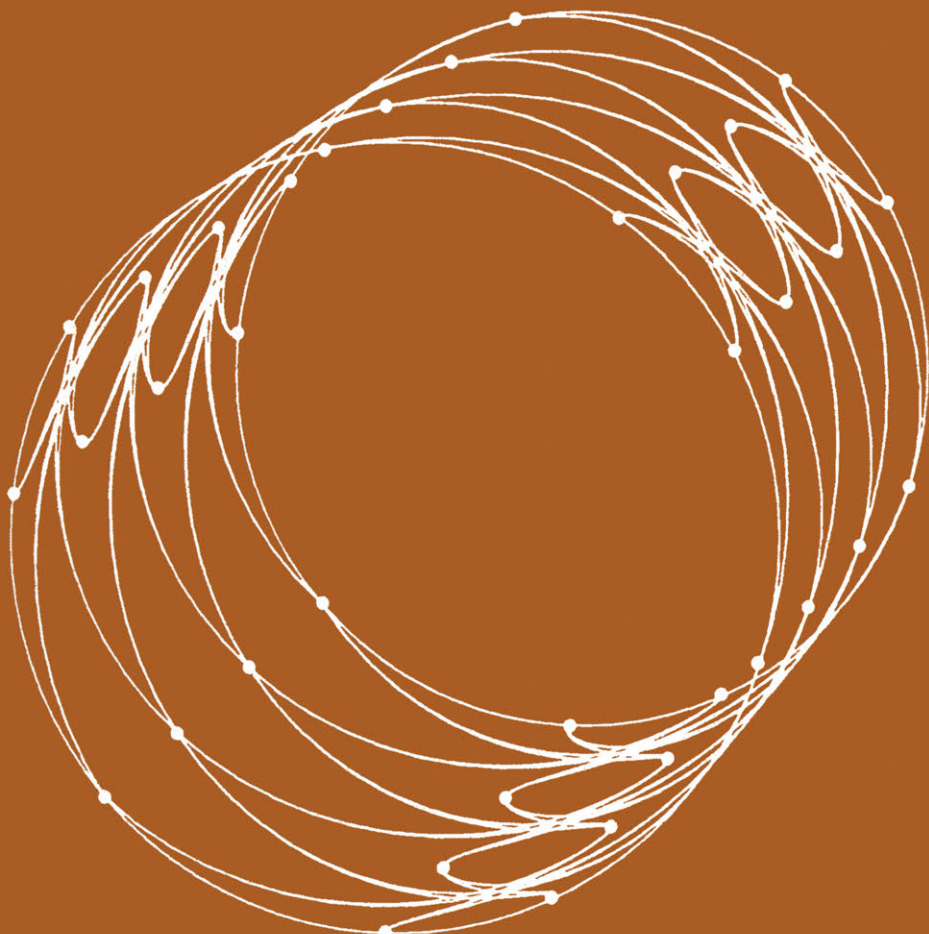


**APPLICATIONS OF COMMUNICATIONS THEORY**

Series Editor: R. W. Lucky



# Digital Phase Modulation

**John B. Anderson, Tor Aulin,  
and Carl-Erik Sundberg**

# **Digital Phase Modulation**

# **Applications of Communications Theory**

**Series Editor: R. W. Lucky, AT & T Bell Laboratories**

---

**COMPUTER NETWORK ARCHITECTURES AND PROTOCOLS**  
Edited by Paul E. Green, Jr.

**DATA TRANSPORTATION AND PROTECTION**  
John E. Hershey and R. K. Rao Yarlagadda

**DEEP SPACE TELECOMMUNICATIONS SYSTEMS ENGINEERING**  
Edited by Joseph H. Yuen

**DIGITAL PHASE MODULATION**  
John B. Anderson, Tor Aulin, and Carl-Erik Sundberg

**ERROR-CORRECTION CODING FOR DIGITAL COMMUNICATIONS**  
George C. Clark, Jr., and J. Bibb Cain

**FIBER OPTICS: Technology and Applications**  
Stewart D. Personick

**FUNDAMENTALS OF DIGITAL SWITCHING**  
Edited by John C. McDonald

**INTRODUCTION TO COMMUNICATION SCIENCE AND SYSTEMS**  
John R. Pierce and Edward C. Posner

**MODELING AND ANALYSIS OF COMPUTER  
COMMUNICATIONS NETWORKS**  
Jeremiah F. Hayes

**MODERN TELECOMMUNICATION**  
E. Bryan Carne

**OPTICAL FIBER TRANSMISSION SYSTEMS**  
Stewart D. Personick

**PRACTICAL COMPUTER DATA COMMUNICATIONS**  
William J. Barksdale

**TELECOMMUNICATIONS SWITCHING**  
J. Gordon Pearce

---

A Continuation Order Plan is available for this series. A continuation order will bring delivery of each new volume immediately upon publication. Volumes are billed only upon actual shipment. For further information please contact the publisher.

# **Digital Phase Modulation**

**John B. Anderson**

Rensselaer Polytechnic Institute  
Troy, New York

**Tor Aulin**

Chalmers University of Technology  
Göteborg, Sweden

**and**

**Carl-Erik Sundberg**

AT & T Bell Laboratories  
Holmdel, New Jersey

**Springer Science+Business Media, LLC**

---

**Library of Congress Cataloging in Publication Data**

**Anderson, John B., 1945-**

Digital phase modulation.

(Applications of communications theory)

Includes bibliographical references and index.

1. Digital modulation. 2. Phase modulation. 3. Modulation theory. I. Aulin, Tor. II.

Sundberg, Carl-Erik. III. Title. IV. Series.

TK5103.7.A53 1986

621.38

86-9430

ISBN 978-1-4899-2033-1

---

10 9 8 7 6 5 4 3 2

ISBN 978-1-4899-2033-1

ISBN 978-1-4899-2031-7 (eBook)

DOI 10.1007/978-1-4899-2031-7

© 1986 Springer Science+Business Media New York

Originally published by Plenum Press, New York in 1986

Softcover reprint of the hardcover 1st edition 1986

All rights reserved

No part of this book may be reproduced, stored in a retrieval system, or transmitted  
in any form or by any means, electronic, mechanical, photocopying, microfilming,  
recording, or otherwise, without written permission from the Publisher

# Preface

The last ten years have seen a great flowering of the theory of digital data modulation. This book is a treatise on digital modulation theory, with an emphasis on these more recent innovations. It has its origins in a collaboration among the authors that began in 1977. At that time it seemed odd to us that the subjects of error-correcting codes and data modulation were so separated; it seemed also that not enough understanding underlay the mostly ad hoc approaches to data transmission. A great many others were intrigued, too, and the result was a large body of new work that makes up most of this book. Now the older disciplines of detection theory and coding theory have been generalized and applied to the point where it is hard to tell where these end and the theories of signal design and modulation begin.

Despite our emphasis on the events of the last ten years, we have included all the traditional topics of digital phase modulation. Signal space concepts are developed, as are simple phase-shift-keyed and pulse-shaped modulations; receiver structures are discussed, from the simple linear receiver to the Viterbi algorithm; the effects of channel filtering and of hardlimiting are described. The volume thus serves well as a pedagogical book for research engineers in industry and second-year graduate students in communications engineering.

The production of a manageable book required that many topics be left out. The major constraint in the book is that it is strictly limited to *phase* modulation. Schemes in which data symbols cause changes in signal amplitude are omitted. Much other exciting new work had to be left out: Channel equalization, new hardware, new error-correcting codes, and multiple-access problems are a few of these subjects. Some readers may seek a more thorough grounding in the mathematical basis of communications theory, since the book assumes a basic knowledge of vector spaces, probability, and random processes. In addition, the rapid treatment of detection theory, information theory, and phase-lock loops may not be enough for some readers.

The book is organized as follows. An introduction expounds the reasons, both technical and commercial, why digital transmission has become so important. Communications theory is the subject of Chapter 2; detection and signal space theory are introduced, along with the error probability and spectrum of a modulation and some simple receivers for it. The older, simpler modulation schemes like phase-shift keying and their real-world behavior provide illustrations of these theories. Chapters 3 and 4 then develop in detail the energy and bandwidth performance of a very general class of modulations called continuous-phase modulations or CPM. Chapter 5 looks at the simultaneous energy and bandwidth performance of these modulations, from the standpoint of both particular schemes and the Shannon theory of modulation. Chapter 6 deals with CPM transmitter structures, while Chapters 7 and 8 discuss more sophisticated receivers than those in Chapter 2. Synchronization and performance with partial phase knowledge form the subject matter of Chapters 9 and 10. Chapter 11 explores the effect of modulations on error-correcting codes. A half-year course in digital modulation could focus on Chapters 1-5 and 7, with other topics chosen to suit the instructor's taste. A shorter, more theoretical course could feature Chapters 2-4.

In writing this book, we have attempted to give some idea of the historical development of the subject, but we have not performed a rigorous literature search and we apologize to the many contributors to the field who have not been referenced by name. We are deeply indebted to our colleagues and co-workers at McMaster University in Canada, the University of Lund and Chalmers Technical University in Sweden, and Rensselaer Polytechnic Institute in the U.S.A., and to our industrial co-workers at INTELSAT, AT & T—Bell Laboratories (U.S.A.), the General Electric (U.S.A.) Corporate Research and Development Center, Codex Corporation (U.S.A.), Ericsson Radio Systems (Sweden), and the European Space Agency. Of this large body of co-workers we must give special mention to Rudi de Buda, Nils Rydbeck, Arne Svensson, and Göran Lindell. It is a special pleasure to acknowledge the typing services of Doris Glöck, Constance Brough, Inga-Britt Holmdahl, Annette Laiacona, and Sandi-jo Rumsey and the patience and guidance of our editor, L. S. Marchand. Certain government agencies were instrumental in the support of the new research in the book; these were the Swedish Board of Technical Development (STU) and the Natural Sciences and Engineering Research Council of Canada.

J. B. Anderson  
*Troy, New York*  
T. Aulin  
*Göteborg, Sweden*  
C.-E. Sundberg  
*Holmdel, New Jersey*

# Contents

<b>Chapter 1. Introduction .....</b>	<b>1</b>
1.1. Why Digital Transmission? .....	1
1.2. Some Basic Digital Channels .....	4
1.3. Some Digital Channel Concepts .....	6
1.4. A Brief History .....	9
1.5. Organization of the Book .....	12
<i>References .....</i>	14
<b>Chapter 2. Signal Analysis and an Overview of Modulation Methods .....</b>	<b>15</b>
2.1. Receiver Principles for Gaussian Noise.....	15
2.1.1. The Maximum Likelihood Receiver .....	15
2.1.2. Probability of Error .....	20
2.2. Phase Modulated Signals .....	22
2.2.1. PSK and FSK .....	23
2.2.2. A Notation for Continuous Phase Modulations .....	25
2.2.3. Euclidean Distance for Phase Modulations .....	26
2.3. Examples of Error Probability Calculations .....	28
2.4. Baseband Receiver and Transmitter Models .....	31
2.5. The Linear Receiver .....	35
2.5.1. Intersymbol Interference and the Receiver Eye .....	36
2.5.2. Channel Filter Effects on MSK and PSK .....	38
2.6. Nyquist-Pulse-Shaped PSK .....	41
2.6.1. Nyquist-Pulse PSK .....	41
2.6.2. Raised Cosine Nyquist Pulses .....	45
2.7. A Summary of Modulation Methods .....	47
2.7.1. Quadrature Modulation Schemes .....	48
2.7.2. CPM Schemes .....	50
<i>References .....</i>	53
<b>Chapter 3. Error Performance .....</b>	<b>55</b>
3.1. System Definition .....	56

<b>3.2. Bounds on the Minimum Euclidean Distance . . . . .</b>	<b>59</b>
3.2.1. Full Response, $H = 1$ . . . . .	60
3.2.2. Partial Response, $H = 1$ . . . . .	71
3.2.3. Full Response, Multi- $h$ . . . . .	79
3.2.4. Partial Response, Multi- $h$ . . . . .	87
3.2.5. Summary . . . . .	90
<b>3.3. The Minimum Euclidean Distance . . . . .</b>	<b>90</b>
3.3.1. Full Response, $H = 1$ . . . . .	92
3.3.2. Partial Response, $H = 1$ . . . . .	96
3.3.3. Full Response, Multi- $h$ . . . . .	105
3.3.4. Partial Response, Multi- $h$ . . . . .	106
3.3.5. Summary . . . . .	109
<b>3.4. Systems with a Trellis Structure . . . . .</b>	<b>111</b>
3.4.1. A State Description for Modulators . . . . .	111
3.4.2. Transfer Function Symbol Error Probability Bounds . . . . .	114
3.4.3. Summary . . . . .	122
<b>3.5. Effects of Filtering and Limiting . . . . .</b>	<b>123</b>
3.5.1. The Euclidean Distance for Mismatched Signal Sets . . . . .	123
3.5.2. Effects of Filtering . . . . .	126
3.5.3. Effects of Filtering and Hard Limitation . . . . .	136
3.5.4. Summary . . . . .	143
<b>3.6. Conclusions . . . . .</b>	<b>144</b>
<b>References . . . . .</b>	<b>144</b>

## **Chapter 4. Spectral Performance . . . . .** 147

<b>4.1. Review of Spectral Calculation Methods . . . . .</b>	<b>147</b>
<b>4.2. A Simple, Fast, and Reliable General Numerical Method . . . . .</b>	<b>149</b>
4.2.1. Derivation of the Method . . . . .	149
4.2.2. Numerical Results . . . . .	154
4.2.3. Generalizations . . . . .	161
4.2.4. Summary of the Autocorrelation Function Method . . . . .	163
<b>4.3. Closed Form Expressions for Some Simple Schemes . . . . .</b>	<b>166</b>
<b>4.4. Asymptotic and Related Behavior of Spectra . . . . .</b>	<b>168</b>
<b>4.5. Effects of Filtering and Amplitude Limitation . . . . .</b>	<b>173</b>
<b>References . . . . .</b>	<b>179</b>

## **Chapter 5. Energy–Bandwidth Comparisons and Shannon Theory for Phase Modulation . . . . .** 181

<b>5.1. Energy and Bandwidth Comparison of Concrete Modulation Systems . . . . .</b>	<b>182</b>
<b>5.2. Basic Ideas of the Shannon Theory . . . . .</b>	<b>186</b>
5.2.1. The Shannon Model of Information Transmission . . . . .	187
5.2.2. Capacity . . . . .	190
5.2.3. Bandwidth and Dimensionality . . . . .	192
<b>5.3. AWGN Channel Capacity and the Phase Modulation Channel . . . . .</b>	<b>194</b>
5.3.1. AWGN Channel Capacity . . . . .	194
5.3.2. A Phase Modulation Channel Model . . . . .	195

Contents	ix
5.4. The Cutoff Rate for Phase Modulation Channels .....	199
5.5. Numerical Results for $R_0$ .....	202
5.6. Energy-Bandwidth Plots Derived from $R_0$ .....	205
<i>References</i> .....	209
 <b>Chapter 6. Transmitters</b> .....	 211
6.1. Read Only Memory Implementations .....	212
6.1.1. ROM Transmitter Theory .....	213
6.1.2. Practical Considerations for ROM Transmitters.....	216
6.2. Phase-Locked Loop Implementations .....	224
6.3. Bandpass Filter and Hard-Limiter Implementation.....	227
6.4. Serial and Parallel MSK Transmitters .....	231
6.5. Conclusions .....	233
<i>References</i> .....	234
 <b>Chapter 7. Receivers</b> .....	 237
7.1. Optimum Coherent and Noncoherent Receivers for CPFSK.....	237
7.1.1. Optimum ML Coherent Receiver for CPFSK .....	238
7.1.2. Optimal ML Noncoherent Receiver for CPFSK.....	242
7.2. Optimum Viterbi Receivers .....	246
7.3. Implementation of the Viterbi Algorithm for CPM .....	252
7.4. Performance Simulation .....	255
7.4.1. Simulating Channel Noise .....	257
7.4.2. Realization of the Viterbi Algorithm and Numerical Results .....	259
7.5. Analysis of Simple Noncoherent Receivers.....	262
7.5.1. Differential Detection .....	263
7.5.2. Discriminator Detection .....	269
7.5.3. Numerical Results .....	271
7.5.4. Application of Sequence Detection .....	275
<i>References</i> .....	276
 <b>Chapter 8. Simplified Receivers</b> .....	 279
8.1. Reduced Complexity Viterbi Detectors .....	279
8.1.1. The Complexity Reduction Concept .....	280
8.1.2. The Performance Measure .....	282
8.1.3. Properties of the Minimum Euclidean Distance for Mismatched Signal Sets .....	285
8.1.4. Optimizing the Reduced-Complexity Receiver .....	287
8.1.5. Numerical Results .....	289
8.1.6. Summary and Tradeoff between Complexity Reduction and Performance	294
8.2. MSK-Type Receivers .....	295
8.2.1. Receiver Principle and Performance .....	296
8.2.2. The Optimum Receiver Filter .....	300
8.2.3. Numerical Results .....	305
8.2.4. Discussion and Comparisons .....	309

<b>8.3. Serial MSK-Type Receivers . . . . .</b>	315
8.3.1. The Concept of Serial Detection . . . . .	315
8.3.2. Error Probability Analysis . . . . .	317
8.3.3. Sensitivity to Phase Errors . . . . .	320
8.3.4. Sensitivity to Timing Errors . . . . .	325
8.3.5. Summary . . . . .	328
<b>8.4. Average Matched Filter Receivers . . . . .</b>	329
8.4.1. AMF Receiver Principles and Structure . . . . .	330
8.4.2. Error Performance of AMF Receivers . . . . .	333
8.4.3. Properties of the Distance and the Uniformly Weighted AMF . . . . .	341
8.4.4. Numerical Results . . . . .	346
8.4.5. Summary . . . . .	349
<b>8.5. Limited Trellis Search Receivers . . . . .</b>	352
<b>References . . . . .</b>	353
<b>Chapter 9. Synchronization . . . . .</b>	357
<b>9.1. Synchronization with a Specified Structure . . . . .</b>	357
9.1.1. Spectral Considerations . . . . .	358
9.1.2. The Synchronizer Structure . . . . .	363
9.1.3. Discrete Component CNRs . . . . .	364
9.1.4. Error Performance . . . . .	367
9.1.5. Multi- $h$ Full Response Synchronization . . . . .	374
<b>9.2. ML Estimation of Data, Phase, and Timing . . . . .</b>	379
<b>9.3. Other Approaches . . . . .</b>	381
<b>References . . . . .</b>	384
<b>Chapter 10. Partially Coherent Receivers . . . . .</b>	387
<b>10.1. Notions of Phase Coherence . . . . .</b>	387
<b>10.2. Partially Coherent Detection; Equivalent Distance . . . . .</b>	388
10.2.1. Derivation of $d_e^2$ . . . . .	390
10.2.2. Some Properties of $d_e^2$ . . . . .	393
<b>10.3. Minimum Equivalent Distance Results . . . . .</b>	397
<b>10.4. Discussion . . . . .</b>	406
<b>References . . . . .</b>	411
<b>Chapter 11. Phase Modulation and Convolutional Codes . . . . .</b>	413
<b>11.1. PSK Set Partition Codes . . . . .</b>	413
<b>11.2. Coded Binary and Quaternary CPFSK . . . . .</b>	417
11.2.1. System Description . . . . .	417
11.2.2. Error Probability and Minimum Euclidean Distance . . . . .	419
11.2.3. Minimum Euclidean Distance: Properties and Calculation . . . . .	420
11.2.4. Symmetries for the Combination of Convolutional Encoder and Mapping Rule . . . . .	423
11.2.5. Numerical Results . . . . .	426
11.2.6. Energy-Bandwidth Tradeoff . . . . .	437

<b>Contents</b>	<b>xi</b>
11.3. Coded Multilevel CPM .....	439
11.3.1. System Description .....	439
11.3.2. Bounds on the Free Euclidean Distance .....	440
11.3.3. Code Search and Tables of Good Codes .....	443
11.3.4. Energy and Bandwidth Efficiency of Coded CPM .....	446
11.3.5. Conclusions .....	450
11.4. Simulations of Coded CPFSK Schemes .....	454
References .....	457
<b>Appendix A. Minimum Distance Calculation Algorithms .....</b>	<b>461</b>
A.1. Limited Sequential Tree Search .....	462
A.2. The Viterbi Algorithm in a Superstate Trellis .....	465
<b>Appendix B. Specification of the Markov Distance Chain and Calculation of <math>R_0</math> .....</b>	<b>469</b>
B.1. A Markov Distance Chain .....	469
B.2. Calculation of $R_0$ .....	471
B.3. Evaluation of $\mathcal{E}[e^{-YE/4N_0}]$ .....	473
<b>Appendix C. Simulation Techniques .....</b>	<b>475</b>
C.1. Statistical Analysis of Error Events .....	475
C.2. The Signal Space Method of Simulation .....	480
<b>Appendix D. Tables of Optimum Codes .....</b>	<b>483</b>
D.1. Optimal Codes for Binary and Quaternary CPFSK .....	483
D.2. Optimal Codes for 8-, 16- and 32-Level CPFSK .....	487
<b>Index .....</b>	<b>493</b>

# Introduction

Communication is the transmission of information to a remote place or a remote time. Digital communication transmits information in discrete quanta. The increasingly complex activities of mankind have forced an exponential growth in communication to sustain them, and revolutions in hardware and in our understanding of electrical communication have decimated the cost of communication and completely changed how it occurs. The foremost innovation in communication has been the advent of digital transmission and the understanding of its importance. This book is about an important method of digital transmission, phase changes in sinusoidal signals.

First it is necessary to set out the causes of the digital communication age, outline the basic scientific issues, and trace some recent history of its technology. Certain themes emerge. Why does the public want to communicate in a digital manner? When is digital transmission a technical necessity? What major engineering quantities must one consider in a system design?

## 1.1. Why Digital Transmission?

All about us we see a revolution in which the older methods of analog transmission are being replaced by digital transmission. Obvious reasons for this include the advent of new, incredibly cheap hardware and of customers with nonanalog data to transmit. A more subtle factor is the nature of communication theory, which may require a digital format in the transmissions systems that we find convenient to use. We will first explore some of these factors.

*New Hardware.* Rapidly advancing electronic technology has caused a revolution in the hardware used in digital communication. Digital circuits

have been reduced to microscopic size, weight, power consumption, and cost. In addition, huge numbers of active devices can be combined into a single integrated circuit. Other types of circuits not based on logic gates have also appeared with all the above advantages, including charge-coupled devices, switched capacitor filters, and various analog integrated circuits. While the hardware revolution is common knowledge, the true depth of it is often unappreciated. The cost of an active device, for instance, has dropped at least a millionfold in a space of 25 years. A change of this magnitude must profoundly affect the design of communications equipment.

Several future generations of integrated circuit technology beyond those now in commercial use exist at this writing in the development stage. These generations relate to the use of submicron structures, new semiconductor materials, fault-tolerant or self-repairing architectures, and computer-aided design aids. It is a fact, however, that knowledge of how to apply these circuits, as opposed to how to construct them, lags behind appearance of the circuits. Much work needs to be done on signal processing hardware and software architectures, and this work will be more expensive than the device development itself.

Microwave hardware has undergone a less publicized but equally exciting development. New solid-state hardware has appeared, such as the Gunn device and field-effect microwave power devices. Stripline and microstrip circuits have appeared, along with new methods for phase shifting and switching microwave energy. Surface acoustic wave devices have undergone a rapid development. These are thin film planar devices that operate over the uhf range by means of elastic waves propagating through a piezoelectric substrate. Since these waves are on the surface, they can be easily tapped, guided, and modified; as a consequence, complex signal filtering can be realized cheaply, at great speed, and in a small space. Other propagating wave devices, such as magnetostatic devices, are on the horizon.

*New Service Demands.* A source of information that is digital in its nature obviously requires digital transmission. Many new sources of this type have appeared. Telex and facsimile transmissions are cheaper than voice or image transmission; electronic data transfer is essential to the operation of widely distributed enterprises like branch banking systems and airlines. A second type of new service demand occurs when those with analog information to transmit discover that digital transmission offers a cost advantage. Voice digitization methods now in use or contemplated require anywhere from 4.8 to 64 kbit/s, depending on quality and terminal complexity, and television transmission consumes from 1 to 40 Mbit/s. The latter figures in both cases represent present commercial standard rates.

*Compatibility and Flexibility.* A complex and costly transmission system is far more useful if it can sustain a variety of information types and patterns of usage. Conversion of all data sources to a common format, bits, means

that all can be handled by the same equipment. Bits can be formed into words or packets at will and different kinds of information can be combined for efficiency. Multiplexing and switching are made easier; new methods of multiple access, such as time division multiple access, become economical.

Some services have special needs that are easier to satisfy with digital transmission. Privacy has become increasingly difficult to guarantee, so that many users demand encryption of their data, a much easier process with a digital signal. Mobile communication favors digital signaling because of privacy and the need to suppress interference. In the rapidly growing cellular mobile service, digital transmission with error control coding leads to increased spectrum economy.

*Fidelity of Reproduction and Error Control.* Digital transmission may be favored by the nature of the channel. Long distance channels are for the most part of two types, terrestrial channels consisting of long chains of repeaters or of other tandem processors such as switches, and satellite transponders. In either case aspects of the channel favor digital signaling. As an example of a channel with many repeaters, consider the microwave radio channel. Microwaves propagate in a line-of-sight fashion so that individual links are limited to about 50 km. If 100 such links are chained to form a 5000-km channel, communications theory shows how much the signal-to-noise ratio (SNR) must be improved in each link so that the total performance is that of an original single link. For an analog system the link SNR must be improved by 20 dB while for a digital system operating at an error rate of  $10^{-5}$  only 2 dB is required.

Satellite channels, on the other hand, are marked by lower power and wide bandwidth. These qualities predispose the channel to digital transmission in another way, as we shall develop.

These channels have a special character that tends to favor digital transmission, but a digital format in any communications network makes it easier to guarantee a given data error rate or fidelity of reproduction. For analog signals that have been digitized, the fidelity of reproduction is set almost entirely by the fineness of the digitizing, and it is easily controlled throughout the system. The error rate in a digital channel generally obeys a threshold rule: Beyond a certain signal power, the receiver error rate falls very rapidly so that as long as signal power exceeds this threshold, a performance level can be virtually guaranteed throughout a system, even if many links and processors are chained. If error performance is not sufficient in one link, digital error correction methods can be used to improve it; in addition, performance of this coding will improve rapidly as a threshold signal power is exceeded.

*Cost.* In cases where one can choose between digital or analog means to transmit information, digital transmission may be cheaper. This may be

true because of the availability of wide bandwidth, the low cost of manufacturing digital equipment, difficulties with error control, or customer factors, like compatibility, flexibility, or need for security.

Disadvantages of digital transmission exist. Some are notorious to the communications engineer; an example is the tendency of digital formats to consume unreasonably wide signal bandwidths. Some more subtle shortcomings exist, however. Digital equipment contains complex and recent technology known only to a few and very expensive to design. To tap the advantages of digital transmission requires the organization of large research efforts.

## 1.2. Some Basic Digital Channels

Communications channels may be divided into those that are forced to be digital because the transmitted information is digital and those that may be either analog or digital because the information is analog. The greatest force for growth in digital communication has come from the second type because analog information sources predominate. Here digital and analog transmission methods compete directly. As far as simple efficiency of transmission is concerned, which approach is superior depends in a complicated way on the available power and bandwidth, the degree to which phase and amplitude relationships are maintained, and the presence of repeater chains. As mentioned before, long repeater chains are a factor favoring digital transmission. A highly nonlinear channel that destroys amplitude relationships also favors digital phase modulation. On the other hand, a channel in which phase relationships are hard to maintain might better employ analog transmission. Power and bandwidth have a strong bearing on the analog-digital choice. Theory shows that if little power is available, signaling must be digital; narrow bandwidth in a channel with reasonably large power demands analog signaling.

To explore further this very complex question of digital vs. analog transmission, we discuss some commonly occurring channels. We concentrate on engineering realities in the channel itself, although economic and networking aspects are equally important to the final system design.

*The Satellite Channel.* No event has more strongly motivated digital transmission research than the communications satellite. This channel consists of a relatively linear high-power amplifier on the ground that feeds an "uplink" and a highly nonlinear low-power amplifier in the satellite that feeds a "downlink" to the ground. Microwave carrier frequencies are normal. The satellite offers an attractive star network topology; it allows communication over long distances at wide bandwidths at relatively low cost.

It appears that digital modulation will eventually predominate in this channel. Compared to other channels, the satellite transmission path is characterized by wide bandwidth, a nonlinear amplitude response, and low power, that is, by very long distances. These factors all point to digital transmission, but the most telling constraint is the low-power one.

As transmitter power drops it becomes increasingly necessary to resort to bandwidth-spreading modulations, including digital ones. Simple analog modulation has at best the same SNR as the radiofrequency channel; and for single sideband modulation, it has the same bandwidth as the information source. Once the SNR drops below 30 dB or so, transmission of telephone-quality voice, for instance, becomes impossible without a bandwidth-spreading modulation like FM. As the SNR drops into the 10-20-dB range encountered in satellite channels, the degree of bandwidth expansion must increase, and the analog transmitter and receiver components must be increasingly wideband. Eventually it becomes more efficient to convert analog signals to digital form and make use of a digital modulation method. New modulation methods will soon become available which, when combined with an efficient analog-to-digital conversion method like adaptive differential PCM, should be more efficient than analog FM over present-day commercial satellites.

Another hallmark of the satellite channel is its nonlinearity. All rf power amplifiers must operate nonlinearly in order to be highly efficient. At the same time, dc power generation on board a satellite is a heavy contributor to launch weight. Satellites are thus compelled to operate as nonlinear amplifiers. The modulations that fare best under these conditions are constant-amplitude modulations, those that have little or no envelope variation; and this narrows the choice to either analog FM or digital phase modulation. A second factor that promotes the use of constant-amplitude modulations is their apparent ability to suppress interference. Interference arises naturally in a satellite link from closely spaced adjacent channels, from the multiple carriers that appear in a multiple-access system, or from spurious carriers that sweep the satellite.

The low power and nonlinearity of the satellite channel require precisely what the channel has in abundance, bandwidth. Bandwidth reduction remains a worthwhile goal, however, since a reduction in signaling bandwidth per data symbol in any channel leads to a correspondingly higher rate of information transfer.

*Terrestrial Microwave Radio Channels.* Except for local service, terrestrial radio networks must use repeaters, a fact that favors digital modulation. But unlike the satellite channel, the SNR in these channels is high and linear operation is available. It is safe to say that analog FM is more efficient here than phase modulation because of its lower bandwidth consumption. New narrow band digital schemes are under development that use both

phase and amplitude modulation, and these may provide stronger competition.

*Coaxial Cables.* These channels are marked by high reliability and freedom from interference, but their electrical nature is such that they require closely spaced repeaters if their operational bandwidth is to be competitive. Thus, digital modulation is strongly preferred. Efficient digital coaxial cable systems have been built having repeaters at 1 km intervals and a data rate of 274 Mbit/s per cable.

*Optical Fibers.* Being guided-wave channels, fibers have the same nature as coaxial cables; but since the carrier is at optical frequencies, their bandwidth is higher and the fiber can be much smaller. The newer optical fibers offer longer repeater intervals than coaxial cables.

*Telephone Line Channels.* A “telephone line” by definition has a certain SNR (about 30 dB) and a certain bandpass (about 300–3300 Hz) and is roughly linear. It need not be a twisted pair of wires. Digital modulation methods used in such channels employ both amplitude and phase modulation because of the linearity and the good SNR. Rates of up to 14.4 kbit/s are carried across any distance over which the defining channel characteristics can be maintained. New methods of phase and amplitude coding are being developed for telephone channels.

*Mobile Channels.* Mobile radio systems operate in the vhf and uhf. They are impaired by fading and phase changes that stem from the rapidly changing signal path and from obstructions and reflections. Consequently, a transmission method is needed that ignores amplitude variations and tends to suppress weaker interfering signals. Analog FM has served well here for a number of years, but much present effort is being devoted to replacing it with a digital modulation. Motivations for this are to better reject interference, to improve message security, and to reduce the use of radio spectrum.

### 1.3. Some Digital Channel Concepts

Our discussion of these channel examples has shown how the nature of the channel directs the choice of modulation. Channels with low power, wide bandwidth, nonlinearity or interference, or a strong combination of these are likely candidates for phase modulation. In perfecting this or any other modulation, certain ideas recur.

*Coding vs. Modulation.* Much of the modulation research of recent times could be described as an integration of error correction coding and modulation into one transmitting system. Here lies the key to more efficient methods and, also, unfortunately, the root of much confusion. Here are

some *traditional* definitions for coding and modulation:

- Encoding: The introduction of redundant symbols to correct errors.
- Modulation: The conversion of symbols to a carrier waveform, usually a sinusoidal function of time.
- Demodulation: The conversion of the carrier waveform back into data, usually symbol by symbol.
- Decoding: The use of redundant symbols to correct data errors.

This definition of encoding seems to imply that coding increases transmission bandwidth through the introduction of extra symbols. Modern coding methods need not do this. As well, it is increasingly common for modulators and demodulators to deal with several signaling intervals at a time in connection with one data symbol because of memory introduced in the modulating operation.

A more modern definition of coding which we shall use is *the imposition of certain patterns onto the transmitted signal*. The decoder knows the set of patterns that are possible, and it chooses one close to the noisy received signal. This definition in effect combines the encoder and modulator into one function, as it does also the demodulator and decoder. The definition includes the idea of parity check coding.

*Bandwidth Compaction.* Before discussing the methods to do this, it is worth recalling that a narrow-spectrum event must be one that lasts a long time. As a modulated signal becomes more band limited, behavior in one signal interval comes to depend on behavior in neighboring ones. This dependence is unavoidable if a transmission method is to be both power and bandwidth efficient at the same time.

A receiver that makes an estimate of the signal under these conditions is called a *sequence estimator*, after the fact that the transmitted symbols are not viewed alone but as a whole sequence. Such receivers are a critical issue in modern research. Correlation among intervals can be effected by bandpass filtering or by introducing intentional correlation into the signal before transmission; modulations of the last type are called *partial response* modulations since the response to a data symbol is spread at the outset over several signaling intervals. Sequence estimation receivers for either case are an important research topic.

A separate approach to bandwidth compaction is source coding, the reduction of the data source, whether analog or digital, into fewer bits per second of digital data. Run-length coding of facsimile and low-rate coding of voice or images are two common source coding measures. We shall not explore this type of approach in this book.

*Channel Filtering.* As already mentioned, one can force band limitation by filtering the transmitted signal. In practice, channel filters are a necessity

because all modulations have an infinitely wide spectrum. Even though the spectrum may decay rapidly, filtering is still necessary to prevent interference to a nearby receiver operating in an adjacent channel. Beyond this, it is common practice to severely filter signals in order to produce a spectrally efficient modulation. Although the result is still called by the name of the original modulation (for instance, “filtered binary phase shift keying”), the output is really a new signaling method with quite different properties. Power efficiency, for instance, falls significantly, and the complexity of an optimal receiver greatly increases.

To the transmission engineer, channel filtering has two primary effects. First, signaling during one interval is spread into others, as mentioned before; when caused by channel filtering, this is called *intersymbol interference*. The use of sequence estimation to reduce this interference is called *equalization*, and several types of equalizers with varying effectiveness have appeared in recent years. The second effect of filtering is the introduction of envelope variations to a signal that might, for instance, have previously had a constant envelope. If the remainder of the channel is nonlinear, these variations are modified yet again in a manner that is hard to predict and compensate. The satellite channel with its uplink and downlink presents a mingling of filtering, noise at various points, and amplitude limiting that is difficult to analyze.

*Bandwidth vs. Power vs. Complexity.* The designer of a digital transmission system finds himself in a morass of conflicting requirements and subtle trade-offs. If one leaves aside networking requirements, political considerations, and the quirks of customers, there remains a question of engineering science: What are the communications engineering trade-offs that occur in a single transmission link? We can define three major engineering commodities that must be “purchased” to achieve a given grade and size of service: Transmission bandwidth, transmission power, and the cost and complexity of the signal processing that is required to achieve the performance specification at the given power and bandwidth. One pays for the consumption of each of these in various ways, including parts cost, dc power generation, regulatory approvals for wider bandwidths, foregone message capacity, engineering design costs, satellite launch weight, and size of antennas.

Each of the three major factors has a cost per unit consumed, and the design of an optimal-cost system depends on these unit costs. In the present age, the complexity/parts cost factor has dropped precipitously so that total cost is likely optimized by a different combination of the three commodities than it was a few years ago. It seems clear that cost-effective future systems will have reduced power and bandwidth and greatly augmented signal processing.

## 1.4. A Brief History

In this section we summarize developments in digital transmission over the last 20 years. The trends exposed here form the basis of the chapters to follow and predict future directions. The references given here form a background reading list for the book.

### *Maturation of Detection Theory (1960–1975)*

The 1960s saw the growth and maturation of detection and estimation theory as they apply to digital communication. Analyses were given for detection of either symbols or waveforms in white or colored Gaussian noise. The theory of signal space analysis, developed earlier by Kotelnikov,<sup>(1)</sup> was popularized in the landmark 1965 text by Wozencraft and Jacobs.<sup>(2)</sup> Optimal detection of a waveform in white Gaussian noise turned out to require a time-invariant linear filter; but detection in colored noise requires a time-varying filter and other unpleasant complications, and design of a simplified, near-optimal receiver for the colored case remains an open question.

In estimation theory, the 1960s saw development of both recursive and block least-squares procedures that could be used in communications to estimate the nature of an unknown channel. As applied to receivers, these methods generally modeled the channel as a time-discrete all-pole filter. We do not emphasize the adaptive receiver in this book; the interested reader is referred to Proakis<sup>(8)</sup> or the early text by Lucky, Salz, and Weldon.<sup>(9)</sup>

The state of detection and estimation theory at the end of the 1960s is summarized in the three-volume treatise by Van Trees.<sup>(13)</sup> Later research in estimation theory has emphasized new estimation and tracking algorithms, notably gradient-following algorithms, some new recursive algorithms, and a new type of channel or system model called the lattice structure. Research continued on the intriguing properties of these lattice filters, the most important of which is a type of orthogonality in the contribution of the sections of the lattice to the total system response.

### *Phase Shift Keying and Binary Coding (1955–1970)*

In the 1960s the basic circuits needed for binary and quaternary phase shift keying (PSK) were worked out, including the modulator and demodulator and useful related circuits like the phase-lock loop. At the same time simple methods of intersymbol interference removal were developed, centering on the zero-forcing (i.e., no feedback of data decisions) equalizer of Lucky.<sup>(3)</sup>

In another stream, binary error correcting codes proposed in the 1950s developed and found implementation; this work is summarized in Clark and Cain,<sup>(4)</sup> Lin and Costello,<sup>(5)</sup> or Blahut.<sup>(6)</sup> These codes generally worked with binary symbols, adding parity check bits to accomplish error correction. They included block codes like BCH and Reed-Solomon codes, for which special decoding algorithms were invented, and convolutional codes, whose tree structure allowed sequential decoding procedures. The latter were based on a method in statistics developed by Wald called sequential analysis, and the best known early procedure was the Fano algorithm. Sequential decoders accept demodulator outputs in short segments until a measure of likelihood indicates that an earlier segment is reliably known; this segment is then released as decoded output and more segments are viewed until the next early segment is felt to be known, and so on until the transmission is decoded. All sequential decoders in this period suffered from occasional erasures, during which the decoding would collapse with no possibility of recovery except through reframing. Sequential decoding, as well as information theory in general, are discussed in the texts by Gallager,<sup>(7)</sup> Viterbi and Omura,<sup>(19)</sup> and Lin and Costello.<sup>(5)</sup>

Early decoders viewed demodulator outputs as symbols and ignored the physical signals and channels that carried the symbols. A partial exception to this was an approach called soft decision decoding that accepted also from the demodulator a measure of the likelihood that its output was correct.

Application of these early PSK systems was limited to low-power, wide-band channels, like the deep space channel. Communications satellites and terrestrial links relied primarily on analog FM.

### *Pulse-Shaped PSK (1965–1980)*

In the 1960s the theory of pulse-amplitude modulation was devised to specify among other things how the shape of a transmitted pulse was related to the signal bandwidth. In the 1970s many methods were proposed to shape the response of the PSK phase to a data symbol in the interest of reducing bandwidth. Rather than a step change of phase from data pulse to data pulse, phase was made to change in a variety of continuous fashions or in an overlapping fashion. Examples include the minimum-shift keying scheme, in which phase changes linearly; sinusoidal frequency shift keying, in which the changes were pieces of sinusoids; and offset-quadrature PSK, where part of the activity in the quadrature modulator was delayed half a symbol interval.

These strategems did succeed in reducing energy at frequencies well removed from the center and, thus, gave signals with less adjacent channel

interference; but they did not much narrow the main part of the spectrum. Details and references for these modulations are given in Chapter 2, and they provide a benchmark against which to measure the power and bandwidth of more efficient modulations in Chapters 3 and 4.

In research parallel to this, the effects of band and amplitude limitation on PSK were studied. In part these effects can be viewed as another kind of pulse shaping, but now intersymbol interference appears. New analytical methods, such as the method of moments, were devised to deal with nonlinear channels. Compensator circuits and channel equalizers were devised, and sequence estimation grew in importance.

### *The Viterbi Algorithm and Sequence Detection (1967- )*

Papers by Viterbi and Forney that appeared in 1967 and 1972 changed the way that researchers viewed the decoding of convolutional codes and the removal of intersymbol interference.

Viterbi<sup>(10)</sup> showed that a convolutional code could be viewed as a structure generated by a finite state machine and could be decoded by an efficient procedure based on keeping track of paths into and out of the machine state. Omura pointed out soon after that the procedure amounted to a dynamic program; Forney showed that the progression of states vs. time could be drawn to good effect on a "trellis" diagram and that the dynamic program solved a shortest route problem on this trellis.

This procedure, which became known as the Viterbi algorithm, caused a revolutionary change in the use of error-correcting codes because it could sequentially decode convolutional codes without erasure. Although the algorithm is really an exhaustive search among all possible decodings, it is the most efficient one possible, and for short, simple codes, it proved to be cost effective. It was amenable to soft decisions, and it could be constructed from an array of parallel processors. Combined with convolutional codes, it gave power gains of 1.5-5 dB with bandwidth expansions in the range 20%-100%, compared to uncoded modulation.

Somewhat after these coding advances, Forney<sup>(11)</sup> showed that ISI could be modeled as a process driven by a finite state machine and that its effects could be optimally removed by the same Viterbi algorithm. This became known as maximum likelihood sequence estimation (MLSE) because it viewed an entire sequence of channel signals and made a maximum likelihood estimate of the uncorrupted signal. Later, Ungerboeck<sup>(12)</sup> extended the generality of the method.

The decision-feedback equalizer appeared during this time and found application. In this equalizer, the algorithm uses already-decided data symbols. Studies in the 1970s detailed what kind of SNR gain could be

obtained from the feedback equalizer and from MLSE. It was shown that for some simple channels MLSE could remove the entire effect of the intersymbol interference, and for others it could not; but it was far superior to the decision-feedback or zero-forcing equalizer. In other channels all three approaches seemed close in performance.

Sequence estimation is a critical issue in the detection of an efficient modulation because a narrow spectrum and, to some degree, power efficiency depend on correlations among signal intervals. Optimal sequence estimation procedures are too complex when applied to signals with real-life filtering, and simplified procedures fall too far short of optimal performance. We discuss sequence receivers in Chapter 7 and simplifications in Chapter 8.

### *Coded Phase and Amplitude Patterns (1975- )*

We have earlier defined coding to be the imposition of a certain set of patterns onto the transmitted signal. By the mid-1970s several implicit schemes of patterning a signal had appeared beyond the parity-check methods of binary symbol coding. Early work by Lender<sup>(14)</sup> showed that partial response that was intentionally inserted could improve the spectral efficiency of an AM format without lowering the energy efficiency. We have mentioned before that a given channel filter produces recognizable signal patterns. As well, a constraint of phase continuity imposes a loose pattern of its own.

These facts inspired a systematic exploration of the ways that patterning of a signal can reduce its consumption of power and bandwidth. Miyakawa, Harashima, and Tanaka<sup>(15)</sup> in 1975 and Anderson and Taylor<sup>(16)</sup> in 1978 explored the idea of varying the modulation index in a cyclic pattern and found that this strategy could simultaneously reduce both signal energy and bandwidth. Aulin, Rydbeck, and Sundberg<sup>(17)</sup> published a thorough investigation of the effects on phase modulation of partial response to a symbol and of smoothing of this response with the same conclusion. Ungerboeck<sup>(18)</sup> devised a type of "set partition" codes that combined convolutional coding with phase and amplitude coding. Taken together, these works create a unified view of modulation and coding and make relatively clear the sources of energy and bandwidth efficiency. They are the precursor of this book.

## **1.5. Organization of the Book**

In Chapter 2 we introduce a framework to describe the existing types of digital modulation, concentrating on phase modulation methods. To

establish a basis for later chapters, some review will be given of detection theory and stochastic processes. Methods to assess the twin measures of a modulation, its energy and bandwidth consumption, are given in Chapters 3 and 4. These ideas are a complex subject that has been the object of much research in the last ten years. The aim is to find the effect on energy and bandwidth of basic modulation characteristics, such as the data symbol alphabet size, the rate of change and smoothness of the phase response, and the length of memory in the modulation.

Chapter 5 evaluates the simultaneous energy and bandwidth consumption of modulations by plotting these quantities in a plane. The chapter then digresses to a theoretical topic, the ultimate performance limits to digital transmission. Techniques devised by Shannon give the ability of a given bandwidth and power to carry information through a Gaussian-noise channel. Other techniques show the ability of constant-envelope phase modulated signals or of parity-check encoders combined with simple modulators. These theoretical upper limits provide an interesting comparison to known, practical schemes, and they suggest how much improvement in power or bandwidth can be hoped for in future research.

Chapters 6–8 address the third major engineering commodity that we have mentioned, processing complexity. Transmitter designs appear in Chapter 6 and receiver designs in Chapters 7 and 8. Optimal receiver designs vary with SNR, and their method of realization depends on the rate at which they must operate. It is important to find simplifications, especially if these lead only to a small performance loss. Many interesting approaches exist, and these are the subject of Chapter 8. However cheap processing may become, it is still important to reduce its cost.

Chapters 9 and 10 discuss the extraction of a phase reference and assess the effect on detection when only partial knowledge of the reference is available. Phase synchronization, often underrated by those new to communications engineering, becomes even more difficult when complexities aimed at reducing energy or bandwidth are imposed on a signal. In some receivers synchronization is obtained only to within a constant, unknown offset, while in others a phase reference is completely unknown; in both cases a reduction occurs in energy efficiency.

Chapter 11 discusses the effect of ordinary parity check coding on a modulation and vice versa. Error correcting codes do provide a way to impose patterns of phase and amplitude on the ultimate sinusoidal carrier; but the receiver cannot be the usual demodulator feeding a binary decoder unless the modulation is very simple, and Hamming distance, which measures the separation between two binary sequences, is rarely useful. In the end, parity check coding must be compared with other techniques that impose signal patterns, such as filtering or direct coding of the signal phase and amplitude.

## References

1. V. A. Kotelnikov, *The Theory of Optimum Noise Immunity*, McGraw-Hill, New York (1959).
2. J. M. Wozencraft and I. M. Jacobs, *Principles of Communications Engineering*, Wiley, New York (1965).
3. R. W. Lucky, A survey of communications theory literature: 1968–1973, *IEEE Trans. Inf. Theory* **IT-19**, 725–739 (1973) (see historical development and reference list).
4. G. S. Clark and J. B. Cain, *Error Correction Coding for Digital Communications*, Plenum, New York (1981).
5. S. Lin and D. J. Costello, Jr., *Error Control Coding: Fundamentals and Applications*, Prentice-Hall, Englewood Cliffs, New Jersey (1983).
6. R. E. Blahut, *Error Control Coding*, Addison-Wesley, Reading, Massachusetts (1983).
7. R. G. Gallager, *Information Theory and Reliable Communication*, Wiley, New York (1968).
8. J. G. Proakis, *Digital Communications*, McGraw-Hill, New York (1983).
9. R. W. Lucky, J. Salz, and E. J. Weldon, *Principles of Data Communication*, McGraw-Hill, New York (1968).
10. A. J. Viterbi, Error bounds for convolutional codes and an asymptotically optimum decoding algorithm, *IEEE Trans. Inf. Theory* **IT-12**, 260–269 (1967).
11. G. D. Forney, Jr., Maximum likelihood sequence estimation of digital sequences in the presence of intersymbol interference, *IEEE Trans. Inf. Theory* **IT-18**, 363–378 (1972).
12. G. Ungerboeck, Adaptive maximum-likelihood receiver for carrier-modulated data-transmission systems, *IEEE Trans. Commun.* **COM-23**, 624–636 (1974).
13. H. L. Van Trees, *Detection, Estimation, and Modulation Theory*, Vol. I, Wiley, New York (1968).
14. A. Lender, The duobinary techniques for high speed data transmission, *IEEE Trans. Commun. Electron.* **82**, 214–218 (1963); see also A. Lender, Correlative digital communication techniques, *IEEE Trans. Commun. Technol.*, 128–135 (1964).
15. H. Miyakawa, H. Harashima, and Y. Tanaka, A new digital modulation scheme, multi-mode binary CPFSK, Proceedings, Third Intern. Conf. Digital Satellite Commun., pp. 105–112, Kyoto, Japan, November (1975).
16. J. B. Anderson and D. P. Taylor, A bandwidth-efficient class of signal space codes, *IEEE Trans. Inf. Theory* **IT-24**, 703–712 (1978).
17. T. Aulin, C.-E. Sundberg, and N. Rydbeck, Continuous phase modulation—Parts I and II, *IEEE Trans. Commun.* **COM-29**, 196–225 (1981).
18. G. Ungerboeck, Channel coding with multilevel/phase signals, *IEEE Trans. Inf. Theory* **IT-28**, 55–67 (1982).
19. A. J. Viterbi and J. K. Omura, *Principles of Digital Communications and Coding*, McGraw-Hill, New York (1979).

# Signal Analysis and an Overview of Modulation Methods

We begin this chapter by setting up ways of handling the signals that appear in a phase modulation system. The concept of signal space is introduced. The simplest phase modulations are then discussed as examples of signal analysis and as introduction to the more general methods that follow in later chapters. Some basic signal processing operations that occur in communications links are introduced, such as baseband conversion, channel filtering, and hard limiting. The chapter requires understanding of the basic ideas of vector spaces and stochastic processes. An excellent treatment of the former from a communications theory point of view appears in Ziemer and Tranter<sup>(1)</sup> and in many other communications theory texts. References for stochastic processes are Papoulis<sup>(2)</sup> or Helstrom.<sup>(3)</sup>

## 2.1. Receiver Principles for Gaussian Noise

We begin by discussing a receiver that makes a maximum likelihood decision about a signaling waveform sent through additive white Gaussian noise, the AWGN channel. In addition to being the most important case of receiver and channel, this case also has a simple analysis in terms of ordinary geometric concepts. Signals and noise are expressed as components over a vector space and error performance depends on Euclidean distances in this space. This analytical scheme will be the method of error analysis for the rest of the book.

### 2.1.1. The Maximum Likelihood Receiver

The maximum likelihood receiver is that receiver that selects the most likely signal sent, given a waveform  $r(t)$  that it has observed. Roughly

speaking, the receiver tries to find the transmitted signal  $s_i(t)$  that maximizes the conditional probability  $f[s_i(t)/r(t)]$  ( $f$  denotes a probability density function). Heuristically, we can use Bayes' rule to express this probability as

$$\frac{f_R[r(t)/s_i(t)] \Pr [s_i(t)]}{f_R[r(t)]} \quad (2.1)$$

Here we have imagined that the received function of time  $r(t)$  has a density function  $f_R$ , even though no such function can be defined if the channel noise is a Gaussian stochastic process; we will repair this oversight later. The denominator probability in (2.1), the unconditional probability of receiving  $r(t)$ , is not a function of  $i$ ; also, when thinking about maximum likelihood detection, we assume that the  $i$ th signal  $s_i(t)$  has the same probability as every other data signal. Thus in the maximization of (2.1) over  $i$ , only  $f_R[r(t)/s_i(t)]$  varies, and attention may be confined to it. This probability is readily available in terms of the AWGN channel model, since, heuristically,  $f_R[r(t)/s_i(t)] = \Pr [n(t) = r(t) - s_i(t)]$ , a probability that stems from the channel noise process  $n(t)$ .

This discussion is not mathematically rigorous because  $n(t)$  and, as a consequence,  $r(t)$  are realizations of a Gaussian stochastic process. The way out of this is to express all these functions as convergent series of special basis functions and then compute probabilities for the weights of the basis functions in the series. The weights are components of vectors in a vector space called a *signal space*.

One needs to show that these collections of weights are indeed vectors in a normed vector space; that is,  $n$ -tuples of weights that will allow calculation of the maximum likelihood receiver error probability satisfy such axioms as closure under addition and multiplication by a scalar, existence of a zero, a negative, a scalar dot product and a norm, or "length," for vectors. We shall not perform these formalities here.

In setting up this normed vector space, we first acquire a set of basis functions  $\{\psi_i(t), i = 1, 2, \dots, n\}$  that is orthonormal and complete. If the inner product of our vector space is defined as

$$\langle h(t), g(t) \rangle = \int h(t)g(t)^* dt \quad (2.2)$$

then an *orthonormal* basis set is one for which  $\langle \psi_i(t), \psi_j(t) \rangle$  is 0 for  $i \neq j$  and 1 for  $i = j$ . The range of integration for the inner product is whatever fixed range has been set for the space. The components in the vector space for a function  $g(t)$  are given by

$$g_j = \langle g(t), \psi_j(t) \rangle \quad (2.3)$$

Suppose we attempt to approximate  $g(t)$  by an expansion in terms of these components, given by

$$\sum_{j=1}^n g_j \psi_j(t) \quad (2.4)$$

If the norm for our vector space is defined as

$$\|g(t)\| = \langle g(t), g(t) \rangle^{1/2} \quad (2.5)$$

then the basis set  $\{\psi_j(t)\}$  is *complete* if the norm

$$\left\| g(t) - \sum_{j=1}^n g_j \psi_j(t) \right\| \rightarrow 0 \quad (2.6)$$

as  $n \rightarrow \infty$ , for any function  $g(t)$  whose square integral is finite. Expression (2.6) says that for a complete basis set the integral of the square error between  $g(t)$  and its expansion tends to zero as the number of terms in the expansion grows large.

It remains to find a suitable complete orthonormal basis set for the signals that appear in the AWGN channel and then to show that this formalism helps explain the behavior of signals in the channel. These signals include a finite set of data-bearing transmitted signals  $\{s_i(t)\}$ , to which is added  $n(t)$ , one of an uncountable set of Gaussian stochastic process realizations. All of these functions are viewed over the same interval as in (2.2). The Karhunen-Loeve expansion (see Van Trees<sup>(4)</sup>) gives a complete orthonormal basis set for this case; for white noise in fact it turns out that any basis set is acceptable provided that it is orthonormal and is complete with regard to the data signals  $\{s_i(t)\}$  alone. Thus, finding a basis set comes down to finding a basis set for just the data signals.

The Gram-Schmidt procedure constructs an orthonormal basis for a given set of functions. The details of this appear in Wozencraft and Jacobs<sup>(5)</sup> or Van Trees,<sup>(4)</sup> and the idea of the procedure is contained in the receiver synthesis procedures of Chapter 7. The importance of the procedure to us now is not its details but the fact that it exists.

Let us then make a basis set  $\{\psi_j(t)\}$  that forms a sufficient basis for all the transmitted signals  $s_i(t)$ . Adopt the notation  $s_{i/j}$  to denote the  $j$ th coefficient in the expansion of the  $i$ th signal; thus,

$$s_i(t) = \sum_{j=1}^{J_s} s_{i/j} \psi_j(t) \quad \text{for each } i$$

$J_s$  is the dimension of the signal space and is at most equal to the number of transmitted signals. The expansion takes place over some time interval of interest,  $[t_1, t_2]$ . The coefficient  $s_{i/j}$  is given by  $\langle s_i(t), \psi_j(t) \rangle$ .

We expand the noise waveform  $n(t)$  by means of the same basis set, obtaining the expansion

$$\sum_{j=1}^{J_1} n_j \psi_j(t) \quad \text{with } n_j = \langle n(t), \psi_j(t) \rangle$$

The expansion of the received signal  $r(t)$  is

$$\sum_{j=1}^{J_1} r_j \psi_j(t)$$

where  $r_j$  equals  $n_j + s_{i/j}$  by the additivity of elements in our signal space. The coefficients  $\{r_j\}$  are Gaussian random variables because they are formed by linear operation on other Gaussian variables. The mean of  $r_j$  conditioned on the  $i$ th signal transmitted is

$$\begin{aligned} \mathcal{E}[R_j / s_i(t)] &= [s_{i/j}] + \mathcal{E}[N_j] \\ &= s_{i/j} + 0 \\ &= s_{i/j}, \quad \text{all } i \text{ and } j \end{aligned}$$

(Here capital letters denote random variables.) The conditional variance is given by

$$\begin{aligned} \text{var}[R_j / s_i(t)] &= \mathcal{E}[(s_{i/j} + N_j) - s_{i/j}]^2 \\ &= \mathcal{E}[N_j^2] \\ &= \mathcal{E}\left[\int n(t)\psi_j(t) dt \int n(u)\psi_j(u) du\right] \end{aligned}$$

in terms of the noise stochastic process  $n(t)$ . For any process, the expectation and integration operations can be commuted so that

$$\begin{aligned} \text{var}[R_j / s_i(t)] &= \iint \mathcal{E}[n(t)n(u)] \psi_j(t)\psi_j(u) dt du \\ &= \iint (N_0/2)\delta(t-u)\psi_j(t)\psi_j(u) dt du \\ &= \int (N_0/2)\psi_j^2(t) dt = N_0/2 \end{aligned}$$

Here  $N_0/2$  is the power spectral density of the white noise  $n(t)$ . A similar calculation shows that the covariance of  $r_k$  and  $r_j$  is zero if  $k \neq j$ , since now the last line above is  $\int (N_0/2)\psi_k(t)\psi_j(t) dt = 0$  by the orthogonality of the basis functions. This shows that the set  $\{r_j\}$  are uncorrelated Gaussian random variables.

Using all these results, we can write down the multivariate density function of  $r_1, r_2, \dots, r_{J_s}$ , conditioned on the transmitted signal  $s_i(t)$ . It is

$$\begin{aligned} f_R(r_1, \dots, r_{J_s} / s_i(t)) &= \prod_{j=1}^{J_s} \frac{\exp [-(r_j - s_{i,j})^2 / N_0]}{(\pi N_0)^{1/2}} \\ &= \frac{\exp [-\sum_{j=1}^{J_s} (r_j - s_{i,j})^2 / N_0]}{(\pi N_0)^{J_s/2}} \end{aligned} \quad (2.7)$$

In (2.1), only (2.7) is subject to variation, so the maximum likelihood receiver finds the maximum of (2.7) over the choice of  $s_i(t)$ . We could have augmented (2.7) to include additional components of  $r(t)$ , which would necessarily be orthogonal to all the transmitted signals, and then modified the denominator of (2.1) accordingly. But the signal  $s_i(t)$  that maximizes (2.1) will not change if we do this.

### Signal Space Distance

It can be seen from (2.7) that the value of the density depends on only one quantity that relates to the signal set,  $\sum_j (r_j - s_{i,j})^2$ . In the normed vector space that we have set up, Parseval's identity can be used to show that this expression equals  $\int [r(t) - s_i(t)]^2 dt$ , which is the square norm of the difference  $r(t) - s_i(t)$ . Rather than norm, communications engineers use the term "square Euclidean distance" between the signals  $r(t)$  and  $s_i(t)$ . From the sum-of-components form of the distance, we see that it is a sum of squares of differences in a set of orthogonal directions. This distance, therefore, has the same Pythagorean character as distance in the ordinary world.

It is also clear from the monotonicity of the  $\exp( )$  function that the density  $f_R$  is maximized by choosing  $s_i(t)$  that is "closest" to  $r(t)$  in the sense of this distance. The maximum likelihood receiver then can be implemented by calculating for each  $i$

$$\int [r(t) - s_i(t)]^2 dt = \int r^2(t) dt + \int s_i^2(t) dt - 2 \int r(t)s_i(t) dt \quad (2.8)$$

Since the first term is constant with respect to  $i$ , the receiver need only form the correlation  $\int r(t)s_i(t) dt$  and subtract it from the second term, which is

the energy of  $s_i(t)$ . If all transmitted signals are of equal energy, only the correlation need be performed. A receiver based on these calculations is called a *correlation receiver*.

Another method of implementing the maximum likelihood receiver is to calculate the distance by expanding  $r(t)$  into coefficients in the signal space, subtracting vectors representing the signals  $s_i(t)$ , and detecting for which  $i$  the difference vector has the least norm. This norm is

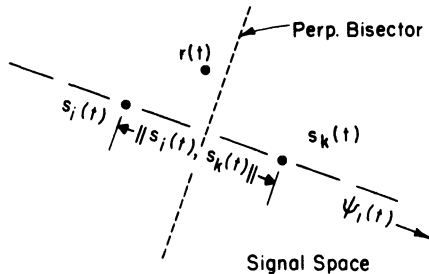
$$\int [r(t) - s_i(t)]^2 dt = \sum_j \left[ \int r(t)\psi_j(t) dt - s_{i/j} \right]^2 \quad (2.9)$$

from which it is apparent that the receiver must evaluate a set of integrals of the form  $\int r(t)\psi_j(t) dt$  and then do subtractions. This receiver is called a *signal space receiver*. It performs one integral for each signal space dimension, while the correlation receiver performs one for each signal that may appear during the integration time followed by a set of subtractions. Thus, when there are about as many signal space directions as there are signals, the correlation receiver is probably simpler to implement.

The integrals in either receiver can be realized by a simple linear filtering operation. Let the integration time be the interval  $[0, NT]$ . By the properties of convolution, the integral  $\int_0^{NT} r(t)s_i(t) dt$  has the same value as the convolution  $r * h$  evaluated at  $NT$ , if  $h(t) = s_i(NT - t)$ . This  $h(t)$  is the function  $s_i(t)$ , time reversed and shifted by  $NT$ . We can interpret  $h * s_i$  as a filtering of  $s_i(t)$  by a filter with impulse response  $h(t)$ .  $h(t)$  is called a *matched filter*, matched in this case to  $s_i(t)$ . We could equally well make a matched filter for  $\psi_j(t)$  for use in a signal space receiver. The use of such matched filters is a standard technique in the construction of receivers, as we shall explore in Chapter 7.

### 2.1.2. Probability of Error

The signal space distance directly determines the probability of symbol error. Let  $P_e(k; i)$  be the probability that the data bearing signal  $s_k(t)$  is detected by the maximum likelihood receiver, given that  $s_i(t)$  was in fact sent. From (2.7), this will happen only if  $s_k(t)$  is closer to the received  $r(t)$  than is  $s_i(t)$ . The situation in signal space is sketched in Figure 2.1. Since white noise is identically distributed along any set of orthogonal axes, let these axes temporarily be chosen so that the first axis runs directly through the signal space points corresponding to  $s_i(t)$  and  $s_k(t)$ . The perpendicular bisector of the line between the signals is the locus of points equidistant from both signals. The probability that  $r(t)$  lies on the “ $s_k(t)$ ” side of the bisector is the probability that the first component  $r_1 - s_{i/1}$  exceeds half of

Figure 2.1.  $s_i(t)$  and  $s_k(t)$  in signal space.

the signal space distance  $\Delta = \|s_i(t) - s_k(t)\|$ . Thus, our error probability is given by

$$P_e(k; i) = \int_{\Delta/2}^{\infty} 1/(\pi N_0)^{1/2} \exp(-u^2/N_0) du \quad (2.10)$$

since  $r_i - s_{i/1}$  is a Gaussian variate with mean 0 and variance  $N_0/2$ .

Next we find the probability that *any* other signal is detected besides  $s_i(t)$ . To do this we use the “union bound” of probability, which states that if  $A_1, A_2, \dots$  are events, the probability  $\Pr\{\text{union } A_i\}$  that one or more happens is overbounded by  $\sum_i \Pr\{A_i\}$ . Consequently, the probability of error if  $s_i(t)$  is sent is bounded by

$$P_e(i) \leq \sum_{k \neq i} \int_{\|s_i(t) - s_k(t)\|/2}^{\infty} 1/(\pi N_0)^{1/2} \exp(-u^2/N_0) du \quad (2.11)$$

The total probability of error is

$$P_e = \sum_i P_e(i) \Pr\{s_i(t) \text{ sent}\} \quad (2.12)$$

In maximum likelihood detection, one assumes that all messages are equally likely. If, in addition,  $P_e(i)$  is the same for all  $i$ , then  $P_e$  and  $P_e(i)$  are identical, but this is only true for simple modulations.

It is convenient to denote the Gaussian integral in (2.11) in terms of the  $Q$  function defined by

$$Q(x) \triangleq (1/2\pi)^{1/2} \int_x^{\infty} e^{-v^2/2} dv \quad (2.13)$$

$Q( )$  can be obtained from the widely tabulated error function by means of  $Q(x) = (1/2)[1 - \text{erf}(x/\sqrt{2})]$ ; alternatively, one can use the bounds

$$(1/2\pi)^{1/2} e^{-x^2/2} \left( \frac{x}{1+x^2} \right) < Q(x) < \begin{cases} (1/2\pi x)^{1/2} e^{-x^2/2} \\ ((1/2) e^{-x^2/2}, \quad x > 0 \end{cases} \quad (2.14)$$

(Tighter bounds appear in Ref. 6.) An increase in signal energy corresponds to an increase in  $x$ ; and as this happens, both bounds become very tight. In terms of  $Q(\cdot)$  we can rewrite (2.11) as

$$P_e(i) \leq \sum_{k \neq i} Q(\|s_i(t) - s_k(t)\|/(2N_0)^{1/2}) \quad (2.15)$$

We shall explore these expressions further in Section 2.2 in terms of phase modulated sinusoidal signals.

The classic explanation of these matters appears in Wozencraft and Jacobs, and the reader in need of tutorial help is directed there. It is of interest to extend the maximum likelihood receiver to the cases of colored Gaussian noise and non-Gaussian noise. While this can be done, the results have less appeal because the concepts of Euclidean distance and simple matched filtering no longer apply. For colored Gaussian noise, a Karhunen-Loeve expansion—not the trivial one here—must be performed to obtain a basis set for the noise and signals; the pattern of logic is similar to ours here, but it leads to more complex results. For non-Gaussian noise, the derivation is even more complex, and it may be quite difficult to solve the Fredholm integral equations that lead to the set of basis functions. These problems are treated in Van Trees. Receivers for the colored Gaussian case were discussed more recently in the papers by Forney<sup>(7)</sup> and Ungerboeck.<sup>(8)</sup>

## 2.2. Phase Modulated Signals

We now apply the signal space analysis just devised to the special case of constant-envelope sinusoidal signals. We begin with a description of simple modulations and then develop notation for the analysis of sophisticated modulations that begins in Chapter 3.

The transmission of data by means of signals over time can be viewed in several ways. In information theory, one considers that information is carried by one of  $S$  signals that can appear over some extended space of time. If the signals are equiprobable,  $\log_2 S$  bits of information are transmitted in this space by the choice of the signal. Such an “extended” reckoning of time is often inconvenient, and it is more natural to think of a sequence of data symbols with each symbol assigned to its own time interval, even though the effect of a symbol may extend outside its interval. Accordingly, let a constant-envelope phase-varying signal be of the form

$$(2E/T)^{1/2} \cos(\omega_0 t + \phi(t)) \quad (2.16)$$

$T$  is the length of a basic signaling interval and  $E$  is the energy expended during this interval, as can be verified by integrating the square of (2.16)

over a  $T$ -length interval. In each interval, an  $M$ -ary data symbol appears and the phase  $\phi(t)$  follows some pattern in response to these symbols.  $\omega_0$  is a carrier frequency, and we will normally simplify calculations by assuming that it is much larger than  $2\pi/T$ .

### 2.2.1. PSK and FSK

The earliest phase modulations were phase-shift keyed (PSK) signals. Here a plot of phase vs. time would show the phase to be constant except for step changes at signaling interval boundaries. In binary PSK, two phases, for instance 0 and  $\pi$ , are available during each symbol interval; in quaternary PSK, the signal can take on four phases, say 0,  $\pi/2$ ,  $\pi$ ,  $3\pi/2$ , during an interval. These phase levels can be offset by a constant so long as the separation is maintained. In a modern PSK system, the rectangular transitions are normally smoothed to produce "smoothed" or "pulse-shaped" PSK. Since the effects of this smoothing can be quite complex, we shall return to the subject at some length in Section 2.6. To avoid confusion, we denote rectangular PSK as "pure" PSK.

In a frequency-shift keyed (FSK) phase modulation,  $\phi(t)$  follows a sequence of straight lines, the slopes of which can be viewed as frequencies. Figure 2.2 shows all the possible trajectories starting from time zero for one type of FSK, continuous phase FSK, in which phase transitions across the interval boundaries are constrained to be continuous. Within any interval, the phase slope is either  $+h\pi/T$  or  $-h\pi/T$ , and the modulation can be viewed as transmitting one of these two frequencies in each interval in response to a (binary) data sequence. Another type of FSK signal is created if discontinuities are allowed at the interval boundaries; this is called discontinuous or "incoherent" FSK. Although it too consists of frequency bursts within each interval, the presence of phase jumps at the interval boundaries changes the power and bandwidth properties of the signal to a surprising degree.

A plot like Figure 2.2 that shows an entire set of phase trajectories is called a *phase tree*. The tree makes clear the transitions of phase across

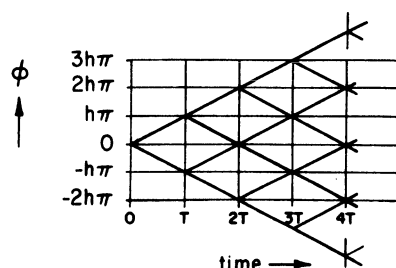


Figure 2.2. Phase trajectories for continuous-phase FSK, displayed in a phase tree (from Anderson & Taylor, IEEE, Nov. 1978).

interval boundaries, and it makes it easier to see the effect of interval-to-interval memory in  $\phi(t)$ . Since phase is modulo- $2\pi$ , a phase tree eventually wraps around itself to form a cylinder whose long axis is time. If the constant  $h$  shown in Figure 2.2 is a ratio of two integers, it will eventually be the case that newly appearing paths fall exactly on top of other paths in the wrapped-around tree; this new structure is called a *trellis*. An example for  $h = 1/2$  appears in Figure 2.3, which shows a section of the FSK cylindrical phase trellis that has been unwrapped and laid flat. After two intervals of growth, the tree of Figure 2.2 with  $h = 1/2$  is such that all future paths more than  $\pi$  radians above the starting phase or less than  $\pi$  below it lie on top of paths within this range. The acquisition of “cylindrical intuition” takes a bit of practice for the human brain, although it is no challenge for a signal processing circuit.

The FSK modulation shown in Figure 2.3, continuous phase FSK with  $h = 1/2$ , was developed around 1970 by de Buda,<sup>(9)</sup> who called it Fast FSK, and by others (see Doelz and Heald<sup>(10)</sup>), who called it minimum-shift keying, or MSK. This scheme plays an important role in the evolution of phase modulation. De Buda observed that the phase continuity imposes a type of memory on the signal phase and that optimal detection required observing the signal over two intervals instead of just one. He went on to propose synchronization and optimal ML detection circuitry. MSK has the same energy requirement as binary or quaternary PSK, but its spectral sidelobes are markedly reduced compared to pure PSK (see Chapter 4).

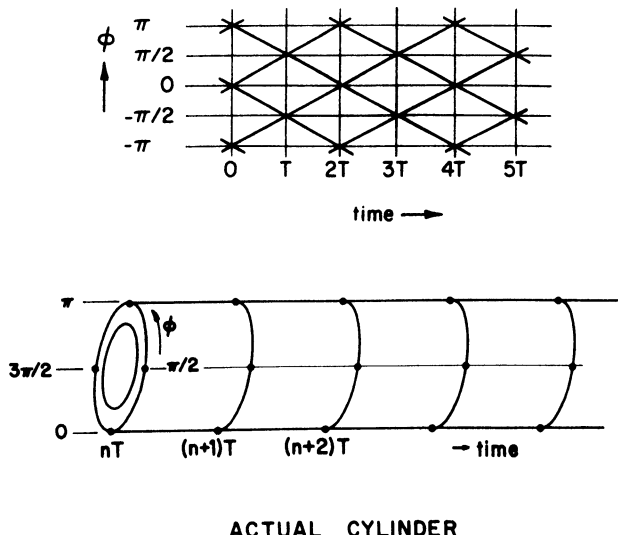


Figure 2.3. Fully developed trellis for MSK; the pattern is wrapped around a cylinder.

Pelchat *et al.*,<sup>(11)</sup> Osborne and Luntz,<sup>(12)</sup> and Schonhoff<sup>(13)</sup> studied continuous-phase FSK with other phase slopes than those implied by  $h = 1/2$ . They showed that all FSKs require a receiver observation time of 2–3 intervals for optimal performance and that the energy and bandwidth requirements varied in a complicated manner as  $h$  changed. Compared to PSK, then, these FSK schemes have several new characteristics: Phase patterns have memory, receivers must observe and calculate information from several intervals, and energy and bandwidth interrelate in such a way that more attractive combinations can be obtained. This behavior of FSK and other more efficient modulations will become clear in succeeding chapters.

### 2.2.2. A Notation for Continuous Phase Modulations

For modulations more complex than PSK, we need a more workable notation to describe patterns of phase. Virtually all phase modulators *convolve* the data sequence, or a simple function of it, with some response function in phase, frequency, or amplitude. They execute thus a linear filtering of the data prior to some simple final operation. (It is interesting to note that most other communications processors, like error correcting coders, data compressors, and filters, are based on some form of convolution.) This motivates the following. Define a phase signal as being determined by a sequence of data symbols  $\alpha_1, \alpha_2, \dots$ , with each  $\alpha_i$  chosen from an  $M$ -ary alphabet  $\pm 1, \pm 3, \dots, \pm(M - 1)$ . It is convenient to restrict  $M$  to be even. Let the total phase in the  $(n + 1)$ st interval satisfy

$$\phi(t) = 2\pi \sum_{i \leq n} \alpha_i h q(t - iT), \quad nT < t \leq (n + 1)T \quad (2.17)$$

Here  $q(\cdot)$  is the *phase smoothing response* that describes how the underlying phase change  $2\pi\alpha_i h$  evolves with time.  $q(t)$  can be any function which before some  $t$  is zero and after some  $t$  is  $1/2$ ; for simple binary PSK modulation  $q(t)$  is a unit step of height  $1/2$  at time zero, and for FSK signals it is a linear increase to  $1/2$  beginning at 0 and ending at  $T$ . Figure 2.4 shows some of these phase responses together with their derivatives, the frequency pulses  $g(t)$ , which are plots of the instantaneous frequency of the individual pulses. It is clear that the instantaneous frequency of the pulse generally lowers as the time lengthens over which the pulse is actively changing. We shall see in Chapter 4 that the actual power spectral density of a modulation also narrows as the frequency pulse lengthens.

The constant of proportionality  $h$  is called the *modulation index*. It determines how much eventual phase change occurs at the appearance of a data symbol, playing a role similar to the modulation index in analog

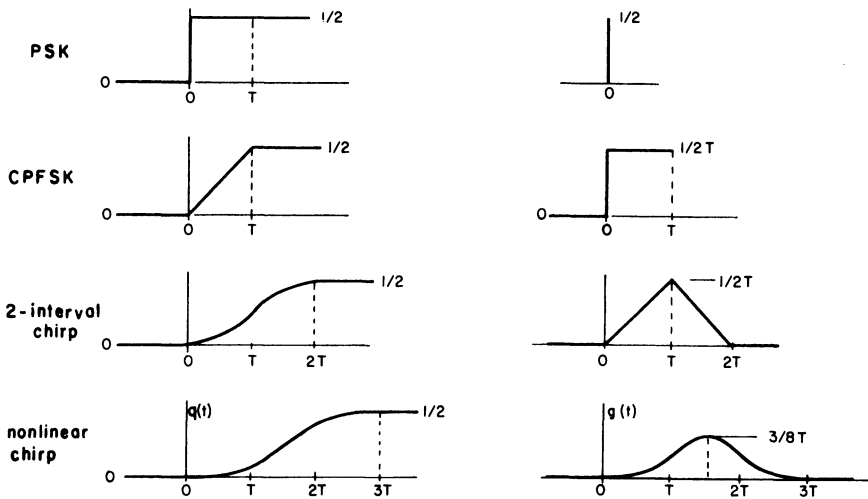


Figure 2.4. Phase smoothing functions  $q(t)$  (left) and their derivatives  $g(t)$  (right). Each pulse has one more derivative than the one above it, and extends over one more interval.

FM. The index  $h$  can be replaced by  $h_i$ , which varies from interval to interval, in which case the signals are said to be a *multi-h* modulation.

### 2.2.3. Euclidean Distance for Phase Modulations

The signal space distance developed in Section 2.1 simplifies considerably for phase-varying signals since the distance between two signals depends only on the phase difference between them.

Suppose two signals  $s_i(t)$  and  $s_k(t)$  differ over  $N$  intervals. Since both are constant envelope with energy  $E$  over a  $T$ -interval, equation (2.8) gives that

$$\int [s_i(t) - s_k(t)]^2 dt = 2NE - 2 \int s_i(t)s_k(t) dt + o(1/\omega_0)$$

where the integrals are over a length  $NT$  seconds and  $o(1/\omega_0)$  denotes a term of order  $1/\omega_0$ . An exercise in trigonometry shows that the cross term becomes

$$2 \int 2(E/T) \cos [\omega_0 + \phi_i(t)] \cos [\omega_0 + \phi_k(t)] dt$$

$$\begin{aligned}
&= 2(E/T) \int \{\cos [\phi_i(t) - \phi_k(t)] + \cos [2\omega_0 + \phi_i(t) + \phi_k(t)]\} dt \\
&= 2(E/T) \int \cos [\phi_i(t) - \phi_k(t)] dt + o(1/\omega_0)
\end{aligned}$$

where  $\phi_i$  and  $\phi_k$  are the phases relative to the carrier of  $s_i$  and  $s_k$ . The distance in the limit of large carrier frequency is

$$2NE - (2E/T) \int \cos \Delta\phi(t) dt \quad (2.18)$$

where  $\Delta\phi(t)$  denotes the phase difference between the signals. A more careful calculation, left to the reader, gives the distance for a particular finite carrier frequency.

This expression is still not the most convenient one. The energy  $E$  is the energy devoted to an interval, not to a data bit. In comparing schemes with differing symbol alphabet size  $M$ , one must normalize  $E$  to form the energy per data bit  $E_b$  in order to assess the total energy consumed by a given message. Since an  $M$ -ary symbol carries  $\log_2 M$  bits of information,  $E$  and  $E_b$  are related by  $E = \log_2 M E_b$ . With this in hand, we define the normalized Euclidean distance function  $d(\cdot, \cdot)$ , between two constant-envelope signals, as

$$d^2(s_i(t), s_k(t)) \triangleq (\log_2 M / T) \int [1 - \cos \Delta\phi(t)] dt \quad (2.19)$$

Here we have incorporated the  $N$  term of (2.18) into the integral. The complete signal space distance between  $s_i(t)$  and  $s_k(t)$  is given by  $2E_b d^2(s_i(t), s_k(t))$ .

### The Minimum Distance

When the ratio of signal energy to noise energy is reasonably high, it turns out that one intersignal distance completely dominates the expression (2.15) that overbounds the total probability of detection error. Imagine that  $s_i(t)$  is transmitted. From (2.14) and (2.15),

$$P_e(i) \leq \sum_{k \neq i} Q(d(s_i(t), s_k(t))(E_b/N_0)^{1/2}) \leq \frac{1}{2} \sum_{k \neq i} e^{-d^2(s_i, s_k)E_b/2N_0} \quad (2.20a)$$

Each exponent contains the ratio  $E_b/N_0$ , the bitwise energy signal-to-noise ratio; throughout this book we call this ratio the *SNR*. If the SNR is not small, the term with the smallest  $d(\cdot, \cdot)$  will strongly dominate (2.20a). At these SNR we can write the approximate bound

$$P_e(i) \leq (K/2) \exp \left\{ -\min_k [d^2(s_i, s_k)] E_b / 2N_0 \right\} \quad (2.20b)$$

and we can bound the total error probability

$$P_e \leq (K/2) \exp \left\{ -\min_{\substack{i,k \\ i \neq k}} [d^2(s_i, s_k)] E_b / 2N_0 \right\} \quad (2.20c)$$

Here  $K$  is the number of signals that attain the minimums in each case. For a strict upper bound at all SNR,  $K$  must be replaced by  $S$ , the total number of signals, but (2.20b) and (2.20c) are good upper bounds at any reasonable SNR.

The final expression for  $P_e$  contains a crucial fact: The worst-case combination of  $s_i(t)$  and  $s_k(t)$  eventually dominates the total error probability for a signal set as the SNR grows. The worst-case distance for any size observation interval  $N$  is called the *minimum distance*. A definition that applies to any set of signals is

$$d_{\min}^2 \triangleq (1/2E_b) \min_{\substack{i,k \\ i \neq k}} \int [s_i(t) - s_k(t)]^2 dt \quad (2.21)$$

Minimum distance and, therefore, error probability as a function of SNR are the subject of Chapter 3.

### 2.3. Examples of Error Probability Calculations

Frequency and phase shift keying provide straightforward examples of error calculation.

Consider a pure binary PSK signal  $s_i(t)$  that begins at time 0. The signals that may appear at the receiver include all  $2^N$  sequences with phase 0 or  $\pi$  in  $N$  intervals. The closest signal to  $s_i(t)$  is the one with the opposite phase in interval 1 (or any other interval) and identical phases in the remaining intervals. Calculation of  $d^2(\cdot, \cdot)$  between these two gives the minimum distance, and from (2.19) evaluated over time  $[0, NT]$ , this square distance is 2. A similar argument shows that for quaternary PSK the minimum distance is the distance between two signals  $\pi/2$  apart in interval

1 and identical otherwise. The integral itself in (2.19) turns out to be  $T$ ; but since  $\log_2 M = 2$ , the square minimum distance of QPSK is 2. Thus, both BPSK and QPSK have the same minimum distance and the same symbol error performance in terms of  $E_b/N_0$  when this ratio is reasonably large.

Note that a total of  $N$  signals lie at the minimum distance away from  $s_i(t)$  for BPSK and  $2N$  signals do for QPSK. This means that the factor  $K$  in the overbound (2.20b) for  $P_e(i)$  is either  $N$  or  $2N$ . Now  $P_e(i)$  is serving as a bound on the probability of receiving correctly an *entire sequence* of  $N$  symbols. By setting  $N$  equal to 1, we have instead the probability of receiving a *single symbol* incorrectly and (2.20a) becomes  $Q((2E_b/N_0)^{1/2})$  for BPSK and  $2Q((2E_b/N_0)^{1/2})$  for QPSK. As an example, suppose a symbol error probability of  $10^{-5}$  is desired. An accurate calculation with the  $Q()$  function shows that  $E_b/N_0 = 9.6$  dB is required while 9.9 dB is required for QPSK; this is because QPSK has twice as many neighbor signals lying at the minimum distance. A plot of these symbol probabilities appears for all  $E_b/N_0$  in Figure 2.5. One can also use the overbound (2.14) on  $Q()$  to obtain the expressions  $(1/2) \exp(-E_b/N_0)$  for BPSK and  $\exp(-E_b/N_0)$  for QPSK. The first, for instance, implies that  $E_b/N_0 = 10.3$  dB is required to attain probability  $10^{-5}$  for BPSK. This answer will converge to that obtained from  $Q()$  itself as the SNR grows further.

The calculation for MSK is more subtle. The phase trellises in Figure 2.2 or 2.3 are made up of many identical diamond-shaped figures. From this symmetry it is clear that every signal  $s_i(t)$  has a neighbor that is one

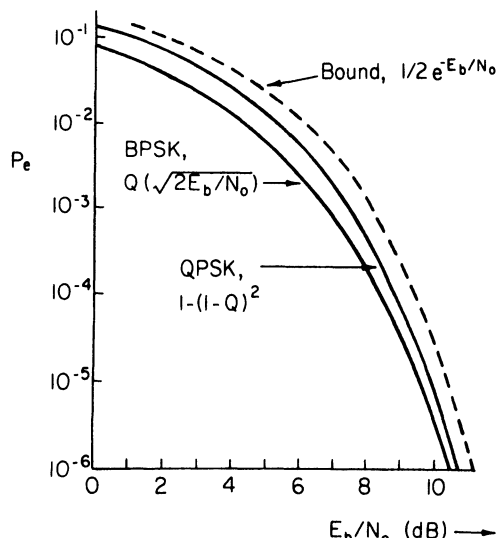


Figure 2.5. Single-symbol error probability for BPSK and QPSK. Note convergence of the two curves. The simple exponential bound is shown for comparison.

diamond “away” from it and otherwise identical. The two signals  $+1, -1, X, X, \dots$  and  $-1, +1, X, X, \dots$ , with  $X, X, \dots$  identical for both, are removed from each other such a diamond shape. For this separation, (2.19) yields 2, which is evidently the minimum distance. Thus, MSK has the same distance as both PSKs.

### *First Symbol Error Probability*

We have distinguished between the error probability of a block of symbols and of a single symbol. Alternately, we could compute the probability that the first symbol is received incorrectly, given that the receiver (and the distance calculation) can view signals that are  $N$  intervals long. This is a more subtle notion than computing the error probability of a signal that has the same duration as the observation window. It turns out to be the natural probability for analyzing error performance of general modulations with memory, the receivers for which need to view more than one symbol interval in order to decide a given symbol. This probability also poses a new question: How long an observation interval is needed to optimally decide a symbol?

To calculate a binary first symbol probability, we fix the first symbol of  $s_i(t)$  at, say  $+1$ , with the remaining symbols arbitrary. The probability of receiving  $\alpha_1 = +1$  incorrectly is the probability that  $s_k(t)$  which is closest to  $r(t)$ , the noisy received signal, over the interval  $[0, NT]$  is one of the signals with  $\alpha_1 = -1$ . The collection of these signals is shown in Figure 2.6 for MSK, where the transmitted signal  $s_i(t)$  appears as a heavy line and the “incorrect subtree,” all tree paths with  $\alpha_1 = -1$ , appears as lighter lines. The number of these paths grows exponentially as  $2^{N-1}$ , but their distance from the transmitted path grows rapidly as well in such a way that the error probability is hardly affected.

We can write an overbound for the first symbol probability just as we did in Section 2.2 consisting of one term for each signal in the incorrect subset. If the observation is restricted to one interval, the bound will be of form (2.20b) with one term, having square distance 1; for two intervals,

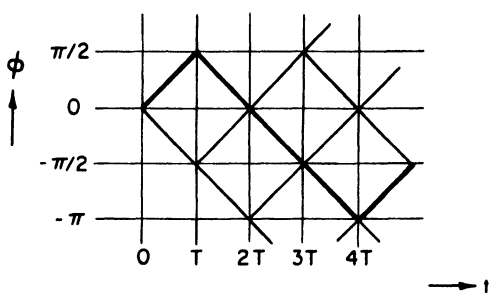


Figure 2.6. Incorrect subtree for sent symbol  $\alpha_1 = +1$  in MSK. Heavy path shows transmitted signal. All light paths are descendants of  $\alpha_1 = -1$ .

there are two terms, one at distance 2 and the other at 3. The first dominates, leading us to the conclusion that MSK with two-interval detection of the first symbol has twice the minimum square distance that it does with one-interval detection; this means that to a close approximation, two-interval MSK requires 3 dB less signal energy for the same error probability. Three-interval observation produces a bound with four terms, the largest of which has  $d^2 = 2$  again. Longer lengths of observation do not improve this minimum distance. The number of terms in the bound increases rapidly, but the size of the terms,  $\exp(-d^2 E_b / N_0)$ , declines more rapidly and the a priori probability of each path declines as well.

The example of MSK underscores the importance of setting a sufficiently wide observation time at detection. This topic will be taken up in detail in Chapter 3 and in Chapter 7, where this shortest observation interval for optimal high SNR performance will be called the path memory.

## 2.4. Baseband Receiver and Transmitter Models

We have already given several optimal receivers based on matched filters; that is, filters whose impulse responses are sinusoids of the form  $A \cos [\omega_0 + \phi(t)]$ . These filters are basically bandpass filters whose response is centered at the rf or if carrier frequency. Some receivers, for instance those based on surface acoustic wave devices, are literally based on such filters. Most, however, convert  $r(t)$  to two signals at zero carrier frequency and carry out detection from these, a process called *converting to baseband*.

Figure 2.7 shows a baseband modulator circuit. It causes a given phase  $\phi(t)$  to modulate a carrier  $\cos(\omega_0 t)$ . Two new signals are created,  $\cos \phi(t)$ , which is called the *in phase component*  $I(t)$ , and  $\sin \phi(t)$ , the *quadrature component*  $Q(t)$ . These are multiplied by  $-A \sin \omega_0 t$  and  $A \cos \omega_0 t$  and added to produce the modulated carrier  $s(t) = A \cos [\omega_0 t + \phi(t)] = AI(t) \cos \omega_0 t - AQ(t) \sin \omega_0 t$ .

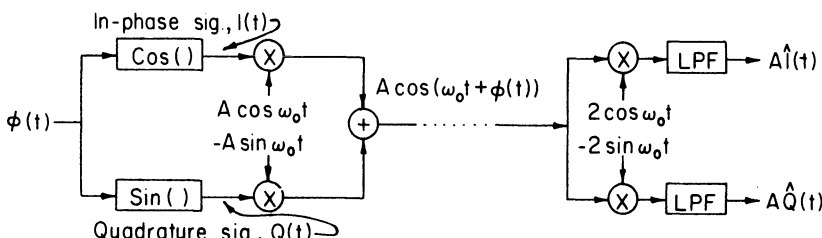


Figure 2.7. Baseband modulator (left) and demodulator (right), showing in-phase and quadrature signals. Channel is assumed to have unity gain.

Next in the figure is shown a baseband demodulator. Here multiplications by  $-2 \sin \omega_0 t$  and  $2 \cos \omega_0 t$  are followed by low-pass filters that remove components at frequency  $2\omega_0$ , leaving baseband components  $A\hat{I}(t)$  and  $A\hat{Q}(t)$  that consist of the transmitted components plus noise. The actual detection, whether matched filtering or something simpler, is performed on these.

Basic trigonometric identities show that the circuit functions in the figures perform as shown there. The  $\sin \omega_0 t / \cos \omega_0 t$  multiplier is called a balanced modulator circuit, and it can be realized relatively simply by mixers or by collections of diodes. A number of circuits are given in Bostian, Krauss, and Raab.<sup>(14)</sup>

Another trigonometric exercise shows how to compute distance from baseband components. Express  $s_i(t)$  as  $(2E/T)^{1/2}[I_i(t) \cos \omega_0 t - Q_i(t) \sin \omega_0 t]$  and  $s_k(t)$  as  $(2E/T)^{1/2}[I_k(t) \cos \omega_0 t - Q_k(t) \sin \omega_0 t]$ , in terms of their  $I$  and  $Q$  baseband components. Expressed thus, the energy of each signal will be  $(E/T) \int I^2(t) + Q^2(t) dt$  in the limit of large  $\omega_0$ ; if we require the condition

$$\mathcal{E} \left[ (1/T) \int_{(n-1)T}^{nT} I^2(t) + Q^2(t) dt \right] = 1 \quad (2.22)$$

then  $E$  will take its accustomed role as the energy per symbol interval. The signal space distance between  $s_i(t)$  and  $s_k(t)$  is

$$\int [s_i(t) - s_k(t)]^2 dt = (E/T) \int [I_i(t) - I_k(t)]^2 + [Q_i(t) - Q_k(t)]^2 dt$$

plus a number of terms that are of order  $1/\omega_0$ . The normalized distance is

$$\begin{aligned} d^2(s_i(t), s_k(t)) &= (\log_2 M)/2T \int [I_i(t) - I_k(t)]^2 \\ &\quad + [Q_i(t) - Q_k(t)]^2 dt \end{aligned} \quad (2.23)$$

From (2.23) we see that  $I$  and  $Q$  must describe the signal in orthogonal directions since the square distance is the sum of the square differences in the  $I$  and  $Q$  directions.

The expression  $[I^2(t) + Q^2(t)]^{1/2}$  is the *envelope* of the rf signal, the instantaneous rms energy in the signal. For a constant-envelope signal, this expression is a constant with time.

### Hard Limited and Filtered Signals

A hard limiter converts a signal with a varying envelope to one with a fixed envelope. The effect of the limiter on the  $I$  and  $Q$  components is to perform the conversion

$$\begin{aligned} I_h(t) &= \frac{I(t)}{[I^2(t) + Q^2(t)]^{1/2}} \\ Q_h(t) &= \frac{Q(t)}{[I^2(t) + Q^2(t)]^{1/2}} \end{aligned} \quad (2.24)$$

The distance between two hard limited signals follows from the phase-signal distance  $d^2$  of (2.23) with  $I_h$ 's and  $Q_h$ 's substituted for the  $I$ 's and  $Q$ 's; an amplitude of  $(2E/T)^{1/2}$  gives a signal with bit energy  $E_b = E/\log_2 M$ . Another way to calculate  $d^2$  is from the phase separation between the two signals. The phase of a hard-limited  $s_i(t)$  is  $\tan^{-1}(I_{h,i}/Q_{h,i})$ ; and by placing this angle and the one for  $s_k(t)$  in (2.19), one gets  $d^2$ .

A filter convolves a modulated signal with the filter impulse response. Most often, a transmitted signal is a narrowband signal centered on a carrier frequency so that signal filters are narrow, bandpass filters. Bandpass channel filters, too, can be “converted to baseband,” where they appear as a pair of lowpass filters. Some transmission systems operate at baseband without a center carrier frequency; and for these, channel filtering is directly a low-pass filter.

The conversion between baseband and bandpass realizations of the same filter is given in Figure 2.8. A bandpass filter impulse response can be expressed as

$$a(t) = 2a_c(t) \cos \omega_0 t - 2a_s(t) \sin \omega_0 t \quad (2.25)$$

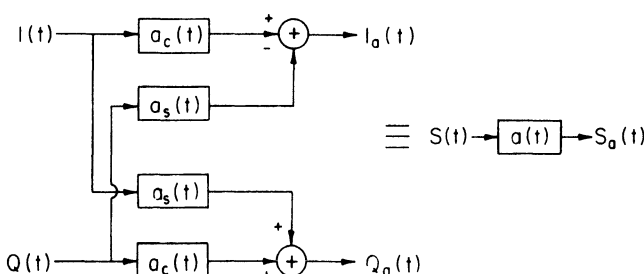


Figure 2.8. Baseband filtering equivalent circuit for bandpass channel filter  $a(t)$  acting on  $s(t)$ .  $a$ ,  $a_c$ , and  $a_s$  are related by (2.25).

When this filters a bandpass signal  $s(t) = I(t) \cos \omega_0 t - Q(t) \sin \omega_0 t$ , the result is another bandpass signal like this but with  $I$  and  $Q$  components

$$\begin{aligned} I_a(t) &= a_c(t) * I(t) - a_s(t) * Q(t) \\ Q_a(t) &= a_c(t) * Q(t) + a_s(t) * I(t) \end{aligned} \quad (2.26)$$

The interested reader can prove this by converting the time signals to the frequency domain and using the fact that both the response and signal have no energy outside a narrow band centered at  $\omega_0$ . Generally speaking,  $a_c$ ,  $a_s$ ,  $I$ , and  $Q$  are all low-pass signals.

The signal space distance between two filtered signals  $s_i(t)$  and  $s_k(t)$  is given by (2.23) with  $I_a$  and  $Q_a$  replacing  $I$  and  $Q$ . Filtering often but not always reduces distance. It also extends the time over which two signals differ so that one must be sure to have an observation time of sufficient width.

### Examples

An  $I$  and  $Q$  channel modulator and demodulator for pure QPSK appears in Figure 2.9. The four phase levels  $\pi/4$ ,  $3\pi/4$ ,  $5\pi/4$ , and  $7\pi/4$  are converted by  $\cos(\cdot)$  and  $\sin(\cdot)$  functions to two outputs  $I$  and  $Q$  that are  $\pm 1/\sqrt{2}$ , from which are generated the modulated carrier. The demodulator reproduces these two with noise added. The next block, called an “Integrate and Dump” circuit, integrates  $\hat{I}$  or  $\hat{Q}$  for the full signal interval, dumps the result at the end of the interval, and begins again from scratch on the next interval. From the dumped result, each decision block puts out  $+1$  if its input lies above 0 and  $-1$  otherwise. In this way the four-level data symbol is regenerated. Carrier and interval-time synchronization must be maintained, but we delay discussion of these to Chapter 9.

This demodulator is actually an optimal, matched filter receiver operating at baseband.  $I(t)$  and  $Q(t)$  take on the constant values  $\pm 1/\sqrt{2}$  during each symbol interval. A matched filter for these is a time-reversed constant;

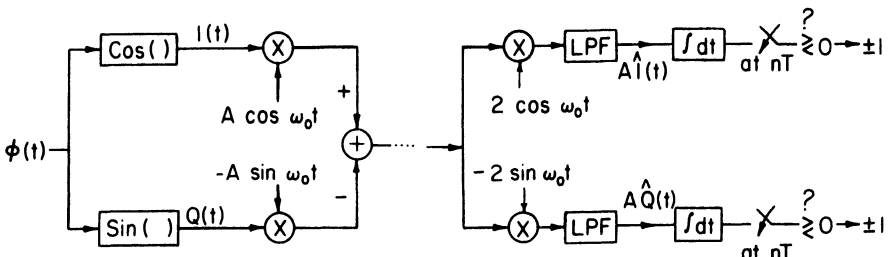


Figure 2.9. Modulator (left) and demodulator (right) for QPSK. These circuits are optimal for pure QPSK.

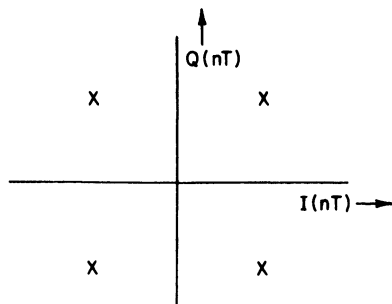


Figure 2.10. Signal space constellation for QPSK; the axes denote the amplitudes of the  $I$  and  $Q$  samples.

i.e., its impulse response is a constant and it is sampled at the interval's end. A filter with this response is precisely the integrator used in the figure. In the terms of 2.1, the signal space has been constructed with the  $I$  and  $Q$  signals as two orthogonal basis vectors. The decision boundaries run along the  $I$  and  $Q$  axes, and the decision blocks act to determine in which quadrant lies the received signal. Figure 2.10 shows the signal space picture of QPSK.

A BPSK modulator/demodulator consists of just the top half of Figure 2.9, the  $I$  channel only. With just this channel, the modulated signal has phase 0 or  $\pi$ . If either BPSK or QPSK are transmitted with pulse shaping of  $I$  and  $Q$ , Figure 2.9 is no longer an optimal receiver because the integrate and dump blocks are no longer matched filters. If the pulse shaping takes place only over one interval, it is possible to replace the integrate and dump with a new matched filter that will produce optimal detection. If the shaping acts over several intervals as it does with narrow band channel filtering, then quite a different, nonlinear receiver is often needed. We will take up this complicated subject in Chapter 8.

An optimal receiver like Figure 2.9 exists for MSK, but its understanding requires some new ideas, which we will put off until Chapter 8. Phase-continuous FSK with modulation index other than 1/2 or with  $M > 2$  cannot be optimally detected by a simple structure like Figure 2.9.

## 2.5. The Linear Receiver

A receiver with the structure of Figure 2.9 is called a *linear receiver*. It consists of the  $\sin \omega_0 t / \cos \omega_0 t$  multipliers, which just move the received signal to baseband, followed by a linear filter, whose output samples, taken once per interval, are converted directly to decoded data. For any modulation scheme, we can ask what is the optimal choice of filter in this receiver,

even if receivers of the linear type are not maximum likelihood. For some modulations, including the Nyquist pulse schemes discussed in Section 2.6, the linear receiver is also maximum likelihood.

### 2.5.1. Intersymbol Interference and the Receiver Eye

When a symbol  $\alpha_n$  that belongs to interval  $n$  causes activity in another symbol interval, the interference is called *intersymbol interference*, or ISI. Filtering to accomplish bandwidth reduction is the primary cause of unwanted ISI. Signal activity relevant to symbol  $\alpha_n$  is convolved with the impulse response of the filter, and the result is a signal spread across a number of intervals. Often, ISI is intentionally introduced in a controlled manner with the idea of improving the energy or bandwidth properties of the signals. Error correction coding is a form of intentional ISI. It can be difficult to separate the concepts of intentional and unintentional ISI; the difference is perhaps mostly psychological. We shall view true ISI as originating in a channel bandpass filter.

It will be simpler to discuss ISI effects in terms of baseband quantities. Suppose that a pulse in  $I(t)$  or  $Q(t)$  like that in Figure 2.11 causes the response at the receiver (in the absence of noise) shown in the figure. Note that the response is not just single-interval pulse shaping since, in addition to smoothing of the pulse rise, parts of the response also appear in later intervals. These later parts will interfere with responses that “belong” in later intervals; and if the parts go on long enough and at sufficient amplitude, they will obscure completely the later intervals.

These effects can be described by an *eye diagram*. Let the modulation be binary and let  $\alpha_n = +1$ . Then plot all the waveforms that can appear in interval  $n$  for each data symbol prehistory  $\dots, \alpha_{n-2}, \alpha_{n-1}$ ; superpose on these all the waveforms with the constraint that  $\alpha_n = -1$  instead. The result, illustrated in Figure 2.12, has an eye-shaped appearance. For quaternary

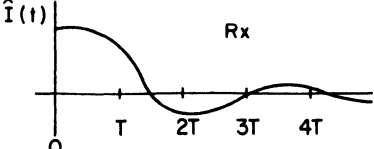
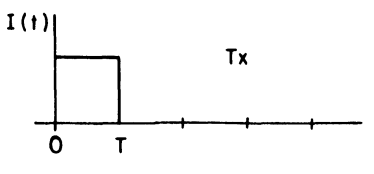
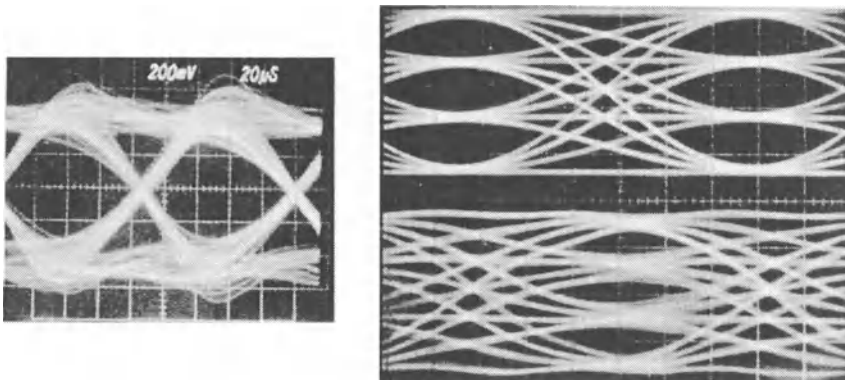


Figure 2.11. Response (below) at receiver to an isolated pulse  $I(t)$  (above) when ISI is present in channel.



**Figure 2.12.** Examples of eye diagrams. (Left) Discriminator output of General Electric Phoenix radio, with 9.6 kbit/s (binary) MSK; smearing is due chiefly to filtering and hardlimiting. (Right) Discriminator output of General Electric Voyager cordless telephone, with four-level 2RC modulation at 16 kbit/s. Top eye is transmitted and bottom eye is as received with moderate filtering. (Courtesy W. Rafferty, GE Corporate Research and Development Center, Schenectady, New York.)

modulation, the pattern will have three eyes, one above the other, as shown also in Figure 2.12. These patterns can easily be generated in the field by connecting an oscilloscope to  $I(t)$  or  $Q(t)$  driven by random data and synchronizing the sweep circuit to the interval timing.

A little thought will show that if the eye(s) are open after front-end filtering as in the figures, then a receiver can perform correct detection simply by sampling  $I$  or  $Q$  at the most open part of the eye and comparing the sample to a set of threshold levels. Such a receiver would have no detection filter at all, aside from its front-end filter. A better design is to add a filter as in Figure 2.9, whose effect will be to average activity over the whole eye before sampling; the design of such a filter may be a complex task, to which we return in Section 2.6 and Chapter 8. It must be stressed that neither of these alternatives need give maximum likelihood detection since this detector does not generally have the linear receiver structure.

Adding channel noise to the waveforms that superpose to form the eye may close the eye further or even reverse the sign of a trace, which causes a detector error in Figure 2.9. Jittery interval timing reduces the total eye opening since certain waveforms are slipped to the left or right. The eye diagram is so useful because no matter what the source of these slips and smears, if the eye remains open over an extended time, error-free detection is likely to occur over that time.

In discussing eye diagrams, we have assumed that the channel filter or pulse shaper is causal and that the main lobe of its response to a pulse at

time  $n$  appears in interval  $n$ . The causality restriction can be removed by superposing waveforms generated by both past and future data symbols, not just past ones. If the main response lobe lies in another interval, then we simply observe the eye and perform the detection in that interval; i.e., at a delay from time  $n$ . Finally, it is tempting to believe that if the eye is “closed” with interference and noise, then consistently correct detection is impossible; but it must be stressed that this is true only for the *linear receiver*.

### 2.5.2. Channel Filter Effects on MSK and PSK

Filter theory tells us that a finite-duration signal must have infinite bandwidth; and, therefore, it is clear that all modulation schemes are somehow filtered. In practice filtering does not materially change phase modulation waveforms until the positive-frequency rf channel bandwidth narrows to 2–4 times  $1/T$ , the interval rate; for instance, a 1-Mbit/s pure BPSK system will not be affected until its bandwidth is constrained to below 1–2 MHz either side of the carrier frequency. For narrower filtering, the ISI increases and its effect in closing the eye diagram eventually exceeds that of the channel noise. In addition, the signal envelope acquires variations. If these pass through a later nonlinearity, they will be modified with a hard-to-assess effect on the signal phase and on the performance of receiver filters.

It is convenient to divide the average power spectral density (hereafter called the spectrum) of a modulation into two regions, the central main lobe and the lower sidelobes. The chief effect of the sidelobes is to interfere with neighboring channels and removal of the sidelobes is primarily a courtesy to them. The main lobe carries the main energy of the modulation; a simple rule of thumb is that filtering will strongly affect the modulation only when it invades the main lobe. Some measured spectra are shown in Figure 2.13 for MSK and BPSK. Figure 2.14 indicates the envelope variation that occurs when MSK and BPSK are filtered by a Chebychev channel filter with the double sideband RF bandwidths indicated. The effect on BPSK is much stronger because BPSK’s main lobe is wider and its side lobes are more prominent.

As the channel filter becomes narrower, ISI increases and more signal energy is required to combat the same level of channel noise. This extra energy for QPSK is plotted in Figure 2.15 as a function of  $(BT)^{-1}$ , where  $T$  is the symbol time and  $B$  is the double sideband RF bandwidth. The solid lines show the energy loss with the integrate and dump receiver of Figure 2.9, while the dashed lines show what happens when the integrator is replaced by a two-pole Butterworth filter having  $BT = 1$ . The figure shows Chebychev channel filters with growing numbers of poles; as the sharpness of the cutoff increases, so does the energy degradation. The losses in the

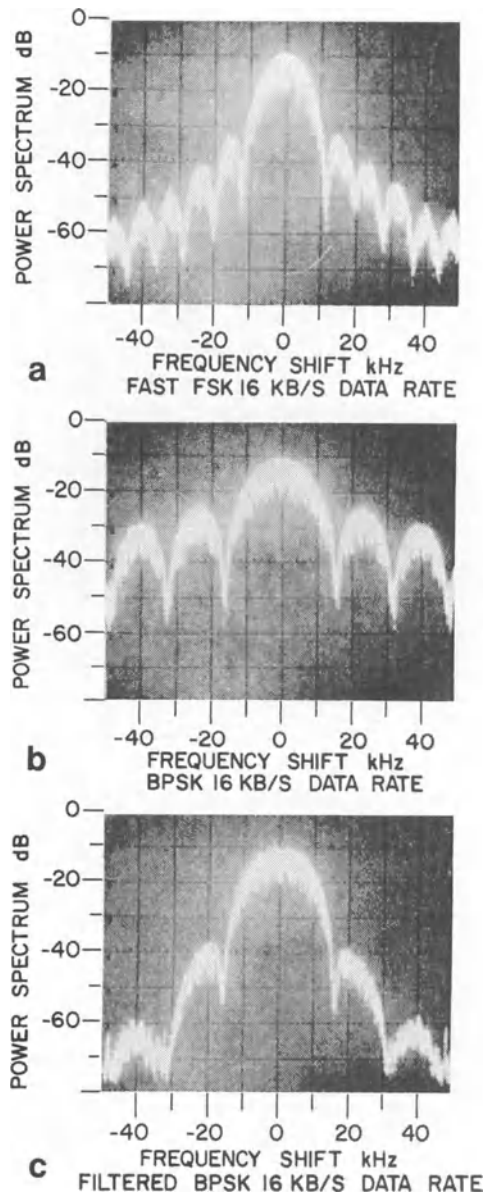


Figure 2.13. Measured spectra of selected modulations, all at 16 kbit/s:  
(a) MSK (also denoted Fast FSK),  
(b) BPSK, (c) BPSK filtered as in Figure 2.14, 30-kHz bandwidth four-pole filter. (Courtesy J. L. Pearce, Communications Research Centre, Government of Canada, Ottawa.)

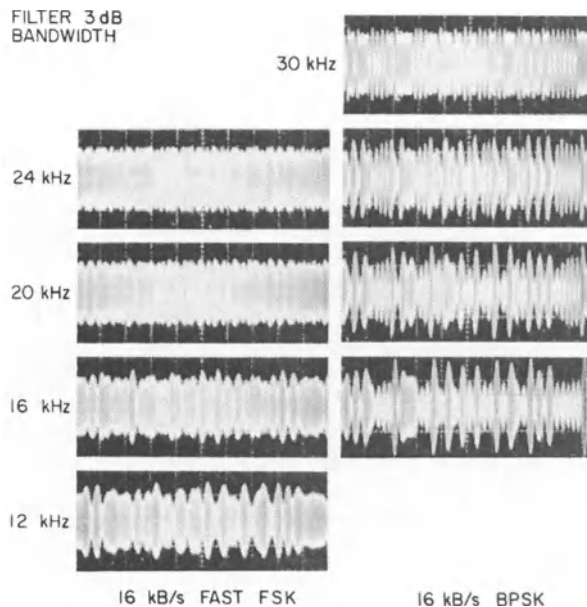


Figure 2.14. Envelope variations caused by filtering of MSK (left) and BPSK (right); 16 kbit/s schemes with Chebychev filter having 3-db double-sideband rf bandwidth indicated. (Courtesy J. L. Pearce, Communications Research Centre, Government of Canada, Ottawa.)

figure were computed analytically, but they do not differ much from experimental measurements.

The Butterworth receiver filter performs better than the integrate and dump because it is apparently closer to the optimal linear receiver filter for these bandlimited signals. An optimal filter would perform even better, and the best receiver structure to combat this channel filtering is not at all the

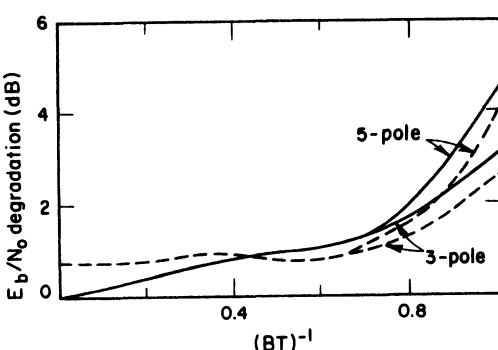


Figure 2.15. Increase of  $E_b/N_0$  required at  $P_e = 10^{-6}$  to combat the effect of Chebychev channel filters.  $B$  is double-sideband rf filter bandwidth;  $T$  is symbol duration. Solid lines represent  $I$  and  $D$  receive filter, dashed lines a two-pole Butterworth filter. (Reprinted from J. J. Jones, Filter distortion and inter-symbol interference effects on PSK signals, *IEEE Trans. Commun.*, COM 19, 120-132, April 1971, © 1971 IEEE.)

linear structure of Figure 2.9. (It is closer to the Viterbi algorithm of Chapter 7.) When  $(BT)^{-1}$  exceeds 0.7 or so, rapidly more signal energy is required. For a linear receiver, the eyes soon close and detection is impossible. In a 1-Mbit/s QPSK system, for instance,  $1/T$  is 500 kHz and degradation rapidly occurs inside a double sideband rf bandwidth of  $500 \text{ kHz}/0.7 = 710 \text{ kHz}$ ; at bandwidth 500 kHz, 3–6 dB extra signal energy is required to offset ISI effects. In a 1-Mbit MSK system these narrowband losses are somewhat greater, but losses in wider bandwidths are similar.

This discussion has illustrated the control of signal bandwidth by bandpass filtering the modulated rf carrier. An alternative is direct shaping of the  $I$  and  $Q$  pulse shapes. Chapters 3 and 4 show in detail the relation of signal energy and bandwidth to the pulse shape and duration, concentrating on shapings that leave the rf envelope constant. A simpler method of shaping  $I$  and  $Q$  is to require that they satisfy a zero-crossing criterion; a constant envelope cannot in general be guaranteed now. This simple and effective method finds wide use, and we turn to it next.

## 2.6. Nyquist-Pulse-Shaped PSK

If the sequence of baseband pulses are so arranged that the  $n$ th pulse passes through zero at every multiple of  $T$  except the  $n$ th, then the amplitude of the  $n$ th pulse can be deduced simply by sampling the total baseband waveform at time  $nT$ , and the data symbol carried by the pulse can be decided from this amplitude. Furthermore, it turns out that a version of the linear receiver exists which will perform maximum likelihood detection of the data. Many practical phase modulation systems are based on this *Nyquist-pulse* PSK.

### 2.6.1. Nyquist-Pulse PSK

A pulse satisfying the *Nyquist-pulse criterion* is one that passes through zero at times  $nT$  for some  $T$ , with  $n = \pm 1, \pm 2, \dots$ . An example of such a pulse is the  $\text{sinc}(\cdot)$  function

$$\text{sinc}(z) \triangleq \sin(\pi z)/\pi z \quad (2.27)$$

when  $z = t/T$ ;  $\text{sinc}(t/T)$  equals 1 at  $t = 0$  and equals 0 at all other integer multiples of  $T$ . Suppose now that a data sequence  $\{\alpha_i\}$  is carried by superposing Nyquist pulses in the manner

$$w(t) = \sum_{i=1}^n \alpha_i \text{sinc}[(t - iT)/T] \quad (2.28)$$

This is illustrated in Figure 2.16. The sinc ( ) pulses in the sum represent successive time shifts by  $T$ . The set of functions  $\{(1/T)^{1/2} \operatorname{sinc}[(t - iT)/T]\}$  are orthonormal since it can be shown that

$$\begin{aligned} \int_{-\infty}^{\infty} (1/T)^{1/2} \operatorname{sinc}[(t - iT)/T] (1/T)^{1/2} \operatorname{sinc}(t - jT)/T dt \\ = \begin{cases} 1, & i = j \\ 0, & \text{otherwise} \end{cases} \end{aligned}$$

As a consequence,

$$\int_{-\infty}^{\infty} w^2(t) dt = T \sum_{i=1}^n \alpha_i^2$$

and the signal  $s(t) = (E/T)^{1/2}w(t)$  has per-symbol energy  $E$  if we require that  $\mathbb{E}[\alpha_i^2] = 1$ .

The signal in (2.28) is a “pulse amplitude modulated” (PAM) signal. If two such PAM signals are applied to the baseband modulator of Figure 2.7, one to the  $I$  and one to the  $Q$  channel, we get an rf version of (2.28) shown in Figure 2.17. This is sinc-pulse-shaped QPSK; retention of the  $I$  channel only gives BPSK. The set of functions  $\{(2/T)^{1/2} \operatorname{sinc}[(t - nT)/T] \cos \omega_0 t\} \cup \{-(2/T)^{1/2} \operatorname{sinc}[(t - nT)/T] \sin \omega_0 t\}$  can be shown to be orthonormal for large  $\omega_0$ . As a consequence, the condition  $(\alpha_i^I)^2 + (\alpha_i^Q)^2 = 1$  implies that  $E$  is the total energy per  $T$  interval where  $\alpha^I$  and  $\alpha^Q$  are the in phase and quadrature data symbols. These symbols are like those in (2.17) except that we shall assign them the values  $\pm 1/\sqrt{2}$ .

A matched filter for  $\operatorname{sinc}(t/T)$  is a filter with this same impulse response [since  $\operatorname{sinc}( )$  is symmetric], and its output sample at time 0 is the correlation between  $+\operatorname{sinc}(t/T)$  and  $I(t)$  or  $Q(t)$ , denoted by  $\rho$  in Figure 2.17. As

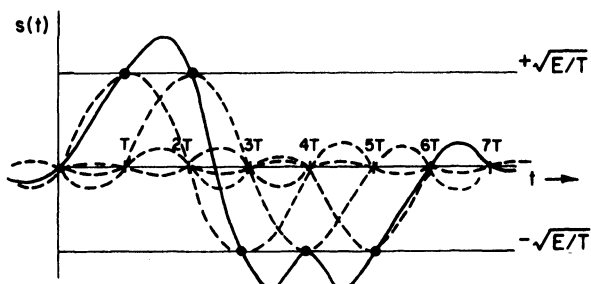


Figure 2.16. A superposition of Nyquist pulses; lighter lines are individual pulses, heavy line is their superposition. Heavy dots show waveform at sample times. Data sequence is  $+1, +1, -1, -1$ .

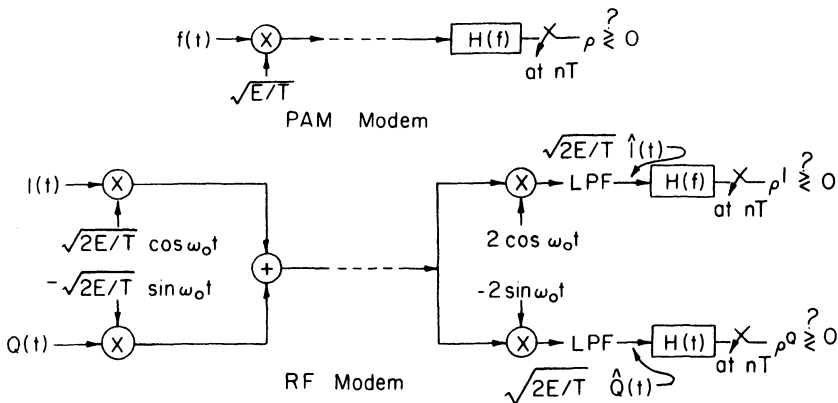


Figure 2.17. PAM and rf transmitter-receivers for pulse-shaped schemes; with Nyquist pulses, the receiver is maximum likelihood.

discussed in Section 2.1, comparison of these correlations to a threshold comprises a maximum likelihood receiver. The matched filter outputs will not be affected by pulses centered at any other multiple of  $T$  since successive pulses are orthogonal. In the spectral domain, the matched filters are perfect low-pass filters  $H(\cdot)$  with pass band  $(-1/2T, +1/2T)$ .

It is easy to show that the error probability of this receiver is the same as that of the pure QPSK receiver evaluated in Section 2.3. Consider the Nyquist QPSK signal

$$s_j(t) = \sum_{i=1}^n \alpha_i^I (2E/T)^{1/2} \operatorname{sinc} [(t - iT)/T] \cos \omega_0 t - \sum_{i=1}^n \alpha_i^Q (2E/T)^{1/2} \operatorname{sinc} [(t - iT)/T] \sin \omega_0 t \quad (2.29)$$

where  $\alpha_i = \pm 1/\sqrt{2}$ . As in Section 2.3, the closest signal to  $s_j(t)$  is the one with a single data symbol reversed, either an  $\alpha_i^I$  or an  $\alpha_i^Q$ . In the latter case, the signal space square distance is

$$\begin{aligned} \|s_j(t) - s_k(t)\|^2 &= \int_{-\infty}^{\infty} [s_j(t) - s_k(t)]^2 dt \\ &= \int_{-\infty}^{\infty} [(2/\sqrt{2})(2E/T)^{1/2} \operatorname{sinc} [(t - iT)/T] \sin \omega_0 t]^2 dt = 2E \end{aligned} \quad (2.30)$$

As defined in Section 2.2.3, the normalized Euclidean distance  $d(s_j(t), s_k(t))$  is related to this distance by  $2E_b d^2 = E$ .  $E_b$ , the energy per data bit, is  $E/2$  since a signal  $s(t)$  in (2.29) carries  $2n$  bits and has total energy  $\|s(t)\|^2 = nE$ . Thus  $d^2 = 2$ . We then can substitute  $d$  into (2.20) to obtain the bound  $2nQ[d(E_b/N_0)^{1/2}]$  on the probability that an error occurs anywhere among the  $2n$  bits carried by (2.29). To bound the probability of a single bit being in error, we set  $n$  to 1 and obtain  $Q[d(E_b/N_0)^{1/2}]$ .

### The Nyquist PSK Spectrum

The Fourier transform of the pulse  $(1/T)^{1/2} \operatorname{sinc}(t/T)$  is

$$\begin{cases} T^{1/2}, & -1/2T < f < 1/2T \\ 0 & \text{otherwise} \end{cases}$$

and for the rf pulses the transforms are

$$(2/T)^{1/2} \operatorname{sinc}(t/T) \cos \omega_0 t: \begin{cases} (T/2)^{1/2}, & -1/2T < f - f_0 < 1/2T \\ 0 & \text{otherwise} \end{cases}$$

$$-(2/T)^{1/2} \operatorname{sinc}(t/T) \sin \omega_0 t: \begin{cases} j(T/2)^{1/2}, & -1/2T < f - f_0 < 1/2T \\ -j(T/2)^{1/2}, & -1/2T < f + f_0 < 1/2T \\ 0 & \text{otherwise} \end{cases}$$

The  $\cos(\omega_0 t)$  transform is shown in Figure 2.18. The transform of (2.29) is a superposition of  $n$  phase shifts of these transforms in such a way that the individual transform energies add. The result is a spectrum whose magnitude is  $(nET/2)^{1/2}$  over the intervals  $(f_0 - 1/2T, f_0 + 1/2T)$  and  $(-f_0 - 1/2T, -f_0 + 1/2T)$ , and zero elsewhere; the total energy in the spectrum is  $nE$ . The phase angle of the spectrum depends on the composition of the data sequence. [We can note that a similar argument gives the power spectral density of pure QPSK; for it, the  $\operatorname{sinc}( )$  pulses in (2.29) are replaced by rectangular pulses and the energies of separate intervals again add orthogonally. The result is (4.37).]

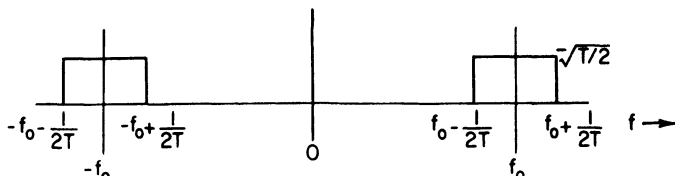


Figure 2.18. Fourier transform of the orthonormal basis function  $(2/T)^{1/2} \operatorname{sinc}(t/T) \cos \omega_0 t$  used in Nyquist QPSK. Note  $f_0 = \omega_0/2\pi$ .

The spectral occupancy of the  $\text{sinc}(\cdot)$  pulse is, in fact, the narrowest of any pulse that satisfies the Nyquist pulse criterion, as a consequence of the *Nyquist sampling theorem*. Suppose that  $g(t)$  is a continuous function that we wish to represent by samples taken every  $T$  seconds. An example is  $s(t)$  in (2.28), where the samples are evidently the data symbols  $\alpha_i$ . Then the theorem says that such samples can be obtained if and only if the sampling rate  $1/T$  is greater than or equal to twice the positive-frequency bandwidth of  $g(t)$ . As a consequence, the data symbols in (2.28) cannot be obtained from  $s(t)$  unless its single-sided bandwidth exceeds  $1/2T$ , or translated to rf, unless its occupancy exceeds  $1/T$ .

In the proof of the sampling theorem it develops that only  $\text{sinc}(\cdot)$  pulses allow the minimum bandwidth. Other pulses that satisfy the pulse criterion will allow  $g(t)$  to be recovered from samples—or in our case, for data symbols to be recovered from  $s(t)$ —but the bandwidth of  $s(t)$  will be larger than  $1/2T$ . We turn now to the most commonly used such class of pulses.

### 2.6.2. Raised Cosine Nyquist Pulses

Using  $\text{sinc}(t/T)$  to carry data leads to a number of difficulties. The pulse is of infinite time duration and is noncausal. In practice, however,  $\text{sinc}(t/T)$  can be truncated to a total width of 10 or so intervals and then delayed for half this width to produce a causal pulse with sufficiently good spectral properties. A more serious problem is the rate of decay of the sidelobes of  $\text{sinc}(t/T)$  in the time domain, which is only of order  $1/(t/T)$ . If the sampling instant in Figure 2.17 wanders somewhat from time  $nT$ , then the sample of  $s(t)$  in (2.28) will contain contributions from many pulses instead of just the  $n$ th. These spurious contributions could be reduced if the pulse sidelobes could be made to decay faster. As well, the time-truncated version of the pulse would be a more accurate representation.

A common approach to these difficulties is to replace the  $\text{sinc}(\cdot)$  pulse generation filter, which at baseband is a perfect low pass filter with a spectral raised-cosine filter as shown at baseband in Figure 2.19. The equation of

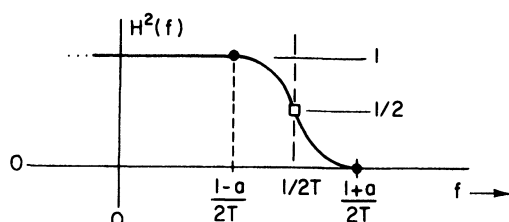


Figure 2.19. Spectral raised-cosine filter response. Response is symmetric about zero hertz; an antisymmetry exists about the point  $(1/2T, 1/2)$  in the plane.

$H^2(f)$  is

$$H^2(f) = \begin{cases} 1; & 0 < |f| < (1-a)/2T \\ \cos^2 \left[ \frac{\pi T}{2a} \left( f - \frac{1-a}{2T} \right) \right], & (1-a)/2T < |f| < (1+a)/2T \\ 0 & \text{elsewhere} \end{cases} \quad (2.31)$$

where the pass band again has been normalized to unity for convenience; this function is symmetrical about the point in the plane  $(1/2T, 1/2)$  which is denoted by the square dot in the figure. The bandwidth of a pulse generated by  $H$  exceeds the bandwidth of  $\text{sinc}(t/T)$  by the factor  $1+a$ ;  $a$  is called the excess bandwidth factor and the pulses themselves are called excess bandwidth pulses. Raised cosine pulses may exceed the  $\text{sinc}(\cdot)$  bandwidth by up to 100%, and it can be shown that the rate of decay of the temporal side lobes is proportional to the factor  $a$ . The usage of raised cosine here is not to be confused with that in Chapter 3 where it refers to the shaping of a *phase* response.

For pulses formed by  $H$  satisfying (2.31), we can show that the linear receiver with receive filter equal to the same  $H$  is a maximum likelihood receiver for these signals. In fact, this can be shown for any  $H$  for which  $H^2(f)$  is symmetrical about the square dot in Figure 2.19. Specifically, we can show that

- i. All filters with  $H^2$  symmetrical about  $(1/2T, 1/2)$  in the sense of Figure 2.19 satisfy the Nyquist pulse criterion;
- ii. The energy of all these pulses, including the  $\text{sinc}(t/T)$  pulse, is the same, and all are symmetric;
- iii. The pulse  $h(t)$  generated by  $H$  is orthogonal to all time shifts of the form  $h(t - nT)$ ,  $n \neq 0$ ;
- iv. The modulation power spectrum consists of replicas of  $H^2(f)$  centered at  $\pm\omega_0/2\pi$ .

To prove result (iii), we can write

$$\int_{-\infty}^{\infty} h(t)h(t - nT) dt = \int_{-\infty}^{\infty} H(f)[H(f) e^{+j2\pi fnT}] df$$

where the equality follows from the generalized Parseval identity. The right-hand side must then be

$$= \int H^2(f) \cos(2\pi fnT) df$$

since the imaginary part of the integral is zero. By consideration of the symmetries of  $H^2$  and  $\cos(2\pi fnT)$ , it can be shown that this last integral is zero. Results (i) and (ii) follow by similar reasoning, and result (iv) follows from (iii).

To show that the linear receiver is maximum likelihood, we proceed as before with sinc( ) pulse transmission, creating the signals of the form (2.29) with  $h( )$  replacing sinc( ), and calculating the distance to the closest neighboring signal exactly as in (2.30), which follows from (iii) above. The receive filter  $H(f)$ , sampled at  $t = nT$ , forms a matched filter receiver for the pulse  $h(t - nT)$  since  $h$  is symmetric and centered at  $nT$  and since the sample at this time contains no contributions from other shifts of  $h$  by  $T$ . Consequently, the probability that a bit is in error is  $Q((2E_b/N_0)^{1/2})$ , as it was with sinc( ) pulses or with pure QPSK.

In a practical system, the filter  $H$  is approximated by a 6–12 pole filter. Filters with excess bandwidth factors larger than  $a = 0.3$  are relatively easy to realize. A 1-Mb/s QPSK system, with  $1/T = 500$  kHz, occupies the double sideband rf bandwidth

$$2(1 + a)(1/2T) = 650 \text{ kHz}$$

for  $a = 0.3$ . This compares to approximately 710 kHz given at the end of Section 2.5 for the last small-loss bandwidth of a pure QPSK signal that is subsequently filtered and detected with an integrate and dump filter. This latter transmission scheme is simpler because it does not require a carefully designed pulse shaping filter and matching receive filter, but it does require an increase in  $E_b$  for the same error performance. The pure QPSK scheme, if it is allowed somewhat more bandwidth, is also close to constant-envelope, while Nyquist-pulse QPSK has a markedly varying envelope. One of our aims in Chapter 3 will be to find a scheme that is both narrow band and constant envelope. Such a scheme will employ more complex pulses and it cannot employ a linear receiver without heavy losses.

## 2.7. A Summary of Modulation Methods

We will now list the important phase modulation formats and terminologies, together with a single-formula or single-sentence explanation of each. The intent is to compile a quick reference list, with details covered elsewhere. The last will be divided into two parts, quadrature methods and continuous-phase modulation (CPM) methods. A format can often be explained in several ways; in particular, a CPM scheme with modulation index 1/2, like MSK, can also be viewed as a quadrature scheme.

### 2.7.1. Quadrature Modulation Schemes

A quadrature scheme can be realized by a circuit like that of Figure 2.7 or 2.9, having in-phase and quadrature signals  $I(t)$  and  $Q(t)$  that multiply  $\cos \omega_0 t$  and  $\sin \omega_0 t$ . These schemes are discussed in Sections 2.4–2.6; the modulated signal satisfies

$$s(t) = (2E/T)^{1/2}[I(t)\cos \omega_0 t - Q(t)\sin \omega_0 t] \quad (2.32)$$

with the constraint (2.22).

**Pure QPSK:** During the  $n$ th symbol interval this scheme is defined by

$$(2E/T)^{1/2}[(1/\sqrt{2})\alpha_n^I \cos \omega_0 t - (1/\sqrt{2})\alpha_n^Q \sin \omega_0 t], \quad nT < t \leq (n+1)T \quad (2.33)$$

where the data symbols  $\alpha_n^I$  and  $\alpha_n^Q$  are both equal  $\pm 1$  and  $E$  is the energy in the 4-ary symbol made up of both  $\alpha$ 's. The signal (2.33) occupies one of the four phases ( $45^\circ$ ,  $135^\circ$ ,  $225^\circ$ ,  $315^\circ$ ) during the entire interval. Pure QPSK is discussed in Sections 2.3 and 2.4, and its spectrum is given in (4.37).

**Pure BPSK:** This is defined by

$$(2E/T)^{1/2}\alpha_n \cos \omega_0 t, \quad nT < t < (n+1)T \quad (2.34)$$

with the data symbol  $\alpha_n$  equal  $\pm 1$  and  $E$  now the energy of a binary transmitted symbol. The signal occupies one of the two signal phases ( $0^\circ$  and  $180^\circ$ ). The detection and spectral properties of BPSK are discussed along with those of QPSK.

**Nyquist PSK:** This is the QPSK of (2.33) in which the rectangular waveform of data symbols has been shaped by pulses  $h(t)$  whose transform satisfies (2.31), a spectrum with a cosine roll-off. Nyquist PSK is discussed in Section 2.6. The signal is

$$(2E/T)^{1/2} \sum_n [(T/\sqrt{2})\alpha_n^I h(t-nT) \cos \omega_0 t - (T/\sqrt{2})\alpha_n^Q h(t-nT) \sin \omega_0 t]$$

**Differential PSK (DPSK):** In a differential scheme, the change from interval to interval is transmitted instead of the actual values of the data symbols. DPSK is BPSK in which the symbols in (2.34) have been encoded by the transformation

Data  $(\alpha_{n-1}, \alpha_n) = (+1, +1)$  or  $(-1, -1)$ : send  $\alpha_n = +1$  in (2.34)

Data  $(\alpha_{n-1}, \alpha_n) = (+1, -1)$  or  $(-1, +1)$ : send  $\alpha_n = -1$  in (2.34)

DPSK may be detected by a special *differential detector* circuit in such a way that a separate carrier acquisition circuit is not needed. The DPSK spectrum is the same as that of BPSK, as is the detection efficiency in the limit of large  $E_b/N_0$ . Extensions to  $M$ -ary PSK exist, but here there is a definite loss in the detector. Differential detection is discussed in Section 8.5 of Chapter 8; for a treatment specifically on DPSK, see Ref. 15.

**2-4PSK:** This is another type of differential encoding in which the sum of all the binary data symbols up to the  $n$ th is converted to a multiple of  $\pi/2$  and sent in pure-QPSK fashion. Rather than an  $I$ - $Q$  formula, it is easier to visualize this modulation in the form

$$(2E/T)^{1/2} \cos \left[ (\pi/2) \left( \sum_{i=0}^n \alpha_i \right) + \omega_0 t \right], \quad nT < t < (n+1)T \quad (2.35)$$

The phases visited are those of QPSK, but only one binary symbol is transmitted in each interval. An advantage of 2-4PSK is that  $180^\circ$  transitions never occur (see OQPSK). 2-4PSK and some generalizations are discussed in Dupontel.<sup>(16)</sup>

**Offset QPSK (OQPSK):** In an offset scheme, the quadrature signal  $Q(t)$  is delayed by  $T/2$  relative to  $I(t)$ . Thus, (2.33) becomes for OQPSK

$$\begin{aligned} & (2E/T)^{1/2} [(1/\sqrt{2})\alpha_n^I \cos \omega_0 t - (1/\sqrt{2})\alpha_{n-1}^Q \sin \omega_0 t], \\ & \quad nT \leq t < (n+1/2)T \\ & (2E/T)^{1/2} [(1/\sqrt{2})\alpha_n^I \cos \omega_0 t - (1/\sqrt{2})\alpha_n^Q \sin \omega_0 t], \\ & \quad (n+1/2) \leq t < (n+1)T \end{aligned} \quad (2.36)$$

The OQPSK phase tree resembles a wall made of bricks in which alternate rows are offset by a half brick. Because of the orthogonality of the  $I$  and  $Q$  channels, neither the AWGN detection probability nor the spectrum of QPSK is affected by this offsetting. However, the modulated OQPSK signal has no  $180^\circ$  phase shifts, unlike QPSK, and therefore keeps a much more constant envelope under amplitude limiting and filtering. An OQPSK receiver is simply Figure 2.9 with the  $Q$ -channel sampler operating at  $t = (n+1/2)T$ . Further details appear in Refs. 15 or 17.

**Minimum Shift Keying (MSK), or Fast FSK:** The different names of this scheme are sometimes used to connote implementation variants; in this book we will consider them the same scheme. It is easiest to visualize MSK as a CPM scheme (see Section 2.7.2), but it can also be viewed as an offset quadrature scheme. Instead of the rectangular rf pulse shaping that occurs in OQPSK, MSK has sinusoidal pulse shaping. Viewed as a CPM scheme, MSK is a binary modulation with symbol interval  $T$ ; but as a quadrature

scheme, it is a quaternary modulation over a double interval  $2T$ . Following the survey article by Pasupathy,<sup>(17)</sup> we divide the binary data stream  $\{\alpha_n\}$  into even and odd symbols and create  $I$  and  $Q$  pulse waveforms from the two streams:

$$\text{For even } n, \quad a_I(t) = \alpha_n, \quad (n-1)T < t \leq (n+1)T$$

$$\text{For odd } n, \quad a_Q(t) = \alpha_n, \quad (n-1)T < t \leq (n+1)T$$

The MSK signal is then

$$s(t) = (2E/T)^{1/2} [a_I(t) \cos(\pi t/2T) \cos \omega_0 t + a_Q(t) \sin(\pi t/2T) \sin \omega_0 t] \quad (2.37)$$

It can be shown that (2.37) is a constant-envelope signal; Figure 2.20 demonstrates how this occurs. MSK is discussed throughout the book, but particularly in Sections 2.3, 4.3 (spectrum), and 8.3 and 8.4 (special receivers).

### 2.7.2. CPM Schemes

In these modulations, the rf signal envelope is constant and phase varies in a continuous manner. All CPM signals are described by

$$s(t) = (2E/T)^{1/2} \cos \left[ \omega_0 t + 2\pi \sum_{i=0}^n \alpha_i h_i q(t - iT) \right], \quad nT < t < (n+1)T \quad (2.38)$$

The data  $\{\alpha_n\}$  are  $M$ -ary data symbols,  $M$  even, taken from the alphabet  $\pm 1, \pm 3, \dots, \pm(M-1)$ ;  $h_i$  is a modulation index, which may vary from interval to interval;  $q(\cdot)$  is the phase response function. CPM schemes are denoted by their phase response function or by its derivative  $g(\cdot)$ , the frequency response function. The most important schemes are listed in Table 2.1 together with their frequency responses. The prefix "L," where it occurs, denotes the length of the response.

The meaning of the abbreviations is

*LRC*—raised cosine, pulse length  $L$ ;

*LSRC*—spectral raised cosine, length  $L$ ;

*LREC*—rectangular frequency pulse, length  $L$ ;

*TFM*—tamed FM;

*GMSK*—Gaussian-shaped MSK.

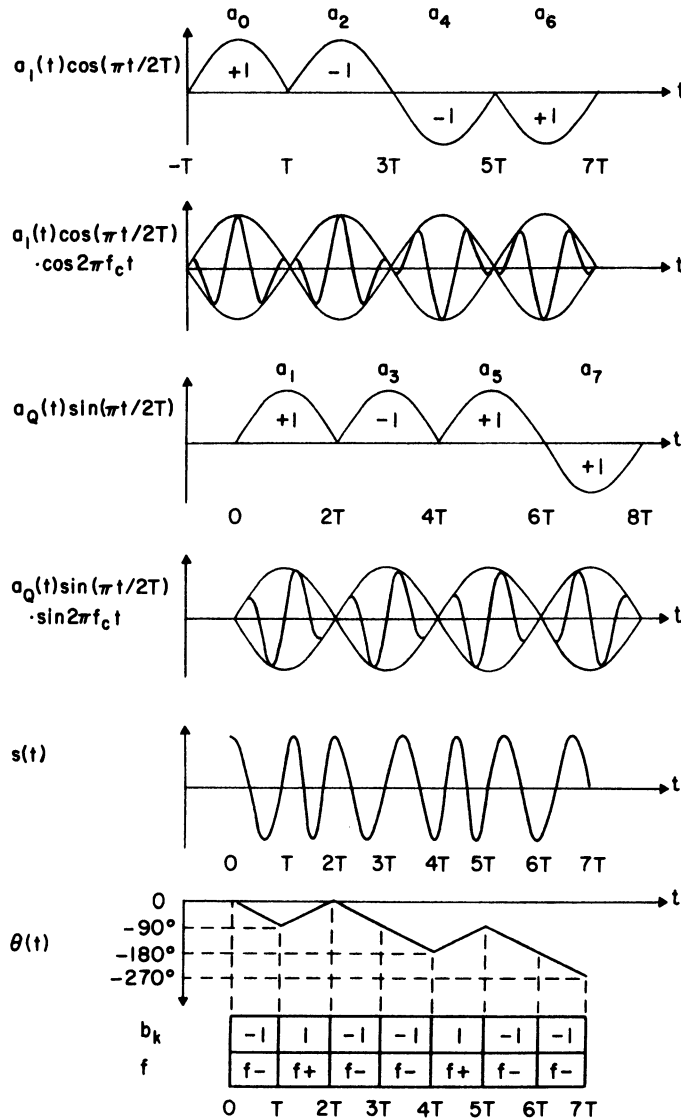


Figure 2.20. The offset quadrature view of MSK.  $T$  is the symbol interval of MSK viewed as a binary modulation;  $b_k$  are the symbols in the CPM view of the scheme. (From Pasupathy,<sup>(17)</sup> © 1979 IEEE.)

**Table 2.1. Definition of Frequency Pulses Referred to in Section 2.7**

LRC	$g(t) = \begin{cases} \frac{1}{2LT} \left[ 1 - \cos \left( \frac{2\pi t}{LT} \right) \right], & 0 \leq t \leq LT \\ 0 & \text{otherwise} \end{cases}$
TFM	$g(t) = \frac{1}{8} [g_0(t-T) + 2g_0(t) + g_0(t+T)]$ $g_0(t) \approx \frac{1}{T} \left[ \frac{\sin \left( \frac{\pi t}{T} \right)}{\frac{\pi t}{T}} - \frac{\pi^2}{24} \frac{2 \sin \left( \frac{\pi t}{T} \right) - \frac{2\pi t}{T} \cos \left( \frac{\pi t}{T} \right) - \left( \frac{\pi t}{T} \right)^2 \sin \left( \frac{\pi t}{T} \right)}{\left( \frac{\pi t}{T} \right)^3} \right]$
LSRC	$g(t) = \frac{1}{LT} \frac{\sin \left( \frac{2\pi t}{LT} \right) \cos \left( \beta \frac{2\pi t}{LT} \right)}{\frac{2\pi t}{LT} - 1 - \left( \frac{4\beta}{LT} t \right)^2}, \quad 0 \leq \beta \leq 1$
GMSK	$g(t) = \frac{1}{2T} \left\{ Q \left[ 2\pi B_b \frac{t - \frac{T}{2}}{(\ln 2)^{1/2}} \right] - Q \left[ 2\pi B_b \frac{t + \frac{T}{2}}{(\ln 2)^{1/2}} \right] \right\}$ $Q(t) = \int_t^\infty \frac{1}{(2\pi)^{1/2}} e^{-\tau^2/2} d\tau$
LREC	$g(t) = \begin{cases} \frac{1}{2LT}, & 0 \leq t \leq LT \\ 0 & \text{otherwise} \end{cases}$

The parameters  $B_b$  in GMSK and  $\beta$  in LSRC are arbitrary and are set to obtain desired distance or spectral properties.

Certain terminology is used with these pulses.

*Multi-h Modulations:* When  $h_i$  varies from interval to interval, a scheme is called multi- $h$ ; otherwise,  $h$  is assumed to be fixed. Generally, a multi- $h$  scheme is one in which  $h_i$  moves cyclically through a set of indices.

*Full vs. Partial Response CPM:* A full response CPM modulation is one whose frequency pulse lasts one signal interval; the most important such schemes are the 1RC and 1REC modulations. Otherwise, the scheme is partial response.

*CPFSK (Continuous Phase FSK):* This is an alternate name for the 1REC family. CPFSK signals are continuous and signal alternatives in a symbol interval are not generally orthogonal unless  $h$  is a multiple of 1/2, unlike FSK schemes of the 1960s, which often were orthogonal and discontinuous. When  $h = 1/2$ , the CPFSK scheme is MSK. Figure 2.20 illustrates

a possible mapping from the data symbols used in the quadrature view of Section 2.7.1 to the symbols in (2.38), which are given the symbol  $b_k$  in Figure 2.20. The value of  $b_k$  at time  $t$  is  $-a_I(t)a_Q(t)$ . Viewed as a CPFSK scheme, MSK is a binary modulation.

**Truncated Pulse CPM:** The GMSK, TFM, and SRC frequency pulses are of infinite time duration and are, therefore, time-truncated in time-domain implementations. The abbreviations GMSKL<sub>T</sub>, TFML<sub>T</sub>, and LSRCL<sub>T</sub> denote these schemes where the frequency pulse  $g(t)$  is truncated to be nonzero for  $L_T$  intervals.

**CORPSK (Correlative PSK) or G-MSK (Generalized MSK):** These terms refer in a general way to PSK, MSK, or even CPM, in which the data symbols have been pre-encoded before modulation. The pre-encoding is effected with a short finite impulse response digital filter. Equivalencies sometimes exist to schemes of the form (2.38).

Chapter 3 discusses the minimum distances of CPM schemes and Chapter 4 discusses their spectra. Additional material on time-truncated schemes appears in Section 8.2.3.

## References

1. R. E. Ziemer and W. H. Tranter, *Principles of Communications*, Houghton Mifflin, Boston (1976).
2. C. W. Helstrom, *Probability and Stochastic Processes for Engineers*, Macmillan, New York (1984).
3. A. Papoulis, *Probability, Random Variables, and Stochastic Processes*, McGraw-Hill, New York (1965).
4. H. L. Van Trees, *Detection, Estimation, and Modulation Theory*, Vol. I, Wiley, New York (1968).
5. J. M. Wozencraft and I. M. Jacobs, *Principles of Communications Engineering*, Wiley, New York (1965).
6. P.-O. Borjesson and C.-E. Sundberg, Simple approximation of the error function  $Q(x)$  for communications applications, *IEEE Trans. Commun.* COM-27, 639–643 (1979).
7. G. D. Forney, Jr., Maximum likelihood sequence estimation of digital sequences in the presence of intersymbol interference, *IEEE Trans. Inf. Theory* IT-18, 363–378 (1972).
8. G. Ungerboeck, Adaptive maximum-likelihood receiver for carrier-modulated data-transmission systems, *IEEE Trans. Commun.* COM-23, 624–636 (1974).
9. R. deBuda, Coherent demodulation of frequency-shift keying with low deviation ratio, *IEEE Trans. Commun.* COM-20, 429–436 (1972).
10. M. L. Doelz and E. T. Heald, Minimum-shift data communication system, U.S. Patent 2,977,417, March 28, 1961.
11. M. G. Pelchat, R. C. Davis, and M. B. Luntz, Coherent demodulation of continuous phase binary FSK signals, Proc., International Telemetering Conference, pp. 181–190, Washington, D.C., 1971.
12. W. P. Osborne and M. B. Luntz, Coherent and noncoherent detection of CPFSK, *IEEE Trans. Commun.* COM-22, 1023–1036 (1974).

13. T. A. Schonhoff, Symbol error probabilities for  $M$ -ary coherent continuous phase frequency-shift keying (CPFSK), Conference Record, International Conference on Communications, pp. 34.5–34.8, San Francisco, California, 1975.
14. H. L. Krauss, C. W. Bostian, and F. H. Raab, *Solid State Radio Engineering*, Wiley, New York (1980).
15. V. K. Bhargava, D. Haccoun, R. Matyas, and P. P. Nuspl, *Digital Communications by Satellite*, Wiley, New York (1981).
16. D. Dupontel, Binary modulations for digital satellite communications link with differential demodulation, Conference Record, Fifth Internal Conference Digital Satellite Communications, Genoa, Italy, pp. 89–98, March 1981.
17. S. Pasupathy, Minimum shift keying: A spectrally efficient modulation, *IEEE Commun. Mag. July*, 14–22 (1979).

## Error Performance

For most digital communication systems, it is of vital importance that the transmitted symbols are detected as reliably as possible at the receiver end, given a specific SNR. A natural and commonly used criterion of goodness among communication engineers is the symbol error probability, which should be minimized. The ultimate conditions under which error probability may be reduced to zero were set up by Shannon,<sup>(1)</sup> and problems of this kind will be further elaborated upon in Chapter 5. What is important here is that Shannon dealt with what are called random codes, whereas we now deal with exact deterministic systems. We also impose the further constraint that the transmitted signal always has a constant envelope.

Even though the systems treated here are exactly defined, the symbol error probability is in most cases beyond our capability to calculate. Instead the union bound introduced in the previous chapter will be used. Furthermore, only large SNR will be considered for which we have

$$P_e \sim Q \left( \left( d_{\min}^2 \frac{E_b}{N_0} \right)^{1/2} \right)$$

as in (2.20a)–(2.20c) of Section 2.2. This one-parameter description of the detection efficiency in terms of  $d_{\min}^2$  greatly simplifies the search for reliable data communication systems, and this chapter deals exclusively with  $d_{\min}^2$ . The plan of the chapter is to first define an upper bound to  $d_{\min}^2$ , called  $d_B^2$ , which will give the overall dependence of distance on the modulation system parameters. We will study this bound for full and partial response modulations, and for systems with both a single modulation index and several indices. Next we will calculate the actual  $d_{\min}^2$ ; it will turn out that  $d_{\min}^2$  is the same as  $d_B^2$ , so long as the observation time of the signals is long enough, except at certain “weak” combinations of parameters.

Next we will develop a state description for modulated signals. This will be used to obtain more accurate error bounds than (2.20a)–(2.20c), and it will find use later in the book, especially in receiver design. Last, we study the effect on  $d_{\min}^2$  of channel filtering and hard limiting. Throughout the chapter we assume the detector is the idealized maximum likelihood (ML) detector of Chapter 2. In studying  $d_{\min}^2$ , we are characterizing the *energy* consumption of ML-detected signals. Chapter 4 will study their bandwidth consumption.

### 3.1. System Definition

It will be convenient to specialize the notations of Chapter 2 slightly and define the transmitted signal as

$$s(t, \alpha) = \left(\frac{2E}{T}\right)^{1/2} \cos [2\pi f_0 t + \phi(t, \alpha) + \phi_0] \quad (3.1)$$

which has a constant amplitude and carries the information in the phase

$$\phi(t, \alpha) = 2\pi \sum_i \alpha_i h_i q(t - iT) \quad (3.2)$$

$\alpha = \dots, \alpha_{-2}, \alpha_{-1}, \alpha_0, \alpha_1, \alpha_2$  is an infinitely long sequence of independent and identically distributed  $M$ -ary data symbols, each taking one of the values

$$\alpha_i = \pm 1, \pm 3, \dots, \pm(M-1), \quad i = 0, \pm 1, \pm 2, \dots$$

with equal probability  $1/M$ .  $M$  will be assumed to be a power of 2 also, but this is not necessary.  $\phi_0$  is an arbitrary constant phase shift which without loss of generality can be set to zero in the case of coherent transmission. This is assumed here. This kind of modulation will be called continuous phase modulation, or CPM, after Aulin,<sup>(15)</sup> or Aulin and Sundberg.<sup>(16)</sup>

The sequence of real constants  $\dots, h_{-2}, h_{-1}, h_0, h_1, h_2, \dots$  are the modulation indices, and the underlined subscript in equation (3.2) means that they appear modulo  $H$ . This means that only  $H$  different constants are used in a cyclical fashion, i.e.  $\dots, h_0, h_1, h_2, \dots, h_{H-1}, h_0, h_1, h_2, \dots$ . These constants are modulation indices. When  $H = 1$ , there is only one modulation index  $h_0$ , which we shall denote  $h$ .

The function  $q(t)$  is the phase response of (2.17), which is obtained from the frequency pulse  $g(t)$  through the relation

$$q(t) = \int_{-\infty}^t g(\tau) d\tau \quad (3.3)$$

It is assumed that the pulse  $g(t)$  is of finite duration, occupying the interval  $[0, LT]$ . For normalization purposes the pulse  $g(t)$  integrates to  $1/2$ . Several examples of frequency pulses  $g(t)$  and their corresponding phase responses  $q(t)$  appeared in Chapter 2.

The transmitted signal can be viewed as being either frequency or phase modulated, with  $g(t)$  acting as an instantaneous frequency smoother and  $q(t)$  as an instantaneous phase smoother. This is illustrated in Figure 3.1, which shows a block diagram of the transmitter. For the purposes of this chapter the phase modulation approach is the preferred one.

Next we consider the detector. The received signal is  $r(t) = s(t, \alpha) + n(t)$ , where  $n(t)$  is the AWGN of Chapter 2. The detector is coherent with perfect synchronization. This means that  $f_0$  and  $\phi_0$  in equation (3.1) are known constants and that the data symbol transition instants  $\dots, -T, 0, T, \dots$  are also known exactly.

Owing to the fact that the phase response  $q(t)$  in equation (3.3) in general is of infinite duration (equal to  $1/2$  for  $t > LT$ ), the phase of the transmitted signal in any particular symbol interval depends not only upon the present data symbol, but also upon all the previous data symbols. In most cases it will also be assumed that the phase  $\phi(t, \alpha)$  is a continuous

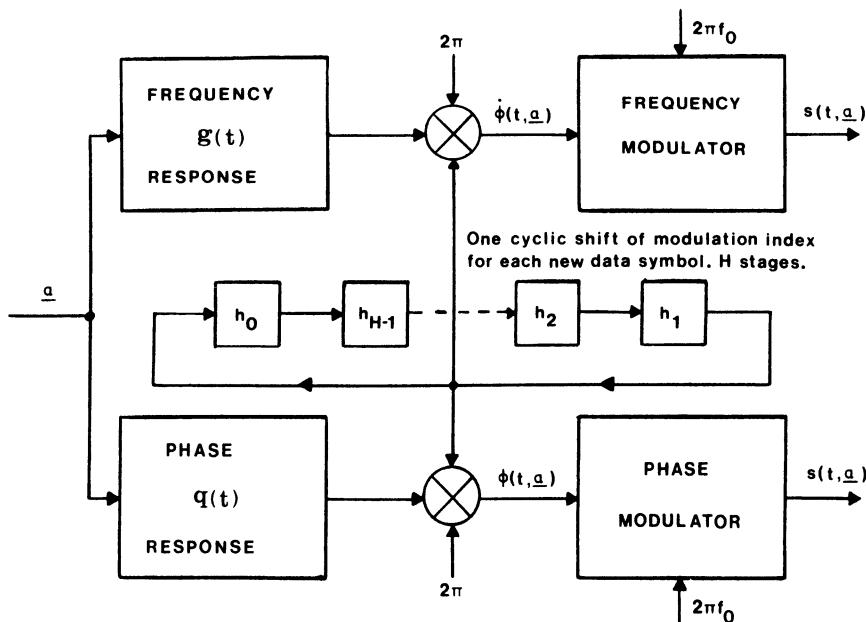


Figure 3.1. A general transmitter block diagram; the upper arm is a frequency modulator, the lower a phase modulator. Both signals are identical. From Ref. 44, © 1984 by John Wiley (UK) Ltd.

function of time, i.e., the frequency pulse contains no impulses. The consequence of this infinite memory in the transmitted signal is that an optimum ML detector must observe many symbol intervals in order to optimally detect a specific data symbol. Actually, the whole sequence of data symbols most likely to have been transmitted must be found. This is called Maximum Likelihood Sequence Detection (MLSD), a very complex procedure in general, both in its implementation and analysis. Instead, the problem of detecting *one* of the data symbols, say  $\alpha_0$ , optimally in the ML sense can be considered. It is assumed that all the data symbols prior to this one have been detected correctly (or are known), and that the receiver is allowed to observe the signal

$$r(t) = s(t, \alpha) + n(t), \quad 0 \leq t \leq NT \quad (3.4)$$

over  $N$  symbol intervals. If we let  $N \rightarrow \infty$  it is clear that  $\alpha_0$  is being detected optimally in the MLSD sense when  $q(t)$  is causal. Further discussion of this point appears in Pelchat *et al.*<sup>(2)</sup> or Osborne and Luntz.<sup>(3)</sup>

For large SNR this one-symbol ML detector correlates the received signal with all the possible transmitted signals over the interval  $[0, NT]$  by a bank of  $M^N$  matched filters or an equivalent method of Section 2.1. The filter giving the best estimated correlation is found, and the first data symbol corresponding to the  $N$  symbol long correlation is taken as the detected data symbol  $\tilde{\alpha}_0$ .

It should be noted that this detector in general only achieves ML detection of the single data symbol  $\alpha_0$ . Assume for instance that the data symbol  $\alpha_1$  is to be detected in the same manner as  $\alpha_0$  and that  $\tilde{\alpha}_0$  is available for this purpose. If  $\tilde{\alpha}_0 = \alpha_0$  there will be no problem, but if  $\tilde{\alpha}_0 \neq \alpha_0$  the assumption that all the data symbols prior to  $\alpha_1$  have been detected correctly no longer holds, and none of the correlations being performed in general match the transmitted signal. The reason for this is that with a general real-valued modulation index  $h$  (or modulation indices  $h_0, h_1, \dots, h_{H-1}$ ), there are infinitely many possible transmitted signal waveforms corresponding to a specific data symbol, depending on all the previous data symbols. This will be discussed further in Section 3.4, where a finite structure for the transmitted signal will be considered.

In spite of the practical problems outlined above, this detector will prove to be a valuable tool. We shall study its first-symbol detection performance over the AWGN channel, by means of the signals' minimum squared Euclidean distance. As a final remark, there is always an MLSD detector having an asymptotic detection performance corresponding to  $d_{\min}^2$ . The discussion above concerning the first-symbol detector is given only to make the understanding of the distance calculations that follow easier.

In describing the modulations that follow, we will move from simple schemes to more complex ones. A scheme having  $L = 1$  is considered to be simpler than a scheme with  $L > 1$ . The former is of the *full response* type since each data symbol affects the instantaneous frequency over one symbol interval only. Schemes with  $L = 2, 3, \dots$  are *partial response* types since the frequency pulses  $g(t)$  now overlap, and the action taken by a specific data symbol can be seen partially over several data symbol intervals. It should be noted that this classification concerns the signals when being viewed as frequency modulated. When viewed as phase modulated, all signals are of partial response type in general.

Schemes with  $H > 1$  will be developed after a discussion of single-index schemes. The former are called *multi-h* schemes; these were introduced in papers by Miyakawa *et al.*,<sup>(18)</sup> Anderson and deBuda,<sup>(19)</sup> Anderson and Taylor,<sup>(20)</sup> and Aulin and Sundberg.<sup>(21,22)</sup>

### 3.2. Bounds on the Minimum Euclidean Distance

This section develops general properties of the minimum Euclidean distance, especially tight upper bounds on this quantity. They will prove to be of great importance for finding  $d_{\min}^2$  itself.

As was shown in Chapter 2, the squared and normalized Euclidean distance measure for a CPM signal is

$$d^2 = \log_2 M \left\{ \frac{1}{T} \int_0^{NT} [1 - \cos \phi(t, \gamma)] dt \right\} \quad (3.5)$$

where

$$\gamma = \alpha - \tilde{\alpha}, \quad \gamma_i = \alpha_i - \tilde{\alpha}_i, \quad i = 0, \pm 1, \pm 2, \dots$$

is the difference between the transmitted data sequence  $\alpha$  and the sequence used by the detector,  $\tilde{\alpha}$ . Note that several different pairs of sequences  $\alpha$  and  $\tilde{\alpha}$  can correspond to a single difference sequence  $\gamma$ . Each component in this difference sequence can take one of the values  $0, \pm 2, \pm 4, \dots, \pm 2(M - 1)$ . It should be noted that the appearance of a difference sequence is a mathematical consequence of the distance measure. To make the properties that follow easier to understand, both pairs of sequences ( $\alpha, \tilde{\alpha}$ ) and a single difference sequence  $\gamma$  will be used. After a while the pair of sequences notation will be dropped.

The Euclidean distance is squared to allow power comparisons, but also since it is most easily handled in this way. This will be evident below. It is also normalized as defined in Chapter 2. For reference,  $d_{\min}^2$  for BPSK or QPSK equals 2.

### 3.2.1. Full Response, $H = 1$

Restriction is made now to CPM signals of full response type, i.e., the frequency pulse  $g(t)$  occupies at most one symbol interval and the shape is arbitrary. A single real-valued modulation index  $h$  is used and the systems are  $M$ -ary. An important tool for finding the properties of  $d_{\min}^2$ , and for actually computing it, is the phase tree. This tree is formed by all phase trajectories  $\phi(t, \alpha)$  having a common starting phase of zero at time  $t = 0$ . Figure 3.2 shows a phase tree for a 1REC scheme over the interval  $[0, 3T]$ . The modulation index  $h$  is general. When  $M = 2$  (a binary system) only

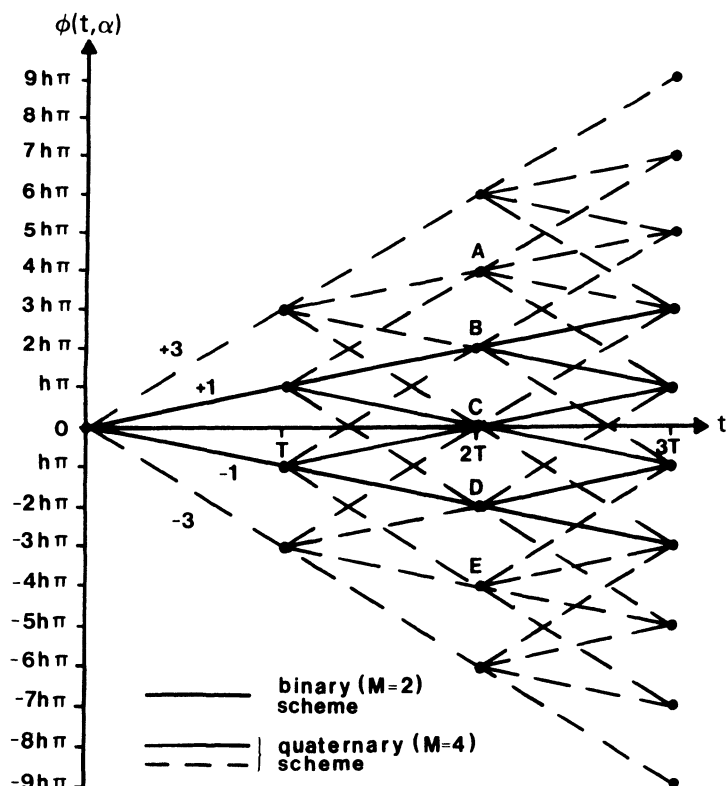


Figure 3.2. A phase tree, showing the ensemble of all phase functions, for a 1REC,  $M = 4$  scheme (dashed lines), and for  $M = 2$  (solid lines). The symbol time is the same in both cases. From Ref. 44, © 1984 by John Wiley Ltd.

the solid trajectories are traced, and when  $M = 4$  (quaternary system) the dashed ones are also. Although the tree in Figure 3.2 is built up from linear phase trajectories, this is not of conceptual importance in what follows.

To calculate  $d_{\min}^2$  for an observation length of  $N$  symbol intervals, all pairs of phase trajectories in the phase tree over  $N$  symbol intervals must be plugged into equation (3.5), after having formed the corresponding difference sequence. The pair of phase trajectories leaving the root node at  $t = 0$  must not coincide, which means that  $\alpha_0 \neq \tilde{\alpha}_0$ . The minimum of all the quantities obtained by using equation (3.5) is the desired result for an observation interval of  $N$  symbols. Since the number of pairs of sequences (or difference sequences) grows exponentially with  $N$ , this procedure very soon turns out to be useless.

When considering the distance properties for CPM signals it is of importance to keep in mind that the phase always must be viewed modulo  $2\pi$ . A practical way to do this is to draw the phase tree on a transparency, then fold this transparency into a cylinder with the time axis along the cylinder. Trajectories which seem to be far apart in the phase tree may actually be close or even coincide when viewed modulo  $2\pi$ . By varying the radius of the cylinder, different modulation indices are obtained.

From (3.5) it is clear that for a given pair of sequences yielding  $\gamma$ , the Euclidean distance is a nondecreasing function of  $N$ . This is because the integrand itself is nonnegative. For construction of an upper bound on  $d_{\min}^2$  we are free to chose *any* fixed pair of sequences. The distance of this pair must obviously equal or exceed  $d_{\min}^2$ .

This philosophy can be employed at any  $N$ , but since  $d_{\min}^2$  is a nondecreasing function of  $N$ , the most interesting case is when  $N \rightarrow \infty$ ; a bound at  $N \rightarrow \infty$  will be a bound at any finite  $N$ . Good candidates for a bound are infinitely long pairs of signals that merge as soon as possible. Since the signals have constant envelope, a merger is obtained when the phases merge. A pair of phase trajectories merge at a certain time if they coincide all the time thereafter. After this merger, the  $d^2$  contribution will be zero. These mergers are *inevitable* if they occur independently of  $h$ .

Applying this method to the binary scheme in Figure 3.2 (solid tree), it is seen that if a pair of sequences

$$\begin{aligned}\alpha &= \dots, +1, -1, \alpha_2, \alpha_3, \dots \\ \tilde{\alpha} &= \dots, -1, +1, \alpha_2, \alpha_3, \dots\end{aligned}\tag{3.6}$$

is chosen, the two phase trajectories coincide for all  $t \geq 2T$ . The merge point is labeled  $C$  in Figure 3.2. The sequences  $\alpha$  and  $\tilde{\alpha}$  can be interchanged with each other, and the resulting  $d^2$  will be the same. The upper bound on the minimum squared normalized Euclidean distance is

$$d_B^2 = 2 - \frac{1}{T} \int_0^{2T} \cos \{2\pi h[2q(t) - 2q(t-T)]\} dt \quad (3.7)$$

where (3.5) was used. For the binary 1REC scheme the result is

$$d_B^2 = 2 \left( 1 - \frac{\sin 2\pi h}{2\pi h} \right) \quad (3.8)$$

For phase trajectories that are linear over each symbol interval, the  $d^2$  measure is simple to obtain analytically. Assuming that the phase separation over a symbol interval is  $\Delta\phi_a$  in the beginning and  $\Delta\phi_b$  at the end, we find the contribution to  $d^2$  over this symbol interval is

$$\begin{aligned} & \left( 1 - \frac{\sin \Delta\phi_a - \sin \Delta\phi_b}{\Delta\phi_a - \Delta\phi_b} \right) \log_2 M, \quad \Delta\phi_a \neq \Delta\phi_b \\ & (1 - \cos \Delta\phi_a) \log_2 M, \quad \Delta\phi_a = \Delta\phi_b \end{aligned} \quad (3.9)$$

Equation (3.8) was obtained in this way with  $\Delta\phi_a = 0$ ,  $\Delta\phi_b = 2\pi h$  over the first bit interval and with  $\Delta\phi_a = 2\pi h$ ,  $\Delta\phi_b = 0$  over the second. For the bit intervals that follow,  $\Delta\phi_a = \Delta\phi_b = 0$ .

It can be noted that instead of using the pair of sequences (3.6), the single difference sequence  $\gamma = +2, -2, 0, 0, \dots$  could have been used directly in (3.5). It is not necessary to consider  $\gamma = -2, +2, 0, 0, \dots$ , since the cosine in (3.5) is an even function. Thus  $\gamma_0$  can always be chosen positive.

Turning to the quaternary case, several pairs of phase trajectories merging at  $t = 2T$  can be found. In Figure 3.2 these mergers are labeled  $A$ ,  $B$ ,  $C$ ,  $D$ , and  $E$  in the phase tree. This is different from the binary case, and two different pairs of phase trajectories can have the same merge point. There are only three distinct phase differences at  $t = T$ , however. These are  $2\pi h$ ,  $4\pi h$ , and  $6\pi h$  when the sign symmetry is removed.

It is easily seen that an upper bound on  $d_{\min}^2$  for the  $M$ -ary case is obtained by using the difference sequences

$$\gamma = \gamma_0, -\gamma_0, 0, 0, \dots; \quad \gamma_0 = 2, 4, 6, \dots, 2(M-1)$$

and taking the minimum of the resulting  $d^2$  quantities,

$$\begin{aligned} d_B^2 &= \log_2 M \min_{1 \leq k \leq M-1} \\ &\times \left( 2 - \frac{1}{T} \int_0^{2T} \cos \{2\pi h 2k[q(t) - q(t-T)]\} dt \right) \end{aligned} \quad (3.10)$$

which for the  $M$ -ary 1REC system, specializes to

$$d_B^2 = \log_2 M \min_{1 \leq k \leq M-1} 2 \left( 1 - \frac{\sin k2\pi h}{k2\pi h} \right) \quad (3.11)$$

Figure 3.3 shows the upper bounds  $d_B^2$  for the  $M$ -ary 1REC schemes for  $M = 2, 4, 8$ , and  $16$ . These bounds are plotted as functions of the modulation index  $h$ . For a fixed value of  $h$ , these bounds grow with  $M$ , and will actually approach  $\infty$  as  $M \rightarrow \infty$ . Also, it will be shown in Section 3.3.1 that it is possible to make  $d_{\min}^2$  equal to  $d_B^2$ , by making the observation interval  $N$  long enough, and that this holds for all  $h$  values except certain discrete ones.

The fact that  $d_B^2$  (and also  $d_{\min}^2$  for any  $N$ ) grows beyond any limit as  $M \rightarrow \infty$  is nothing fundamentally new. According to the work of Shannon,<sup>(1)</sup> such a signal set can exist. For sufficiently large but finite SNR, the error probability can be arbitrarily small as  $M$  grows. The  $M$ -ary 1REC scheme is one such system; another example is given in Wozencraft and Jacobs,<sup>(23)</sup>

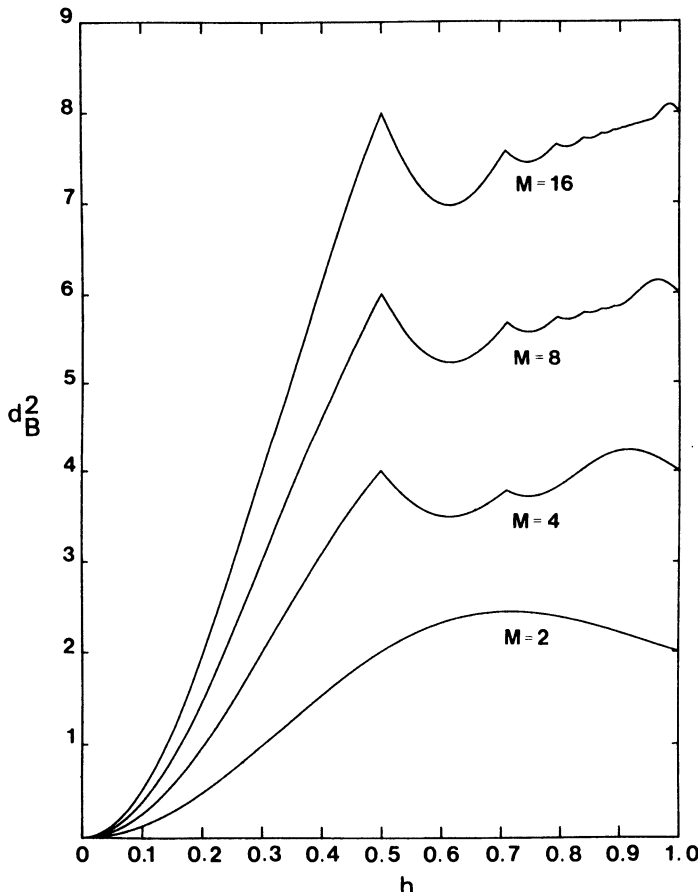


Figure 3.3. The upper bound  $d_B^2$  as a function of  $h$  for  $M$ -ary 1REC modulations,  $M = 2, 4, 8, 16$ . From Ref. 44, © 1984 by John Wiley Ltd.

pp. 290–292, or Viterbi,<sup>(24)</sup> p. 227. The problem is that the bandwidth of the transmitted signal also grows with  $M$ , and thus requires an infinite bandwidth for error-free transmissions. Such tradeoffs and discussions will be considered in detail in Chapter 5.

It can be shown that for all full response CPM systems with the property

$$\int_0^T g(\tau) d\tau = 0 \quad (3.12)$$

a merger can occur at  $t = T$  in the phase tree and thus the difference sequences

$$\gamma = \gamma_0, 0, 0, 0, \dots, \quad \gamma_0 = 2, 4, 6, \dots, 2(M - 1)$$

yield the upper bound

$$d_B^2 = \log_2 M \min_{1 \leq k \leq M-1} \left[ 1 - \frac{1}{T} \int_0^T \cos 4\pi h k q(t) dt \right] \quad (3.13)$$

Because of the early merger at  $t = T$ , the potential Euclidean distance increment over the interval  $[T, 2T]$  is lost, and the overall distance properties are poor. Pulses of this type will be called “weak.” They will not be considered further in this chapter. In Chapter 4 it will be shown that from a spectral point of view also, such systems have unattractive properties. In the sequel we will concentrate on positive frequency pulses having the property

$$g(t) = g(T - t), \quad 0 \leq t \leq T \quad (3.14)$$

i.e., they are symmetric with respect to the middle of the duration of the pulse.

It is of interest to study the influence of the specific shape of  $g(t)$  upon  $d_B^2$ , and for this purpose we pick

$$g(t) = \begin{cases} 0, & t \leq 0, \quad t \geq T \\ \frac{\pi}{4T} \sin \frac{\pi t}{T}, & 0 \leq t \leq T \end{cases} \quad (3.15)$$

with the corresponding phase response

$$q(t) = \begin{cases} 0, & t \leq 0 \\ \frac{1}{4}(1 - \cos(\pi t/T)), & 0 \leq t \leq T \\ \frac{1}{2}, & t \geq T \end{cases} \quad (3.16)$$

Just like the 1REC pulse, this pulse has no continuous derivatives at the end points. The pulse itself is continuous, however, unlike 1REC. Since the

frequency pulse (3.15) is a half cycle sinusoid, this scheme will be referred to as HCS. Another pulse of interest is the raised cosine, introduced in Chapter 2, here used in its 1RC version.

Figure 3.4 shows  $d_B^2$  as a function of  $h$  for the three schemes 1REC, HCS, and 1RC when  $M = 2$ . Equation (3.7) was used for calculation of  $d_B^2$ , and numerical integration was used for HCS and 1RC. First of all it is seen that when  $h = 1/2$ , all the curves coincide and are equal to two. The 1REC scheme corresponds to MSK and the 1RC scheme to SFSK. This property will later be shown to be true for all nonweak pulses  $g(t)$  having the symmetry property (3.14). What is more important right now is that there is no single pulse  $g(t)$  which is uniformly best for all modulation indices. Figures 3.5 and 3.6 show  $d_B^2$  for the same three schemes when  $M = 4$  and  $M = 8$ . It is clear that a scheme which is good for low  $h$  values is bad for large  $h$  values. We are interested, then, in the pulse  $g(t)$  which maximizes  $d_B^2$  for a given  $h$  and  $M$ . This problem is partly solved now.

#### *Optimization of the Upper Bound $d_B^2$*

For frequency pulses  $g(t)$  having the symmetry property (3.14), the expression for the upper bound in equation (3.10) can be written

$$d_B^2 = \log_2 M \min_{1 \leq k \leq M-1} \left\{ 2 \left[ 1 - \frac{1}{T} \int_0^T \cos 4\pi h k q(t) dt \right] \right\} \quad (3.17)$$

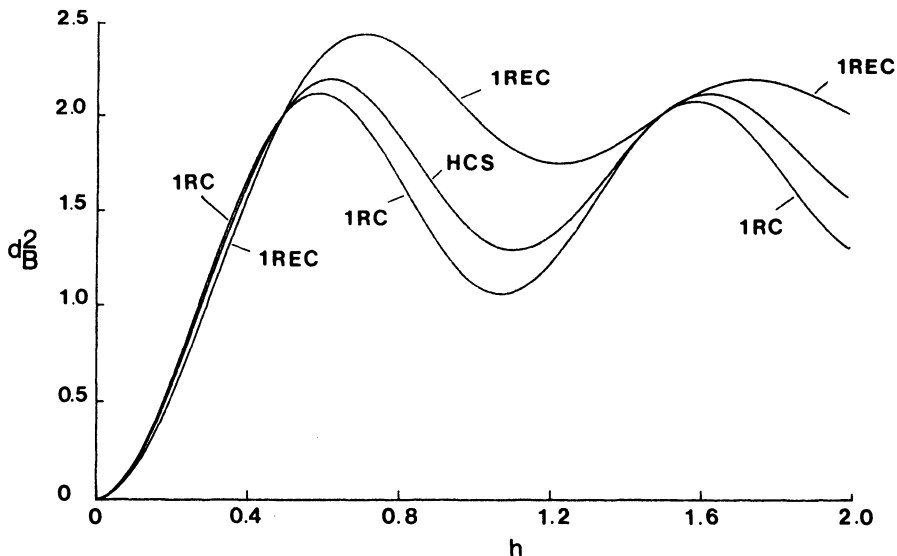


Figure 3.4. The upper bounds  $d_B^2$  for the three binary schemes 1REC, HCS, and 1RC.

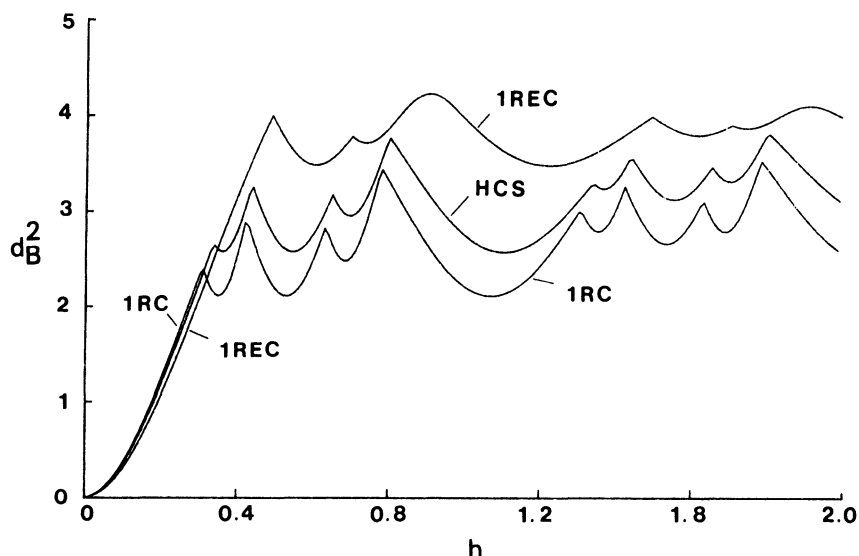


Figure 3.5. The upper bounds  $d_B^2$  for the three quaternary schemes 1REC, HCS, and 1RC.

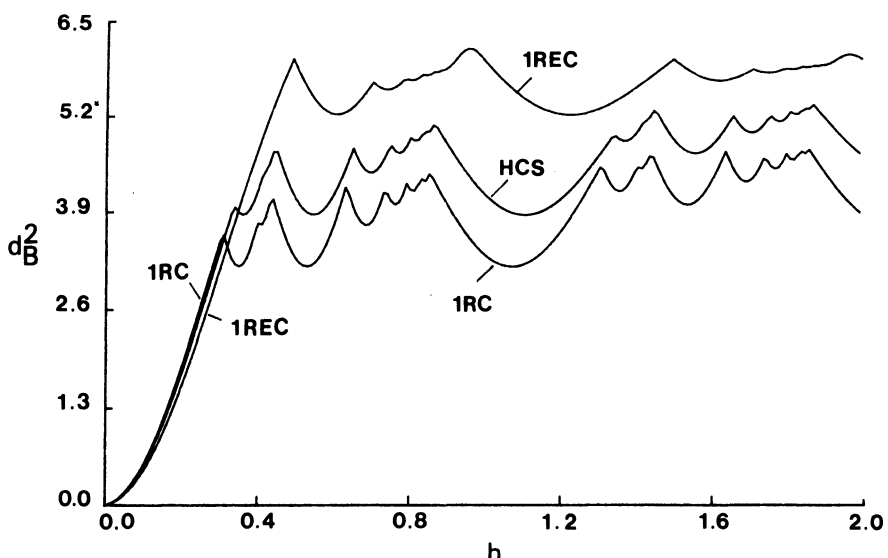


Figure 3.6. The upper bounds  $d_B^2$  for the octal schemes 1REC, HCS, and 1RC.

i.e.,  $d_B^2$  is twice the distance calculated over the first symbol interval. Since  $\cos(\cdot) \geq -1$ ,  $d_B^2$  can never exceed  $4 \log_2 M$ . Thus, at most an improvement of 3 db in  $E_b/N_0$  for a large SNR might be obtained in the binary case ( $M = 2$ ) compared to MSK or BPSK.

Furthermore, equation (3.17) can also be written

$$d_B^2 = \log_2 M \min_{1 \leq k \leq M-1} \times \left[ 2 \left( 1 - 2 \cos \pi h k \frac{1}{T} \int_0^{T/2} \cos [4\pi h k q_0(t) - \pi h k] dt \right) \right] \quad (3.18)$$

where

$$q_0(t) = q(t + T/2), \quad 0 \leq t \leq T/2$$

Consider first the binary case ( $M = 2$ ). Here

$$d_B^2 = 2 \left( 1 - 2 \cos \pi h \frac{1}{T} \int_0^{T/2} \cos [4\pi h q_0(t) - \pi h] dt \right) \quad (3.19)$$

Observe that  $\cos \pi h = 0$  for  $h = 1/2, 3/2, 5/2$ , etc., so that the upper bound equals 2, independent of the shape of the symmetric pulse  $g(t)$ . Actually, this is true for all pulses except weak ones. This is of particular interest since much attention has been devoted to the binary case with  $h = 1/2$ . Examples of such schemes are MSK, FFSK, SFSK, OQPSK, and variations. Actually  $M = 2$ ,  $h = 1/2$  can be viewed as offset amplitude modulation in the two quadrature channels  $I$  and  $Q$ , in which the pulses are nonoverlapping and of duration  $2T_b$ . For MSK the shape is a half cycle sinusoid, and for OQPSK a rectangle. Thus full response CPM schemes with  $M = 2$  and  $h = 1/2$  can be viewed as being either frequency, phase, or amplitude modulated.

To maximize  $d_B^2$  for the binary case, the last term in equation (3.19) must be minimized. Two cases can be distinguished:

Case I:  $0 \leq h \leq 1/2$ , where  $\cos \pi h \geq 0$ .

Case II:  $1/2 \leq h \leq 1$ , where  $\cos \pi h \leq 0$ .

The integral in (3.19) must be minimized for Case I and maximized for Case II. It is also clear that the pulse, which maximizes  $d_B^2$  for Case I, will minimize  $d_B^2$  for Case II and vice versa.

To make the integral in (3.19) as small as possible, the argument inside the cosine must be as close to  $\pi$  as possible. This yields for the interval  $0 \leq h \leq 1$

$$q_0(t) = 1/2, \quad \text{Case I}$$

$$q_0(t) = 1/4, \quad \text{Case II}$$

with the resulting phase responses

$$q_I(t) = \begin{cases} 0, & 0 \leq t \leq T/2 \\ 1/2, & t > T/2 \end{cases} \quad \text{Case I}$$

and

$$q_{II}(t) = \begin{cases} 0, & t = 0 \\ 1/4, & 0 < t < T \\ 1/2, & t \geq T \end{cases} \quad \text{Case II}$$

From the sign symmetry, to minimize  $d_B^2$  the phase responses above have to be interchanged for the respective cases. The upper bound  $d_B^2$  for the two phase responses is now found as

$$\begin{aligned} d_B^2 &= 1 - \cos 2\pi h && \text{using } q_I(t) \\ d_B^2 &= 2(1 - \cos \pi h) && \text{using } q_{II}(t) \end{aligned} \quad (3.20)$$

so for any binary scheme,  $d_B^2$  is bounded by

$$\begin{aligned} 1 - \cos 2\pi h &\leq d_B^2 \leq 2(1 - \cos \pi h), & 0 \leq h \leq 1/2 \\ 2(1 - \cos \pi h) &\leq d_B^2 \leq 1 - \cos 2\pi h, & 1/2 \leq h \leq 1 \end{aligned} \quad (3.21)$$

An analogous technique can be used to derive bounds for  $h \geq 1$ .

Hence when  $h = 1/2$ ,  $q_I(t)$  corresponds to binary PSK but with a  $T_b/2$  time offset. The phase response  $q_{II}(t)$  also corresponds to a kind of PSK system, where the total phase shift is split up into two phase shifts of equal magnitude and separated by  $T_b$ .

The two phase responses  $q_I(t)$  and  $q_{II}(t)$  are both members of the class of  $(\alpha, \beta)$  functions defined by

$$\begin{aligned} & \frac{\beta}{2\alpha} \frac{t}{T}, \quad 0 \leq t \leq \alpha T \\ & \frac{\alpha}{2} \frac{1 - 2\beta}{1 - 2\alpha} \frac{t}{T} + \frac{\beta}{2}, \quad \alpha T \leq t \leq (1 - \alpha)T \\ & \frac{\beta}{2\alpha} \left( \frac{t}{T} - 1 \right) + \frac{1}{2}, \quad (1 - \alpha)T \leq t \leq T \\ & \frac{1}{2}, \quad t \geq T \end{aligned} \tag{3.22}$$

which is shown in Figure 3.7. The phase response  $q_I(t)$  is obtained with  $(\alpha, \beta) = (0, 0)$  and  $q_{II}$  is obtained with  $(\alpha, \beta) = (0, 1/2)$ . Figure 3.8 shows the upper and lower bounds on  $d_B^2$ , and also  $d_B^2$  for two other combinations of  $(\alpha, \beta)$  plus the schemes 1REC, 1RC ( $h = 1/2, 1/4$ , and  $1/8$ ) and HCS. It is seen that the different bounds  $d_B^2$  never cross each other and that 1RC is in between that of  $(\alpha, \beta) = (1/4, 0)$  and HCS.

The phase response  $q_{II}(t)$  belongs to the class of *plateau functions* in which the phase changes only in the beginning and the end of the symbol interval. In the middle the phase remains constant, forming a plateau. All  $(\alpha, \beta)$  functions are plateau functions when  $\beta = 1/2$ . For this subclass of the  $(\alpha, \beta)$  functions the upper bound is

$$d_B^2 = 2 \left[ 1 - (1 - 2\alpha) \cos \pi h - \frac{\alpha}{h\pi} \sin 2\pi h \right] \tag{3.23}$$

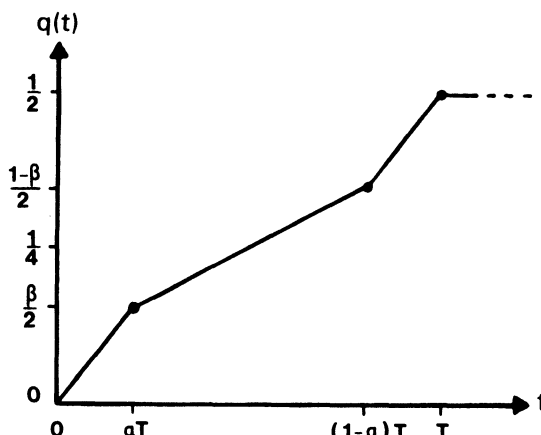


Figure 3.7. The  $(\alpha, \beta)$  class of phase function  $q(t)$ .

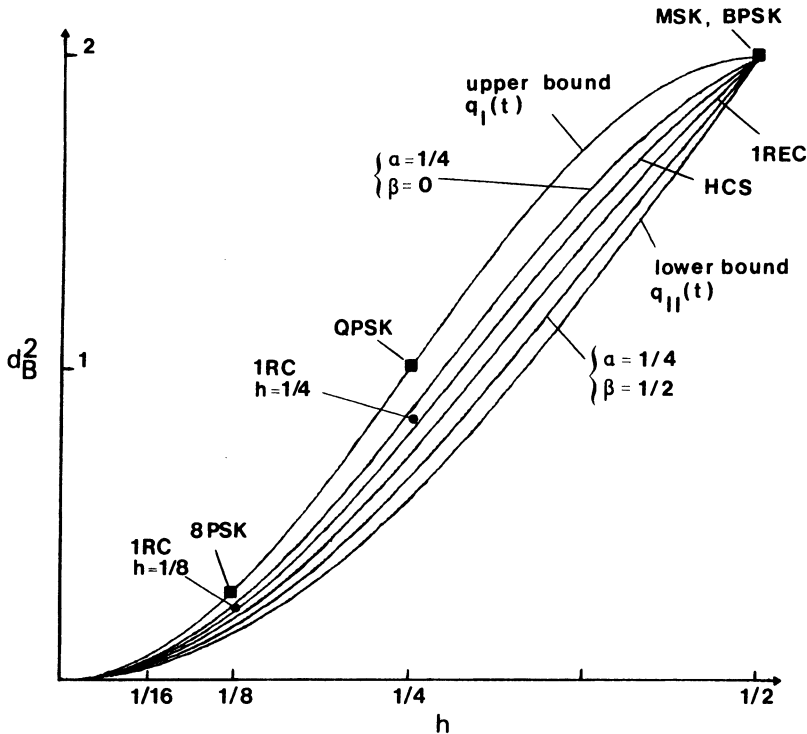


Figure 3.8. Comparison of upper bounds for  $M = 2$ ,  $0 \leq h \leq 1/2$ ;  $q_I(t)$  is the upper bound on all upper bounds  $d_B^2$ , and  $q_{II}(t)$  is the lower bound on all upper bounds. All schemes have  $L = 1$ .

which is easily obtained by using (3.22) in (3.7) or (3.16). For small values of  $\alpha$ , this  $d_B^2$  approaches a value of 4 when  $h = 1$ . As will be seen in Section 3.3.1 this is a weak modulation index, which means that  $d_{\min}^2$  can never be made equal to  $d_B^2$ , even if an infinite observation interval ( $N \rightarrow \infty$ ) is used. By choosing  $h$  close to 1, however,  $d_{\min}^2$  can be made equal to  $d_B^2$ .

The problem of finding frequency pulses  $g(t)$  that optimize  $d_B^2$ , given  $h$  and  $M$ , is far more complicated in the general  $M$ -ary case than for the binary case. The general problem is still unsolved. Here the upper bound must be constructed from the minimum of several functions, and when  $h$  varies with fixed  $M$ , different functions take the minimum value. This is true also for fixed  $h$  and  $M$  when the shape of the frequency pulse  $g(t)$  is varied. For an  $M$ -ary scheme with  $0 \leq h \leq 1/M$ , however, the binary bounds (3.21) still apply after a multiplication with  $\log_2 M$ .

It is always true that for  $M$ -ary schemes  $d_B^2 \leq 4 \log_2 M$ . Since the bound  $d_B^2$  now is formed by taking the minimum of several component functions, this maximum value can never be reached. An incomplete search in the

$(\alpha, \beta)$  class of phase responses gave the maximum  $d_B^2 = 4.62$  in the quaternary case ( $M = 4$ ). This maximum was found for  $(\alpha, \beta) = (0, 0.17)$  and  $h = 0.62$ . By comparison, the maximum value of  $d_B^2$  for a quaternary 1REC scheme is 4.232 when  $h = 0.914$  (see Figure 3.3).

### 3.2.2. Partial Response, $H = 1$

In the previous section the phase tree was seen to be an important tool for calculations of Euclidean distances and especially upper bounds on this quantity. This tree is formed by the ensemble of phase trajectories having a common start phase, or root, say zero, at time  $t = 0$ . Since it is assumed that all the data symbols prior to  $t = 0$  are known it follows that  $\alpha_i = \dot{\alpha}_i$ ;  $i < 0$ . Thus when pairs of phase trajectories are considered, they coincide up to time  $t = 0$ .

Figure 3.9 shows an example of a phase tree for a binary partial response scheme. The frequency pulse is 3REC (see Section 2.7). In Figure 3.9 the phase tree has been drawn for the case where all the data symbols prior to  $t = 0$  are +1. A major difference between phase trees for full response ( $L = 1$ ) and partial response ( $L = 2, 3, \dots$ ) schemes is that in the latter case the shape of the trajectories starting from a specific node depends upon which node is chosen. In Figure 3.9 it can be seen that there are two different shapes of phase trajectories corresponding to the data +1. The shape is uniquely determined by the present data symbol and the  $L - 1$  last data

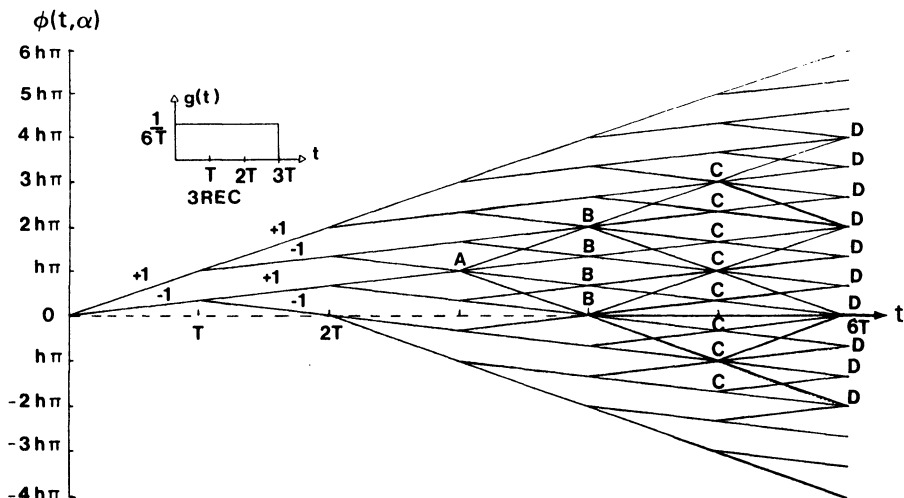


Figure 3.9. The phase tree when the frequency pulse  $g(t)$  is constant and of length  $L = 3$ ; the data symbols are binary and prior to  $t = 0$  are all +1. Point A is a crossing, not a merger; points B, C, and D denote the first, second, and third mergers. From Ref. 44, © 1984 by John Wiley Ltd.

symbols. The data symbols prior to a certain node forms what is called the *prehistory*.

Since we are interested in calculation of Euclidean distances, or an upper bound on the minimum of this quantity, one might wonder if this distance measure depends upon which prehistory is taken. Fortunately it does not; this is seen by considering (3.5). Since the data symbols prior to the root of the tree are equal, it follows that the components  $\gamma_i$ ,  $i < 0$  in the difference sequence used in (3.5) are all equal to zero. Thus from a distance calculation point of view, the prehistory is completely canceled. We have only to consider difference sequences with components satisfying the conditions

$$\begin{aligned}\gamma_i &= 0, \quad i < 0 \\ \gamma_0 &= 2, 4, 6, \dots, 2(M-1) \\ \gamma_i &= 0, \pm 2, \pm 4, \dots, \pm 2(M-1), \quad i \geq 1\end{aligned}\tag{3.24}$$

Note that  $\gamma_0 \neq 0$  since  $\alpha_0$  and  $\tilde{\alpha}_0$  must not be equal. It is also sufficient to consider only positive  $\gamma_0$ , since the cosine in (3.5) is an even function.

A phase tree formed by using those difference sequences  $\gamma$  with components  $\gamma_i$  as in (3.24), instead of the sequences  $\alpha$ , is called a *phase difference tree*. Figure 3.10 shows such a tree for the case considered in Figure 3.9,

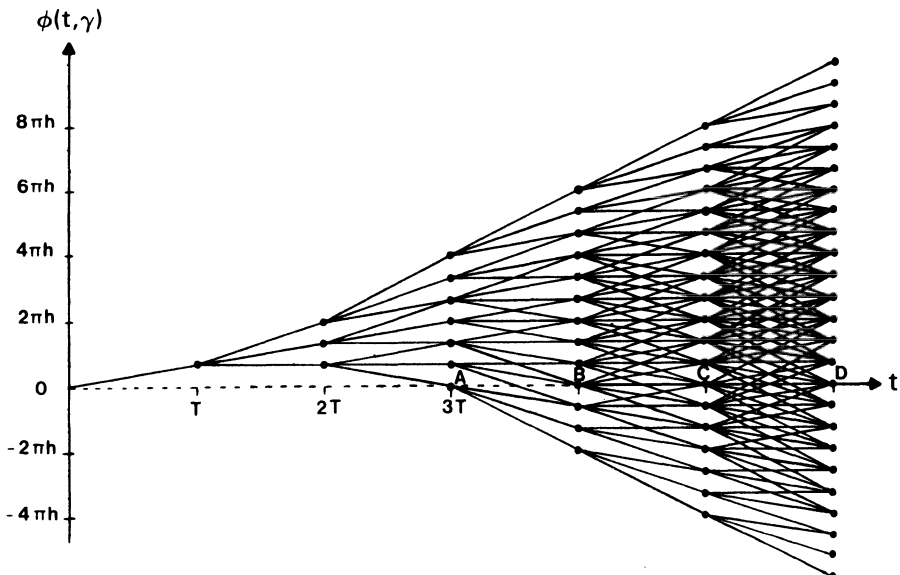


Figure 3.10. The phase difference tree for the  $g(t)$  in Fig. 3.9. B, C, and D are again mergers; A cannot be since no future trajectory from it is identically zero. From Ref. 44, © 1984 by John Wiley Ltd.

binary 3REC. The tree shows the entire ensemble of phase difference trajectories.

The construction of an upper bound on the minimum Euclidean distance for partial response schemes for all observation lengths  $N$  including infinity, is quite similar to the one for full response schemes. Pairs of sequences  $\alpha$  and  $\tilde{\alpha}$ , yielding early mergers in the phase tree are identified and considered to be infinitely long. In Figure 3.9, mergers are identified by the property that the phases coincide at a specific time  $t_m$ , and do so ever after. In the phase difference tree, Figure 3.10, the mergers are trajectories identically equal to zero for all  $t \geq t_m$ . Note that the integration in equation (3.11) has only to be performed over the interval  $0 \leq t \leq t_m$ , even though an infinite observation interval is considered.

The first time instant after which a phase difference trajectory can be made zero ever after is in general  $t = (L + 1)T$ , where  $L$  is the length of the frequency pulse  $g(t)$ , measured in symbol intervals. This is called the *first merger*, and the phase difference trajectories giving this merger are obtained by choosing the difference sequences

$$\gamma_i = \begin{cases} 0, & i < 0 \\ \gamma_0 = 2, 4, 6, \dots, 2(M - 1), & i = 0 \\ -\gamma_0, & i = 1 \\ 0, & i > 1 \end{cases} \quad (3.25)$$

The phase difference trajectories are

$$\phi(t, \gamma) = \begin{cases} 0, & t \leq 0 \\ \gamma_0 2\pi h q(t), & 0 \leq t \leq T \\ \gamma_0 2\pi h [q(t) - q(t - T)], & T \leq t \leq (L + 1)T \\ \gamma_0 2\pi h [q((L + 1)T - q(LT))] = 0, & t \geq (L + 1)T \end{cases} \quad (3.26)$$

By calculating the minimum of the Euclidean distances associated with the phase difference in (3.26) via (3.5), an upper bound is obtained on the minimum Euclidean distance as a function of  $h$ , for fixed  $M$  and  $g(t)$ , just as it was for the full response case treated in the previous section.

One can also consider *second mergers*, that is, phase difference trajectories which merge at  $t = (L + 2)T$ . These phase difference trajectories are obtained from (3.2) by using

$$\gamma_i = \begin{cases} 0, & i < 0 \\ 2, 4, 6, \dots, 2(M - 1), & i = 0 \\ 0, \pm 2, \pm 4, \dots, \pm 2(M - 1), & i = 1, 2 \\ 0, & i > 2 \end{cases} \quad (3.27)$$

satisfying

$$\sum_{i=0}^2 \gamma_i = 0$$

Of course such mergers occur also for the full response case, but as will be shown in Section 3.3.1 the Euclidean distances associated with these (and all) later mergers are always larger than those for the first merger. For partial response schemes it can happen that this is not the case, as will be seen in numerical examples that will follow. Hence the former upper bound can be tightened by also taking the minimum of the Euclidean distances associated with second mergers. This new upper bound might also be further tightened by taking the third merger into account, and so on.

The exact number of mergers needed to give an upper bound on the minimum Euclidean distance which cannot be further tightened is not known exactly, but in no known case were mergers later than the  $L$ th needed. For the full response case, it can be proven that the first mergers give the tight bound. It is obvious that the difference sequences giving the  $m$ th mergers are

$$\gamma_i = \begin{cases} 0, & i < 0 \\ 2, 4, 6, \dots, 2(M-1), & i = 0 \\ 0, \pm 2, \pm 4, \dots, \pm 2(M-1), & 0 < i < m+1 \\ 0, & i \geq m+1 \end{cases} \quad (3.28)$$

satisfying

$$\sum_{i=0}^m \gamma_i = 0$$

In Figure 3.11 are the Euclidean distances corresponding to the first, second, and third mergers for the binary 3REC scheme plotted as functions of  $h$ . For the first and second mergers there is only one component to the upper bound, whereas there are several cases for the third merger. It is seen that over the interval considered  $0 \leq h \leq 2.5$  only one of the three third-merger components actually tightens the overall bound.

In the previous section weak frequency pulses  $g(t)$  were defined to be those for which  $q(LT) = 0$ , i.e.,  $g(t)$  integrates to zero. Such pulses are also weak for partial response schemes because the first merger does not occur at  $t = (L+1)T$  but instead at  $t = LT$ . Thus the Euclidean distance is built up over a shorter time interval, yielding a poor system with small  $d_{\min}^2$ . There are, however, partial response schemes which have earlier mergers,

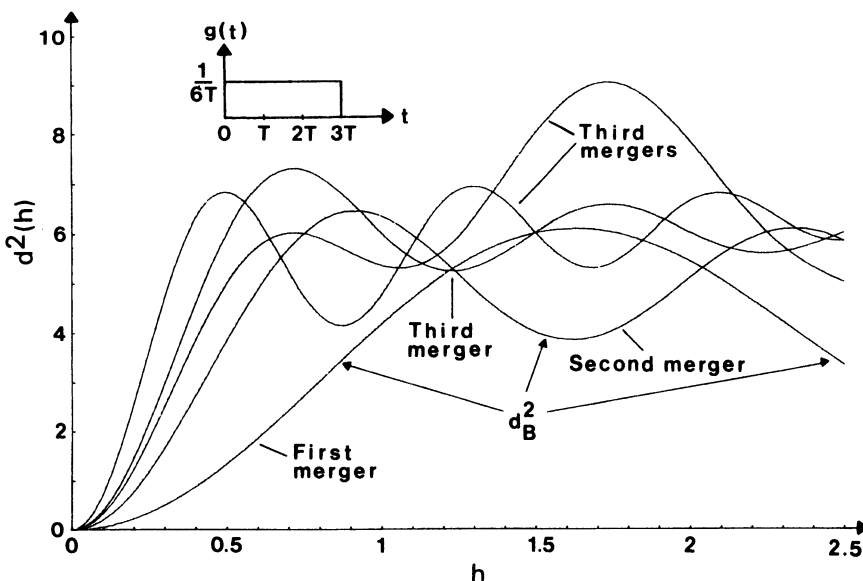


Figure 3.11. Construction of the upper bound on the minimum distance for the scheme with the  $g(t)$  of Figures 3.9 and 3.10. Only one of the third-merger curves contributes. From Ref. 44, © 1984 by John Wiley Ltd.

depending on the shape of the frequency pulse  $g(t)$  and the number of levels  $M$ , but not the modulation index  $h$ . A partial response system is weak of order  $L_c$ , if the first inevitable (independent of  $h$ ) merger occurs at  $t = (L + 1 - L_c)T$ . Schemes with  $q(LT) = 0$  are thus weak of the first order. An example of a second-order weak system is the binary 4REC. Here the difference sequence built up from repetitions of the subdifference sequence  $+2, -2, -2, +2$  (or its negative) yields a merger at  $t = 3T$ . It can be noted that because of (3.5), the transmitted data sequence  $\alpha$  must be  $+1, -1, -1, +1$  or  $-1, +1, +1, -1$  periodically repeated. The a priori probability for this to happen of course goes to zero as the length of the specific transmitted sequence goes to infinity. Thus the dependence upon the transmitted sequence makes this weakness less dangerous.

Next plots of  $d_B^2$  will be presented for some specific schemes. Figure 3.12 shows this bound for binary schemes with frequency pulses 1RC, 2RC, ..., 6RC. It can be clearly seen that when  $L \geq 2$ ,  $d_B^2$  is built up from segments of several different functions. Numerical integration was used for the calculation of these curves. The general trend in Figure 3.12 is obvious: By increasing the pulse length  $L$ ,  $d_B^2$  gets smaller for low modulation indices but larger for high modulation indices. For all the schemes in Figure 3.12, the first merger occurs at  $t = (L + 1)T$ . It turns out that 8RC is a weak

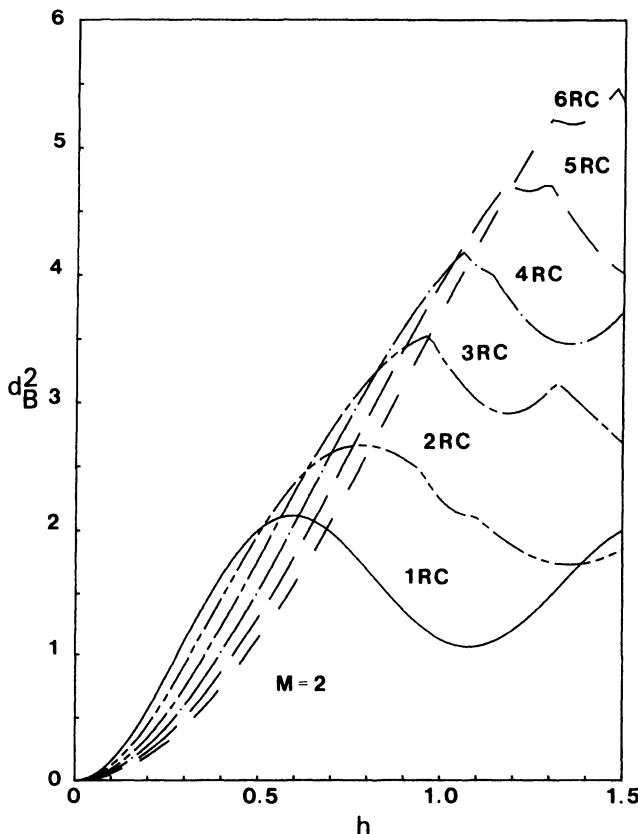


Figure 3.12. The upper bounds  $d_B^2$  for the binary schemes 1RC to 6RC. From Ref. 44, © 1984 by John Wiley Ltd.

system and 7RC is almost so. Thus  $L = 6$  is the practical limit of smoothing for RC pulses.

By looking at a phase tree, it is easy to see why  $d_B^2$  is reduced when  $L$  is increased. For low modulation indices, the difference sequence  $\gamma = \dots, +2, -2, 0, 0, \dots$  gives the upper bound for all the schemes. By identifying such a pair of phase trajectories in the phase tree for 4RC, shown in Figure 3.13, it is seen that they are very much closer together than for a full response scheme; compare with the tree for binary 1REC (solid tree) in Figure 3.2. Although the phases are separated over 5-bit intervals for the 4RC scheme, they are so much closer together that the net result is a decreased  $d_B^2$ . The only way to separate the phases for a given  $L$  is to increase  $h$ . For sufficiently large  $h$ ,  $d_B^2$  will start decreasing; this is because phase always must be reckoned modulo  $2\pi$ . This will be further discussed in Section 3.3.

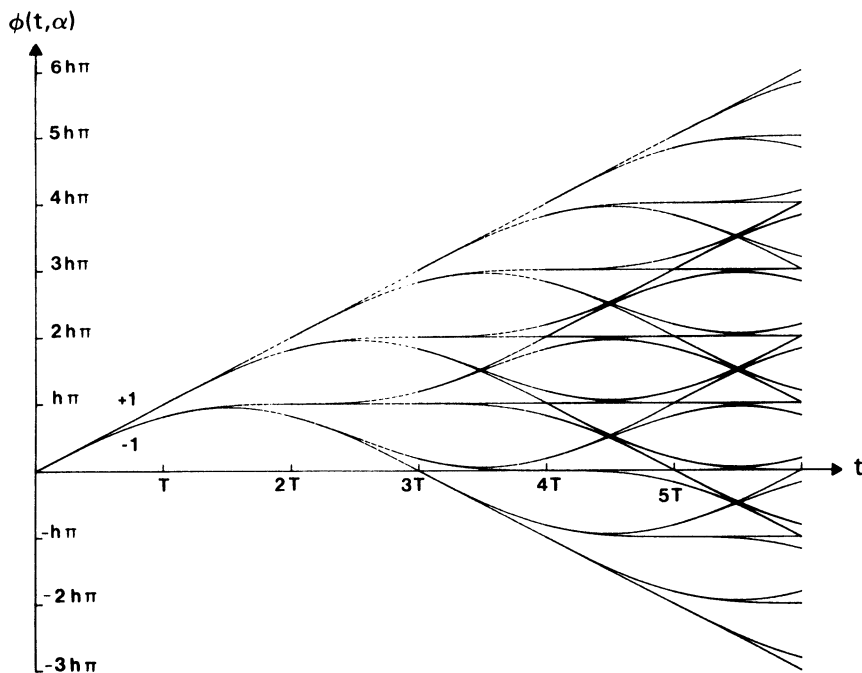


Figure 3.13. The phase tree for binary 4RC; data symbols prior to  $t = 0$  are all +1. From Ref. 44, © 1984 by John Wiley Ltd.

For full response schemes it was found that choosing an  $M$  larger than 2 gave larger  $d_B^2$  for the same modulation index. The same is true for partial response schemes. This is exemplified in Figure 3.14, which shows  $d_B^2$  as a function of  $h$  for the quaternary ( $M = 4$ ) schemes 1RC, 2RC, and 3RC. Quaternary 4RC is a weak system, but 3RC is far from weak. Note that the duration of the frequency pulse  $g(t)$  now is measured in symbol intervals. This means that  $L = 3$  in this quaternary system corresponds to a pulse of duration 6-bit intervals.

The phase tree for the quaternary 2RC scheme is shown in Figure 3.15 over the interval  $0 \leq t \leq 4T$ . In this figure, there are  $4^4 = 256$  different phase trajectories. Just as in Figure 3.2, drawn for 1REC, the phase tree in Figure 3.15 also contains the binary 2RC tree. This is obtained by picking only the inner two phase trajectories at each node.

Finally octal systems are studied, and Figure 3.16 shows  $d_B^2$  for the frequency pulses 1RC, 2RC, and 3RC. Since 4RC was weak when  $M = 4$ , it is clear that it is weak also when  $M = 8$ . It is seen that  $d_B^2$  for the 3RC scheme takes very large values when  $h$  is large. What is more interesting is that  $d_B^2 = 2$  (the case for MSK, BPSK, and QPSK) can be achieved for

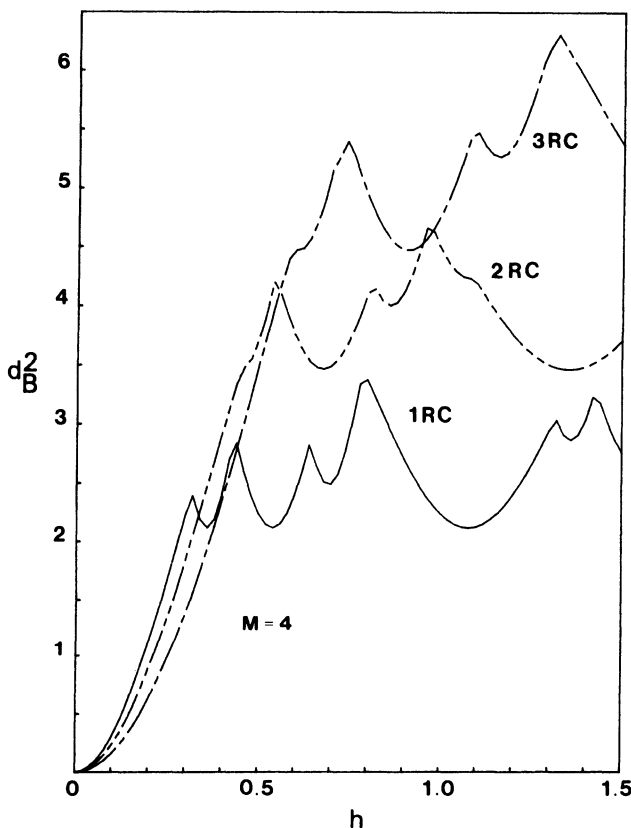


Figure 3.14. The upper bounds  $d_B^2$  for quaternary schemes 1RC to 3RC. From Ref. 44, © 1984 by John Wiley Ltd.

very small  $h$ -values. This is of interest because reducing  $h$  can improve the spectral performance of the system.

Although numerical results have been given only for RC pulses, the general trends carry over to other pulse shapes, so long as  $g(\cdot)$  is positive over the interval  $0 \leq t \leq LT$ .

Another interesting class of frequency pulses are the SRC pulses with mainlobe width  $L$  symbol intervals, truncated symmetrically to  $L_T$  symbol intervals ( $L_T \geq L$ ). It has been observed that the phase trees for SRC and RC pulses are very similar, if  $L_T$  is not too close to  $L$ . As a rule of thumb,  $L_T = L + 4$  is good enough. Since the phase trees are almost identical, it follows that  $d_B^2$  for the class SRC is almost identical to  $d_B^2$  for the RC class of frequency pulses.  $M$  and  $L$  must of course be the same. Actual calculations of  $d_B^2$  for SRC pulses have also been performed in some cases. It was found from comparison with the corresponding RC pulses that the Euclidean

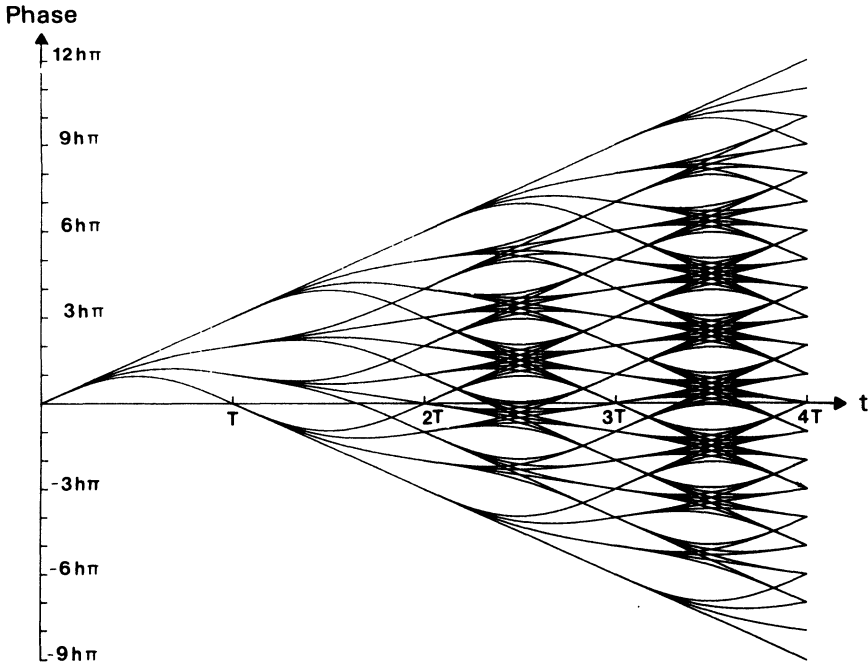


Figure 3.15. The phase tree for the quaternary scheme 2RC.

distances agree to three decimal places. Thus SRC and RC pulses have the same error performance on the AWGN channel. The difference in spectral performance will be studied in Chapter 4.

### 3.2.3. Full Response, Multi- $h$

The idea behind the use of multi- $h$  schemes is shown in Figure 3.17. Here the phase tree for a binary  $2 - h$  ( $H = 2$ ) scheme with frequency pulse 1REC is shown. The tree is drawn for  $h_2 = 5h_1/6$ , but this is not conceptually important so long as  $h_1 \neq h_2$ . By using  $H$  different modulation indices in a cyclic manner, the first inevitable merger is delayed from  $t = 2T$  for a  $H = 1$  scheme (compare Section 3.2.1) to  $t = (H + 1)T$ . This is exemplified in Figure 3.17, where the first inevitable merger occurs at  $t = 3T$ . This means that compared to a  $H = 1$  scheme the Euclidean distance is potentially larger since the integration interval in (3.5) is longer. By using (3.9), which holds for linear phase trajectories, we get the first-merger component in the upper bound on distance

$$d_{B,1}^2 = 3 - 2 \frac{\sin 2\pi h_1}{2\pi h_1} - \cos 2\pi h_1$$

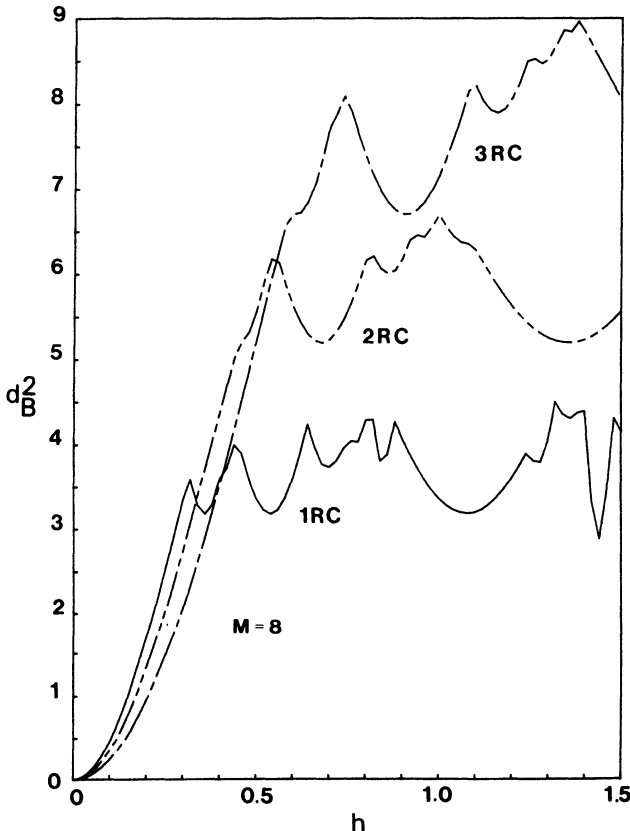


Figure 3.16. The upper bounds  $d_B^2$  for octal schemes 1RC to 3RC. From Ref. 44, © 1984 by John Wiley Ltd.

It is noted that  $d_B^2$  is a function of  $h_1$  only. The difference sequence corresponding to this merger is  $\gamma = \dots, +2, 0, -2, \dots$ . By considering another node in the phase tree starting with the modulation index  $h_2$  another component is

$$d_{B,2}^2 = 3 - 2 \frac{\sin 2\pi h_2}{2\pi h_2} - \cos 2\pi h_2$$

and an upper bound can now be formed as

$$d_B^2 = \min \{d_{B,1}^2, d_{B,2}^2\} \quad (3.29)$$

The Euclidean distance for multi- $h$  schemes is not independent of which node is taken as a root node. There are in general  $H$  different nodes which

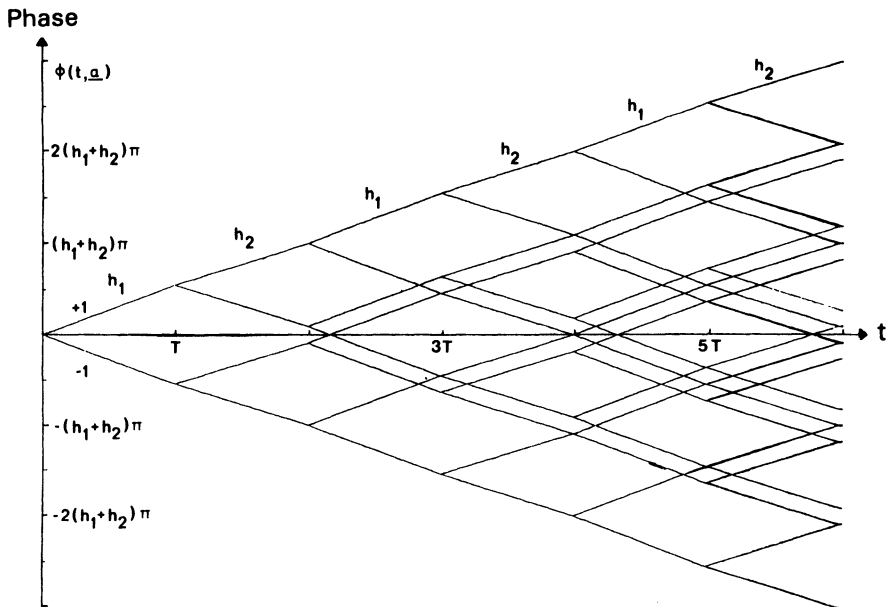


Figure 3.17. The phase tree for the binary  $2-h$  scheme based on the 1REC pulse. Phases are linear within each interval. In the case shown,  $h_2 = (5/6)h_1$ . From Ref. 21, © 1982 by IEEE.

must be considered as root nodes. By choosing the first merger for these  $H$  different cases, and taking the minimum, an upper bound  $d_B^2$  can be found.

For  $H = 1$ , full response schemes, the first mergers yielded a tight upper bound. It has empirically been found that this is not the case when  $H > 1$ . Even for the  $2 - h$ , 1REC scheme illustrated in Figure 3.17, it has been found that in some regions of the  $h_1, h_2$  plane, mergers occurring at  $t = 7T$  give contributions to the upper bound. The difference sequences that were found to form a tight upper bound in the region  $0 \leq h_1, h_2 \leq 1$  are

$$\gamma = \begin{cases} +2, 0, -2, 0, 0, \dots \\ +2, +2, -2, -2, 0, 0, \dots \\ +2, -2, -2, +2, 0, 0, \dots \\ +2, -2, 0, +2, -2, 0, \dots \\ +2, -2, +2, 0, -2, +2, -2, 0, 0, \dots \end{cases} \quad (3.30)$$

starting with both  $h_1$  and  $h_2$ . This gives 10 upper-bound components, and the minimum of these is shown in the three-dimensional plot in Figure 3.18. The maximum value of  $d_B^2$  is 4.0 in the region considered; for a proof see Ref. 21. This maximum occurs when  $h_1 = h_2 = 1/2$ . Since the two modulation indices are equal we are back in the  $H = 1$  case. It is possible to choose

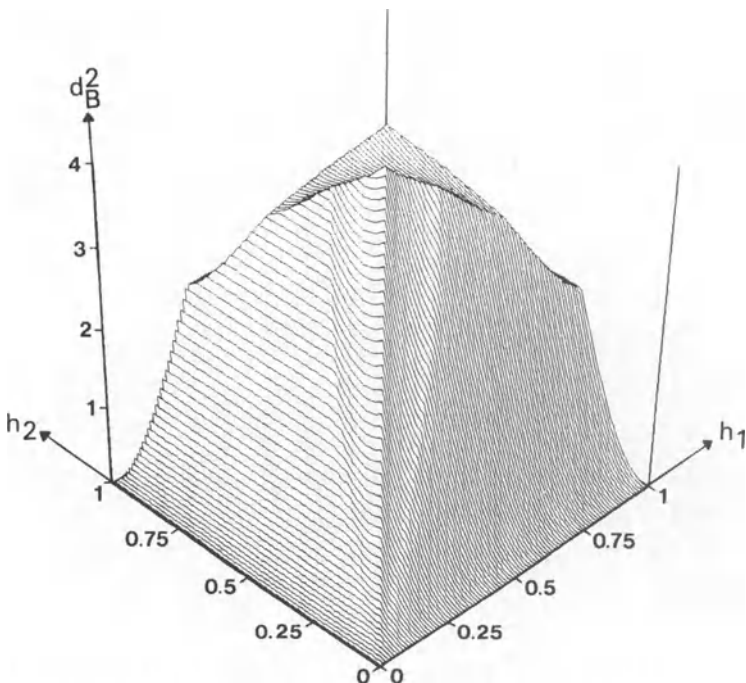


Figure 3.18. The upper bound  $d_B^2$  for binary  $2-h$  1REC schemes, when both  $h$ 's lie in the interval  $(0, 1)$ . The maximum value 4.0 occurs for both  $h_1$  and  $h_2$  near 0.5. From Ref. 21, © 1982 by IEEE.

$h_1$  and  $h_2$  arbitrarily close to  $1/2$  of course. Thus there are no binary  $2 - h$  schemes using 1REC pulses with minimum squared normalized Euclidean distance values larger than 4 for this practically interesting range of modulation indices.

The technique to construct an upper bound for the  $M$ -ary case with  $M \geq 4$  is similar to the one in Section 3.2.1. The upper bound for the  $2 - h$  scheme can also be written as a function of the two  $h$  values  $h_1$  and  $h_2$ , i.e.,  $d_B^2(h_1, h_2)$ . Thus one can write

$$d_{B|M\text{-ary}}^2(h_1, h_2) = \log_2 M \min_{1 \leq k_1, k_2 \leq M-1} \{d_{B|\text{binary}}^2(k_1 h_1, k_2 h_2)\} \quad (3.31)$$

This bound is plotted for  $M = 4$  in the three-dimensional Figure 3.19. Now the maximum value 6.49 is obtained when  $h_1 = h_2 = 0.77$  in the region considered. Actual calculations of  $d_{\min}^2$ , which are presented in Section 3.3.3, indicate that the bound (3.31) is quite useful for the  $M = 4$  case.

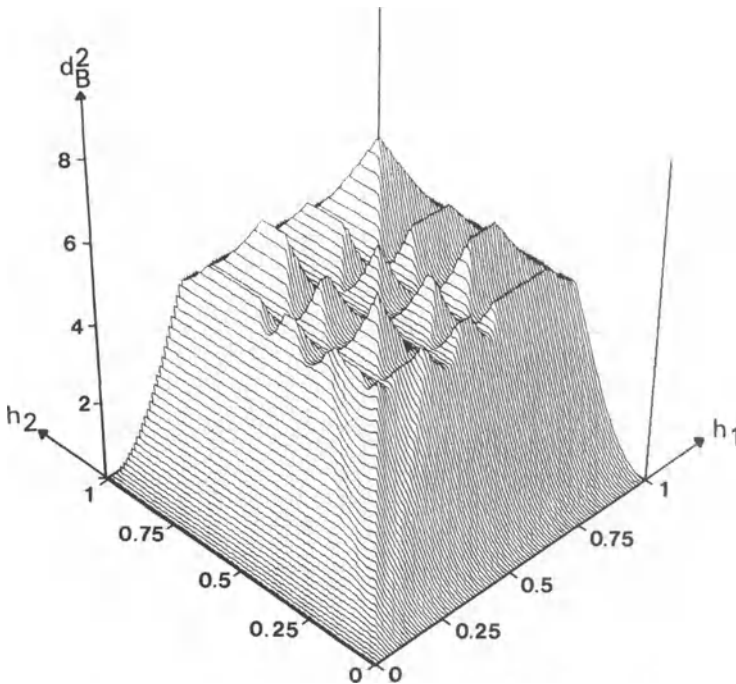


Figure 3.19. The upper bound  $d_B^2$  as in Figure 3.19, but for quaternary instead of binary 1REC. The maximum value 6.49 occurs when both  $h_1$  and  $h_2$  are near 0.77. From Ref. 21, © 1982 by IEEE.

In the remainder of this section we develop bounds for schemes with more than two  $h$ 's. The material is more complicated and should be skipped on first reading. Its importance lies in the producing of upper bounds to the performance available from  $M$ -ary schemes for each number of  $h$ 's. Restriction will be made to the 1REC pulse, although the same development can be done when other pulse shapes are used.

First we study the case  $H = 3$ . The following difference sequences yield mergers in the binary case at  $t = 4T, 5T$ , and  $6T$ :

$$\gamma = \begin{cases} +2, 0, 0, -2, 0, 0, \dots \\ +2, -2, 0, -2, +2, 0, 0, \dots \\ +2, +2, +2, -2, -2, -2, 0, 0, \dots \\ +2, +2, -2, -2, -2, +2, 0, 0, \dots \\ +2, -2, +2, -2, +2, -2, 0, 0, \dots \\ +2, -2, -2, -2, +2, +2, 0, 0, \dots \end{cases} \quad (3.32)$$

Just as with  $H = 2$ , the trees starting with  $h_1$ ,  $h_2$ , and  $h_3$  must all be taken into account; this gives 18 components in the construction of the upper bound. Similarly, when  $H = 4$ ,

$$\gamma = \begin{cases} +2, 0, 0, 0, -2, 0, 0, \dots \\ +2, +2, 0, 0, -2, -2, 0, 0, \dots \\ +2, -2, 0, 0, -2, +2, 0, 0, \dots \\ +2, +2, +2, 0, -2, -2, -2, 0, 0, \dots \\ +2, +2, -2, 0, -2, -2, +2, 0, 0, \dots \\ +2, -2, +2, 0, -2, +2, -2, 0, 0, \dots \\ +2, -2, -2, 0, -2, +2, +2, 0, 0, \dots \end{cases} \quad (3.33)$$

define the mergers at  $t = 5T$ ,  $6T$ , and  $7T$ . Now there are 28 components in the construction of the upper bound, and the minimum is taken of them all to give the resulting upper bound. It is straightforward if lengthy to write down the closed form expressions for the bound components by the use of these sequences, and equation (3.9).

By studying (3.30), (3.32), and (3.33), it is easy to see how to choose  $\gamma$ -sequences for a general multi- $h$  scheme with  $H$  different modulation indices giving a merger, without ever drawing the actual phase difference tree. By taking either the even- or odd-numbered components of  $\gamma$  in (3.30), which is for  $H = 2$ , it is seen that either set always sums to zero. The same holds for (3.32), which is for  $H = 3$ , by adding every third component, and for (3.33), by adding every fourth component. Each of the  $H$  sums corresponds to one and the same  $h$  value. The condition that these sums all must be equal to zero assumes that a phase shift caused by a specific  $h$ -value can in general only be canceled by using the same  $h$  value again. Thus it is possible to enumerate difference sequences  $\gamma$ , corresponding to mergers, by requiring that

$$\sum_{i=0}^m \gamma_{iH+j} = 0, \quad j = 0, 1, 2, \dots, H-1$$

$$\gamma_i = 0, \quad i \leq -1, \quad i \geq H+m \quad (3.34)$$

where  $m$  denotes the  $m$ th merger. All  $H$  different root nodes must also be considered. The values of the components in  $\gamma$  must also be chosen as in (3.24), in accordance with the alphabet size.

By maximizing the upper bounds obtained in an exhaustive fashion for the binary  $H = 1, 2, 3$ , and 4 schemes, the peak distance bound values presented in Table 3.1 are obtained. A close study of the bound component functions shows that the region for each  $h_i$  where a peak can occur is limited to only a part of the interval  $0 \leq h_i \leq 1$ . When  $H = 3$ , for instance, it is

**Table 3.1. Maximum Values of the Upper Bound  $d_B^2$  for Binary Multi- $h$  Linear Phase Systems**

$H$	Max $d_B^2$	dB gain compared to PSK	$h_1$	$h_2$	$h_3$	$h_4$	$\bar{h}$
1	2.43	0.85	0.715				0.715
2	4.0	3.0	0.5	0.5			0.5
3	4.88	3.87	0.620	0.686	0.714		0.673
4	5.69	4.54	0.73	0.55	0.73	0.55	0.64

sufficient to search for maxima in the regions  $0.35 \leq h_i \leq 0.75$ , where the corresponding bound component for the very first merger is larger than 4.5. This approach was followed in the search for bound peaks.

From Table 3.1 it can be concluded that most of the good 2-, 3-, and 4- $h$  schemes occur for low and moderate values of  $h_i$ , and that the  $h_i$  are also close together. Thus it is of interest to study the upper bound for the case  $h_i = h$ , a constant. This gives, of course, an  $H = 1$  scheme and thus should yield weak  $H = 2, 3$ , and 4 schemes, but it will give an approximate bound for schemes whose  $h_i$  are close to equal. For the  $h_i = h$  case, the bound functions corresponding to the three first inevitable mergers when  $H = 2, 3, 4$  are

$$\begin{aligned} d_{\text{I}}^2 &= 2 \left( 1 - \frac{\sin 2\pi h}{2\pi h} \right) + (H-1)(1 - \cos 2\pi h) \\ d_{\text{II}}^2 &= 4 \left( 1 - \frac{\sin 4\pi h}{4\pi h} \right) + (H-2)(1 - \cos 4\pi h) \\ d_{\text{III}}^2 &= 4 \left( 1 - \frac{\sin 2\pi h}{2\pi h} \right) \end{aligned} \quad (3.35)$$

Both  $d_{\text{I}}^2$  and  $d_{\text{II}}^2$  grow linearly with  $H$ , so that eventually only  $d_{\text{III}}^2$ , which is constant with  $H$ , controls the value of the minimum. This implies that the use of many indices is of limited use in improving the minimum distance.

The upper bound (3.35) is plotted in Figure 3.20 for the cases of 2, 3, and 4 indices. The overall bound peaks for the same cases are also shown; now the  $h_i$  are not constrained to be constant. The horizontal axis in the figure is

$$\bar{h} = \frac{1}{H} \sum_{i=1}^H h_i \quad (3.36)$$

which is the mean modulation index for the multi- $h$  scheme. The motive for this choice is that the spectral characteristics of a multi- $h$  scheme where

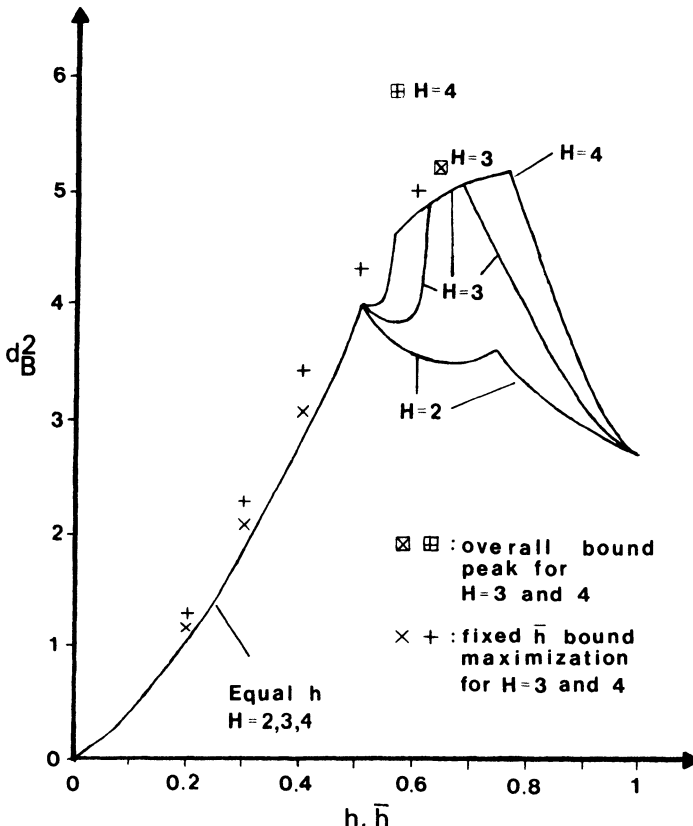


Figure 3.20. The upper bounds  $d_B^2$  when  $H = 2, 3, 4$ . Solid lines show the equal  $h$  bounds; the overall peaks and the optimizations for fixed  $h$  are also shown when  $H = 2, 3$ .

the  $h_i$  values are close together is similar to a  $H = 1$  scheme with  $h = \bar{h}$ , as shown in Refs. 24 and 25.  $\bar{h}$  also appears in Table 3.1.

By restricting all the  $h_i$  to be the same, we avoid the difficulty of maximizing over  $H$  variables. Another way to reduce this difficulty somewhat is to search for the maximizing set of indices, with the constraint that  $\bar{h}$  is fixed. The result of this search is shown for certain  $\bar{h}$  in Figure 3.20. The points indicate true overbounds, but only for a small region of indices whose  $\bar{h}$  is near the horizontal coordinate. Nonetheless, they appear to give a useful indication of the minimum distance of multi- $h$  codes. The distance grows to a maximum of about 6 that occurs when the average of the indices is near 0.6.

The upper bound results above for the binary 1REC schemes can easily be generalized to the  $M$ -ary case for each value of  $H$  by using the same

technique as in (3.31), i.e.,

$$\begin{aligned} d_B^2|_{M\text{-ary}}(h_1, h_2, \dots, h_H) \\ = \log_2 M \min_{1 \leq k_1, k_2, \dots, k_H \leq M-1} [d_B^2|_{\text{binary}}(k_1 h_1, k_2 h_2, \dots, k_H h_H)] \end{aligned}$$

By a nonexhaustive search, some peak values of  $d_B^2$  for the case  $H = 2$ , 3 and  $M = 4, 8$  have been found. (The frequency pulse is still 1REC.) The search was performed in the neighborhood  $h_i \approx h$ , all  $i$ , and for  $h_i \leq 1$ . The bound peaks occur at an average  $\bar{h}$  that is close to the  $h$  at which a single- $h$  scheme has its peaks. The results are summarized in Table 3.2 for single and multiple index schemes. Note the significantly higher peak values for the  $M = 4$  and  $M = 8$  cases, compared to the corresponding Table 3.1 for the binary case.

The upper-bound results are summarized in Figure 3.21. The trends described earlier can now be clearly seen. For  $M = 2$  the bound of the type (3.35) is a factor of 2 (3 dB) above the  $H = 1$  case for  $h \leq 1/2$  when  $H \geq 2$ . "True" minimum distances (from a nonexhaustive search) are also shown against the variable  $\bar{h}$ . By going from  $H = 1$  to  $H = 2$ , the bounds increase by a factor of 2, but only small gains are obtained by using  $H \geq 3$ . This is true for  $M = 2, 4$ , and 8. Increasing  $M$  leads to significant gains. It can also be concluded that there exist many-level  $H = 1$  schemes that give equal or better bound results than binary multi- $h$  schemes. These figures give a good picture of how the parameters  $H$  and  $M$  will influence the performance for 1REC schemes, but the bounds are only approximate, as we shall see in Section 3.3.3.

### 3.2.4. Partial Response, Multi- $h$

The technique used in the previous section—finding pairs of phase trajectories in the phase tree with inevitable mergers—can be directly applied

**Table 3.2. Maximum Upper Bound Values for Some Quaternary and Octal Multi- $h$  Linear Phase Schemes with  $H = 1, 2$ , and 3**

$M$	$H$	Max $d_B^2$	dB gain compared to PSK	$h_1$	$h_2$	$h_3$
4	1	4.23	3.25	0.914		
4	2	6.54	5.15	0.772	0.772	
4	3	7.65	5.83	0.795	0.795	0.795
8	1	6.14	4.87	0.964		
8	2	7.50	5.74	0.883	0.883	
8	3	8.40	6.23	0.879	0.879	0.879

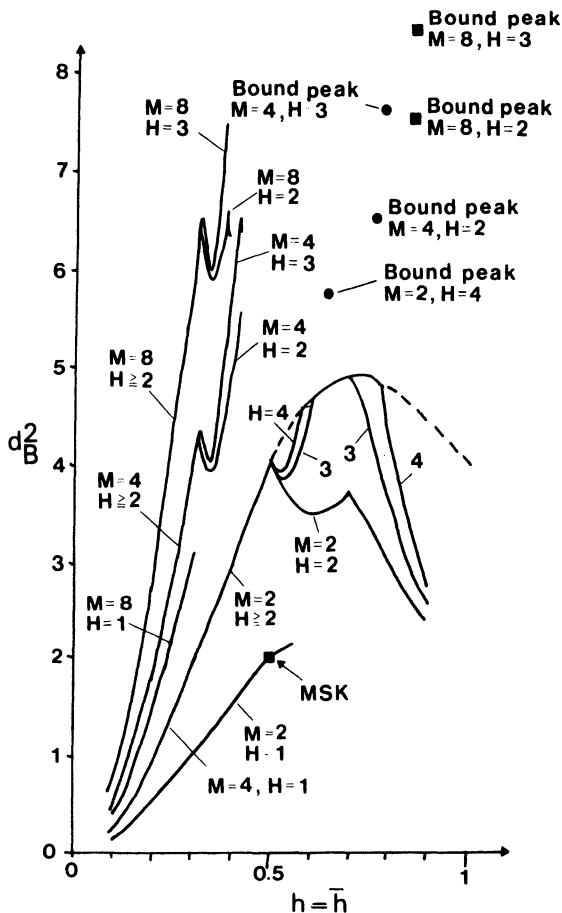


Figure 3.21. A summary of the upper bounds on minimum distance for several  $M$  and  $H$ . Some individual bound peaks are also shown. From Ref. 21, © 1982 by IEEE.

when the frequency pulse width  $L$  exceeds a single interval. The difference sequences yielding mergers must still satisfy condition (3.34) even though  $L \geq 2$ . The first merger now occurs at  $t = (L + H)T$  in general, for a partial response scheme using  $H$  different cyclical  $h$  values.

Recall that in Section 3.2.2 the first through  $L$ th mergers [which occur at  $t = (L + 1)T, (L + 2)T, \dots, 2LT$ ] were each used to generate a distance bound function; our upper bound to minimum distance was then the minimum at each  $h$  of these functions. It was empirically found for this  $H = 1$  case that the final bound could not be improved by using functions from later inevitable mergers. On the other hand, Section 3.2.3 showed that for multi- $h$  schemes with  $L$  equal only 1 as much as the fifth merger

contributed to the final bound. This was true even when  $H$  and  $M$  were only 2.

We can relatively easily extend the calculations of Section 3.2.3 to the case of partial response modulation with two indices. The distance bounds so obtained appear in Section 3.3.4, with the numerical results for the actual minimum distance. In the construction of the upper bounds *all* inevitable mergers from the first to the  $(L + 3)$ rd have been used. It should be noted that there are more second mergers than there are first mergers, etc. As will be seen in Section 3.3.4, where actual  $d_{\min}^2$  results are presented, this is not quite enough, and taking into account even later mergers, the upper bound can be further tightened. Since the number of inevitable mergers grows very rapidly with the depth of the merger, it is probably unrealistic to consider mergers later than the  $(L + 3)$ rd. The obvious conclusion is that one has to be satisfied with an upper bound  $d_B^2$  which is not tight everywhere.

An example of a phase tree for a binary  $H = 2$  scheme with  $L = 2$  is shown in Figure 3.22. The  $S$  class of pulses used there are obtained by successive convolutions of the rectangular pulses of duration 1 with itself. Thus  $1S$  equals 1RFC, and  $2S$  is triangular with duration  $2T$ . This means that the phase trajectories in Figure 3.22 are segments of second-order polynomials.

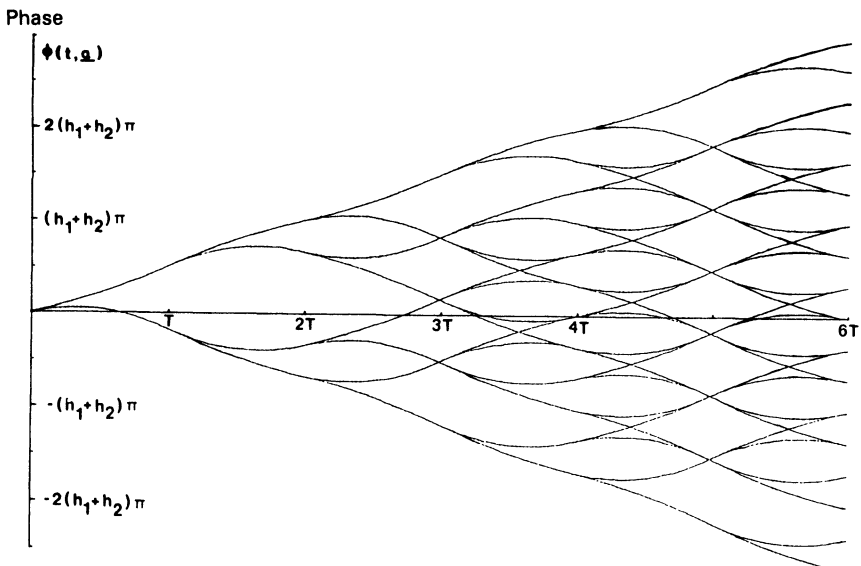


Figure 3.22. The phase tree for a binary  $2-h$  scheme based on the  $2S$  pulse; the first inevitable merger occurs at  $t = 4T$ .  $h_2 = (1/2)h_1$  in this example, and data symbols prior to  $t = 0$  are +1. From Ref. 22, © 1982 by IEEE.

### 3.2.5. Summary

Section 3.2 contains techniques for the construction of upper bounds on the minimum squared Euclidean distance for the phase modulated systems emphasized in this book. The most general scheme is the partial response multi- $h$  system.

It must be stressed that the eventual product of these bounds will be a fast algorithm to bound the error probability of various systems. This is particularly true for the  $H = 1$  case. As well, the very shape of  $d_B^2$  is a powerful tool for the classification of different systems. By plotting  $d_B^2$  as a function of  $h$ , a whole family of systems can be compared. The next section will show that  $d_B^2$  is also useful for efficient calculation of  $d_{\min}^2$  for different observation widths. This is done by using a heavily reduced tree search algorithm which is described in Appendix A.

Finally, it can be noted that  $d_B^2$  values significantly larger than 2 ( $d_{\min}^2 = 2$  for MSK and QPSK, for instance) can be obtained. No redundant bits are transmitted over the channel, as is the case with error-correcting codes. A particularly effective way of increasing the distance is to increase the alphabet size  $M$ .

## 3.3. The Minimum Euclidean Distance

This section considers the problem of calculating the minimum squared normalized Euclidean distance,  $d_{\min}^2$ , for a given observation width of  $N$  symbol intervals. This quantity can be calculated by using the difference sequences  $\gamma_N$  through

$$d_{\min}^2 = \log_2 M \min_{\gamma_N} \left[ N - \frac{1}{T} \int_0^{NT} \cos \phi(t, \gamma_N) dt \right] \quad (3.37)$$

with restriction that

$$\gamma_i = 0, \quad i < 0$$

$$\gamma_0 = 2, 4, 6, \dots, 2(M-1)$$

$$\gamma_i = 0, \pm 2, \pm 4, \dots, \pm 2(M-1), \quad i = 1, 2, \dots, N-1$$

$$\gamma_i = 0, \quad i > N$$

In Section 3.2, inevitable mergers were used for the construction of an upper bound,  $d_B^2$ , on  $d_{\min}^2$ . There are other kinds of mergers too, that depend upon the specific modulation index  $h$ . These will be the case if there is a phase difference trajectory that equals a nonzero multiple of  $2\pi$  beyond a

certain time. The magnitude of this constant phase difference trajectory depends upon  $h$ , and it is always possible to choose  $h$ 's such that the constant equals zero modulo  $2\pi$ . For reasons that will be clear below, these  $h$  values will be called *weak*. These  $h$ -dependent mergers can occur prior to the first inevitable merger at  $t = (L + 1)T$  for a  $H = 1$  system.

Since any phase difference trajectory is achieved by feeding the difference sequence into a filter having the impulse response  $q(t)$  and multiplying the output of this filter by  $2\pi h$ , the first time at which a constant difference trajectory is obtained is at  $t_w = LT$ . This will occur if  $\gamma_0 = 2, 4, 6, \dots, 2(M - 1)$  and all the other  $\gamma_i$  equal zero. Note that this holds for multi- $h$  schemes also. This is because for frequency pulses  $g(t)$  of length  $L$  symbol intervals  $q(t) = q(LT)$ ,  $t \geq LT$ . Sometimes a constant phase difference can occur also for  $t_w = (L - 1)T, (L - 2)T$ , and so on, but only for specific phase responses  $q(t)$ . Ignoring this case, the constant phase difference trajectory is made equal to zero modulo  $2\pi$  if

$$2\pi h_w \gamma_0 q(LT) = k2\pi, \quad k = 1, 2, \dots, \gamma_0 = 2, 4, 6, \dots, 2(M - 1)$$

where it is assumed that  $q(LT) \neq 0$ . Thus for the weak modulation indices

$$h_w = \frac{k}{\gamma_0 q(LT)}, \quad k = 1, 2, \dots, \gamma_0 = 2, 4, 6, \dots, 2(M - 1) \quad (3.38)$$

a merger occurs at  $t_w = LT$ , modulo  $2\pi$ .

In a similar way, the phase difference trajectory can be made constant for all  $t \geq (L + \Delta L)T$  by choosing

$$\gamma_0 = \begin{cases} 0, & i < 0 \\ 2, 4, 6, \dots, 2(M - 1), & i = 0 \\ 0, \pm 2, \pm 4, \dots, \pm 2(M - 1), & i = 1, 2, \dots, \Delta L \\ 0, & i > \Delta L \end{cases}$$

and the weak modulation indices now are

$$h_w = \frac{k}{q(LT) \sum_{i=0}^{\Delta L} \gamma_i}, \quad k = 1, 2, 3, \dots \quad (3.39)$$

$$\sum_{i=0}^{\Delta L} \gamma_i \neq 0$$

We shall say the modulation indices are weak of order 1, 2, ... if  $\Delta L = 1, 2, \dots$ . As will be seen below,  $d_{\min}^2$  can be below the upper bound  $d_B^2$  at these indices (and only these), for all values of  $N$ , hence the term weak. If

it is considerably below the upper bound, the term *catastrophic* will be applied.

Next follows numerical results on  $d_{\min}^2$  for various systems in the form of plots. These present  $d_{\min}^2$  versus the modulation index  $h$ , for different values of  $N$ , the number of symbol intervals observed by the receiver. The influence of the weak modulation indices will be evident, and it will be clear how large  $N$  has to be made in a specific situation to make  $d_{\min}^2$  equal to  $d_B^2$ . This value of  $N$  is denoted  $N_B$ . An algorithm for calculation of  $d_{\min}^2$  is presented in Appendix A.

### 3.3.1. Full Response, $H = 1$

As an introductory example the binary scheme with frequency pulse 1REC is chosen. Figure 3.23 shows  $d_{\min}^2$  versus  $h$  for  $N = 1, 2, 3, 4$ , and 5. The upper bound  $d_B^2$  is also shown dashed where it is not yet reached with  $N = 5$ . For this system  $h_w = 1, 2, \dots$  are weak of the first order according to (3.38), with the early merger occurring at  $t = T$ . This can be seen in Figure 3.2 (solid tree), where the two nodes  $+h\pi$  and  $-h\pi$  coincide for these  $h_w$ . It is also apparent in Figure 3.23;  $d_{\min}^2$  at  $h_w = 1$  cannot be made larger than 1 for any  $N$ .

Note that  $h = 1/2$  corresponds to MSK and gives  $d_{\min}^2 = 2$  when  $N \geq 2$ . This is the same  $d_{\min}^2$  as antipodal signaling, e.g., BPSK. The required observation interval for BPSK is one bit interval, and for detectors making bit-by-bit decisions, PSK in fact achieves the largest distance of any binary scheme.<sup>(23)</sup> The required observation interval for MSK is two-bit intervals, and the asymptotic performance in terms of error probability is the same as that for BPSK. The optimum modulation index for the 1REC system is  $h = 0.715$  when  $N = 3$ . This gives  $d_{\min}^2 = 2.43$  and thus a gain of 0.85 db in terms of  $E_b/N_0$  is obtained compared to MSK or BPSK. The upper bound  $d_B^2$  is twice as large as  $d_{\min}^2$  for  $N = 1$ . This is because of the symmetry condition (3.14).

The minimum normalized squared Euclidean distance versus the modulation index  $h$  is shown in Figure 3.24 for the quaternary 1REC system. Note that  $d_B^2$  (shown dashed where it is not reached) is often as much as twice  $d_{\min}^2$  at  $N = 1$  symbol interval. The maximum value of  $d_B^2$  is almost reached for eight observed symbol intervals. From (3.38) we can see that the first-order weak modulation indices in the interval  $0 \leq h \leq 2$  are  $h_w = 1/3, 1/2, 2/3, 1, 4/3, 3/2, 5/3$ , and 2. The effect of these early mergers can be clearly seen in Figure 3.24. Note that most of these weak  $h$  values must be considered catastrophic, since  $d_{\min}^2$  is restricted to 2.

It is interesting to compare  $d_{\min}^2$  for the quaternary 1REC system to QPSK (whose phase response has  $h = 1/4$  and  $M = 4$ ). As is indicated in Figure 3.24,  $d_{\min}^2 = 2$  for QPSK, but the quaternary 1REC system lies slightly

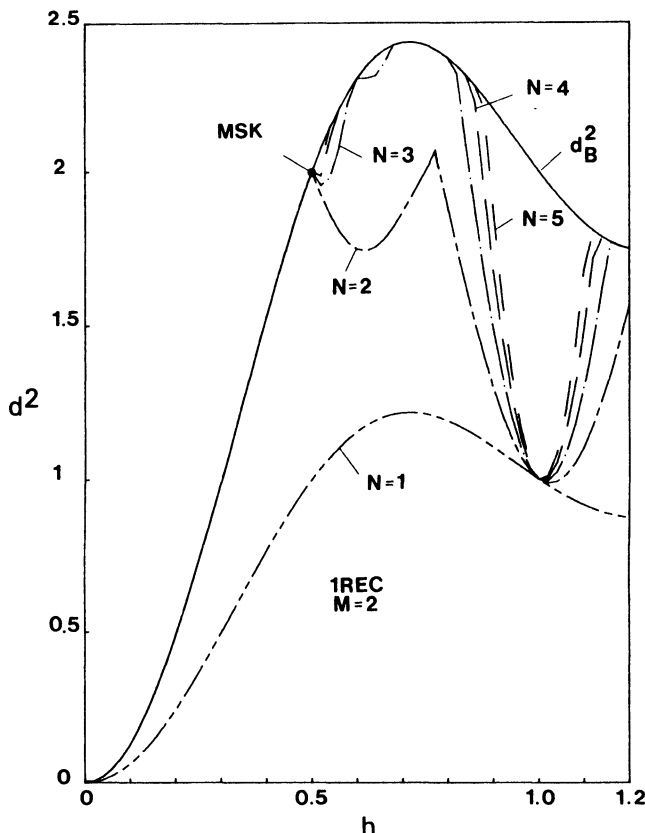


Figure 3.23. A comparison of the normalized distance upper bound  $d_B^2$  (solid line) to the actual  $d_{\min}^2$ , plotted against  $h$  for binary 1REC. The cases for  $N = 1, \dots, 5$  observation intervals are shown. From Ref. 44, © 1984 by John Wiley Ltd.

below this value for  $h = 1/4$ . For  $M = 2$  and  $h = 1/2$ , on the other hand, all schemes have  $d_{\min}^2 = 2$ , 1REC and BPSK included.

The minimum distance for the octal ( $M = 8$ ) 1REC system is given in Figure 3.25 for  $N = 1, 2, 3$  and in some intervals for  $N = 4$  and 5. Like the quaternary case, the upper bound  $d_B^2$  is reached with two observed symbol intervals for low  $h$  values. Compared to the quaternary case, and especially the binary, the number of first-order weak  $h$ -values has greatly increased in the interval  $0.3 \leq h \leq 1$ . Larger values of  $N$  are also required to reach  $d_B^2$  when  $h \neq h_w$ . Most of the weak indices are catastrophic.

The scheme 8PSK [ $q_1(t)$  in Section 3.2.1,  $h = 1/8$ ,  $M = 8$ ], which was shown in Section 3.2.1 to maximize  $d_B^2$  when  $h = 1/8$ , is also indicated in Figure 3.25. It is seen that if  $h$  is slightly larger than  $h = 1/8$  and if  $N$

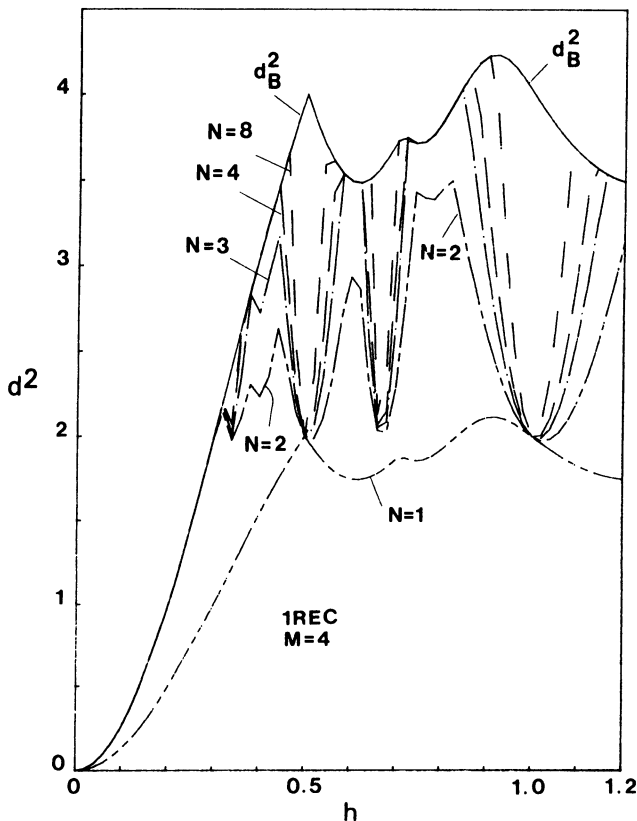


Figure 3.24. Minimum distance vs.  $h$  for quaternary 1REC. From Ref. 44, © 1984 by John Wiley Ltd.

is 2, the octal 1REC scheme yields the same  $d_{\min}^2$ . Much larger distances can be obtained for the octal 1REC system by choosing for instance  $h \approx 0.45$  and  $N = 5$ .

General conclusions concerning the minimum distance properties of 1REC schemes with larger values of  $M$  are most easily achieved by studying the tightness of the upper bound, and the distance growth with  $N$  for  $h$  values close to  $h_w$ .

#### *Tightness of the Upper Bound $d_B^2$*

It will now be shown that for all full response,  $H = 1$  schemes, except at weak modulation indices of the first order, the minimum Euclidean distance itself equals this bound if the observation interval  $N$  is long enough. The least  $N$  for which this occurs is denoted  $N_B$ .

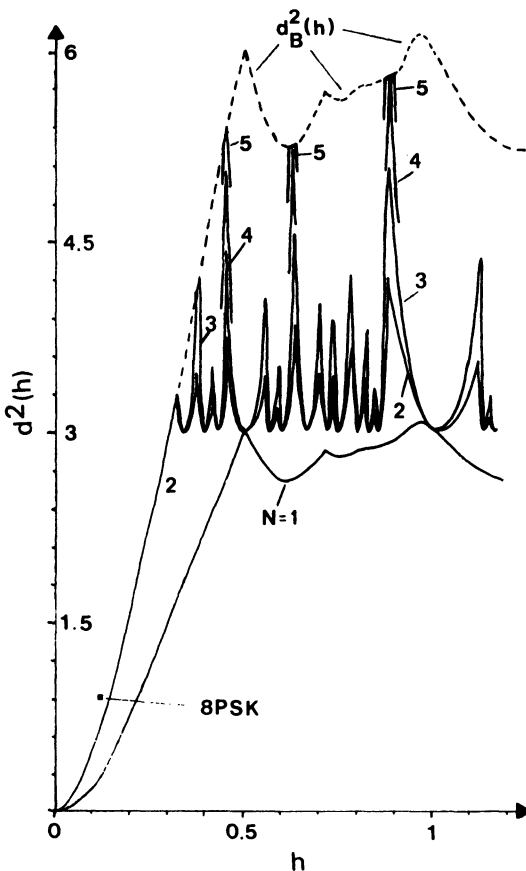


Figure 3.25. Minimum distance vs.  $h$  for octal 1REC. From Ref. 16, © 1981 by IEEE.

If a specific pair of full-response phase trajectories never merges, in phase, the Euclidean distance will grow without limit with  $N$ . This is because the Euclidean distance increment calculated over each symbol interval is positive. Since  $d_{\min}^2$  previously was shown to be upper bounded, the pair of phase trajectories giving the minimum distance must eventually merge. For a modulation index close to a first-order weak modulation index, the difference sequence with only  $\gamma_0 \neq 0$  and all other  $\gamma_i$  equal to zero gives the smallest growing Euclidean distance with  $N$ . Its distance is

$$d^2 = \log_2 M \min_{1 \leq k \leq M-1} \left[ 1 - \frac{1}{T} \int_0^T \cos 2\pi h k \gamma_0 q(t) dt + (N-1)(1 - \cos \pi h k \gamma_0) \right] \quad (3.40)$$

The smallest growth rate per symbol interval is apparent from the second term, and this is

$$\log_2 M \min_{1 \leq k \leq M-1} (1 - \cos \pi h k \gamma_0) \quad (3.41)$$

For sufficiently large  $N$  in (3.40), with  $h$  near but not identical to a weak index, the minimum distance for  $h$  is given by  $d_B^2$  since  $d^2$  in (3.40) will exceed  $d_B^2$ .

By using (3.40) it is possible to find  $N_B$  for the modulation index  $h_{\text{opt}}$  which maximizes  $d_B^2$  for any  $M$ -ary 1REC scheme. When  $M \geq 4$ ,  $h_{\text{opt}}$  is near 1, even though  $h = 1$  is a weak index of first order, with poor performance. The results are summarized in Table 3.3. The maximum attainable minimum distance value grows with  $M$ , but the number of first-order weak (catastrophic) modulation index values also grows with  $M$ , as does  $N_B$ . For  $h \leq 0.3$ ,  $N_B = 2$  for all  $M$ . For other pulse shapes  $g(t)$  such as HCS or 1RC, the general conclusions above still hold. A comparison between such schemes was made in Section 3.2.1 on a  $d_B^2$  basis, and the discussion of the last few pages is easily modified. Generally,  $d_{\text{min}}^2$  achieves  $d_B^2$  except at weak modulation indices. For details see the references and figures given there.

### 3.3.2. Partial Response, $H = 1$

A great many partial response schemes have been studied. Rather than cover all of these, we discuss as representative modulations the RC and REC classes; the REC class is a generalization of FSK signaling, while the RC results are typical of those for smoothed phase pulses. It will be evident that  $d_B^2$  constructed as in Section 3.2.2 will be a tight bound on  $d_{\text{min}}^2$  for all pulse classes, except at certain weak  $h$  values.

First a simple example will be studied in some detail, and the  $d_{\text{min}}^2$  behavior explained. For this purpose the binary 3REC scheme is selected. It uses the phase tree in Figure 3.9 and the phase difference tree shown in

**Table 3.3. Optimum  $h$ -Values and Corresponding Normalized Euclidean Distances for  $M$ -ary 1REC Schemes**

$M$	Optimum $h$ ( $h_{\text{opt}}$ )	$d_B^2(h_{\text{opt}})$	$N_B$
2	0.715	2.434	3
4	0.914	4.232	9
8	0.964	6.141	41
16	0.983	8.088	178
32	0.992	10.050	777

Figure 3.10. Figure 3.26 shows  $d_{\min}^2$  for this scheme for  $N = 1, 2, \dots, 10$  observed bit intervals. The upper bound is shown in Figure 3.11.

In Figure 3.26 it is seen that for most  $h$  values  $d_{\min}^2$  increases up to the upper bound with  $N$ , but not for the weak modulation indices.  $h_w = 3/4, 1, 9/8, 6/5, 9/7, 3/2$ , etc. By studying (3.39), it can also be seen that "weak" modulation indices like  $h_w = 4/5, 7/8$  do not affect the growth of  $d_{\min}^2$  with  $N$ . This is because only some of the weak modulation indices of the first few orders actually degrade  $d_{\min}^2$ . For full response schemes ( $L = 1$ ) only the very first order affected  $d_{\min}^2$ , and the others have distance values on or above  $d_B^2$ .

The 3REC scheme is special in that some of the weak modulation indices are so because of the pulse shape  $g(t)$ . By studying the phase difference tree in Figure 3.10, one can see that there are trajectories which are constant for  $t \geq T$ ,  $t \geq 2T$ ,  $t \geq 3T$ , and so on. In the general case this will not occur until  $t \geq LT$ , which is  $3T$  here. The offending difference sequence now is  $\gamma = \dots, +2, -2, 0, +2, -2, 0 \dots$ , periodically repeated. A merger at  $t = T$  is obtained modulo  $2\pi$  if

$$\frac{2\pi h}{3} = k2\pi, \quad k = 1, 2, \dots \Leftrightarrow h = 3k, \quad k = 1, 2, \dots$$

The effect of this cannot be seen in Figure 3.26 owing to the limited range

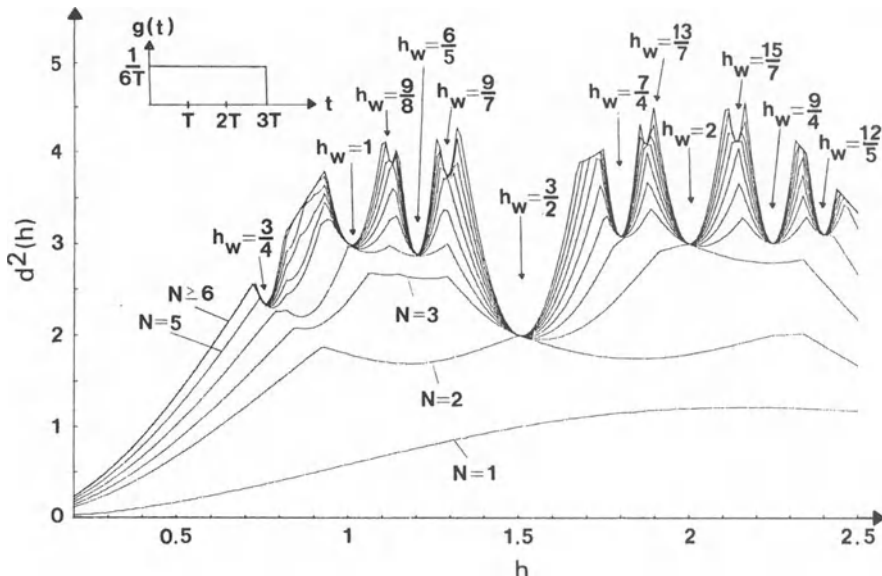


Figure 3.26. Minimum distance vs.  $h$  for binary 3REC, with  $N = 1, \dots, 10$  symbols observation interval. Weak modulation indices  $h_w$  are indicated by arrows. From Ref. 44, © 1984 by John Wiley Ltd.

of  $h$  shown. There exists another phase difference trajectory which is constant for  $t \geq 2T$ , if  $\gamma = \dots, +2, 0, -2, +2, 0, -2, \dots$  periodically repeated. A merger of  $t = 2T$ , modulo  $2\pi$  is obtained if

$$\frac{4\pi h}{3} = k2\pi; \quad k = 1, 2, \dots \Leftrightarrow h = \frac{3k}{2}, \quad k = 1, 2, \dots$$

This one can be seen in Figure 3.26 for  $h = \frac{3}{2}$  ( $k = 1$ ). Note that  $N = 2$  now leads to the maximum  $d_{\min}^2$ . As will be seen from studying binary 3RC, this kind of weak  $h$  value can be removed by changing the pulse shape. As well, the probability of these (or any) special sequences rapidly drops as their length increases. By making  $N$  large, these weak-index events can be made very unlikely.

### Binary Systems

The RC class will now be analyzed in terms of  $d_{\min}^2$ . Figure 3.27 shows the minimum normalized squared Euclidean distance for the 2RC scheme. The receiver observation interval is 1 to 5 bit intervals. For  $h = 1/2$ , all binary  $H = 1$  full response systems including MSK  $d_{\min}^2 = 2$  with  $N_B = 2$ . For this  $h$  value the 2RC system yields almost the same distance, but with  $N = 3$ . (The exact figure is 1.97.) Hence MSK and 2RC with  $h = 1/2$  have almost the same performance in terms of bit error probability for large SNR, but the optimum detector for the 2RC system must observe one bit interval

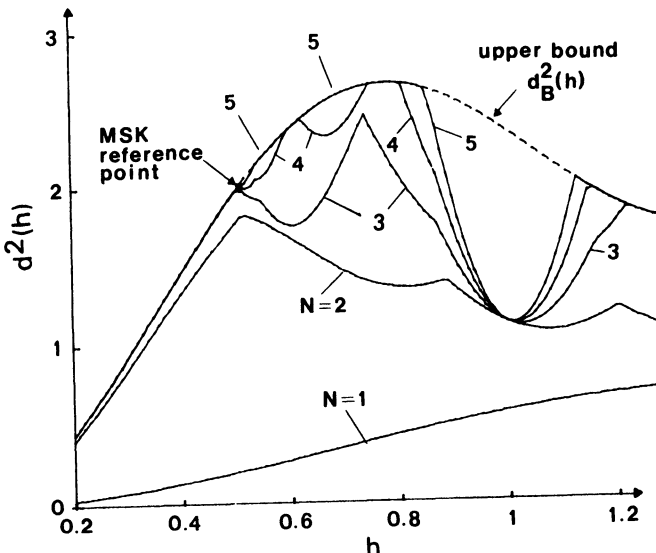


Figure 3.27. Minimum distance vs.  $h$  for the binary 2RC scheme, with up to five observation intervals. From Ref. 17, © 1981 by IEEE.

more than that for the MSK system. It can be expected, however, that the 2RC,  $h = 1/2$  system has a more compact spectrum; this will be discussed in Chapter 4.

For the binary 1REC system, the maximum value of  $d_{\min}^2$  is 2.43 when  $h = 0.715$  and  $N = 3$ . Larger values can be obtained with the 2RC system. Figure 3.27 shows that when  $h \approx 0.8$ ,  $d_{\min}^2$  equals 2.65 for  $N = 4$ . It is also seen that in the region  $0 < h \leq 1/2$ ,  $d_B^2$  is reached with  $N = 3$  observed bit intervals.

The phase tree for the binary 3RC scheme is shown in Figure 3.28. As with 3REC, the specific shape of a phase trajectory over a bit interval depends not only upon the present data symbol, but also on the two preceding ones; Figure 3.28 is drawn for the case where  $\alpha_{-1} = \alpha_{-2} = +1$ . Straight lines occur in the phase tree for a sequence of constant data. These lines occur for all RC schemes with  $L \geq 2$  (see 4RC in Figure 3.13) and they can be used for synchronization, as will be discussed in Chapter 9.

The minimum normalized squared Euclidean distances for the 3RC scheme are shown in Figure 3.29 for  $N = 1, 2, \dots, 6$  and  $N = 15$  observed bit intervals. The upper bound  $d_B^2$  has been calculated according to the method in Section 3.2.2, using the first, second, and third mergers.

For  $N = 1$  observed symbol interval,  $d_{\min}^2$  is very poor for almost every modulation index, but already with  $N = 2$  it significantly increases, and when  $N = 4$  the upper bound is reached in the region  $0 < h \leq 0.6$ . The upper bound in this region is lower than for the 2RC system, as shown in Figure 3.12. Outside this region larger values of  $d_{\min}^2$  can be obtained, and for  $h \approx 0.85$  the upper bound value of 3.35 is reached with six observed bit intervals. The maximum value of the upper bound occurs for an  $h$ -value slightly smaller than unity.

There is an apparent weak modulation index when  $h = 2/3$ , but this is not a true weak modulation index since  $d_{\min}^2$  in fact increases (by a small amount) when  $N$  is increased. This behavior is caused by crossings in the phase tree, and not a merger. After the first crossing the phase trajectories are close together, crossing each other once every symbol interval.

For the binary schemes 4RC and 5RC, the upper bounds on  $d_{\min}^2$  are shown in Figure 3.12 and the corresponding  $d_{\min}^2$  curves can be found in the reference. Instead the binary 6RC system is studied for all modulation indices and the  $d_{\min}^2$  vs.  $h$  plot is shown in Figure 3.30. The peak  $d_{\min}^2$  value is larger than those for the shorter pulses and it occurs at a larger  $h$  value, but the distance at  $h$  values below 1/2 is smaller than for shorter pulses. Figure 3.30 also shows that longer pulses require longer observation intervals. For the binary 6RC system, minimum squared Euclidean distance values above 5 can be obtained when  $h \approx 1.25$  and  $N = 30$  observed bit intervals. This corresponds to an asymptotic gain in SNR of at least 4 db compared to MSK.

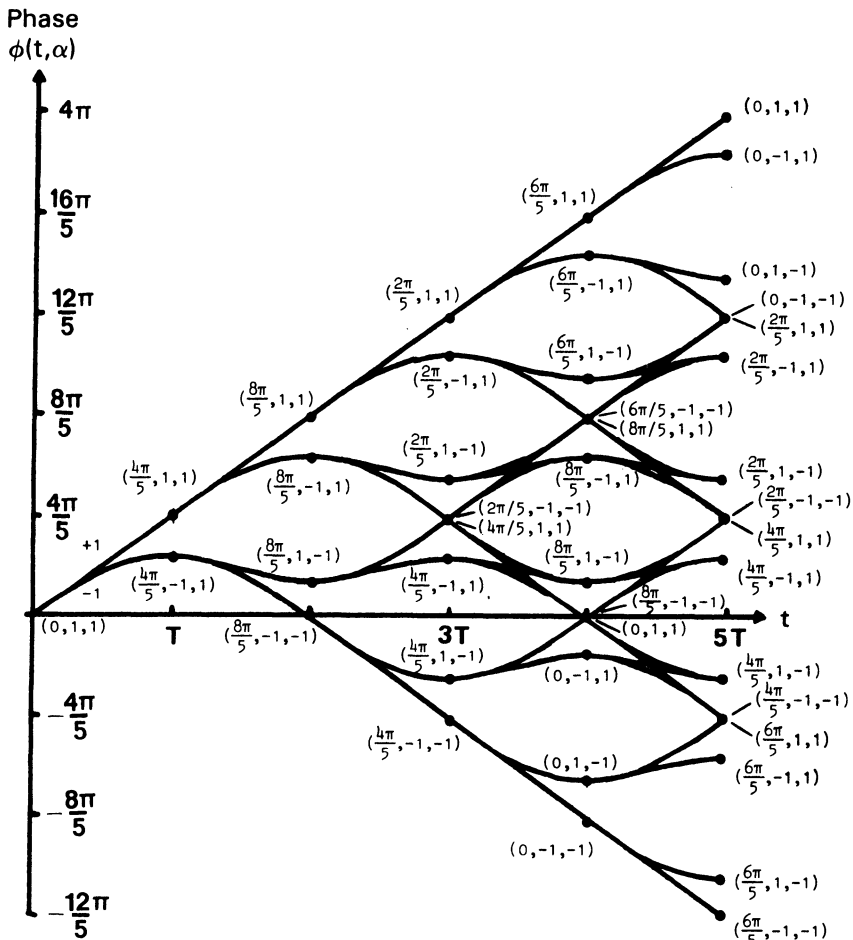


Figure 3.28. The phase tree for the binary 3RC scheme with  $h = 4/5$ . The labeling of the nodes is that of Section 3.4. From Ref. 17, © 1981 by IEEE.

In the study of yet longer pulses than 6RC, it is found that 8RC is a second-order weak scheme, i.e., the upper bound on the minimum Euclidean distance calculated by the inevitable merger difference sequence can be further tightened by also taking into account the sequence giving the early merger at  $t = 7T$ . The two systems 7RC and 9RC are not weak according to our definition, but since they are very close to the 8RC system they are “nearly” weak, and  $N$  must be very large for all modulation indices to make the Euclidean distance equal to the upper bound  $d_B^2$ .

As will be made clear in Chapter 4, it can be advantageous from a spectral point of view to use strictly band limited frequency pulses  $g(t)$ .

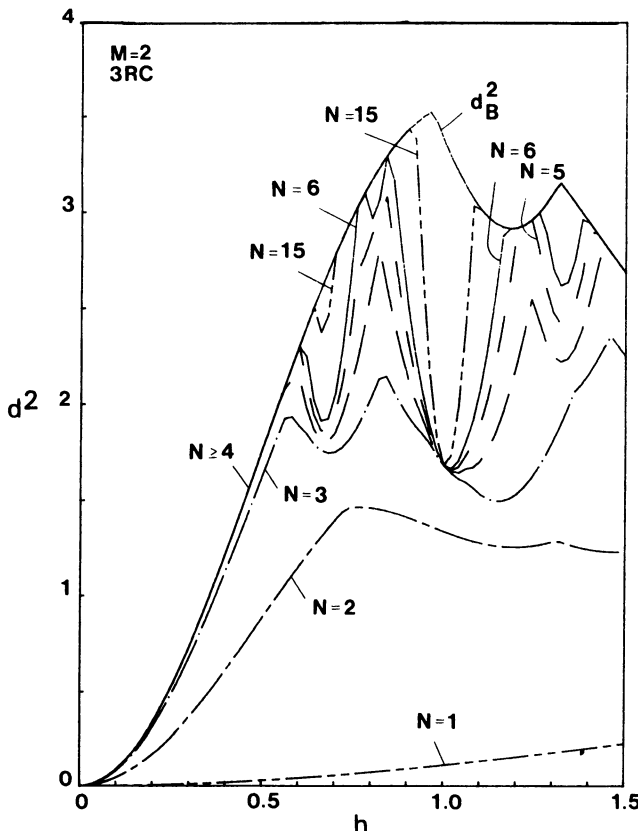


Figure 3.29. The minimum distance vs.  $h$  for binary 3RC. From Ref. 44, © 1984 by John Wiley Ltd.

An example of such a pulse is the SRC pulse (see Table 2.1) with main lobe width  $L_M$  symbol intervals. Another example is the TFM scheme. These pulses are of course of infinite duration, and must be truncated symmetrically to  $L_T$  symbol intervals.

The phase tree for the binary 3SRC scheme with  $L_T = 7$  is very similar to the 3RC phase tree in Figure 3.28. (Here “3” is the value of  $L_M$ .) It is believed that an optimum detector for the 3RC system works well if the transmitted signal is 3SRC. The distortion due to the truncation in the 3SRC phase tree will appear as a slightly increased noise level. This noise level can be reduced to a negligible amount if  $L_T$  is increased.

Calculations of both  $d_B^2$  and  $d_{\min}^2$  for different  $N$  have shown that the two binary schemes 3RC and 3SRC with  $L_T = 7$  are almost identical. Owing to the time-domain tails of the truncated 3SRC pulse, the number of observed

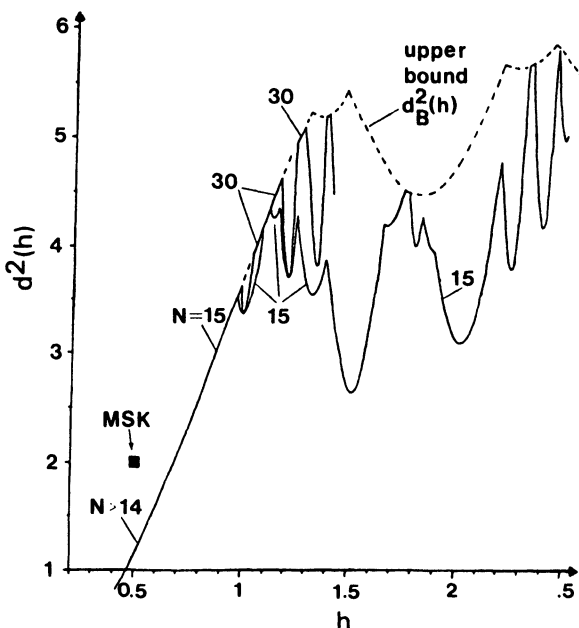


Figure 3.30. The minimum distance vs.  $h$  for binary 6RC with  $N = 15$  and 30 intervals observation. From Ref. 17, © 1981 by IEEE.

symbol intervals needed to reach the upper bound must be increased for the 3SRC system. By instead using a 3RC detector for the transmitted signal 3SRC, the  $N$ -values can be reduced to those for the 3RC system. More on this subject will appear in Chapter 8.

Calculations of  $d_B^2$  and  $d_{\min}^2$  for different  $N$  have also been performed for the TFM scheme. Originally this scheme was only proposed for  $h = 1/2$ , but it has since been generalized to include all real-valued modulation indices. The result of the distance calculations closely agree with the trends for RC pulses. The main lobe of the frequency pulse  $g(t)$  for the TFM system is approximately  $3.7T$ . For  $h = 1/2$   $d_B^2$  is reached with 10 observed bit intervals and equals 1.58. The pulse  $g(t)$  was truncated to  $7T$ . The value of  $d_B^2$  for 3RC and 4RC when  $h = 1/2$  is 1.76 and 1.51, respectively.

### *Quaternary and Octal Systems*

It was found in Section 3.3.1 that  $M$ -ary systems with  $M \geq 4$  yield larger minimum Euclidean distances than binary systems. This will prove true in the partial response case as well. A phase tree for a two-interval partial response, 2RC, appears in Figure 3.15. This is the simplest case;

now four phase branches leave every node in the phase tree, corresponding to data symbols  $\pm 1, \pm 3$ . The first mergers occur at  $t = 3T$ .

Actual distance calculations for  $M = 4$  will be presented here only for the 3RC system. The other RC systems will be described in terms of trends. Figure 3.31 shows the 3RC results; the observation intervals  $N = 1, 2, 3, 6$ , and 12 only are shown for clarity. Very large values of the minimum Euclidean distance are obtained in the region  $h \approx 1.3$  and a receiver observation interval of  $N = 15$  symbol intervals is enough to make  $d_{\min}^2$  equal to  $d_B^2$ . For these  $h$  values  $d_{\min}^2$  takes values around 6.28. This corresponds to an asymptotic gain of 5 db compared to MSK or QPSK. The effect of weak indices is not too serious.

Minimum Euclidean distance calculations have also been performed for octal ( $M = 8$ ) and hexadecimal ( $M = 16$ ) systems using the frequency

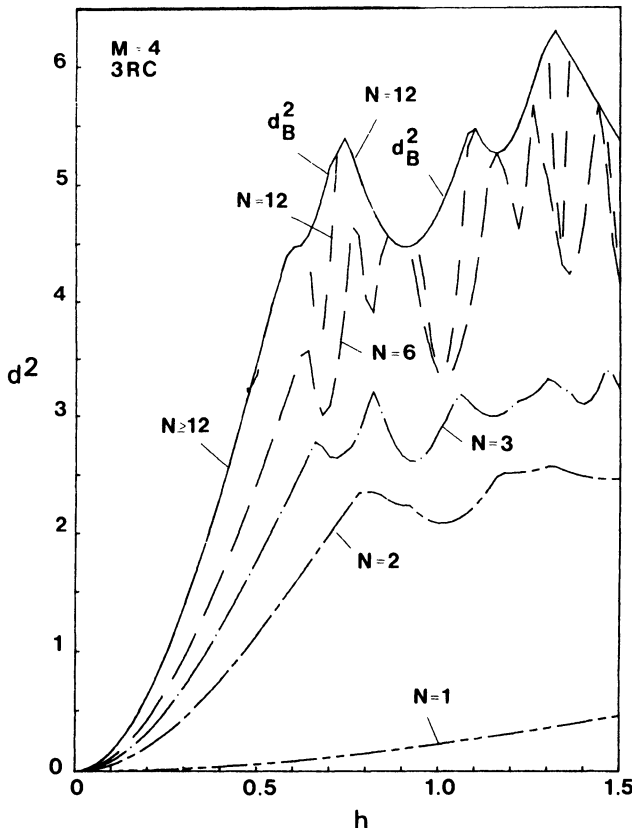


Figure 3.31. The minimum distance vs.  $h$  for quaternary 3RC with  $N = 1, 2, 3, 6$  and 12 interval observation.  $N_B = 12$  for  $h$  in the region  $(0, 0.5)$ . From Ref. 44, © 1984 by John Wiley Ltd.

pulses 2RC and 3RC. Figure 3.32 shows the results for the  $M = 8$ , 3RC case. The main conclusion concerning all of these results is that the trends with increasing  $L$  in binary systems hold here too, i.e., lower values of  $d_B^2$  for low modulation indices, larger values of  $d_B^2$  for large modulation indices up to a point, and an increased number of symbol intervals required in order to make  $d_{\min}^2$  equal to  $d_B^2$ . As is seen in Figure 3.32, the octal 3RC system yields a minimum Euclidean distance of 9.03 with  $N = 12$  symbol intervals. The asymptotic gain in terms of  $E_b/N_0$  compared to MSK or QPSK is 6.5 db.

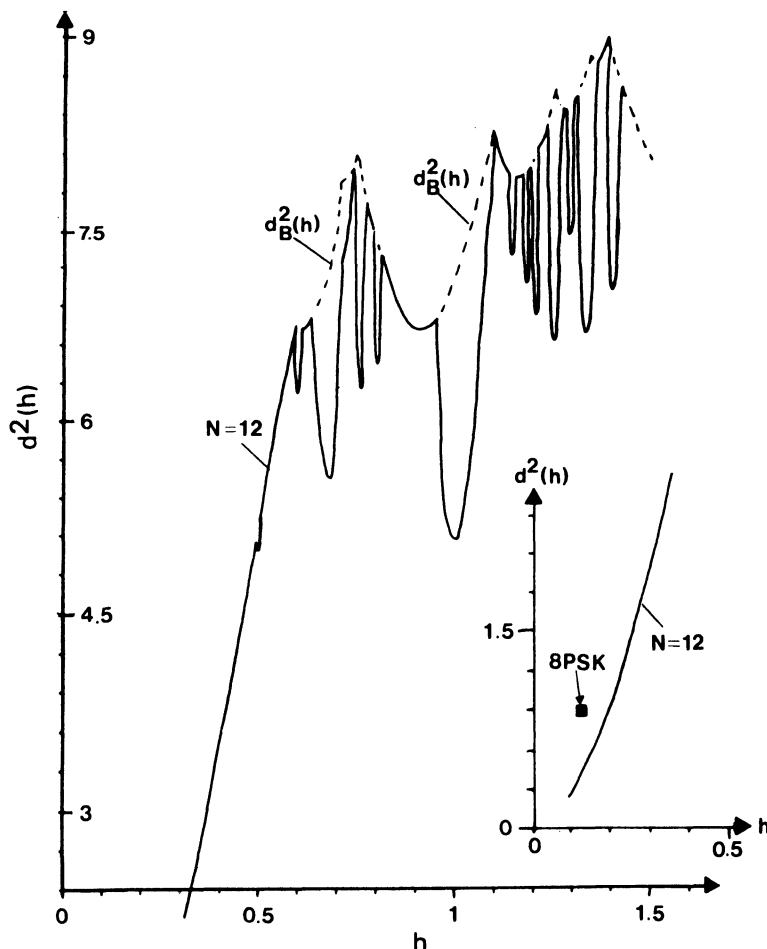


Figure 3.32. Minimum distance vs.  $h$  octal 3RC. The upper bound is reached at  $N = 12$  in the  $h$  region  $(0, 0.59)$ ;  $h = 0.5$  is slightly "weak."

### 3.3.3. Full Response, Multi- $h$

The reduced tree search algorithm described in Appendix A has been used with success for calculation of  $d_{\min}^2$  for two-index schemes. Note that the search must be repeated with each  $h_i$  as the starting index, in order to find the worst case. We shall discuss only the case of 1REC pulses with two indices and  $M = 2$  and 4. By using the trellis algorithm in Appendix A,  $H = 3$  and 4 can be studied.

Figure 3.33 shows  $d_{\min}^2$  for a fixed  $h_1 = 1/2$  as a function of  $h_2$  for a receiver observation interval of  $N = 30$  bits (solid curve). Here the scheme is binary. The upper bound from Section 3.2.3 is shown dashed. The upper

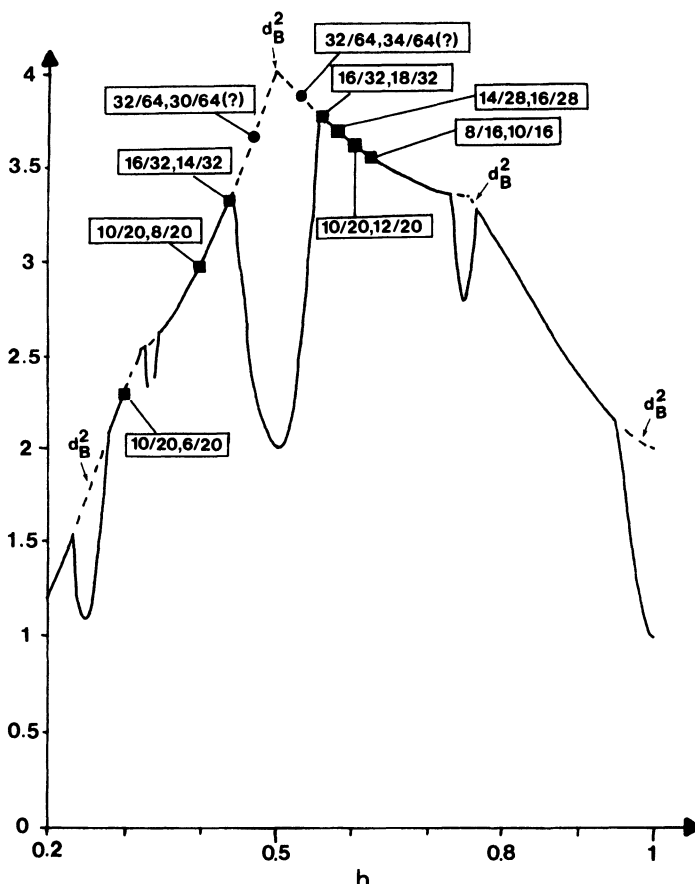


Figure 3.33. Minimum distance vs.  $h_2$  for the binary two-index 1REC scheme with  $h_1 = 1/2$ ; the other index is the horizontal axis. Specific schemes are denoted by dots and the two indices. The observation interval is  $N = 30$ . From Ref. 21, © 1982 by IEEE.

bound is generally tight, except for some weak or catastrophic combinations of the two modulation indices. The weak  $h_1, h_2$  values occur for certain linear combinations of the modulation indices. For example the relation  $h_2 = h_1/2$  gives a weak combination when  $\gamma = \dots, +2, -2, +2, 0, 0, \dots$ , starting with  $h_2$  at time 0. The same holds for  $h_2 = 2h_1$ , with the same  $\gamma$  sequence, but starting with  $h_1$ . This merger at  $t = 3T$  occurs only for this combination.

The case  $h_1 = h_2$  is clearly a weak, or even catastrophic, two-index scheme (and is also for  $H > 2$ ), because we now have a fixed  $h$  scheme. For  $h_1 = 1$  or  $h_2 = 1$ , a merger occurs independently of  $h_2$  or  $h_1$ , respectively, at  $t = T$ , since the phase separation is  $0 \bmod 2\pi$ . Below, other weak  $h_1, h_2$  values than those mentioned here will be noticed.

In Figure 3.33 the combination  $h_1 = h_2 = 1/2$  is especially interesting. This is where the upper bound  $d_B^2$  has its global maximum at distance 4. Yet  $h_1 = h_2 = 1/2$  corresponds to MSK, which is known to have  $d_{\min}^2 = 2$  for  $N = 2$ . By choosing an  $h_1, h_2$  combination close but not equal to this weak one, it is possible to have  $d_{\min}^2$  arbitrarily close to 4 when  $N$  is made large. In Figure 3.33 are also indicated some specific schemes which have been analyzed by the use of a trellis search algorithm similar to the one in Appendix A.<sup>(20)</sup> The  $h_1, h_2$  values are shown as rational numbers for reasons that will be clear in Section 3.4.

Actual  $d_{\min}^2$  results for binary  $H = 3$  and  $H = 4$  schemes are comparable to the upper bounds from Section 3.2.3. We can conclude that the upper bounds are quite tight, especially for  $\bar{h} \leq 1/2$  and for  $H = 3$ .

Next quaternary  $H = 2$  schemes will be considered. Figure 3.34 shows  $d_{\min}^2$  as a function of  $h_2$  when  $h_1 = 0.4$  and Figure 3.35 shows this when  $h_1 = 0.8$ . The global maximum of  $d_B^2$  in the region  $0 \leq h_1, h_2 \leq 1$  occurs at  $h_1 = h_2 = 0.77$ , where  $d_B^2 = 6.49$ . In order to illustrate behavior near this weak pair  $d_{\min}^2$  has been calculated in Figure 3.35 with  $N = 60$  in the region  $0.77 \leq h_2 \leq 0.78$ . The value of  $d_{\min}^2$  for  $h_1 = 0.8, h_2 = 0.77$  equals 6.14. By reducing  $h_1$  somewhat this value can probably be increased somewhat, but at the expense of a significantly increased  $N$ .

### 3.3.4. Partial Response, Multi- $h$

In Section 3.2.4, we saw that it was a difficult task to calculate a tight upper bound for a general multi- $h$  scheme, especially if  $H$  and  $L$  are large. Therefore only a fairly limited number of mergers has been used for calculation of components of  $d_B^2$ . By using the reduced tree search algorithm, supported by  $d_B^2$  (see Appendix A), for actual  $d_{\min}^2$  calculations, it can be observed whether  $d_B^2$  is tight or not. The true  $d_B^2$  can be found by letting  $N$  grow large. For the reduced tree search algorithm to work, it is not

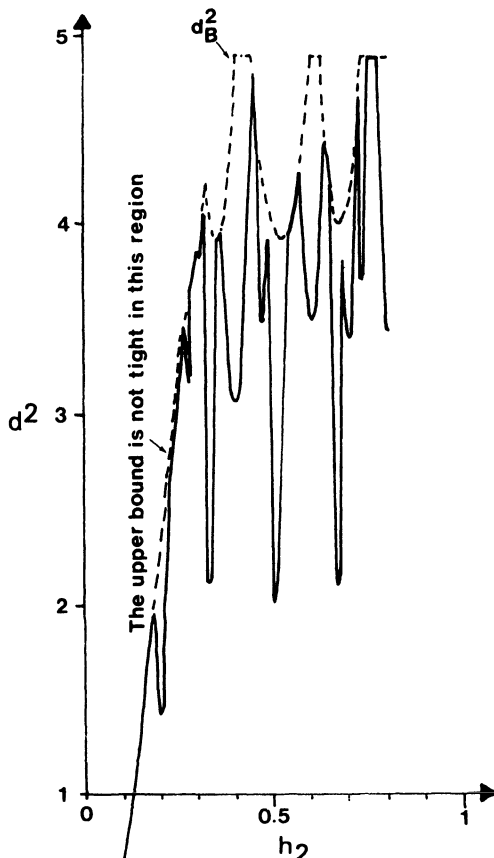


Figure 3.34. Minimum distance vs.  $h_2$  for the quaternary two-index 1REC scheme with  $h_1 = 0.4$ ; here  $N = 30$ . From Ref. 21, © 1982 by IEEE.

necessary to know a tight upper bound, just an upper bound. The lower the better, however.

Several binary  $H = 2$  partial response schemes have been analyzed in this way. Data are available for the pulse shapes 2RC, 3RC, 4RC and 2S, 3S, and 4S. In the figures below  $d_{\min}^2$  is plotted for  $N = 30$  observed bit intervals together with the upper bound. Mergers up to the  $(L + 3)$ rd have been used for the upper bound.

Figure 3.36 shows  $d_{\min}^2$  as a function of  $h_2$  for the  $H = 2$ , 2RC scheme with  $h_1 = 1/2$ . The upper bound is plotted dashed. Note that there are regions where the upper bound is not tight. This was ascertained by calculating  $d_{\min}^2$  for  $N$  up to 30 and observing that  $d_{\min}^2$  stopped growing after a while. Thus a tighter upper bound exists, if one has the motivation to find it. It is interesting to make comparisons with the single-index binary 2RC

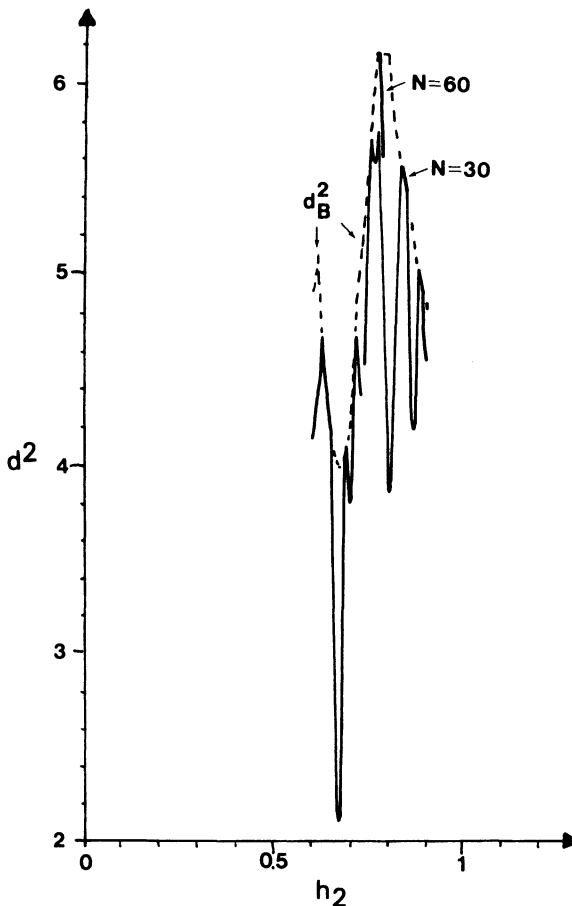


Figure 3.35. Minimum distance vs.  $h_2$  for the same scheme as in Fig. 3.34, but with  $h_1 = 0.80$ .  $N$  is 30, except in the region (0.77, 0.78), where it is 60. From Ref. 21, © 1982 by IEEE.

scheme, also shown in Figure 3.36. It is seen that one indeed gets a distance gain by using a two-index scheme. However, the  $H = 2$  scheme is not as simple as the fixed  $h$  scheme.

Figure 3.37 shows the binary  $H = 2, 3$ RC scheme for the fixed  $h_1$  values 0.5 and 0.8. As before,  $N = 30$ . These are, of course, only limited calculations, but they expose certain trends. Distance gains are obtained for low  $h$  values, i.e.,  $h_1, h_2 \leq 0.5$ , and systems with performance gain over binary  $H = 1$  schemes can be found there. For large  $h$  values the distance of the  $H = 2$  schemes does not grow very much beyond that of the  $H = 1$  scheme.

By using 2S or 3S pulses instead of 2RC or 3RC pulses, the same relative behavior is maintained in the binary case. It is worth noting that

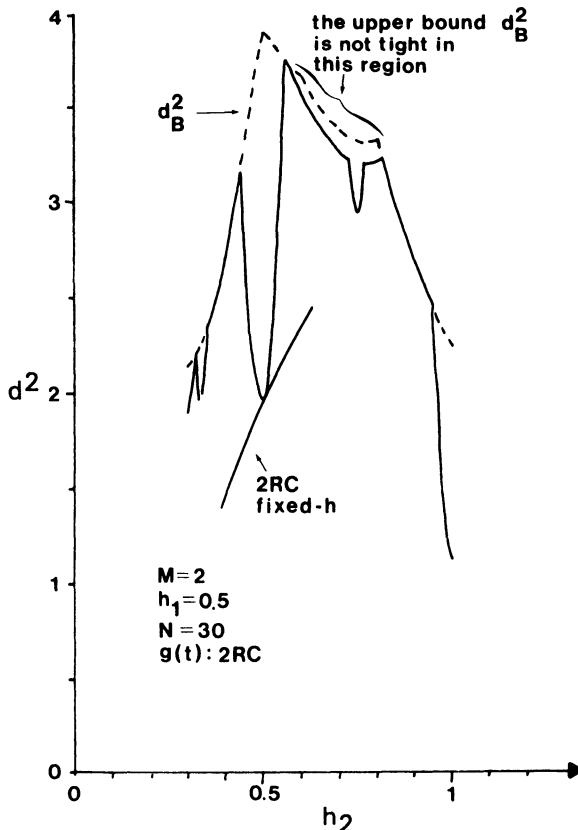


Figure 3.36. Minimum distance vs.  $h_2$  for the binary two-index 2RC scheme, when  $h_1 = 1/2$ ;  $N = 30$ . As comparison,  $d_{\min}^2$  for the single-index 2RC scheme is shown as a function of  $h = h_2$  in the region near  $h = 1/2$ . From Ref. 22, © 1982 by IEEE.

distance values above 4 can be reached with  $H = 2, 3RC$  and  $4RC$  schemes. This is not possible with the binary  $1REC$ ,  $H = 3$  case. Nor is it possible with  $H = 1, 3RC$  schemes. However, distance values considerably above 4 can be reached by using binary  $H = 1$  schemes based on long pulses, e.g.,  $5RC$ ,  $6RC$ . For the pulses  $4S$  and  $4RC$  the gain by going from  $H = 1$  to  $H = 2$  is smaller than for the pulses of duration 2 and 3 bit intervals.

### 3.3.5. Summary

The calculation of  $d_{\min}^2$  gives the details of the basic trends shown by the upper bound function. We have seen that except for weak modulation indices,  $d_{\min}^2$  can be made equal to  $d_B^2$  by increasing the observation interval up to some finite  $N_B$ . This is the least  $N$  needed for asymptotically optimum

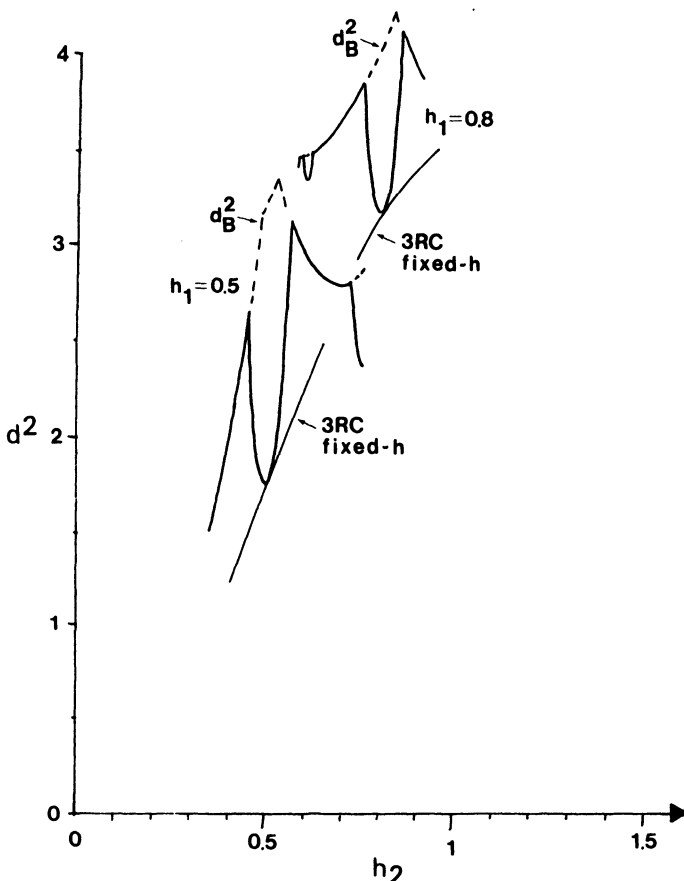


Figure 3.37. Minimum distance vs.  $h_2$  for the binary two-index 3RC scheme, when  $h_1$  is 0.5 and 0.8. Fixed- $h$  3RC is also shown.

error performance. By plotting  $d_{\min}^2$  as a function of  $N$ , the column distance function (CDF),<sup>(31)</sup> previously used to describe the Hamming distance structures of convolutional codes, is obtained. In Chapters 7 and 8 we will relate  $N$  to receiver memory and find that  $N_B$  gives the largest required memory under certain conditions.

It has been verified that it is possible to have constant envelope digital modulation systems which are more power efficient than QPSK and MSK, for example. In some cases the power gain is considerable; complex block or convolutional codes would be needed to achieve it with traditional memoryless modulation methods, and their check symbols would increase bandwidth. In the schemes presented here, the code is built into the modulator itself. The redundancy of the transmitted signal lies in its tree structure,

and not in the insertion of extra check symbols, and thus all the schemes have an information rate which is larger than or equal to one. This is of great importance to the bandwidth occupancy of the transmitted signal.

Many classes of digital phase modulation are available, and this gives the system designer a large amount of freedom. For a given value of  $d_{\min}^2$ , many different systems with different properties are available to choose from. Euclidean distance is most easily increased by increasing the alphabet size or the pulse response length.

### 3.4. Systems with a Trellis Structure

On calculating minimum distance, we have assumed that the maximum likelihood receiver of Chapter 2 views the phase tree of the signal over a time span of  $N$  symbol intervals, to make a ML decision of the first symbol present in that time interval. The major problem with envisioning a detector in this way is that even though the data symbols are  $M$ -ary, there is an exponentially growing number of branches in the tree corresponding to each data symbol. To do the necessary correlations in the detector (see Section 2.1) would require a receiver of potentially infinite size. Such receivers naturally do not exist, although it is in principle possible to analyze them in terms of  $d_{\min}^2$ , as we have done. A way out of this dilemma is to create a state description for modulations. We will also give symbol error probability bounds for receivers based on this concept.

#### 3.4.1. A State Description for Modulators

We can rewrite (3.2), the phase relative to the carrier of the transmitted signal, as (letting  $i' = i \bmod H$ )

$$\begin{aligned}\phi(t, \alpha) &= 2\pi \sum_{i=-\infty}^n \alpha_i h_{i'} q(t - iT) \\ &= 2\pi \sum_{i=n-L+1}^n \alpha_i h_{i'} q(t - iT) \\ &\quad + \pi \sum_{i=-\infty}^{n-L} \alpha_i h_{i'}, \quad nT \leq t \leq (n+1)T\end{aligned}\tag{3.42}$$

by using the properties that  $q(t) \equiv 0$ ,  $t < 0$  and  $q(t) \equiv 1/2$ ,  $t > LT$ . Hence, given  $h_1, h_2, \dots, h_H$  and  $g(t)$ , for any symbol interval  $n$  the phase  $\phi(t, \alpha)$

is uniquely defined by the present data symbol  $\alpha_n$ , the *correlative state vector*  $(\alpha_{n-1}, \alpha_{n-2}, \dots, \alpha_{n-L+1})$ , and the *phase state*  $\theta_n$ , where

$$\theta_n = \left[ \pi \sum_{i=-\infty}^{n-L} \alpha_i h_{i'} \right] \text{modulo } 2\pi \quad (3.43)$$

The number of correlative states is finite and equal to  $M^{(L-1)}$ . For rational modulation indices, let us define the modulation indices in terms of integers as

$$h_{i'} = \frac{2k_{i'}}{p}, \quad i' = 1, 2, \dots, H \quad (3.44)$$

There are thus  $p$  different phase states with values

$$\theta_n \in \left\{ 0, \frac{2\pi}{p}, \frac{4\pi}{p}, \dots, \frac{(p-1)2\pi}{p} \right\}$$

In (3.43)  $k_{i'}$  and  $p$  are integers with no factors in common. Thus the total state of the transmitted phase (and also signal) is the  $L$ -tuple

$$\sigma_n = (\theta_n, \alpha_{n-1}, \alpha_{n-2}, \dots, \alpha_{n-L+1}) \quad (3.45)$$

and there are  $pM^{(L-1)}$  distinct states. The current data symbol  $\alpha_n$  directs the transition from the state  $\sigma_n$  to the next state  $\sigma_{n+1}$ , and this transition defines the actual function of time that is transmitted.

Figure 3.28 shows a phase tree for the binary 3RC scheme with  $H = 1$  and  $h = 4/5$  with the states labeled. In this case there are  $5 \cdot 4 = 20$  different states, and the nodes in the tree have been assigned states according to (3.45). The root node at time  $t = 0$  has been given the phase state zero. Close observation of Figure 3.28 reveals that a pattern of repetition exists among the states. We can clarify this by making a list of the states and writing down all the states that can be reached from each state. If we do this in the style of Figure 3.38, it will become clear that  $M$  transitions leave every node on the left and  $M$  enter each node on the right. If a number of "units" like Figure 3.38 are appended side by side, we will have a trellis structure, like the phase trellis introduced in Chapter 2, called a *state trellis*. A finite number,  $pM^L$ , of signal alternatives exist in each signal interval.

It is now possible to let the detector operate by using this state trellis instead of the tree. An efficient and optimum way of finding the ML path through a trellis is by using the Viterbi algorithm (VA). Here the path closest to the transmitted signal leading into each state is taken as a tentative decision. Alternatively, the path producing the largest correlation can be

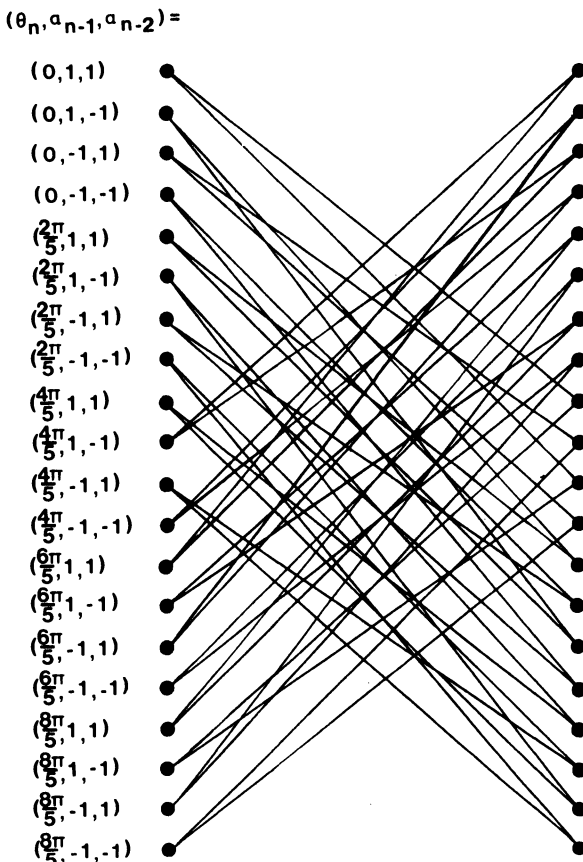


Figure 3.38. The state trellis diagram for binary 3RC with  $h = 4/5$ . Compare to Figure 3.28, which assigns the states to phase tree nodes. From Ref. 44, © 1984 by John Wiley Ltd.

selected. This is done recursively from symbol interval to symbol interval. The path leading up to the state having the largest correlation is taken as the detected path. There is a high probability that all the selected paths (the "survivors") up to symbol interval  $n$  will be the same up to time  $n - N_T$  symbol intervals. Therefore the initial segment of the ML sequence is known up to time  $n - N_T$  symbol intervals and can form the output of the detectors. The effect of different choices of  $N_T$  will be studied below.

A receiver using this concept is described in detail in Chapter 7. For now, we can say that the VA is a recursive optimal procedure to detect the state sequence of a discrete time finite state Markov process observed in memoryless noise. The VA with an unlimited  $N_T$  is optimum in the sense that the likelihood function is maximized, and hence a ML estimate of the

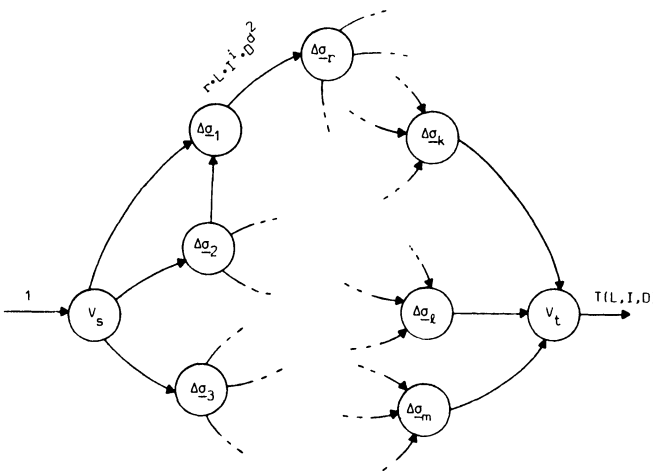


Figure 3.39. A split averaged difference state graph; dummy variables  $L$ ,  $I$ , and  $D$  correspond to each branch and the averaging over the transmitted sequence is performed by multiplying each branch gain by  $r$ . From Ref. 29, © 1981 by IEEE.

sequence of states is produced. Since also a specific sequence of states must uniquely correspond to a sequence of data symbols, an ML estimate of the data sequence is also obtained.

In what follows,  $H = 1$  will be assumed. In this case the phase states behave in a very specific way when  $p$  is even. Define the *even* phase states  $\{0, 4\pi/p, 8\pi/p, \dots, (p-2)2\pi/p\}$  and the *odd* phase states  $\{2\pi/p, 6\pi/p, 10\pi/p, \dots, (p-1)2\pi/p\}$ . With this division of the set of phase states, it can be shown that if during any specific symbol interval one of the even (odd) phase states is used, then during the next symbol interval, one of the odd (even) phase states must be used. By utilizing this, the “effective” number of phase states is cut in half.

### 3.4.2. Transfer Function Symbol Error Probability Bounds

This error bound will require a new type of notation. We need first to develop the concept of error events as they occur in ML state sequence estimation. An error event starts when the path produced by the detector for the first time diverges from the path produced by the transmitter. The error event ends when the two paths merge again. The difference between two signals can be characterized by states, just as can the signals themselves. A *difference state vector* is defined as

$$\Delta\sigma_n = (\Delta\theta_n, \gamma_{n-1}, \gamma_{n-2}, \dots, \gamma_{n-L+1}) \quad (3.46)$$

where

$$\Delta\theta_n = \left[ h\pi \sum_{i < n-L} \gamma_i \right] \text{modulo } 2\pi$$

is the difference phase state and  $(\gamma_{n-1}, \gamma_{n-2}, \dots, \gamma_{n-L+1})$  is the difference correlative state vector. For these difference states  $\Delta\sigma_n$ , a difference trellis or a difference state graph can be constructed, just as for  $\sigma_n$ . Now a path through the all-zero difference state corresponds to correct transmission. By splitting this error-free state into a start state  $V_s$  and a terminal state  $V_t$  in the difference state graph, the structure of all error events can be described, including those that are infinitely long. The reason for using these difference states will be apparent as we proceed.

Let the dummy variables  $L$ ,  $I$ , and  $D$  now be defined; these will be associated with trellis branches when we derive our error bound.  $L$  [not to be confused with the duration of the frequency pulse  $g(t)$ ] is a counter for the length of a specific error event and is attached to every branch. The exponent of  $I$  is 1 if an error is made ( $\gamma \neq 0$ ); otherwise it is zero, and  $D$  will carry the normalized squared Euclidean distance, associated with the phase difference trajectory, in its exponent. Finally, we need to define a branch gain with the general form

$$r \cdot L \cdot I^i \cdot D^{d^2}$$

A factor  $r$  has been included to account for the dependence upon the transmitted data. Since the transmitted data symbol takes  $M$  different values with equal probability and since a specific value of a component in the difference sequence  $\gamma$  corresponds to  $M - |\gamma|/2$  different pairs of transmitted and detected symbols, the factor  $r$  must be

$$r = \frac{M - |\gamma|/2}{M}$$

Hence, given a value of  $\gamma$ , impossible pairs of transmitted and detected data symbols are not counted.

Now the *transfer function* is defined as the output from the graph when a 1 is given as input. A general example is shown in Figure 3.39. The averaged transfer function is written

$$T(L, I, D) = \sum_{i=1}^{\infty} r_i L^i I^{v_i} D^{d^2_i} \quad (3.47)$$

where  $\nu_i$  is the number of symbol errors for the  $i$ th path from  $V_s$  to  $V_t$ . What  $T(L, I, D)$  does is to describe *all* possible paths through the split difference state graph. In (3.47) it gives the duration of the error event by the exponent of  $L$ , the total number of errors by the exponent of  $I$ , and the distance is through the exponent of  $D$ . An excellent introduction to the transfer function technique appears in Viterbi and Omura,<sup>(43)</sup> we will not repeat that material now.

The quantity  $N_T$  is called path memory length (see Section 7.3) since in practice only sequences (paths) of length  $N_T$  leading to each of the states are retained in memory. We will first assume that this memory is of infinite size.

### *Infinite Path Memory*

By considering all possible error events and by using the union bound, the upper bound on the error event probability is

$$p(\epsilon) \leq \sum_{i=1}^{\infty} r_i Q\left(\left(d_i^2 \frac{E_b}{N_0}\right)^{1/2}\right) \quad (3.48)$$

and the upper bound on the symbol error probability is

$$p_s \leq \sum_{i=1}^{\infty} r_i \nu_i Q\left(\left(d_i^2 \frac{E_b}{N_0}\right)^{1/2}\right) \quad (3.49)$$

In (3.48) and (3.49) the summation index  $i$  is a counter for all the error events. The analogy between (3.47) on the one hand and (3.48) and (3.49) is obvious. It assumes, however, that  $T(L, I, D)$  is given in the form (3.47), i.e., as a series expansion. To avoid this, the inequality

$$Q((x + y)^{1/2}) \leq Q(x^{1/2}) e^{-y/2}, \quad x, y > 0 \quad (3.50)$$

is used, which yields a somewhat looser but still exponentially tight bound

$$p(\epsilon) \leq Q\left(\left(d_{\min}^2 \frac{E_b}{N_0}\right)^{1/2}\right) \exp\left(\frac{d_{\min}^2}{2} \frac{E_b}{N_0}\right) T(L, I, D) \Big|_{\substack{L=1 \\ I=1 \\ D=e^{-E_b/2N_0}}} \quad (3.51)$$

and

$$p_s \leq Q\left(\left(d_{\min}^2 \frac{E_b}{N_0}\right)^{1/2}\right) \exp\left(\frac{d_{\min}^2}{2} \frac{E_b}{N_0}\right) \frac{\partial T(L, I, D)}{\partial I} \Big|_{\substack{L=1 \\ I=1 \\ D=e^{-E_b/2N_0}}} \quad (3.52)$$

which avoids the series expansion.  $d_{\min}^2$  is the minimum normalized squared Euclidean distance associated with all the error events. In the distance plots in Section 3.3, this is  $d_{\min}^2$  for  $N \rightarrow \infty$ .

It is still assumed that  $T(L, I, D)$  is given as a closed form expression. This is in most cases impossible to obtain and numerical methods suited for computer calculations must be used. Such a method is now described.

The averaged difference state transition matrix  $\mathbf{A}$  is an alternative way of describing the averaged split difference state graph. This matrix describes the branch gains according to

$$\mathbf{A} = \begin{bmatrix} V_s & V_1 & V_2 & \cdots & V_t \\ V_s & 0 & T_{s,1}(L, I, D) & T_{s,2}(L, I, D) & \cdots & 0 \\ V_1 & 0 & T_{1,1}(L, I, D) & T_{1,2}(L, I, D) & \cdots & T_{1,t}(L, I, D) \\ V_2 & 0 & T_{2,1}(L, I, D) & T_{2,2}(L, I, D) & \cdots & T_{2,t}(L, I, D) \\ \vdots & \vdots & \vdots & \vdots & \ddots & \vdots \\ V_{N_s} & 0 & T_{N_s,1}(L, I, D) & T_{N_s,2}(L, I, D) & \cdots & T_{N_s,t}(L, I, D) \\ V_t & 0 & 0 & 0 & \cdots & 0 \end{bmatrix} \quad (3.53)$$

where  $V_1, V_2, \dots, V_{N_s}$  are the error states. Since  $\mathbf{A}$  describes all transitions over one symbol interval,  $\mathbf{A}^2$  describes all transitions over two symbol intervals, and so on. Thus the  $(s, t)$  element in the matrix

$$\mathbf{T} = \mathbf{A} + \mathbf{A}^2 + \mathbf{A}^3 + \cdots = \mathbf{A}(\mathbf{I} - \mathbf{A})^{-1} \quad (3.54)$$

is the average transfer function  $T(L, I, D)$ .  $\mathbf{I}$  is the identity matrix.

Thus for fixed  $E_b/N_0$ ,  $L = 1$ ,  $I = 1$ , and  $D = e^{-E_b/2N_0}$ , all entries in  $\mathbf{A}$  are real numbers and  $\mathbf{T}$  can be found from numerical calculations, especially the  $(s, t)$  element. The derivative in (3.52) can be found numerically through

$$\frac{\partial T(L, I, D)}{\partial I} \Big|_{I=1} \approx \frac{T(L, I = 1 + \varepsilon, D) - T(L, I = 1, D)}{\varepsilon} \quad (3.55)$$

It is easy to construct lower bounds on both the error event and symbol error probability. This merely corresponds to choosing the path through the state graph with which  $d_{\min}^2$  is associated. Both  $d_{\min}^2$  and the path can be found by using any of the methods in Appendix A. It can be concluded that the upper and lower bounds are asymptotically tight since  $d_{\min}^2$  dominates for large SNR.

For an example of the transfer function technique, the binary  $H = 1$ , 1REC scheme with  $h = 2/3$  is chosen. Straightforward calculations give the

necessary parameters for the branch gains, and the result is shown in Figure 3.40. The notation

$$\begin{aligned} d_I^2 &= 1 + \frac{3\sqrt{3}}{8\pi} \\ d_{II}^2 &= 1 - \frac{3\sqrt{3}}{4\pi} \\ d_{III}^2 &= \frac{3}{2} \end{aligned} \quad (3.56)$$

is used for the Euclidean distance increments. From this we find

$$A = \begin{bmatrix} V_s & 4\pi/3 & 8\pi/3 & V_t \\ V_s & 0 & \frac{1}{2}LID^{d_I^2} & \frac{1}{2}LID^{d_I^2} & 0 \\ 4\pi/3 & 0 & LD^{d_{III}^2} & \frac{1}{2}LID^{d_{III}^2} & \frac{1}{2}LID^{d_I^2} \\ 8\pi/3 & 0 & \frac{1}{2}LID^{d_{III}^2} & LD^{d_{III}^2} & \frac{1}{2}LID^{d_I^2} \\ V_t & 0 & 0 & 0 & 0 \end{bmatrix} \quad (3.57)$$

The  $(s, t)$  element of the matrix  $T$  is

$$T(L, I, D) = \frac{\frac{1}{4}L^3I^3D^{2d_I^2+d_{III}^2} + \frac{1}{2}(1-LD^{d_{III}^2})L^2I^2D^{2d_I^2}}{(1-LD^{d_{III}^2})^2 - \frac{1}{4}L^2I^2D^{2d_{III}^2}} \quad (3.58)$$

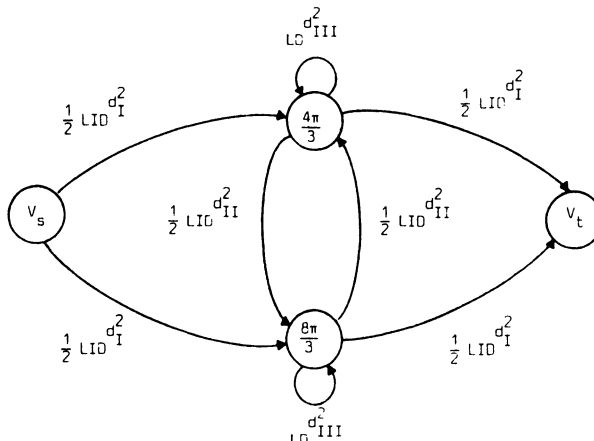


Figure 3.40. Split averaged difference state graph for the binary single-index 1REC scheme with  $h = 2/3$ . From Ref. 29, © 1981 by IEEE.

Taking the partial derivative with respect to  $I$  at  $I = 1$  and  $L = 1$ , we get the expansion

$$\begin{aligned} \frac{\partial T(L, I, D)}{\partial I} \Bigg|_{\substack{L=1 \\ I=1}} &= D^{2d_1^2} \left[ (1 + \frac{1}{4}D^{d_{11}^2} + \frac{1}{4}D^{2d_{11}^2}) \right. \\ &\times \sum_{i=0}^{\infty} \sum_{\substack{j=0 \\ j \text{ even}}}^i 2^{-j} \binom{i}{j} D^{jd_{11}^2} D^{(i-j)d_{11}^2} + (1 + \frac{1}{4}D^{2d_{11}^2}) \\ &\times \left. \sum_{i=0}^{\infty} \sum_{\substack{j=0 \\ j \text{ odd}}}^i 2^{-j} \binom{i}{j} D^{jd_{11}^2} D^{(i-j)d_{11}^2} \right] \end{aligned} \quad (3.59)$$

which shows that the dominating term in the expression for the symbol error probability upper bound is

$$Q \left( \left( 2d_1^2 \frac{E_b}{N_0} \right)^{1/2} \right) = Q \left( \left[ \left( 2 + \frac{3\sqrt{3}}{4\pi} \right) \frac{E_b}{N_0} \right]^{1/2} \right) \quad (3.60)$$

The minimum Euclidean distance for this scheme is  $d_{\min}^2 = 2d_1^2$ , and the corresponding error event can be easily identified in Figure 3.40. Note that there are two symbol errors in this error event, and it could be expected that the symbol error probability would be twice as large as in (3.60). The reason why this is not so is the dependence on the transmitted sequence, which in Figure 3.40 introduces a factor of 1/2.

This example was chosen also to demonstrate the complexity of the expansion of  $T(L, I, D)$  even for this simple case. In practice numerical methods must be used.

### *Finite Path Memory*

The effect of a truncated path memory of duration  $N_T$  symbol intervals in the detector will now be considered. It has been shown for convolutional codes<sup>(32)</sup> that if unmerged error events, unmerged over at least  $N_T$  symbol intervals, are included with those previously considered, an upper bound on the probability of error events for path memory  $N_T$  is obtained. This directly carries over to the schemes considered here.

Consider a split averaged difference state graph as before. The sum of the transfer functions from the state  $V_s$  to the states  $V_1, V_2, \dots, V_{N_s}$ , having terms in which the exponent of the dummy variable  $L$  is at least  $N_T$ , describes all these other kinds of error events. By forming the matrix

$$\mathbf{T}_{N_T} = \mathbf{A}^{N_T} + \mathbf{A}^{N_T+1} + \mathbf{A}^{N_T+2} + \dots = \mathbf{A}^{N_T}(\mathbf{I} - \mathbf{A})^{-1} \quad (3.61)$$

the desired transfer function  $T_{N_T}(L, I, D)$  is given by the sum of the elements  $(s, 1), (s, 2), \dots, (s, N_s)$  in the matrix  $\mathbf{T}_{N_T}$ . By using union bound again and replacing  $T(L, I, D)$  by  $T(L, I, D) + T_{N_T}(L, I, D)$  and proceeding exactly as above, we get the desired upper bounds on both  $P(\varepsilon)$  and  $P_s$  for finite  $N_T$ . In equations (3.51) and (3.52),  $d_{\min}^2$  must be replaced by  $d_{\min}^2$  for an observation interval of  $N_T$  symbol intervals, as in Section 3.3.

It is now clear that if  $N_T \geq N_B$ , the detector will have an asymptotically optimum error performance. This is because  $d_{\min}^2$  is upper-bounded by  $d_B^2$ , and cannot be increased by making the observation interval longer than  $N_B$ .

### *Numerical Examples*

Two numerical examples will be given, where the numerical method above has been used. The first is binary 4RC with  $H = 1$  and  $h = 4/5$ . In this case the number of states in the trellis, with which the detector works, is 40. The upper and lower bounds on the bit error probability are shown in Figure 3.41; upper bounds are shown for  $N_T = 1, 2, \dots, 15$  and also  $N_T = \infty$ . For comparison, the exact bit error probability for BPSK is shown dashed.

The lower and upper bounds are quite tight when  $N_T \geq 12$  and  $E_b/N_0$  is larger than 6 dB. The asymptotic performance of the detector can be found by calculation of  $d_{\min}^2$  for different observation intervals  $N$ , as in Section 3.3.

Figure 3.41 also shows that there is a gain in terms of  $E_b/N_0$  compared to BPSK. At which SNR this gain starts to be noticed is hard to tell from Figure 3.41, and at low SNR the union bound is quite loose. For a reliable answer, simulations must be performed, as discussed in Chapter 7.

As the other example of upper and lower bounds on the symbol error probability, the quaternary ( $M = 4$ ) scheme 3RC with  $H = 1$  and  $h = 1/2$  is chosen. The results appear in Figure 3.42. The attractive properties observed for the previous binary scheme remain for this quaternary scheme. This has been found to be true for other quaternary schemes. Comparisons can be made to Figure 3.31, where  $d_{\min}^2$  is given for  $N = 1, 2, 3$ , and 15, to obtain the asymptotic behavior for the curves in Figure 3.42.

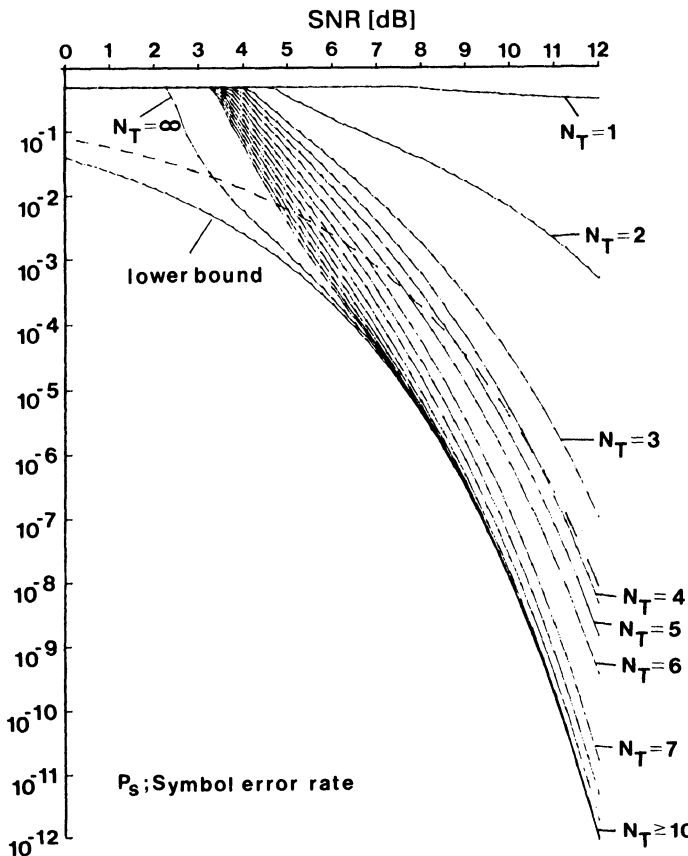


Figure 3.41. Upper bounds on the bit error probability for binary 4RC with  $h = 4/5$ ; the detector has path memory lengths  $N_T$  as indicated. The BPSK bit error probability is shown dashed. From Ref. 29, © 1981 by IEEE.

#### *Generalization to Multi- $h$*

In the multi- $h$  case, the state graph is time varying in a cyclical manner with a period of  $H$  symbol intervals. It can be broken up into  $H$  time-invariant graphs, one for each of the  $H$  modulation indices. At the end of each symbol interval (each transition in the graph), one has to move to the corresponding state in the graph for the next active modulation index.  $T_i(L, I, D)$  will denote the transfer function obtained by starting in graph  $i$ . The total transfer function is

$$T(L, I, D) = \frac{1}{H} \sum_{i=1}^H T_i(L, I, D) \quad (3.62)$$

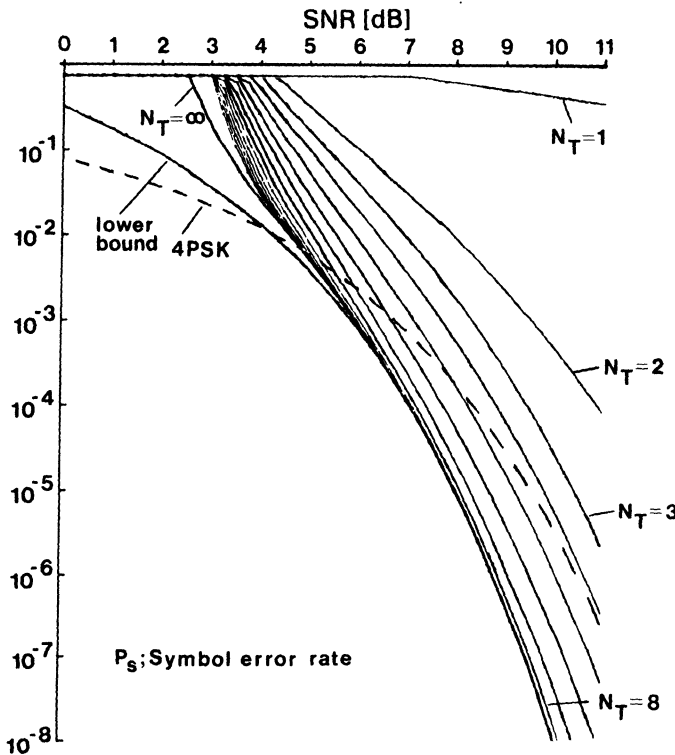


Figure 3.42. Upper bounds on the symbol error probability for quaternary 3RC with  $h = 1/2$ . The path memory length is as shown; for this modulation  $N_B = 11$  symbols. From Ref. 29, © 1981 by IEEE.

which is used exactly as in the  $H = 1$  case for obtaining upper bounds on the error event and symbol error probabilities. More details appear in Ref. 30.

### 3.4.3. Summary

By restricting oneself to CPM schemes where the modulation indices are rational, the structure of the transmitted signal becomes finite, and can be described as a finite state time-invariant Markov process. This means that the tree structure used for general real-valued modulation indices folds into a trellis. There are efficient ways of finding the ML path through such a trellis (e.g., the Viterbi algorithm). What is more important is that the receiver structure is finite and thus implementable.

By developing upper and lower bounds for the symbol error probability, it was found that this detector performs as well as the hypothetical tree detector. From the two examples, it is apparent that the asymptotic error

performance indicated by  $d_{\min}^2$  was obtained for realistic SNRs. This makes the trellis decoder/demodulator interesting from a practical point of view. Other modulations have also been studied,<sup>(15,27,28,29,30)</sup> with results consistent with the behavior in Figures 3.41 and 3.42.

### 3.5. Effects of Filtering and Limiting

If a band-limiting or amplitude-limiting filter is put between the transmitter and the optimum detector for the AWGN channel, this detector is no longer optimum. Viewed in signal space, the signal vectors are moved around; the dimension of the signal space may even be changed. By measuring the minimum Euclidean distance between vectors corresponding to different data symbols, the asymptotic performance can be obtained for the receiver which is matched to the distorted signals. This error performance may be better or worse than for unfiltered signals. Distance measures for distorted CPM signals with optimum detectors were given in Section 2.4, in equations (2.22)–(2.26).

It is also of interest to examine the asymptotic performance of a receiver which is optimum for undistorted signals in the AWGN channel, but is used nonetheless to detect distorted signals. This receiver is now of course suboptimum, and by comparing its performance relative to the optimum receiver, the effect of the distorting element can be clearly seen. A distance measure for mismatched signal sets will be derived below. This will then be used for CPM systems with distorting elements such as a band pass filter or a filter combined with a hard amplitude limiter.

#### 3.5.1. The Euclidean Distance for Mismatched Signal Sets

Our derivation of the Euclidean distance measure for receivers mismatched to a signal set is very general and will apply to other situations than distorted CPM signals transmitted over an AWGN channel. All that is assumed is that the detector is coherent and that there is AWGN before the receiver. The results arrived at here will be used at several places in the book.

It is assumed that the transmitter sends the signals  $\{s_T(t, \alpha)\}$  and that the detector correlates the received signal with all the alternatives in a different receiver signal set  $\{s_R(t, \tilde{\alpha})\}$ , where the sequence  $\tilde{\alpha}$  is varied. This is done over the interval  $0 \leq t \leq NT$  and the maximum correlation is found. The first data symbol in the observed time interval is taken as the detected symbol.

The receiver principle and the critical parameters are illustrated in two dimensions in Figure 3.43. The signals are represented in a signal space

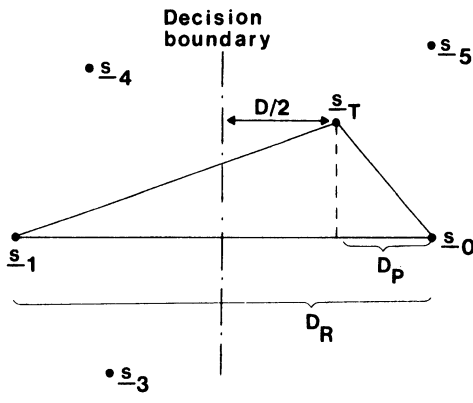


Figure 3.43. Distances in the receiver signal space.

large enough to accommodate all receivable signals. Let the vector  $s_0$  represent the receiver alternative corresponding to the transmitted sequence  $\alpha$ . Other receiver alternatives are  $s_1$ ,  $s_2$ , and  $s_3$ . The transmitted signal is represented by the vector  $s_T$ . Since the receiver selects the signal alternative corresponding to the largest correlation, this corresponds to the signal point in its set which has the smallest Euclidean distance to the point in the transmitter set. Figure 3.43 shows the noiseless case; with AWGN, a noise vector is added to the signal point  $s_T$ . When the noise vector is such that the transmitted signal is moved to the other side of the decision boundary, an error occurs.

As a consequence, the distance parameter  $D$  is of interest for all pairs of received signals  $(s_0, s_j)$ ,  $j = 1, 2, \dots$ , for a given transmitted signal  $s_T$ . The minimum of these distance parameters, where the minimization is also over all transmitted signals  $s_T$ , determines the error performance of the system for large SNR.

Simple geometry applied to Figure 3.43 yields that

$$\frac{1}{2}D = \frac{1}{2}D_R - D_p \quad (3.63)$$

where

$$D_R^2 = |s_0 - s_1|^2 \quad (3.64)$$

is the squared signal space distance between the receiver alternatives, henceforth simply called the *receiver distance*.  $D_p$  is the projection of the signal  $s_T - s_0$  on the signal  $s_1 - s_0$ , which is

$$D_p = \frac{\langle s_T - s_0, s_1 - s_0 \rangle}{|s_1 - s_0|} \quad (3.65)$$

Insertion now gives

$$D_p = \frac{1}{2D_R} (D_R^2 - D_A^2) \quad (3.66)$$

where

$$D_A^2 = |\mathbf{s}_1 - \mathbf{s}_T|^2 - |\mathbf{s}_0 - \mathbf{s}_T|^2 \quad (3.67)$$

and we can characterize  $D$ , our quantity of interest, as simply

$$D = \frac{D_A^2}{D_R} \quad (3.68)$$

As before, normalized squared Euclidean distances can be formed according to

$$d_A^2 = \frac{D_A^2}{2E_b}, \quad d_R^2 = \frac{D_R^2}{2E_b} \quad (3.69)$$

so that

$$d^2 = \frac{D^2}{2E_b} = \frac{d_A^4}{d_R^2} \quad (3.70)$$

The distance measure  $d_R^2$  stems from the receiver signal space alone, and  $d^2$  from both the transmitter signal space and receiver signal space. Considering only the transmitter signal space, we define

$$d_T^2 = \frac{1}{2E_b} \int_0^{NT} [s_T(t, \alpha) - s_T(t, \tilde{\alpha})]^2 dt \quad (3.71)$$

$d_T^2$  is the distance measure for an optimum detector for the signals  $\{s_T(t, \alpha)\}$ . By using a suboptimum detector instead, the performance, measured by  $d$ , cannot be improved and consequently

$$d^2 \leq d_T^2 \Leftrightarrow d_A^4 \leq d_T^2 d_R^2 \quad (3.72)$$

Note, however, that it is possible to have  $d^2 \geq d_R^2$ , and this will be exemplified below. This means that by changing the transmitter and keeping the receiver the same, performance actually can be improved.

### 3.5.2. Effects of Filtering

Three modulation systems related to the one just discussed are needed for an understanding of the asymptotic error performance of a filtered CPM signal. These three systems are shown schematically in Figure 3.44, and are denoted

- OCPM: Optimum CPM
- OFCPM: Optimum Filtered CPM
- SFCPM: Suboptimum Filtered CPM

We now consider  $s_0(t, \alpha)$  to be a filtered signal. For all three systems AWGN is present at the front end of the receiver. The two first systems are optimum, and the third one is suboptimum with respect to the second one. The impulse response  $a(t)$  of the bandpass filter is given by equation (2.25), expressed by its baseband equivalents  $a_c(t)$  and  $a_s(t)$ . The envelope

$$e_a(t, \alpha) = [I_a^2(t, \alpha) + Q_a^2(t, \alpha)]^{1/2}$$

of the filtered signal with quadrature components  $I_a(t, \alpha)$  and  $Q_a(t, \alpha)$  (with respect to  $\cos 2\pi f_0 t$  and  $\sin 2\pi f_0 t$ ), is in general time-varying. Expressions for  $I_a(t, \alpha)$  and  $Q_a(t, \alpha)$  are given in (2.26).

The nonconstant envelope means that the quantity  $E$ , which used to denote the energy per symbol in  $s(t, \alpha)$ , does not have this meaning for the signal  $s_0(t, \alpha)$ . The symbol energy now depends upon the specific data

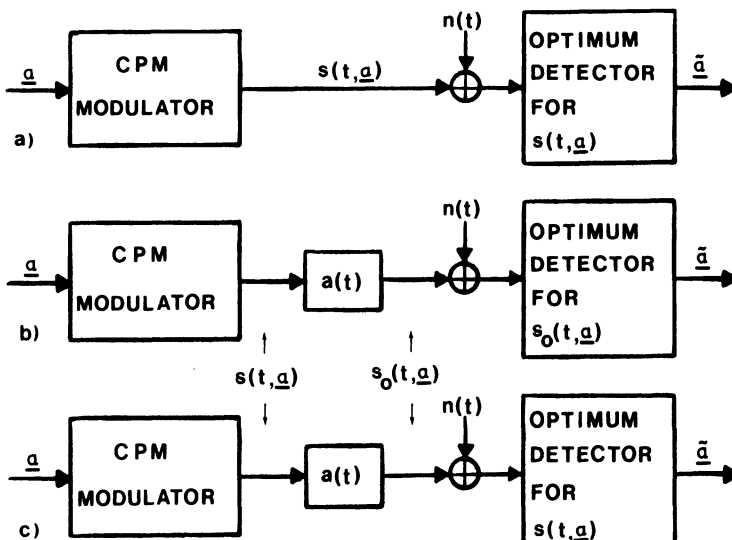


Figure 3.44. Block diagrams for the combinations (a) OCPM, (b) OFCPM, (c) SFCPM. From Ref. 35, © 1982 by IEEE.

sequence  $\alpha$  and also the amplitudes of the baseband impulse responses  $a_c(t)$  and  $a_s(t)$ . By proper scaling of these impulse responses, however, it is possible to generate a signal  $s_0(t, \alpha)$  where the *average* energy per data symbol is  $E$ . The average is over the data sequences  $\alpha$ . It is assumed that  $a_c(t)$  and  $a_s(t)$  are normalized in this way; this is important for a fair comparison of the detection performance that will follow.

The detector in the modulation system OFCPM makes exhaustive correlations with the received signal for all possible signals  $s_0(t, \alpha)$ , and decides the signal with the largest correlation. It is possible that this detector makes infinitely many correlations, even for a finite observation interval  $NT$ , because the impulse responses  $a_c(t)$  and  $a_s(t)$  may have an infinite duration. To avoid this it is assumed that the impulse response is causal and of duration  $L_a$  symbol intervals.

Because of the group delay of the bandpass filter, the signal  $s_0(t, \alpha)$  will of course be delayed. The detector in the OFCPM system takes this into account. The detector in the SFCPM system neglects the influence of the bandpass filter and is therefore suboptimum. It is assumed that this suboptimum detector observes the received signal over the interval  $\lambda T \leq t \leq (N + \lambda)T$ , where  $\lambda$  is chosen to maximize  $d_{\min}^2$  for the SFCPM system; these merely correspond to an adjustment of the symbol timing. In the numerical examples below, the bandpass filter always has a linear phase, and  $\lambda = L_a/2$  is chosen.

Now expressions for  $d^2$  for the three systems in Figure 3.44 will be given. For the two optimum systems we have, by straightforward use of the definition,

$$d^2 = \frac{1}{2E_b} \int_0^{NT} [s(t, \alpha) - s(t, \tilde{\alpha})]^2 dt, \quad \text{OCPM}$$

$$d^2 = \frac{1}{2E_b} \int_0^{NT} [s_0(t, \alpha) - s_0(t, \tilde{\alpha})]^2 dt, \quad \text{OFCPM}$$

This reduces to

$$d^2 = \log_2 M \frac{1}{T} \int_0^{NT} [1 - \cos \phi(t, \gamma)] dt, \quad \text{OCPM}$$

$$d^2 = \frac{1}{2} \log_2 M \frac{1}{T} \int_0^{NT} [I_a(t, \alpha) - I_a(t, \tilde{\alpha})]^2 dt + \frac{1}{2} \log_2 M \frac{1}{T} \int_0^{NT} [Q_a(t, \alpha) - Q_a(t, \tilde{\alpha})]^2 dt, \quad \text{OFCPM} \quad (3.73)$$

where  $\gamma = \alpha - \tilde{\alpha}$  as usual. Note that the difference sequence cannot be used for the OFCPM system in general. For the system SFCPM, the development leading to (3.70) is used but with signals instead of the vectors in Section 3.5.1. This gives

$$\begin{aligned} d^2 &= \frac{d_A^4}{d_R^2} \\ d_A^2 &= \log_2 M \frac{1}{T} \int_0^{NT} I_a(t + \lambda T, \alpha) [I(t, \alpha) - I(t, \tilde{\alpha})] dt \\ &\quad + \log_2 M \frac{1}{T} \int_0^{NT} Q_a(t + \lambda T, \alpha) [Q(t, \alpha) - Q(t, \tilde{\alpha})] dt, \quad \text{SFCPM} \\ d_R^2 &= \log_2 M \frac{1}{T} \int_0^{NT} [1 - \cos \phi(t, \gamma)] dt \end{aligned} \quad (3.74)$$

by insertion of relevant quantities. Just like the OFCPM system, the difference sequence  $\gamma$  cannot be used for the SFCPM system in general.

#### *A Memory Analysis of $I_a(t, \alpha)$ and $Q_a(t, \alpha)$*

It is important to investigate the influence of the data symbols  $\alpha$  on the calculation of  $d_{\min}^2$ , especially for the systems OFCPM and SFCPM. For an unfiltered CPM signal, it was shown in Section 3.4.1 that the phase  $\phi(t, \alpha)$ , over any symbol interval, could be divided into a correlative phase transition and a phase shift. More precisely we can write

$$\phi(t, \alpha) = \theta(t, \alpha_n) + \theta_n, \quad nT \leq t \leq (n+1)T \quad (3.75)$$

where

$$\begin{aligned} \alpha_n &= (\alpha_n, \alpha_{n-1}, \dots, \alpha_{n-L+1}) \\ \theta(t, \alpha_n) &= 2\pi h \sum_{i=n-L+1}^n \alpha_i q(t - iT), \quad nT \leq t \leq (n+1)T \\ \theta_n &= h\pi \sum_{i \leq n-L} \alpha_i \end{aligned}$$

Now the quadrature components  $I_a(t, \alpha)$  and  $Q_a(t, \alpha)$  for the signal  $s_0(t, \alpha)$  are considered. It will be convenient to use the complex preenvelope notation for these components. This alternative is fully equivalent to the quadrature components notation of Section 2.4. Now we express

$$\tilde{s}_0(t, \alpha) = I_a(t, \alpha) + jQ_a(t, \alpha) \quad (3.76)$$

from which the modulated signal  $s_0(t, \alpha)$  is obtained by

$$s_0(t, \alpha) = \left( \frac{2E}{T} \right)^{1/2} \operatorname{Re} [\tilde{s}_0(t, \alpha) e^{j2\pi f_0 t}] \quad (3.77)$$

The operation of the bandpass filter can be written as [compare (2.26)]

$$\tilde{s}_0(t, \alpha) = \int_{t-L_a T}^t e^{j\phi(\tau, \alpha)} \tilde{a}(t-\tau) d\tau \quad (3.78)$$

Here  $\tilde{a}(t)$  is the complex envelope of the impulse response  $a(t)$  for the bandpass filter, i.e.,  $\tilde{a}(t) = a_c(t) + ja_s(t)$ .

Insertion of  $\theta(t, \alpha_n)$  and  $\theta_n$  from (3.75) gives

$$\begin{aligned} \tilde{s}_0(t, \alpha) &= e^{j\theta_{n-L_a}} \int_{t-L_a T}^{(n-L_a+1)T} e^{j\theta(\tau, \alpha_{n-L_a})} \tilde{a}(t-\tau) d\tau \\ &\quad + \sum_{i=1}^{L_a-1} e^{j\theta_{n-L_a+i}} \int_{(n-L_a+i)T}^{(n-L_a+i+1)T} e^{j\theta(\tau, \alpha_{n-L_a+i})} \tilde{a}(t-\tau) d\tau \\ &\quad + e^{j\theta_n} \int_{nT}^t e^{j\theta(\tau, \alpha_n)} \tilde{a}(t-\tau) d\tau, \quad nT \leq t \leq (n+1)T \end{aligned} \quad (3.79)$$

where the integral in (3.78) has been divided over the respective symbol intervals. It follows from this that over the interval  $[nT, (n+1)T]$ , the quadrature components  $I_a(t, \alpha)$  and  $Q_a(t, \alpha)$  are uniquely determined by the present data symbol  $\alpha_n$ , the *augmented state vector*

$$\alpha'_n = (\alpha_{n-1}, \dots, \alpha_{n-L_a}, \dots, \alpha_{n-L-L_a+1}) \quad (3.80)$$

and the phase shift

$$\theta'_n = h\pi \sum_{i \leq n-L-L_a} \alpha_i = \theta_{n-L_a} \quad (3.81)$$

Hence there are  $M^{(L+L_a-1)}$  different augmented correlative state vectors, and for a rational modulation index there is only a finite number of phase states, coinciding with those for unfiltered CPM. The trellis structure of the signal is not destroyed by the filtering so long as  $L_a$  is finite, but the number of states does grow.

### $d_B^2$ for OFCPM and SFCPM

The technique of finding inevitable mergers, developed in Section 3.2 for unfiltered modulations, can also be used here for a construction of an upper bound  $d_B^2$  on the minimum squared normalized Euclidean distance. As before, we require  $\alpha_i = \tilde{\alpha}_i$  when  $i < 0$  and  $\alpha_0 \neq \tilde{\alpha}_0$ .

First the OFCPM system is considered. Since a filtered CPM signal is uniquely defined by  $\alpha_n$ , the augmented state vector  $\alpha'_n$  and the phase shift  $\theta'_n$ , it is clear that if two signals have these quantities equal, they are indistinguishable from each other. We are interested in finding a merger that occurs for all  $h$ -values. It can be seen that the first merger of this kind occurs at  $t = (L + L_a + 1)T$  by making the augmented state vectors  $\alpha'_{L+L_a+1}$  and  $\tilde{\alpha}'_{L+L_a+1}$  identical, and also by choosing  $\alpha_1$  and  $\tilde{\alpha}_1$  in such a way that

$$\theta'_{L+L_a+1} = \tilde{\theta}'_{L+L_a+1} \Leftrightarrow \alpha_0 + \alpha_1 = \tilde{\alpha}_0 + \tilde{\alpha}_1$$

which in the binary case only can be accomplished by putting  $\alpha_1 = -\alpha_0$  and  $\tilde{\alpha}_1 = -\tilde{\alpha}_0$ .

As was the case for unfiltered CPM, there are also later mergers, and it turns out that the pair of sequences  $\alpha, \tilde{\alpha}$  yielding these mergers satisfies the merger constraint for the difference sequence  $\gamma$  in (3.28). By using these later mergers, it is possible to tighten  $d_B^2$ .

For unfiltered CPM it is irrelevant for calculation of distance how the data symbols prior to  $t = 0$  are chosen, so long as they are equal. For OFCPM this is not so, and by studying the expression for  $d^2$ , one finds that  $L - 1$  data symbols before  $t = 0$  have an influence on  $d_B^2$ . One also finds that the last  $L_a$  data symbols prior to the merger affect  $d_B^2$ . All these data symbols must be varied when calculating an upper bound function for OFCPM, and the minimum taken.

Next the SFCPM system is considered. In this case the expression for  $d^2$  involves the two quantities  $d_A^2$  and  $d_R^2$  in (3.74). Difference sequences can be used for calculating  $d_R^2$ , as is clear from (3.74), so it remains to study  $d_A^2$  in more detail. In the expression for  $d_A^2$  in (3.74), the integrands can be made equal to zero by making  $I(t, \alpha) = I(t, \tilde{\alpha})$  and  $Q(t, \alpha) = Q(t, \tilde{\alpha})$  for some  $t \geq t_m$ . Since these mergers occur for the quadrature components of the unfiltered CPM signal, for which the detection SFCPM is optimized, it follows that the first inevitable merger occurs at  $t = (L + 1)T$ . The merger sequences are those given by (3.28), with  $\gamma$  replaced by  $\alpha - \tilde{\alpha}$ . Note that the *detector* defines the merger for the suboptimum system, and that this is true in general.

The dependence upon  $\alpha$  and  $\tilde{\alpha}$  in the expression for  $d_B^2$  is also of interest. One finds that the  $L + L_a - \lambda - 1$  data symbols prior to  $t = 0$  must be varied in calculating  $d_B^2$ . For the  $m$ th merger in the original unfiltered

trellis,  $d_B^2$  is also affected by the data symbols with indices

$$i = (L + m + \lfloor \lambda \rfloor - L_a - 1), \dots, (m + \lfloor \lambda \rfloor - L_a + 2), (m + \lfloor \lambda \rfloor - L_a + 1)$$

and also the data symbols after the merger with indices

$$i = (L + m + 1), \dots, (L + m + \lceil \lambda \rceil - 2), (L + m + \lceil \lambda \rceil - 1).$$

This is partly due to the time shift  $\lambda$  between the receiver and transmitter, and partly to the longer memory in the signal  $s_0(t, \alpha)$  compared to  $s(t, \alpha)$ .

### Numerical Results

Examples of  $d_B^2$  and  $d_{\min}^2$  with different  $N$ -values will be given for the three systems OCPM, OFCPM, and SFCPM. Only binary schemes will be considered. The underlying unfiltered CPM schemes are either LREC or LRC with  $L = 1, 2$ , and  $3$ . Two classes of bandpass filters  $a_c(t)$  are also used; their responses are also either RC shaped or REC shaped, and are causal and of duration  $L_a$  bit intervals. In all cases  $a_s(t)$  is identically zero. Thus the filtering is done symmetrically with respect to the carrier frequency  $f_0$ . Figure 3.45 shows the squared magnitude of the Fourier transform of  $a_c(t)$  for the two classes of filters at equivalent baseband. The first nulls in these spectra occur at  $fT_b = 2/L_a$  for RC filtering and at  $fT_b = 1/L_a$  for REC filtering.

As a first example, Figure 3.46 shows  $d_{\min}^2$  for 1RC, OCPM and also for 1RC/1REC, SFCPM. Here the notation means that  $g(t)$  is 1RC and  $a(t)$  is 1REC. The number of observed bit intervals are  $N = 1, 2, 3$ , and  $4$  for both schemes. It can be seen that for low  $h$  values,  $d_{\min}^2$  for SFCPM is smaller than for OCPM. For larger  $h$  values, however, ( $0.6 < h < 0.9$ ) the situation is reversed, surprisingly enough. It must be remembered that SFCPM is suboptimum relative to OFCPM not OCPM. Thus insertion of a band-limiting filter can sometimes improve the performance.

By studying upper bound for the three systems OCPM, OFCPM, and SFCPM, this effect can be seen more clearly. In Figure 3.47 the three upper bounds  $d_B^2$  are shown for 1RC, OCPM and OFCPM, SFCPM when 1RC/2RC is transmitted. Note that  $d_B^2$  for SFCPM is always smaller than  $d_B^2$  for OFCPM, and that  $d_B^2$  for SFCPM is sometimes larger than  $d_B^2$  for OCPM.

In Figure 3.48 actual  $d_{\min}^2$  curves are shown for OFCPM, 1RC/2RC when  $N = 1, 2, \dots, 7$  observed bit intervals. The upper bound from Figure 3.47 is shown dashed where it is not reached with  $N = 7$ ; the tightness of  $d_B^2$  is obvious.

For the sake of completeness, actual  $d_{\min}^2$  curves are shown in Figure 3.49 for SFCPM, 1RC/2RC when  $N = 1, 2, \dots, 6$ . The upper bound is shown also here. It is seen that for  $h$  values slightly above  $h = 1$ ,  $d_{\min}^2$  is

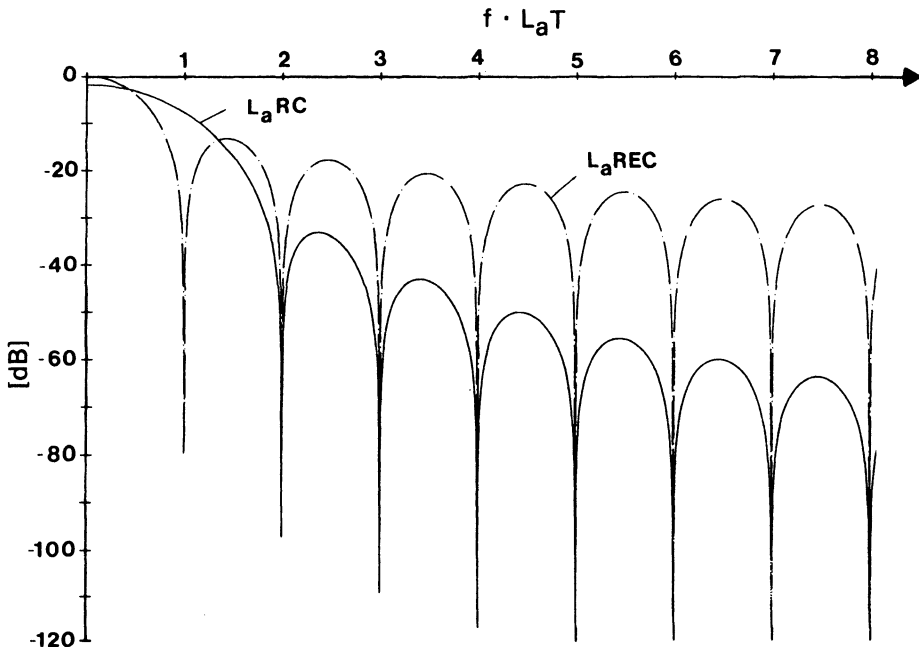


Figure 3.45. Spectral characteristics  $|A(f)|^2$  in db for the filters  $L_a$ REC and  $L_a$ RC.

not a nondecreasing function of  $N$ . This is a phenomenon that can occur for suboptimum detectors, but never for optimum ones. Thus it is of importance to find the best  $N$ , and not just make  $N$  large, for a suboptimal detector.

Some further behavior of the upper bounds appears in Figure 3.50. Here  $d_B^2$  is shown for the schemes 2RC, OCPM and also for OFCPM, SFCPM when 2RC/2RC is transmitted. Here  $d_B^2$  for SFCPM is still larger than  $d_B^2$  for OCPM, but for a smaller region of  $h$  values than was the case in Figure 3.47. This trend occurs when  $L$  is increased; as  $L$  is increased further the region of  $h$  values will shift to larger  $h$  values and eventually disappear.

A final example of actual  $d_{\min}^2$  curves appears in Figure 3.51. Here  $d_{\min}^2$  is shown for the two schemes 3RC, OCPM and 3RC/2REC, SFCPM. For both schemes  $N = 1, 2, 3$ , and 4. It is seen that for low  $h$  values the SFCPM scheme is about as good as the OCPM scheme with  $N = 2$ . For these low  $h$  values,  $d_{\min}^2$  for SFCPM has reached the upper bound  $d_B^2$ , and thus the asymptotic performance cannot be improved for the SFCPM scheme by making  $N$  larger than 4.

It can also be seen that when  $h = 1$ ,  $d_{\min}^2$  for the SFCPM scheme equals zero for all  $N$ . This is because the 2REC filter has a spectral null at

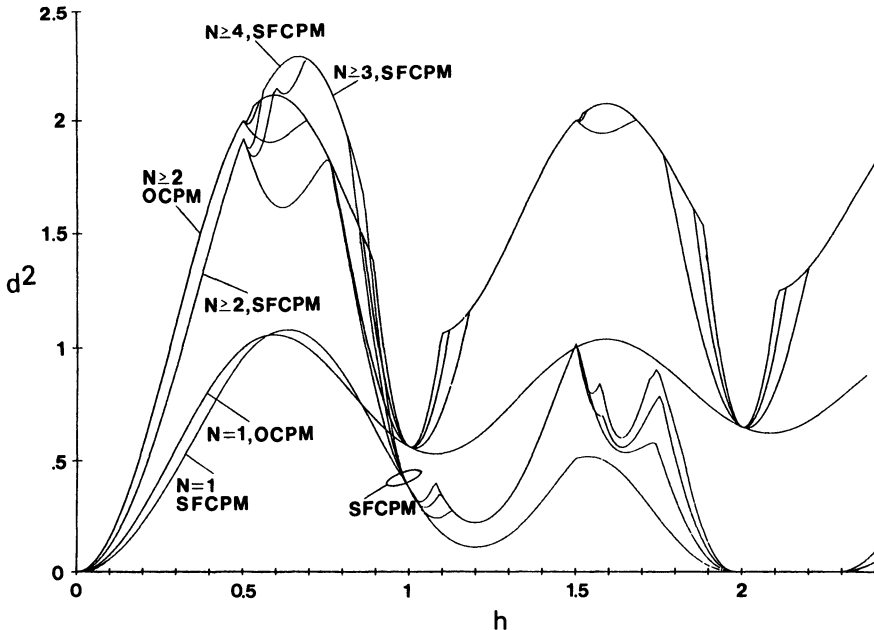


Figure 3.46. Minimum distance 1RC, OCPM and 1RC/1REC, SFCPM;  $N = 1, \dots, 4$  symbol observation interval.

$fT_b = \pm 1/2$ , and when  $h = 1$ , the instantaneous frequency for constant data for the 3RC scheme is exactly  $\pm 1/2 T_b$ . Thus the filter removes the transmitted signal entirely for the worst data case and the detector observes only AWGN. So it must be that  $d_{\min}^2 = 0$ .

Since a bandpass filter makes the envelope at the output of the filter time-varying, it is important to study this envelope variation. For the scheme considered in the previous figure, 3RC/2REC, this envelope is shown in Figure 3.52 for the case when  $h = 0.8$ . The plot shows the trajectory of  $I_a(t, \alpha)$  and  $Q_a(t, \alpha)$  as time evolves. From Section 3.4.1 it is known that the underlying CPM signal has  $p = 5$  phase states. This can be seen clearly in the fivefold symmetry of Figure 3.52. It is easy to show that any envelope diagram for a filtered CPM signal with  $p$  phase states is invariant to a rotation which is a multiple of  $2\pi/p$  radians.

### General Observations

Our method becomes too complex with long impulse responses, so we are prevented from analyzing very narrow band filtering. Nonetheless, some general observations and suggestions can be made.

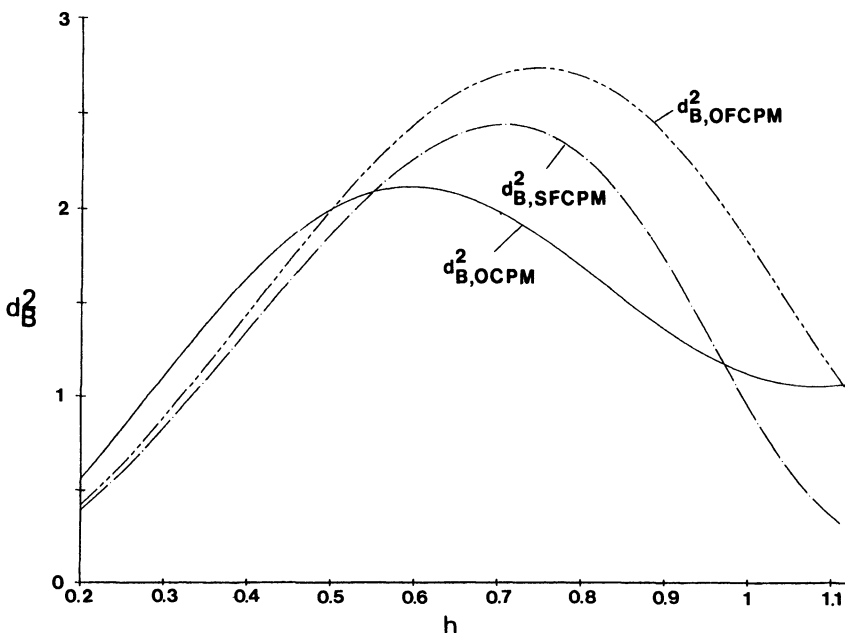


Figure 3.47. Upper bounds on  $d_{\min}^2$  for OCPM when 1RC is transmitted, and for OFCPM and SFCPM when 1RC/2RC is transmitted.

Firstly, it has been observed that for low  $h$  values ( $h \leq 0.5$ ) the performance after bandpass filtering is always degraded. This is true also when the optimum detector for the filtering is used. This performance degradation gets more and more pronounced with narrower filtering. It is also of interest to study the performance for a fixed bandpass filter, when the length of smoothing of the underlying CPM signal is increased ( $L$  is increased). Table 3.4 shows this. Asymptotic degradation in db in terms of  $E_b/N_0$  relative to unfiltered CPM is shown for several combinations of frequency pulses  $g(t)$  and bandpass filters  $a_c(t)$  when  $h = 1/2$  and  $M = 2$ . Reading the table horizontally, one sees that the degradation increases as the filtering is made narrower. Reading vertically, one sees that for fixed  $a_c(t)$  the performance gets worse with the duration of  $g(t)$ . As will be shown in Chapter 4, an increased  $L$  makes the power spectrum of the CPM signal narrower. Thus a narrow band CPM scheme is degraded more than a wider band scheme, for the same band-limiting filter!

For somewhat larger modulation indices ( $h \approx 0.8$ ), the effect is the same, although when  $L$  is small a performance gain can be obtained. This gain turns into a loss as  $L$  is increased. A possible explanation to this general behavior follows from studying the envelope diagram in Figure 3.52. It can be observed that when the phase varies slowly with time, the envelope is

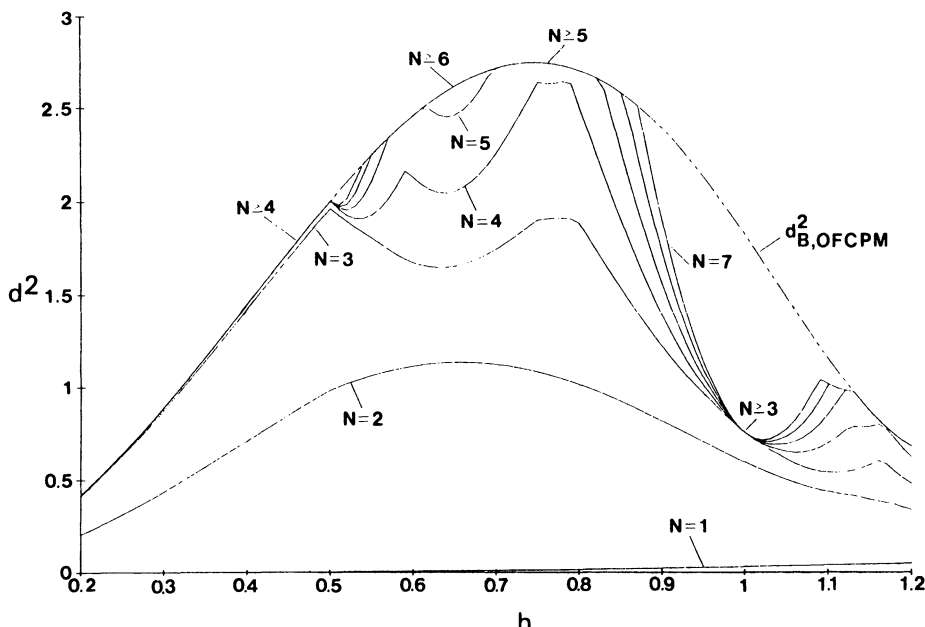


Figure 3.48. Upper bound and minimum distance for OFCPM when 1RC/2RC is transmitted;  $N = 1, \dots, 7$  observation intervals. From Ref. 35, © 1982 by IEEE.

large and vice versa. For CPM schemes with phase trees having straight lines for constant data ( $\pm\alpha = \dots, 1, 1, 1, \dots$ ) there is also a small inner circle appearing in the envelope diagram. This means that by using smoother and smoother CPM schemes, the phase prior to bandpass filtering is forced to vary more slowly during a larger portion of time, relatively speaking. Therefore the envelope gets larger during a longer portion of time. But in all CPM schemes considered here (except 1RC), the two sequences of constant data above always cause a large phase variation, irrespective of  $L$ . Since the average power per transmitted data symbol must be the same as for unfiltered CPM, the inner circle in the envelope diagram gets smaller and smaller with increased smoothing of the phase.

For low  $h$  values the transmitted and received data sequences associated with  $d_{\min}^2$  are

$$\alpha = \dots, +1, +1, -1, +1, +1, +1, \dots$$

$$\tilde{\alpha} = \dots, \underset{t=0}{+1}, -1, +1, +1, +1, +1, \dots$$

or the corresponding sign reversed sequences. Since filters of the types

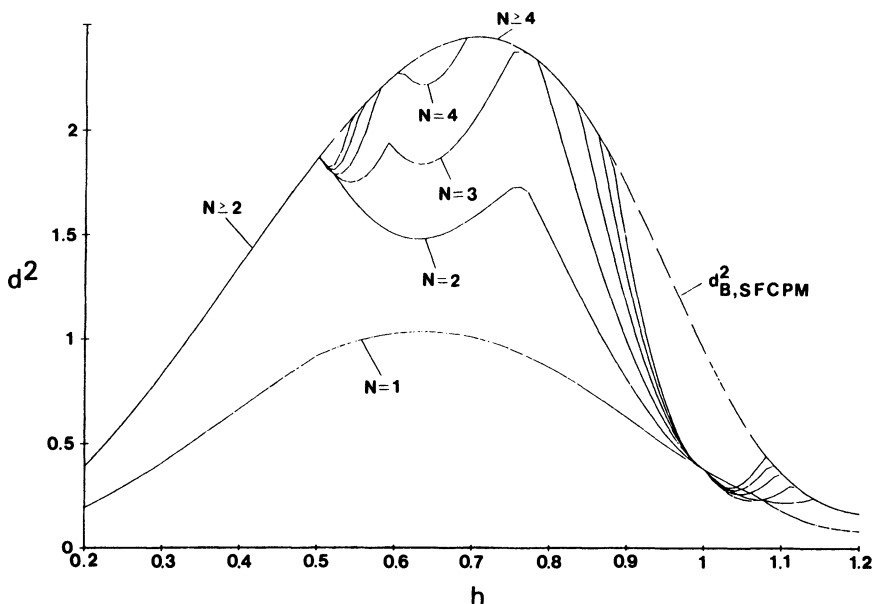


Figure 3.49. Upper bound and minimum distance for SFCPM when 1RC/2RC is transmitted; observation intervals  $N = 1, \dots, 6$ . From Ref. 35, © 1982 by IEEE.

$L_a$ REC and  $L_a$ RC have spectra which decrease slowly down to the first spectral null, large degradations are obtained even for mild filtering. It is believed that ideal bandpass filtering degrades the performance less.

With increased  $L$ , the occurrence of a constant transmitted frequency gets less probable. This makes the worst case error event very unprobable, which means that for a real system large values of  $E_b/N_0$  are needed before the performance loss is dominated by  $d_{\min}^2$ .

There are in principle three ways to improve the performance of a bandpass filtered CPM system. The first is to choose a more suitable transmitter filter, the second is to construct a more efficient suboptimum detector of equal complexity, and the third is to combine both of these approaches. At  $h = 1/2$ , we recall that both the OCPM and OFCPM schemes have the same  $d_B^2$ .

### 3.5.3. Effects of Filtering and Hard Limitation

By inserting a hard amplitude limiter after the filtered schemes just considered, we arrived at the three schemes in Figure 3.53, which we now study. The notation

OCPM: Optimum CPM

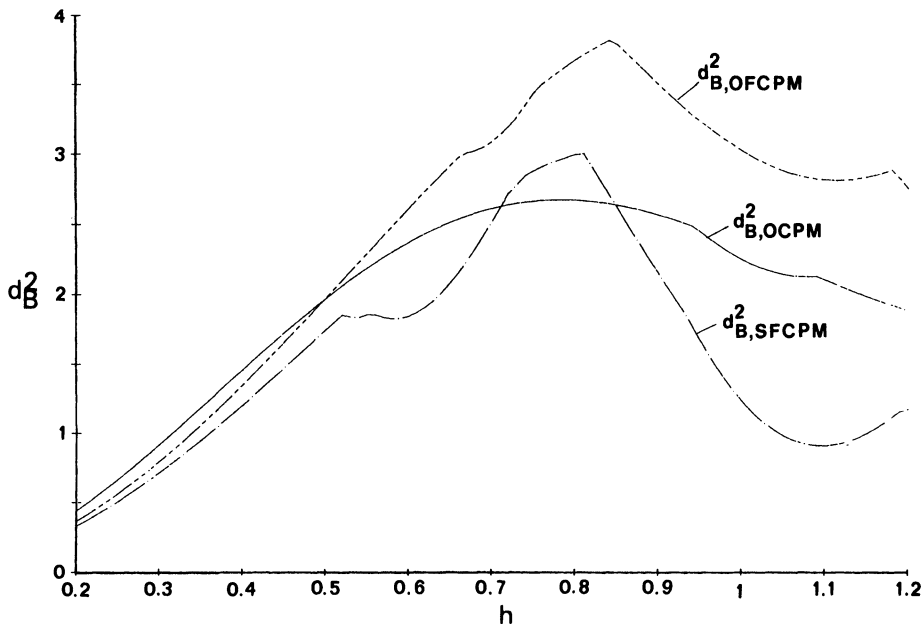


Figure 3.50. Upper bounds for OCPM when 2RC is transmitted, compared to OFCPM and SFCPM when 2RC/2RC is transmitted.

OFLCPM: Optimum Filtered and Limited CPM

SFLCPM: Suboptimum Filtered and Limited CPM

will be used for these schemes, in analogy with the previous section.

The addition of a hard limiter actually simplifies the problem of analyzing the asymptotic error performance, since the phase  $\phi_1(t, \alpha)$  now completely describes the constant envelope signal  $s_1(t, \alpha)$ . This phase is at every instant the same as the one before the hard limiter, and only the amplitude is changed. Since the hard limiter performs a memoryless operation on the input signal, it follows that the signal state description and dependence of  $d_B^2$  and  $d_{\min}^2$  on the data sequence are the same for  $s_1(t, \alpha)$  as for  $s_0(t, \alpha)$ . We can thus proceed directly to calculations of distance.

The normalized squared Euclidean distances for the three systems in Figure 3.53 are

$$d^2 = \log_2 M \frac{1}{T} \int_0^{NT} [1 - \cos \phi(t, \gamma)] dt, \quad \text{OCPM}$$

$$d^2 = \log_2 M \frac{1}{T} \int_0^{NT} \{1 - \cos [\phi_1(t, \alpha) - \phi_1(t, \tilde{\alpha})]\} dt, \quad \text{OFLCPM}$$

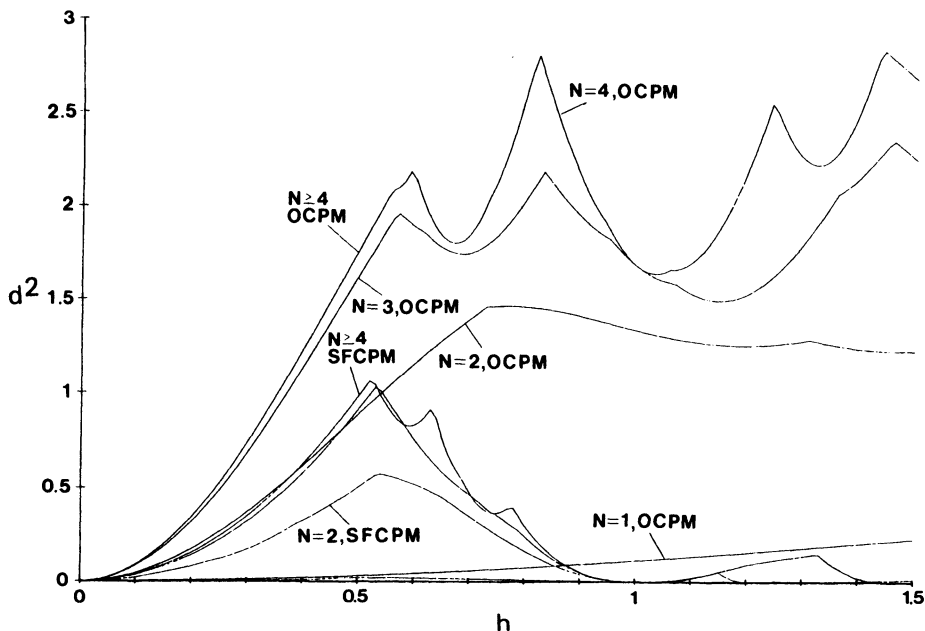


Figure 3.51. Minimum distances for 3RC under OCPM and 3RC/2REC under SFCPM.

$$d^2 = \frac{d_A^4}{d_R^2}$$

$$d_A^2 = \log_2 M \frac{1}{T} \int_0^{NT} \{ \cos [\phi_1(t + \lambda T, \alpha) - \phi(t, \alpha)] \\ - \cos [\phi_1(t + \lambda T, \alpha) - \phi(t, \tilde{\alpha})] \} dt, \quad \text{SFLCPM} \quad (3.82)$$

$$d_R^2 = \log_2 M \frac{1}{T} \int_0^{NT} [1 - \cos \phi(t, \gamma)] dt$$

Here  $\lambda T$  is the time shift between transmitter and receiver. It should be noted that the phase  $\phi_1(t, \alpha)$  in general is not linearly modulated by the data, which means that

$$\phi_1(t, \alpha) \neq 2\pi h \sum_i \alpha_i q_1(t - iT)$$

for all possible phase responses  $q_1(t)$ . Thus difference sequences cannot be used for OFLCPM and SFLCPM.

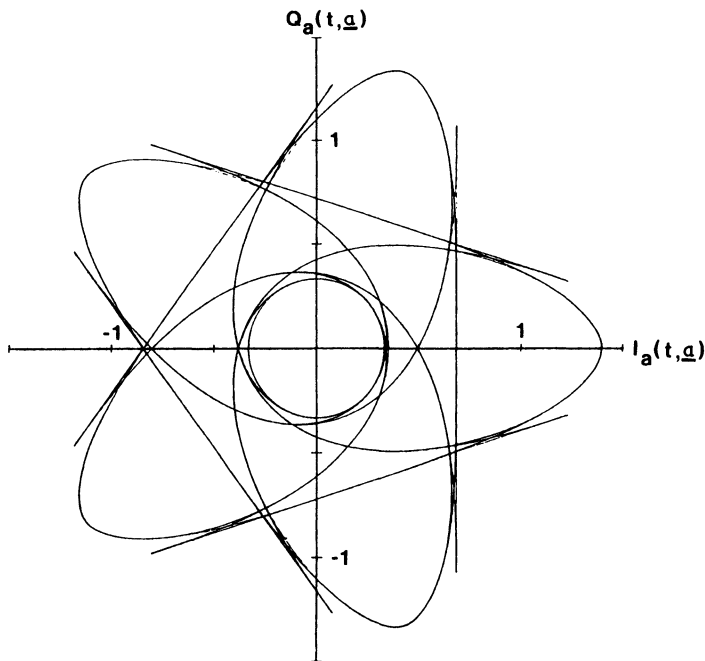


Figure 3.52. The envelope diagram for the scheme 3RC/2REC with  $h = 0.8$ .

For the numerical results, the same frequency pulses  $g(t)$  and bandpass filters  $a_c(t)$  as in Section 3.5.2 have been used. The shorthand notation  $g(t)/a_c(t)/\text{LIM}$  will be used for the band- and amplitude-limited signals. Only binary schemes are considered, and we will concentrate on the representative case 2RC/2RC/LIM.

Figure 3.54 shows the three upper bounds  $d_B^2$  for the schemes 2RC, OCPM, for 2RC/2RC/LIM, OFLCPM and for SFLCPM. The introduction of the bandpass hard limiter yields larger bound values for the last two over the first, when  $h \geq 0.75$ . This will be commented upon.

**Table 3.4. Asymptotic Degradation in dB in Terms of  $E_b/N_0$  Relative to Unfiltered CPM,  $M = 2$  and  $h = 1/2$**

$a_c(t)$ $g(t)$	1RC	1REC	2RC	2REC
1RC	0.04	0.18	0.29	1.56
2RC	0.10	0.31	0.52	2.03
3RC	0.19	0.51	0.79	2.56

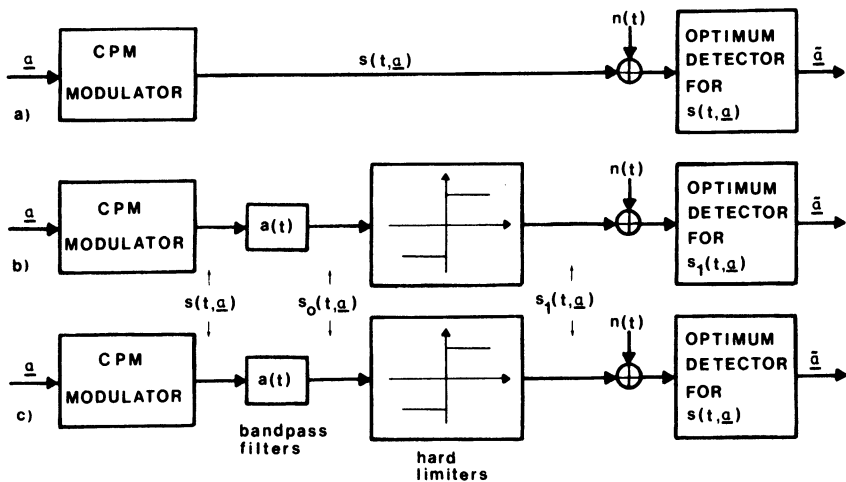


Figure 3.53. Block diagrams for the three hard limited combinations (a) OCPM (no limiting), (b) OFLCPM, and (c) SFLCPM. From Ref. 36, © 1983 by IEEE.

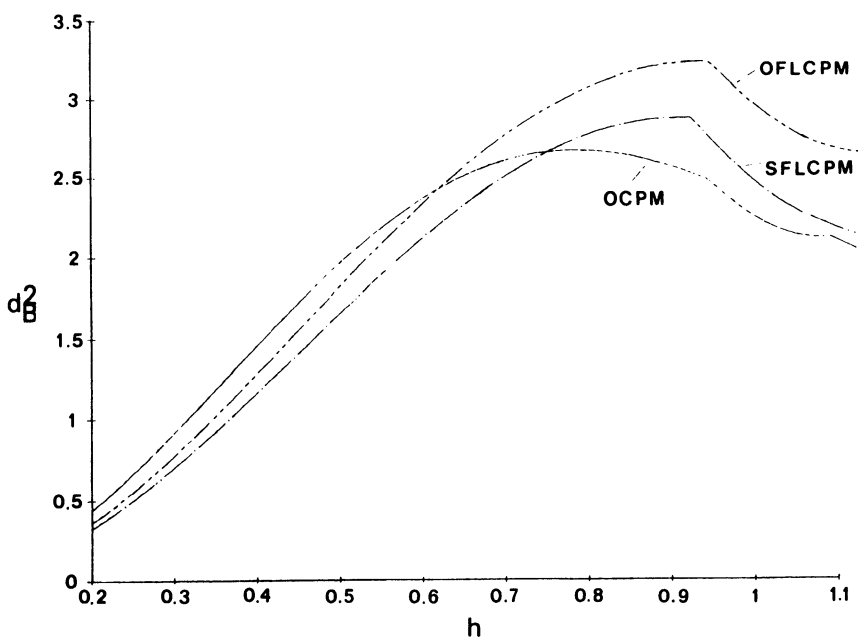


Figure 3.54. Upper bounds for 2RC under OCPM, and for 2RC/2RC/LIM under OFLCPM and SFLCPM.

In Figure 3.55 actual  $d_{\min}^2$  curves are given for the OFLCPM scheme with transmitted signal 2RC/2RC/LIM together with the upper bound from Figure 3.54. The observation interval is  $N = 1, 2, \dots, 7$  bit intervals. It is seen that  $d_B^2$  is reached with  $N = 5$  for low  $h$  values.

The scheme SFLCPM is considered in Figure 3.56 when  $N = 1, 2, \dots, 6$  observed bit intervals. The upper bound is reached with  $N = 5$  around  $h = 0.8$ , which confirms that a power gain relative to the scheme OCPM can really be achieved. This gain is accomplished merely by the insertion of the bandpass filter and the hard amplitude limiter on the original 2RC CPM system.

Since the phase  $\phi_1(t, \alpha)$  completely determines the signal  $s_1(t, \alpha)$ , it is useful to draw a phase tree. The signal 2RC/2REC/LIM with  $h = 1/2$  has such a tree according to Figure 3.57 when  $M = 2$ . The first merger in this tree occurs at  $t = 5T$ , as would have been the case for a linearly phase modulated CPM signal with  $L = 4$ . Actually the phase tree  $\phi_1(t, \alpha)$  is very similar to the phase tree  $\phi(t, \alpha)$  for the binary CPM signal 4RC. It has been observed that by convolving  $g(t)$  and  $a_c(t)$  and then replacing  $g(t)$  with this convolved pulse, the so constructed phase tree  $\phi(t, \alpha)$  is very similar to the phase tree  $\phi_1(t, \alpha)$ .

Some general conclusions can be made for bandpass filtered and hard amplitude limited CPM. The combination of these two devices acts like a

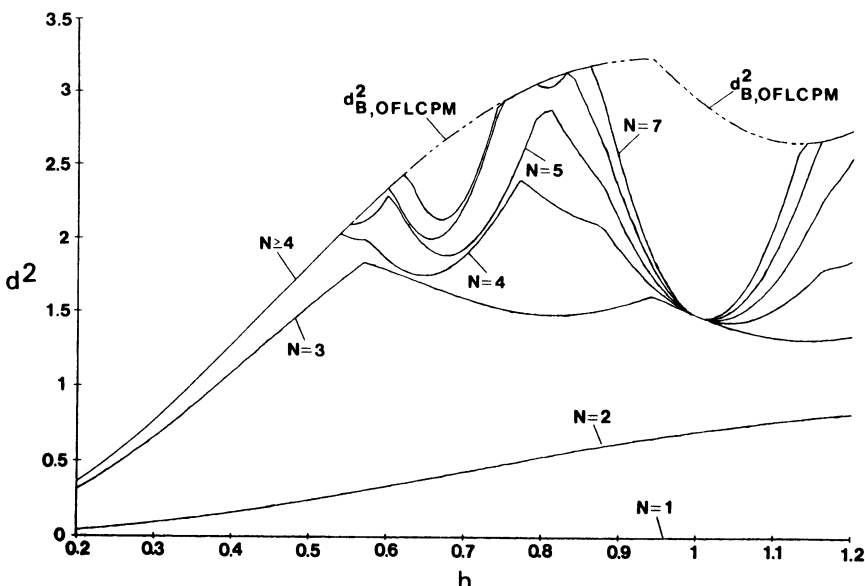


Figure 3.55.  $d_{B,\text{OFLCPM}}^2$  and  $d_{\min}^2$  for binary 2RC/2RC/LIM with  $N = 1, \dots, 7$  interval observation.

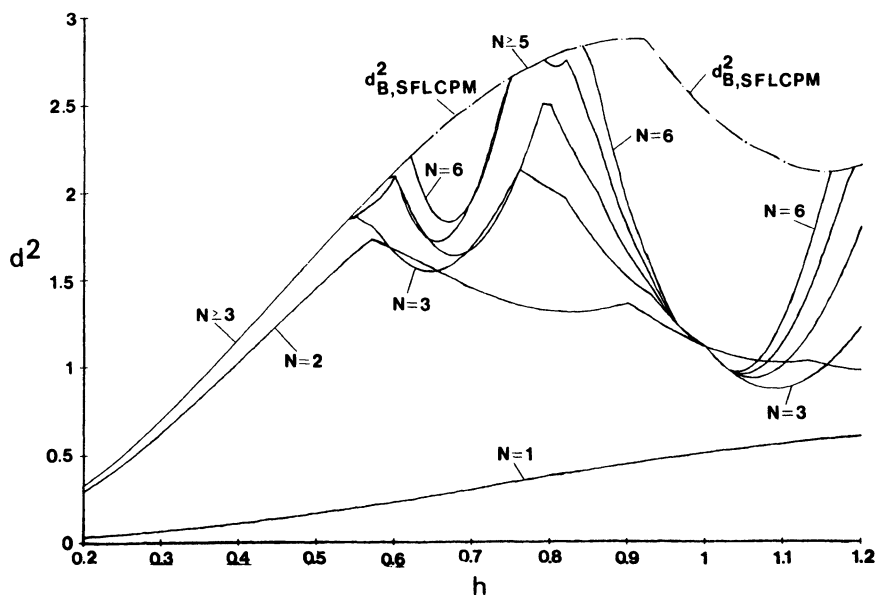


Figure 3.56. Upper bound and minimum distance for the scheme 2RC/2RC/LIM under combination SFLCPM, with  $N = 1, \dots, 6$  interval observation.

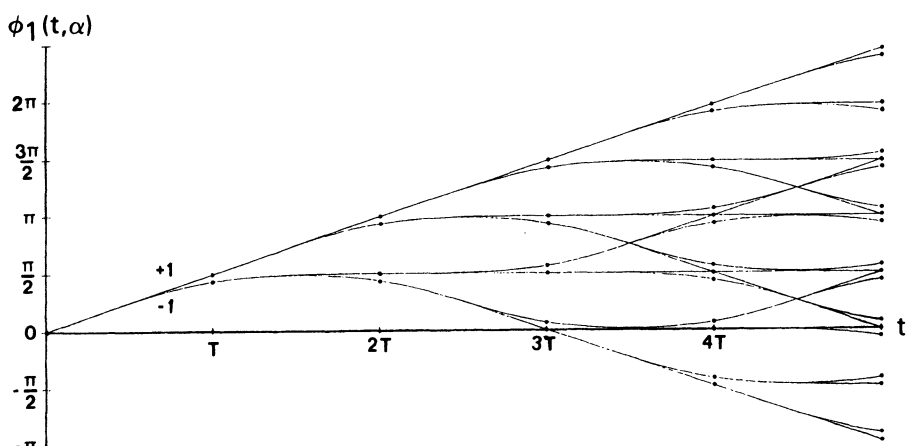


Figure 3.57. The phase tree for the signal 2RC/2REC/LIM with  $h = 1/2$ . This tree is very close to that of the scheme 4RC. From Ref. 36, © 1983 by IEEE.

phase smoother on the original CPM signal. The new signal is also a CPM signal, not linearly phase modulated but close to being so, and it has a larger  $L$ . Thus the trends pointed out in Section 3.2.2 concerning the behavior of  $d_B^2$  with increasing  $L$  also hold here, especially for low modulation indices.

### 3.5.4. Summary

We have applied the idea of the Euclidean distance measure to two kinds of distortion operations on a CPM signal. Although the analysis that followed for these two distorting elements was performed only for the case  $H = 1$ , it can easily be generalized to include multi- $h$  schemes.

The major problem that arises in calculating  $d_{\min}^2$  is the computational effort, which grows exponentially with the duration of the impulse response of the bandpass filter. Bandpass filters in practical applications will have a large  $L_a$ , and one should turn to simulations as done in Refs. 37, 39, 41, and 42.

Another problem that has not yet been solved is to construct upper and lower bounds on the symbol error probability for these distorted schemes, in the style of Section 3.4.2. This is of interest because in mismatched systems there is larger difference between the worst-case error event and typical event distances. Thus the performance gain/degradation indicated by  $d_{\min}^2$  may occur only at very low error rates, i.e.,  $d_{\min}^2$  is a pessimistic performance measure for low and intermediate SNRs. Another difficulty with bit error probability bound calculations is that the Euclidean distance measure for mismatched signal sets is not additive from symbol interval to symbol interval, as it is for optimum systems. This also means that reduced tree search algorithm for finding  $d_{\min}^2$  in Appendix A in general cannot be used. Brute force must be used instead.

An analytic approach for evaluation of the error performance, using upper and lower bounds on the bit error probability, is performed in Ref. 38. Only MSK and OQPSK are considered when band-limiting filters are used at the transmitter and receiver front end. This makes the analysis simple, and the procedure in Ref. 38 can be applied to any binary CPM system with  $h = 1/2$ .

A performance analysis of a quadrature partial response (QPRS) signal which is hard limited, transmitted over an AWGN channel, and coherently detected, has been performed by Amoroso.<sup>(40)</sup> A similar system is considered in Ref. 41, but no analysis of the error performance is presented. Note that QPRS is a priori an amplitude modulation system.

Finally, we stress that if the CPM signal has a trellis structure before any of the two kinds of distortion considered here, it will have one after. The number of states will grow, because of the extra memory (intersymbol interference) introduced by the bandpass filter.

### 3.6. Conclusions

This whole chapter, with the exception of Section 3.4, has dealt with the single quantity  $d_{\min}^2$  for a multitude of digital phase modulation schemes. For binary PSK or QPSK this quantity equals 2, and for decades this has been *the* distance figure used by communication engineers. We now see that  $d_{\min}$  should really be viewed as a function of  $h$ . Plots of  $d_{\min}$  vs.  $h$  give the whole story about the error performance for a family of phase modulation methods, even at relatively high error rates such as  $10^{-4}$ .  $d_{\min}^2$  is a simple one-parameter description of the energy consumption of a whole communications scheme.

The methods presented for calculation of  $d_{\min}^2$  and  $d_B^2$  are quite straightforward to use. They make it possible to analyze a new modulation system designed for particular needs, and to analyze its error performance.

The major conclusion from the results in this chapter is that it is quite possible to design digital constant envelope modulation schemes which are significantly more power efficient than BPSK and QPSK. We have to accept that to have this power gain, more signal processing is required at the receiver side. If a receiver must make its decision solely on the basis of one symbol interval, antipodal signals such as BPSK minimize the bit error probability.

A good error performance is not the only quality measure for a digital phase modulation system. The spectral occupancy of the transmitted signal is a very different but equally important measure. This will be dealt with in the next chapter, and in Chapter 5 both these performance measures are put together and studied jointly.

## References

1. C. E. Shannon, A mathematical theory of communication, *Bell. Syst. Tech. J.* **27**, 379–423 (1948).
2. M. G. Pelchat, R. C. Davis, and M. B. Luntz, Coherent demodulation of continuous phase binary FSK signals, Proc. Int. Telemetering Conf., Washington, D.C., pp. 181–190, 1971.
3. W. P. Osborne and M. B. Luntz, Coherent and noncoherent detection of CPFSK, *IEEE Trans. Commun.* **COM-22**, 1023–1036 (1974).
4. R. deBuda, Coherent demodulation of frequency-shift keying with low deviation ratio, *IEEE Trans. Commun.* **COM-20**, 429–436 (1972).
5. T. A. Schonhoff, Symbol error probabilities for  $M$ -ary coherent continuous phase frequency-shift keying (CPFSK), IEEE Int. Conf. Commun., Conf. Record, San Francisco, pp. 34.5–34.8, 1975.
6. T. A. Schonhoff, Bandwidth vs. performance considerations for CPFSK, IEEE National Telecommun., Conf. Record, pp. 38.1–38.5, 1975.
7. T. A. Schonhoff, Symbol error probabilities for  $M$ -ary CPFSK: Coherent and noncoherent detection, *IEEE Trans. Commun.* **COM-24**, 644–652 (1976).

8. T. Aulin and C.-E. Sundberg, Bounds on the performance of binary CPFSK type of signaling with input data symbol pulse shaping, *IEEE National Telecommun., Conf. Record*, Birmingham, Alabama, pp. 6.5.1-6.5.5, 1978.
9. T. Aulin and C.-E. Sundberg, *M*-ary CPFSK type of signaling with input data symbol pulse shaping—Minimum distance and spectrum, *IEEE Int. Conf. Commun., Conf. Record*, Boston, pp. 42.3.1-42.3.6, 1979.
10. A. Lender, The duobinary technique for high speed data transmission, *IEEE Trans. Commun. Electron. COM-11*, 214-218 (1963).
11. A. Lender, Correlative level coding for binary data transmission, *IEEE Spectrum* 3, 104-115 (1966).
12. P. Kabal and S. Pasupathy, Partial response signaling, *IEEE Trans. Commun. COM-23*, 921-934 (1975).
13. T. Aulin, N. Rydbeck, and C.-E. Sundberg, Bandwidth efficient constant-envelope digital signaling with phase tree demodulation, *Electron Lett.* 14, 487-489 (1978).
14. T. Aulin, N. Rydbeck, and C.-E. Sundberg, Bandwidth efficient digital FM with coherent phase tree demodulation, *IEEE Int. Conf. Commun., Conf. Record*, Boston, pp. 42.4.1-42.4.6, 1979.
15. T. Aulin, CPM—A power and bandwidth efficient digital constant envelope modulation scheme, Doctoral Thesis, *Telecommun. Theory*, Univ. of Lund, Lund, Sweden, November 1979.
16. T. Aulin and C.-E. Sundberg, Continuous phase modulation—Part I: Full response signaling, *IEEE Trans. Commun. COM-29*, 196-209 (1981).
17. T. Aulin and C.-E. Sundberg, Continuous phase modulation—Part II: Partial response signaling, *IEEE Trans. Commun. COM-29*, 210-225 (1981).
18. H. Miyakawa, H. Harashima, and Y. Tanaka, A new digital modulation scheme—Multi-mode binary CPFSK, *Third Int. Conf. Dig. Satellite Commun., Conf. Record*, Kyoto, Japan, pp. 105-112, 1975.
19. J. B. Anderson and R. deBuda, Better phase-modulation error performance using trellis phase codes, *Electron. Lett.* 12, 587-588 (1976).
20. J. B. Anderson and D. P. Taylor, A bandwidth-efficient class of signal space codes, *IEEE Trans. Inf. Theory IT-24*, 703-712 (1978).
21. T. Aulin and C.-E. Sundberg, On the minimum Euclidean distance for a class of signal space codes, *IEEE Trans. Inf. Theory IT-28*, 43-55 (1982).
22. T. Aulin and C.-E. Sundberg, Minimum Euclidean distance and power spectrum for a class of smoothed phase modulation codes with constant envelope, *IEEE Trans. Commun. COM-30*, 1721-1729 (1982).
23. J. Wozencraft and I. M. Jacobs, *Principles of Communication Engineering*, Wiley, New York (1965).
24. A. Viterbi, *Principles of Coherent Communication*, McGraw-Hill, New York (1966).
25. A. T. Lereim, Spectral properties of multi- $h$  phase codes, M. Eng. thesis, McMaster Univ., Technical Report No. CRL-57, Communications Research Laboratory, Hamilton, Ontario, Canada, July 1978.
26. J. B. Anderson, D. P. Taylor, and A. T. Lereim, A class of trellis phase modulation codes for coding without bandwidth expansion, *Int. Conf. on Commun., Conf. Record*, Toronto, Ontario, Canada, pp. 50.3.1-50.3.5, June 1978.
27. J. K. Omura and D. Jackson, Cutoff rates for channels using bandwidth efficient modulations, *Nat. Telecommun. Conf., Conf. Record*, Houston, pp. 14.1.1-14.1.11, November 1980.
28. T. Aulin, Viterbi detection of continuous phase modulated signals, *Nat. Telecommun. Conf., Conf. Record*, Houston, pp. 14.2.1-14.2.7, November 1980.
29. T. Aulin, Symbol error probability bounds for coherently Viterbi detected continuous phase modulated signals, *IEEE Trans. Commun. COM-29*, 1707-1715 (1981).

30. S. G. Wilson, J. H. Highfill, and C.-D. Hsu, Error bounds for multi- $h$  phase codes, *IEEE Trans. Inf. Theory* **IT-28**, 660–665 (1982).
31. S. Lin and D. J. Costello, *Error Control Coding: Fundamentals and Applications*, Prentice Hall, Englewood Cliffs, New Jersey (1983).
32. F. Hemmati and D. J. Costello, Jr., Truncation error probability in Viterbi decoding, *IEEE Trans. Commun.* **COM-25**, 530–532 (1977).
33. T. Aulin, C.-E. Sundberg, and A. Svensson, Viterbi detectors with reduced complexity for partial response continuous phase modulation, *Nat. Telecommun., Conf. Record*, New Orleans, pp. D8.3.1–D8.3.7, December 1981.
34. A. Svensson, C.-E. Sundberg, and T. Aulin, Distance measure for simplified receivers, *Electron. Lett.* **19**(23), 953–954 (1983).
35. T. Aulin and C.-E. Sundberg, Detection performance of band-limited continuous phase modulation, *Globecom '82, Conf. Record*, Miami, pp. E7.6.1–E7.6.7, December 1982.
36. T. Aulin and C.-E. Sundberg, Optimum and sub-optimum detectors for band and amplitude limited continuous phase modulation, *Int. Conf. on Commun., Conf. Record*, Boston, pp. A6.1.1–A6.1.6, June 1983.
37. D. P. Taylor and H. C. Chan, A simulation study of two bandwidth-efficient modulation techniques, *IEEE Trans. Commun.* **COM-29**, 267–275 (1981).
38. I. Korn, OQPSK and MSK systems with bandlimiting filters in transmitter and receiver and various detector filters, *Proc. IEE, Part F*, 439–447 (1980).
39. H. Singh and T. T. Thjung, Error-rate measurements for SFSK with band limitation, *Electron. Lett.* **16**(2), 64–66 (1980).
40. F. Amoroso, The use of quasi-bandlimited pulses in MSK transmission, *IEEE Trans. Commun.* **COM-27**, 1616–1624 (1979).
41. M. C. Austin and M. U. Chang, Quadrature overlapped raised-cosine modulation, *Int. Conf. on Commun., Conf. Record*, Seattle, pp. 26.7.1–26.7.5, June 1980.
42. M. Atobe, Y. Matsumoto, and Y. Tagashira, One solution for constant envelope modulation, *4th Int. Conf. on Diag. Sat. Commun., Conf. Record*, Montreal, pp. 45–50, October 1978.
43. A. J. Viterbi and J. Omura, *Principles of Digital Communications and Coding*, McGraw-Hill, New York (1979).
44. T. Aulin and C.-E. Sundberg, CPM—An efficient constant amplitude modulation scheme, *Int. J. Satellite Commun.* **2**, 161–186 (1984).

# Spectral Performance

The bandwidth that a signal occupies is an important aspect of its total performance, as important as its error performance. The radiofrequency spectrum is a limited and valuable resource and its use is controlled by international law. It is thus important to consume as little of it as possible.

There is no single definition of bandwidth. Constant-envelope signals by nature are not bandlimited, even if they are infinite in duration. Different measures, like power outside a certain frequency or the position of spectral nulls, are appropriate for the effect of different types of equipment on the signal. In this chapter we explore ways to compute the distribution of energy with frequency in a signal, its power spectral density (PSD). Traditionally, this calculation has required long computations and formulas of legendary size. After a survey of some older methods, we will present in Section 4.3 a new method that provides a fast and accurate numerical calculation of the PSD for a general digital phase modulated signal. Representative PSDs will follow and the effects of filtering and amplitude limiting will be studied.

## 4.1. Review of Spectral Calculation Methods

The fundamental difficulty in the calculation of spectra is that a typical modulation system driven by random data does not produce a wide-sense stationary output. Samples at two times of the modulated signal have one set of statistics if the times lie within the same symbol interval and quite another set if the times lie in different intervals, even if the interval between the times is the same in both cases. This means that no process autocorrelation function can be defined, and so the power spectral density of the process, which is ordinarily taken as the Fourier transform of the autocorrelation function, cannot be defined.

Communications engineers have avoided this difficulty by computing instead an *average* power spectral density. In different methods, this averaging is performed in different senses. In some methods, the transmitted signal is subjected to a random phase shift or time shift and the spectrum computed for the average of such random signals; this randomized signal is wide-sense stationary. In all methods, the spectrum is averaged at some point over the ensemble of transmitted data sequences. As a consequence, the average power spectral density is a long-term average, and we must hope that local spectral characteristics will not deviate too much from it. Throughout this book, we will be dealing with these averaged spectral densities, even though we will normally drop the term "average." Usually the spectra will be computed by the method of Section 4.2.

The reference list of this chapter is collection of some of the key papers in the calculation of the PSD of a digital phase modulated signal. An early method was the *direct approach* of Anderson and Salz;<sup>(5)</sup> see also Refs. 3 and 4. Here one takes the Fourier transform of the deterministic signal  $s(t, \alpha)$  and then forms the average over  $\alpha$  and  $\phi_0$  of these transforms according to

$$\lim_{N \rightarrow \infty} \frac{1}{NT} \mathcal{E}\{|S_N(f, \alpha)|^2\}$$

$\phi_0$  is an offset to the signal phase, distributed uniformly over  $(0, 2\pi)$ , and  $S_N$  is the transform of  $s(t, \alpha)$  truncated to  $(0, NT)$ . No autocorrelation function is ever computed. Complicated equations result for most schemes and two-dimensional numerical integrations are required. Closed-form formulas can be had for full response CPFSK.

Another approach is the *autocorrelation method*; see Greenstein<sup>(16)</sup> and Refs. 3, 4, 15, 17, 20, 21, 22, 24. Here the product of  $s(t, \alpha)$  and  $s(t + \tau, \alpha)$  is formed and the average of this product is taken for  $t$  in the interval  $(0, T)$ . This product is then averaged with respect to the data sequence  $\alpha$ . Next this time-averaged autocorrelation is Fourier transformed. Greenstein's original method was fast to calculate, but it applied only to frequency pulses that integrate to zero. The method we will develop in Section 4.2 is of the autocorrelation type, but it applies to any frequency pulse.

A numerical method was proposed by Garrison<sup>(11)</sup> in which the phase response  $q(t)$  of the modulation is broken into a piecewise-linear approximation; the spectrum for each linear section can be expressed in closed form and the modulation spectrum is approximately the superposition of all the section spectra. The computation with this method grows rapidly with the number of sections and the method cannot provide accurate results for the sidelobes. Other approaches exploit the Markov chain nature of the

modulation.<sup>1,8,10,13,14,19</sup> Finally, it is always possible to simulate a scheme (or transmit it) and measure its spectrum.

None of these methods has proved really satisfactory, as they apply only to limited cases or involve very large formulas and long computation. We will list some of the closed-form cases in Section 4.3. Generally, these are the cases of binary, equiprobable data and frequency pulses of length at most two. Certain “analytical” formulas have been published that are really infinite series expansions of Bessel or Frensel integrals, often of fractional order; see Refs. 6, 12, 17, 18.

The spectra of  $I$  and  $Q$  channel modulations like QPSK and BPSK were discussed in Section 2.6. For these, successive pulses in the  $I$  and  $Q$  channels are all orthogonal to each other, so that the total spectrum is just a scaled-up version of the spectrum of one pulse.

## 4.2. A Simple, Fast, and Reliable General Numerical Method

### 4.2.1. Derivation of the Method

In this section a method for calculation of PSDs for a general CPM signal is given. It is simple to use and the computational effort is small. A complete derivation is given, but it is not necessary to read this to be able to use the method. A short summary of the method is given in Section 4.2.4, where it is assumed that the notation is known. First consider the rf signal

$$s(t, \alpha) = (2P)^{1/2} \cos [2\pi f_0 t + \phi(t, \alpha)] \quad (4.1)$$

for which the PSD is to be calculated.  $f_0$  denotes the rf center (or “carrier”) frequency. Here  $P$  is the constant transmitted power  $E/T$  and  $\phi(t, \alpha)$  is the information carrying phase. This notation coincides with that in Chapter 2, except that  $E/T$  has been replaced by  $P$ . A single modulation index  $h$  and a single phase response  $q(t)$  are used to produce

$$\phi(t, \alpha) = 2\pi h \sum_{i=-\infty}^{\infty} \alpha_i q(t - iT)$$

where the sequence  $\alpha = \dots, \alpha_{-1}, \alpha_0, \alpha_1, \dots$  of random data symbols are  $M$ -ary [ $\alpha_i = \pm 1, \pm 3, \dots, \pm(M-1)$ ;  $i = 0, \pm 1, \pm 2, \dots$ ] and statistically independent. The data symbols are also identically distributed with *a priori* probabilities

$$P_j = P\{\alpha_i = j\}, \quad j = \pm 1, \pm 3, \dots, \pm(M-1), \\ i = 0, \pm 1, \pm 2, \dots \quad (4.2)$$

where  $\sum P_j = 1$ . It is possible to consider a yet more general case where the modulation index is cyclically varying (multi- $h$ ) and the sequence of data symbols are correlated. This will be treated in Section 4.2.3.

To calculate the PSD, the autocorrelation function is first found, and then Fourier-transformed. This approach was originally taken by Greenstein,<sup>(16)</sup> who considered time-limited phase responses  $q(t)$ . As will be seen below, this facilitates the solution but also leads to power spectra with undesirable properties. It is convenient to work with complex notation so the CPM signal (4.1) is written [see (3.76) and (3.77) in Section 3.5.2]

$$s(t, \alpha) = (2P)^{1/2} \operatorname{Re} \{ e^{j\phi(t, \alpha)} e^{j2\pi f_0 t} \} \quad (4.3)$$

where  $\operatorname{Re}\{\cdot\}$  denotes the real part. By definition the autocorrelation function is

$$r(\tau) = \langle \mathcal{E}\{s(t + \tau, \alpha)s^*(t, \alpha)\} \rangle \quad (4.4)$$

where the operator  $\langle \cdot \rangle$  denotes averaging with respect to the random variable  $t$ , uniformly distributed over the interval  $[0, T]$ .  $\mathcal{E}\{\cdot\}$  is the averaging operator with respect to the sequence  $\alpha$ . The signal  $s(t, \alpha)$  is actually cyclostationary, but by introducing the operator  $\langle \cdot \rangle$  this property is removed. The resulting ensemble of signals is stationary.

By insertion of (4.3) into (4.4) we obtain

$$r(\tau) = P \operatorname{Re} \{ R(\tau) e^{j2\pi f_0 \tau} \} \quad (4.5)$$

if the signal is narrow-band, meaning  $f_0 T \gg 1$ ; here  $R(\tau)$  is the complex baseband autocorrelation function

$$R(\tau) = \langle \mathcal{E}\{e^{j\phi(t+\tau, \alpha)} e^{-j\phi(t, \alpha)}\} \rangle \quad (4.6)$$

For our signal this can be written

$$R(\tau) = \langle \mathcal{E}\{e^{j2\pi h \sum_i \alpha_i [q(t+\tau-iT) - q(t-iT)]}\} \rangle \quad (4.7)$$

The sum in the exponent can be written as a product of exponentials

$$R(\tau) = \left\langle \mathcal{E}\left\{ \prod_i \exp(j2\pi h \alpha_i [q(t + \tau - iT) - q(t - iT)]) \right\} \right\rangle \quad (4.8)$$

and since the data symbols in the sequence  $\alpha$  are statistically independent, the averaging with respect to the sequence is simply performed as

$$R(\tau) = \left\langle \prod_i \left\{ \sum_{\substack{k=-(M-1) \\ k \text{ odd}}}^{M-1} P_k \exp(j2\pi h k [q(t + \tau - iT) - q(t - iT)]) \right\} \right\rangle \quad (4.9)$$

where the prior probabilities for the data symbols were used. The product above contains infinitely many factors. But the frequency pulse  $g(t)$  is identically equal to zero outside the interval  $[0, LT]$ , and the phase response  $q(t)$  is zero for  $t < 0$  and equal to  $1/2$  for  $t > LT$ . This makes the exponent in (4.9) cancel to zero for all but a finite number of factors. By assuming that  $\tau \geq 0$  and writing

$$\tau = \tau' + mT, \quad 0 \leq \tau' < T, \quad m = 0, 1, 2, \dots \quad (4.10)$$

it can be shown that<sup>(24)</sup>

$$\begin{aligned} R(\tau) &= R(\tau' + mT) \\ &= \frac{1}{T} \int_0^T \prod_{i=1-L}^{m+1} \left\{ \sum_{\substack{k=-(M-1) \\ k \text{ odd}}}^{M-1} P_k \exp(j2\pi h k [q(t + \tau' - (i-m)T) \right. \\ &\quad \left. - q(t - iT)]) \right\} dt \end{aligned} \quad (4.11)$$

where the operation  $\langle \cdot \rangle$  has been expressed explicitly. Note that the case  $\tau \leq 0$  adds no difficulty to the problem since it is possible to write

$$R(\tau) = R_c(\tau) + jR_s(\tau), \quad R_c(\tau), \quad R_s(\tau) \text{ real}$$

and the real and imaginary parts satisfy

$$\begin{aligned} R_c(-\tau) &= R_c(\tau) \\ R_s(-\tau) &= -R_s(\tau) \end{aligned} \quad (4.12)$$

which is a property possessed by all autocorrelation functions.

In a simple way the baseband autocorrelation function  $R(\tau)$  for a general CPM signal has been found. What remains in finding the power spectrum is to perform the Fourier transformation

$$S(f) = \mathcal{F}\{R(\tau)\} = \int_{-\infty}^{\infty} R(\tau) e^{-j2\pi f\tau} d\tau \quad (4.13)$$

numerically without any truncation errors. Note that

$$S(f) = 2 \operatorname{Re} \left\{ \int_0^\infty R(\tau) e^{-j2\pi f\tau} d\tau \right\} \quad (4.14)$$

because of (4.12), in which  $\tau \geq 0$ . We now study the expression for  $R(\tau)$  in (4.11) for  $\tau = \tau' + mT \geq LT$ . For this case we have

$$\begin{aligned} R(\tau) &= R(\tau' + mT) \\ &= C_\alpha^{m-L} \frac{1}{T} \int_0^T \prod_{i=1-L}^0 \left\{ \sum_{\substack{k=-M-1 \\ k \text{ odd}}}^{M-1} P_k \exp(j2\pi h k [q(LT) - q(t - iT)]) \right\} \\ &\quad \times \prod_{i=1-L}^1 \left\{ \sum_{\substack{k=-M-1 \\ k \text{ odd}}}^{M-1} P_k \exp[j2\pi h k q(t + \tau' - iT)] \right\} dt, \quad m \geq L \end{aligned} \quad (4.15)$$

where

$$C_\alpha = \sum_{\substack{k=-M-1 \\ k \text{ odd}}}^{M-1} P_k e^{j2\pi h k q(LT)}$$

is a constant, independent of  $\tau$ . What is important is that the integrand in (4.15) is independent of the variable  $m$ , and depends only on  $\tau'$ . The conclusion is that when  $\tau \geq LT$ ,  $R()$  always has the form

$$R(\tau) = R(\tau' + mT) = C_\alpha^{m-L} \psi(\tau'), \quad m \geq L, \quad 0 \leq \tau' < T \quad (4.16)$$

i.e., it is separable in the arguments  $m$  and  $\tau'$ . The function  $\psi(\tau')$  is the integral in (4.15) and has only to be calculated over the interval  $0 \leq \tau' < T$ .  $R(\tau)$  then follows from successive multiplications by  $C_\alpha$ , and has therefore a *geometric decay* from symbol interval to symbol interval.

Now we return to the Fourier transform (4.14). It is seen from (4.15) that  $|C_\alpha| \leq 1$ , and to start with assume that  $|C_\alpha| < 1$ . The integral in (4.14) can be divided as

$$\int_0^\infty R(\tau) e^{-j2\pi f\tau} d\tau = \int_0^{LT} R(\tau) e^{-j2\pi f\tau} d\tau + \int_{LT}^\infty R(\tau) e^{-j2\pi f\tau} d\tau$$

where the last term can be written as

$$\int_{LT}^\infty R(\tau) e^{-j2\pi f\tau} d\tau = \sum_{m=L}^\infty \int_{mT}^{(m+1)T} C_\alpha^{m-L} \psi(\tau') e^{-j2\pi f(\tau'+mT)} d\tau$$

By putting  $m = L$  in equation (4.16) we find

$$\psi(\tau') = R(\tau' + LT), \quad 0 \leq \tau' < T$$

and thus

$$\begin{aligned} \int_{LT}^{\infty} R(\tau) e^{-j2\pi f\tau} d\tau &= e^{-j2\pi fLT} \int_0^T \\ &\times R(\tau' + LT) e^{-j2\pi f\tau'} d\tau' \sum_{m=0}^{\infty} C_{\alpha}^m e^{-j2\pi fmT} \end{aligned} \quad (4.17)$$

The sum in (4.17) is geometric and adds to

$$\sum_{m=0}^{\infty} C_{\alpha}^m e^{-j2\pi fmT} = \frac{1}{1 - C_{\alpha} e^{-j2\pi fT}} \quad (4.18)$$

This finally gives

$$\int_{LT}^{\infty} R(\tau) e^{-j2\pi f\tau} d\tau = \frac{e^{-j2\pi fLT}}{1 - C_{\alpha} e^{-j2\pi fT}} \int_0^T R(\tau + LT) e^{-j2\pi f\tau} d\tau \quad (4.19)$$

and so

$$\begin{aligned} S(f) &= 2 \operatorname{Re} \left\{ \int_0^{LT} R(\tau) e^{-j2\pi f\tau} d\tau \right. \\ &\quad \left. + \frac{e^{-j2\pi fLT}}{1 - C_{\alpha} e^{-j2\pi fT}} \int_0^T R(\tau + LT) e^{-j2\pi f\tau} d\tau \right\} \end{aligned} \quad (4.20)$$

It is seen that  $R(\tau)$  only has to be calculated over the interval  $[0, (L+1)T]$  and that the Fourier transform can be found numerically from equation (4.20). The autocorrelation function  $R(\tau)$  is most easily calculated by using equation (4.11). Thus equations (4.11), (4.15), and (4.20) are the only equations needed to find the PSD for a general CPM signal when  $|C_{\alpha}| < 1$ .

The decay constant  $C_{\alpha}$  is easy to interpret. So far it has been assumed that  $|C_{\alpha}| < 1$  which guarantees that the sum (4.18) converges for all values of  $f$ . If  $|C_{\alpha}| = 1$  one can put

$$C_{\alpha} = e^{j2\pi\beta}, \quad 0 \leq \beta < 1 \quad (4.21)$$

and from (4.16) it follows that for  $|\tau| \geq LT$ ,  $R(\tau)$  is periodic in  $\tau$  with period  $T$ . Extend the periodic part of  $R(\tau)$  to cover also the interval  $[-LT, LT]$  and call this part  $R_{\text{dis}}(\tau)$ ; one can write

$$R(\tau) = R_{\text{con}}(\tau) + R_{\text{dis}}(\tau) \quad (4.22)$$

Since the function  $R_{\text{dis}}(\tau)$  is periodic with period  $T$  it follows that its Fourier transform contains only impulses located at frequencies

$$f_{\text{dis}} = (\beta + k)1/T, \quad k = 0, \pm 1, 2, \dots$$

the magnitudes can be found from the Fourier transform coefficients of the Fourier series expansion for  $R_{\text{dis}}(\tau)$ . Thus  $R_{\text{dis}}(\tau)$  yields the discrete spectral components in the PSD. The function  $R_{\text{con}}(\tau)$  is identically zero outside the interval  $|\tau| \geq LT$  and yields the continuous part of the PSD. Thus the PSD for a general CPM signal can be easily found numerically, whether or not  $|C_\alpha| < 1$ , and when  $|C_\alpha| = 1$ , discrete spectral components occur in the power spectrum.

It is easy to check whether  $|C_\alpha| < 1$ . When  $q(LT) = 0$ ,  $C_\alpha = 1$ . Thus all CPM signals having a frequency pulse  $g(t)$  integrating to zero will have a PSD containing discrete spectral components. This is not a desirable property since part of the transmitted power is wasted in the discrete components, which carry no information.

Finally we note the very simple form of (4.20) for the case  $C_\alpha = 0$ ,

$$S(f) = 2 \operatorname{Re} \left\{ \int_0^{(L+1)T} R(\tau) e^{-j2\pi f\tau} d\tau \right\} \quad (4.23)$$

In the binary case this is obtained only when  $h = 1/2, 3/2, 5/2, \dots$  and  $P_{+1} = P_{-1} = 1/2$ . The pure QPSK modulation of Section 2.6 can be viewed as a pair of these modulations in quadrature, with  $h = 1/2$ .

#### 4.2.2. Numerical Results

This section contains examples of PSDs obtained by using the numerical method above. The method requires very little computational effort; it grows only linearly with the duration of the frequency pulse  $g(t)$ , whereas other methods require a computational effort growing exponentially or faster with this quantity. The speed of the method is a consequence of the exponential form of (4.16).

First, however, the general binary case ( $M = 2$ ) will be studied with regard to the appearance of discrete spectral components. It is sufficient to concentrate attention on  $C_\alpha$ , which is

$$C_\alpha = \cos[h\pi] + j(p_{+1} - p_{-1}) \sin[h\pi] \quad (4.24)$$

It is assumed that the frequency pulse  $g(t)$  does not integrate to zero. Viewed in the complex plane,  $C_\alpha$  forms an ellipse as  $h$  varies. When either  $p_{+1} = 1$  or  $p_{-1} = 1$  we have  $|C_\alpha| = 1$  and now

$$C_\alpha = \begin{cases} e^{jh\pi}, & p_{+1} = 1 \\ e^{-jh\pi}, & p_{-1} = 1 \end{cases}$$

Therefore discrete spectral components will occur at

$$f_{\text{dis}} = \begin{cases} \frac{h}{2T} + k \frac{1}{T} \\ -\frac{h}{2T} + k \frac{1}{T} \end{cases}, \quad k = 0, \pm 1, \pm 2, \dots \quad (4.25)$$

If  $p_{+1}$  or  $p_{-1}$  are not allowed to be equal to 1, the only way to have  $|C_\alpha| = 1$  is

$$C_\alpha = -1, \quad h \text{ odd integer}$$

$$C_\alpha = +1, \quad h \text{ even integer}$$

$$f_{\text{dis}} = \begin{cases} \pm \frac{1}{2T}, \pm \frac{3}{2T}, \pm \frac{5}{2T}, \dots, & h \text{ odd integer} \\ 0, \pm \frac{1}{T}, \pm \frac{2}{T}, \dots, & h \text{ even integer} \end{cases} \quad (4.26)$$

As will be seen in Chapter 9, the ability to produce discrete spectral components by considering integer valued modulation indices can be used for synchronization of a general CPM signal. However, it is possible that the magnitude of some (even all) of the discrete components may be equal to zero. This depends upon the specific shape of the frequency pulse  $g(t)$ .

Now we turn to a study of the continuous spectral component. In Figure 4.1  $R(\tau)$  is shown in the complex plane [ $R_s(\tau)$  plotted against  $R_c(\tau)$ ] for the quaternary scheme ( $M = 4$ ) 1SRC with  $h = 5/8$ . The *a priori* probabilities for the data symbols have been chosen as  $(p_{-3}, p_{-1}, p_{+1}, p_{+3}) = (0.05, 0.45, 0.05, 0.45)$ . The variable  $\tau$  varies along the trajectory shown in Figure 4.1, starting at  $(R_c(\tau), R_s(\tau)) = (1, 0)$  for  $\tau = 0$ . It can be seen that when  $\tau$  has increased somewhat, the form of the trajectory is regular and roughly repetitive, the amplitude becomes smaller and smaller, and rotation takes place. Equation (4.20) describes this mathematically since multiplication by a complex valued constant corresponds to a scaling and a phase shift. This occurs repeatedly as  $\tau$  is increased by  $T$ , when  $\tau \geq LT$ . (In Figure 4.1 the interval  $0 \leq \tau \leq 15T$  has been used.) Note that  $R(\tau)$  for  $\tau < 0$  is the mirror image of Figure 4.1 about the real axis.

Another illustration of (4.20) is shown in Figure 4.2. Here  $R_c(\tau)$  and  $R_s(\tau)$  are shown as functions of  $\tau$  for the binary scheme 1RC with modulation index  $h = 1/2$ . The *a priori* probabilities for data symbols are

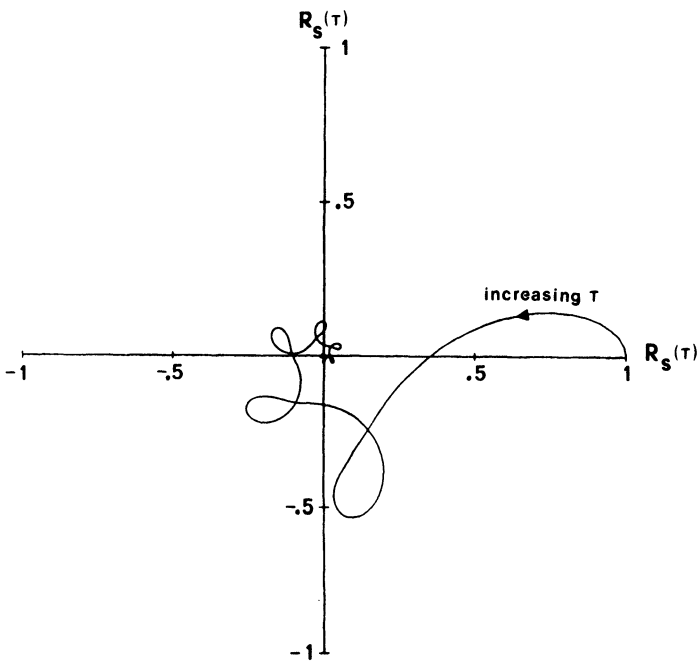


Figure 4.1. Plot of  $R(\tau)$  in the complex plane; the modulation is 1SRC,  $M = 4$  and  $h = 5/8$ .  $\tau$  varies along the curve. The PDF for the data symbols is  $(0.05, 0.45, 0.05, 0.45)$ .

$(p_{-1}, p_{+1}) = (1/4, 3/4)$  and this gives  $C_\alpha = j/2$ . The trajectory is traced over  $0 \leq \tau \leq 5T$ . This autocorrelation function is completely determined by its values over the interval  $0 \leq \tau \leq 2T$ .  $R_c(\tau)$  over the interval  $2T \leq \tau \leq 3T$  equals  $-R_s(\tau)/2$  over the interval  $T \leq \tau \leq 2T$ , and similarly  $R_s(\tau)$  over the interval  $2T \leq \tau \leq 3T$  equals  $R_c(\tau)/2$  over the interval  $R \leq \tau \leq 2T$ . This is because the complex valued constant  $C_\alpha$  is completely imaginary and of magnitude  $1/2$ . In Figure 4.3 the PSD is shown by the solid curve; for comparison the PSD for MSK [ $M = 2$ ,  $g(t) = 1\text{REC}$ ,  $h = 1/2$ ,  $p_{-1} = p_{+1}$ ] is shown by the broken curve. The MSK spectrum is symmetrical because the data are equiprobable, but its sidelobes decay more slowly because  $g(t)$  is less smooth.

Next schemes with longer  $g(t)$  pulses are considered. In the binary case three different *a priori* probabilities for the data symbols have been used:

$$(p_{-1}, p_{+1}) = \begin{cases} (1/2, 1/2) & \text{B1} \\ (1/4, 3/4) & \text{B2} \\ (1/10, 9/10) & \text{B3} \end{cases} \quad (4.27)$$

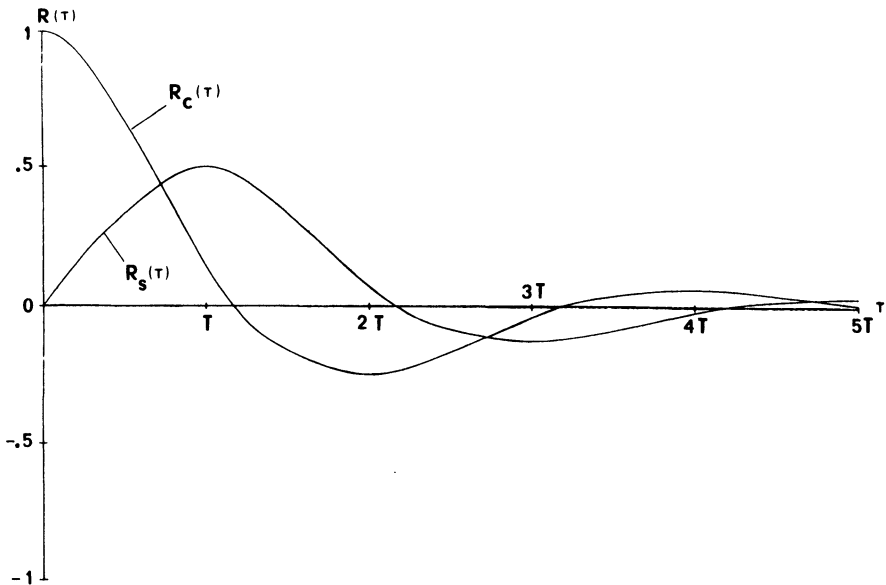


Figure 4.2. The autocorrelation function for 1RC,  $M = 2$ ,  $h = 1/2$ , when  $(p_{-1}, p_{+1}) = (1/4, 3/4)$ .

In the quaternary case also there are three cases:

$$(p_{-3}, p_{-1}, p_{+1}, p_{+3}) = \begin{cases} (1/4, 1/4, 1/4, 1/4) & Q1 \\ (1/10, 2/10, 3/10, 4/10) & Q2 \\ (5/100, 10/100, 15/100, 70/100) & Q3 \end{cases} \quad (4.28)$$

Note the notation B1, B2, B3 and Q1, Q2, Q3. The power spectrum will always be shown as a function of the dimensionless quantity  $fT_b$ , where  $T = T_b \log_2 M$ . The normalized PSD will integrate to unity in all cases since now  $R(0) = 1$ .

First the two binary schemes (4RC,  $h = 1/2$ ) and TFM are considered. In both cases the data symbols +1 and -1 will be equiprobable, which is case B1. The scheme TFM has a frequency pulse  $g(t)$  with a Fourier transform

$$G(f) = F\{g(t)\} = \frac{1}{2} \cos^2 \pi f T \frac{\pi f T}{\sin \pi f T} \quad (4.29)$$

No analytical expression has been found for  $g(t)$ ; instead, one can inverse-transform (4.29) numerically and truncate the pulse in time. As in Section 3.3.2, we have truncated here to  $7T$  to get a pulse with main lobe width

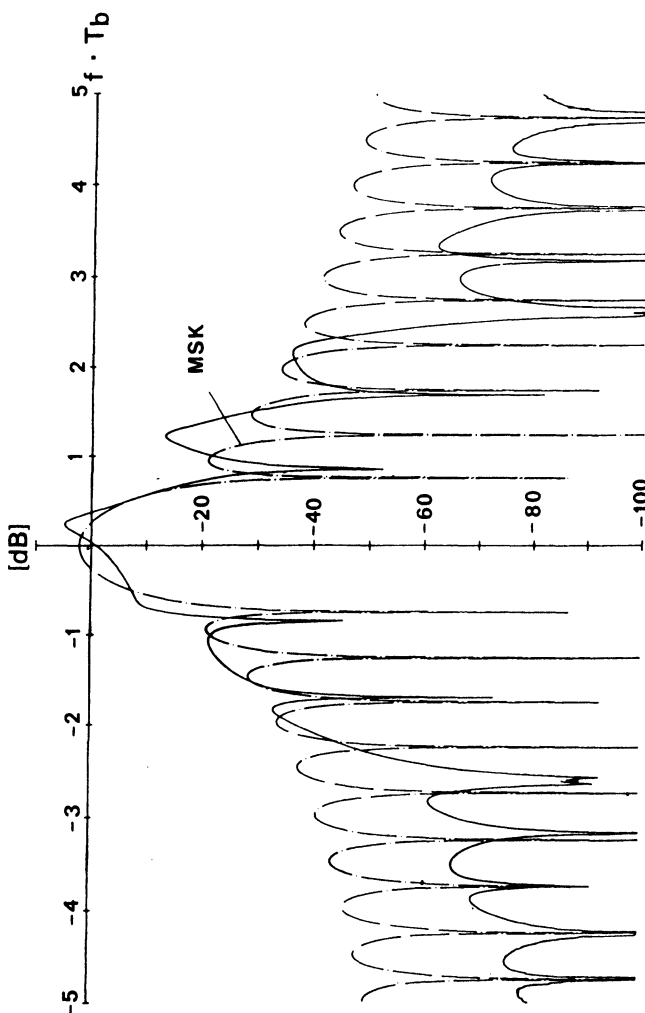


Figure 4.3. PSD for 1RC,  $M = 2$ ,  $h = 1/2$ , when  $(p_{-1}, p_{+1}) = (1/4, 3/4)$ .

$3.7T$  and with shape close to that in Table 2.1. The PSDs for the two modulations are compared in Figure 4.4. The fast autocorrelation method is used for the PSD of the TFM scheme, and it can be seen that the method loses accuracy at about  $-90$  dB. A more accurate (but more time consuming) method was used for the (4RC,  $h = 1/2$ ) spectrum; we shall take this method up again in Section 4.4.

The two spectra in the figure are almost identical down to  $-50$  dB. The TFM spectrum has a knee around  $-75$  dB which is due to the time-truncation of its  $g(t)$ ; the knee can be lowered by having a wider truncation than  $7T$ . Recall that it was found in Section 3.3.2 that the distance properties of TFM are very close to those of the RC family, if optimally detected.

As other examples of PSDs the schemes 6RC and 6SRC, both having  $M = 2$  and  $h = 1/4$ , are considered. The frequency pulse  $g(t)$  for 6SRC has been truncated to  $16T$ , symmetrically around the mainlobe. Figure 4.5 shows the PSD for the 6RC scheme and Figure 4.6 for the 6SRC scheme; in both figures the prior probabilities for the data symbols are  $B_1$ ,  $B_2$ , and  $B_3$ . As the data symbol  $+1$  becomes more probable a peak starts to develop at the frequency  $f = h/2T_b$ . This is consistent with (4.25), but it can also be justified by the fact that a constant frequency (linear phase) is transmitted for all RC schemes except 1RC for constant data. This is also true for SRC schemes having pulses  $g(t)$  without truncation and is approximately true otherwise.

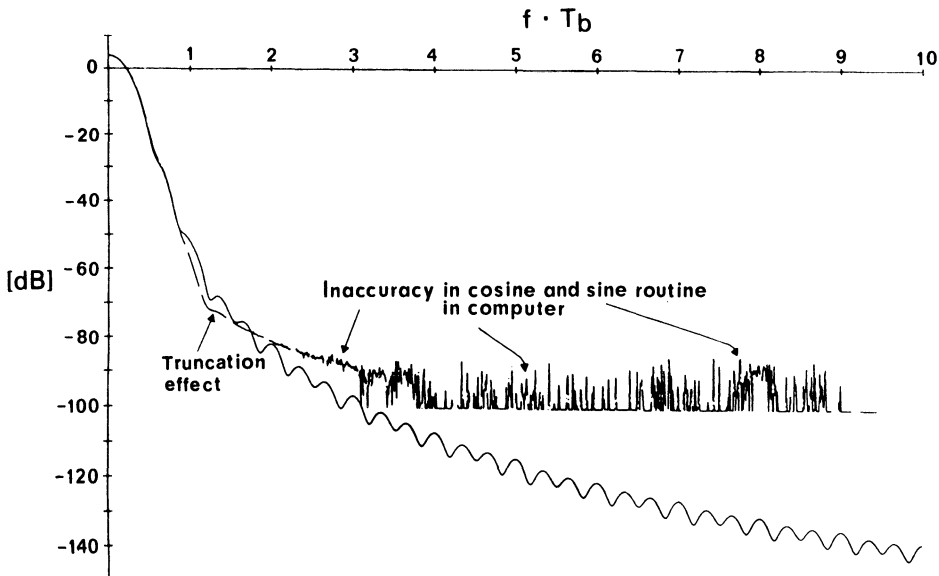


Figure 4.4. PSDs for binary 4RC with  $h = 1/2$  (solid) and TFM (dash-dotted) with  $g(t)$  truncated to  $7T$ ; equiprobable data symbols.

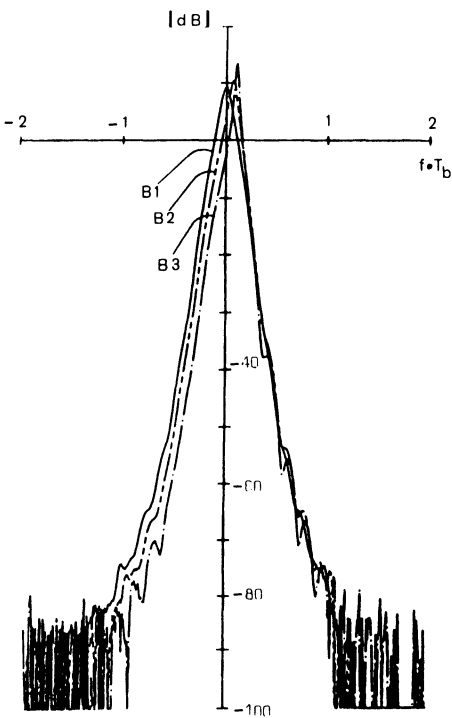


Figure 4.5. PSDs for 6RC,  $M = 2$ ,  $h = 1/4$ ; several symbol distributions.

The PSDs in Figures 4.5 and 4.6 are very similar, and are practically identical down to  $-50$  dB. Using the frequency pulse 6SRC instead of 6RC, however, the small sidelobes below  $-50$  dB in the 6RC scheme disappear. This phenomenon has been observed for other combinations of RC and SRC schemes, irrespective of the modulation index  $h$ .

Figures 4.7 and 4.8 are for the same conditions as Figures 4.5 and 4.6 except that the modulation index  $h$  has been changed from  $1/4$  to  $1/2$ . This widens the PSDs, but the conclusions made concerning Figures 4.5 and 4.6 still apply.

Two quaternary schemes will be considered. The frequency pulses are 3RC and 3SRC, both with  $h = 1/4$ , in Figures 4.9 and 4.10. The truncation length for the 3SRC pulse is  $13T$  symmetrically. This correspond to 26-bit intervals. Just as in the binary case, the small sidelobes for the 3RC scheme disappear for the 3SRC scheme. This result has been observed in all other quaternary schemes, and also in cases with even larger  $M$ .

Finally, we consider the *fractional out of band power*. This is given by

$$P_{\text{ob}}(B) = \frac{\int_{-\infty}^{\infty} S(f) df - \int_{-B}^{B} S(f) df}{\int_{-\infty}^{\infty} S(f) df} = 1 - \int_{-B}^{B} S(f) df \quad (4.30)$$

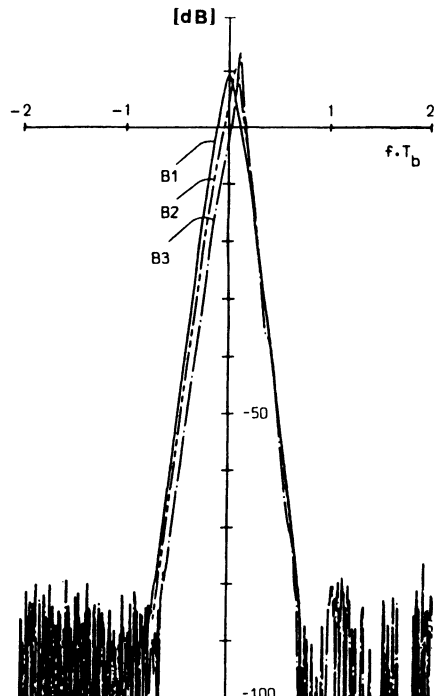


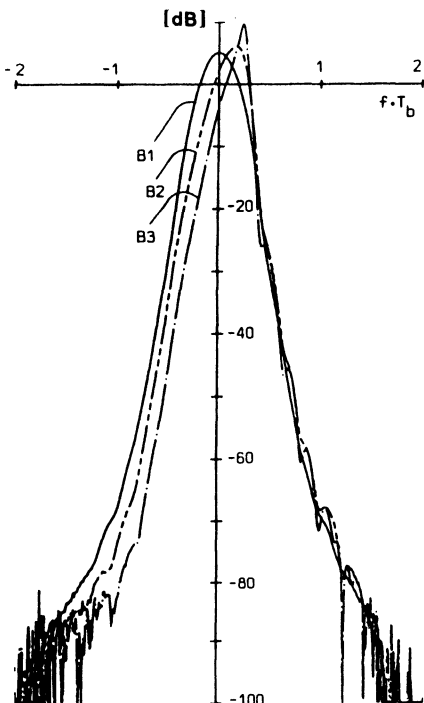
Figure 4.6. PSDs for 6SRC,  $M = 2$ ,  $h = 1/4$ .

since all the PSDs are normalized to integrate to unity. The function  $P_{ob}(B)$  shows the fraction of the power falling outside the band  $-BT \leq fT \leq BT$ , with  $B$  treated as a variable. It is common practice to plot  $P_{ob}(B)$  in a decibel scale, where for instance  $-20$  dB corresponds to 1%. Figure 4.11 shows such a plot for the binary scheme 6SRC with  $h = 1/4, 1/2, 3/4$ , with MSK shown as a reference. In all cases the data symbols  $+1$  and  $-1$  are equiprobable. The results shown in Figure 4.11 were obtained by numerical integration of the respective PSDs; in all cases the autocorrelation function method was used to obtain these PSDs. The curve for MSK is always above the others and the curves for 6SRC are very steep.

#### 4.2.3. Generalizations

There are two obvious generalizations to the model for the CPM signal which can be made, the use of multi- $h$  schemes and the case of correlated data symbols. A combination of these two cases is also possible.

In multi- $h$  schemes  $H$  different modulation indices  $h_1, h_2, \dots, h_H$  are used in a cyclical manner from symbol interval to symbol interval, as developed in Chapter 3. It is possible to use the autocorrelation function

Figure 4.7. PSDs for 6RC,  $M = 2$ ,  $h = 1/2$ .

method also for this case, and the derivation of the relevant expressions follows closely the one given in Section 4.2.1. Only an outline will be given now. The introduction of  $H$  different modulation indices does not change the cyclostationary property of the process  $s(t, \alpha)$ , but it does change the period of the cycle from  $T$  to  $HT$ . Therefore by changing the meaning of the time-averaging operator  $\langle \cdot \rangle$  from an average over the interval  $[0, T]$  to an average over the interval  $[0, HT]$  in the derivation for the autocorrelation, the correct result will be found. Now the autocorrelation function is completely determined by its values over the interval  $0 \leq \tau \leq (L + H)T$ . Next, we write  $\tau = \tau' + mHT$ , where  $0 \leq \tau' < HT$  and  $m = 0, 1, 2, \dots$ . The autocorrelation function will still decay geometrically, but now over blocks of  $H$  intervals. This means that if  $R(\tau)$  is known over the interval  $[LT, (L + H)T]$ ,  $R(\tau)$  over the interval  $[(L + H)T, (L + 2HT)]$  is found from multiplication by a complex-valued constant  $C_\alpha$ . The expression for  $C_\alpha$  will differ from (4.15) and will now be a function of  $h_1, h_2, \dots, h_H$ . Just as for  $H = 1$ ,  $|C_\alpha| = 1$  will imply discrete spectral components.

The case with correlated data symbols (but  $H = 1$ ) is treated in Ref. 20. Here the correlation is introduced by using a finite-state sequential

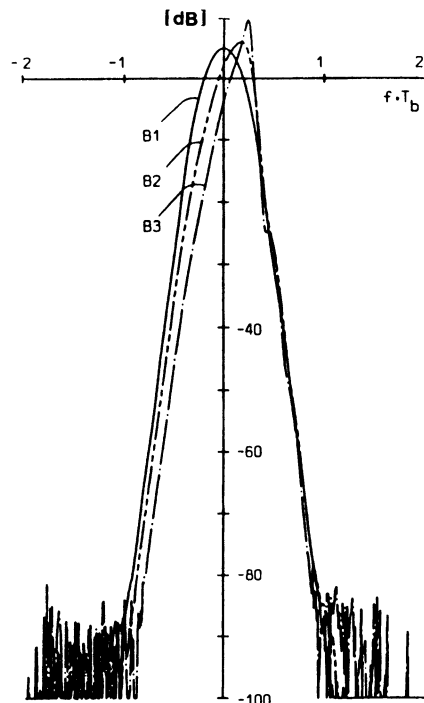
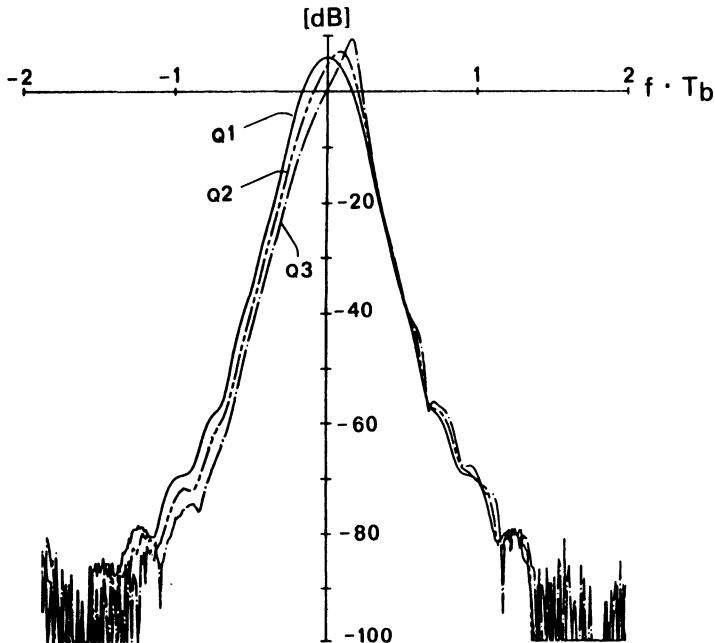


Figure 4.8. PSDs for 6SRC,  $M = 2$ ,  $h = 1/2$ .

machine whose input is a sequence of mutually independent symbols and whose output is a function of the state of the machine and the current input symbol. This generalization adds a lot to the difficulty of deriving the expressions for  $R(\tau)$  and  $S(f)$ ; the computer time required increases and memory requirements grow with the square of the number of states in the sequential machine. In Pierobon *et al.*<sup>(20)</sup> a PSD is calculated for a binary scheme with a frequency pulse of duration 20-bit intervals and a sequential machine with two states. What sets the practical limit is probably the number of these states, which must be kept very low since large matrices must be inverted. If the sequential machine is removed, the method in Ref. 20 is the same as the autocorrelation function method presented in Section 4.2.1.

#### 4.2.4. Summary of the Autocorrelation Function Method

It is convenient to have the equations for this method gathered in one place. This section will serve that purpose. Only the case  $|C_\alpha| < 1$  (no discrete spectral components) which is of most practical interest, will be considered.

Figure 4.9. PSDs for 3RC,  $M = 4$ ,  $h = 1/4$ .

## (1) Calculate the autocorrelation function

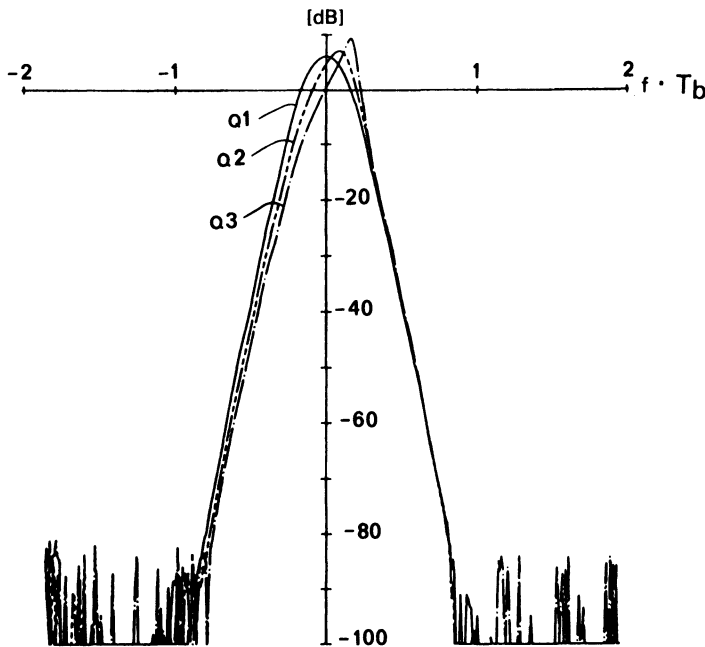
$$R(\tau) = R(\tau' + mT)$$

$$\begin{aligned}
 &= \frac{1}{T} \int_0^T \prod_{i=1-L}^{m+1} \left\{ \sum_{\substack{k=-M-1 \\ k \text{ odd}}}^{M-1} P_k \exp(j2\pi hk[q(t+\tau'-(i-m)T) \right. \\
 &\quad \left. - q(t-iT)]) \right\} \quad (4.31)
 \end{aligned}$$

over the interval  $[0, (L+1)T]$ . The time difference  $\tau$  has been written as  $\tau = \tau' + mT$  with  $0 \leq \tau' < 1$  and  $m = 0, 1, 2, \dots$

## (2) Calculate

$$C_\alpha = \sum_{k=-M-1}^{M-1} P_k e^{j\hbar\pi k} \quad (4.32)$$

Figure 4.10. PSDs for 3SRC,  $M = 4$ ,  $h = 1/4$ .

(3) The PSD is

$$S(f) = 2 \operatorname{Re} \left\{ \int_0^{LT} R(\tau) e^{-j2\pi f\tau} d\tau + \frac{e^{-j2\pi fLT}}{1 - C_\alpha e^{-j2\pi fT}} \int_0^T R(\tau + LT) e^{-j2\pi f\tau} d\tau \right\} \quad (4.33)$$

Note that all quantities are real valued when  $P_k = 1/M$ ,  $k = \pm 1, \pm 3, \dots, \pm(M-1)$ . We have in this case

$$R(\tau) = \frac{1}{T} \int_0^T \prod_{i=1-L}^{[\tau/T]} \frac{1}{M} \frac{\sin 2\pi hM[q(t+\tau-iT) - q(t-iT)]}{\sin 2\pi h[q(t+\tau-iT) - q(t-iT)]} dt \quad (4.34)$$

and

$$S(f) = 2 \left[ \int_0^{LT} R(\tau) \cos 2\pi f\tau d\tau + \frac{1 - C_\alpha \cos 2\pi fT}{1 + C_\alpha^2 - 2C_\alpha \cos 2\pi fT} \int_{LT}^{(L+1)T} R(\tau) \cos 2\pi f\tau d\tau \right] \quad (4.35)$$

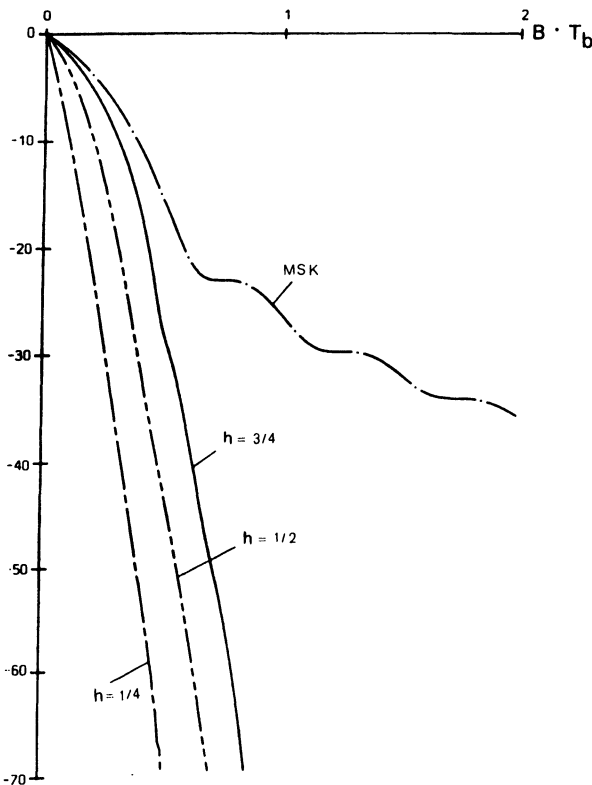


Figure 4.11. Fractional out of band power (in decibels) for 6SRC,  $M = 2$  with equiprobable symbol distribution;  $h = 1/4, 1/2$ , and  $3/4$  are shown with comparison to MSK.

where

$$C_\alpha = \frac{1}{M} \frac{\sin M\pi h}{\sin \pi h} \quad (4.36)$$

### 4.3. Closed Form Expressions for Some Simple Schemes

We will now collect in one place the few simple spectral formulas that are now known. The PSDs of most sophisticated modulations do not have a closed form. In some cases very complicated formulas are known, but we refer to the references for these. Fortunately, the commonly used simple modulations do have simple formulas.

In the expressions that follow, the frequency variable is normalized to the data bit rate, that is, true frequency is scaled by  $T_b$  and given the symbol

$f$ , a quantity with dimensions Hz/bit/s. Recall that the symbol time  $T$  is related to the data bit time  $T_b$  by  $T = \log_2 M T_b$ . The data symbols are equiprobable. The energy per data bit  $E_b$  is unity.

#### *M-ary PSK (pure)*

$$S(f) = \frac{T}{T_b} \frac{\sin^2(\pi f(T/T_b))}{[\pi f(T/T_b)]^2} \quad (4.37)$$

A simple derivation of this in terms of orthogonal pulses was given in Section 2.6 for BPSK and QPSK; the general formula follows from the analysis of Section 4.2.1. Spectral nulls occur when  $f$  is a multiple of  $1/\log_2 M$ .

#### *QPSK (Nyquist)*

$$S(f) = H^2(f) \quad (4.38)$$

Here  $H()$  is the Nyquist pulse shaping function of Section 2.6, an example of which is the raised-cosine pulse of (2.31), with  $f$  normalized as specified above. The antisymmetry point (see Figure 2.19) appears at normalized frequency 1/4.

#### *MSK*

$$S(f) = \frac{16}{\pi^2} \left( \frac{\cos 2\pi f}{1 - 16f^2} \right)^2 \quad (4.39)$$

The first spectral null occurs at  $f = 0.75$ ; thereafter nulls occur at  $0.75 + 0.5n$ .

#### *M-ary 1REC*

$$S(f) = \frac{T}{T_b} \frac{2}{M} \sum_{i=1}^M \left( \frac{1}{2} \frac{\sin^2 \gamma_i}{\gamma_i^2} + \frac{1}{M} \sum_{j=1}^M \frac{A_{ij} \sin \gamma_i \sin \gamma_j}{\gamma_i \gamma_j} \right) \quad (4.40)$$

where

$$\begin{aligned} \gamma_i &= \left[ f \frac{T}{T_b} - (2i - M - 1) \frac{h}{2} \right] \pi \\ A_{ij} &= \frac{\cos(\gamma_i + \gamma_j) - C_\alpha \cos(\gamma_i + \gamma_j - 2\pi f(T/T_b))}{1 - 2C_\alpha \cos(2\pi f(T/T_b)) + C_\alpha^2} \\ C_\alpha &= \frac{1}{M} \frac{\sin M\pi h}{\sin \pi h} \end{aligned}$$

#### 4.4. Asymptotic and Related Behavior of Spectra

It is often of interest to know the behavior of a spectrum in its far side lobes. This information is needed to assess the adjacent channel interference caused by a modulation. Asymptotic estimates also help us to measure the error in a numerical computation method; typically, methods like that of Section 4.2 begin to show error when the spectra that they calculate become very small.

A general property of PSDs for frequencies far from the center frequency was verified by Baker.<sup>(9)</sup> If the frequency pulse  $g(t)$  has  $c$  continuous derivatives [or if  $q(t)$  has  $c + 1$ ], then the PSD decreases asymptotically as

$$S(f) \sim |f|^{-(2c+6)} \quad (4.41)$$

This occurs for any length pulse, and for any  $h$  or  $M$ . Thus it is possible in principle to design a phase modulation scheme with any desired rate of decay in the PSD, merely by shaping the pulse  $g(t)$ . However, the decay may occur very far from the center frequency. If the pulse length  $L$  is kept fixed, experience shows that a large  $c$  will also yield a large main lobe and first side lobe. Generally speaking, increasing  $c$  is not the best way to achieve a bandwidth efficient modulation.

A more elegant proof of Baker's result appears in Ref. 23. The method of proof is by successive integration by parts of the PSD formula, to produce an infinite series. A term similar to (4.41) dominates this series at large  $f$ .

It follows that the PSD for all PSK-type schemes behaves like  $|f|^{-2}$ , for all REC schemes like  $|f|^{-4}$ , and for all RC schemes like  $|f|^{-8}$ , asymptotically. Note especially that for SRC schemes the PSD decreases faster than any power of  $f$ , asymptotically, if the frequency pulse is not truncated. A good way to truncate SRC pulses is to cut them at the zero-crossings. Then the PSD will decrease like  $f^{-6}$  for frequencies far away from the carrier. By using long enough frequency pulses, the knee in the PSD due to the truncation can be moved down to start at  $-100$  dB or so, a level which in practice can be ignored.

Sometimes it is of interest to calculate the PSD down to such a low level that the fast autocorrelation method Section 4.2 gives noisy results. The asymptotic argument that leads to (4.41) can be expanded and improved to achieve virtually exact results for these tail frequencies. Such a method is described in Ref. 23, and only a summary will be given now.

Define

$$I(f, \alpha_{L+k}) = \int_0^1 \exp \left\{ j2\pi h \sum_{i=1}^L \alpha_{i+k} q[(\tau - i + L)T] \right\} e^{-j2\pi f\tau} d\tau \quad (4.42)$$

where the components of the vector

$$\boldsymbol{\alpha}_{L+k} = (\alpha_{k+1}, \alpha_{k+2}, \dots, \alpha_{k+L})$$

are the  $M$ -ary statistically independent and identically distributed data symbols. It has been shown by Baker<sup>(9)</sup> that the PSD is

$$\begin{aligned} \frac{2}{T} S(f) &= \mathcal{E}\{|I(f, \boldsymbol{\alpha}_L)|^2\} \\ &+ 2 \operatorname{Re} \left\{ \sum_{K=1}^{L-1} e^{-j2\pi kf} \mathcal{E} \left\{ I(f, \boldsymbol{\alpha}_{L+k}) I^*(f, \boldsymbol{\alpha}_L) \right. \right. \\ &\quad \times \exp \left[ j2\pi h \sum_{m=1}^k \alpha_m q(LT) \right] \left. \right\} \\ &+ 2 \operatorname{Re} \left\{ \frac{e^{-j2\pi fL}}{1 - C_\alpha e^{-j2\pi f}} \mathcal{E}\{I(f, \boldsymbol{\alpha}_L)\} \right. \\ &\quad \times \mathcal{E} \left\{ I^*(f, \boldsymbol{\alpha}_L) \exp \left[ j2\pi h \sum_{m=1}^L \alpha_m q(LT) \right] \right\} \quad (4.43) \end{aligned}$$

in the nonsingular case (i.e., no discrete frequency components). Here the expectation  $\mathcal{E}\{\cdot\}$  is over the sequence of data symbols and represents a countable sum. The PSD integrates to unity and the frequency is normalized with the symbol rate  $1/T$ .

It is of importance that the integral  $I(\cdot, \cdot)$  be calculated very accurately using numerical integration (e.g., Simpson's formula). By using the  $p$ th derivative of  $I(\cdot, \cdot)$ , premultiplied by  $(2\pi f)^{2p}$ , i.e.,

$$\begin{aligned} I_p(f, \boldsymbol{\alpha}_{L+k}) &= \left( \frac{-j}{2\pi f} \right)^p \int_0^1 \\ &\quad \times e^{-j2\pi f\tau} \frac{d^{(p)}}{d\tau^{(p)}} \left\{ e^{j2\pi h} \sum_{i=1}^L \alpha_{i+k} q[(\tau - i + L)T] \right\} d\tau \quad (4.44) \end{aligned}$$

instead of  $I(\cdot, \cdot)$  in (4.43), it is shown in Ref. 23 that the resulting spectrum will be the same after averaging with respect to the sequence of data symbols. The derivative in (4.44) can be calculated by using the relation

$$\frac{d^{(p)} e^{\phi(t)}}{dt^{(p)}} = \sum_{k=1}^p \binom{p-1}{k-1} \phi^{(k)}(t) \frac{d^{(p-k)} e^{\phi(t)}}{dt^{(p-k)}}$$

What is important in (4.44) is the factor in front of the integral. By choosing a value for  $p$  such that the asymptotic behavior is met, the integral does not have to be calculated very accurately. For  $f$  values close to zero,  $p = 0$  can be chosen, and in this case the method coincides with the direct method given by Anderson and Salz,<sup>(5)</sup> except for the averaging with respect to the data. For larger  $f$ , a larger value of  $p$  should be chosen, and it has been observed that accurate results are obtained for  $f > 1/2$  if  $p$  is chosen as  $p = c + 2$ , where  $c$  is the number of continuous derivatives of the frequency pulse  $g(t)$ . To make the numerical integration easy for large  $f$ , an integration by parts can be made, yielding

$$\begin{aligned} I_p(f, \alpha_{L+k}) = & -\left(-\frac{j}{2\pi f}\right)^{p+1} \\ & \times \left[ e^{-j2\pi fz} \frac{d^{(p)}}{dz^{(p)}} \left( \exp \left\{ j2\pi h \sum_{i=1}^L \alpha_{i+k} q[(z-i+L)T] \right\} \right) \right]_{z=0+}^{1-} \\ & + \left(-\frac{j}{2\pi f}\right)^{p+1} \int_0^1 e^{-j2\pi f\tau} \frac{d^{(p+1)}}{d\tau^{(p+1)}} \\ & \times \left( \exp \left\{ j2\pi h \sum_{i=1}^L \alpha_{i+k} q[(\tau-i+L)T] \right\} \right) d\tau \end{aligned} \quad (4.45)$$

When the asymptotic behavior of the PSD has been established, the power spectrum can be written<sup>(23)</sup>

$$S(f) = \frac{\Psi(f)}{(2\pi f)^{2c+6}} \quad (4.46)$$

where  $\Psi(f)$  is a periodic function with some period  $f_p$ . Thus

$$\Psi(f_0) = \Psi(f_0 + kf_p), \quad k = 0, 1, 2, \dots$$

where  $f_0$  is sufficiently large. Hence,

$$\begin{aligned} S(f_0) &= \frac{\Psi(f_0)}{(2\pi f_0)^{2c+6}} \\ S(f_0 + kf_p) &= \frac{\Psi(f_0 + kf_p)}{[2\pi(f_0 + kf_p)]^{2c+6}} = \frac{\Psi(f_0)}{[2\pi(f_0 + kf_p)]^{2c+6}}, \quad k = 0, 1, 2, \dots \end{aligned}$$

and elimination of  $\Psi(f_0)$  yields

$$S(f_0 + kf_p) = \left( \frac{f_0}{f_0 + kf_p} \right)^{2c+6} S(f_0), \quad k = 0, 1, 2, \dots \quad (4.47)$$

or in dB

$$10 \log_{10} S(f_0 + kf_p) = 10 \log_{10} S(f_0) - 10(2c + 6) \log_{10} (k + f_0/f_p); \\ k = 0, 1, 2, \dots$$

This relation can be used to extend a PSD over a larger frequency interval, once the asymptotic behavior has been established. The asymptotic behavior can be checked against the part of the spectrum already calculated by numerical integration by testing if (4.47) holds.

Some numerical results obtained by using this method will now be given. The PSDs are, as before, normalized to integrate to unity and the frequency is normalized with the data bit rate  $1/T_b$ . In all cases the raised cosine class of frequency pulses has been used, and it has also been assumed that the distribution of the data symbols (or sequences) is uniform.

Figure 4.12 shows the power spectra for the binary schemes 1RC, 2RC, 3RC, 4RC, and 5RC when  $h = 1/2$ . The 1RC case coincides with SFSK

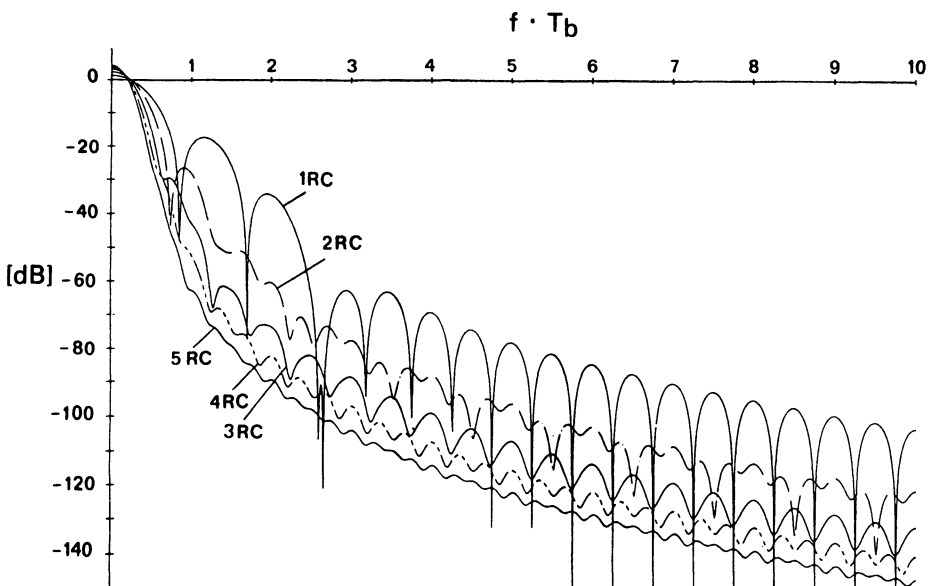


Figure 4.12. Power spectra for binary RC schemes when  $h = 1/2$ , showing 1RC through 5RC with equiprobable data.

and its maximum instantaneous frequency is separated from the carrier by  $1/2T_b$ . For the partial response schemes this maximum is only half as big. This is clearly reflected in Figure 4.12, where it can be seen that the first two side lobes are quite large for the 1RC case; for  $L = 2$  these sidelobes have dropped considerably.

The PSDs for the binary schemes 4RC with modulation index  $h = 0.3$ , 0.5, and 0.8 are shown in Figure 4.13. The sidelobes can hardly be distinguished, and the mainlobe is narrow. The power in the signal is to a large extent confined to the frequency interval  $[0, 0.2]$  when  $h \leq 1/2$ . Note that when  $h = 0.3$  and 0.8 there is little evidence of the spectral peaking that occurs when  $h$  nears 0 or 1.

In Figure 4.14 are the PSDs for QPSK, MSK and also for the quaternary ( $M = 4$ ) scheme 3RC with  $h = 0.3$ . This choice of spectra is motivated by the fact that the error performance in AWGN is almost the same. Note that the mainlobe of the partial response scheme is narrower than that for QPSK when  $fT_b \leq 0.5$  and larger (by a small amount) only in an extremely small interval around  $fT_b = 0.5$ .

A general conclusion from these plots is that increasing the size of the signalling alphabet  $M$  or the pulse duration  $L$  leads to a more compact spectrum with side lobes that fall off more smoothly.

The price that has to be paid is quite high for PSDs with high accuracy in the spectral tails. A complex-valued integral must be solved numerically

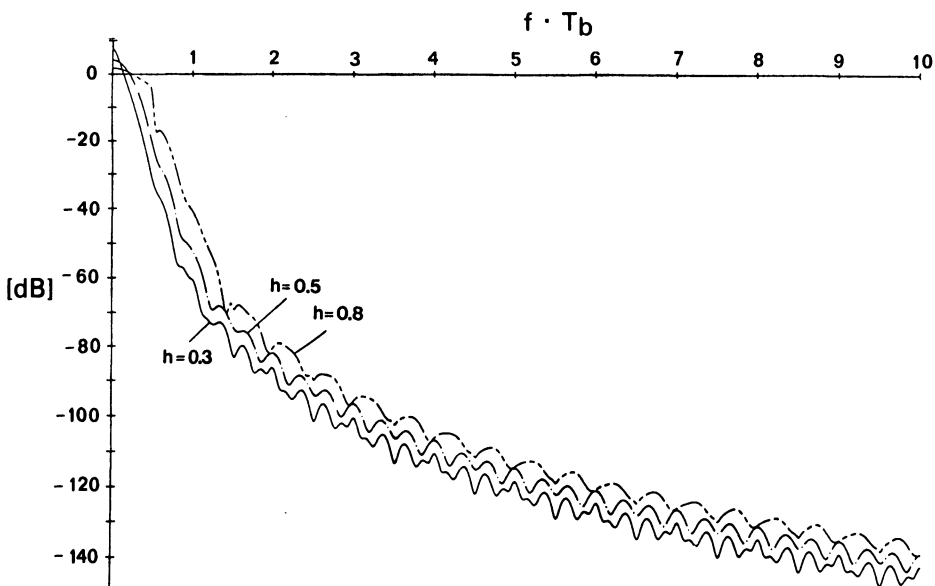


Figure 4.13. Power spectra for binary 4RC schemes with  $h = 0.3, 0.5$ , and 0.8.

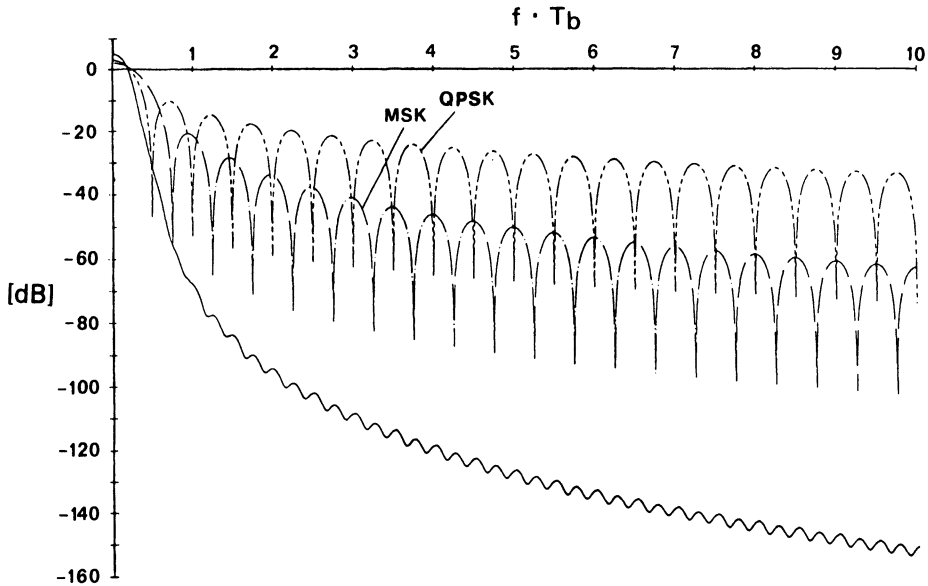


Figure 4.14. Power spectra for quaternary 3RC with  $h = 0.3$ , QPSK, and MSK.

$M^{2L}$  times. This is because the averaging with respect to the data has not been done analytically, but rather must be done in an enumerative fashion.

*Numerical Accuracy of the Fast Autocorrelation Method.* It can be seen in Figure 4.4 that the PSD calculation for the TFM scheme becomes erratic below  $-80$  or  $-90$  dB. Comparison to accurate calculations made using the method of this section shows that the TFM spectrum is indeed inaccurate in this region. This occurs because of computer word length constraints; investigation has shown that the principal villain is often the sine/cosine routines, which are generally limited in accuracy to 10 decimal digits. By using double precision sines and cosines and double precision arithmetic, another 10–20 dB extension can be gained in the PSD accuracy, but there are few situations where this small extension is worth the much longer computation time.

#### 4.5. Effects of Filtering and Amplitude Limitation

By bandpass filtering of a constant envelope signal it is possible to improve the spectral characteristics at the expense of producing a time-varying envelope. Through hard amplitude limitation the envelope can be made constant again, but now at the expense of a changed PSD. The minimum Euclidean distance aspects of such operations were studied in Chapter 3; here the spectral properties are analyzed.

The same notation will be used as in Chapter 3. Thus the constant envelope modulated signal is

$$s(t, \alpha) = (2P)^{1/2} \operatorname{Re} \{ \tilde{s}(t, \alpha) e^{j2\pi f_0 t} \} \quad (3.77')$$

$$\tilde{s}(t, \alpha) = e^{j\phi(t, \alpha)} \quad (3.76')$$

The bandpass filter has the impulse response

$$a(t) = 2 \operatorname{Re} \{ \tilde{a}(t) e^{j2\pi f_0 t} \}$$

$$\tilde{a}(t) = a_c(t) + j a_s(t)$$

and the filtered CPM signal is

$$s_0(t, \alpha) = (2P)^{1/2} \operatorname{Re} \{ \tilde{s}_0(t, \alpha) e^{j2\pi f_0 t} \} \quad (4.48)$$

$$\tilde{s}_0(t, \alpha) = I_a(t, \alpha) + j Q_a(t, \alpha)$$

It is well known from standard textbooks that the filtering operation is described by a complex convolution of the complex envelopes of the input signal and the bandpass filter, i.e.,

$$\tilde{s}_0(t, \alpha) = \tilde{s}(t, \alpha) * \tilde{a}(t)$$

Once the PSD  $S(f)$  for the nonfiltered CPM signal has been calculated, it is easy to find the PSD  $S_0(f)$  for the filtered signal by the usual formula

$$S_0(f) = S(f) |\tilde{A}(f)|^2$$

where  $\tilde{A}(f)$  is the Fourier transform of  $\tilde{a}(t)$ . The amplitude of the filter  $a(t)$  is preferably scaled such that  $S_0(f)$  integrates to unity, just as  $S(f)$  does. This will give a fair comparison between  $S(f)$  and  $S_0(f)$  and guarantees that the signal  $s_0(t, \alpha)$  has the same average power  $P$  as the constant-power signal  $s(t, \alpha)$ .

We concentrate now on finding a method for calculation of  $S_1(f)$ , the PSD of the hard amplitude limited signal  $s_1(t, \alpha)$ . This is also a bandpass signal and the hard limiting operation is described through

$$s_1(t, \alpha) = (2P)^{1/2} \operatorname{Re} \{ \tilde{s}_1(t, \alpha) e^{j2\pi f_0 t} \} \quad (4.49)$$

$$\tilde{s}_1(t, \alpha) = \frac{\tilde{s}_0(t, \alpha)}{|\tilde{s}_0(t, \alpha)|}$$

just as in Chapter 3. Only systems having the property that  $|\tilde{s}_0(t, \alpha)| \neq 0$  for all  $t$  and  $\alpha$  are allowed.

$S_1(f)$  is calculated by using the autocorrelation function method just as in Section 4.2. Thus we have

$$r_1(\tau) = \langle \mathcal{E}\{s_1(t + \tau, \alpha) s_1(t, \alpha)\} \rangle$$

where the operators  $\mathcal{E}\{\cdot\}$  and  $\langle \cdot \rangle$  are the same as in Section 4.2. By using the narrow-band property of the rf signal  $s_1(t, \alpha)$  we have

$$\begin{aligned} r_1(\tau) &= P \operatorname{Re} \{ R_1(\tau) e^{j2\pi f_0 \tau} \} \\ R_1(\tau) &= \langle \mathcal{E}\{\tilde{s}_1(t + \tau, \alpha)\tilde{s}_1^*(t, \alpha)\} \rangle \end{aligned} \quad (4.50)$$

and now  $S_1(f)$  is the Fourier transform of  $R_1(\tau)$ . It is assumed that the impulse response  $a(t)$  is of finite duration  $L_a$  symbol intervals. The reason for this will be made clear below. Without loss of generality it is also assumed that the bandpass filter is causal. Straightforward insertion of relevant quantities into (4.50) gives

$$\begin{aligned} R_1(\tau) &= \left\langle \mathcal{E} \left\{ \frac{\int_0^{L_a T} \tilde{a}(\theta) \exp[j\phi(t + \tau - \theta, \alpha)] d\theta}{|\int_0^{L_a T} \tilde{a}(\theta) \exp[j\phi(t + \tau - \theta, \alpha)] d\theta|} \right\} \right. \\ &\quad \times \left. \frac{\int_0^{L_a T} \tilde{a}^*(\theta) \exp[-j\phi(t - \theta, \alpha)] d\theta}{|\int_0^{L_a T} \tilde{a}(\theta) \exp[j\phi(t - \theta, \alpha)] d\theta|} \right\rangle \end{aligned} \quad (4.51)$$

By inserting the expression for the information carrying phase  $\phi(t, \alpha)$  and writing  $\tau = \tau' + mT \geq 0$ ;  $0 \leq \tau' < T$ ,  $m = 0, 1, 2, \dots$ , it is found that the expectation with respect to the sequence  $\alpha$  only has to be performed with respect to the sequence

$$\alpha_m = (\alpha_{1-L-L_a}, \dots, \alpha_m, \alpha_{m+1})$$

which is of finite length when  $\tau < \infty$ . This guarantees that the operation  $\mathcal{E}\{\cdot\}$  can be performed numerically without any truncation errors. This is why  $L_a$  is assumed to be finite.

The autocorrelation function  $R_1(\tau)$  has almost identical properties to these of the autocorrelation function  $R(\tau)$  treated in Section 4.2. It can easily be shown that

$$\begin{aligned} R_1(\tau) &= R_1(\tau' + mT) = C_\alpha^{m-L-L_a} \Psi_1(\tau'), \\ m &\geq L + L_a, \quad 0 \leq \tau' < T \end{aligned} \quad (4.52)$$

i.e., when  $\tau \geq (L + L_a)T$ . This can be compared to the expression (4.16) for  $R(\tau)$  when  $\tau \geq LT$ . Thus the procedure for calculating  $S_1(f)$  from  $R_1(\tau)$  parallels the derivation in Section 4.2 for calculating  $S(f)$  from  $R(\tau)$ . The quantity  $C_\alpha$  in equation (4.52) is the same as in (4.15). The summary in Section 4.2.4 applies also to this case except that  $R_1(\tau)$  should be calculated over the interval  $[0, (L + L_a + 1)T]$  using equation (4.51). Then  $S_1(f)$  is found from  $R_1(\tau)$  in the same way except that  $L$  is to be substituted for  $L + L_a$ .

It takes much more time to calculate  $R_1(\tau)$  than  $R(\tau)$ . The reason for this is that we now have extra integration (with respect to  $\theta$ ) but also that

the averaging with respect to the sequence  $\alpha_m$  takes much longer to enumerate. There are  $M^{(L+L_a+1+m)}$  such sequences, and this puts a practical limit on the schemes which can be considered.

The autocorrelation function  $R_1(\tau)$  is in general complex valued but is real if the data symbols are uniformly distributed and the impulse response  $\tilde{a}(t)$  is real [so  $A(f)$  is symmetric with respect to  $f = 0$ ]. In this important case  $S_1(f)$  has only to be calculated for nonnegative  $f$ , due to symmetry. This special case is treated in some numerical examples below. It has furthermore been assumed that  $M = 2$  and  $h = 1/2$ . In this case  $R_1(\tau)$  is of finite duration, identically equal to zero when  $|\tau| \geq (L + L_a + 1)T$ .

Figure 4.15 shows the three PSDs  $S(f)$ ,  $S_0(f)$ , and  $S_1(f)$ . The frequency pulse  $g(t)$  is chosen to be 1REC and  $a_c(t)$  is also 1REC. Note that  $a_s(t) \equiv 0$ . In this figure the three spectra are labeled 1REC, 1REC/1REC, and 1REC/1REC/LIM. This notation is obvious from the context. It is seen that the mainlobe of the PSD for 1REC/1REC/LIM is nearly the same as for 1REC/1REC. Thus the mainlobe is not widened by the influence of the hard limiter. Also note that the PSD for 1REC/1REC/LIM is sometimes below that of 1REC/1REC when  $|fT_b| > 2.5$ . It seems that  $S_0(f)$  and  $S_1(f)$  have the same asymptotic falloff rate.

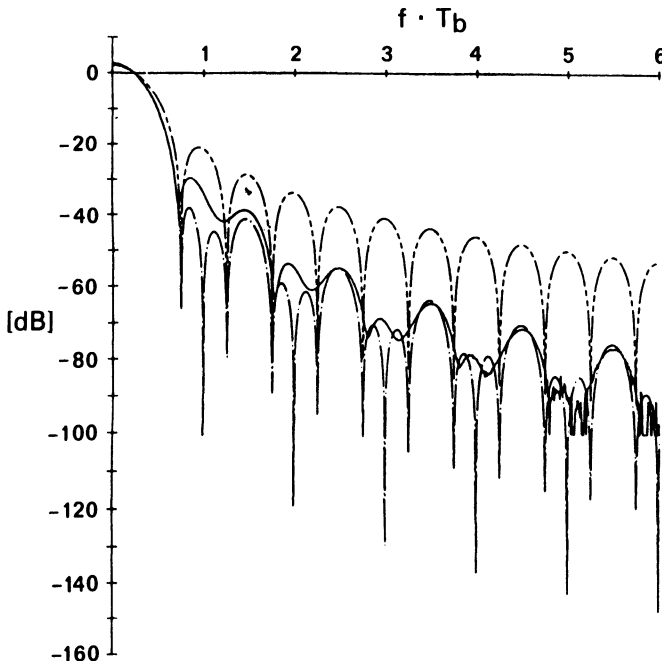


Figure 4.15. Power spectra for the modulator/filter/limiter combinations 1REC, 1REC/1REC, and 1REC/1REC/LIM.

In Figure 4.16,  $a_c(t)$  has been chosen to be 2REC instead, keeping everything else the same. The PSDs  $S(f)$ ,  $S_0(f)$ , and  $S_1(f)$  are now labeled 1REC, 1REC/2REC, and 1REC/2REC/LIM. The first spectral null due to the filtering now appears at  $fT_b = 1/2$ . Now the limiter widens the main lobe of the PSD for the filtered signal. On the other hand, the hard limiter has also reduced the level of the PSD when  $|fT_b| \geq 2$ . Thus hard limitation of a signal does not always have to be a spectrum spreading operation.

Finally, Figure 4.17 shows the case when  $g(t)$  is chosen to be 3RC and  $a_c(t)$  is 2REC. It is seen that  $S_1(f)$  is accurate down to  $-90\text{dB}$ .  $S(f)$  has been calculated by using the high-precision method in Section 4.4 and  $S_0(f)$  is  $S(f)|\tilde{A}(f)|^2$ . Over the interval  $0.25 \leq fT_b \leq 2.00$  the PSD for the 3RC/2REC/LIM signal is in between those for 3RC and 3RC/2REC.

In Section 4.4 it was stated that if the frequency pulse  $g(t)$  has  $c$  continuous derivatives, the PSD will decay like  $|f|^{-(2c+6)}$  for frequencies far away from the carrier. Actually the number of continuous derivatives can be referred to the signal itself ( $e^{j\phi(t,\alpha)}$ ) or the instantaneous phase  $[\phi(t, \alpha)]$ . Both these have  $c + 1$  continuous derivatives. The bandpass filter  $\tilde{a}(t)$  performs a smoothing operation on this signal. If  $\tilde{a}(t)$  has  $c_a$  continuous derivatives it follows that the filtered signal has  $c + c_a + 2$  continuous derivatives. The hard limiter performs a continuous memoryless operation

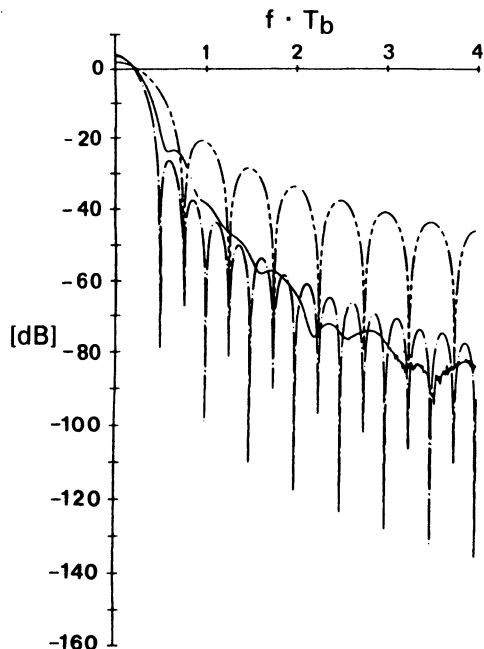


Figure 4.16. Power spectra for the binary modulator combinations 1REC, 1REC/2REC, and 1REC/2REC/LIM;  $h$  is  $1/2$ . Note behavior for  $fT_b > 2$ .

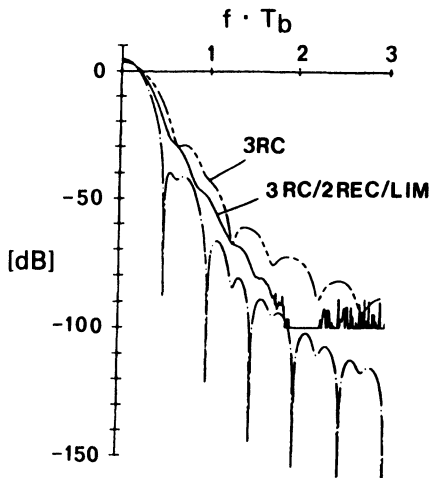


Figure 4.17. Power spectra for the binary modulator combinations 3RC, 3RC/2REC, and 3RC/2REC/LIM when  $h = 1/2$ . Note behavior near  $fT_b = 2$ .

on the filtered signal and it follows that the hard limited signal also has  $c + c_a + 2$  continuous derivatives. Thus it follows that the PSD  $S_1(f)$  will decay like  $|f|^{-[2(c+c_a+2)+6]}$ , or  $|f|^{-[2(c+c_a)+10]}$ . When no bandpass filter is present,  $c_a = -2$  and the previous result from Section 4.4 is obtained again. For REC pulses,  $c$  (or  $c_a$ ) equals  $-1$  and for RC pulses it equals  $+1$ . We conclude that the PSDs  $S_0(f)$  and  $S_1(f)$  in Figures 4.15 and 4.16 decay like  $|f|^{-6}$  and in Figure 4.17 like  $|f|^{-10}$ , asymptotically.

It follows from the presentation of the calculation of PSDs for signals transmitted over band- and amplitude-limited channels that the method can easily be generalized to include any memoryless nonlinearity, e.g., soft limiter, TWT. What needs to be changed is the nonlinear transformation of  $\tilde{s}_0(t, \alpha)$  into  $\tilde{s}_1(t, \alpha)$  in (4.49). Investigation shows that the important relationship (4.52) still holds. The expression for  $C_\alpha$  changes, however.

Other methods for calculation of PSDs for digitally modulated signals over band-limited nonlinear channels are given in Refs. 25 and 26. There it is assumed that the transmitted signal is the quadrature amplitude modulated signal

$$\begin{aligned} S(t) &= A \left[ \sum_{n=-\infty}^{\infty} a_n p_c(t - 2nT) \right] \cos 2\pi f_0 t \\ &\quad + A \left[ \sum_{n=-\infty}^{\infty} b_n p_s(t - 2nT) \right] \sin 2\pi f_0 t, \quad a_n, b_n = \pm 1 \end{aligned}$$

The pulse shapes  $p_c(t)$  and  $p_s(t)$  are of finite duration. Important special cases are QPSK, SQPSK, QORC, SQORC, and MSK. In Ref. 25 a matrix approach based on the technique described in Ref. 1 is used, and in Ref. 26 the autocorrelation function method is used.

## References

1. R. C. Titsworth and L. R. Welch, "Power Spectra of Signals Modulated by Random or Pseudorandom Sequences," Jet Propulsion Laboratory, Pasadena, California, Technical Report 32-140, October 10, 1961.
2. W. Postl, "Die Spektrale Leistungsdichte bei Frequenzmodulation eines Trägers mit einem Stochastischen Telegraphiesignal," *Frequenz* **17**, 107-110 (1963).
3. W. R. Bennett and S. O. Rice, "Spectral Density and Autocorrelation Function Associated with Binary Frequency-Shift Keying," *Bell Syst. Tech. J.* **43**, 2355-2385 (1963).
4. M. G. Pelchat, "The Autocorrelation Function and Power Spectrum of PCM/FM with Random Binary Modulating Waveforms," *IEEE Trans. on Space Electronics and Telemetry SET-10*, 39-44 (1964).
5. R. R. Anderson and J. Salz, "Spectra of Digital FM," *Bell Syst. Tech. J.* **44**, 1165-1189 (1965).
6. T. T. Tjhung, "Power Spectra and Power Distributions of Random Binary FM Signals with Premodulation Shaping," *Electronics Letters* **1**, 176-178 (1965).
7. L. Lundquist, "Digital PM Spectra by Transform Techniques," *Bell Syst. Tech. J.* **48**, 397-411 (1969).
8. V. K. Prabhu and H. E. Rowe, "Spectra of Digital Phase Modulation by Matrix Methods," *Bell Syst. Tech. J.* **53**, 899-935 (1974).
9. T. J. Baker, "Asymptotic Behaviour of Digital FM Spectra," *IEEE Trans. Commun. COM-22*, 1585-1594 (1974).
10. H. E. Rowe and V. K. Prabhu, "Power Spectrum of a Digital Frequency-Modulation Signal," *Bell Syst. Tech. J.* **54**, 1095-1125 (1975).
11. G. J. Garrison, "A Power Spectral Analysis for Digital FM," *IEEE Trans. Commun. COM-23*, 1228-1243 (1975).
12. F. Amoroso, "Pulse and Spectrum Manipulation in the Minimum (Frequency) Shift Keying (MSK) Format," *IEEE Trans. Commun. COM-24*, 381-384 (1976).
13. V. K. Prabhu, "Spectral Occupancy of Digital Angle-Modulation Signals," *Bell Syst. Tech. J.* **55**, 429-453 (1976).
14. S. A. Gronemeyer and A. L. McBride, "MSK and Offset QPSK Modulation," *IEEE Trans. Commun. COM-24*, 809-820 (1976).
15. M. K. Simon, "A Generalization of Minimum-Shift-Keying (MSK)-Type Signaling Based Upon Input Data Symbol Pulse Shaping," *IEEE Trans. Commun. COM-24*, 845-856 (1976).
16. L. J. Greenstein, "Spectra of PSK Signals with Overlapping Base-band Pulses," *IEEE Trans. Commun. COM-25*, 523-530 (1977).
17. M. Rabzel and S. Pasupathy, "Spectral Shaping in Minimum Shift Keying (MSK)-Type Signals," *IEEE Trans. Commun. COM-26*, 189-195 (1978).
18. T. Aulin, G. Lindell, and C-E. Sundberg, "Selecting Smoothing Pulses for Partial Response Digital FM," *Proceedings of the IEE, Part F: Communication, Radar and Signal Processing*, **128**, 237-244 (1981).
19. P. Galko and S. Pasupathy, "The Mean Power Spectral Density of Markov Chain Driven Signals," *IEEE Trans. Inf. Theory IT-27*, 746-754 (1981).
20. G. L. Pierobon, S. G. Pupolin, and G. P. Tronca, "Power Spectrum of Angle Modulated Correlated Digital Signals," *IEEE Trans. Comm. COM-30*, 389-396 (1982).
21. T. Aulin and C-E. Sundberg, "Calculating Digital FM Spectra by Means of Autocorrelation," *IEEE Trans. Commun. COM-30*, 1199-1208 (1982).
22. T. Aulin and C-E. Sundberg, "Autocorrelation Functions and Power Spectral Densities for Band-Pass Filtered and Hard-Limited Continuous Phase Modulation," International Conference on Communications, ICC '82, Philadelphia, Pennsylvania, June 13-17, 1982. Conference Record, pp. 6F.6.1-6F.6.5.

23. T. Aulin and C-E. Sundberg, "Exact Asymptotic Behaviour of Digital FM Spectra," *IEEE Trans. Commun.* **COM-30**, 2438–2449 (1982).
24. T. Aulin and C-E. Sundberg, "An Easy Way to Calculate the Power Spectrum for Digital FM," *Proceedings of the IEE, Part F: Communication, Radar and Signal Processing*, **130**(6), 519–526 (1983).
25. F. Amoroso, "The Use of Quasi-Bandlimited Pulses in MSK Transmission," *IEEE Trans. Commun.* **COM-27**, 1616–1624 (1979).
26. D. Divsalar and M. K. Simon, "The Power Spectral Density of Digital Modulations Transmitted Over Nonlinear Channels," *IEEE Trans. Commun.* **COM-30**, 142–151 (1982).

## Energy–Bandwidth Comparisons and Shannon Theory for Phase Modulation

Neither energy nor bandwidth consumption alone is a sufficient measure of a modulation system. It is a simple matter to reduce the bandwidth of a scheme if large energy is available, and similarly high energy is not needed for a low error probability if a large bandwidth can be tapped. What is much more difficult is reducing one of these without reducing consumption of the other.

At the same time, energy and bandwidth are different in nature and cannot be directly compared. In this chapter we will evade this difficulty by plotting positions of schemes in an energy–bandwidth plane. Now schemes of similar “worth” will lie along contours in the plane. Of course, many transmission links have an absolute energy or bandwidth constraint; in this case the modulations of interest lie along horizontal or vertical lines in the plane.

The chapter begins by comparing concrete systems, using the energy and bandwidth results of Chapters 3 and 4. The object will be to clarify which modulation parameters change the overall worth of a system and which only readjust the system to work at a new combination of energy and bandwidth. To gain insight into the ultimate capabilities of phase modulation, we must turn to the Shannon theory of information. We will need to make a distinction between the concrete schemes of Chapters 3 and 4, which we will call *modulations*, and another means of transporting information, called *Shannon codes*. The Shannon theory produces bound parameters like capacity and the cutoff rate that tie together energy and bandwidth and give upper bounds to the consumption of these in any constant-envelope scheme, including those not yet explicitly known.

## 5.1. Energy and Bandwidth Comparison of Concrete Modulation Systems

In the previous chapter, we developed the means to compute the bandwidth occupancy of a modulation. In Chapter 3, we characterized its energy consumption in terms of the minimum distance  $d_{\min}$ . In this section we will plot these quantities in an energy–bandwidth plane. The trends that will appear help make clear which combinations of parameters lead to an inherently strong modulation.

It is important to properly normalize the energy and bandwidth of different schemes so that they may be fairly compared. As in Chapter 4, let  $2BT_b$  denote the double sideband rf bandwidth of a signal, counting positive frequencies only. This bandwidth has been normalized to the data rate in terms of *bits* carried per second, so that schemes with different signaling alphabets may be compared. (Recall that  $T_b = T/\log_2 M$ , where  $T$  is the symbol interval time and  $M$  is the modulation alphabet size.) For a measure of energy consumption, it will be convenient to use the normalized Euclidean distance  $d_{\min}$  that was featured in Chapter 3, rather than directly use energy. Further,  $d_{\min}^2$  will be expressed in decibels compared to the distance of QPSK or MSK, which is 2; that is, our distance measure will be  $10 \log_{10}(d_{\min}^2/2)$ . Recall from Section 2.2 that the probability of symbol error is about

$$P_e \approx Q((d_{\min}^2 E_b / N_0)^{1/2})$$

from which it is clear that an increase of  $X$  dB in  $d_{\min}^2$  can be traded for a reduction of  $X$  dB in  $E_b$  for the same approximate error probability. In this sense our measure is a statement of per-bit energy consumption.

Figure 5.1 plots  $10 \log_{10}(d_{\min}^2/2)$  vs.  $2BT_b$  for a variety of 1REC (i.e., continuous phase FSK) schemes with different modulation indices and alphabet sizes. MSK is shown as a square dot. Bandwidth is measured in terms of fractional out of band power, and two families of curves are shown, one for 99% power inside  $2BT_b$ , and one for 99.9% power inside. All of the 99.9% curves lie further to the right than the 99% curves, since the 99.9% bandwidth is a wider measure. Better modulations lie toward the upper left. The largest index  $h$  used is shown at the top of each curve. As one moves down the curves, smaller  $h$  are employed, which causes the scheme to use less bandwidth but more power.

It is clear from Figure 5.1 that  $M = 2$  is a poor alphabet size to use at either power bandwidth, since these curves lie well to the lower right of the others. An alphabet size of 4 is almost as good as the best alphabet size, which seems to be close to 8. A size of 16 is clearly worse than 8. We can

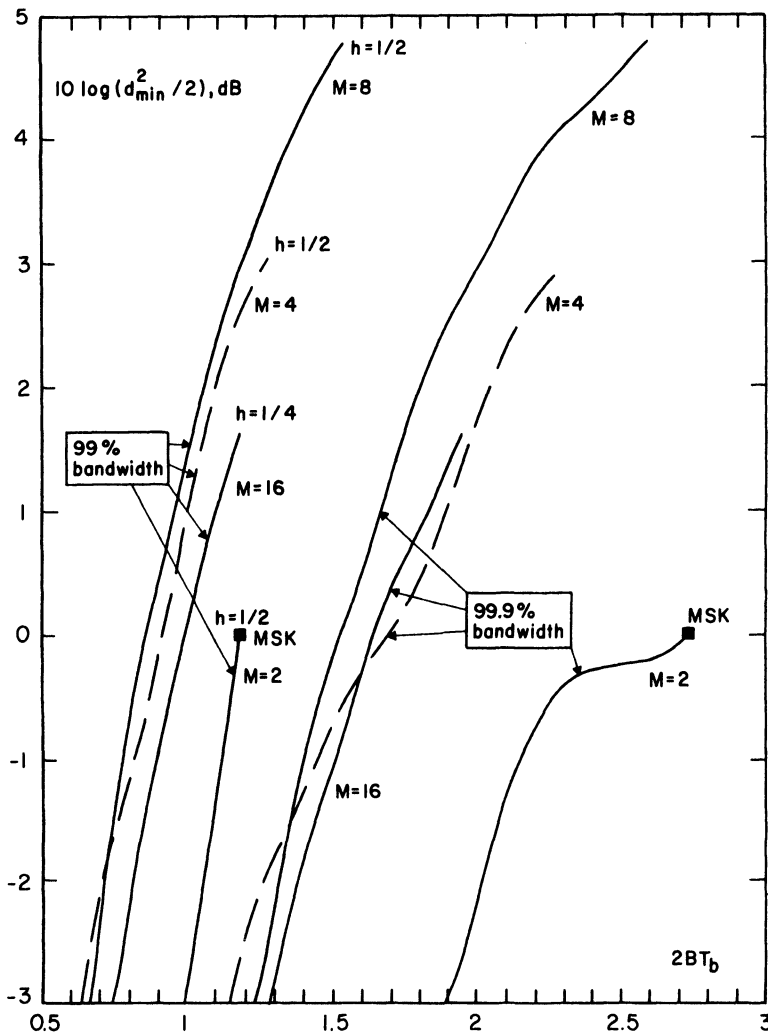


Figure 5.1. Energy-bandwidth tradeoff for CPFSK (1REC) with 99% and 99.9% power-in-band bandwidths. From Ref. 10.

conclude that  $M = 4$  is a good size to use for FSK schemes, since it leads to a simple system and it performs essentially as well as any other. The index  $h$  seems only to trade off energy for bandwidth. Although large distance gains are possible, they are inexorably linked to bandwidth expansion. The weakness of  $M = 2$  systems at practical values of  $E_b/N_0$  is predicted by signal space theory (see Wozencraft and Jacobs<sup>(6)</sup>) and has been noticed in practical applications.

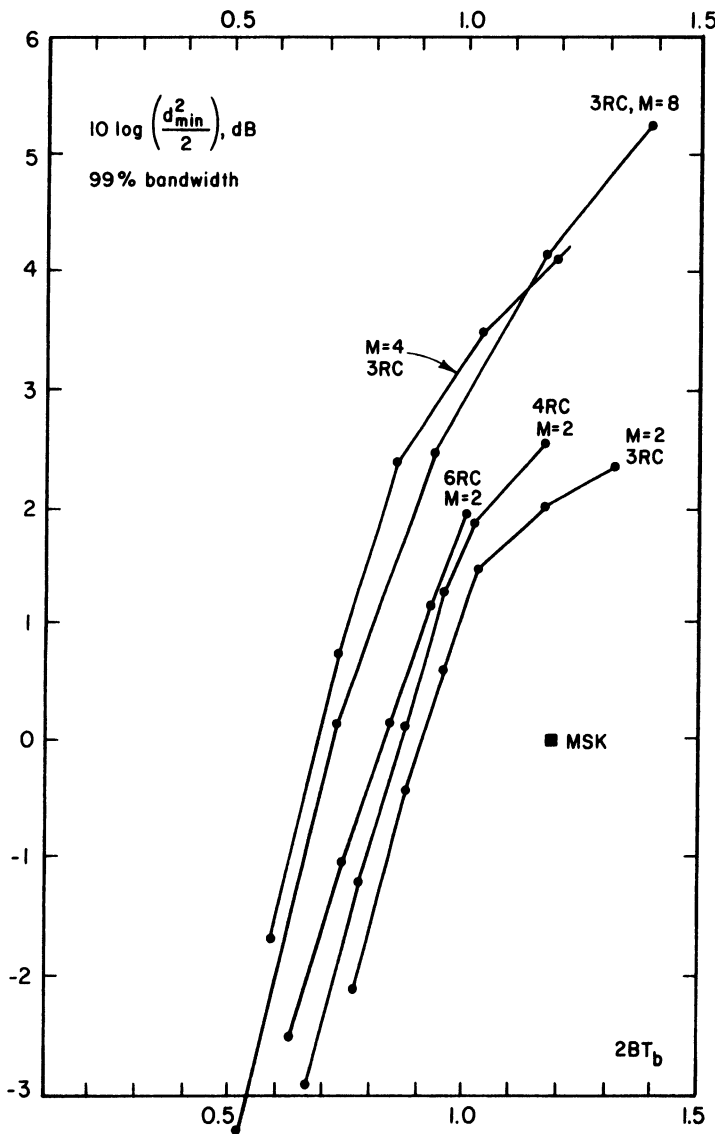


Figure 5.2. Energy-bandwidth tradeoffs for CPM schemes with RC pulses; bandwidth is the 99% power-in-band definition. Straight lines interconnect points that denote specific schemes. From Ref. 10.

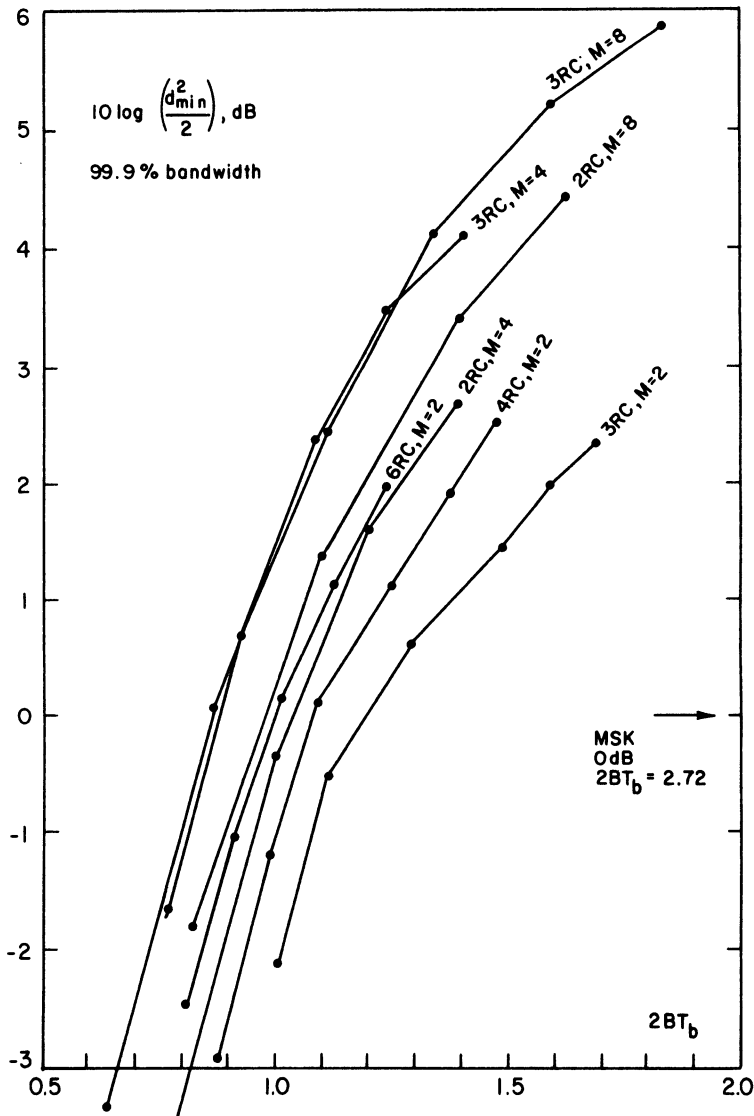


Figure 5.3. Energy-bandwidth tradeoffs as in Figure 5.2, but with 99.9% bandwidth definition. From Ref. 10.

Figure 5.2 plots RC-pulse modulations at their 99% bandwidth, with the same style as Figure 5.1. MSK is shown for reference. Here again  $M = 2$  schemes are poor, and  $M = 4$  seems to be the best choice. There is a small improvement in the modulations as the pulse lengthens but alphabet size has the greater influence. Here “improvement” means better energy, better bandwidth, or if desired by the designer, both at once. The RC systems of Figure 5.2 are only somewhat better than the FSK systems of Figure 5.1 for the 99% bandwidth criterion. This reflects the fact that the spectral main lobes are not much different.

Figure 5.3 shows RC-pulse systems compared in terms of 99.9% bandwidth. This criterion stresses spectral side lobes and gives a good indication of the adjacent-channel interference of a modulation. Now an increase in pulse length has a strong effect and produces a much better modulation. This is true at all the alphabet sizes, but  $M = 4$  is still close to the best size except in the wide bandwidth/low energy region. The 99.9% curves of Figure 5.1 are much worse than the curves of Figure 5.3.

These plots show that longer, smoother phase responses dramatically improve energy-bandwidth performance only if the bandwidth criterion takes some account of spectral side lobes. Otherwise there is only moderate improvement; this reflects the basic difficulty of narrowing the spectral main lobe in a constant-envelope modulation. A second feature of these plots is the strong influence of alphabet size.

All of these results are for specific constant-envelope schemes that we can now imagine and construct, and the ultimate abilities of pure phase modulation, by means of schemes as yet undiscovered, is a matter for speculation. The Shannon theory will be of help here.

## 5.2. Basic Ideas of the Shannon Theory

We now shift course, and introduce quite a different way of viewing the energy and bandwidth of a transmission, the Shannon theory of information. This theory contains several new concepts, such as the information contained in a sequence and the capacity of a channel, and a new approach to generation of signals called random coding. The theory gives an idea of the ultimate performance of methods like phase modulation to which we can compare the performance of the concrete schemes in this book. At present, information theory has developed a theory of finite-state channels that in principle is sufficient to analyze channels of the phase modulation type, but the details of it have not been worked out for this application. Results are available, however, for a simple channel parameter, the cutoff rate. These will give us an effective simultaneous analysis of energy and bandwidth in phase modulation, which will follow in Section 5.4.

### 5.2.1. The Shannon Model of Information Transmission

In the Shannon theory of communication, both the channel and the transmitted information are viewed as probabilistic objects. Two processors, called the channel *encoder* and *decoder*, convert the data to be transmitted into a form suitable for the channel and then after transmission back again into the form of the data. An important theorem, originally due to Shannon, shows that encoders and decoders exist that guarantee virtually error-free transmission, provided that the quantity of information carried falls below a certain limit called the *channel capacity*.

Figure 5.4 shows a basic form of the Shannon model that will suit our purposes. Sequences of  $M$ -ary data symbols  $\underline{u}^K$  enter the channel encoder in blocks of  $K$ ; these symbols are independent and occur each with probability  $1/M$ . (Extensions of the theory allow for sources with dependent or unequally distributed letters.) The essential feature is that the data are viewed not in terms of the identity of their symbols, but in terms of their probability distribution. The information content of a symbol  $u$  is measured by the entropy function

$$H(U) = - \sum_i P_u(u_i) \log_2 P_u(u_i) \quad (5.1)$$

where the sum runs over the symbol alphabet and  $P_u$  is the distribution of a symbol. The entropy of the random variable  $U^K$ , a block of independent and identically distributed (IID) symbols, is given by  $H(U^K) = KH(U)$ . In case the alphabet of  $U$  is  $M$ -ary,

$$H(U) = \log_2 M$$

The encoder in Figure 5.4 converts  $U^K$  by means of an invertible mapping to a new sequence  $X^N$ , a block of  $N$  symbols, possibly from a new alphabet. The purpose of the encoder is to match the data to the conditions imposed by the channel. If the data and channel input alphabets are both binary, the encoder ordinarily will add parity check digits to the data stream. These will enable the decoder to correct channel errors. In the phase modulation channels, the input alphabet is much more complex and we shall wait until Section 5.3 to define it properly. As mentioned in Section 1.3, an encoder is best thought of as imposing certain patterns, defined by the data, onto the transmitted signal, rather than as adding extra



Figure 5.4. A Shannon communication system.

symbols. A decoder looks for one of these patterns close to the noisy pattern that is received. If the patterns in the set are distant enough from each other, the encoder/decoder combination will effectively combat the channel effects.

The degree of symbol expansion in the encoder is described by its *rate*. In case both the  $u$  and  $x$  alphabets are the same, the rate may be defined as  $K/N$  data symbols per use of the channel. Otherwise, the definition is more complicated, and it may be inappropriate to define the rate in terms of channel uses in the Shannon sense.

A central concept in information theory, devised by Shannon himself, has been the *random code*. To create such a code, words  $x^N$  are selected at random according to a distribution  $P_x$ . Additional words are selected with the same distribution until one exists for each data sequence  $u^K$ . Many such codes are very poor; conceivably, all words selected could even be the same. Random codes have no structure and thus require computing and storage resources that grow exponentially with the length of the code. But information theory concludes typically that a sufficiently long code selected this way will with high probability have optimal performance. We will develop random phase modulation codes in Section 5.3.

The next block in Figure 5.4 is the channel. A channel is defined by a conditional probability distribution  $P_{y|x}(Y|X)$  between a sequence of channel inputs and outputs,  $X$  and  $Y$ . Each channel input symbol is converted in a probabilistic way to one of the channel output symbols. The alphabet of  $Y$  may differ from that of  $X$ , and either alphabet may be continuous or discrete. A channel is memoryless if for all symbol sequences  $x^N$  and  $y^N$  the relation

$$P_{y|x}(Y|X) = \prod_{i=1}^N P_{y|x}(Y_i|X_i) \quad (5.2)$$

holds. In case the input alphabet is finite and discrete and (5.2) holds, we will call the channel an *input-discrete memoryless channel* (IDMC). A few phase modulation channels can be sufficiently modeled by the IDMC, but most require an input-discrete channel model with memory, which we will take up in the next section. All the models we will need are input discrete.

Figure 5.5 shows several classic channel models of the IDMC type. The binary symmetric channel, or BSC, assumes that both input and output alphabets are binary. To match the usage in the rest of the book, we have used +1 and -1 to denote the symbols, but these letters are purely symbolic and any other notation would do as well. The BSC diagram shows graphically that each symbol is converted to the other with probability  $p$  and is transmitted correctly with probability  $(1-p)$ . The BSC is appropriate to parity-check coding over a binary channel when we cannot gain access to

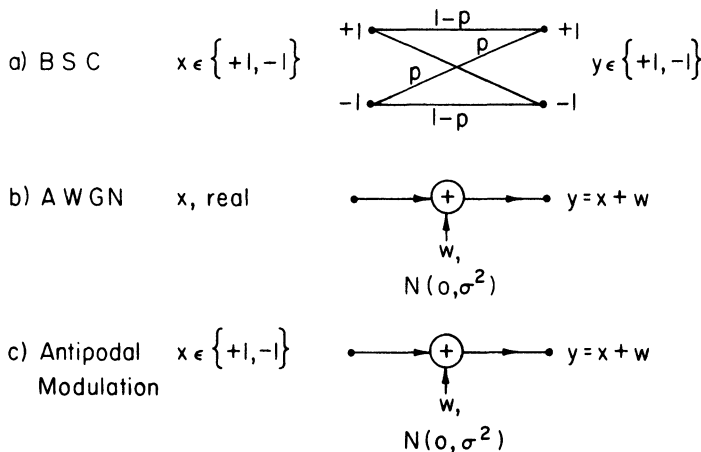


Figure 5.5. Same basic channel models; (a) binary symmetric channel, (b) additive white Gaussian noise channel, and (c) antipodal modulation channel.

the mechanism of the channel. When more information is known, for instance, when the channel is in reality phase modulation with a known type of noise, the BSC is apt to be a strongly inaccurate model.

Figure 5.5b diagrams the additive white Gaussian noise, or AWGN, channel. In this, a zero-mean uncorrelated Gaussian noise variate adds to an input letter to produce a continuous-alphabet output. Both input and output alphabets are not purely symbolic, but represent parts of the real line. In the language of Chapter 2, collections of input letters correspond to vectors in signal space, with each letter indicating a displacement along an orthogonal signal space direction. The effect of white channel noise is to add an uncorrelated Gaussian variate to each vector component. The AWGN channel model takes accurate account of an important noise mechanism and gives a good model for modulations in which the signal space components of the modulated signal behave in an independent manner.

The antipodal modulation channel in Figure 5.5c describes the special case when the symbols of  $x^N$  can be viewed as each corresponding to an orthogonal direction in signal space, or to its opposite direction. All signals have equal energy. The input letters  $\pm 1$  in the model are points on the real line. Figure 5.5c accurately models BPSK, either pure or Nyquist shaped, and MSK (viewed as offset QPSK); QPSK is modeled by two such channels operating independently. Partial response phase modulations or modulations with index other than 1/2 are not adequately modeled. These require an extension to a more complicated input alphabet, or more seriously, a channel model with memory.

### 5.2.2. Capacity

For an IDMC, the channel capacity is defined to be

$$C \triangleq \max_{P_x} \sum_y \sum_x P_x(x) P_{y/x}(y/x) \ln \frac{P_{y/x}(y/x)}{\sum_{x'} P_x(x') P_{y/x}(y/x')} \quad (5.3)$$

where  $P_x(x)$  is the distribution function of the channel input variate. If  $y$  is continuous, the  $y$ -sum is replaced by an integral. Capacity thus results from a maximization over the possible input distributions, and it is a function of the transition probabilities of the channel. This reiterates how all the quantities in the Shannon theory are functions only of probability distributions. The following theory, proven originally by Shannon, shows the significance of the channel capacity.

*Theorem 5.1* (Channel Coding Theorem). For any IDMC, there exists an encoder of rate  $R$  bits per channel use for which the error probability of a maximum likelihood decoder is bounded by

$$P_e \leq K_0 2^{-NE(R)} \quad (5.4)$$

Here  $K_0$  is a constant, symbols appear in blocks of  $N$ , and  $P_e$  is the probability of incorrect reception.  $E(R)$  is a convex decreasing positive function of  $R$  for  $R$  in the range  $[0, C]$ .

The theorem shows that at any transmission rate short of capacity, virtually error-free transmission is possible in the limit of large code block length. The calculation of  $C$  is quite difficult, and the reader is referred to the techniques given in Gallager<sup>(1)</sup> or Viterbi and Omura.<sup>(2)</sup> These texts prove Theorem 5.1 by showing how to compute the error exponent  $E(R)$ , which sets the rate of decay of  $P_e$  with  $N$ . They give as well a proof of the converse to Theorem 5.1, which states that no code exists with  $R > C$  for which the decoder error probability tends to zero with  $N$ . For transmission at rates near capacity, the channel input distribution must be near the maximizing  $P_x$  in (5.3), so that an additional requirement on the encoder is to produce this distribution at its output.

For the BSC of Figure 5.5a, it is clear from symmetry that the maximizing  $P_x$  is  $P_x(1) = P_x(-1) = 1/2$ . Since  $P_{y/x}(y/x)$  equals  $1 - p$  when  $x$  and  $y$  agree and  $p$  otherwise, (5.3) gives for the BSC capacity

$$C = 1 - p \log_2 (1/p) - (1 - p) \log_2 [1/(1 - p)], \quad (5.5)$$

measured in bits per channel use. For the antipodal modulation channel of Figure 5.5c, symmetry of the channel again implies that  $P_x(1) = P_x(-1) = 1/2$ ; the fact that  $P_{y/x}(y/1) = P_{y/x}(-y/-1)$  implies that

$$C = -\log_2 (2\pi e)^{1/2} - \int_{-\infty}^{\infty} \frac{[P_{y|x}(y|-1) + P_{y|x}(-y|-1)]}{2} \\ \times \log_2 \frac{[P_{y|x}(y|-1) + P_{y|x}(-y|-1)]}{2} dy \quad (5.6)$$

where we have again substituted into (5.3). Here,  $P_{y/x}(y/-1)$  is set by the Gaussian channel, and is equal to

$$P_{y/x}(y/-1) = \frac{1}{(2\pi)^{1/2}} \exp \{-[y - (2E_b/N_0)^{1/2}]^2/2\} \quad (5.7)$$

where  $E_b/N_0$  is the ratio of data bit energy to noise energy from Section 2.2.

Computation of the capacities in (5.5) and (5.6) allows us to compare the antipodal modulation channel model with the much cruder BSC model. When the BSC models an antipodal with a matched-filter demodulator, the error probability  $p$  is  $Q((2E_b/N_0)^{1/2})$ , and making this substitution in (5.5) gives  $C$  for the equivalent BSC model. Viterbi and Omura, p. 153ff, calculate these capacities, and Figure 5.6 reproduces some of their results. They find that at low energy-to-noise ratios,  $C$  for the BSC is about  $(2/\pi)E_b/N_0$ , while  $C$  for the antipodal modulation channel is about  $E_b/N_0$ . Thus  $C$  for the BSC falls short by  $2/\pi$  and we can interpret this as a loss of 1.96 dB in the energy  $E_b$ . Viterbi and Omura also show that an octal quantization of the continuous output of the modulation channel, to produce a two-input eight-output IDMC, will recover almost all this loss.

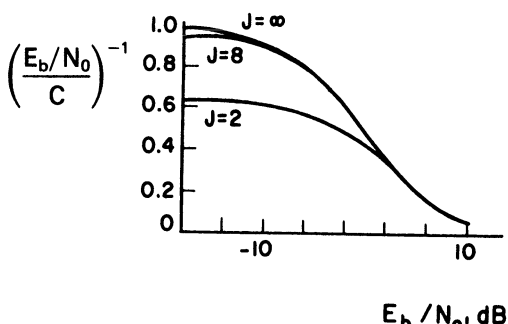


Figure 5.6. Capacity of the quantized AWGN channel, normalized by  $E_b/N_0$ , as a function of  $E_b/N_0$  in decibels.  $J = 2$  is the BSC (two-level quantization of the channel output),  $J = 8$  is eight-level quantization, and infinity denotes no quantization, i.e., the antipodal modulation channel. From Viterbi and Omura.<sup>(2)</sup>

Both of these capacities must fall below 1 bit/channel use, since the input alphabets in both cases are binary. The capacity of the AWGN channel of Figure 5.5b can lie much higher than 1 for the same  $E_b/N_0$ . We will delay computation of this capacity to Section 5.3.

One block remains in Figure 5.4, the decoder. In computing capacities and proving coding theorems with the Shannon theory, one assumes that the decoder is the maximum likelihood detector of Section 2.1. In the context of the Shannon channel model, this means that the decoder finds the most likely  $\hat{\mathbf{u}}^K$ , given that  $\mathbf{y}^N$  is received. If  $\hat{\mathbf{u}} \neq \mathbf{u}$ , the entire code word is considered to be in error. The decoder uses  $P_x$  and  $P_{y/x}$  in making its maximum likelihood decision.

### 5.2.3. Bandwidth and Dimensionality

The Shannon theory, as we have summarized it above, includes the concept of signal energy, but makes no mention of the bandwidth of signals. Rather, it considers that information is transmitted in words  $\mathbf{x}^N$ , in which each letter represents an independent position, or in the language of signal space theory, an orthogonal dimension. In order for the Shannon theory to have a meaningful relation to modulation theory, it is necessary to relate dimensionality to bandwidth.

It is not difficult to make a heuristic argument that an interval of bandwidth  $(-W, W)$  and a time interval of duration  $T_0$  can give rise to about  $2WT_0$  signal space dimensions. Suppose that data are carried by the function

$$\text{sinc}(t) = \frac{\sin(\pi t/T)}{\pi t/T}, \quad -\infty < t < \infty$$

that is, each  $T$  seconds a new function  $a_i \text{sinc}(\cdot)$  is initiated, with the amplitude  $a_i$  carrying information. The total transmitted signal is

$$s(t) = \sum_i a_i \text{sinc}(t - iT)$$

The  $\text{sinc}(\cdot)$  functions in this sum are orthogonal (see Section 2.6) in the sense that by sampling  $s(t)$  at time  $iT$ , we can recover the data-bearing variable  $a_i$ . This transmission system is simply the baseband part of the Nyquist-pulse-shaped QPSK system that was discussed in Chapter 2, with  $\text{sinc}(\cdot)$  pulses used in place of excess-bandwidth pulses.

The bandwidth of any superposition of  $\text{sinc}(\cdot)$  pulses like  $s(t)$  is precisely  $(-1/2T, 1/2T)$ . After a long time  $T_0$ ,  $T_0/T$  dimensions will have been carried by  $s(t)$ . With the substitution  $W = 1/2T$ , this amounts to  $2WT_0$  dimensions.

Our reasoning is not quite accurate because  $s(t)$  is not time limited to an interval of length  $T$ . For large  $T$  it is clear that  $s(t)$ 's time duration is fractionally only a little larger than  $T$ , but in any strict sense,  $s(t)$  has infinite duration. Furthermore, the theory of Fourier transforms tells us that any effort to time-limit  $s(t)$  will cause its spectrum to have infinite width. In fact, one cannot simultaneously time- and band-limit any function. A careful proof of the result that dimensionality is about  $2WT_0$  must define  $W$  and  $T_0$  as the bandwidth or time outside which lies only a small fraction of these commodities.

The construction of such a proof is a subtle exercise. In Theorem 5.2 we use the result of Landau and Pollak,<sup>(3)</sup> which followed work by Slepian and Pollak.<sup>(4)</sup> Another result of this type was given by Shannon<sup>(5)</sup>; the reader is also referred to an approach in Chapter 8 of the text by Gallager.

**Theorem 5.2.** Consider a set of  $N$  orthogonal basis functions  $\{\phi_i(t)\}$  chosen so that (i) for each  $i$ ,  $\phi_i(t)$  is zero outside the interval  $[-T_0/2, T_0/2]$ ; (ii) each  $\phi_i(t)$  has unit energy, that is,

$$\int_{-T_0/2}^{T_0/2} \phi_i(t)^2 dt = \int_{-\infty}^{\infty} |\Phi_i(f)|^2 df = 1$$

(iii) all but a fraction  $\delta$  of this lies inside the band  $[-W, W]$ , that is,

$$\int_{-W}^W |\Phi_i(f)|^2 df = 1 - \delta$$

Then the number of such functions that can be found lies in the range

$$2WT_0 < N < 2(1 + \varepsilon)WT_0 \quad (5.8)$$

where  $\varepsilon > 0$  and  $\delta > 0$  both tend to 0 as  $T_0$  grows large.

The proof of Theorem 5.2 is complicated, and the reader is directed to the relatively legible account in Appendix 5A of Wozencraft and Jacobs.<sup>(6)</sup> Equation (5.8) shows that if bandwidth  $W$  and sufficient time  $T_0$  are available, a signal space of dimension about  $2WT_0$  can be set up. Then the  $N$ -tuple input  $x^N$  to the AWGN channel of Figure 5.5b corresponds to a point in this space. Each component of  $x$  is affected by AWGN of variance  $N_0/2$ , where  $N_0$ , as in Chapter 2, is the power spectral density of the white noise. The maximum likelihood decoder in Figure 5.4 can in principle be realized by one of the matched filter receivers of Section 2.1, consisting of filters matched to each  $x$ , that is, to each function of the form

$$s(t) = \sum_{i=1}^N x_i \phi_i(t)$$

We have seen that sinc( ) pulse shaped PSK can realize a number of signal space dimensions roughly in accordance with (5.8). Nyquist pulse shaping will generate a factor  $1/(1+a)$  fewer dimensions for the same  $W$  and  $T_0$ , where  $a$  is defined as in (2.31) or Fig. 2.19. For the continuous phase modulated signals of Chapter 3, the situation is considerably more subtle. CPM signals do not fully exploit the signal space of their signals in the sense that the signals have only small components along many of the basis directions. We will see additional evidence of this in Chapter 8, where it will be seen that receivers with reduced dimensional complexity are almost as effective as those that view the full signal space. Thus the bandwidth consumption of a CPM scheme that apparently needs  $N$  dimensions for its expression may be less than that implied by (5.8) in a practical system.

### 5.3. AWGN Channel Capacity and the Phase Modulation Channel

In this section, we shall give the capacity of the AWGN channel, deferring again the complex proof of this result to one of the texts on information theory. We then consider channel models for general phase modulation, for which successive signal intervals are dependent and the antipodal modulation channel of Fig. 5.5c does not apply. These channels are not memoryless. Techniques exist to compute these capacities but they are difficult, and no numerical results yet exist for these channels.

#### 5.3.1. AWGN Channel Capacity

Before stating the capacity theorem, we must take care to define the data rates that appear in Figures 5.4 and 5.5b. The theorem will be written in terms of  $C_d$ ,  $R_d$ , and  $E_d$ , the capacity, transmission rate, and energy *per dimension* of the signal space. Each  $N$ -tuple word that passes through the channel carries  $NR_d$  bits and consumes an average  $NE_d$  joules of energy.

*Theorem 5.3.* The capacity  $C_d$  in bits per dimension for the AWGN channel is given by

$$C_d = \frac{1}{2} \log_2 (1 + 2(E_d / N_0)) \quad (5.9)$$

If the rate  $R_d$  in bits per dimension is less than  $C_d$ , some code exists such that the maximum likelihood decoder error probability tends to zero as  $N$  grows. Conversely, if  $R_d$  exceeds  $C_d$ , any code has error probability near one.

The customary proof of Theorem 5.3 is a long exercise in the geometry of the  $N$ -dimensional signal space in which the code word vectors  $\mathbf{x}$  reside.

The volume of signal space occupied by these is approximately

$$[(\pi E_d)^{1/2}]^N / (N/2)!, \quad N \text{ even}$$

the volume of an  $N$ -dimensional sphere of radius  $\sqrt{E_d}$ . The theorem shows how many code points may be distributed in this volume in such a way that the signal space distance grows without limit as  $N$  grows. A readable proof of the theorem appears in Wozencraft and Jacobs.<sup>(6)</sup> This proof assumes the code points are randomly distributed through the energy sphere; the input alphabet in Fig. 5.5b is thus best considered to be the segment  $[-\sqrt{E_d}, \sqrt{E_d}]$  of the real line. De Buda and Kassem<sup>(7)</sup> have proven Theorem 5.3 when the code points are constrained to fall on the points of a lattice in signal space. In this kind of code, each letter of  $x$  is taken from a (possibly different) finite subset of  $[-\sqrt{E_d}, \sqrt{E_d}]$ .

Theorem 5.3 is a theorem about signal space, and it does not consider the bandwidth of signals. However, Theorem 5.2 tells us that a bandwidth  $W$  will make available about  $2WT_0$  dimensions in time  $T_0$ , or about  $2W$  dimensions per second. Since the capacity of the AWGN channel is  $C_d$  bits per dimension, the capacity in bits per second must be about

$$C = W \log_2 (1 + 2(E_d / N_0)) \quad (5.10)$$

An additional substitution can replace the energy  $E_d$ , measured in joules, with the signal power  $P$ , measured in watts.  $P$  must be equal the energy per dimension times the rate of appearance of dimensions, and the latter is about  $2W$ , so that  $P$  equals  $2WE_d$ . This gives the AWGN capacity in its power and bandwidth form,

$$C = W \log_2 (1 + P / WN_0) \text{ bit/s} \quad (5.11)$$

Note that the ratio inside the parentheses is the ratio of the total signal power  $P$  to the total noise power,  $2W(N_0/2)$ .

Capacity formulas (5.9)–(5.11) give the ultimate limit to transmission rate in a Gaussian channel, in terms of the noise density and the signal energy, power, and bandwidth. The coding theorem makes no comment on what type of signals might reach near this limit. We do not at this point know whether phase modulated signals or constant-envelope signals, for instance, fall short of this limit.

### 5.3.2. A Phase Modulation Channel Model

In Chapter 2 we have set out two types of phase modulation, Nyquist pulse-shaped modulation and continuous phase constant-envelope modulation. In the former case, the antipodal modulation channel is an adequate model, and it was shown in Section 2.6 that the linear receiver is an optimal

receiver for uncoded, Nyquist-pulse modulation. In the second case, however, the continuous phase requirement and the partial response nature (if the modulation is so designed) mean that the proper model is normally a channel with memory.

In a discrete channel with memory, the transition probabilities at time  $n$  depend on the *state* of the channel at time  $n - 1$ . The states of the channel evolve in a Markov fashion, in which the probabilities of transiting to a new state depend on the state at the previous time. There exist thus two sets of “transition” probabilities, one relating to the train of states and another that determines the channel probabilities. In some channels with memory, the state transitions are independent of the channel inputs  $x$ . An example of this is the fading channel, modeled as a two-state channel with a “clear” state and a “faded” state, the so-called Gilbert–Elliott model. Transitions between these two states occur independently of the transmitted data, but the channel transition probabilities depend on the state and become much worse during the “faded” state. In other channels, the state depends entirely on the channel inputs. The classic example of this is the intersymbol interference channel, in which a certain length of previous input symbols interferes with the channel in a way that depends only on the symbols. One can then denote the channel transition probabilities in the form

$$P_{y/x}(y_n/x_n; \sigma_{n-1}) = P_{y/x}(y_n/x_n; x_{n-1}, \dots, x_0)$$

which expresses that fact that the probability of channel output  $y$  at time  $n$  depends on the input  $x$  at that time and a state that in turn depends on the previous inputs. It is this ISI channel that is the focus of this section.

To define the ISI channel that is appropriate for the continuous-phase constant-envelope modulation channel, we first recall the definitions (3.1) and (3.2), the latter of which was (for constant  $h$ )

$$\phi(t, \alpha) = 2\pi h \sum_{i=0}^n \alpha_i q(t - iT), \quad nT < t < (n+1)T \quad (5.12)$$

In Chapter 3 the  $\{a_i\}$  were data symbols,  $q(\cdot)$  was the phase response function, and  $h$  was the modulation index. Modulations were studied in which  $q(\cdot)$  was active for  $L$  symbols, after which it assumed the constant value  $1/2$ . This means that the underlying Markov chain is not as complicated as (5.12) suggests. As we did in Section 3.4.1, we can rewrite (5.12) as

$$\phi(t, \alpha) = 2\pi h \sum_{i=n-L+1}^n \alpha_i q(t - iT) + \pi h \sum_{i=0}^{n-L} \alpha_i \quad (5.13)$$

which expresses the fact that symbols more than  $L$  intervals before the present simply form a constant offset in the phase shaping process. This motivates defining the state of the channel during interval  $n$  to be

$\sigma_n = (\theta_n, \alpha_{n-1}, \dots, \alpha_{n-L+1})$ , where  $\theta_n$  is the phase state

$$\theta_n = \left( \pi h \sum_{i=0}^{n-L} \alpha_i \right) \bmod 2\pi$$

of (3.43) and  $\alpha_{n-1}, \dots, \alpha_{n-L+1}$  form the correlative state vector. The phase in the  $(n+1)$ -st interval in (5.13) is determined by  $\sigma_n$  and the data symbol  $\alpha_n$ , or equivalently, by the transition from  $\sigma_n$  to  $\sigma_{n+1}$ .

As shown in Section 3.4.1, the state space has cardinality  $\eta M^{L-1}$ , if  $h$  is a multiple of  $1/2\eta$ . Typically, most of these states are not reachable from a given state in one transition, but for modulations of the form (5.13) every state is reachable in finite time from every other state. Such a state space is called *indecomposable*. We will assume  $h$  is rational, so that the space is also finite.

To complete the channel modeling, we must connect (5.13) and the state definition following to the AWGN channel of Figure 5.5b. The data symbols  $\alpha_i$  do not themselves appear in the AWGN channel, but rather are transformed by (5.13) into a phased sinusoid, which is then converted to a vector  $\mathbf{x}$  in signal space. The dimension of this space cannot be larger than  $2M^L$ , because the signal shape is defined by the previous state and the present data symbol, and an in-phase and quadrature dimension are sufficient to define all  $\eta$  phase shifts that can appear. Thus a sequence of symbols  $\alpha^N$  leads to a sequence  $\mathbf{x}^{N\xi}$  which is longer by the factor  $\xi$ , the dimension of the per-interval signal space. The modification to the AWGN channel is diagrammed in Figure 5.7.

It remains to incorporate the concept of random coding into our phase modulation model, since this concept is fundamental to the Shannon theory and we must use it in the sequel. The phase code words are completely defined by the sequence  $\alpha^N$ , if  $h, q(\cdot)$ , etc. are taken as given. By a random phase modulation code, we will mean a set of phase trajectories of a length  $N$  intervals for which the  $\alpha^N$  sequences were chosen at random according to some specified distribution. To choose a code of rate  $R$  bits/interval means to select  $2^{NR}$  words independently by this process. We will call these codes *Shannon codes*.

It is important to distinguish between a *modulation*, which has rate  $\log_2 M$  bits/interval, data symbols that are identical to  $\alpha$ , and a fixed

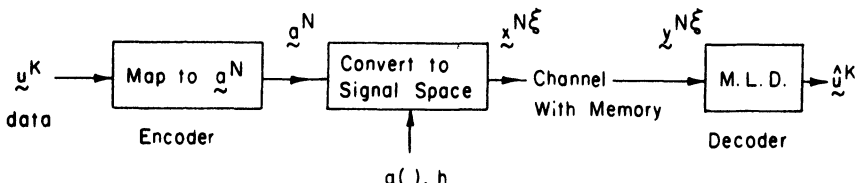


Figure 5.7. Model of channel with memory, for phase modulation over  $N$  T-intervals; rate of transmission is  $R = \log_2 K/N$  bits/T interval.

probability of error determined by the signal energy, the free distance, and the noise density; and a Shannon code, which has a rate set by the number of words in its codebook, data symbols  $u^K$  that are mapped to the larger-cardinality set of  $\alpha^N$ , and an error that can be driven to zero if the rate falls below capacity. The rate of a Shannon code is limited to  $\log_2 M$  bits/interval, but it will ordinarily be less. The communications model that employs such a code is shown in Figure 5.7.

A simple example of a phase modulation channel is provided by binary CPFSK with  $h = 1/4$ . Phase transitions in this scheme are linear and depend for their shape only on the present symbol; the transition begins at a phase equal to  $\pi h$  times the sum of all the previous symbols  $\alpha_i$ , mod  $2\pi$ . Figure 5.8a shows the transitions,  $\eta M^L$ , or 8 in number; a signal space of size  $2M^L$ , or 4, will be required to express these transitions as inputs to an AWGN channel. The extension of this example to the 2REC channel is tedious but straightforward. There will now be 16 transitions, some of which look identical but stem from different state transitions. As many as eight signal space dimensions may be required; an enumeration of the needed phase transitions shows that in fact six will do.

A Shannon code for use in the CPFSK channel will contain a set of phase trajectories, or “words,” that are identical to certain CPFSK modulator outputs, but not all the outputs will appear in the code. Instead, the fraction  $2^{NR}/M^N$  will appear; the missing words contribute by their absence

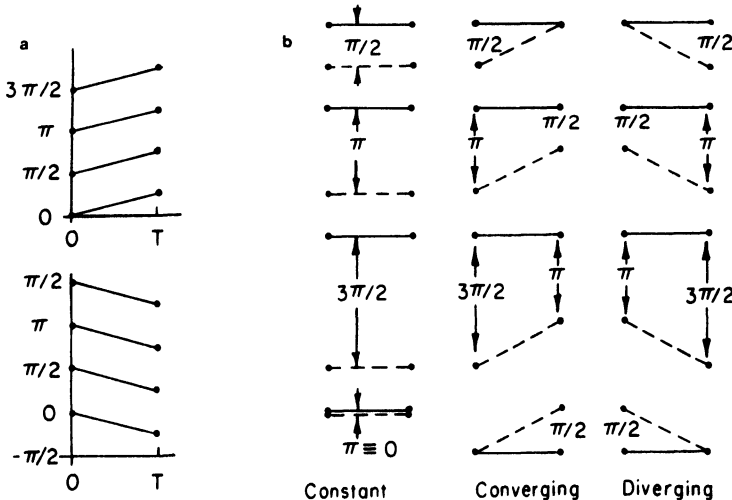


Figure 5.8.ab: Binary CPFSK (1REC) with  $h = 1/4$ . (a) Phase transitions possible in one signal interval; note that the sets of transitions in alternate intervals are shifted by  $\pi/4$ . (b) Differences between phase transitions of two random signals possible in one signal interval; pairs of signals offset by a constant are not shown.

to the code distance properties, leading to a signaling scheme with error probability tending to zero with  $N$ . For the CPFSK and 2REC examples, a Shannon code of length 10 and rate 1/2 will contain 512 words out of a possible 1024. A modulator, on the other hand, can have all 1024 outputs; its error probability, however, is fixed, no matter how large is  $N$ .

### *Capacity of the Phase Modulation Channel*

Known results of the finite state channel are summarized in Gallager.<sup>(1)</sup> Any indecomposable channel like ours has a unique capacity; channels that are not indecomposable have a capacity that depends on the starting state, but this capacity must lie between certain bounds. For certain channels, capacity can be computed by a method that finds the largest eigenvalue of a matrix whose dimension is related to the number of states, and then optimizes over the distribution of  $\alpha$ . Some inkling of this method can be gained from Appendix B, where we use an eigenvalue method to find the cutoff rate of a phase channel. However, the capacity calculation is difficult, and no numerical results are available in the literature. This motivates us to consider the simpler cutoff rate computation.

## 5.4. The Cutoff Rate for Phase Modulation Channels

In this section we introduce the concept of the cutoff rate, a relatively simple underbound to capacity. We will need to consider the phase differences between a *pair* of signals that can arise in a random phase code, and to model these with a “difference” Markov chain. An eigenvalue method then gives the cutoff rate.

### *The Cutoff Rate*

Consider two signals  $s_1(t)$  and  $s_2(t)$ , constant-envelope phase code words that have been chosen at random and made part of a code. Although these signals could be expressed in the vector notation of the last section, it is more direct to denote them as the equivalent time functions. From (2.15)–(2.19), the probability that a maximum likelihood decoder picks  $s_2$  given that  $s_1$  was transmitted is

$$P_{2,e} = \mathcal{E}[Q(\|s_1 - s_2\|/(2N_0)^{1/2})] \quad (5.14)$$

where  $\|s_1(t) - s_2(t)\|$  is the signal space distance between the signals and (2.15) has been specialized to the case of just two signals. The expectation

operator is over the code choice distribution. From Section 2.2,  $\|s_1 - s_2\|^2 = 2E_b d^2(s_1, s_2)$ , with

$$d^2(s_1, s_2) = (\log_2 M)/T \int [1 - \cos \Delta\phi(t, \alpha)] dt$$

If  $R$  is the rate of the code in bits per signal interval and the code extends over  $N$  signal intervals, then the code contains  $2^{NR}$  words, each selected by the same as yet unnamed probability distribution.

The union bound of probability states that the overall probability of error when  $s_1$  is transmitted is overbounded by  $2^{NR}P_{2,e}$ , since by the method of code selection, all the properties of the remaining words are identically distributed.

Now define the bound parameter  $R_0$  to be

$$R_0 = -(1/N) \log_2 P_{2,e} \quad (5.15)$$

Then the union-bound overbound becomes  $2^{-N(R_0 - R)}$ . This tends exponentially to zero with the code word length whenever  $R < R_0$ . The same bound must apply to all transmitted sequences  $s_i$ , since the choice of all is identically distributed. We have thus shown that one can choose a code and then use a word of it to transmit data, with arbitrarily small error probability.

The simple error exponent  $(R - R_0)$  is generally weaker than the exponent  $E(R)$  that appears in (5.4), and in particular,  $R_0$  is less than capacity so that  $(R - R_0)$  is useless for a range of rates between  $R_0$  and  $C$ . The situation is shown in Figure 5.9, which compares a typical  $E(R)$  for

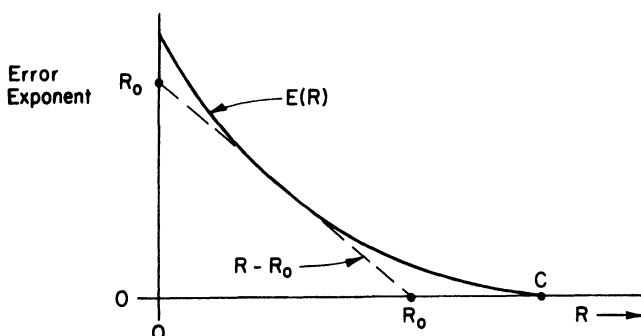


Figure 5.9. Comparison of cutoff rate bound  $(R - R_0)$  to actual error exponent  $E(R)$ , showing approximate relationship.

an IDMC to  $(R - R_0)$ . The two exponents are similar over the middle range of rates. For the antipodal modulation channel of Figure 5.5c, it is known that  $R_0 = C/2$  and that the best exponent  $E(R)$  is the same as  $(R - R_0)$  for rates below  $C/4$ ; however, one should beware of extending such results to more complicated channels or to channels with memory. An exposition on the exponent  $E(R)$  appears in Gallager<sup>(1)</sup> or Viterbi and Omura.<sup>(2)</sup>

The quantity  $R_0$  is closely related to the *cutoff rate*  $R'_0$ , which we shall define as the maximization of  $R_0$  over the choice of the distribution function of the code word choice. In a IDMC with binary inputs it is clear from symmetry that the choice of code word letters should be equiprobable and analysis shows that they should be independently selected as well. For the general phase modulation channel, which is not memoryless, finding  $R'_0$  devolves into optimizing the distribution of the sequence of symbols  $\alpha^N$ . It is not clear that the individual  $\alpha_i$  should be selected independently, or in the case of a nonbinary  $\alpha_i$ , that it should be selected equiprobably. To circumvent these difficulties, we always choose the letters of  $\alpha$  independently and equiprobably, and denote the bound parameter so obtained as  $R_0$ .  $R_0$  may fall somewhat below the true cutoff rate.

Several authors, notably Massey,<sup>(8)</sup> have shown that the cutoff rate is a fundamental parameter of a channel. It is closely related to the performance of convolutional codes on the BSC and to the computation required by sequential decoding methods. Studies of IDMCs have shown that the optimized  $R'_0$  is often little different from the uniform-distribution  $R_0$  (see Wozencraft and Jacobs<sup>(6)</sup>).  $R_0$  for phase modulation channels was explored in our paper, Ref. 9.

### *A Markov Chain for Signal Phase Differences*

Suppose that a phase code word has been generated by the sequence  $\alpha_0, \alpha_1, \dots$ . The symbol  $\alpha_n$  occurs just after time  $nT$  and the function  $q(\cdot)$  distributes and smooths the resulting phase change out over the next  $LT$  seconds. In any one interval, the effects of  $(L - 1)$  of the  $\alpha_i$  superpose via (5.13). Recall that even though we have carried over the notation  $\alpha$ , these are no longer the data symbols.

To derive a bound of the cutoff rate type, we need to consider the distance between two signals of the same amplitude but different phase. This distance depends on the phase difference  $\Delta\phi(t)$  through (2.19), and  $\Delta\phi(t)$  itself is a linear function of the difference of the two  $\alpha$  sequences because of the linearity of (5.12). Carrying over the notation of Chapter 3, we can denote this difference as  $\gamma$ . As an example, consider the case of Figure 5.8, 1REC phase smoothing. From (5.13) the phase difference in the

interval  $nT < t \leq (n+1)T$  is

$$\begin{aligned}\Delta\phi(t, \gamma) &= 2\pi h \sum_{i=n-L+1}^n [\alpha_i(2) - \alpha_i(1)] q(t - iT) + \pi h \sum_{i=0}^{n-L} [\alpha_i(2) - \alpha_i(1)] \\ &= 2\pi h \gamma_n(t - nT)/2T + \Delta\theta_n\end{aligned}\quad (5.16)$$

Figure 5.8b shows all the phase differences that can occur in a signaling interval for a binary  $\alpha$  sequence and  $h = 1/4$ . Note that if two phase trajectories in a pair are deflected by identical  $\alpha_n$ 's, their separation will remain fixed, and this case is shown only once.

From (5.13) it is clear that  $\phi(t, \gamma)$  in an interval forms a Markov chain, and this will be a finite state chain if the differences  $\gamma$  are constrained to be multiples of  $2\pi/\eta$ . This will be the case if  $h$  is a multiple of  $1/\eta$ . The full specification of the difference Markov chain is tedious and we will postpone a sketch of it to Appendix B. Once the chain is defined, it is necessary to compute the expectation in (5.14) for two long phase trajectories. The signal space distance  $\|s_1 - s_2\|$  grows in a Markov manner, driven by the phase difference chain; the expectation follows from the eigenvalues of a matrix derived from the state transition matrix of this chain. These technicalities also appear in Appendix B.

## 5.5. Numerical Results for $R_0$

Figures 5.10–5.12 show numerical values of  $R_0$  as a function of the energy  $E$  available in an interval. Note that this is not the data symbol energy because each interval no longer carries a full symbol. The three

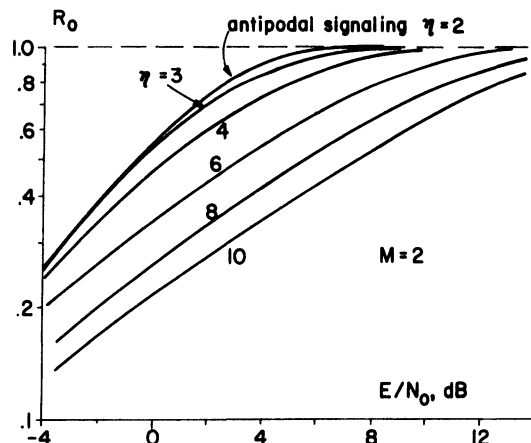


Figure 5.10.  $R_0$  (in bit/T) as a function of normalized interval energy,  $E/N_0$ , for modulation indices  $1/\eta$ ; binary CPFSK (1REC) Shannon phase codes. From Ref. 9.

figures show  $R_0$  vs.  $E$  for different modulation indices  $h = 1/\eta$ , symbol alphabets for the symbols  $\alpha_n$ , and degrees of smoothing. Generally, the results show that if a reasonable signal energy is available, there is a strong preference for larger symbol alphabets and smoothing leads to little degradation.

In Figure 5.10, the symbol alphabet  $M$  is fixed at two choices out of each phase trellis node while  $\eta$  varies up to 10. Linear phase, or CPFSK (1REC), smoothing applies. As  $\eta$  increases, the modulation index contracts, phase paths converge and diverge more slowly from each other, and  $R_0$  is reduced. The bandwidth, however, is falling dramatically at the same time. When  $\eta = 2$ ,  $R_0$  is identical to the cutoff rate for pure BPSK or QPSK, that is, for antipodal signaling on the orthogonal modulation channel. We repeat this curve on the next two figures for reference.

Figure 5.11 fixes  $\eta$  at 4 and varies the alphabet of  $\alpha$ , describing therefore the Shannon codes with phase changes that are some multiple of  $2h\pi = \pi/2$ . At large  $E/N_0$  ratio,  $R_0$  tends to  $\log_2 M$ , the maximum rate of an  $M$ -ary transmission system. The capacity of an  $M$ -ary input AWGN is  $\log_2 M$  as well, but the capacity for the AWGN channel of Figure 5.5b, which has arbitrary inputs, is presumably much larger at this energy. At low  $E/N_0$ , all curves converge to the antipodal signaling reference. Above 0 dB,  $R_0$

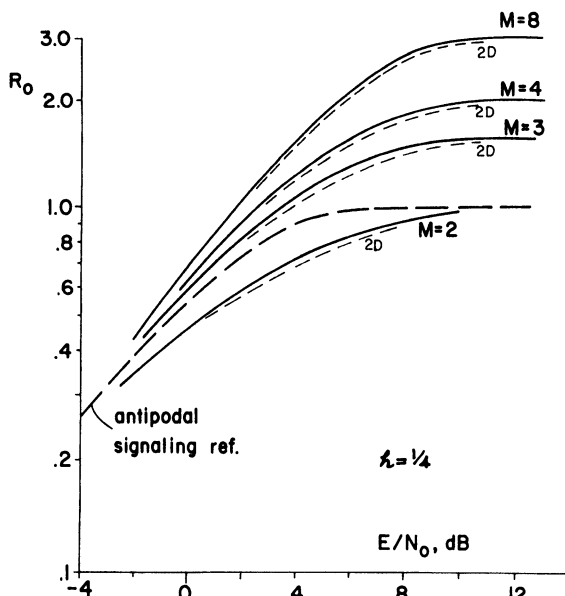


Figure 5.11.  $R_0$  (in bit/ $T$ ) as a function of  $E/N_0$  at modulation index  $1/4$ , for alphabet sizes 2, 3, 4, and 8. Solid curves are CPFSK, dashed curves are 2D, a 2-interval quadratic smoothing of phase. Only slight degradation occurs. From Ref. 9.

rapidly improves as more slope choices become available, and so long as  $M > 2$ , it lies well above antipodal signaling;  $M$ -ary signaling should thus have much better error performance at the same rate compared to binary signaling.

Figure 5.12 shows the effect of successively higher smoothing, spread over from 0 to 3 intervals, with the symbol alphabet set at 4 and  $h = 1/4$ . 2RC and 3RC smoothing were discussed in Chapter 3; 2D and 3D refer to quadratic and cubic smoothing, which are defined in Ref. 9. In all cases, the numeral is  $L$ , the number of intervals over which a phase change is spread.

There is a degradation of perhaps 3% for each unit increase in  $L$ . It is striking how little  $R_0$  is degraded by higher smoothing order, considering the bandwidth improvements that stem from smoothing. A pair of smoothed phase paths are forced to remain close together once they approach each other and to remain apart once separated; apparently, these two effects roughly counterbalance. The small drop in  $R_0$  may be made up by a small increase in signal energy or in code complexity. Consider for example a

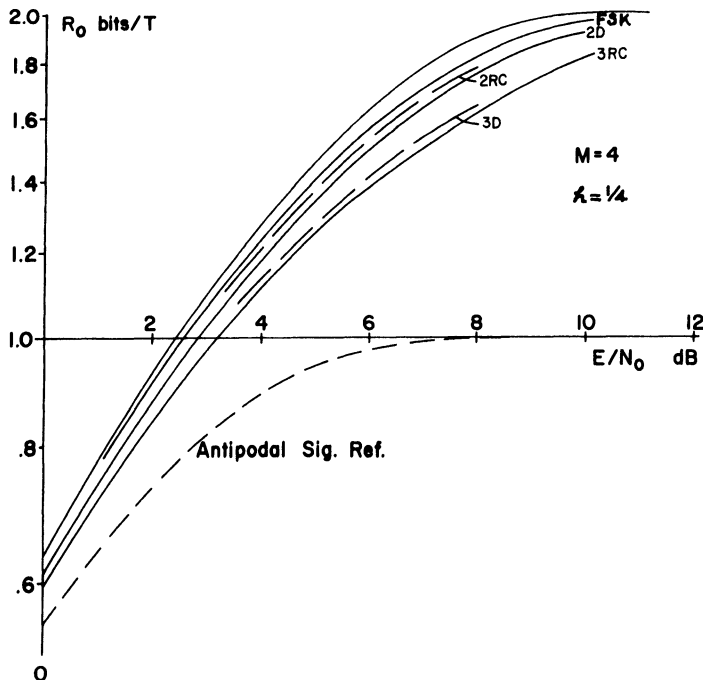


Figure 5.12.  $R_0$  (in bit/T) as a function of  $E/N_0$  for modulation index 1/4 and alphabet size 4, showing the effect of degree and type of smoothing. The  $R_0$  scale is expanded to show changes more clearly. The topmost curve represents QPSK-like signals. From Ref. 9.

code carrying 1 data bit/ $T$ -interval at  $E/N_0 = 6$  dB. With an  $\alpha$ -alphabet of 4 and  $\eta = 4$ ,  $R_0 = 1.52$  for 2RC smoothing and 1.56 for 1REC smoothing; the error probability of a good random code is thus bounded asymptotically by  $\exp_2(-0.52N)$  for 2RC and  $\exp_2(-0.56N)$  for 1REC. Thus 2RC smoothing requires a 7% increase in the code word length  $N$  for the same error bound, or alternately, the figure shows that a 0.4-dB energy increase will suffice.

## 5.6. Energy–Bandwidth Plots Derived from $R_0$

The parameter  $R_0$  provides an effective tool for simultaneously comparing the energy and bandwidth of different types of phase modulation codes. If a code has rate  $R$  bits/ $T$ -interval and if it consumes  $E$  joules in each interval, its energy consumption per data bit  $E_b$  is  $E/R$  and the time devoted to each data bit  $T_b$  is  $T/R$ . The bandwidth consumed by a smoothed signal driven by random symbols  $\alpha$  at the rate of one per  $T$  seconds has been computed in Chapter 4. If  $B$  is this bandwidth, reckoned in some sense like, for instance, in-band power, the bandwidth consumption per data bit is  $BT_b$ . Counting positive frequencies only rf bandwidth is  $2BT_b$ . We have thus converted energy and bandwidth to per-data-bit quantities by scaling  $E$  and  $B$  by  $1/R$  and  $T/R$ .  $R$  can be at least as large as  $R_0$ , so that these scalings are at least as small as  $1/R_0$  and  $T/R_0$ .

Figures 5.13–5.15 show the trajectories in the energy–bandwidth plane that occur as  $R_0$  is varied by means of changing the interval energy  $E$ . The definition of bandwidth is the bandwidth inside which lies 99% of the power; this means that the power out of band is 20 dB below that which is in band. Figure 5.13 depicts the case of binary symbol choice, and 5.14 the case of quaternary choice, while 5.15 summarizes all cases and compares them to the performance of parity check coding. Figures 5.13 and 5.14 consist of a number of superposed curves, one for each modulation index  $h$ . As a rule, each  $h$  minimizes energy and bandwidth over only a short range of these commodities, compared with other  $h$  used in the calculations.  $R_0$  does not explicitly appear in the plots, but it is generally true that if  $h$  and  $E/N_0$  are well chosen,  $R_0$  will be at 85%–95% of  $\log_2 M$ . The direction of better performance in these plots is down and to the left.

In Figure 5.13 solid curves show linear smoothing over one interval and dashed curves show cubic smoothing spread over three intervals. For linearly smoothed transmission at 1 Hz/bit (double-sideband), for example, the best  $h$  evidently lies between 1/4 and 1/6, but at 1.4 Hz/bit, such an  $h$  causes an unnecessary bandwidth expansion of about 40%. Viewed in the energy dimension, 1 Hz/bit may be obtained with  $E_b/N_0 = 8$  dB using the optimal  $h$ , but requires 9 dB with  $h = 1/8$  and is not possible at all with  $h$

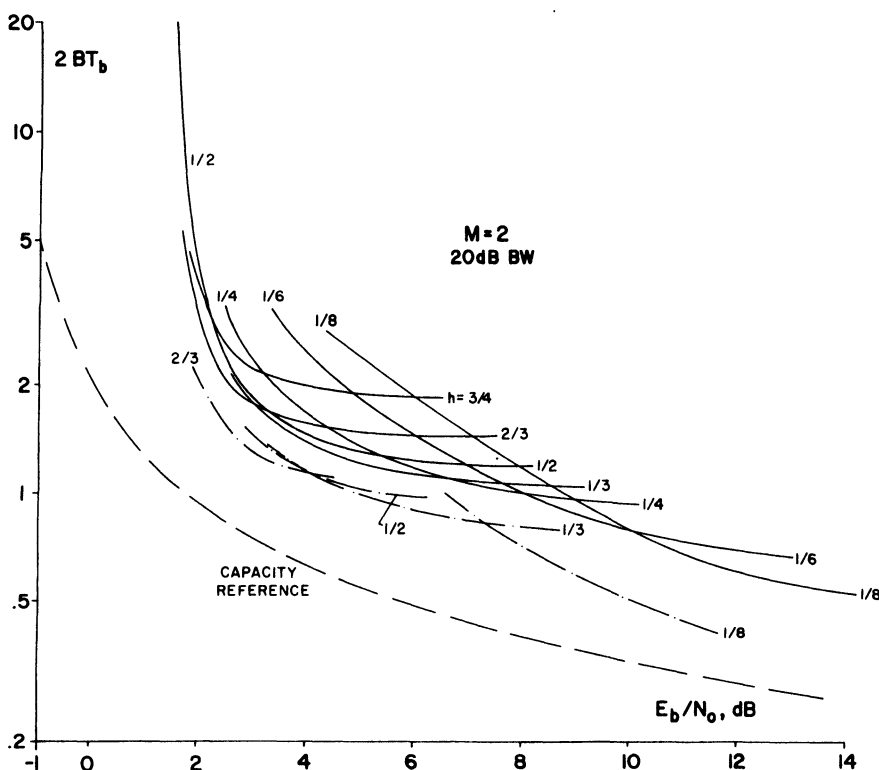


Figure 5.13. Energy-bandwidth plot of Shannon phase codes. The interval energy and  $R_0$  vary along each curve. CPFSK and order-3 smoothing curves are shown, one for each modulation index; 99% (20 dB) power bandwidth and alphabet size 2. From Ref. 9.

greater than  $1/4$ . It is interesting that  $h = 1/2$ , which produces an ensemble of signals that resemble MSK, is not preferred at any bandwidth. The dashed curves show that three-interval cubic smoothing consistently reduces bandwidth by 20% or more; this shows that the bandwidth-reducing effect of smoothing has overwhelmed the slightly degraded  $R_0$ .

Figure 5.14 portrays linear, 2RC, and 3RC smoothing when the symbol alphabet is quaternary. Besides the 20-dB power bandwidth, the wider 40-dB bandwidth appears as well. Third-order smoothing again leads to a 20% bandwidth reduction of the 20-dB bandwidth, and a 60% reduction of the 40-dB bandwidth. This is because smoothing more dramatically affects the spectral tails than the main lobe. Figure 5.15 summarizes these two plots as well as other data. It is clear that a quaternary alphabet of phase choices is much better than a binary one in the range of  $E_b/N_0$  that is of practical interest. A 30%–40% bandwidth savings occurs, or alternately, perhaps 5 dB energy can be saved. A change to an octal alphabet produces another

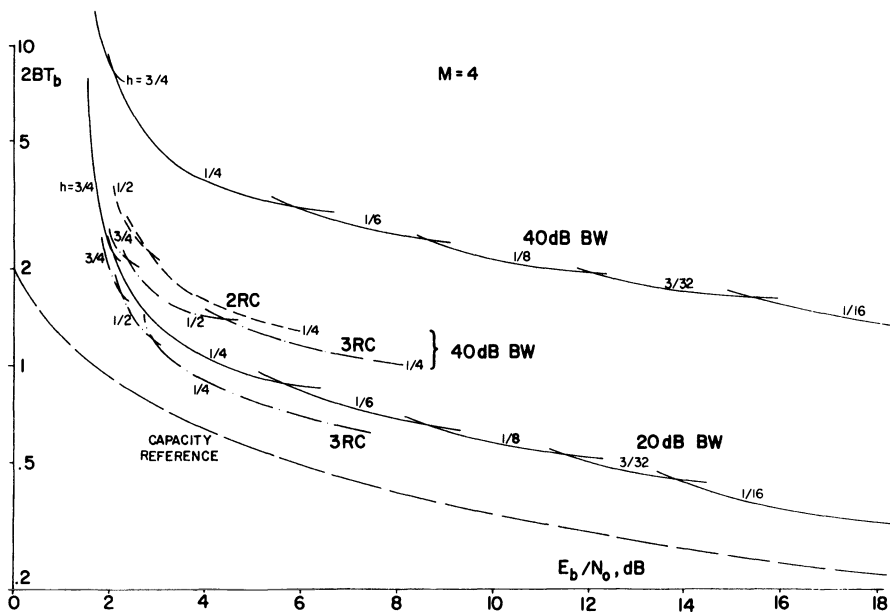


Figure 5.14. Energy-bandwidth plot of Shannon phase codes. CPFSK (solid curves), 2RC and 3RC smoothing and alphabet size 4; 99% (20 dB) and 99.99% (40 dB) power bandwidths are shown. From Ref. 9.

small improvement, but the main gain is from binary to quaternary. These conclusions are similar to those in Section 5.1, which were based on Euclidean distance.

#### *Comparison to BSC and Parity Check Coding*

By computing the corresponding cutoff rates, we can compare phase modulation codes to coding with a simpler channel model like the BSC or to coding with parity check coding and modulation that occur in separate blocks. The cutoff rate for BSC with crossover probability  $p$  is

$$R'_0 = 1 - \log_2 \{1 + 2[p(1-p)]^{1/2}\} \quad (5.17)$$

In this channel model,  $p = Q((2E/N_0)^{1/2})$ , on the assumption that the interval energy  $E$  is devoted to an antipodal signaling method; codes exist with rates at least  $R'_0$  bits/interval. The cutoff rate for the antipodal modulation channel (often called a "soft decision" channel) is

$$R'_0 = 1 - \log_2 [1 + \exp_e(-E/N_0)] \quad (5.18)$$

a larger quantity. The inputs to both these channel models are binary

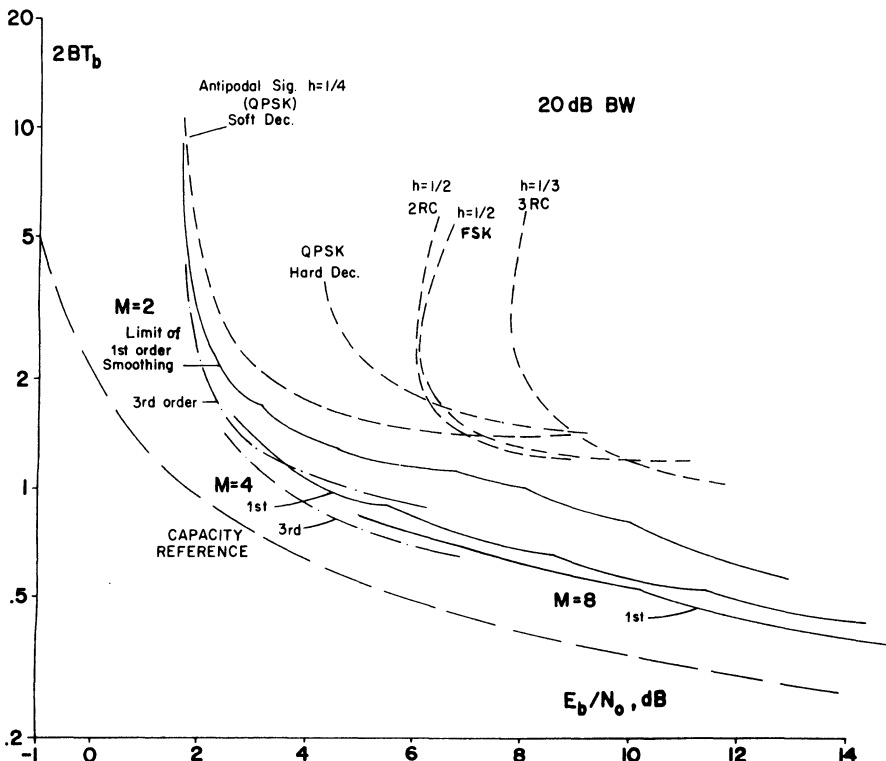


Figure 5.15. Summary of energy-bandwidth performances, showing limit to performance with alphabet size 2, 4, and 8, and CPFSK and 3RC smoothing. Dashed curves show performance of modulation-plus-binary coding with signal space decoding, including QPSK with and without soft decisions, and CPFSK, 2RC, and 3RC modulations combined with binary coding. 20-dB bandwidth is used, except 15 dB for QPSK (20-dB bandwidth is 3 times larger). From Ref. 9.

sequences and code words are made up of these symbols, one per signal interval; both cutoff rates are overbounded by 1 bit/interval. The coding could be, for instance, parity check coding.

A set of trajectories appear in Figure 5.15 for these two types of transmission. Pure QPSK is assumed for the modulation and the bandwidth used is the 15-dB out-of-band power bandwidth, which is about 1/3 of the 20-dB bandwidth, so that the curves are optimistic compared to the others. (As an alternative, one might use Nyquist-pulse QPSK, but this will be a nonconstant envelope scheme; it will occupy a similar bandwidth.) It can be seen from the figure that these less direct forms of coding perform considerably worse than the full phase modulation coding approach, as judged by this cutoff rate method of comparison. Bandwidth is perhaps twice as large and energy consumption is 3–5 dB worse.

Finally, we can plot the case of binary coding combined with a more sophisticated modulator of the type developed in Chapter 3. We will assume that the demodulator has a sufficiently long observation interval, that it is maximum likelihood, and that the error events that do occur are randomized by perfect interleaving. The ensuing error rate is assumed to be that of a BSC, whose cutoff rate for binary encoding is given by (5.17). In Figure 5.15 appear the cases of MSK, 2RC smoothing with the same modulation index,  $1/2$ , and a 3RC modulator with  $h = 1/3$ . In all cases, the performance is much worse than direct phase modulation coding with the same  $h$  and smoothing.

All the schemes in Figures 5.13–5.15 have constant signal envelope. For comparison, a capacity reference curve has been plotted, which represents the capacity of a Gaussian channel with the same power level and bandwidth as implied by the coordinates of the plot. One must beware of an exact comparison to such a curve, which among other sins does not consider bandwidth in the “20-dB” sense. Nonetheless it appears that constant-envelope signaling, with its tolerance of nonlinear rf amplifiers, etc., does not lie far off from capacity. It is also clear from the plots that narrowband constant-envelope signaling requires in theory small modulation indices; these in turn place a strain on synchronization circuitry.

## References

1. R. G. Gallager, *Information Theory and Reliable Communications*, Wiley, New York, 1968.
2. A. J. Viterbi and J. K. Omura, *Principles of Digital Communications and Coding*, McGraw-Hill, New York, 1979.
3. H. J. Landau and H. O. Pollak, Prolate spheroidal wave functions, Fourier analysis and uncertainty, Part III: The dimension of the space of essentially time- and band-limited signals, *Bell Syst. Tech. J.* **41**, 1295–1336 (1962).
4. D. Slepian and H. O. Pollak, Prolate spheroidal wave functions, Fourier analysis and uncertainty, Part I, *Bell Syst. Tech. J.* **40**, 43–64 (1961).
5. C. E. Shannon, Probability of error for optimal codes in a Gaussian channel, *Bell Syst. Tech. J.* **38**, 611–656 (1959).
6. J. M. Wozencraft and I. M. Jacobs, *Principles of Communications Engineering*, Wiley, New York, 1965.
7. R. de Buda and W. Kassem, About lattices and the random coding theorem, *IEEE Trans. Inf. Theory*, in press (1985).
8. J. Massey, Coding and modulation in digital communications, Proceedings, Int. Zurich Seminar on Digital Communications, Zurich, Switzerland, March 1974.
9. J. B. Anderson, C.-E. Sundberg, T. Aulin, and N. Rydbeck, “Power-bandwidth performance of smoothed phase modulation codes,” *IEEE Trans. Commun. COM-29*, 187–195 (1981).
10. T. Aulin and C.-E. Sundberg, CPM—An efficient constant amplitude modulation scheme, *Int. J. Satellite Commun.* **2**, 3, 161–186 (1984).

# Transmitters

In this chapter we investigate implementation aspects of different CPM modulators. Only CPM schemes with fixed modulation index  $h$  are considered. Thus multi- $h$  schemes and coded phase modulation are not considered, but it is straightforward to generalize the transmitters that we discuss. We will first give some general structures and then discuss the practical implementation aspects of each with a few special cases in mind. More details on this subject are in the study reports in Refs. [1 and 2].

A conceptual transmitter structure is shown in Figure 6.1. It has been mentioned in Chapter 2 and in a more general form in Chapter 3. Because of the exact relation needed between the symbol rate and the modulation index, this structure is not easily converted into a practical modulator. An advantage is that the structure can be used interchangeably with digital and analog input. de Jager and Dekker<sup>(3)</sup> recently studied the practical aspects of this structure, and found that the VCO sensitivity must be monitored by a control circuit to prevent a large cumulative phase error. In this chapter we will concentrate on transmitter structures other than this direct one.

Section 6.1 deals with the general quadrature transmitter structure of Figure 6.2. This structure is referred to as the ROM-structure in the sequel. Section 6.2 deals with a structure based on a simple PSK modulator followed by a phase-locked loop<sup>(6)</sup> with a certain loop-transfer function; see Figure 6.3. This structure has certain limitations on the  $g(t)$  pulses that can be

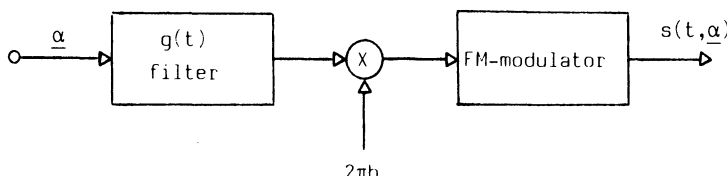


Figure 6.1. Conceptual modulator for fixed  $h$  CPM.

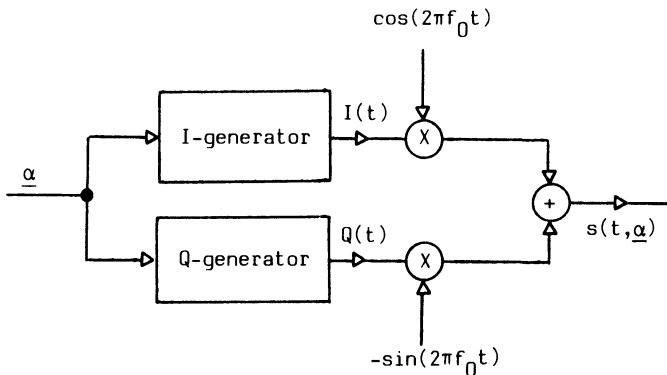


Figure 6.2. Basic quadrature transmitter structure.

implemented. It is also limited in the maximum modulation index. In terms of speed it has advantages, though. Section 6.3 describes a simple modulator followed by a bandpass filter and limiter,<sup>(5)</sup> as in Figure 6.4. This approach is not easy to analyze exactly. A theoretical analysis applicable for small modulation indices is included. In practical terms this modulator is similar to the PLL approach.

Some alternative approaches for important special cases of CPM are discussed in Section 6.4, including serial generation of MSK.

### 6.1. Read Only Memory Implementations

The most general and most straightforward way of implementing a CPM transmitter is to use the basic formula for the modulated signal separated into quadrature components. These are stored in sampled and quantized form in look-up tables, e.g., in read only memories (ROMs). In this way one can design a transmitter capable of changing between different modulation systems just by changing the contents of the ROM storages. This transmitter structure is also very well suited for implementation in very large-scale integrated circuits (VLSI). It is possible to integrate the full modulator in only one VLSI circuit even for fairly high-speed applications. The ROM implementation has gained great popularity in recent years in

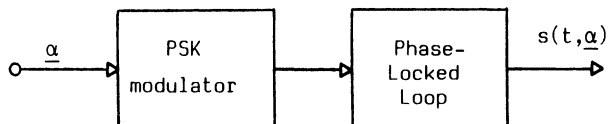


Figure 6.3. Phase-locked loop modulator for CPM.

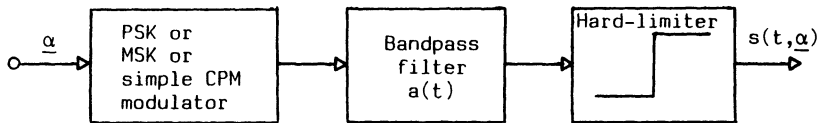


Figure 6.4. CPM modulator with a bandpass filter and hard-limiter.

telephone modem and mobile radio applications. In the following we first give the theoretical background in a condensed form and then continue by discussing practical implementation aspects. For background information, see Chapters 2 and 3.

### 6.1.1. ROM Transmitter Theory

The normalized transmitted signal  $s_0(t, \alpha_n)$  is

$$s_0(t, \alpha_n) = \cos(2\pi f_0 t + \phi(t, \alpha_n)) \quad (6.1)$$

where subscript  $n$  denotes that we are considering the normalized transmitted signal over the time interval corresponding to the  $M$ -ary data symbol  $\alpha_n$ . Dividing  $s_0(t, \alpha_n)$  into quadrature components yields

$$s_0(t, \alpha_n) = I(t) \cos(2\pi f_0 t) - Q(t) \sin(2\pi f_0 t) \quad (6.2)$$

where, as in Section 2.4

$$I(t) = \cos[\phi(t, \alpha_n)]$$

$$Q(t) = \sin[\phi(t, \alpha_n)]$$

The modulated phase is

$$\phi(t, \alpha_n) = \theta(t, \alpha_n) + \theta_n \quad (6.3)$$

where

$$\begin{aligned} \theta(t, \alpha_n) &= 2\pi h \sum_{i=n-L+1}^n \alpha_i q(t - iT) \\ \theta_n &= \pi h \sum_{-\infty}^{n-L} \alpha_i \end{aligned}$$

$\theta_n$  represents the phase state and  $\theta(t, \alpha_n)$ ,  $nT \leq t < (n+1)T$ , is the branch in the phase trellis; state descriptions are discussed in Section 3.4.1.

The quadrature transmitter in Figure 6.2 avoids the problems of Figure 6.1 since the  $I(t)$  and  $Q(t)$  generators are clocked with a multiple of the bit rate. The  $I(t)$  and  $Q(t)$  generators for a general  $M$ -ary system can be implemented in many ways.<sup>(1,4,11)</sup> One straightforward solution is shown in Figure 6.5. This transmitter is a generalization to arbitrary  $h$  values of the transmitter proposed in the original TFM paper by de Jager and Dekker.<sup>(3)</sup> In this solution all possible  $I(t)$  and  $Q(t)$  shapes over one symbol interval  $T$  are stored in memories and addressed by the states  $(\alpha_{n-1}, \theta_n)$  and the present input symbol  $\alpha_n$ . The phase states  $\theta_n$  are generated by a sequential machine consisting of a phase state ROM and a delay of length one symbol interval  $T$ . At each symbol time the data sequence  $\alpha_n$  and the phase state  $\theta_n$  determines the next phase state  $\theta_{n+1}$ . The phase state machine is preferably constructed with phase state serial numbers  $v_n$  instead of actual phase state values  $\theta_n$ . In this case it can often be implemented as an up/down counter, with the  $v_n$  related to the phase values  $\theta_n$  by the equation

$$\theta_n = (h\pi v_n + \phi_0) \bmod (2\pi) \quad (6.4)$$

where  $\phi_0$  is an arbitrary phase constant. In the following  $\phi_0$  is set to zero. The  $I(t)$  and  $Q(t)$  shapes are swept by a counter  $C$  at the rate  $m(1/T)$ , where  $m$  is the number of stored samples per symbol interval  $T$ .

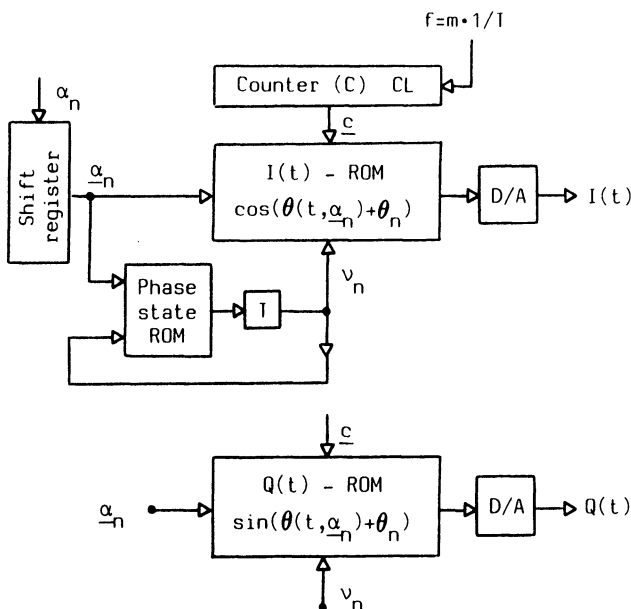


Figure 6.5. ROM Transmitter.  $I$ - and  $Q$ -generator structure. The phase state number  $v_n$  corresponds to the phase state value  $\theta_n$ .

In general the  $I(t)$  ROM size is given by

$$R_s = pM^L mm_q \quad (6.5)$$

where  $m_q$  is the number of bits per sample (i.e., quantization accuracy) and  $p$  is the number of phase states ( $h = 2k/p$ ). Each signal in the ROM is identified by an address of length  $L$   $M$ -ary data symbols and a phase state number. The  $Q(t)$  ROM is of course the same size. As an example, the size of the  $I(t)$  ROM is 1024 bits for  $M = 2$ , 3RC ( $L = 3$ ),  $h = 0.5$ ,  $m = 4$ , and  $m_q = 8$ . The size of the phase state ROM is normally very small compared to  $R_s$ . In the example above the phase state ROM size is only 16 bits.

The  $I(t)$  and  $Q(t)$  ROM size can be reduced by a factor  $p$  by rewriting  $I(t)$  and  $Q(t)$  as

$$\begin{aligned} I(t) &= \cos [\theta(t, \alpha_n) + \theta_n] \\ &= \cos [\theta(t, \alpha_n)] \cos (\theta_n) - \sin [\theta(t, \alpha_n)] \sin (\theta_n) \end{aligned} \quad (6.6a)$$

$$\begin{aligned} Q(t) &= \sin [\theta(t, \alpha_n) + \theta_n] \\ &= \cos [\theta(t, \alpha_n)] \sin (\theta_n) + \sin [\theta(t, \alpha_n)] \cos (\theta_n) \end{aligned} \quad (6.6b)$$

A transmitter implementation based on the above formula is given in Figure 6.6. The penalty for the  $p$ -fold ROM reduction is four multipliers and two small ROMs [ $\cos(\theta_n)$  and  $\sin(\theta_n)$ ] of size  $pm_q$  bits.

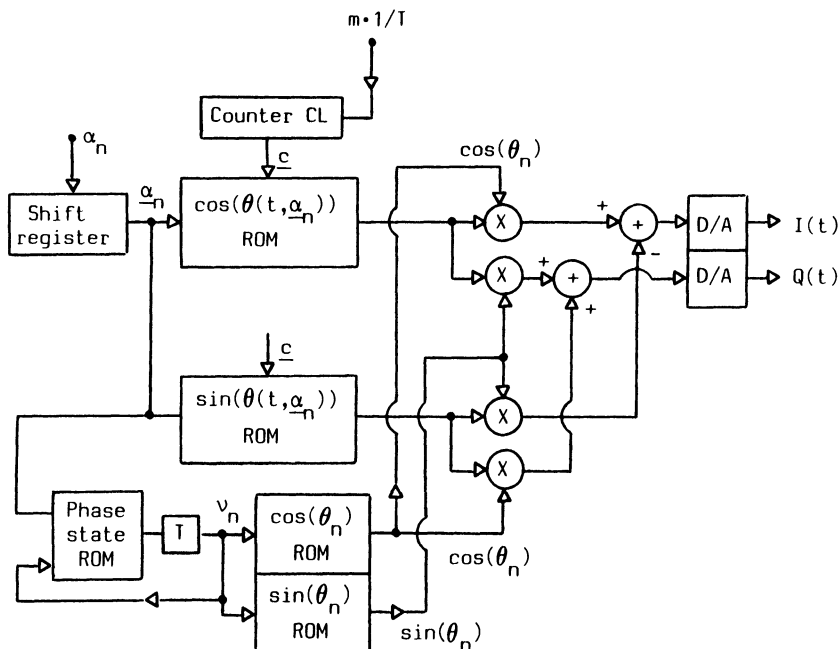


Figure 6.6. ROM Transmitter.  $I(t)$  and  $Q(t)$  generators with reduced ROMs.

Another possibly better transmitter structure is based on stored phase values instead of stored cosines and sines. This structure is shown in Figure 6.7. The scheme avoids multipliers and double cos/sin ROMs but adds one cos-sin converting ROM at the end. This final ROM must be able to “fold” input values  $\pm(M - 1)h\pi$  outside the normal  $\pm\pi$  range. The phase path ROM contains all possible phase paths  $\theta(t, \alpha_n)$ . The phase state sequential machine generates the successive phase state serial numbers  $v_n$ . These numbers are converted to actual phase values  $\theta_n$  in a small converting ROM. The phase paths  $\theta(t, \alpha_n)$  and  $\theta_n$  are then added in a digital adder and converted to  $I(t)$  and  $Q(t)$  in a fairly small cos/sin ROM.

The total ROM size of this transmitter is sometimes smaller than that of the previous one. The main reason is that only one phase path ROM and one phase state converting ROM is needed instead of two in the transmitter in Figure 6.6. The saving in ROM size by this should be compared to the size of the converting output ROMs. Further implementation aspects are covered in Refs. [1 and 4].

Recently it has been suggested that simplified ROM transmitters can be implemented simply by storing  $\cos[2\pi f_i t + \phi(t, \alpha)]$  in sample form. The frequency  $f_i$  is a suitably chosen intermediate frequency. The rf signal is obtained after straightforward up conversion.

### 6.1.2. Practical Considerations for ROM Transmitters

In this section we present some of the results of the implementation studies in Ref. 1. The results concentrate on the following three topics: Numerical precision, discrete MSI implementation with high-speed ECL circuitry, and LSI implementation.

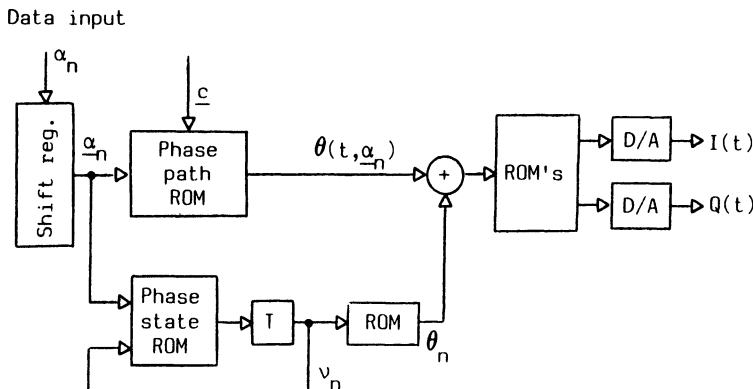


Figure 6.7. Transmitter structure with phase ROMs instead of “ $I$  and  $Q$ ” ROMs. The output ROM must tolerate input addresses from  $-\pi - (M - 1) \cdot h\pi$  to  $\pi + (M - 1) \cdot h\pi$  for positive  $g(t)$  pulses and slightly more for  $g(t)$  pulses with side lobes.

In the ROM transmitter solution discussed above the ROM contain a number  $m$  of phase branch samples for each symbol time. These samples are stored with a certain numerical precision, i.e., with a certain number of bits per sample. The number of samples per symbol  $m$  and the number of bits per sample  $m_q$  (quantization) differs for different applications. For example, if the number of samples per symbol is too low the spectrum will replicate too close to the desired spectrum and thus give a form of aliasing distortion and difficulties with the final filtering; compare Figures 6.8 and 6.9. The simulations presented in these figures show the behavior of the transmitter spectrum with four and eight samples per symbol time. The frequency scale is normalized to the bit rate. Further examples are given in Ref. 1.

We have assumed that the ROM transmitter produces a staircase output waveform, thus giving a  $(\sin x)/x$  envelope to the periodically repeating power spectrum. It is obvious that the analog low-pass filtering following the ROM transmitter must be narrow enough to reduce the repeated power spectrum peak further. This is a straightforward filtering problem.

The quantization noise created by the limited number of bits per sample is likely to appear as a more or less white background noise. The magnitude of this noise can be estimated to be of the order of one half of a quantization

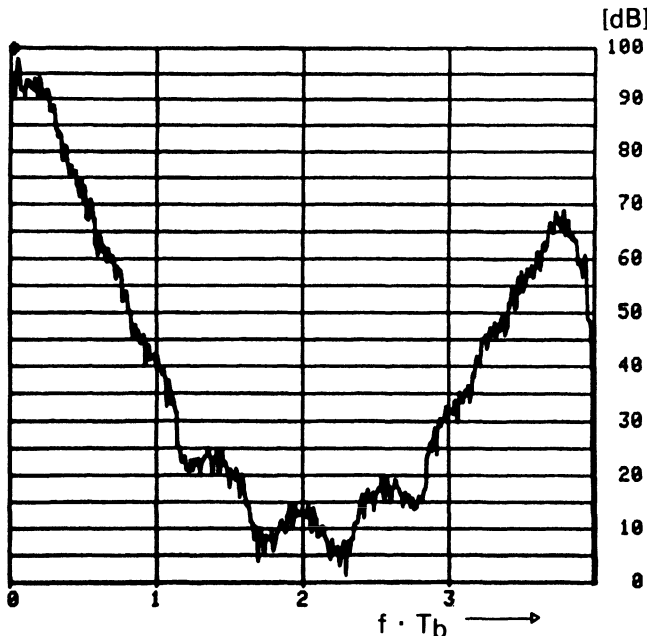


Figure 6.8. Simulated power spectrum for 2RC,  $M = 4$  with  $h = 1/3$ ,  $m = 8$  samples/symbol.

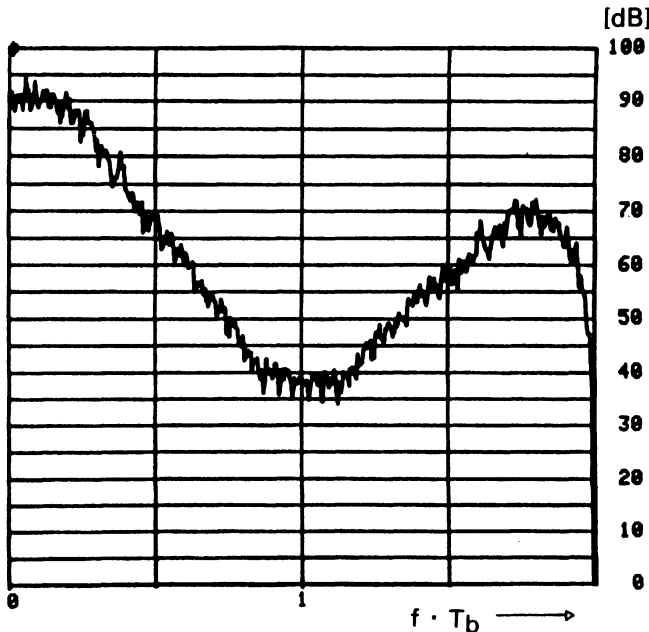


Figure 6.9. Simulated power spectrum for 2RC,  $M = 4$  with  $h = 1/3$ ,  $m = 4$  samples/symbol.

step. Thus with  $m_q$  bit/sample this noise level will be of order  $-20 \log_{10}[2^{(m_q+1)}] = -6(m_q + 1)$  dB below the carrier level. This means that if an adjacent channel level of at least  $-30$  dB is required, at least 5-6 bit quantization is needed in the ROM transmitter. For other applications, such as mobile radio systems with adjacent channel requirements of  $-70$  dB, 10-12 bits per sample seem to be necessary. A number of computer simulations concerning quantization and sampling effects have been carried out in Ref. 1. The simulations use a ROM transmitter with different quantizations on the  $I(t)$  and the  $Q(t)$  signals. The power spectrum simulations are based on 512 samples and the power spectra are average over eight such 512 sample frames. The basic computer precision is about 16 bits, thus making the highest obtainable quantization approximately  $m_q \approx 16$ . The frequency scales in the power spectra in the figures below are normalized with the bit rate. The spectra are shown from the carrier to the aliasing point (i.e., half the sampling frequency). The effect of the quantization on the  $I(t)$  signal is also shown for certain parameter values. The data word length is 64 bits.

Figure 6.10 shows the result of the simulations of the quantization noise. We notice that the straight line  $-6(m_q + 1)$  is a fairly good approximation for  $m_q = 4\text{-}14$  bits. Figures 6.11a-6.11c show the spectrum of a quaternary 2RC scheme with modulation index  $h = 1/3$ ,  $m_q = 16, 8$ , and 4 bit

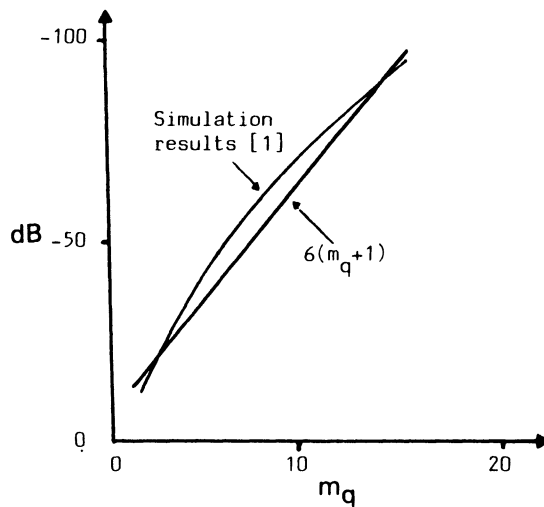


Figure 6.10. Quantization noise versus the number of bits per sample  $m_q$ .

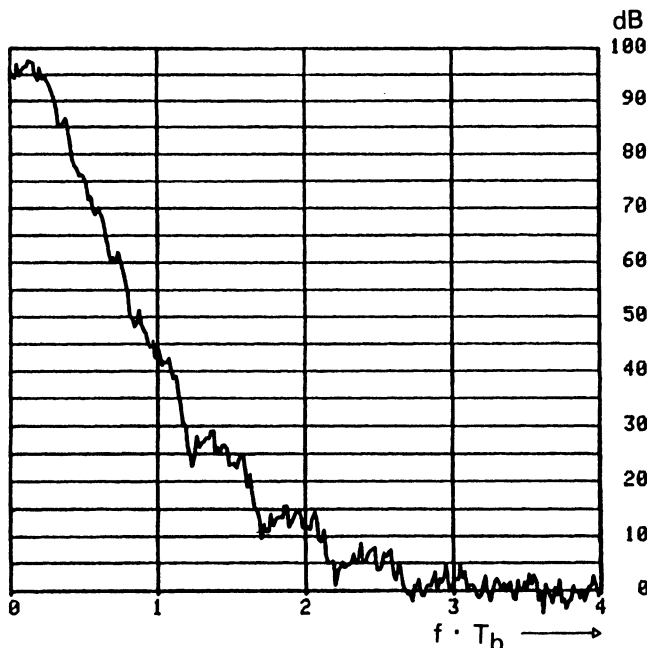


Figure 6.11a. Simulated power spectrum for quaternary 2RC with  $h = 1/3$ ,  $m = 16$ ,  $m_q = 16$ .

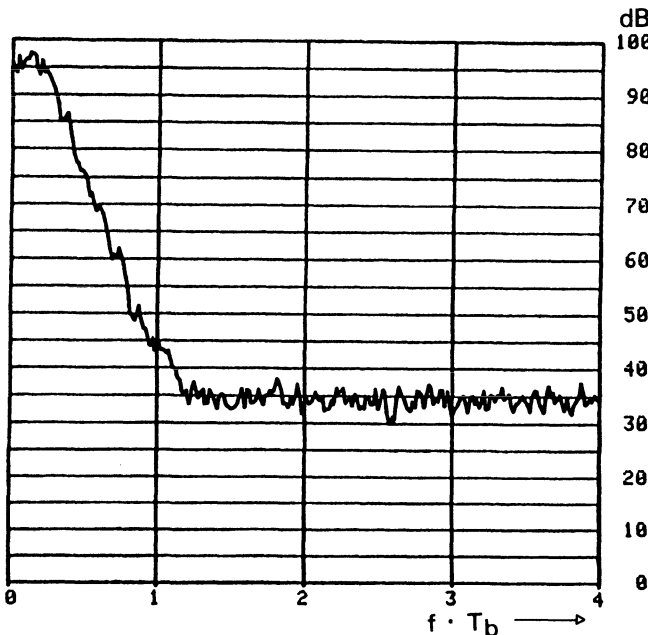


Figure 6.11b. Simulated power spectrum for quaternary 2RC with  $h = 1/3$ ,  $m = 16$ ,  $m_q = 8$ .

quantization and  $m = 16$  samples per symbol. We notice that the noise is approximately linearly decreasing with the number of quantization bits  $m_q$ . The same thing is noticed for other systems in Ref. 1. Figure 6.12 shows the  $M = 2$ , 4RC case with  $h = 1/2$ ,  $m = 8$  and  $m_q = 16$ .

Figures 6.13a–6.13b show a quadrature time signal  $I(t)$  for the sample above with 16- and 4-bit quantization. The quantization distortion can be seen by comparing these figures. The length of these diagrams corresponds to 64 data bits.

As an illustration to what can actually be built with existing components we now give the following design example. With changing technology and faster components, the numbers can easily be scaled accordingly.

In 1982 there were ROM or PROM circuits in ECL techniques with address access times of 15 ns or less. In a direct implementation approach this gives a constraint on the maximum speeds obtainable with the ROM transmitter approach. A similar constraint applies to the components of the  $I$  and  $Q$  generator structures; the basic components here are the input shift register, sweep counter, phase branch ROMs, phase state ROM with delay and D/A converters. All these components are shown in Figure 6.14 for a quaternary CPM modulator with a  $g(t)$  pulse length of less than or equal to two symbols (four bits) and less than or equal to eight phase states

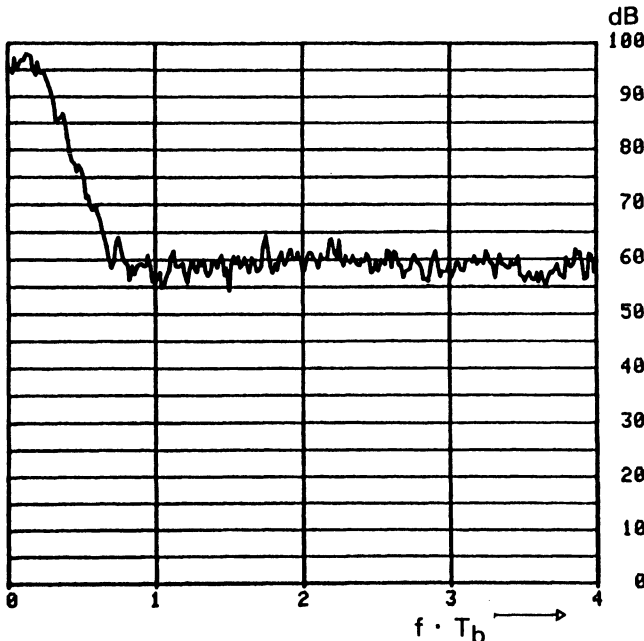


Fig. 6.11c. Simulated power spectrum for quaternary 2RC with  $h = 1/3$ ,  $m = 16$ ,  $m_q = 4$ .

( $p \leq 8$ ). This means that one can for example implement a 2RC  $h = 1/3$  ( $p = 6$ ),  $M = 4$  scheme. The modulation indices  $h = 2/3$  ( $p = 3$ ),  $h = 1/2$  ( $p = 4$ ) and  $h = 1/4$  ( $p = 8$ ) are also allowed by this design. All other alternative pulse forms  $g(t)$  with  $L = 2$  are also possible.

From Figure 6.14 it can be seen that the speed-limiting signal path is through the synchronous count-to-four circuit, the ROM and the latch in front of the D/A converter. With a 15-ns ROM, and ECL circuitry, it is realistic to assume a total delay of 25 ns for this critical path. With four samples per symbol this gives a maximum symbol rate of 1/100 ns which is equivalent to a maximum bit rate of roughly 20 Mb/s for a quaternary system. To achieve higher speed we have to go to more clever solutions. For example we may address the four samples in each symbol at the same time and use a multiplexer after the ROMs to serialize the samples.

For longer pulses ( $L \geq 3$ ) the above arguments are still applicable; the only difference is that larger memories and a longer input shift register are required. For binary schemes the main difference is that the input shift register is only one bit wide. To obtain the same power spectrum the length will have to increase, however. This means that total memory size will be roughly the same. For binary systems the symbol rate is the same as the bit rate. Thus it seems that the maximum obtainable bit rate is larger for

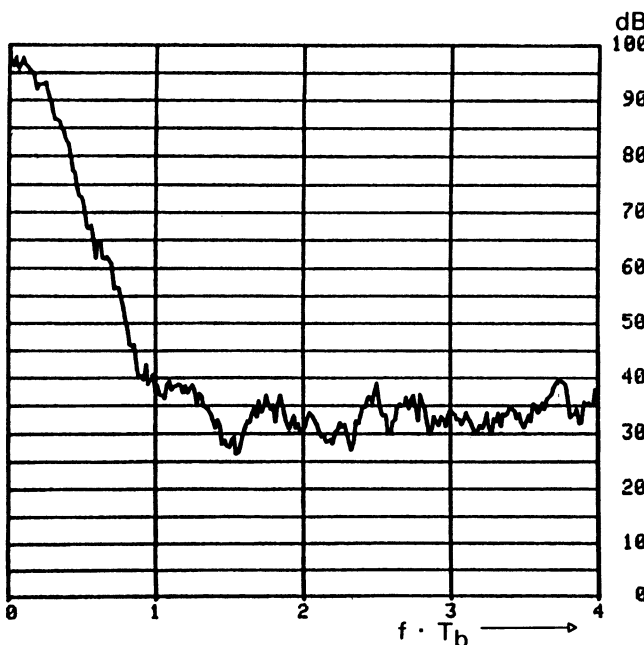


Figure 6.12. Simulated power spectrum for binary 4RC with  $h = 1/2$ ,  $m = 8$ ,  $m_q = 8$ .

quaternary systems. However, this probably is not the case because quaternary systems will normally use twice as many samples per symbol; see for example Figures 6.11 and 6.12 and Ref. 1.

For future designs it is interesting to investigate the possibilities for the ROM modulator in a large-scale integrated (LSI) implementation. Such a circuit will have smaller size, cost, and power consumption, and higher reliability. These are of particular importance in mobile applications. The most convenient implementation technique for the ROM modulator is

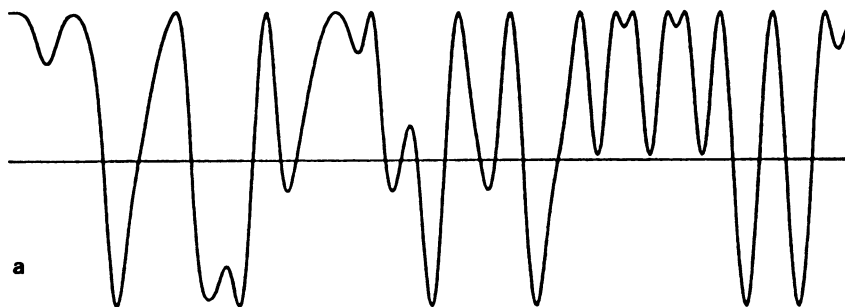


Figure 6.13a. A quadrature time signal  $I(t)$  from a ROM transmitter for  $M = 4$ , 2RC,  $h = 1/3$  with  $m = 16$ ,  $m_q = 16$  (virtually no quantization).

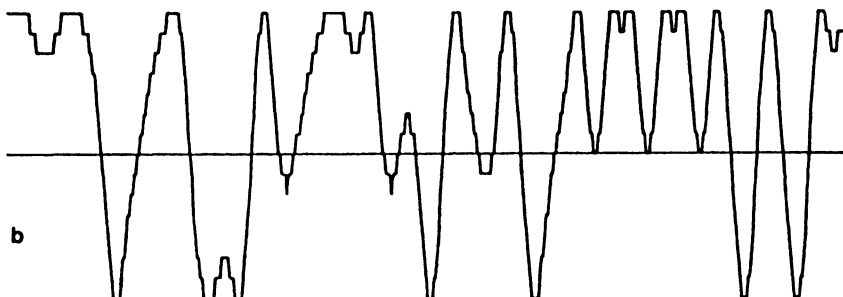


Figure 6.13b. A quadrature time signal  $I(t)$  from a ROM transmitter for  $M = 4$ ,  $2RC$ ,  $h = 1/3$  with  $m = 16$ ,  $m_q = 4$ . The quantization can be clearly seen by comparing with the same waveform without quantization in Figure 6.13a.

perhaps CMOS-LSI circuitry. With this technique it is possible to include everything, including the ROMs and possibly even the D/A converters, in a single circuit. As of 1982, the speed of CMOS circuitry varies from a gate delay of about 30 ns for rather slow techniques to about 3 ns for the fastest silicon on sapphire (SOS) techniques. This implies that these techniques are capable of producing ROM modulators for the speed range 1 Mbit/s to at least 10 Mbit/s in a single low-power circuit. The estimated power for

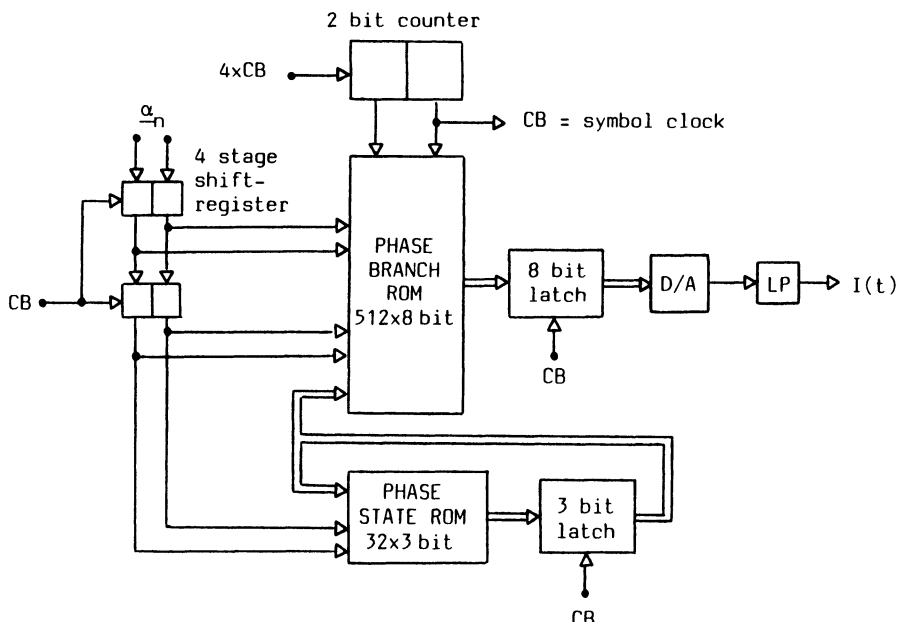


Figure 6.14.  $I$ -generator with high-speed logic.

a 100-kbit/s modulator implemented with this technique is of the order of 10 mW.

## 6.2. Phase-Locked Loop Implementations

A structure based on a normal PSK modulator followed by a phase-locked loop (PLL) with a certain loop filter function is a reasonably easy way of constructing a CPM modulator. This technique is in many ways related to the bandpass limiter technique studied in the next section of this chapter. The basic function of the PLL or bandpass filter is to do a smoothing of the incoming waveform, thus creating a signal with correlation over several symbol intervals and a narrower spectrum. We now show that by careful choice of the filtering function, it is possible to approximately achieve CPM signals very close to many of these considered in this book.

From a speed point of view, the PLL transmitter, like the bandpass and hard-limiter transmitter, is good. With a PSK modulator in front of a PLL there are no specific limits (to hundreds of megabits per second) to the maximum achievable data rate. PSK modulators can be constructed for very high rates. However, a problem with the PLL is the limitation in modulation index, and the linear phase detector. At high speeds it is desirable to use a conventional mixer for the phase detector; this will probably even further limit the maximum modulation index.

Figure 6.3 shows a transmitter based on a standard PSK modulator followed by a PLL. This transmitter is shown in more detail in Figure 6.15. The  $M$ -ary PSK modulator produces a phase change  $\alpha h\pi$  for each data symbol  $\alpha$ . In the binary PSK case the phase change is  $\pm\pi/2$  ( $h = 1/2$ ) and in the quaternary (QPSK) case,  $\pm\pi/4$ ,  $\pm3\pi/4$  ( $h = 1/4$ ). The so-called 2-4 PSK,<sup>(19)</sup> or alternatively OQPSK,<sup>(20)</sup> should be used, in which amplitudes are never zero. Following the analysis in Ref. 1 we will now study the modulator in Figure 6.15 more closely.

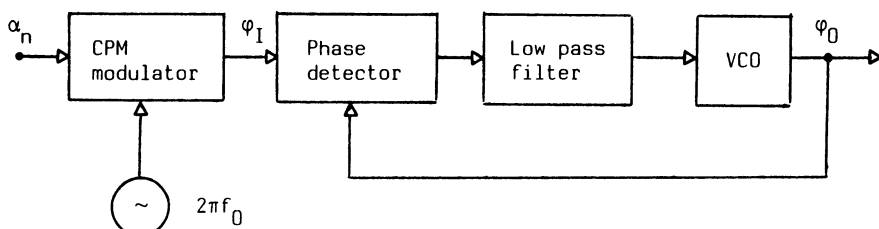


Figure 6.15. Phase locked loop modulator with CPM input. For an alternative structure, replace the CPM modulator with an  $M$ -PSK modulator. Compare Figure 6.3.

It is assumed that the PLL in the first approximation is a linear device acting on the phase, with the transfer function

$$H(s) = \phi_0(s)/\phi_I(s) \quad (6.7)$$

If we consider only the first data symbol at  $t = 0$ ,  $\phi_I(t)$  is  $\alpha h \pi \sigma(t)$ , where  $\sigma(t)$  is the unit step function. Its transform is  $\phi_I(s) = \alpha h \pi / s$ . The output phase  $\phi_O(s)$  can be written as

$$\phi_O(s) = (\alpha h \pi / s) H(s) = \alpha h \pi H_1(s) \quad (6.8)$$

or in the time domain,

$$\phi_0(t) = \alpha h \pi h_1(t) \quad (6.9)$$

where

$$H_1(s) = H(s)/s$$

$h_1(t)$  is its impulse response.

For CPM the phase function is

$$\phi(t) = 2\pi h \alpha q(t)$$

which is the same as the PLL output if

$$h_1(t) = 2q(t)$$

The transfer function of the PLL is

$$H(s) = \frac{F(s)}{s + F(s)} \quad (6.10)$$

where  $F(s)$  is the transfer function of the loop filter, including constants for the phase detector and the VCO. This gives

$$H_1(s) = \frac{F(s)}{s[s + F(s)]} \quad (6.11)$$

With this form it may not be possible to realize an arbitrary desired phase function  $h_1(t)$  exactly (e.g., a raised cosine frequency pulse), but good approximations are probably possible to achieve. One example is described in Ref. 6.

Above we have assumed that the PLL is linear. The phase error  $\phi_I - \phi_O$  must therefore be within the linear region of the phase detector. The best phase detector, built with digital techniques, is linear from  $-\pi$  to  $+\pi$ ; see Refs. 1, 12, 13. With this, the phase error must never exceed  $\pm\pi$ , and this gives an upper limit to the modulation index  $h$ . The limit also depends on the phase length ( $L$ ) and the number of levels ( $M$ ). A rough estimation is that for an RC-like frequency pulse of length  $L$ , the limit is given by

$$(L + 1)h(M - 1) < 2 \quad (6.12)$$

Two examples that fall within this limit are binary 3RC with  $h = 0.5$  and quaternary 2RC with  $h = 0.1$ .<sup>(1)</sup>

For high-speed applications it may be preferable to use a normal mixer instead of the linear phase detector assumed in the calculations. This will limit the maximum usable phase error and thus the maximum usable modulation index even further.

Above we considered a PLL transmitter/MPSK modulator combination. A slightly different PLL transmitter is actually shown in Figure 6.15, in which the MPSK modulator is replaced by a simple CPM modulator. In this form the PLL modulator is even more similar to the bandpass limiter modulator shown in Figure 6.17. Problems with the phase detector are probably reduced if we use a CPM modulator with more or less continuous phase; in this case high-speed modulators may probably be constructed with normal mixers for the phase detection. Our estimates indicate that the modulation indices mentioned above may now be achieved without the linear phase detector. However, the speed problem is not quite solved, because we must implement the CPM modulator with a high-speed technique. A first suggestion is to use an MSK modulator in front of the PLL. MSK can be generated for very high speeds with rather conventional circuitry; see, e.g., Ref. 14. The approximate derivation for the PLL modulator with MSK input is very similar to the one just given for PSK. The main difference is that the input is now a ramp instead of a step function.

In general we can write the input phase from the simple CPM modulator as

$$\phi_I(t) = \sum_i \alpha_i h 2\pi q_I(t - iT)$$

Assuming that the PLL behaves as a linear device with the impulse response  $h(t)$  we have the output phase

$$\phi_O(t) = \sum_i \alpha_i h 2\pi q_I(t - iT) * h(t)$$

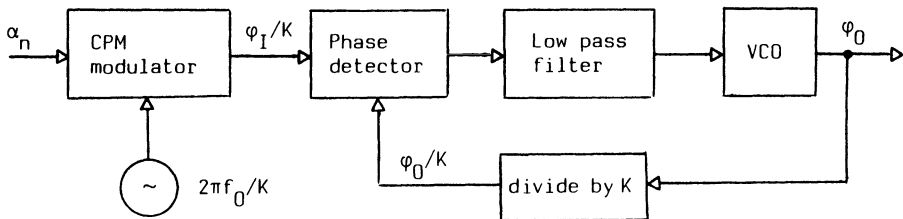


Figure 6.16. Phase-locked loop modulator with higher maximum modulation index.

where \* denotes convolution. Comparing this to the general phase formula for CPM gives the relation

$$q(t) = q_I(t) * h(t) \quad (6.13)$$

Thus it is fairly easy to synthesize CPM schemes with this structure.

An additional idea<sup>(1)</sup> for achieving higher modulation indices is shown in Figure 6.16. Here we use a divide-by- $K$  counter in the feedback loop of the PLL. This requires a CPM modulator with a modulation index of only  $1/K$  times the desired modulation index. From an implementation point of view this modulator probably has more problems with speed than the two examples above. The first problem is the simple CPM modulator with modulation index  $h/K$ , which is not always easy to achieve without, for example, the ROM transmitter. Another speed problem is the divide-by- $K$  counter operating on the carrier frequency.

### 6.3. Bandpass Filter and Hard-Limiter Implementation

Figure 6.4 shows a transmitter based on a simple CPM modulator followed by a bandpass filter and a limiter. In Section 3.5 and in Ref. 5 it is shown that the spectrum and phase tree for this type of transmitter can be made very similar to those of an ordinary CPM transmitter. This means that this type of transmitter may be used as a way of simplifying a more complex CPM transmitter. It is reasonable to assume that the bandpass filter and the limiter can be easily implemented for almost any realistic data rate, so that all speed constraints are on the simple CPM transmitter in front of the filter. A filter with a particular impulse response can be approximately implemented with ordinary filter techniques; more exactly specified impulse responses may be implemented by, for example, a surface-acoustic wave (SAW) filter. We will show that the bandpass filter to a first approximation (for low modulation indices) acts as a filter on the baseband phase. This makes it possible to calculate the bandpass filter impulse response needed to create a certain pulse  $g(t)$  with simple means.

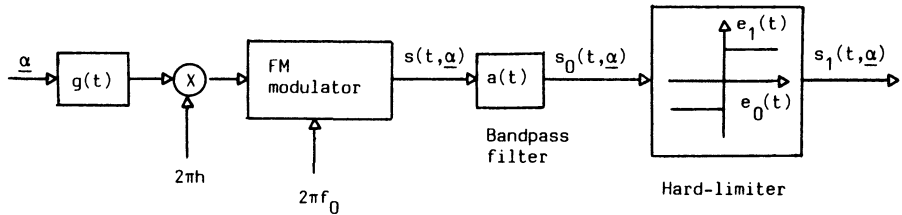


Figure 6.17. Block diagram showing the transmitted signal  $s_1(t, \alpha)$  and its generation.

In Figure 6.17 the modulation concept is shown in block diagrams and Figure 6.18 shows the corresponding baseband equivalent. In Figure 6.19 the complex envelope notations used are illustrated. The notations and the theory for CPM signal transmission through a bandpass filter and a hard limiter is described above in Sections 2.4 and 3.5. By using

$$\phi_1(t, \alpha) = \arg \{ \tilde{s}_1(t, \alpha) \} = \arg \{ \tilde{s}_0(t, \alpha) \} \quad (6.14)$$

where  $\arg \{ z \}$  denotes the argument of the complex quantity  $z$ , the produced signal can be written

$$s_1(t, \alpha) = (2P)^{1/2} \cos [2\pi f_0 t + \phi_1(t, \alpha)] \quad (6.15)$$

which is recognized as a CPM signal. For this signal, however, the relationship

$$\phi_1(t, \alpha) \neq 2\pi h \sum_{i=-\infty}^{\infty} \alpha_i q_1(t - iT)$$

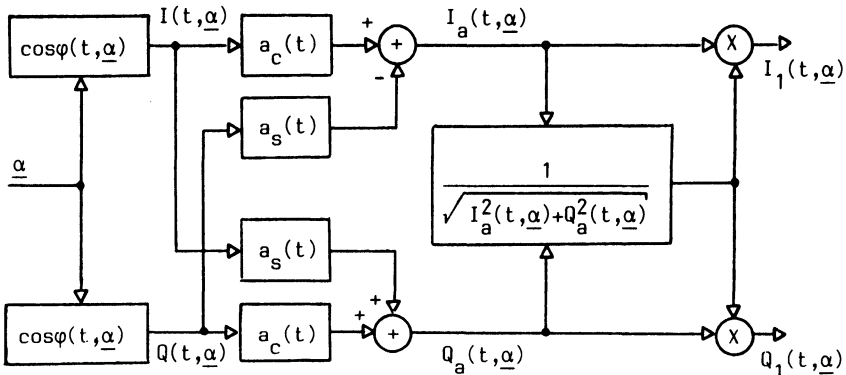


Figure 6.18. Baseband model for generation of the nonlinear CPM signal  $s_1(t, \alpha)$ .  $I_1(t, \alpha)$  and  $Q_1(t, \alpha)$  are the quadrature components of  $s_1(t, \alpha)$ .

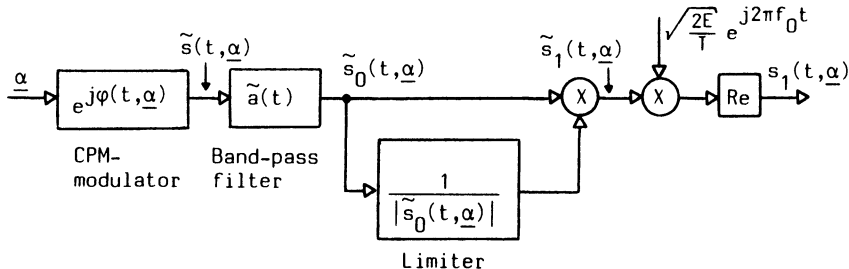


Figure 6.19. Illustration of the complex notations for the considered modulation scheme.  $P = E/T$ .

does not in general hold, i.e., the phase of the CPM signal is no longer linearly modulated by the data sequence  $\alpha$ . In fact this is one way of producing a nonlinearly modulated CPM signal. The envelope prior to hard limiting must never be zero, because the output from the hard limiter is then not defined.

For low modulation indices we can further simplify the formula for the phase after the bandpass limiter. First, observe that

$$\phi_1(t, \alpha) = \arg \{ \tilde{s}_0(t, \alpha) \} = \arg \{ \tilde{s}(t, \alpha) * \tilde{a}(t) \}$$

or

$$\phi(t, \alpha) = \arg \{ e^{j\phi(t, \alpha)} * \tilde{a}(t) \} \quad (6.16)$$

We now use the property that both  $q(t)$  and  $\tilde{a}(t)$  are assumed to be time limited, so that  $\phi(t, \alpha)$  may be written as

$$\phi(t, \alpha) = 2\pi h \sum_{i=n-L+1}^n \alpha_i q(t - iT) + \theta_n$$

where  $\theta_n$  is a constant for each symbol interval. For low modulation indices, the time varying part of  $\phi(t, \alpha)$  may be regarded as small enough to expand the exponential function into a Taylor series. This may be written as

$$\phi_1(t, \alpha) = \arg \left\{ \left[ 1 + j\phi(t, \alpha) - \frac{\phi^2(t, \alpha)}{2} \dots \right] * \tilde{a}(t) \right\}, \quad (6.17)$$

which is to a first-order approximation,

$$\phi_1(t, \alpha) = \arg \{ [1 + j\phi(t, \alpha)] * \tilde{a}(t) \} \quad (6.18)$$

If we assume that  $\tilde{a}(t) = a_c(t)$  is real (the bandpass filter has a symmetric frequency response) we can write

$$\begin{aligned}\phi_1(t, \alpha) &= \arg \{[1 + j\phi(t, \alpha)] * a_c(t)\} \\ &= \arctan \left[ \frac{\phi(t, \alpha) * a_c(t)}{1 * a_c(t)} \right]\end{aligned}\quad (6.19)$$

For small  $h$  values the arctan may be omitted. The denominator is a constant  $A$ , so that

$$\phi_1(t, \alpha) \approx \phi(t, \alpha) * \frac{\tilde{a}(t)}{A}$$

or

$$\phi_1(t, \alpha) \approx 2\pi h \sum_{i=-\infty}^{\infty} \alpha_i q(t - iT) * \frac{\tilde{a}(t)}{A} \quad (6.20)$$

If this formula is compared to the normal CPM expression for the information carrying phase, we notice that the bandpass filter to a first approximation acts as a linear filter on the phase response. Thus it is fairly easy to synthesize bandpass filters to obtain a desired  $g(t)$  pulse. As an example, Figure 6.20 shows the phase tree for a 1REC,  $h = 1/2$ , CPM signal

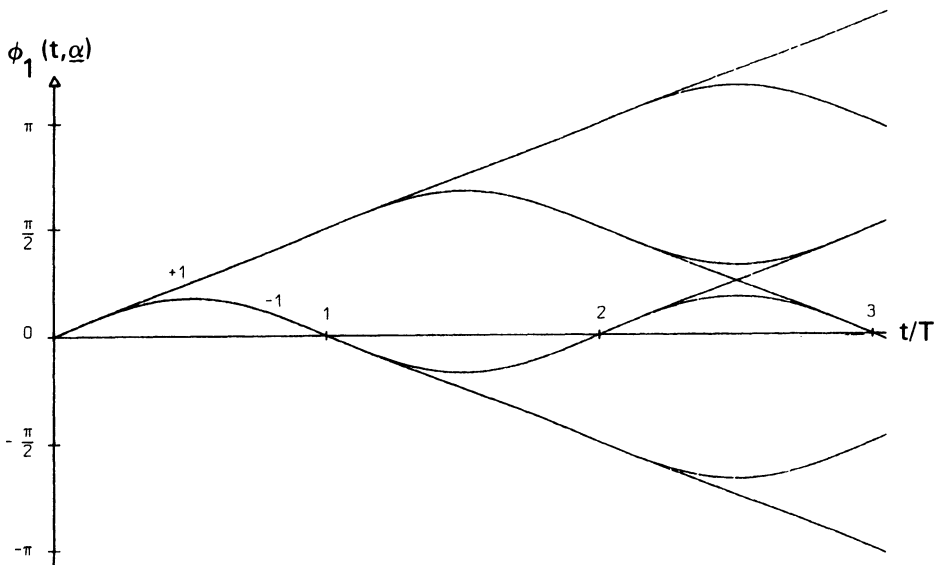


Figure 6.20. Phase tree for a 1REC  $h = 1/2$  CPM signal sent through a 1RC filter followed by a limiter. The signal is nonlinearly phase modulated and the shape of the tree changes with the modulation index  $h$ . For  $h = 1/2$  we notice the close resemblance to a 2RC phase tree.

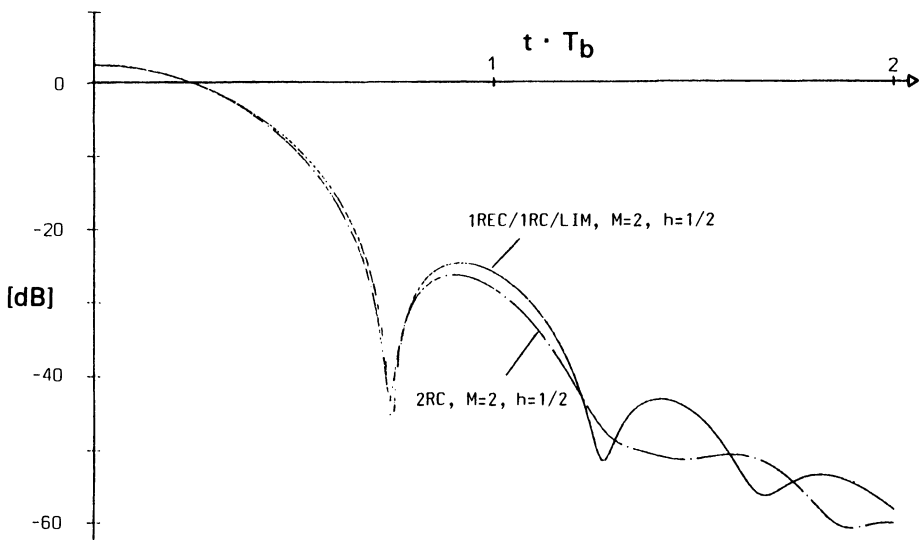


Figure 6.21. Comparison between calculated spectra for pure 2RC,  $M = 2$ ,  $h = 1/2$  and 1REC/1RC/LIM when  $M = 2$ ,  $h = 1/2$ .

filtered with a 1RC (in the time domain) filter followed by a limiter. The tree is almost exactly the same as a 2RC phase tree. Figure 6.21 shows the power spectrum of this filtered CPM signal compared with a 2RC,  $h = 1/2$ , power spectrum. Even here the resemblance is very close. More details are found in Section 3.5 and in Ref. 1, where bandpass filtering and hard limiting are considered as types of channel imperfections in the transmission of a CPM signal.

#### 6.4. Serial and Parallel MSK Transmitters

Several special modulator structures have been devised for MSK. Because MSK is a quadrature-multiplexed modulation scheme, it can be optimally detected by coherently demodulating its in-phase and quadrature components in parallel, in the manner of Sections 2.4 and 2.6. Clearly, the quadrature channels of the modulator and demodulator must be time synchronized, amplitude balanced, and in phase quadrature to avoid overall system degradation. This becomes more difficult as the data rate increases.<sup>(18)</sup> References 20 and 21 give a more extensive discussion of the parallel approach to modem implementation for QPSK, OQPSK, and MSK. The *serial* method is an alternative approach to parallel modulation and demodulation of MSK which avoids its problems. It was first publicized by Amoroso

and Kivett<sup>(8)</sup> in 1977, and later implemented at 760 Mbit/s by Ryan, Hambley, and Vogt.<sup>(14)</sup> Serial MSK transmitters are well described in Refs. 8 and 18 and practical realization aspects are in Refs. 9, 10, 14, and 17.

The serial modulation of MSK is somewhat more subtle to grasp than the parallel method. A serial modulator structure for serial MSK is illustrated in Figure 6.22. It consists of a pure BPSK modulator with carrier frequency of  $f_0 - 1/4T$ , Hz, and a bandpass conversion filter with impulse response

$$h(t) = \begin{cases} (1/T) \sin [2(f_0 + 1/4T)t] & 0 \leq t \leq T \\ 0 & \text{otherwise} \end{cases} \quad (6.21)$$

which corresponds to a  $(\sin x)/x$ -shaped transfer function. A frequency-domain proof<sup>(18)</sup> of the validity of the serial modulation technique for MSK is provided by considering the product of the power spectrum of the BPSK signal and the magnitude squared of the transfer function of the conversion filter, whose center frequency is offset from the BPSK carrier by one-half the data rate. The resulting signal has the MSK power spectrum shown in Chapter 4. When mathematically expressed in terms of single-sided spectra, the BPSK spectrum is proportional to

$$S_{\text{BPSK}}(f) = 2 \operatorname{sinc}^2 [(f - f_0)T + 0.25]$$

where  $\operatorname{sinc}(x) = (\sin \pi x)/(\pi x)$ . The conversion filter transfer function is

$$G(f) = \operatorname{sinc} [(f - f_0)T - 0.25] \exp(-j2\pi f t_0) \quad (6.22)$$

where  $t_0$  represents an arbitrary delay for the filter. The product of  $S_{\text{BPSK}}(f)$  and  $|G(f)|^2$  can be simplified to

$$S_{\text{MSK}}(f) = |G(f)|^2 S_{\text{BPSK}}(f) = \frac{16}{\pi^2} \left[ \frac{\cos 2\pi(f - f_0)T}{1 - 16T^2(f - f_0)^2} \right]^2 \quad (6.23)$$

which is the power spectrum of MSK given in Section 4.3.

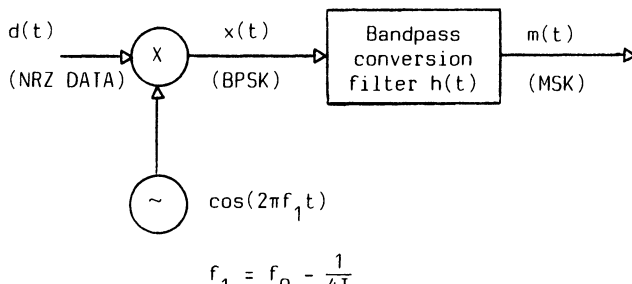


Figure 6.22. Implementation of a serial MSK modulator utilizing bandpass conversion and matched filters.

It is not clear how this idea might be generalized to a serial partial response transmitter. MSK is very special, since it corresponds to linear modulation in the quadrature arms. This is not the case for partial response CPM with for instance 4RC,  $M = 2$ ,  $h = 1/2$ . Serial MSK-type detection can, however, be applied to partial response CPM.<sup>(15,16)</sup> This will be discussed in Chapter 8. Another technique is described in Ref. 7, where transmitter is described for duobinary MSK (2REC,  $h = 1/2$ , which is called FSOQ in Ref. 7). The key idea is switching between two simple transmitters. It is not evident how this technique can be generalized to more general cases either.

Serial MSK modulations have the advantage that all operations are performed serially, and therefore offer significant implementation trade-offs at high data rates. The precise synchronization and balancing required for the quadrature signals of the parallel structures are no longer present.

Although conversion filters have been implemented with surface acoustic wave (SAW) devices, the maximum bandwidth of SAW devices is about 10%–30% of the center frequency employed. For production SAWs, center frequencies of a few hundred megahertz represent the upper limit, assuming normal fabrication techniques, with 1 GHz representing the upper limit if laser trimming and other special techniques are used. Thus, the use of SAW filters implies an upper limit on data rate of about 100 Mbit/s, assuming normal fabrication. Alternative filters are considered in Ref. 18.

## 6.5. Conclusions

In this chapter we have studied principles of various CPM transmitter structures from an implementation point of view. It seems reasonable that general CPM ROM-transmitter structures are capable of at least 30 Mbit/s speeds with 1982 technology. The transmitter part can be made very low cost and compact by the use of ECL-LSI technology. Low-power, extremely compact, transmitters may be implemented in CMOS-LSI technology for bit rates below 10 Mbit/s. It is shown in Ref. 1 that 5–6 bit resolution and 4–8 samples per symbol are reasonable design parameters for satellite applications.

Transmitters based on simple CPM modulators followed by PLLs or a bandpass filter and hard limiter structure are studied in the last sections. These structures can be used for very high-speed applications; operating bit rates of 120 Mbit/s seem realistic.

These transmitter structures are quite general and applicable to a wide range of CPM schemes. There are a variety of other special techniques described in the literature. We mention especially the so-called *serial MSK*

technique,<sup>(8,9)</sup> which has been used to implement MSK (1REC,  $h = 1/2$ ) at data rates above 500 Mbit/s.<sup>(10)</sup> The serial MSK technique might be used to implement the simple CPM modulator in the general CPM transmitter of Figure 6.15.

## References

1. T. Aulin, B. Persson, N. Rydbeck, and C-E. Sundberg, "Spectrally-Efficient Constant-Amplitude Digital Modulation Schemes for Communication Satellite Applications," May 1982, Study Report, European Space Agency—ESTEC, contract No. 4765/81/NL/MD, Vol. I and Vol. II. In part published in Conference Record, The Sixth International Conference on Digital Satellite Communications, Phoenix, Arizona, September 1983.
2. D. Muilwijk and J. H. Schadé, "Correlative Phase Modulation for Fixed Satellite Services," January 1983, Study Report ESTEC 4485/80/NL/MS, Philips Telecommunicatie Industrie B.V., Hilversum, The Netherlands.
3. F. de Jager and C. B. Dekker, "Tamed Frequency Modulation, A Novel Method to Achieve Spectrum Economy in Digital Transmission," *IEEE Transactions on Communications COM-26(5)*, 534-542 (1978).
4. T. Aulin, N. Rydbeck, and C-E. Sundberg, "Continuous Phase Modulation (CPM) Part II, Partial Response Signalling," *IEEE Communication Transactions COM-29*, 210-225 (1981).
5. T. Aulin and C-E. Sundberg, "Authocorrelation Functions and Power Spectral Densities for Bandpass Filtered and Hard-limited Continuous Phase Modulation," ICC'82, Conference Record, pp. 6F6.1-6F6.5.
6. K. Honma, E. Murate, and Y. Rikou, "On a Method of Constant Envelope Modulation for Digital Mobile Radio Communication," ICC'80, Conference Record, pp. 24.1.1-24.1.5.
7. S. A. Rhodes, "FSQO, A New Modulation Method that yields a Constant Envelope," NTC'80, Conference Record, pp. 51.1.1-5.1.17.
8. F. Amoroso and J. A. Kivett, "Simplified MSK Signalling Technique," *IEEE Transactions on Communications COM-25*, 443-441 (1977).
9. F. Amoroso, "Experimental Results on Constant Envelope Signalling with Reduced Sidelobes," ICC'81, Conference Record, pp. 47.1-47.1.5.
10. C. R. Ryan, "Advances in Serial MSK Modems," NTC'81, Conference Record, pp. G3.6.1-G3.6.5.
11. T. Aulin, N. Rydbeck and C-E. Sundberg, "Transmitter Receiver Structures for  $M$ -ary Partial Transmitter and Receiver Structures for  $M$ -ary Partial Response FM," 1980 International Zürich Seminar on Digital Communications, March 4-6, 1980, Conference Record, pp. A.2.1-A.2.6.
12. F. Gardner, *Phaselock Techniques*, 2nd Edition, Wiley, New York (1979).
13. W. C. Lindsey and M. K. Simon, *Telecommunications System Engineering*, Prentice-Hall, Englewood Cliffs, New Jersey (1973).
14. C. R. Ryan, A. R. Hambley, and D. E. Vogt, "760 Mbit/s Serial MSK Microwave Modem," *IEEE Transactions on Communications COM-28(5)*, 771-777 (1980).
15. C-E. Sundberg and A. Svensson, "Parallel and Serial MSK-type Detection of Partial Response Continuous Phase Modulation," Mediterranean Electrotechnical Conference, MELECON'83, Athens, Greece, May 1983, Conference Record, paper B8-01.
16. A. Svensson and C-E. Sundberg, "Serial MSK-type Detection of Partial Response Continuous Phase Modulation," *IEEE Transactions on Communications COM-33*, (1), 44-52 (1985).

17. R-E. Ziemer, C. R. Ryan and J. H. Stilwell, "Conversion and Matched Filter Approximations for Serial Minimum Shift Keyed Modulation," *IEEE Transactions on Communications* COM-30(3), 495-509 (1982).
18. R. E. Ziemer and C. R. Ryan, "Minimum-Shift Keyed Modem Implementations for High Data Rates," *IEEE Communications Magazine* 21(7), 28-37 (1983).
19. D. Dupontel, "Binary Modulations for Digital Satellite Communications Link with Differential Demodulation," Fifth International Conference on Digital Satellite Communications, Genoa, Italy, March 1981, Conference Record, pp. 89-98.
20. V. K. Bhargava, D. Haccoun, R. Matyas, and P. Nuspl, *Digital Communications by Satellite Modulation, Multiple Access and Coding*, Wiley, New York (1981).
21. S. Pasupathy, "Minimum Shift Keying: A Spectrally Efficient Modulation," *IEEE Communications Magazine* 17, 14-22 (1979).
22. F. Amoroso, "The Bandwidth of Digital Data Signals," *IEEE Communications Magazine* 18, 13-24 (1980).
23. J. J. Spilker, Jr., *Digital Communications by Satellite*, Prentice-Hall, Englewood Cliffs, New Jersey (1977).

---

# Receivers

In this chapter we will discuss ideal coherent receiver principles for CPFSK and CPM. It will be assumed that synchronization is established, i.e., that the carrier phase and the symbol timing are precisely known by the receiver. Methods for extraction of these parameters from the received noisy signal are discussed in Chapter 9. Noncoherent reception will also be considered. In this case we assume that the receiver only knows the symbol timing while the carrier phase is completely unknown (and remains unknown) to the receiver; we will consider both optimum and suboptimum receivers of this type. The in-between case of partially coherent detection will be delayed to Chapter 10.

Throughout this chapter the channel is assumed to be a white additive Gaussian channel. The optimum coherent and noncoherent receiver of Osborne and Luntz<sup>(4)</sup> for CPFSK over this channel is described in Section 7.1. We then describe the optimum coherent maximum likelihood sequence estimation (MLSE) receiver for CPM. It utilizes the Viterbi algorithm, which is discussed in Section 7.3. Performance simulations for partial response CPM and CPFSK are in Section 7.4. Simple noncoherent receivers are developed in Section 7.5. Simplified suboptimum coherent receivers will be discussed in detail in Chapter 8, and detailed analysis of the noncoherent receiver appears in Chapter 10.

## 7.1. Optimum Coherent and Noncoherent Receivers for CPFSK

We have developed the basics of maximum likelihood (ML) detection in Section 2.1 and followed it in Section 2.6 with a discussion of the optimum receiver for pure and Nyquist pulse shaped PSK. The PSK receiver needed only to be a linear receiver, observing a single interval, because the signal behavior with independent data was independent from interval to interval.

The receiver in the present section detects CPFSK signals, that is CPM with 1REC phase response. These signals have memory between intervals because of the phase continuity constraint of CPFSK. This leads to a better bandwidth and energy performance, as we have seen in Chapters 2 and 3. Obtaining this performance requires a multiple interval observation rather than the symbol-by-symbol decisions in Section 2.6.

Despite the fact that we will emphasize CPFSK, the receivers in this section are quite general and apply to CPM schemes with any pulse shape and any modulation index. We have already considered the coherent case implicitly in the distance calculations of Chapter 3. Indeed, it could be said that the optimum receiver is useful mostly to provide a theoretical performance benchmark, but in certain applications a receiver with the architecture here proves useful. In addition, very simple optimal coherent receivers exist for the special case of full response CPM with  $M = 2$  and  $h = 1/2$ , e.g., 1REC.

### 7.1.1. Optimum ML Coherent Receiver for CPFSK

This receiver makes a decision about one symbol only, based on observation of a sequence of consecutive symbols. Once the decision is made, the receiver in principle starts from scratch again, processing the following symbol by sliding the observation interval.

Much of the development in this and the succeeding section 7.1.2 follows Schonhoff<sup>(5)</sup> and parallels the theoretical binary development in Osborne and Luntz.<sup>(4)</sup> The received  $M$ -ary CPFSK signal during the  $i$ th symbol is modelled as

$$r(t) = \left(\frac{2E}{T}\right)^{1/2} \cos \left\{ 2\pi f_0 t + \frac{\alpha_i \pi h [t - (i-1)T]}{T} + \pi h \sum_{j=1}^{i-1} \alpha_j + \varphi_0 \right\} \\ + n(t), \quad (i-1)T < t < iT \quad (7.1)$$

where we use the notations from Chapters 2 and 3. In (7.1) it is assumed that  $\sum_{j=1}^{i-1} \alpha_j = 0$  for  $i = 1$ . The possible phase trajectories (the phase tree) using the phase term  $\alpha_i \pi h [t - (i-1)T]/T + \pi h \sum_{j=1}^{i-1} \alpha_j + \varphi_0$  are shown in Figure 3.2, Chapter 3, for quaternary modulation and  $\varphi_0 = 0$ . For quaternary modulation we have  $\alpha_i = \pm 1, \pm 3$ . Figure 7.1 shows for comparison the phase tree for binary 3RC, which will be considered below.

In determining the optimum receiver structure for detecting symbol  $\alpha_1$ , we shall use a shorthand notation developed in Refs. 4 and 5 for the received signal,

$$r(t) = s(t, \alpha_1, D_k) + n(t) \quad (7.2)$$

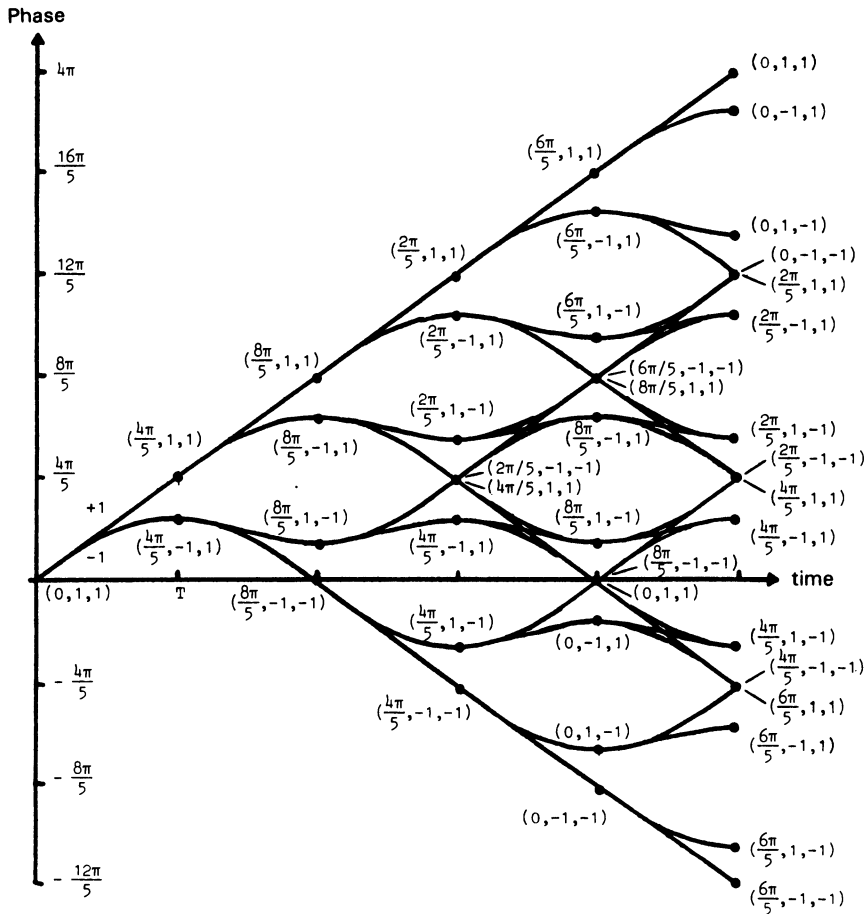


Figure 7.1. Binary phase tree for a 3RC scheme for  $h = 4/5$ . The state description is also given in the tree.

where  $\alpha_1$  is the first symbol, and  $D_k$  is the  $(N - 1)$ -tuple  $D_k = \{\alpha_2, \dots, \alpha_N\}$ . For coherent detection, the starting phase  $\varphi_0$  is assumed known, and hence will be assumed to be 0 with no loss in generality.

The optimum receiver determines the  $M$  likelihood parameters<sup>(8,9)</sup>

$$l_1 = \int \exp \left[ \frac{2}{N_0} \int_0^{NT} r(t) s(t, 1, D_k) dt \right] f(D_k) dD_k$$

$$l_2 = \int \exp \left[ \frac{2}{N_0} \int_0^{NT} r(t) s(t, -1, D_k) dt \right] f(D_k) dD_k$$

1

$$l_{M-1} = \int \exp \left[ \frac{2}{N_0} \int_0^{NT} r(t) s(t, M-1, D_k) dt \right] f(D_k) dD_k \quad (7.3)$$

$$l_M = \int \exp \left[ \frac{2}{N_0} \int_0^{NT} r(t) s(t, -(M-1), D_k) dt \right] f(D_k) dD_k$$

where  $f(D_k)$  is the discrete probability density function (PDF) of  $D_k$ . The integral  $\int f(D_k) dD_k$  is more precisely  $(N-1)$ -fold integral

$$\int \int \int \cdots \int f(\alpha_2) f(\alpha_3) \cdots f(\alpha_N) d\alpha_2 d\alpha_3 \cdots d\alpha_N$$

and each of the discrete PDFs  $f(\alpha_\mu)$ ,  $\mu = 2 \dots N$  is given by

$$f(\alpha_\mu) = \frac{1}{M} \sum_{j=-(M-1) \text{ by steps of } 2}^{(M-1)} \delta(\alpha_\mu - j), \quad \mu = 2, \dots, N$$

where  $\delta(\ )$  is a Dirac  $\delta$ -function. Since  $D_k$  can have  $m = M^{N-1}$  different possibilities, the integrals over  $D$  can be evaluated. Thus the  $M$  parameters  $l_1, l_2, \dots, l_M$  are obtained.

$$\begin{aligned} l_1 &= \sum_{j=1}^m \exp \left[ \frac{2}{N_0} \int_0^{NT} r(t) s(t, 1, D_j) dt \right] \\ l_2 &= \sum_{j=1}^m \exp \left[ \frac{2}{N_0} \int_0^{NT} r(t) s(t, -1, D_j) dt \right] \\ &\vdots && \vdots \\ l_{M-1} &= \sum_{j=1}^m \exp \left[ \frac{2}{N_0} \int_0^{NT} r(t) s(t, M-1, D_j) dt \right] \\ l_M &= \sum_{j=1}^m \exp \left[ \frac{2}{N_0} \int_0^{NT} r(t) s(t, -(M-1), D_j) dt \right] \end{aligned} \quad (7.4)$$

The receiver then decides the data symbol  $\alpha_1$  that corresponds to the largest of  $l_1$  to  $l_M$ . This optimum coherent maximum likelihood (*ML*) receiver is shown in Figure 7.2.

Unfortunately, it is not possible to analyze the error performance of this receiver exactly, but we can compute bounds on performance which are tight at high or low SNR. The derivation of the low SNR result leads to the so-called average matched filter receiver, which we will take up in

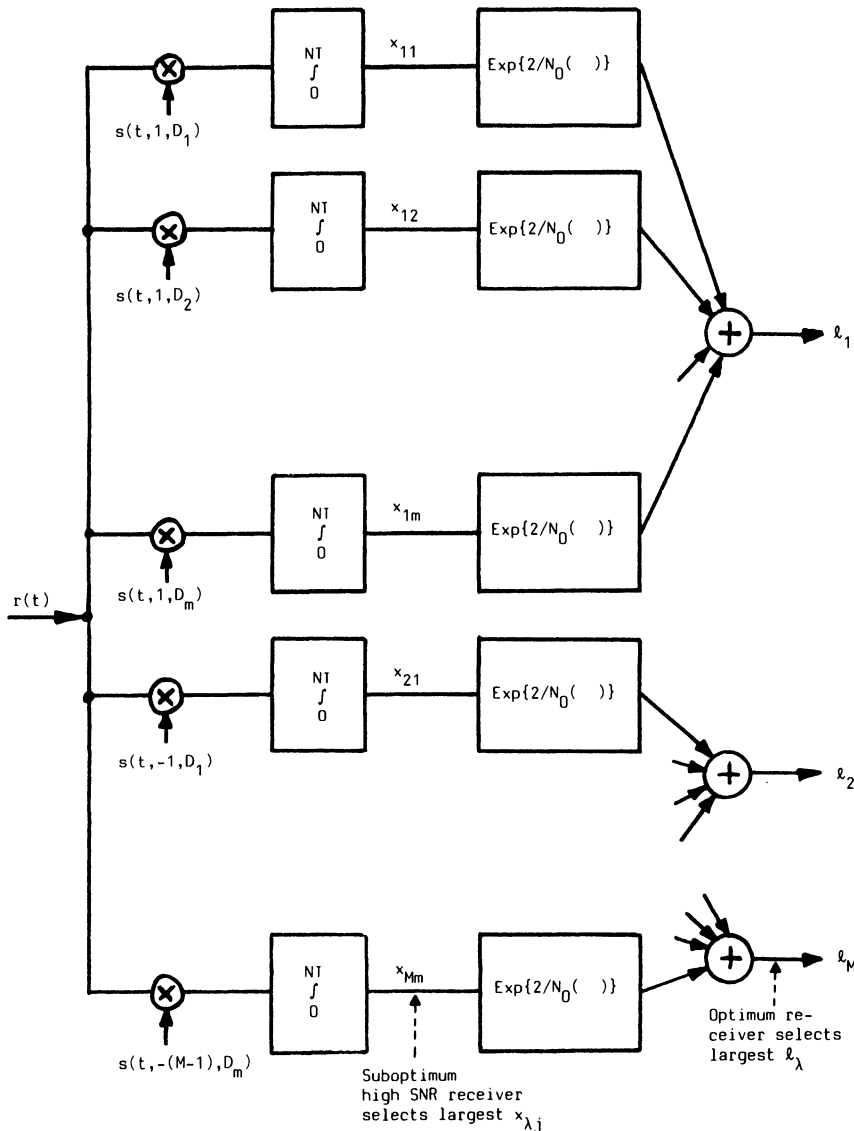


Figure 7.2. Optimum and high-SNR suboptimum CPFSK coherent receivers of Osborne and Luntz type.<sup>(4)</sup>

Section 8.4. At high SNR, the error probability is dominated by the minimum distance already found in Chapter 3. We define the parameters  $x_{\lambda j}$  as

$$x_{\lambda j} = \begin{cases} \int_0^{NT} r(t) s(t, \lambda, D_j) dt, & \lambda \text{ odd} \\ \int_0^{NT} r(t) s(t, -(\lambda - 1), D_j) dt, & \lambda \text{ even} \end{cases} \quad (7.5)$$

The  $M$  likelihood parameters can now be written as

$$l_\lambda = \sum_{j=1}^m \exp\left(\frac{2}{N_0} x_{\lambda j}\right), \quad \lambda = 1, \dots, M.$$

For large SNR we use the approximation

$$\sum_{j=1}^m \exp\left(\frac{2}{N_0} x_{\lambda j}\right) \approx \exp\left(\frac{2}{N_0} x_\Lambda\right) \quad (7.6)$$

where  $x_\Lambda$  is the largest of the  $x_{\lambda j}$ . From (7.5) and Section 2.2, the normalized Euclidean distance  $d$  is related to  $x$  by  $d^2 = (\text{NE} - x)/E_b$ , so that the smallest  $d$  dominates (7.6) as claimed and the error probability is  $P_e \approx Q((d_{\min}^2 E_b / N_0)^{1/2})$ . Thus the high SNR performance of Figure 7.2 follows from the distance results of Chapter 3. The above discussion can be extended to any CPM scheme simply by replacing the transmitted signal  $s(t)$ .

### 7.1.2. Optimal ML Noncoherent Receiver for CPFSK

For noncoherent detection, the initial phase  $\Phi = \phi_0$  in (7.1) is assumed unknown. Furthermore we assume a uniform PDF from 0 to  $2\pi$ . Again following Refs. 4 and 5, the received signal is written in shorthand notation as

$$r(t) = s(t, \alpha_{n+1}, \Delta_k, \Phi) + n(t) \quad (7.7)$$

Here, the signal is observed for  $N = 2n + 1$  symbols. The receiver makes a decision on the middle symbol  $\alpha_{n+1}$ .  $\Delta_k$  is defined as the  $2n$ -tuple consisting of

$$\Delta_k = \{\alpha_1, \alpha_2, \dots, \alpha_n, \alpha_{n+2}, \dots, \alpha_{2n+1}\}$$

$\Delta_k$  can take on  $\mu$  values where  $\mu = M^{2n}$ . The optimum noncoherent ML receiver determines the  $M$  likelihood parameters

$$\begin{aligned} l_1 &= \int_{\Phi} \int_{\Delta} f(\Delta) f(\Phi) \exp \left[ \frac{2}{N_0} \int r(t) s(t, 1, \Delta_k, \Phi) dt \right] d\Phi d\Delta \\ l_2 &= \int_{\Phi} \int_{\Delta} f(\Delta) f(\Phi) \exp \left[ \frac{2}{N_0} \int r(t) s(t, -1, \Delta_k, \Phi) dt \right] d\Phi d\Delta \\ &\vdots && \vdots \\ l_{M-1} &= \int_{\Phi} \int_{\Delta} f(\Delta) f(\Phi) \exp \left[ \frac{2}{N_0} \int r(t) s(t, M-1, \Delta_k, \Phi) dt \right] d\Phi d\Delta \\ l_M &= \int_{\Phi} \int_{\Delta} f(\Delta) f(\Phi) \exp \left[ \frac{2}{N_0} \int r(t) s(t, -(M-1), \Delta_k, \Phi) dt \right] d\Phi d\Delta \end{aligned} \quad (7.8)$$

In the above expressions  $f(\Delta)$  is the discrete PDF of  $\Delta$  and  $f(\Phi)$  is the PDF of  $\Phi$ . As can be expected, these likelihood parameters are similar to the coherent likelihood parameters of (7.3) except for the added integral over the initial phase  $\Phi$ . The integral  $\int_{\Delta} f(\Delta) d\Delta$  is a  $2n$ -fold integral

$$\int_{\alpha_1} \int_{\alpha_2} \dots \int_{\alpha_{2n+1}}^{\text{but not } \alpha_{n+1}} f(\alpha_1) f(\alpha_2) \dots f(\alpha_{2n+1}) d\alpha_1 d\alpha_2 \dots d\alpha_{2n+1}$$

Integrating over  $\Delta$  as was done in the coherent case, we get the  $M$  likelihood parameters

$$\begin{aligned} l_1 &= \int_{\Phi} \frac{1}{\mu} \sum_{k=1}^{\mu} \exp \left[ \frac{2}{N_0} \int r(t) s(t, 1, \Delta_k, \Phi) dt \right] f(\Phi) d\Phi \\ l_2 &= \int_{\Phi} \frac{1}{\mu} \sum_{k=1}^{\mu} \exp \left[ \frac{2}{N_0} \int r(t) s(t, -1, \Delta_k, \Phi) dt \right] f(\Phi) d\Phi \\ &\vdots \\ l_M &= \int_{\Phi} \frac{1}{\mu} \sum_{k=1}^{\mu} \exp \left[ \frac{2}{N_0} \int r(t) s(t, -(M-1), \Delta_k, \Phi) dt \right] f(\Phi) d\Phi \end{aligned} \quad (7.9)$$

$$l_M = \int_{\Phi} \frac{1}{\mu} \sum_{k=1}^{\mu} \exp \left[ \frac{2}{N_0} \int r(t) s(t, -(M-1), \Delta_k, \Phi) dt \right] f(\Phi) d\Phi$$

Averaging over the phase  $\Phi$  gives the zeroth-order modified Bessel function. Thus we can write

$$\begin{aligned} l_1 &= \frac{1}{\mu} \sum_{k=1}^{\mu} I_0\left(\frac{2}{N_0} z_{1k}\right) \\ l_2 &= \frac{1}{\mu} \sum_{k=1}^{\mu} I_0\left(\frac{2}{N_0} z_{2k}\right) \\ &\quad \vdots \\ l_M &= \frac{1}{\mu} \sum_{k=1}^{\mu} I_0\left(\frac{2}{N_0} z_{Mk}\right) \end{aligned} \tag{7.10}$$

where

$$z_{ak}^2 = x_{ak}^2 + y_{ak}^2$$

$$x_{ak} = \begin{cases} \int r(t)s(t, a, \Delta_k, 0) dt, & a \text{ odd} \\ \int r(t)s(t, -(a-1), \Delta_k, 0) dt, & a \text{ even} \end{cases}$$

and

$$y_{ak} = \begin{cases} \int r(t)s(t, a, \Delta_k, \pi/2) dt, & a \text{ odd} \\ \int r(t)s(t, -(a-1), \Delta_k, \pi/2) dt, & a \text{ even} \end{cases}$$

$z_{ak}$  is a random variable with a Rician distribution.<sup>(10)</sup>

The optimum noncoherent (ML) receiver structure is shown in Figure 7.3. This receiver structure is optimum independent of SNR. Unfortunately, as in the case of coherent detection, the performance of this receiver is difficult to calculate accurately. Hence a high-SNR approximation is made and a resulting high-SNR receiver structure is developed. A suboptimum receiver structure which examines all the  $z_{ak}$ ,  $a = 1, \dots, M$  and  $k = 1, \dots, \mu$ , and then decides the  $\alpha_{n+1}$  corresponding to the largest performs well for high SNR. This follows from the following. The Bessel function  $I_0(\cdot)$  is a monotonic function. For large SNR we have with good approximation

$$\sum_{k=1}^{\mu} I_0(z_{ak}) \approx I_0(z_{a\Delta}) \tag{7.11}$$

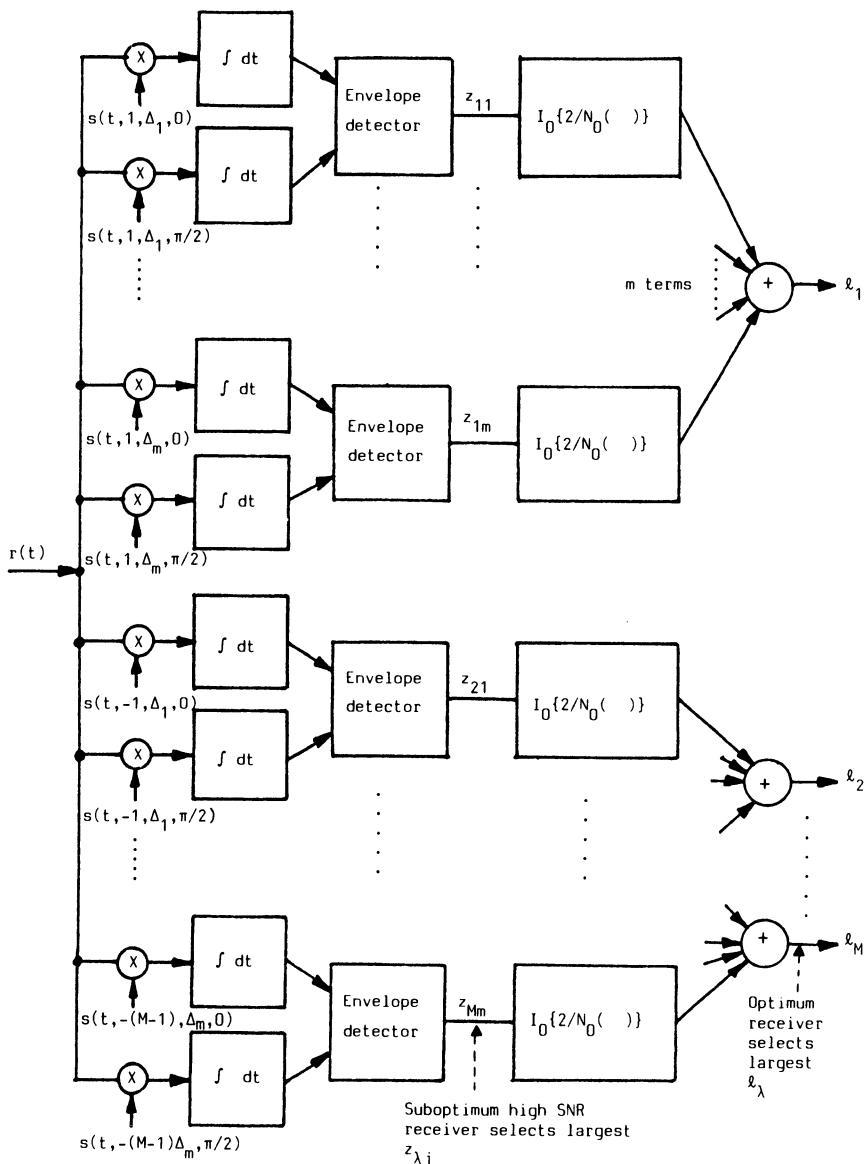


Figure 7.3. Optimum and high-SNR suboptimum CPFSK noncoherent receivers of Osborne and Luntz type.<sup>(4)</sup>

where  $z_{a\Delta}$  is the largest of the  $z_{ak}$ . The suboptimum noncoherent large high-SNR receiver is also shown in Figure 7.3.

The asymptotic behavior for high SNR of the receiver structure in Figure 7.3 is analyzed in Chapter 10 by means of distance results. The generalizations to other CPM schemes are obvious. Results for some partial response schemes are also given in Chapter 10.

The optimum and suboptimum structures in this section apply for general partial response CPM, but they become unreasonably complex. As well it is unclear how successive symbol decisions can be made in a convenient way using the structures in Figures 7.2 and 7.3. In the next section we will derive a general coherent high-SNR receiver for partial response CPM, where the ML sequence estimation is done by means of a Viterbi processor. We will see that this structure is convenient for construction of a general receiver that employs successive real time symbol decisions.

## 7.2. Optimum Viterbi Receivers

In this section we will describe a class of optimum receivers of the maximum likelihood sequence estimation type. The text will be in terms of partial response CPM, but with minor modifications the principles apply also to multi- $h$  CPM and to coded CPM. The material in this section can be found in Refs. 11-14, 37, and 15-21. The Viterbi receiver for multi- $h$  CPM is considered in some detail in Appendix C and in Refs. 22, 25-27.

First we briefly repeat the trellis development from Section 3.4.1. It is assumed that the pulse  $g(t)$  has finite length  $LT$ , i.e.,  $g(t) = 0$  for  $t < 0$  and  $t > LT$ . Since  $g(t)$  is time limited,  $q(t)$  is 0 for  $t \leq 0$  and constant at  $q(LT)$  for  $t \geq LT$ . For positive pulses  $g(t)$ ,  $q(LT) = 1/2$ . Thus the information-carrying phase can be written as

$$\begin{aligned}\phi(t, \alpha) &= 2\pi h \sum_{i=-\infty}^n \alpha_i q(t - iT) = \theta(t, \alpha_n) + \theta_n \\ &= 2\pi h \sum_{i=n-L+1}^n \alpha_i q(t - iT) + h\pi \sum_{i=-\infty}^{n-L} \alpha_i, \\ nT &\leq t \leq (n+1)T\end{aligned}\quad (7.12)$$

For  $h$  and  $g(t)$  and for any symbol interval  $n$ , the phase  $\phi(t, \alpha)$  is defined by  $\alpha_n$ , the correlative state vector  $(\alpha_{n-1}, \alpha_{n-2}, \dots, \alpha_{n-L+1})$  and the phase state  $\theta_n$ , where

$$\theta_n = h\pi \sum_{i=-\infty}^{n-L} \alpha_i \bmod 2\pi \quad (7.13)$$

The number of correlative states is finite and equal to  $M^{(L-1)}$ . For rational modulation indices the phase tree is reduced to a phase trellis.<sup>(15,11-14)</sup> For  $h = 2k/p$  ( $k, p$  integers) there are  $p$  different phase states with values  $0, 2\pi/p, 2 \cdot 2\pi/p, \dots, (p-1)2\pi/p$ . The total state is defined by the  $L$ -tuple  $\sigma_n = (\theta_n, \alpha_{n-1}, \alpha_{n-2}, \dots, \alpha_{n-L+1})$ , and the number of such states is

$$S = pM^{(L-1)}$$

All of these properties are critical to the receiver structures in this section.

Figure 7.1 shows the phase tree for a binary system with a raised cosine pulse of length  $L = 3$  (3RC) for  $h = 4/5$ . Phase states and correlative states are assigned to the nodes in the phase tree. The root node is arbitrarily given phase state 0. Each node in the tree is labeled with the state  $(\theta_n, \alpha_{n-1}, \alpha_{n-2})$ . The state trellis diagram can be derived from Figure 7.1 by viewing the phases modulo  $2\pi$ . By folding the phase tree in Figure 7.1 into a cylinder, the so-called phase cylinder in Figure 7.4 is obtained. The 20-state trellis is shown in Figure 7.5.

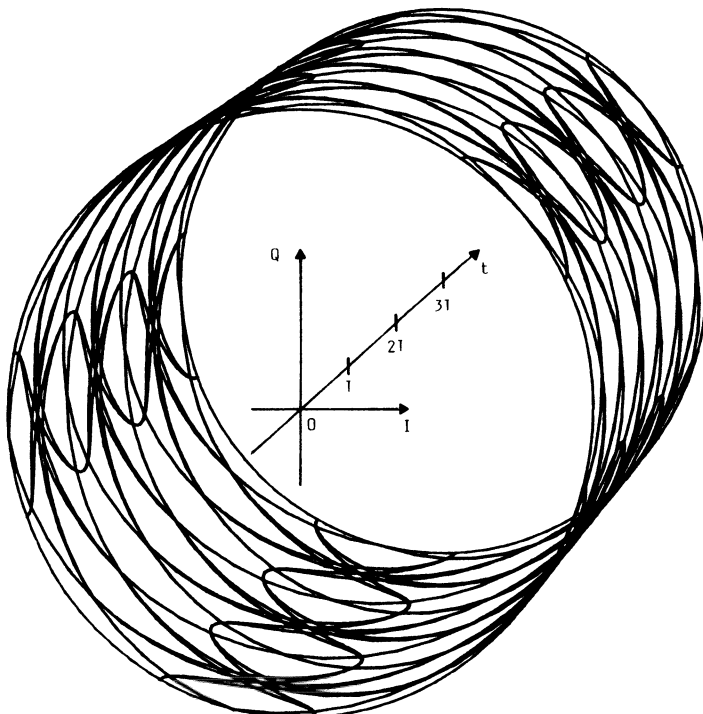


Figure 7.4. Phase cylinder for  $M = 2$ , 3RC with  $h = 4/5$ . Compare Figures 7.1 and 7.5. All signal paths are shown over three symbol intervals on the surface of the cylinder. Phase relative to the carrier is shown.

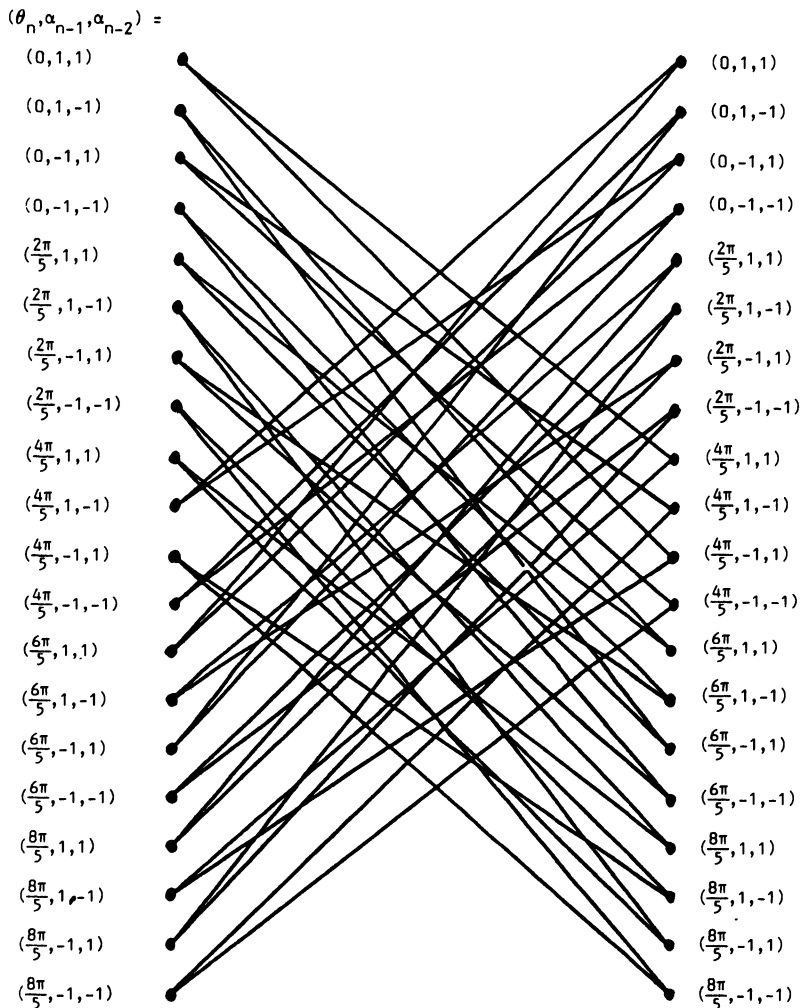


Figure 7.5. Trellis diagram for the binary 3RC scheme with  $h = 4/5$ . Compare the phase tree in Figure 7.1, where the different states are assigned to the nodes. Also compare the phase cylinder in Figure 7.4.

The receiver observes the signal  $r(t) = s(t, \alpha) + n(t)$ , where the noise  $n(t)$  is Gaussian and white. As we developed in Section 2.1, the maximum likelihood sequence estimating (MLSE) receiver maximizes the log likelihood function <sup>(16)</sup>

$$\log_e [p_{r(t)|\tilde{\alpha}}(r(t))|\tilde{\alpha}]] \approx - \int_{-\infty}^{\infty} [r(t) - s(t, \tilde{\alpha})]^2 dt \quad (7.14)$$

with respect to the infinitely long estimated sequence  $\tilde{\alpha}$ . The maximizing sequence  $\tilde{\alpha}$  is the maximum likelihood sequence estimate and  $p_{r(t)|\tilde{\alpha}}$  is the probability density function for the observed signal  $r(t)$  conditioned on the infinitely long sequence  $\tilde{\alpha}$ . It is equivalent to maximize the correlation

$$J(\tilde{\alpha}) = \int_{-\infty}^{\infty} r(t)s(t, \tilde{\alpha}) dt \quad (7.15)$$

In principle, the operation (7.15) is the basis for a correlation receiver, in which all possible transmitted signals  $s(t, \alpha)$  are correlated with the received signal and the data sequence  $\tilde{\alpha}$  maximizing the correlation is chosen as the received data. This is not a feasible structure in practice, not even with reasonably short data bursts.

Now define

$$J_n(\tilde{\alpha}) = \int_{-nT}^{(n+1)T} r(t)s(t, \tilde{\alpha}) dt \quad (7.16)$$

Thus we can write

$$J_n(\tilde{\alpha}) = J_{n-1}(\tilde{\alpha}) + Z_n(\tilde{\alpha}) \quad (7.17)$$

where

$$Z_n(\tilde{\alpha}) = \int_{nT}^{(n+1)T} r(t) \cos [\omega_0 t + \phi(t, \tilde{\alpha})] dt$$

By using the above formulas it is possible to calculate the function  $J(\tilde{\alpha})$  recursively through (7.17) and the metric  $Z_n(\tilde{\alpha})$ . This metric can be recognized as a correlation between the received signal and an estimated signal over the  $n$ th symbol interval.

The Viterbi algorithm is a recursive procedure to choose those sequences that maximize the log likelihood function up to the  $n$ th symbol interval. The possible extensions of those sequences are portrayed in the state trellis. The receiver computes  $Z_n(\tilde{\alpha}_n, \tilde{\theta}_n)$  for all  $M^L$  possible sequences  $\tilde{\alpha}_n = \{\tilde{\alpha}_n, \tilde{\alpha}_{n-1}, \dots, \tilde{\alpha}_{n-L+1}\}$  and all  $p$  possible  $\tilde{\theta}_n$ . This makes  $pM^L$  different values of  $Z_n$ . Rewriting (7.17) using (7.13) yields

$$Z_n(\tilde{\alpha}_n, \tilde{\theta}_n) = \int_{nT}^{(n+1)T} r(t) \cos (\omega_0 t + \theta(t, \tilde{\alpha}_n) + \tilde{\theta}_n) dt \quad (7.18)$$

It is seen that  $Z_n(\tilde{\alpha}_n, \tilde{\theta}_n)$  is obtained by feeding the signal  $r(t)$  into a filter and sampling the output of the filter at  $t = (n + 1)T$ , and that a bank of

such filters must be used. The receiver correlates the received signal over one symbol interval with all possible transmitted alternatives over that symbol interval. By using the finite state description of the signals, the correlation receiver can now be implemented without exponential growth of the number of receiver signal alternatives.

The noise  $n(t)$  can be expressed in the bandpass form

$$n(t) = x(t) \cos \omega_0 t - y(t) \sin \omega_0 t \quad (7.19)$$

Using the basic quadrature receiver of Figure 7.6, the received quadrature components are

$$\begin{aligned} \hat{I}(t) &= \left[ \left( \frac{2E}{T} \right)^{1/2} I(t) + x(t) \right] \\ \hat{Q}(t) &= \left[ \left( \frac{2E}{T} \right)^{1/2} Q(t) + y(t) \right] \end{aligned} \quad (7.20)$$

By inserting these components in (7.18) and omitting double frequency terms, we have

$$\begin{aligned} Z_n(\tilde{\alpha}_n, \tilde{\theta}_n) &= \cos(\tilde{\theta}_n) \int_{nT}^{(n+1)T} \hat{I}(t) \cos[\theta(t, \tilde{\alpha}_n)] dt \\ &\quad + \cos(\tilde{\theta}_n) \int_{nT}^{(n+1)T} \hat{Q}(t) \sin[\theta(t, \tilde{\alpha}_n)] dt \\ &\quad + \sin(\tilde{\theta}_n) \int_{nT}^{(n+1)T} \hat{Q}(t) \cos[\theta(t, \tilde{\alpha}_n)] dt \\ &\quad - \sin(\tilde{\theta}_n) \int_{nT}^{(n+1)T} \hat{I}(t) \sin[\theta(t, \tilde{\alpha}_n)] dt \end{aligned} \quad (7.21)$$

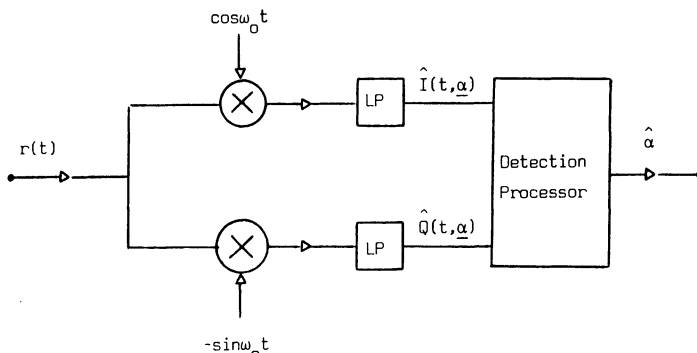


Figure 7.6. Basic quadrature receiver. The LP-filters only remove double carrier frequency terms.  $r(t) = I(t) \cos(\omega_0 t) - Q(t) \sin(\omega_0 t) + n(t)$ .

This can be interpreted as  $4M^L$  baseband filters with the impulse responses

$$h_c(t, \tilde{\alpha}_n) = \begin{cases} \cos \left[ 2\pi h \sum_{j=-L+1}^0 \tilde{\alpha}_j q((1-j)T - t) \right] \\ 0 \quad \text{for } t \text{ outside } [0, T] \end{cases}$$

and

$$h_s(t, \tilde{\alpha}_n) = \begin{cases} \sin \left[ 2\pi h \sum_{j=-L+1}^0 \tilde{\alpha}_j q((1-j)T - t) \right] \\ 0 \quad \text{for } t \text{ outside } [0, T] \end{cases} \quad (7.22)$$

The number of filters required can be reduced by a factor of 2 by observing that every  $\tilde{\alpha}$ -sequence has a corresponding sequence with reversed sign. Figure 7.7 shows an optimum receiver with  $2M^L$  matched filters. The outputs of these filters are sampled once every symbol interval, which produces the metrics  $Z_n(\tilde{\alpha}_n, \tilde{\theta}_n)$  in (7.21).

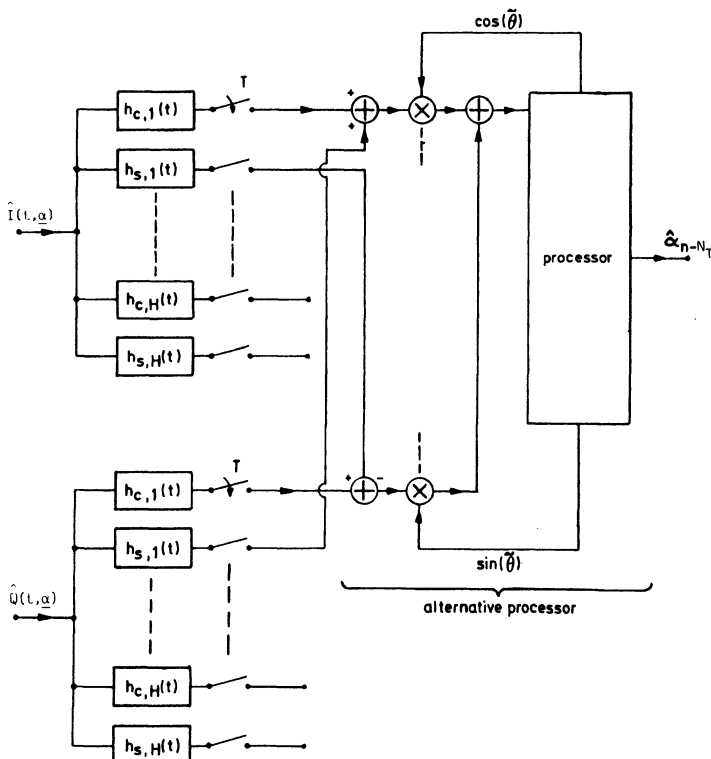


Figure 7.7. Receiver with baseband filterbank. The filters are given by equation (7.22).

The Viterbi algorithm (VA) is a recursive optimal solution to the problem of estimating the state sequence of a discrete time finite state Markov process observed in memoryless noise. The VA is optimum in the sense that the likelihood estimate of the sequence of states is obtained. Since a specific sequence of state transitions gives a unique sequence of data symbols, a maximum likelihood estimate of the data sequence is also obtained. This is referred to as maximum likelihood sequence estimation (MLSE). Note that the Osborne and Luntz receiver in Section 7.1 is optimum with a different criterion: It finds the optimum estimate of the first data symbol.

In its basic form, the Viterbi algorithm assumes that all possible transmitted finite sequences start from one common state and end in another common state. The decision about the most likely transmitted sequence is delayed at the receiver until the whole sequence is received. The metrics of all candidate state paths are successively updated at each trellis section; all possible state transitions are extended and all paths are deleted at the next trellis section except the path with highest likelihood entering each node. When the whole signal sequence is received, all candidate state paths terminate in the same common node at the far end of the trellis, and the most likely of these is the MLSE output.

We will now modify this scheme for practical application to CPM reception. Tutorial treatments of the Viterbi algorithm are widely available; particularly recommended are those available in Refs. 7, 17, and 21. Some alternative Viterbi receiver structures appear in Refs. 18–20, and 13.

### 7.3. Implementation of the Viterbi Algorithm for CPM

We will emphasize here details of the Viterbi approach that are important in a phase demodulator. We have seen from Chapter 3 and the previous section that the CPM signals have a finite number of states for any rational modulation index. Figure 7.8 shows one more example with 3RC,  $h = 2/3$ ,  $M = 2$  which we will carry along as an illustration. This has a trellis with 12 states, shown in Figure 7.9. With the recursive metric of (7.17) we can now perform Viterbi detection of the received signal by means of the structure in Figure 7.7. A bank of matched filters computes the metrics.

Decoding a block of the CPM signal can mimic the method of decoding a block or convolutional code with an inserted tail.<sup>(21)</sup> However, in practice, this is not the most feasible method of demodulating. The CPM signal is normally not block-structured with common states at certain intervals. Furthermore, the long delays are often unwanted. Therefore a modified Viterbi algorithm is used for CPM, much the same way as a modified Viterbi algorithm is used for decoding convolutional codes.<sup>(17,21)</sup> It successively

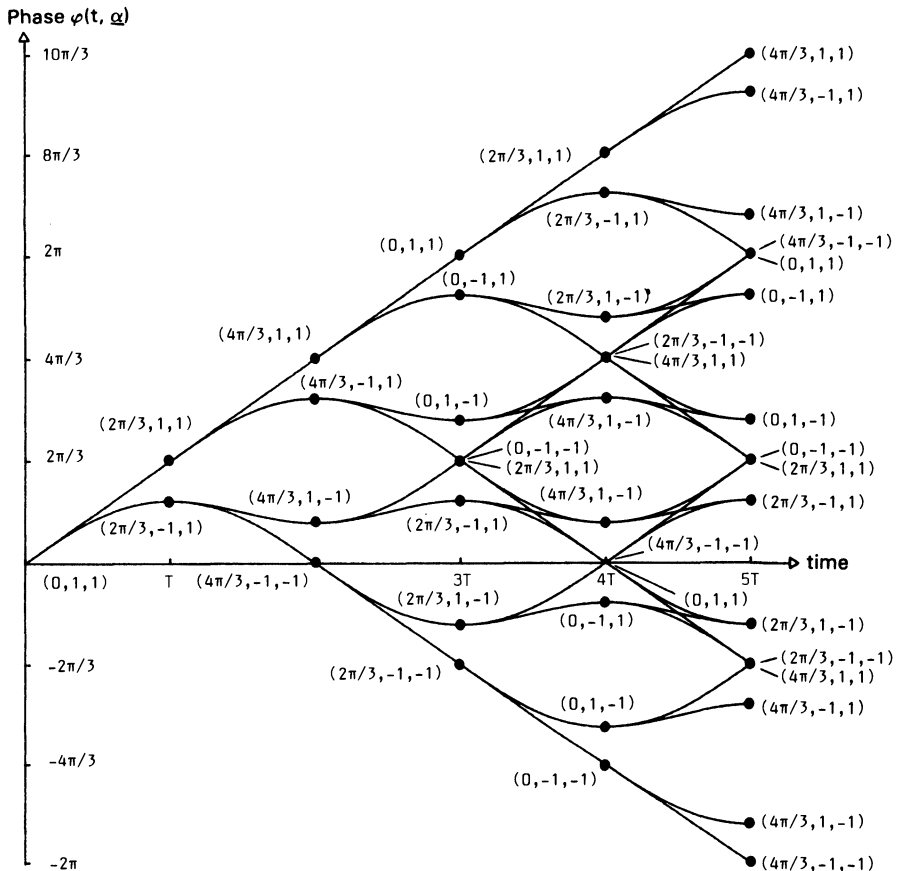


Figure 7.8. Binary phase tree for 3RC when  $h = 2/3$ . The assignment of states is shown.

outputs symbols after a decoding delay that is the same for each symbol, and it accepts sequences of indefinite length. At each state in the trellis, the surviving paths are saved only back to a certain point, a length called the *path memory*  $N_T$ . At this delay a decision on the oldest symbol is forced by, for instance, taking a majority decision among the state paths, or releasing the symbol corresponding to the most likely path, or by simply choosing at random; the best criterion depends on conditions like the SNR. By doing this we are relying on the fact that for well-behaved CPM systems, a path which has split from the correct path will accumulate distance from it in proportion to the length of the unmerged span. Incorrect paths will have a low probability of having a long unmerged span.

The minimum distance calculations in Chapter 3 guide us in choosing the path memory  $N_T$ . Figure 3.29 shows the minimum squared Euclidean

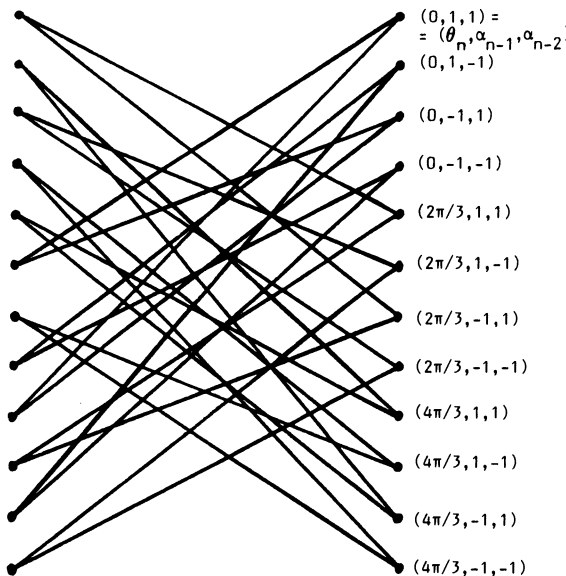


Figure 7.9. State trellis for the binary 3RC scheme with  $h = 2/3$ . Compare the phase tree in Figure 7.8.

distance as a function of  $h$  and the observation interval length  $N$ . The upper bound on the minimum squared Euclidean distance is reached for  $N \geq N_B$ . It is clear from the analysis behind Figure 3.29 that the path memory should be selected at least as large as  $N_B$ , and experiment has shown that  $N_B$  is almost always enough. The length of the path memory is normally a function of the modulation index. From Figure 3.29 we can conclude for example that for  $h \leq 0.5$ ,  $N_B = 4$  while for  $h \approx 2/3$ ,  $N_B$  is about 20. The reason for this is obvious from Figure 7.10, where two unmerged paths are close and a long observation interval is required before their distance is larger than the bound  $d_B^2$ . Compare the phase cylinder for  $h = 1/2$  shown in Figure 7.11; in this case no unmerged paths have smaller distance than the pair giving  $d_{\min}^2 = d_B^2$  for  $N = N_B = 4$ .

A further illustration to the trellis structure of CPM is given in Figure 7.12. Here four successive symbol intervals are shown in the trellis for 3RC,  $h = 2/3$ ,  $M = 2$ . Two pairs of paths with distance  $d_B^2$  are shown. (Compare the phase tree in Figure 7.8 and the phase cylinder in Figure 7.10; the full trellis section in Figure 7.8 and the phase cylinder in Figure 7.10; the full trellis section in Figure 7.9 is used to construct Figure 7.12.) Although the paths in Figure 7.12 have merged, the path memory for a Viterbi detector with 3RC,  $h = 2/3$ ,  $M = 2$  should be of the order of  $N_T \approx N_B \approx 20$ . Here, unmerged neighbors are more important than merged neighbors in setting  $N_T$ .

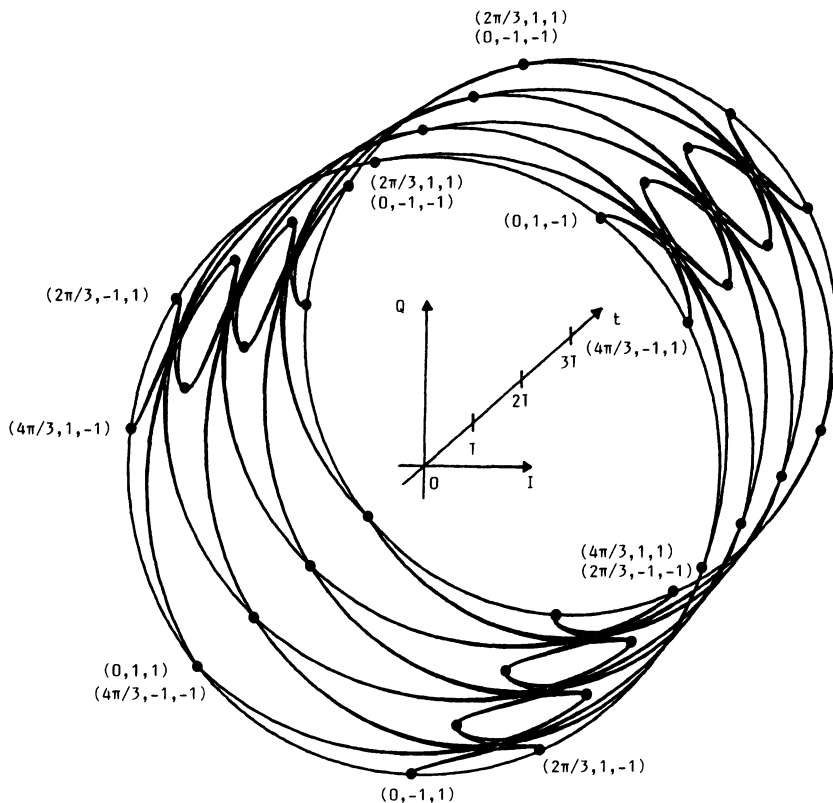


Figure 7.10. Phase cylinder for  $M = 2$ , 3RC with  $h = 2/3$ . Compare the trellis in Figure 7.9 and the phase tree in Figure 7.8. Note the arbitrary phase offset between the phase in the tree in Figure 7.8 and the cylinder in Figure 7.10.

Another implementation problem with Viterbi decoders is metric quantization. For convolutional codes used with QPSK or BPSK modulation, 3-bit A/D conversion seems sufficient in practice.<sup>(21)</sup> For CPM reception, it still remains to investigate the best choice of the number of bits in the metric quantization. Most likely, the loss with 3 bits is larger for CPM. This is discussed somewhat in Chapter 11.

#### 7.4. Performance Simulation

In this section we will explore the measurement of receiver error performance by simulation, and present some representative results for partial response CPM schemes. Other numerical results appear elsewhere

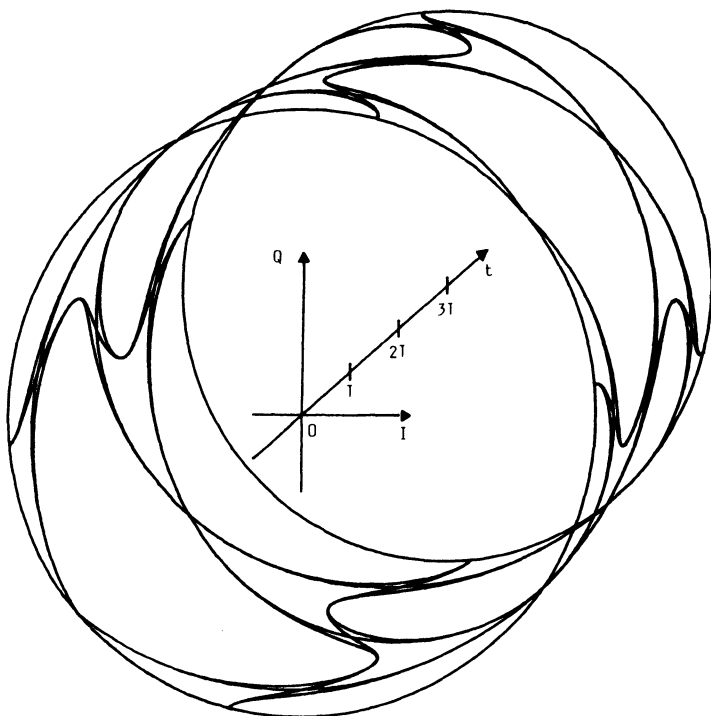


Figure 7.11. Phase cylinder for  $M = 2$ , 3RC with  $h = 1/2$ .

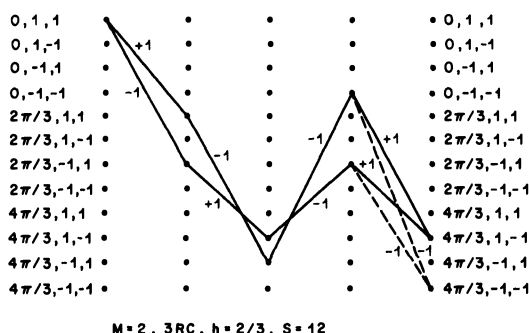


Figure 7.12. Examples of two pairs of paths in the trellis which are on distance  $d_B^2$ . Compare the corresponding paths in the phase tree in Figure 7.8. The full trellis section in Figure 7.9 have been used.

in the book: Simulations of convolutionally coded CPM appear in Chapter 11 and results for multi- $h$  modulations<sup>(23-30)</sup> are featured in Appendix C. It should be stressed that what is simulated is channel noise, not the receiver. The receiver is simply implemented in software, a common approach in practical applications.

#### 7.4.1. Simulating Channel Noise

The problem of measuring receiver error by simulation may be broken into three parts: (i) simulating the effect of channel noise, (ii) constructing a receiver, and (iii) analyzing statistically the error events that occur. The last topic is the subject of Appendix C, and we will discuss the first topic now.

The Viterbi receiver calculates the metric increment  $Z_n(\tilde{\alpha}_n, \tilde{\theta}_n)$  of (7.18), which is the correlation over the  $n$ th interval of a certain signal and the received signal plus noise, denoted  $r(t)$ . If we assume that  $r(t) = s(t) + n(t)$ , with  $s(t)$  the transmitted signal and  $n(t)$  white Gaussian noise, then  $Z_n$  is a correlated Gaussian variable with mean

$$\begin{aligned} \mathcal{E}[Z_n] &= 0 + (2E/T)^{1/2} \int_{nT}^{(n+1)T} \cos[\omega_0 t + \psi(t)] \cos[\omega_0 t + \Phi(t)] dt \\ &= (1/2)(2E/T)^{1/2} \int_{nT}^{(n+1)T} \cos[\psi(t) - \Phi(t)] dt \end{aligned} \quad (7.23)$$

Here  $s(t) = (2E/T)^{1/2} \cos[\omega_0 t + \psi(t)]$  and the signal to which the correlator is matched is  $\cos[\omega_0 t + \Phi(t)]$ . The second moment of  $Z_n$  is

$$\begin{aligned} \mathcal{E}[Z_n^2] &= \left[ (2E/T)^{1/2} \int_{nT}^{(n+1)T} \cos[\omega_0 t + \psi(t)] \cos[\omega_0 t + \Phi(t)] dt \right]^2 + 0 \\ &\quad + \mathcal{E} \left[ \int_{nT}^{(n+1)T} \int_{nT}^{(n+1)T} n(t)n(\tau) \cos[\omega_0 t + \Phi(t)] \right. \\ &\quad \times \cos[\omega_0 \tau + \Phi(\tau)] dt d\tau \\ &= \mathcal{E}^2[Z_n] + \int_{nT}^{(n+1)T} (N_0/2) \cos^2[\omega_0 t + \Phi(t)] dt \\ &= \mathcal{E}^2[Z_n] + N_0 T/4 \end{aligned} \quad (7.24)$$

where the last line holds in the limit of large carrier frequency. The difficulty of simulating the channel noise lies in the fact that  $Z_n$  is correlated in a nasty manner.

One approach to simulation would be to generate correlated noise variates  $Z_n - \mathcal{E}[Z_n]$  and add these to the noise-free filter outputs; thus far, this method has not been explored. Another procedure, in common use, is to form a discrete-time approximation to the modulated signal. The signal is sampled each  $1/\xi T$  second, or  $\xi$  times each interval, and the assumption is made that the signal holds that sample value throughout the  $1/\xi T$ -second subinterval. During the subinterval,  $s(t)$  holds a constant value and therefore occupies a single orthogonal dimension of signal space; the effect of the noise on this piece of signal is to add to its value an uncorrelated Gaussian variate. The correlation (7.18) is converted to the summation

$$Z_{\text{dis}} = \frac{T}{\xi} \sum_{k=1}^{\xi} r\left(\frac{kT}{\xi}\right) \cos(\omega_0 kT/\xi + \Phi(kT/\xi)) \quad (7.25)$$

where the index  $k$  runs over the sample points in the  $n$ th interval.

For the discretized signal, (7.23) becomes

$$\mathcal{E}[Z_{\text{dis}}] = (1/2)(2E/T)^{1/2} \frac{T}{\xi} \sum_{k=1}^{\xi} \cos[\psi(kT/\xi) - \Phi(kT/\xi)] \quad (7.26)$$

which converges to (7.23) as  $\xi$  grows large, by the fundamental theorem of calculus. The variance expression becomes

$$\begin{aligned} \mathcal{E}[Z_{\text{dis}}^2] &= \mathcal{E}^2[Z_{\text{dis}}] \\ &\quad + \mathcal{E}\left[ \sum_{k=1}^{\xi} \sum_{l=1}^{\xi} (T/\xi)^2 n[kT/\xi] n[lT/\xi] \cos[(\omega_0 lT/\xi) + \Phi(lT/\xi)] \right. \\ &\quad \times \cos[(\omega_0 kT/\xi) + \Phi(kT/\xi)] \Bigg] \\ &= \mathcal{E}^2[Z_{\text{dis}}] + \sum_{k=1}^{\xi} (T/\xi)^2 \sigma^2 \cos^2[(\omega_0 kT/\xi) + \Phi(kT/\xi)] \\ &\rightarrow \sigma^2 T^2 / 2\xi + \mathcal{E}^2[Z_{\text{dis}}] \quad \text{as } \xi \rightarrow \infty \end{aligned} \quad (7.27)$$

Here  $\sigma^2$  is the variance of the IID Gaussian variates  $n(k)$  that are added to each signal sample. Equating (7.27) and (7.24), we find that

$$\sigma^2 = N_0 \xi / 2T \quad (7.28)$$

will produce in the limit an effect similar to stochastic-process noise with a power spectral density of  $N_0/2$ .

The intention of this derivation is to give the idea behind the "discrete sample" method. A more effective use of the method requires that the foregoing be recast in terms of the baseband components  $I(t)$  and  $Q(t)$ . If this is done, only 4-16 points per interval are needed to give a good approximation for a reasonably smooth CPM signal; the proper number of points is best found experimentally by increasing the point count until no change in the results occurs. In any simulation, it is necessary to test a known case in order to be sure that all scalings and constants are correct.

Another method of simulating channel noise is to express the signals in terms of components along the orthogonal directions of a signal space, the so-called "signal space" method. After a signal is broken down in this way, an IID Gaussian variate of variance  $N_0/2$  is added to each component to form the components of the noisy signal. The signal space method is more effective than the discrete sample method if the signals that the modulation can produce in an interval are expressible in a small signal space. In LREC schemes, for instance,  $4L$  dimensions are required; for  $L = 1$  (CPFSK) the signal space method is attractive. This method is illustrated for multi- $h$  codes in Appendix C.

#### 7.4.2. Realization of the Viterbi Algorithm and Numerical Results

In constructing the Viterbi algorithm, an effective procedure is to store the identity of the trellis in tables. One table is used to store the state transitions caused by each data symbol from each state. To increase speed, another table stores "backwards" state information, the states from which it is possible to enter each state. The transmitter uses the first table and the receiver the second. For each state, a memory "cell" is maintained, in which are stored the metric of the best path leading into the state at the present time, the identity of the path (i.e., the data symbols corresponding to it), and certain temporary information.

During the operation of the receiver, the algorithm seeks the best metric path leading into each state at the next time. There are  $M$  paths out of each state at the present time and into each state at the next time. Each of these corresponds to a signal, and these signals are correlated with the channel signal by means of (7.18); the process takes place numerically as described in Section 7.4.1. The identity of a path is kept in the state cell until it exceeds the path memory length, and thereafter path symbols are either truncated or released to the use one by one as the algorithm proceeds through the trellis.

In order to measure the error performance of the receiver, its output symbols are compared to the known transmitted symbols. For an accurate statistical treatment, it is essential to keep track of error *events*, not simply symbol errors. An event begins when the receiver-output trellis path splits

from the transmitted path and it ends when the paths merge again. Further discussion of error event analysis appears in Appendix C. Generally speaking, it is difficult to simulate receiver performance at low error rate because events seldom occur and their statistics are therefore unreliable.

### Numerical Results

Simulations for a few selected schemes will now be presented. As a reference, the bit error probability for binary PSK,  $Q((2E_b/N_0)^{1/2})$ , appears in the figures; this is an approximate estimate for QPSK. A lower bound on the bit error probability is also shown; this bound is derived by considering the minimum distance event only, and for an  $M$ -ary scheme it is

$$P_b \geq \frac{2}{\log_2 M} \frac{M^2 - 2}{M^2} Q((d_{\min}^2 E_b / N_0)^{1/2}) \quad (7.29)$$

The bound is tight at high SNR.

The path memory for the Viterbi detector in Figure 7.13 has been set to 50 symbol intervals, which is more than enough for the minimum distance path to occur.  $\xi = 20$  sample points per symbol interval have been used. Figure 7.13 shows two eight-level CPFSK schemes. The modulation indices are  $1/4$  and  $5/11$ . The eight-level information symbols are Gray coded according to Table 7.1; this is a good mapping rule for uncoded CPFSK, but not necessarily the preferred one for coded CPFSK (see Chapter 11).

We now turn to simulations of 3RC schemes. A method has been described in Chapter 3 for calculation of upper bounds on the symbol error probability for a Viterbi detector having a path memory of length  $N_T$  symbol intervals. Figure 7.14 shows the result of this calculation for the binary 3RC scheme with  $h = 4/5$  when  $N_T = 1, 2, \dots, 20$  and  $N_T = \infty$ . The asymptotic behavior cannot be improved by making  $N_T > N_B$ , where  $N_B$  is the value of  $N$  where  $d_{\min}^2 = d_B^2$ . The lower bound shown in Figure 7.14 is based on the minimum Euclidean distance and it is seen that if  $N_T \geq N_B$ , the upper and lower bounds are close even for fairly large error probabilities. By increasing  $N_T$ , improvement is achieved for low SNR, but at low SNR the upper bounds are loose.  $d_{\min}^2$  is 3.17, so the asymptotic gain in  $E_b/N_0$  is 2.0 dB compared to QPSK. From Figure 7.14, it is seen that this gain is achieved even at fairly low SNR. This conclusion holds for a large variety of schemes and it can be concluded that the minimum Euclidean distance is sufficient for the characterization of performance in terms of symbol error probability. Even where the upper bound is loose the minimum distance appears to be accurate.

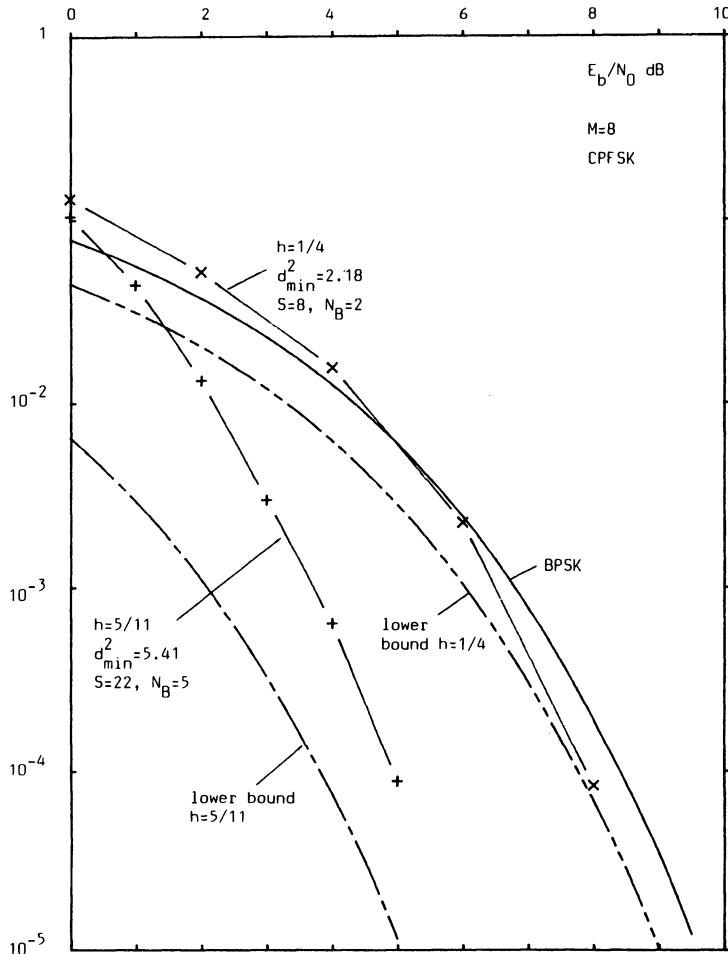


Figure 7.13. Simulated bit error probability  $P_b$  for uncoded eight-level CPFSK. Comparisons with asymptotic lower bounds from equation (7.34). See Table 7.1.

Table 7.1. The Gray Code (Mapping Rule) Used by the Eight-Level Uncoded CPFSK Schemes

Binary representation	000	001	010	011	100	101	110	111
$\alpha$ symbol value	-1	-3	-7	-5	1	3	7	5

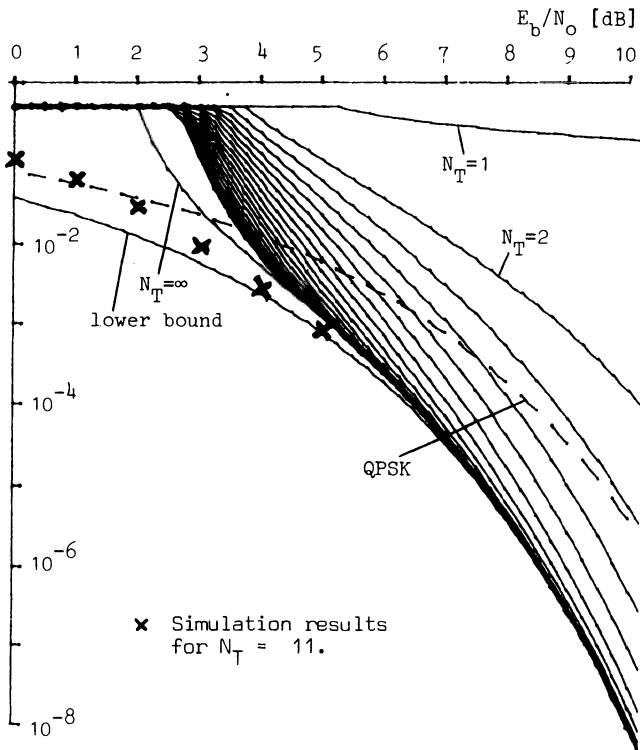
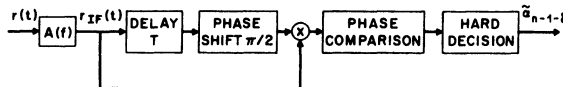


Figure 7.14. Computer simulations of  $M = 2$ , 3RC,  $h = 4/5$ ,  $N_T = 11$ . Upper bounds for  $N_T = 1, 2, \dots, 20$  and a lower bound are also shown. Compare QPSK (BPSK) for reference (shown dashed).

With these bounds as comparison, some 3RC simulation results are shown in Figure 7.14. These are for a coherent Viterbi detector with path memory 11. Results similar in appearance have been obtained for a wide variety of modulations; see for instance Refs. 13, 20, and 38.

## 7.5. Analysis of Simple Noncoherent Receivers

The bulk of the analytical treatment of receivers for CPM available in the literature considers ideal coherent receivers. In applications, however, noncoherent receivers are often used because they are simpler and less expensive. Unfortunately, they are often very difficult to analyze because of their nonlinear nature, which leads to non-Gaussian noise. There are some analytical results available for differential detection and discriminator detection of CPM with symbol-by-symbol decisions. These will be presented in this section together with some modified schemes and simulation results.

Figure 7.15. Differential detector with delay  $T$ .

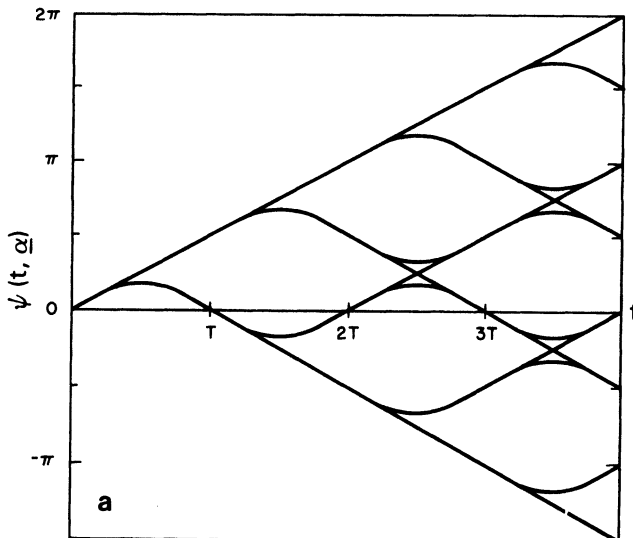
### 7.5.1. Differential Detection

We will first consider differential detection of binary partial response CPM. The receiver is shown in Figure 7.15. The received signal  $r(t)$  is filtered by an IF filter  $A(f)$  which band limits  $r(t)$ . This creates a time-varying signal envelope  $(2E_b/T)^{1/2}\mathcal{A}(t, \alpha)$  and a distorted phase  $\psi(t, \alpha)$ :

$$r_{\text{IF}}(t) = \left(\frac{2E_b}{T}\right)^{1/2} \mathcal{A}(t, \alpha) \cos [\omega_0 t + \psi(t, \alpha)] + n'(t) \quad (7.30)$$

where  $n'(t)$  is the filtered noise process and  $E = E_b$ . For the calculation of  $\mathcal{A}(t, \alpha)$  and  $\psi(t, \alpha)$  see Section 3.5 or Ref. 51. Figures 7.16 and 7.17 give some examples of the envelope and the phase tree for filtered CPM schemes. Using the quadrature representation of the bandpass noise

$$n'(t) = \sqrt{2}n'_c(t) \cos [\omega_0 t + \psi(t, \alpha)] - \sqrt{2}n'_s(t) \sin [\omega_0 t + \psi(t, \alpha)]$$

Figure 7.16a. Phase tree for MSK (1REC,  $h = 1/2$ ) filtered in a 1RC filter.

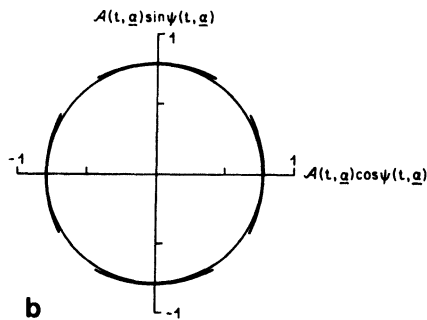


Figure 7.16b. Envelope for MSK filtered in a 1RC filter.

we get the polar representation of  $r_{IF}(t)$

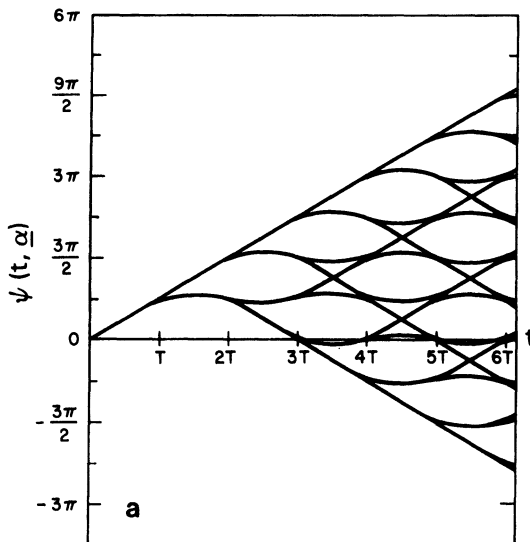
$$r_{IF}(t) = \mathcal{R}(t, \alpha) \cos [\omega_0 t + \psi(t, \alpha) + \eta(t)] \quad (7.31)$$

where

$$\mathcal{R}(t, \alpha) = \sqrt{2} \left\{ \left[ \left( \frac{E_b}{T} \right)^{1/2} \mathcal{A}(t, \alpha) + n'_c(t) \right]^2 + n'^2_s(t) \right\}^{1/2}$$

and

$$\eta(t) = -\arctan \frac{n'_s(t)}{\left( \frac{E_b}{T} \right)^{1/2} \mathcal{A}(t, \alpha) + n'_c(t)}$$

Figure 7.17a. Phase tree for 1REC with  $h = 3/4$  filtered in a 3RC filter.

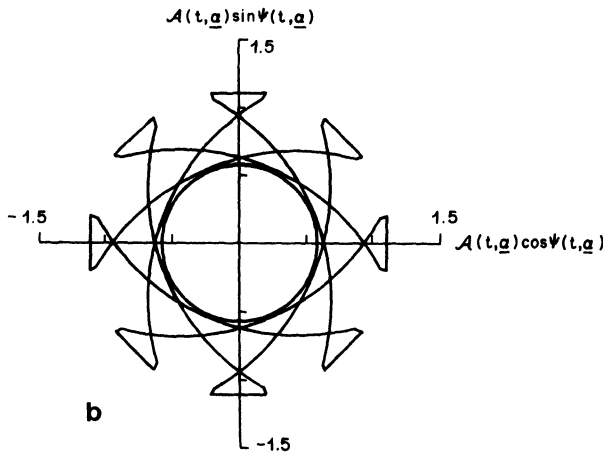


Figure 7.17b. Envelope for 1REC with  $h = 3/4$  filtered in a 3RC filter.

Here  $n'_s$  and  $n'_c$  are low-pass Gaussian processes. We will often use the raised cosine filter given by

$$a(t) = \begin{cases} \left(\frac{2}{3L_A T}\right)^{1/2} \left(1 - \cos \frac{2\pi t}{L_A T}\right), & 0 \leq t \leq L_A T \\ 0, & \text{otherwise} \end{cases} \quad (7.32)$$

The *differential detector* multiplies  $r_{IF}(t)$  by a one-symbol interval delayed and  $90^\circ$  phase shifted version of itself, resulting in

$$y(t) = \frac{\mathcal{R}(t, \alpha) \cdot \mathcal{R}(t - T, \alpha)}{2} \sin [\omega_0 T + \Delta\psi(t, T, \alpha)] \quad (7.33)$$

where

$$\begin{aligned} \Delta\psi(t, T, \alpha) &= [\Delta\psi(t, T, \alpha) + \eta(t) - \eta(t - T)] \text{ modulo } 2\pi \\ &= [\psi(t, \alpha) - \psi(t - T, \alpha) + \eta(t) - \eta(t - T)] \text{ modulo } 2\pi \end{aligned}$$

and second harmonic terms are ignored.  $\Delta\psi(t, T, \alpha)$  represents the change over one symbol interval of the filtered signal phase  $\Delta\psi(t, T, \alpha) = \psi(t, \alpha) - \psi(t - T, \alpha)$  plus the change in phase  $\eta(t) - \eta(t - T)$  contributed by the additive white Gaussian noise.

Assuming  $\omega_0 T = 2k\pi$  leads to

$$y(t) = \frac{\mathcal{R}(t, \alpha) \cdot \mathcal{R}(t - T, \alpha)}{2} \sin \Delta\psi(t, T, \alpha) \quad (7.34)$$

This signal is sampled when the ensemble of phase differences  $\psi(t, \alpha) - \psi(t - T, \alpha)$  has an open eye. This time is easily seen to be<sup>(12,51)</sup>

$$\begin{aligned} t_0 &= nT && \text{if } L + L_A \text{ odd} \\ t_0 &= (n + 1/2)T && \text{if } L + L_A \text{ even} \end{aligned} \quad (7.35)$$

where  $L_A$  is the length in symbol intervals of the filter impulse response  $a(t)$ .

Figure 7.18 shows the ensemble of  $\psi(t, \alpha) - \psi(t - T, \alpha)$  for the unfiltered CPM scheme 2RC, i.e.,  $\phi(t, \alpha) - \phi(t - T, \alpha)$ . At this time instant the receiver makes a decision about  $\alpha_{n-1-\delta}$  where  $\delta$  is the delay given by

$$\delta = \left\lceil \frac{L + L_A}{2} \right\rceil - 1$$

and  $\lceil (L + L_A)/2 \rceil$  is the nearest integer larger than or equal to  $(L + L_A)/2$ . The receiver decides  $\tilde{\alpha}_{n-1-\delta} = 1$  if  $y(t_0) > 0$  and otherwise decides  $\tilde{\alpha}_{n-1-\delta} = -1$ . An equivalent decision rule is  $\tilde{\alpha}_{n-1-\delta} = 1$  if  $\sin \Delta\psi(t_0, T, \alpha) > 0$  and  $\tilde{\alpha}_{n-1-\delta} = -1$  if  $\sin \Delta\psi(t_0, T, \alpha) \leq 0$ .

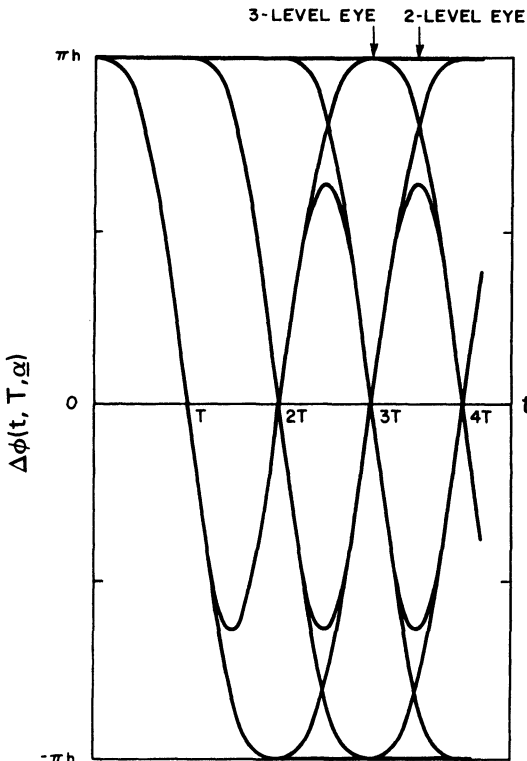


Figure 7.18. Phase difference diagram for 2RC, when the delay is  $T$ .

If  $\tilde{\alpha}_{n-1-\delta} = 1$  is transmitted, an error occurs with the probability

$$P(\alpha) = \Pr \{ \sin \Delta\psi(t_0, T, \alpha) \leq 0 \mid \alpha \} \quad (7.36)$$

In Simon and Wang<sup>(42)</sup> it is shown that this is given by

$$\begin{aligned} P(\alpha) &= \frac{1}{2} \left[ 1 - \left( 1 - \frac{\beta^2}{\alpha^2} \right)^{1/2} I_e \left( \frac{\beta}{\alpha}, \frac{E_b \alpha}{N_0} \right) \right] \\ &= \frac{(\alpha^2 - \beta^2)^{1/2}}{2\pi} \int_0^\pi \frac{\exp [-E_b(\alpha - \beta \cos \theta)/N_0]}{\alpha - \beta \cos \theta} d\theta \end{aligned} \quad (7.37)$$

where  $I_e(\beta/\alpha, E_b \alpha / N_0)$  is the Rice function.<sup>(46)</sup> The variables  $\alpha$  and  $\beta$  (note the difference between  $\alpha$  and  $\alpha$ ) are given by

$$\begin{aligned} \alpha &= \frac{U - rW \cos \Delta\psi(t_0, T, \alpha)}{1 - r^2} \\ \beta &= \left[ \alpha^2 - \frac{W^2 \sin^2 \Delta\psi(t_0, T, \alpha)}{1 - r^2} \right]^{1/2} \end{aligned}$$

where  $U, W, \Delta\psi(t_0, \alpha)$  are functions of  $\alpha$  given by

$$\begin{aligned} U &= \frac{\mathcal{A}^2(t_0, \alpha) + \mathcal{A}^2(t_0 - T, \alpha)}{2T \int_{-\infty}^{\infty} |A(f)|^2 df} \\ W &= \frac{\mathcal{A}(t_0, \alpha) \mathcal{A}(t_0 - T, \alpha)}{T \int_{-\infty}^{\infty} |A(f)|^2 df} \\ \Delta\psi(t_0, T, \alpha) &= \psi(t_0, \alpha) - \psi(t_0 - T, \alpha) \end{aligned}$$

and  $r$  is the noise correlation at  $T$

$$r = \frac{\mathcal{E}[n'(t_0)n'(t_0 - T)]}{N_0 \int_{-\infty}^{\infty} |A(f)|^2 df}$$

The average error probability is given by

$$P_e = \frac{1}{m} \sum_{\alpha} P(\alpha) \quad (7.38)$$

where  $m$  is the total number of sequences that need to be considered. It can be shown that

$$m = M^{L+L_A+l}$$

where

$$\begin{aligned} l &= 0 && \text{if } L + L_A \text{ odd} \\ l &= 1 && \text{if } L + L_A \text{ even} \end{aligned}$$

Since  $P(\alpha) = P(-\alpha)$  the number of terms can be reduced by 1/2.

For large SNRs the error probability  $P(\alpha)$  can be approximated. When  $E_b/N_0$  is large, it is known<sup>(46)</sup> that

$$\begin{aligned} I_e\left(\frac{\beta}{\alpha}, \frac{E_b}{N_0}\alpha\right) &\approx \frac{1}{\left[1 - \left(\frac{\beta}{\alpha}\right)^2\right]^{1/2}} \\ &- \frac{1}{\left[2\frac{\beta}{\alpha}\left(1 - \frac{\beta}{\alpha}\right)\right]^{1/2}} 2Q\left(\left[2\frac{E_b}{N_0}\alpha\left(1 - \frac{\beta}{\alpha}\right)\right]^{1/2}\right) \end{aligned} \quad (7.39)$$

for large SNRs

$$P(\alpha) \approx \left(\frac{\alpha + \beta}{2\beta}\right)^{1/2} Q\left(\left[\frac{2E_b}{N_0}(\alpha - \beta)\right]^{1/2}\right) \quad (7.40)$$

From this, we can define an equivalent to the Euclidean distance<sup>(40,41,10)</sup> for differential detection,

$$d_e^2 = 2(\alpha - \beta) \quad (7.41)$$

and write the error probability asymptotically as

$$P(\alpha) \approx Q\left(\left(\frac{d_e^2 E_b}{N_0}\right)^{1/2}\right) \quad (7.42)$$

The minimum equivalent distance  $d_{\min}^2$  gives the asymptotic value of the average error probability  $P_e$ , i.e.,

$$P_e \approx Q\left(\left(d_{\min}^2 \frac{E_b}{N_0}\right)^{1/2}\right) \quad (7.43)$$

where

$$d_{\min}^2 = \min_{\alpha} d_e^2$$

There is a large number of further results on differential detection of CPM, e.g., Refs. 31, 47, 48.

### 7.5.2. Discriminator Detection

In this section discriminator detection of binary partial response continuous phase modulation will be considered. The received signal is again filtered in an IF filter  $A(f)$ . Then  $r_{IF}(t)$  is passed through a limiter and a discriminator. The receiver is shown in Figure 7.19. The output of the discriminator is the derivative of the phase  $\psi(t, \alpha)$ , and an integrate and dump filter following the discriminator produces a phase difference  $\Delta\Psi(t, T, \alpha)$ <sup>(42,43,39)</sup> given by

$$\begin{aligned} \Delta\Psi(t, T, \alpha) &= \psi(t, \alpha) - \psi(t - T, \alpha) + [\eta(t) - \eta(t - T)] \bmod (2\pi) \\ &\quad + 2\pi N(t - T, t) \end{aligned} \quad (7.44)$$

where  $N(t - T, t)$  is the number of clicks, that is, the number of  $2\pi$  rotations, in the interval  $t - T$  to  $t$ . The receiver decides  $\tilde{\alpha}_{n-1-\delta} = 1$  if  $\Delta\Psi(t_0, T, \alpha) > 0$  and  $\tilde{\alpha}_{n-1-\delta} = -1$  otherwise, with the decision times as in Section 7.5.1. The ability of the receiver to make correct decisions depends on the statistics of  $[\eta(t_0) - \eta(t_0 - T)] \bmod (2\pi)$  and  $N(t_0 - T, t_0)$ . From Refs. 43, 44 and references therein, e.g., Ref. 58, it is known that the error probability can be divided into two terms, each taking care of one of the above possibilities, i.e.,

$$P(\alpha) = \Pr \{ \text{no clicks} \} P_{\text{cont}}(\alpha) + P_{\text{click}}(\alpha) \quad (7.45)$$

From Ref. 44,  $P_{\text{cont}}(\alpha)$  is given by

$$\begin{aligned} P_{\text{cont}}(\alpha) &= \Pr \{ \Delta\psi(t_0, T, \alpha) - \pi \leq \psi(t_0, \alpha) - \psi(t_0 - T, \alpha) \\ &\quad + [\eta(t_0) - \eta(t_0 - T)] \bmod (2\pi) \leq 0 | \alpha \} \end{aligned}$$



Figure 7.19. Discriminator detector.

From Refs. 43, 45 it is known that this is given by

$$\begin{aligned}
 P_{\text{cont}}(\alpha) = & \frac{W \sin \Delta\psi(t_0, T, \alpha)}{4\pi} \\
 & \times \int_{-\pi/2}^{\pi/2} \frac{\exp \left[ -\frac{E_b}{N_0} \frac{U - V \sin \theta - W \cos \Delta\psi(t_0, T, \alpha) \cos \theta}{1 - r \cos \theta} \right]}{U - V \sin \theta - W \cos \Delta\psi(T, \alpha) \cos \theta} d\theta \\
 & + \frac{r \sin \Delta\psi(t_0, T, \alpha)}{4\pi} \\
 & \times \int_{-\pi/2}^{\pi/2} \frac{\exp \left[ -\frac{E_b}{N_0} \frac{U - V \sin \theta + W \cos \theta}{1 + r \cos \Delta\psi(t_0, T, \alpha) \cos \theta} \right]}{1 + r \cos \Delta\psi(t_0, T, \alpha) \cos \theta} d\theta \quad (7.46)
 \end{aligned}$$

where

$$V = \frac{\mathcal{A}^2(t_0, \alpha) - \mathcal{A}^2(t_0 - T, \alpha)}{2T \int_{-\infty}^{\infty} |A(f)|^2 df}$$

and other variables are given in (7.37).

Now consider the random variable  $N(t - T, t)$ . This is assumed to be a discrete random variable with a Poisson distribution<sup>(43,44)</sup>

$$\Pr \{ N = k \} = \frac{e^{-\bar{N}(\alpha)} \bar{N}(\alpha)^k}{k!}, \quad k = 0, 1, 2, \dots \quad (7.47)$$

where  $\bar{N}(\alpha)$  is the average number of clicks in the time interval  $t - T$  to  $t$ , given by

$$\bar{N}(\alpha) = \int_{t-T}^t \frac{\dot{\psi}(\tau, \alpha)}{2\pi} e^{-(E_b/N_0)\rho(\tau, \alpha)} d\tau$$

$\dot{\psi}(\tau, \alpha)$  is the derivative of  $\psi(t, \alpha)$  and  $(E_b/N_0)\rho(\tau, \alpha)$  is the instantaneous SNR given by

$$\rho(\tau, \alpha) = \frac{\mathcal{A}^2(\tau, \alpha)}{T \int_{-\infty}^{\infty} |A(f)|^2 df}$$

Thus the error probability  $P(\alpha)$  is given by

$$P(\alpha) = e^{-\bar{N}(\alpha)} P_{\text{cont}}(\alpha) + (1 - e^{-\bar{N}(\alpha)}) \quad (7.48)$$

and the average error probability is then given by

$$P_e = \frac{1}{m} \sum_{\alpha} P(\alpha) \quad (7.49)$$

where  $m$  is given in Section 7.5.1.

In Ref. 43 there are also comparisons between the above time domain method to the frequency domain method in Tjhung and Wittke.<sup>(57)</sup>

### 7.5.3. Numerical Results

In this section selected numerical results are presented for differential and discriminator detection.

Figures 7.20 and 7.21 show error probabilities for some filtered 1REC and 1RC schemes with  $h = 0.5$ . All filtered schemes will be denoted transmitted scheme/filter type, e.g., 1REC/1RC. Differential detection is best suited for schemes with modulation indices around  $h = 1/2$ . With larger modulation indices the difference phase over one symbol interval gets close to  $\pi$  and the error increases. The equivalent distances for these schemes are summarized in Table 7.2.

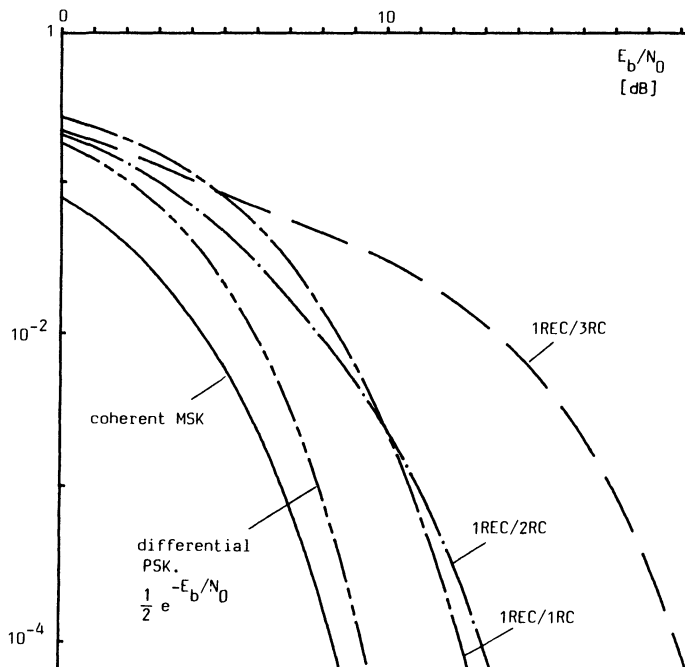


Figure 7.20. Error probabilities for differential detection of filtered 1REC with  $h = 1/2$ .

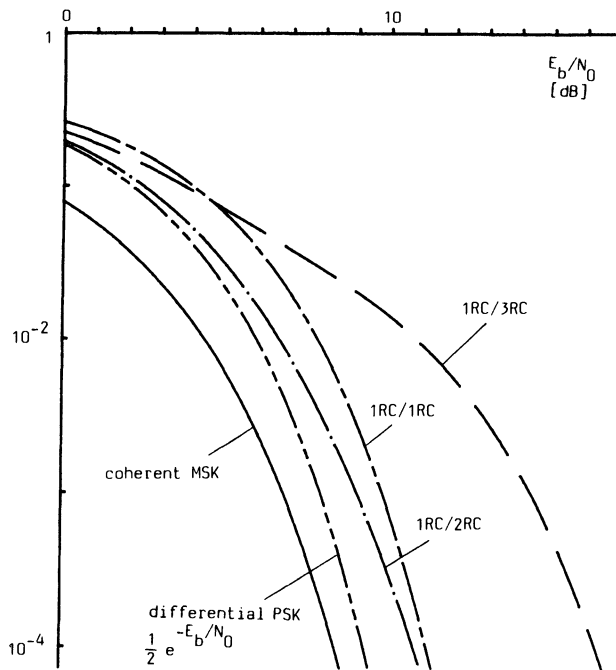


Figure 7.21. Error probabilities for differential detection of 1RC with  $h = 1/2$ .

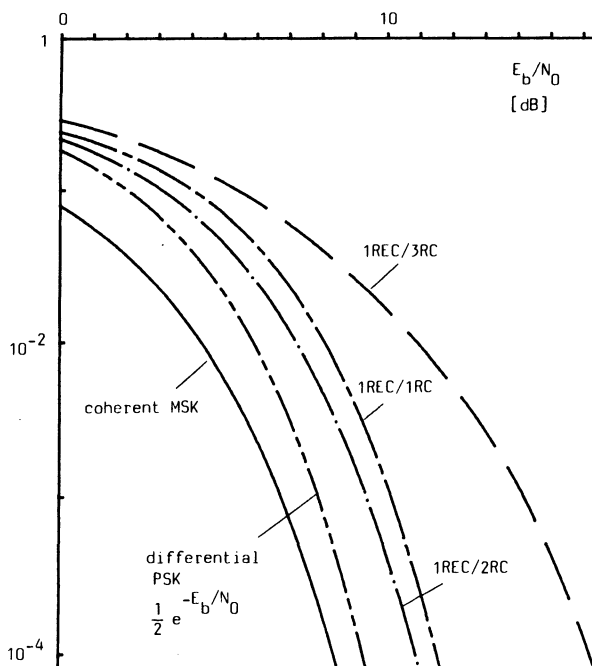


Figure 7.22. Error probabilities for discriminator detection of 1REC with  $h = 0.718$ .

**Table 7.2. Minimum Equivalent Euclidean Distance for Various Schemes with Differential Detection**

$h = 0.4$							$h = 0.5$						
Scheme	1REC/1RC	1REC/2RC	1REC/3RC	1REC/1RC	1REC/2RC	1REC/3EC	1REC/1RC	1RC/2RC	1RC/3RC	1RC/2RC	1RC/3RC	1RC/2RC	1RC/3RC
$d_e^2$	0.4792	0.3850	0.0868	0.7150	0.5764	0.1329	0.7681	0.6611	0.1740				
<hr/>													
$h = 0.5$							$h = 0.4$						
Scheme	1REC/1RC	1REC/2RC	1REC/3RC	2RC/1RC	2RC/2RC	2RC/3RC	2RC/1RC	2RC/2RC	2RC/3RC	2RC/1RC	2RC/2RC	2RC/3RC	2RC/3RC
$d_e^2$	1.1228	0.9702	0.2564	0.2945	0.2431	0.0376	0.4491	0.3714	0.0606				

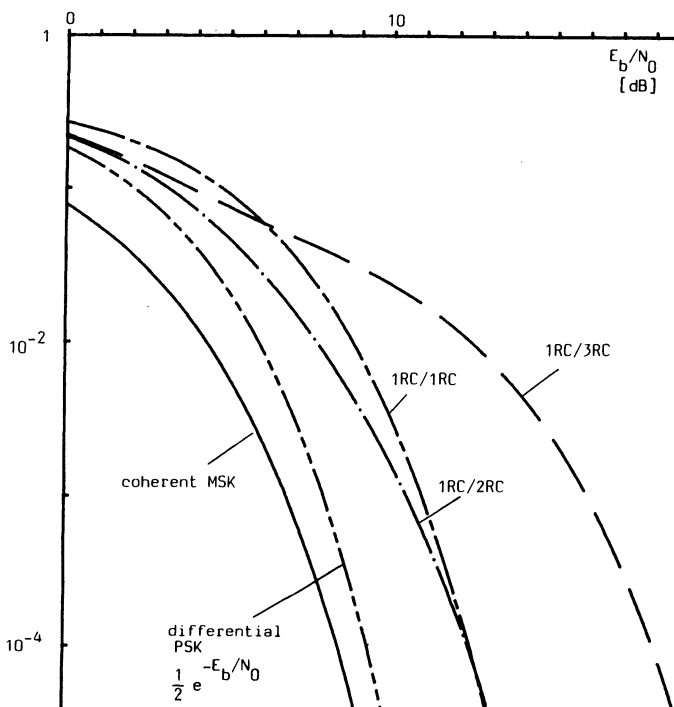


Figure 7.23. Error probabilities for discriminator detection of 1RC with  $h = 0.4$ .

The error probability for discriminator detection of  $h = 1/2$  schemes is very close to the results above for differential detection. Thus only schemes with  $h \neq 1/2$  will be considered henceforth. Figures 7.22–7.24 show some results; for discriminator detection the error probability can be decreased by increasing the modulation index. Further numerical results appear in Ref. 39, and methods for receiver filter optimization are also considered there.

Good combinations of modulations and differential and discriminator detectors have been found, where the loss at error rate  $10^{-6}$  is only in the order of 2 dB compared to coherent MSK. These schemes have, however, a slightly wider power spectrum. The performance of noncoherently detected schemes depends on many parameters, such as IF-filter bandwidth, bandwidth of the transmitted scheme, and noise correlations. Thus it is a difficult problem to find optimized schemes with noncoherent detection. We have given some tools for analyzing certain noncoherent schemes, but much work remains to be done in this area.

In Refs. 39, 49, four-level schemes both with differential and discriminator detection are considered. Results are presented and compared to those in Refs. 52 and 53, which were obtained by means of simulations.

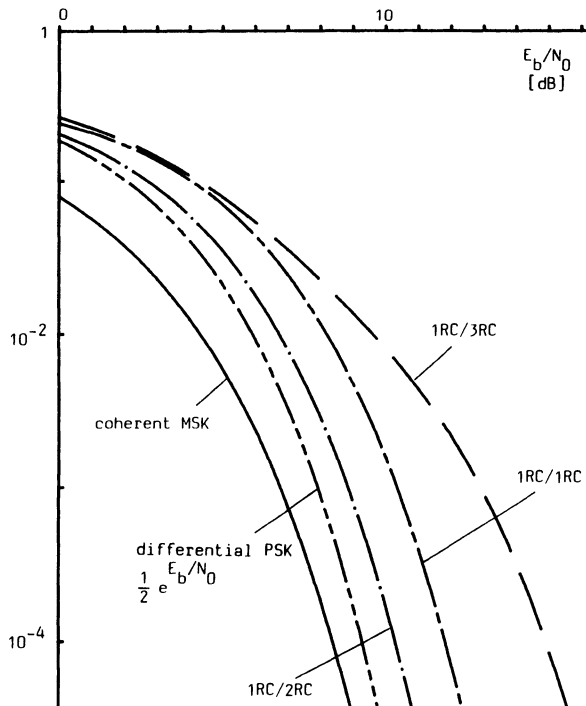


Figure 7.24. Error probabilities for discriminator detection of 1RC with  $h = 0.62$ .

Optimized receiver filters and receiver simulation results are also presented in Ref. 39.

#### 7.5.4. Application of Sequence Detection

In this section we will limit ourselves to mention some examples of noncoherent suboptimum reception of CPM with sequence detection.

At this time sequence detection discriminators are still evolving, and few analytical results are available. It is clear that the memory in the continuous phase also helps in noncoherent reception and should be utilized for example in Viterbi processing following the discriminator<sup>(32,33,54,39)</sup> or differential detectors.<sup>(35,36,54,56,39)</sup> These receivers are difficult to analyze and optimize. One seems to be forced to use computer simulations and/or measurements.

A noncoherent receiver based on the detection of a generalized tamed frequency modulated (GTFM) signal by a frequency discriminator is described in Ref. 32. The received binary data are decided from the output of the frequency discriminator by a decoder, which takes the form of either

a simple bit-by-bit detector or a maximum-likelihood sequence estimator (MLSE) of low complexity. The bit error rates in the presence of Gaussian noise have been studied by means of computer simulations for several GFTM signals. All these signals share the good spectral properties of tamed frequency modulation (TFM). It is shown that the error rate performance of the proposed discriminator detection scheme can be optimized by means of an appropriate choice of parameters in GTFM signal generation at the transmitter. It is also shown that the GTFM signal with discriminator and Viterbi detection requires at least 3 dB more in signal-to-noise ratio than coherent MSK. For further details see Refs. 32–35.

## References

1. W. R. Bennett and S. O. Rice, "Spectral Density and Autocorrelation Functions Associated with Binary Frequency-Shift Keying," *Bell System Technical Journal* Sep., 2355–2385 (1962).
2. M. G. Pelchat, "The Autocorrelation Function and Power Spectrum of PCM/FM with Random Binary Modulating Waveforms," *IEEE Transactions on Space Electronics and Telemetry* March, 39–44 (1964).
3. R. R. Anderson and J. Salz, "Spectra of Digital FM," *Bell System Technical Journal* 44, 1165–1189 (1965).
4. W. P. Osborne and M. B. Luntz, "Coherent and Noncoherent Detection of CPFSK," *IEEE Transactions on Communications* COM-22, 1023–1036 (1974).
5. T. A. Schonhoff, "Symbol Error Probabilities for  $M$ -ary CPFSK: Coherent and Noncoherent Detection," *IEEE Transactions on Communications* COM-24 (6) 644–652(76).
6. R. de Buda, "Coherent Demodulation of Frequency Shift Keying with Low Deviation Ratio," *IEEE Transactions on Communications* June, 429–435 (1972).
7. G. D. Forney, Jr., "The Viterbi Algorithm," *Proceedings of the IEEE* 61, 268–278 (1973).
8. J. J. Stiffler, *Theory of Synchronous Communications*, Prentice-Hall, Englewood Cliffs, New Jersey (1971).
9. J. G. Proakis, *Digital Communications*, McGraw-Hill, New York (1982).
10. M. Schwartz, W. R. Bennett, and S. Stein, *Communication Systems and Techniques*, McGraw-Hill, New York (1966), Secs. 8.2 and 8.3.
11. T. Aulin and C-E. Sundberg, "Continuous Phase Modulation—Part I: Full Response Signaling," *IEEE Transactions on Communications* COM-29(3), 196–210 (1981).
12. T. Aulin, N. Rydbeck, and C-E. Sundberg, "Continuous Phase Modulation—Part II: Partial Response Signaling," *IEEE Transactions on Communications* COM-29(3), 210–226 (1981).
13. T. Aulin, "Three Papers on Continuous Phase Modulation (CPM)," Thesis, University of Lund, November 1979.
14. T. Aulin, N. Rydbeck, and C-E. Sundberg, "Transmitter and Receiver Structures for  $M$ -ary Partial Response FM," Proc. 1980 Int. Zürich Seminar on Digital Commun., March 4–6, 1980, pp. A2.1–A2.6.
15. J. B. Anderson and R. de Buda, "Better Phase-Modulation Error Performance Using Trellis Phase Codes," *Electronics Letters* 12, 587–588 (1976).
16. J. M. Wozencraft and I. M. Jacobs, *Principles of Communication Engineering*, Wiley, New York (1965).
17. A. J. Viterbi and J. K. Omura, *Principles of Digital Communication and Coding*, McGraw-Hill, New York (1979).

18. T. A. Schonhoff, H. E. Nichols, and H. M. Gibbons, "Use of the MLSE Algorithm to Demodulate CPFSK," *Proc. Int. Conf. on Commun.*, Toronto, Canada, 1978, 25.4.1-25.4.5.
19. R. C. Davis, "An Experimental 4-ary CPFSK Modem for Line-Of-Sight Microwave Digital Data Transmission," *EASCON Conference Record*, Washington, DC, 1978, pp. 674-682.
20. T. Aulin, "Symbol Error Probability Bounds for Coherently Viterbi Detected Continuous Phase Modulated Signals," *IEEE Transactions on Communications COM-29*, 1707-1715 (1981).
21. G. L. Clark and J. B. Cain, *Error Correction Coding for Digital Communications*, Plenum Press, New York (1981).
22. J. B. Anderson, Simulated Error Performance of Multi- $h$  Phase Codes, *IEEE Transactions on Information Theory IT-27*(3), 357-362 (1981).
23. T. A. Schonhoff, "Symbol Error Probabilities for  $M$ -ary CPFSK," Conference Record Int. Conf. on Communications, San Francisco, June 1975. See also ICC 1978.
24. H. Miyakawa, H. Harashima, and Y. Tanaka, "A New Digital Modulation Scheme-Multi-Mode Binary CPFSK," *Proc. 3rd Int. Conf. on Digital Satellite Communications*, November 1975, pp. 105-112.
25. J. B. Anderson and D. P. Taylor, "A Bandwidth-Efficient Class of Signal-Space Codes," *IEEE Transactions on Information Theory IT-24*, 703-712 (1978).
26. T. Aulin and C-E. Sundberg, "On the Minimum Euclidean Distance for a Class of Signal Space Codes," *IEEE Transactions on Information Theory IT-28*(1), 43-45 (1982).
27. T. Aulin and C-E. Sundberg, "Minimum Euclidean Distance and Power Spectrum for a Class of Smoothed Phase Modulation Codes," *IEEE Transactions on Communications COM-30*(7), 1721-1729 (1982).
28. D. E. Knuth, *The Art of Computer Programming*, Vol. II, Addison-Wesley, Reading, Massachusetts (1969).
29. D. R. Cox and P. R. Lewis, *The Statistical Analysis of Series of Events*, Methuen, London (1966), Chaps. 5 and 6.
30. J. B. Anderson and K. Srivatsa, "Trellis Decoded Error Events are Apparently Independent," Proc. 1980 Princeton Conf. on Information Sciences and Systems, Princeton, New Jersey, March 1980.
31. T. Masamura, S. Samejima, Y. Morihiro, and H. Fuketa, "Differential Detection of MSK with Nonredundant Error Correction," *IEEE Transactions on Communications COM-27*(6), 912 (1979).
32. K. S. Chung, "A Noncoherent Receiver for GTFM Signals," *GLOBECOM'82*, Miami, December 1982. Conference Record, pp. B3.5.1-B3.5.5.
33. K. S. Chung and L. E. Zegers, "Generalized Tamed Frequency Modulation," *Proc. IEEE International Conf. on Acoustics, Speech and Signal Processing*, Vol. 3, pp. 1805-1808, Paris, May 1982.
34. F. de Jager and C. B. Dekker, "Tamed Frequency Modulation, a Novel Approach to Achieve Spectral Economy in Digital Transmission," *IEEE Transactions on Communications COM-26*(5), 534-542 (1978).
35. K. Murota and K. Hirade, "GMSK Modulation for Digital Mobile Radio Telephone," *IEEE Transactions on Communications COM-29*(7), 1044-1050 (1981).
36. K. Hirade, M. Ishizuka, F. Adachi, and K. Ohtani, "Error-Rate Performance of Digital FM with Differential Detection in Mobile Radio Channels," *IEEE Transactions on Vehicular Technology VT-28*, 204-212 (1979).
37. T. Aulin and C-E. Sundberg, "CPM-An Efficient Constant Amplitude Modulation Scheme," *International Journal of Satellite Communications*, 2(3), 161-186 (1984).
38. G. Lindell, C-E. Sundberg, and A. Svensson, "Error Probability of Multilevel CPM with High Rate Convolutional Codes," 1984 International Zürich Seminar on Digital

- Communications, Zürich, Switzerland, March 1984. Conference Proceedings (IEEE No. 84CH1998-4), pp. 93-100.
- 39. A. Svensson and C-E. Sundberg, "On Error Probability for Several Types of Noncoherent Detection of CPM," Global Telecommunications Conference, GLOBECOM'84, Atlanta, Georgia, November 1984. Conference Record, pp. 22.5.1-22.5.7.
  - 40. T. Aulin and C-E. Sundberg, "Partially Coherent Detection of Digital Full Response Continuous Phase Modulated Signals," *IEEE Transactions on Communications COM-30(5)*, 1096-1117 (1982).
  - 41. A. Svensson, C-E. Sundberg, and T. Aulin, "Partial Response Continuous Phase Modulation with Partially Coherent Detection," International Conference on Communications, ICC'83, Boston, Massachusetts, June 20-22, 1983. Conference Record, pp. A6.5.1-A6.5.9.
  - 42. M. K. Simon and C. C. Wang, "Differential Versus Limiter-Discriminator Detection of Narrow-Band FM," *IEEE Transactions on Communications COM-31(11)*, 1227-1234 (1983).
  - 43. T. T. Tjhung, C. S. Ng, K. K. Yeo, and P. H. Wittke, "Error Performance Analysis for Narrow-band Duobinary FM with Discriminator Detection," *IEEE Transactions on Communications*, To appear.
  - 44. R. F. Pawula, "On the Theory of Error Rates for Narrow-Band Digital FM," *IEEE Trans. on Communications*, COM-29(11), 1634-1643 (1981).
  - 45. R. F. Pawula, S. O. Rice, and J. H. Roberts, "Distribution of the Phase Angle Between Two Vectors Perturbed by Gaussian Noise," *IEEE Trans. on Communications* COM-30(8), 1828-1841 (1982).
  - 46. J. H. Roberts, *Angle Modulation: The Theory of System Assessment*, Peter Peregrinus Ltd (1977).
  - 47. S. Haykin, *Communication Systems*, Second Edition, Wiley, New York (1983).
  - 48. D. Dupontel, "Binary Modulations for Digital Satellite Communications Link with Differential Detection," Fifth International Conference on Digital Satellite Communications, Genoa, Italy, March 23-26, 1981. Conference Record, pp. 89-98.
  - 49. M. Schwartz, W. R. Bennett, and S. Stein, *Communication Systems and Techniques*, McGraw-Hill, New York (1966).
  - 50. S. Parl, "A New Method of Calculating the Generalized Q Function," *IEEE Trans. on Information Theory IT-26(1)*, 121-124 (1980).
  - 51. T. Aulin and C-E. Sundberg, "Detection Performance of Band-Limited Continuous Phase Modulation," Global Telecommunication Conference, GLOBECOM'82, Miami, Florida, November 29-December 2, 1982. Conference Record, pp. E7.6.1-E7.6.7.
  - 52. M. Ikoma, K. Kimura, N. Saegusa, Y. Akaiwa, and I. Takase, "Narrow-Band Digital Mobile Radio Equipment," International Conference on Communications, ICC'81, Denver, Colorado, June, 1981. Conference Record, pp. 23.3.1-23.3.5.
  - 53. Y. Akaiwa, I. Takase, S. Kojima, M. Ikoma, and N. Saegusa, "Performance of Baseband-Bandlimited Multilevel FM with Discriminator Detection for Digital Mobile Telephony," *The Transactions of the IECE of Japan* E64(7), pp. 463-469 (1981).
  - 54. J-E. Stjernvall and J. Uddenfeldt, "Gaussian MSK with Different Demodulators and Channel Coding for Mobile Telephony," International Conference on Communications, ICC'84, Amsterdam, The Netherlands, May 14-17. Conference Record, pp. 1219-1222.
  - 55. K. S. Chung and L. E. Zegers, "Generalized Tamed Frequency Modulation," *Philips Journal of Research*, 37, pp. 165-177 (1982).
  - 56. K. Hirade, K. Murota, and M. Hata, "GMSK Transmission Performance in Land Mobile Radio," GLOBECOM'82. Conference Record, pp. B3.4.1-B3.4.6.
  - 57. T. T. Tjhung and P. H. Wittke, "Carrier Transmission of Binary Data in a Restricted Band," *IEEE Transactions on Communications Technology*, COM-18, 295-304 (1970).
  - 58. J. E. Mazo and J. Salz, "The Theory of Error Rates for Digital FM," *Bell System Technical Journal*, 45, pp. 1511-1535 (1966).

# Simplified Receivers

The optimum coherent receiver for CPM is described in Chapter 7. Its complexity grows exponentially in proportion to  $M^L$ . In Chapter 8 we will present four different methods for constructing simplified suboptimum coherent receivers for CPM. We will see that their level of complexity, performance degradation, and degree of applicability are interconnected.

The most general class of simplified receivers comprises two methods of construction of reduced-complexity Viterbi detectors presented in Sections 8.1 and 8.5. In Section 8.1 the receiver is a full Viterbi receiver for a simpler CPM scheme than the one transmitted. The simpler scheme is a good approximation of the transmitted one. The simplest type of receivers are the so-called MSK-type receivers presented in their parallel form in Section 8.2 and in their serial form in Section 8.3. The applicability of these receivers is limited. Finally various types of average matched filter receivers are discussed in Section 8.4.

Throughout this chapter coherent detection of a CPM scheme is assumed. Perfect carrier recovery and synchronization is normally assumed. It is also assumed that the channel is an additive white Gaussian noise channel, and that the data symbols are independent and identically distributed. Some practical aspects of receivers for CPM are presented in the recent studies.<sup>(46-50)</sup>

## 8.1. Reduced Complexity Viterbi Detectors

It has been shown above that schemes with combined good spectral properties and detection properties can be obtained in the CPM family. The schemes with combined attractive spectra and error probability often require a maximum likelihood sequence detector implemented by means of a Viterbi detector. The optimum receiver exploits the structure of the

transmitted phase trajectories, and uses the Viterbi algorithm to perform maximum likelihood sequence estimation (MLSE). These receivers typically consist of a filter bank followed by a Viterbi processor, where the number of states can be quite large (see Chapter 7 and Refs. 1–9).

In this section a new class of reduced-complexity Viterbi detectors is considered. It is shown that good performance can be obtained with a Viterbi receiver in which the number of filters and states is reduced. The key idea is to approximate the phase tree (the ensemble of all possible transmitted phase vs. time functions) with a phase tree based on a shorter frequency response, and use the Viterbi receiver for this shorter scheme instead as a receiver. This scheme, used by the receiver, can be optimized to give the best possible performance at a given complexity level.

### 8.1.1. The Complexity Reduction Concept

In a CPM scheme all the information is contained in the transmitted phase. The instantaneous frequency is a linear sum of overlapping frequency pulses, where the amplitude of the pulses depends on the data symbols. The length in symbol intervals and the shape of the pulses determines the performance of the modulation system. In this section the frequency pulse is of rectangular (REC) or raised cosine (RC) shape. Since the frequency pulse is time limited, the transmitted phase can be divided into two terms, as in Section 3.4. One term depends only on the last  $L$  symbols, where  $LT$  is the length of the frequency pulse and the other term is the sum of the previous symbols. For rational values of  $h$  the second term only takes a finite number of values, modulo  $2\pi$ . For these  $h$  values the phase tree reduces to a phase trellis. The states in the trellis are defined by the phase state and the correlative state vector, i.e., the prehistory symbols; the transmitted phase in a symbol interval only depends on the phase state, the correlative state vector, and the last transmitted data symbol. The total number of states in the trellis is  $S = pM^{(L-1)}$ , where  $p$  is the number of phase states,  $M$  is the number of levels, and  $L$  is the length of the frequency response in symbol intervals. In Chapter 7 it is shown that the log likelihood function can be calculated recursively by filtering and can be used as a metric in a Viterbi detector. The receiver there consists mainly of a bank of filters and a Viterbi processor, and it requires  $2M^L$  filters.

The class of coherent suboptimum receivers considered in this section is also of maximum likelihood sequence estimating type. The principal idea is the following. The receiver uses a shorter pulse than the transmitter, thus approximating the phase tree; the receiver frequency pulse  $g_R(t)$  is chosen in such a way that the tree generated by  $g_R(t)$  is a reasonably good approximation of the phase tree generated by the transmitter frequency pulse  $g_T(t)$ . The receiver based on  $g_R(t)$  is built according to the optimum

receiver principles, and is the optimum receiver for the case  $g_T(t) = g_R(t)$ . If the transmitter pulse length in symbol intervals is  $L_T$  and the receiver pulse length is  $L_R$ , then the complexity reduction factor is  $M^{(L_T - L_R)}$ , both in terms of the number of receiver states and receiver filters.

Figure 8.1 shows a transmitter tree based on 3RC and a simplified receiver with a phase tree based on the shorter 2REC pulse. The two trees are shown with a small phase offset relative to the best alignment so that they can be more easily distinguished. It is clear that the 2REC tree, with properly chosen phase and time offset ( $T/2$  in this case), approximates the 3RC scheme fairly well. The quality of this approximation is analyzed in Section 8.1.2. The complexity reduction in this example is a factor of 2.

Several interesting observations can be made by studying Figure 8.1. For example, a transmitted sequence of binary symbols, e.g.,  $+1, -1, -1, +1, \dots$ , does not in general correspond exactly to the same phase path in the transmitter and receiver phase trees. This is of course a consequence of the approximation made, and it occurs even if there is no noise at all in the transmission link. We will say that the transmitter and receiver signal sets are *mismatched*. This mismatch should of course not be too large, because then detection errors are made even without noise. It is also clear from the example above that the phase synchronization and timing between the transmitter and receiver trees is of great importance. This problem will also be addressed below.

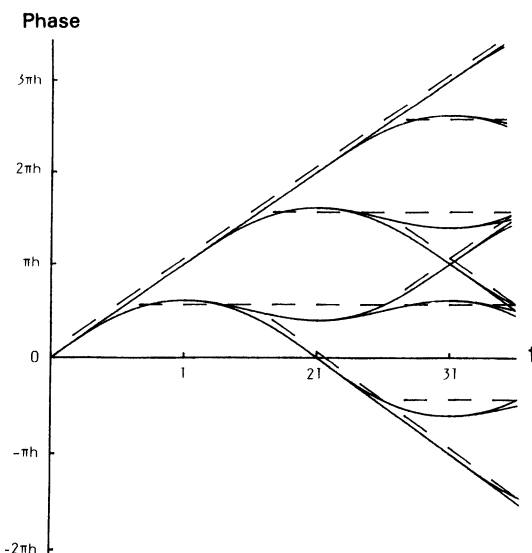


Figure 8.1. Transmitter phase tree (solid) for 3RC and receiver phase tree for 2REC. Correct symbol timing, small phase offset.

### 8.1.2. The Performance Measure

In Chapter 3 the minimum normalized squared Euclidean distance is introduced as a performance measure. For the optimum detector the minimum normalized squared Euclidean distance in the signal space is

$$\frac{D_{\min}^2}{2E_b} = d_{\min}^2 = \min_{\substack{\alpha, \beta \\ \alpha_0 \neq \beta_0}} \left\{ \frac{1}{2E_b} \int_0^{NT} [s(t, \alpha) - s(t, \beta)]^2 dt \right\} \quad (8.1)$$

where  $s(t, \alpha)$  is the transmitted CPM signal,  $E_b$  is the bit energy,  $NT$  is the length of the observation interval, and  $\alpha$  and  $\beta$  are data sequences which are different in the first symbol. The distance depends on the difference sequence  $\gamma = \alpha - \beta$  rather than the individual data sequences themselves. If  $2\pi f_0 T \gg 1$ , (8.1) can be rewritten

$$d_{\min}^2 = \min_{\gamma, \gamma_0 \neq 0} \left\{ \log_2(M) \frac{1}{T} \int_0^{NT} [1 - \cos(\phi(t, \gamma))] dt \right\} \quad (8.2)$$

where  $\phi(t, \gamma)$  is the transmitted phase,  $\gamma_i = \alpha_i - \beta_i$  and  $M$  the number of transmitted levels.

Let us now consider the reduced-complexity receiver. The receiver is assumed to correlate the received signal with all alternative in the receiver library of signals and choose the alternative with the largest correlation. The receiver principle and the critical parameters are illustrated in Figure 3.43, and discussed in Section 3.5.1. By using the mismatched Euclidean distance introduced there, the error probability at large SNR can be estimated for a given signal and reduced-complexity receiver. Let the transmitted signal for a given  $\alpha$  be

$$s_T(t, \alpha) = \left( \frac{2E}{T} \right)^{1/2} \cos [\omega_0 t + \phi(t, \alpha)] \quad (8.3)$$

Below we are considering all signals over a time interval of length  $NT$ . The receiver generates its library of possible signal alternatives (where  $\alpha$  is varying)

$$s_R(t, \alpha) = \left( \frac{2E}{T} \right)^{1/2} \cos [\omega_0 t + \psi(t, \alpha)] \quad (8.4)$$

These signals are viewed over the same time interval as the transmitted signal, and  $\phi(t, \alpha)$  and  $\psi(t, \alpha)$  are calculated from  $g_T(t)$  and  $g_R(t)$ , respectively.  $\psi(t, \alpha)$  is based on a shorter frequency response than  $\phi(t, \alpha)$ .

Both the transmitter and the receiver signals are represented in one signal vector space.  $\mathbf{s}_T$  denotes the transmitted signal point in this context. Let  $\mathbf{s}_0$  represent the receiver alternative which corresponds to the correct sequence  $\alpha$ , i.e., the transmitted data sequence, and let  $\mathbf{s}_1, \mathbf{s}_2, \mathbf{s}_3, \dots$  represent other receiver alternatives. Suppose the signal alternative  $\mathbf{s}_1$  corresponds to the signal

$$s_R(t, \beta) = \left(\frac{2E}{T}\right)^{1/2} \cos [\omega_0 t + \psi(t, \beta)]$$

The receiver selects the signal alternative which corresponds to the largest correlation with this. This corresponds to the signal point which has the smallest distance to the received signal point. Figure 3.43 shows the situation in the noiseless case. With additive white Gaussian noise, the signal point  $\mathbf{s}_T$  is added to a noise vector. When the magnitude of the noise vector is such that the received signal point is located on the other side of the decision boundary, an error occurs. Thus the distance  $D$  in (8.6) is of interest for all pairs of receiver signals  $(\mathbf{s}_0, \mathbf{s}_j)$   $j = 1, \dots$  for a given transmitted signal  $\mathbf{s}_T$ . Note that  $D$  is the distance in the  $\mathbf{s}_j - \mathbf{s}_0$  direction, which is a vector in the receiver subset of the signal space. It is possible to project the transmitted signals into the receiver signal space and calculate the distance in this space instead. For large signal-to-noise ratios the smallest  $D$  is of particular interest since it is the minimum Euclidean distance for the mismatched signal set. This parameter determines the error probability behavior for large signal-to-noise ratios.

Simple geometry yields that  $D = D_A^2/D_R$  where  $D_R^2 = |\mathbf{s}_0 - \mathbf{s}_1|^2$  is the Euclidean distance between the receiver alternatives and  $|\cdot|$  is a norm in the Euclidean space. This is the receiver distance referred to below. The numerator  $D_A^2$  is considered in Section 3.5 and is shown to be

$$D_A^2 = |\mathbf{s}_1 - \mathbf{s}_T|^2 - |\mathbf{s}_0 - \mathbf{s}_T|^2 \quad (8.5)$$

This is by definition a positive quantity. We will use the usual normalized squared distances

$$d^2 = D^2/2E_b = (D_A^2/D_R)^2 = d_A^4/d_R^2 \quad (8.6)$$

where  $d_R^2 = D_R^2/2E_b$  and  $d_A^2 = D_A^2/2E_b$ .

From the analysis in Chapter 3, the receiver performance for large SNRs is determined by the minimum distance  $d_{\min}^2$ , where the minimization is carried out both over transmitter sequences and receiver sequences. For the special case of no mismatch, i.e.,  $\phi(t, \alpha) = \psi(t, \alpha)$ , we have  $d_A^2 = d_R^2$

and thus  $d^2 = d_R^2$ . In this case, the error probability is determined by the minimum distance in the signal set,  $d_R^2$ . Using (8.1)–(8.3) in (8.6) and assuming  $\omega_0 T \gg 1$ , we get

$$d_A^2 = (\log_2 M) \left\{ \frac{1}{T} \int_0^{NT} \cos [\phi(t, \alpha) - \psi(t, \alpha)] dt - \frac{1}{T} \int_0^{NT} \cos [\phi(t, \alpha) - \psi(t, \beta)] dt \right\} \quad (8.7)$$

and

$$d_R^2 = (\log_2 M) \frac{1}{T} \int_0^{NT} \{1 - \cos [\psi(t, \beta) - \psi(t, \alpha)]\} dt \quad (8.8)$$

Equations (8.6)–(8.8) are the key to the analysis of the behavior of mismatched signal sets and thus reduced-complexity Viterbi receivers for large SNRs.  $d_{\min}^2$ , the minimum of  $d^2$ , gives the asymptotic performance of the considered signal with the given receiver. Thus for large signal-to-noise ratios, the error probability behavior is given by

$$P_e \sim Q((E_b d_{\min}^2 / N_0)^{1/2})$$

By studying (8.7) and (8.8) we can see that  $d_A^2$  and  $d_R^2$  can be calculated recursively when  $N$  is increased. This observation can be used for computing  $d^2$  efficiently; see Refs. 1–4 and 37 for details.

It is clear that this reduced-complexity receiver is suboptimum. An optimum receiver is matched to the pulse  $g_T(t)$ , and thus the squared Euclidean distance is

$$d_T^2 = (\log_2 M) \left\{ N - \frac{1}{T} \int_0^{NT} \cos [\phi(t, \alpha) - \phi(t, \beta)] dt \right\}$$

the minimum Euclidean distance for the suboptimum receiver cannot be larger, since in that case the suboptimum receiver performs better than the optimum receiver for large signal-to-noise ratios. Thus we have the inequality

$$\min(d^2) = \min(d_A^4/d_R^2) \leq \min(d_T^2) \quad (8.9)$$

It is interesting to note that for a specific  $\alpha$  and  $\beta$  it can possibly be the case that  $\min(d_A^4/d_R^2) > \min(d_R^2)$ ; this can occur if and only if  $d_A > d_R$ . This implies that it is possible to start with a scheme with matched receiver and transmitter and then obtain a larger minimum Euclidean distance by changing the transmitter into another one, now mismatched, with larger  $d_T$ . For detailed examples, see Ref. 3.

### 8.1.3. Properties of the Minimum Euclidean Distance for Mismatched Signal Sets

The properties of the mismatched distance measure will now be investigated more precisely. First we will look into the usefulness of difference sequences. Then upper bounds  $d_B^2$  on the minimum distance are calculated.

For calculation of Euclidean distances for optimum receivers, only the phase difference  $\phi(t, \alpha) - \phi(t, \beta) = \phi(t, \alpha - \beta)$  has to be considered, which means that only the difference sequence  $\gamma = \alpha - \beta$  has to be considered. It will now be investigated if and when difference sequences also can be used for calculation of Euclidean distances for mismatched receivers. The crucial quantities which have to be investigated are  $\phi(t, \alpha) - \psi(t, \alpha)$  and  $\phi(t, \alpha) - \psi(t, \beta)$  in (8.7). The first difference is

$$\begin{aligned}\phi(t, \alpha) - \psi(t, \alpha) &\triangleq \varepsilon(t, \alpha) = 2\pi h \sum_i \alpha_i [q_T(t - iT) - q_R(t - iT)] \\ &= 2\pi h \sum_i \alpha_i q_\Delta(t - iT)\end{aligned}\quad (8.10)$$

where

$$q_\Delta(t) = q_T(t) - g_R(t) = \int_{-\infty}^t [g_T(\tau) - g_R(\tau)] d\tau$$

The symbol timing between the transmitter and the receiver is defined by letting  $g_R(t)$  occupy the interval  $[0, L_R T]$  and  $g_T(t)$  occupy the interval  $[-L_\Delta T, (L_T - L_\Delta)T]$ , where  $L_T \geq L_R$  and

$$L_\Delta = \frac{L_T - L_R}{2} \quad (8.11)$$

A phase offset  $\psi_0$  to the receiver phase will assure the best fit between the two phase trees given by the ensembles of  $\phi(t, \alpha)$  and  $\psi(t, \alpha)$ . The properties of  $q_R(t)$  and  $q_T(t)$  lead to  $q_\Delta(t) = 0$  when  $t \leq -L_\Delta T$  and  $t \geq (L_T - L_\Delta)T$ . Thus it can be seen that the dependence of  $\alpha$  in  $\varepsilon(t, \alpha)$  in the interval  $nT \leq t \leq (n+1)T$  lies in the  $(2\Lambda_\Delta + L_R)$ -ary vector

$$(\alpha_{n-L_R+1-\Lambda_\Delta}, \dots, \alpha_n, \dots, \alpha_{n+\Lambda_\Delta}) = \alpha_{n+\Lambda_\Delta} \quad (8.12)$$

where

$$\Lambda_\Delta = \left\lceil \frac{L_T - L_R}{2} \right\rceil$$

( $\lceil \cdot \rceil$  means “smallest integer less than”.)

Now the expression  $\phi(t, \alpha) - \psi(t, \beta)$  is considered. By constraining  $t$  to the interval  $nT \leq t < (n+1)T$  and using the properties of  $q_T(t)$  and  $q_R(t)$ , we have

$$\begin{aligned} \phi(t, \alpha) - \psi(t, \beta) = h\pi \sum_{i \leq n-L_R-\Lambda_\Delta} (\alpha_i - \beta_i) - h\pi \sum_{i=n-L_R-\Lambda_\Delta+1}^{n-L_R} \beta_i \\ + 2\pi h \sum_{i=n-L_R-\Lambda_\Delta+1}^{n-L_R} \alpha_i q_T(t - iT) \\ + 2\pi h \sum_{i=n-L_R+1}^n [\alpha_i q_T(t - iT) - \beta_i q_R(t - iT)] \\ + 2\pi h \sum_{i=n+1}^{n+\Lambda_\Delta} \alpha_i q_T(t - iT) \end{aligned} \quad (8.13)$$

and only the first term depends on  $\alpha - \beta$ . For the other terms the two  $(2\Lambda_\Delta + L_R)$ -ary vector  $\alpha_{n+\Lambda_\Delta}$  and  $\beta_{n+\Lambda_\Delta}$  defined by (8.12) must be used. Thus for an observation interval  $N \leq L_R + \Lambda_\Delta$  intervals, both the  $\alpha$  and  $\beta$  sequences must be used to obtain all the Euclidean distances. For  $N > L_R + \Lambda_\Delta$  intervals, however, the phase separation created by the initial  $N - L_R - \Lambda_\Delta$  data symbols can be expressed by means of a sum of elements of the difference sequence  $\alpha - \beta$ .

### Upper Bound $d_B^2(h)$

The minimum Euclidean distance for optimum receivers was upper bounded in Section 3.2 by identifying so-called mergers in the phase tree. For mismatched receivers mergers do not exist in general, at least not mergers of the kind of Section 3.2. It is possible, however, to choose sequences  $\alpha$  and  $\beta$  such that the calculation of  $d_A^2$  only has to be performed over a finite interval, even though  $\alpha$  and  $\beta$  are infinitely long. The sequences  $\alpha$  and  $\beta$  are chosen exactly as the merger sequences in Section 3.2:

$$\alpha = \dots, \alpha_{-2}, \alpha_{-1}, +1, -1, \alpha_2, \dots$$

$$\beta = \dots, \beta_{-2}, \beta_{-1}, -1, +1, \beta_2, \dots$$

where  $\alpha_i = \beta_i$  when  $i \neq 0, 1$ . This is the “first merger” in the binary case. Now this pair of sequences yields a merger at  $t = (L_R + 1)T$  in the phase tree given by the ensemble of  $\psi(t, \alpha)$ . It remains to study (8.7) for this pair of sequences and an infinite observation length  $-\infty < t < \infty$ . Since

$\alpha_i = \beta_i$ ,  $i < 0$  it is clear that  $\psi(t, \alpha) = \psi(t, \beta)$  for all  $t \leq 0$ . For all  $t > (L_R + 1)T$  we know from the previous discussion about difference sequences that  $\psi(t, \alpha) = \psi(t, \beta)$ , since the influence of  $\alpha_0, \alpha_1$  and  $\beta_0, \beta_1$  does not affect the shape of these two phase trajectories. Only the separation between these two phase trajectories is affected by these symbols. This separation equals zero since  $\sum_i \alpha_i = \sum_i \beta_i$ , and thus  $\psi(t, \alpha) = \psi(t, \beta)$  for all  $t \leq 0$  and  $t \geq (L_R + 1)T$ . This is equivalent to

$$\phi(t, \alpha) - \psi(t, \alpha) = \phi(t, \alpha) - \psi(t, \beta), \quad t \leq 0, \quad t \geq (L_R + 1)T$$

and so the two integrals in (8.7) are equal over these intervals. Thus it is sufficient to calculate  $d_A^2$  over the time interval where the trajectories in the receiver phase tree are unmerged.

In the  $M$ -ary case there are more merger sequences, and in any case there are also mergers later than the first. In some cases the upper bound on  $d^2$  can be improved by also taking such mergers into account. Unlike the case for matched receivers, the upper bound can also depend upon a finite number of the prehistory data symbols  $\alpha_{-1}, \alpha_{-2}, \dots$  and  $\beta_{-1}, \beta_{-2}, \dots$ . Only one prehistory sequence needs to be considered, however, since  $\alpha_i$  equals  $\beta_i$ ,  $i < 0$ .

#### 8.1.4. Optimizing the Reduced-Complexity Receiver

The aim of this section is to find the optimum reduced-complexity receiver, in the manner of Refs. 1, 2, 37. A natural function to optimize is the error probability at a given SNR, but this is unrealistic. Therefore the minimum Euclidean distance has been chosen instead, which will optimize the asymptotic error probability. We will find the receiver frequency response  $g_R(t)$  that maximizes the minimum Euclidean distance, given by (8.6)–(8.8). An analytic solution to this seems difficult to find. With a numerical maximization, it would in principle be possible to find the optimum reduced-complexity receiver, to a given transmitted scheme, a given modulation index, and a given complexity reduction, for every observation length of  $N$  symbol intervals, but the computational efforts to do this are very large. Therefore, the upper bound on the minimum Euclidean distance is maximized instead. A tight upper bound seems always to be available and it is possible to find an observation length sufficiently large for the minimum distance to reach this upper bound.

We will choose the phase response  $q_R(t)$  to be a piecewise linear function for  $0 < t < L_R T$  which is allowed to be discontinuous at  $t = 0$  and

at  $t = L_R T$ :

$$q_R(t) = \begin{cases} 0, & t \leq 0 \\ q_i + \frac{2N_1(q_{i+1} - q_i)}{L_R T} \left( t - i \frac{L_R T}{2N_1} \right), & i \frac{L_R T}{2N_1} < t \leq (i+1) \frac{L_R T}{2N_1}, \quad i = 0, 1, \dots, N_1 - 1 \\ 1/2 - q_R(L_R T - t), & L_R T/2 < t < L_R T \\ 1/2, & t \geq L_R T \end{cases} \quad (8.14)$$

Figure 8.2 depicts this; in the figure  $q_{N_1} = 1/4$  always.

Since the transmitter pulse  $g_T(t)$  is symmetric around  $t = L_T T/2$  it is assumed that also the receiver pulse  $g_R(t)$  is symmetric around  $t = L_R T/2$ . Maximizations without this assumption have shown that this is likely the case. This means that the interval  $0 \leq t \leq L_R T/2$  is divided into  $N_1$  subintervals, over which  $q_R(t)$  is linear. The variables  $q_i$  are the values at the end points of these intervals and  $q_{N_1} = q_R(L_R T/2) = 1/4$  owing to symmetry. Then  $q_R(t)$  for  $L_R T/2 < t \leq L_R T$  is given by symmetry. The set of  $q_i$ ,  $i = 0, \dots, N_1 - 1$ , maximizing the upper bound, has to be found. This can

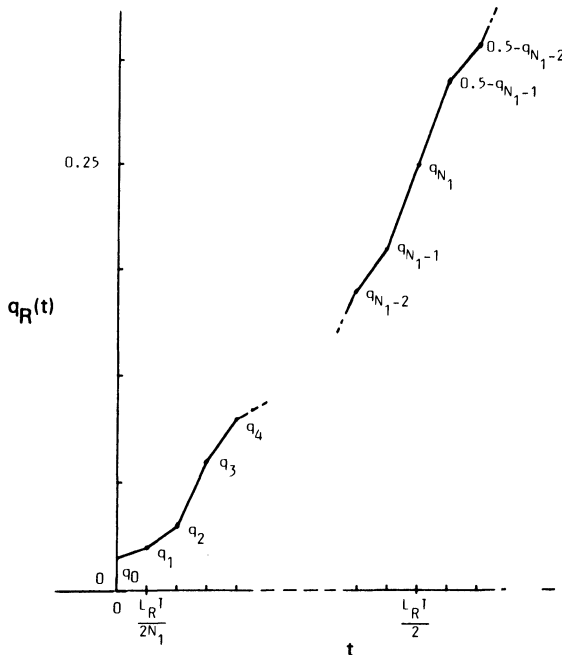


Figure 8.2. The piecewise linear phase response of the reduced-complexity receiver, where  $q(t) = \frac{1}{2} - q(L_R T - t)$  for  $L_R T/2 \leq t \leq L_R T$ .

be done by a steepest descent algorithm.<sup>(12,37)</sup> The results show that in general  $q_0 \neq 0$  yields the optimum. By choosing  $N_1$  large, it is possible to approximate every continuous phase response  $q_R(t)$  (except at  $t = 0$  and  $t = L_R T$ ) that corresponds to a symmetric frequency response  $g_R(t)$ .

### 8.1.5. Numerical Results

In this section both distance results and simulated error probability results will be given for reduced-complexity Viterbi receivers based on approximate short frequency response pulses.

#### *Distance Results*

Normalized Euclidean distance results are given in Figures 8.3-8.6 for several combinations of transmitter and receiver pulse shapes. The distance of Section 8.1.2 is plotted against the modulation index for several observation intervals  $N$ ; the latter are always measured in the receiver tree. Results

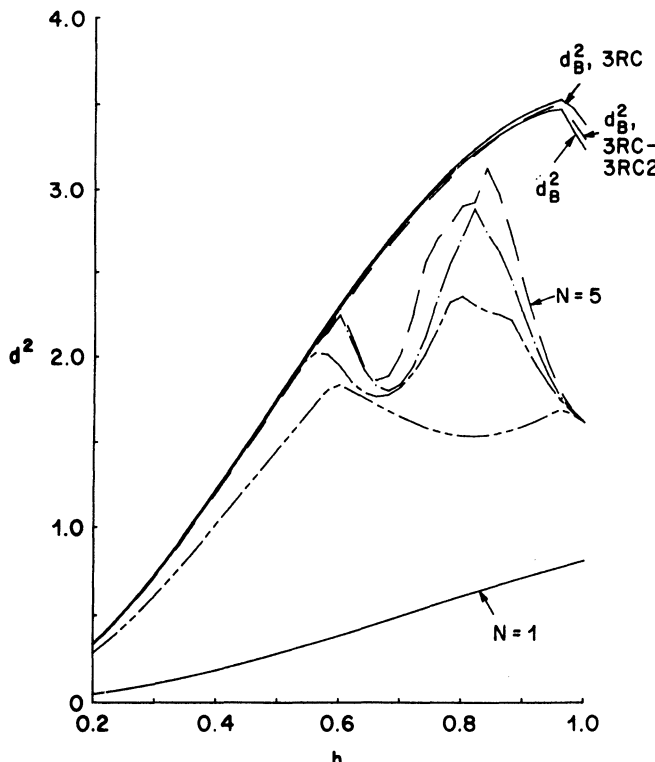


Figure 8.3. Minimum distance for binary 3RC-2T0.75. Note that this receiver is optimum only for  $h = 3/4$ .

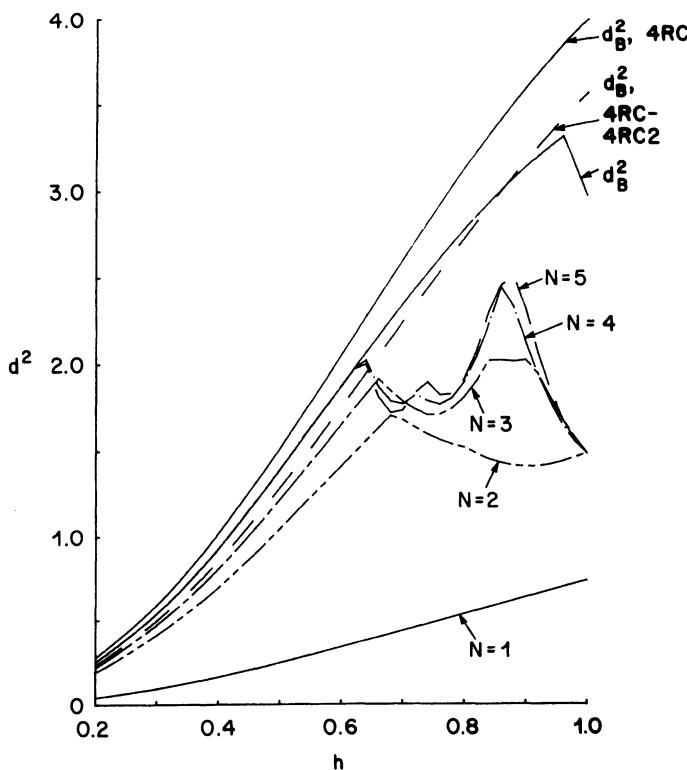


Figure 8.4. Minimum distance for binary 4RC-2T0.50. Note that this receiver is optimum only for  $h = 1/2$ .

appear for both *ad hoc* receiver pulses and pulses optimized by the method of Section 8.1.4. The optimized short pulses will be denoted  $L_T RC - L_R Th$ , where  $L_T$  and  $L_R$  are the lengths of the transmitter and receiver pulses in symbol intervals, and  $h$  is the modulation index for which this receiver is optimum. The *ad hoc* reduced-complexity receivers will in like manner be denoted transmitted scheme-receiver scheme, as in for instance 3RC-1REC. For all the optimized pulses, the maximization is performed with  $N_1 = 10$ , that is, the interval  $0 \leq t \leq L_R T$  is divided into 20 subintervals.

Figure 8.3 shows a scheme with a complexity reduction of 2, 3RC-2T0.75. For comparison the upper bound for the 3RC-3RC2 scheme,<sup>(37)</sup> and the upper bound for the optimum 3RC receiver are given. It is shown in Ref. 37 that the phase tree given by the optimum  $g_R(t)$  pulse approximates the 3RC phase tree very well, and it is clear here that the distance is very close to the upper bound for the optimum 3RC receiver. The loss at  $h = 3/4$  compared to optimum 3RC is small for both reduced-complexity receivers.

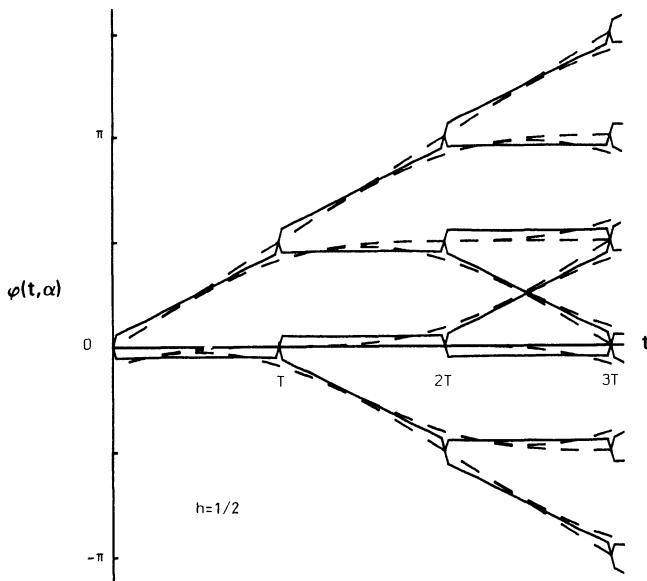


Figure 8.5. Phase tree for binary 4RC-2T0.50 (solid) and 4RC (dashed).

Note that this receiver phase response for 3RC-2T0.75 is not optimum for  $h$  near 1.

The degradation compared to the optimum scheme for the reduced-complexity receivers optimum at other modulation indices is very close to the degradation for 3RC-2T0.75.<sup>(37)</sup>

Now consider transmitted 4RC. Figure 8.4 gives the results for 4RC-2T0.50, which has a complexity reduction factor of 4. The phase tree of the optimum reduced-complexity receiver, shown in Figure 8.5, approximates the 4RC phase tree fairly well. The loss at  $h = 1/2$  compared to the optimum 4RC receiver is about 0.35 dB. As seen from the distance graph, the reduced-receiver upper bound is reached with an observation length of 4 symbol intervals.

Optimizations and distance calculations for some quaternary ( $M = 4$ ) schemes have also been done. Figure 8.6 shows the results for quaternary 2RC-1T0.25. The complexity reduction factor is now 4. Note that the calculated values are marked with •, ×, +, or □ and the lines only connect these values. The distances shown are normalized with the bit energy  $E_b$  and are therefore comparable with the binary results. The loss at  $h = 1/4$  compared to the optimum 2RC receiver is about 0.35 dB. The upper bound at  $h = 1/4$  is reached with an observation length  $N = 3$ .

Some results for other pulses are available in Refs. 1-4 and 37.

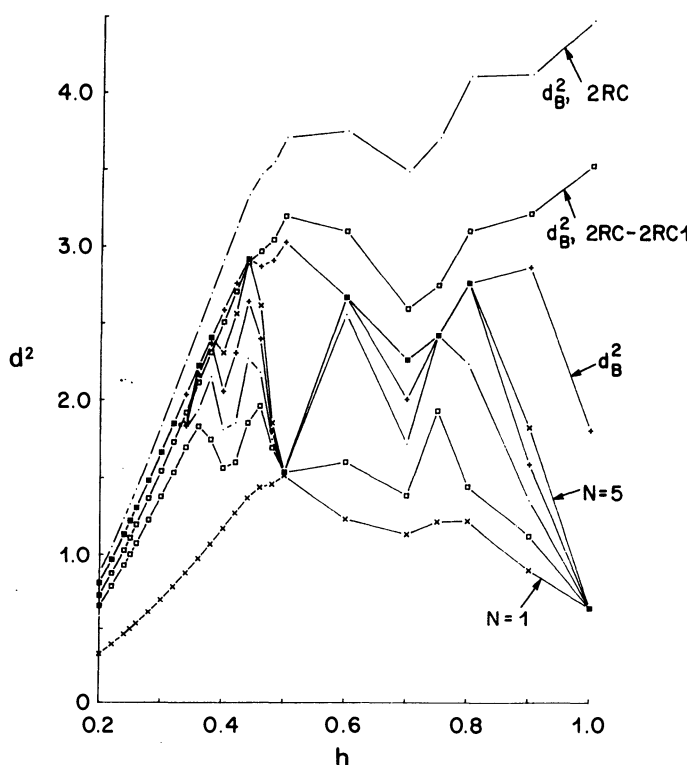


Figure 8.6. Minimum distance for quaternary 2RC-1T0.25. Note that this receiver is optimum only for  $h = 1/4$ .

### *Simulated Error Probabilities*

The minimum distance calculations give the error probability behavior for large signal-to-noise ratios. For low signal-to-noise ratios it is necessary to perform computed simulations. This is so for the optimum Viterbi receiver as well. However, simulations are even more appropriate for the reduced-complexity receiver. From the distance considerations in the previous sections it follows that relatively speaking, the error event corresponding to the minimum Euclidean distance is a more unusual event for the reduced-complexity receiver than for the optimum receiver. A specific prehistory must have occurred in the phase tree for the minimum distance error event to take place, and this not so for the optimum receiver. A minimum distance can occur there for any prehistory since the phase difference is the same independent of the prehistory.

Simulations are available for transmitted 4RC with  $h = 1/2$  and transmitted quaternary 2RC with  $h = 1/4$ . The receivers used are the optimum

Viterbi receiver, the optimum reduced-complexity receiver, and the *ad hoc* reduced-complexity receiver with the largest  $d_{\min}^2$ . Results are based on runs of 2500 errors and the path memory in the Viterbi detector is 20 symbol intervals, which for all the schemes is enough to reach the asymptotic performance given by  $d_{\min}^2$ . The lower bound on the error probability for the optimum Viterbi receiver (see Chapter 3) is also given as comparison. Note that the error probabilities actually obtained are marked with  $\times$ ,  $+$ , or  $\square$  and then connected with a straight line. This is also the case for the lower bound.

Figure 8.7 shows the results for 4RC-4RC2 (+), 4RC-2T0.50 ( $\times$ ), and optimum 4RC ( $\square$ ), together with the lower bound for  $h = 1/2$ . It is seen that the reduced-complexity receivers perform approximately equally for low SNRs, while the optimum receiver performs about 0.1 dB better at  $P = 10^{-2}$ . The losses at low SNRs for the reduced-complexity receivers are not at all as large as the minimum distances suggest. This is because the probability for the error event giving minimum distance to occur is very low.

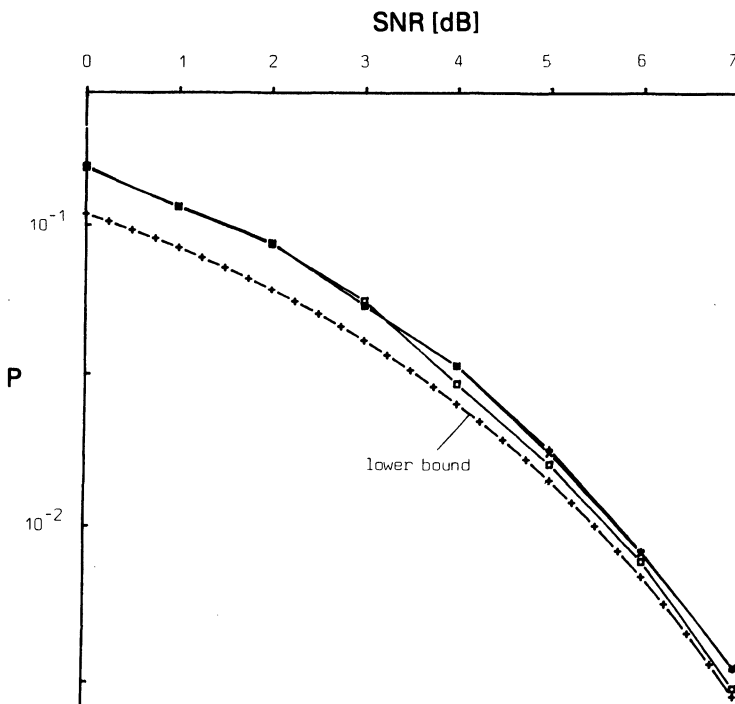


Figure 8.7. Simulated bit error probability for 4RC-4RC2 (+), 4RC-2T0.50 ( $\times$ ), and optimum 4RC ( $\square$ ) for  $h = 1/2$ . The lower bound for the optimum receiver is also shown. The results are based on 2500 errors.

Figure 8.8 portrays some quaternary schemes. These are 2RC-2RC1 (+), 2RC-1T0.25 ( $\times$ ), and optimum 2RC ( $\square$ ) for  $h = 1/4$ . The lower bound for the optimum scheme is also shown. In this case 2RC-1T0.25 performs in between the other two schemes. Still the loss compared to the optimum scheme is low. Further numerical results are in Refs. 1, 37.

### 8.1.6. Summary and Tradeoff between Complexity Reduction and Performance

To illustrate the tradeoff between complexity reduction and performance degradation we have selected data from some of the schemes in the distance results just given and from 1–4, 37. By complexity reduction we mean the factor  $M^{(L_T - L_R)}$  by which the number of states and filters in the suboptimum receiver is reduced compared to the optimum receiver. By performance degradation we mean the factor  $10 \log_{10} (d_T^2 / d_{\min}^2)$ , i.e., the difference in power in decibels between the optimum scheme and the suboptimum scheme for large SNRs. The performance degradation varies with  $h$  while the complexity reduction factor only is a function of  $M$  and  $L_T - L_R$ .

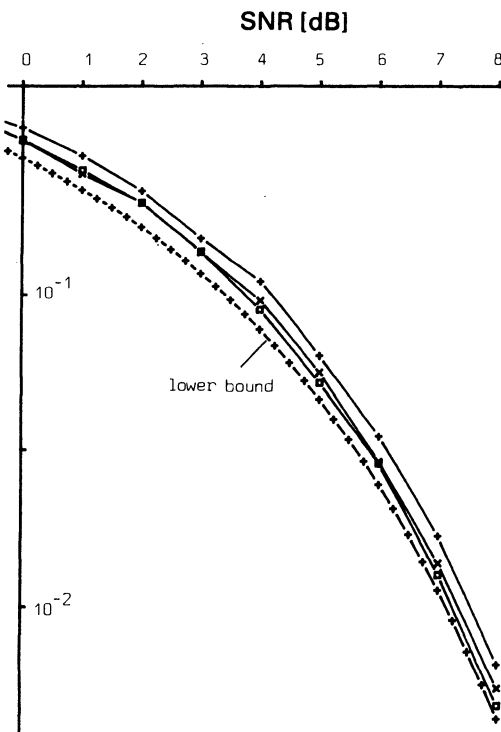


Figure 8.8. Simulated symbol error probability for quaternary 2RC-2RC1 (+), 2RC-1T0.25 ( $\times$ ), and optimum 2RC ( $\square$ ) for  $h = 1/4$ . The lower bound for the optimum receiver is also shown. The results are based on 2500 errors.

**Table 8.1. Power Degradation Versus Complexity Reduction for the Optimum Reduced-Complexity Receiver Compared to the Optimum Receiver for  $h = 3/4$**

Transmitted scheme	$M = 2$ 2RC	$M = 2$ 3RC	$M = 2$ 4RC	$M = 2$ 3RC	$M = 2$ 4RC	$M = 4$ 2RC	$M = 2$ 4RC
$L_R$	1	2	3	1	2	1	1
Degradation [dB]	0.13	0.02	0.02	0.86	0.36	1.28	2.40
$M^{L_T - L_R}$	2	2	2	4	4	4	8

Table 8.1 shows the asymptotic performance degradation for the optimum reduced-complexity receiver compared to the optimum receiver versus the corresponding complexity reduction factor, for  $h = 3/4$ . It is seen that the degradation is very small for a low complexity reduction factor while it is increasing for larger factors. Useful complexity reductions are possible with almost no loss. If larger losses can be tolerated, very smooth transmitted modulations can be detected by quite simple receivers.

The reduced-complexity receiver is a robust receiver and the idea of approximating the phase tree can also be applied to other types of smooth frequency responses, e.g., TFM, GMSK, SRC, and CORPSK.<sup>(10,23,6,11,51)</sup> Similar results can be expected for these schemes.

An analytic optimization has not been done and seems very difficult to do. However, the results here seem to be very close to an absolute optimum reduced-complexity receiver. A comparison with the results for the *ad hoc* pulses indicate that the minimum distance is not especially sensitive to small variations in the pulse shape.

With the receiver in this section, the signal spectrum is unaffected, and only receiver complexity is reduced. Thus the very low sidelobes of, for instance, 3RC can be maintained with simpler detectors. The technique is quite general and applies to nonbinary CPM schemes and rational modulation indices not necessarily equal 1/2.

## 8.2. MSK-Type Receivers

For some cases of CPM it is not necessary to use the Viterbi detector. Recently, much work has been devoted to the MSK-type of receiver.<sup>(24,14-23,25,26,37)</sup> This receiver has only two filters and only a small amount of processing. The receiver makes single symbol decisions. This simplified receiver is of course in general suboptimum, but it works well for binary modulation with modulation index  $h = 1/2$ . Various ideas in selecting the receiver filters are analyzed in Refs. 10, 16, 23, 27 and an

optimum filter is derived in Refs. 21, 19 for various correlative FSK schemes (piecewise linear phase functions) and for smooth pulses in Refs. 37, 14, 15. In Ref. 25 a filter based on a minimum squared error approach is given and analyzed for a TFM scheme. The performance for this receiver is almost equal to the optimum receiver for schemes with a moderate degree of smoothing, i.e., overlapping frequency pulses of length up to 3-4 symbol intervals (mainlobe width).

In this section the parallel MSK type of receiver is analyzed for a general  $h = 1/2$  binary CPM signal and the best such receivers are derived. A distance measure giving the asymptotic performance on the Gaussian channel is introduced. Error probability formulas are given both for the Gaussian and the Rayleigh fading additive channels. Diversity schemes are also considered. The material in this section first appeared in Refs. 15 and 17.

### 8.2.1. Receiver Principle and Performance

The MSK-type receiver is based on the structure of the parallel MSK receiver, which was introduced in Section 2.7 and is repeated in Figure 8.9. Signals with modulation index 1/2 have attractive properties that can be used to formulate a simple receiver, and we will exploit those here. Besides assuming  $h = 1/2$ , we will assume binary signaling, perfect carrier recovery, and symmetric frequency pulses  $g(t)$ . The decisions are made every  $2T$  in

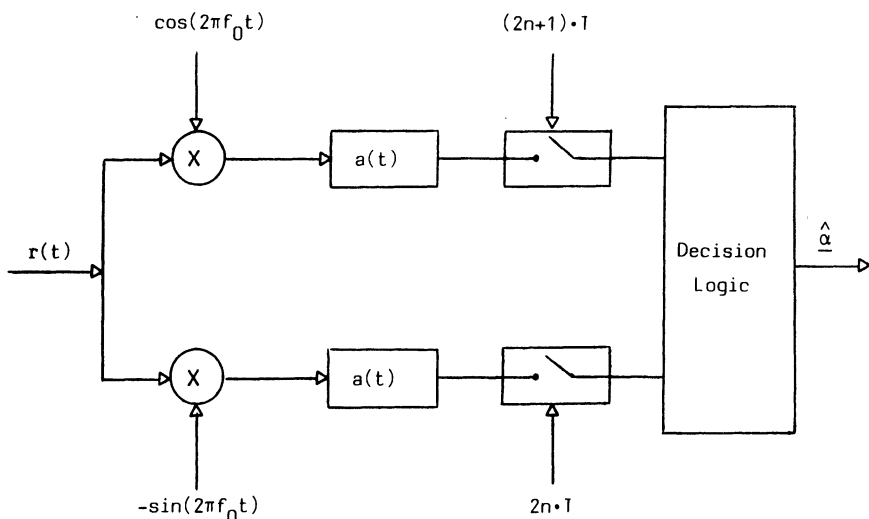


Figure 8.9. Receiver structure for the parallel MSK-type receiver for partial response CPM.  $a(t)$  is the receiver filter.

alternate quadrature arms. "Decision logic" in Figure 8.9 also consists of differential decoding and time demultiplexing as explained for MSK in Chapter 2.

We have found in earlier chapters that MSK (1REC,  $h = 1/2$ ) is in fact a linear modulation in two quadrature arms and that the linear receiver of Figure 8.9 is an ML receiver. We can employ a linear receiver for partial response schemes with  $h = 1/2$ , although it may not be possible to express these as linear modulation in the quadrature arms, and the receiver may not be ML. In these schemes, we will detect the *phase node sequence* defined by Ref. 16

$$\vartheta_n = (\pi/2) \sum_{i \leq n} \alpha_i \quad (8.15)$$

This phase node can only take four different values, 0,  $\pi/2$ ,  $\pi$ , and  $3\pi/2$ . The data symbols can easily be calculated from  $\vartheta_n$ , by using  $\alpha_n = (2/\pi)(\vartheta_n - \vartheta_{n-1})$ . This can also be effected by differential encoding.<sup>(16,21,24)</sup>

Receiver decisions in one of the quadrature arms will be made just from the  $\cos \phi(t, \alpha)$  eye pattern. Figure 8.10 gives an example for 3RC ( $L = 3$  in LRC in Table 2.1). These signals will be denoted  $\tilde{s}(t, \alpha)$ . The ensemble of signals  $\tilde{s}(t, \alpha)$  can be divided into two subsets. Let  $t_0$  denote the time when the decision is made. The subset having  $\tilde{s}(t_0, \alpha) > 0$  will be denoted  $S^+$ , while the subset having  $\tilde{s}(t_0, \alpha) < 0$  will be denoted  $S^-$ . The corresponding data sequences will in the same manner be denoted  $\alpha^+$  if the sequence gives rise to a signal in  $S^+$  and  $\alpha^-$  if the corresponding signal belongs to  $S^-$ . In the vector signal space the signals will be denoted  $s_i^+$  or

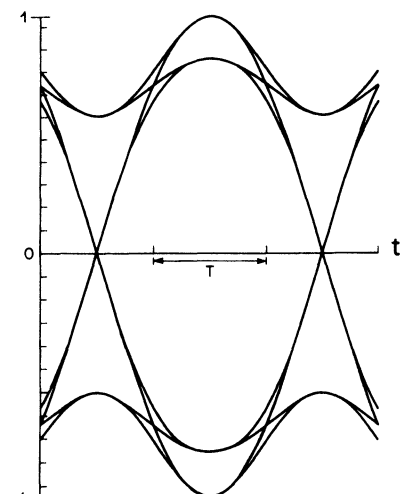


Figure 8.10.  $\cos \phi(t, \alpha)$  eye pattern of a binary 3RC,  $h = 1/2$ , scheme.

$\mathbf{s}_i^-$  where  $\mathbf{s}_i^+ \in S^+$  and  $\mathbf{s}_i^- \in S^-$ ,  $i = 1, \dots, m/2$ .  $m$  is the total number of signals. Owing to the fact that  $h = 1/2$ , the signals in  $S^-$  are equal to  $-\mathbf{s}_i^+$ ,  $i = 1, \dots, m/2$ .

Following Refs. 14, 15, and 37, the normalized received signal is given by  $\tilde{\mathbf{r}}(t) = \tilde{\mathbf{s}}(t, \boldsymbol{\alpha}) + (T/E_b)^{1/2} n_c(t)$ , where  $n_c(t)$  is the quadrature component given by  $n(t) = \sqrt{2}n_c(t) \cos \omega_0 t - \sqrt{2}n_s(t) \sin \omega_0 t$ . Thus the binary hypothesis testing problem is

$$\begin{aligned} H^+: \quad \mathbf{r} &= \mathbf{s}_i^+ + \mathbf{n}, \quad \mathbf{s}_i^+ \in S^+ \\ H^-: \quad \mathbf{r} &= \mathbf{s}_i^- + \mathbf{n}, \quad \mathbf{s}_i^- \in S^- \end{aligned}$$

where  $\mathbf{n}$  represents the additive noise and  $\mathbf{r}$  the received signal in the vector signal space. Since the data symbols  $\pm 1$  occur with equal probability, the probability of the signals  $\mathbf{s}_i^+$  and  $\mathbf{s}_i^-$  is equal to  $1/m$ . The linear receiver for this problem is that of Figure 8.9, with threshold equal to zero because of the symmetry of the signal sets  $S^+$  and  $S^-$ . The symmetry implies also that there are  $m/2$  signal points corresponding to  $H^+$  and  $m/2$  signal points corresponding to  $H^-$  in the signal space, and that the signal space has thus been split into two decision regions.

The optimum receiver filter in vector form was given by Galko<sup>(21)</sup> as

$$\mathbf{a} = \sum_{i=1}^{m/2} a_i \mathbf{s}_i^+ \quad (8.16)$$

in terms of an impulse response, the filter is  $a(t) = \sum_{i=1}^{m/2} a_i \tilde{\mathbf{s}}(t, \boldsymbol{\alpha}_i^+)$ . The coefficients  $a_i$ ,  $i = 1, 2, \dots, m/2$ , should be chosen to minimize the average error probability  $P$ . The normalized squared distance assuming  $\mathbf{s}_j^+$  is transmitted is given by

$$d_j^2 = \frac{2}{T} \frac{[\langle \mathbf{s}_j^+, \mathbf{a} \rangle]^2}{|\mathbf{a}|^2} = \frac{2}{T} \cdot \frac{[\int_I a(-t) \tilde{\mathbf{s}}(t, \boldsymbol{\alpha}_j^+) dt]^2}{\int_I a^2(t) dt} \quad (8.17)$$

where  $I$  denotes the  $N_F$  symbol observation interval. For MSK the squared normalized distance is 2, with matched filters of length  $N_F = 2$ . The asymptotic performance for large SNR is determined by the minimum of these distances  $d_{\min}^2 = \min_j \{d_j^2\}$ . The error probability in estimating the phase node  $\vartheta_n$  on the Gaussian channel is obtained by averaging over all possible transmitted waveforms to get

$$P = \frac{1}{m} \sum_{j=1}^m Q \left( \left( d_j^2 \frac{E_b}{N_0} \right)^{1/2} \right) \quad (8.18)$$

The function  $Q(x)$  is the Gaussian error function defined in Chapter 2.

Because an error in estimating  $\vartheta_n$  will affect both  $\alpha_n$  and  $\alpha_{n+1}$ , the bit error probability  $P_e$  in estimating the data sequence  $\alpha_n$  will be about a factor of 2 larger than  $P$ . With differential encoding for resolving the relationship between phase nodes and data symbols and filters shorter than two symbol intervals,<sup>(10,24)</sup> we will have  $P_e = 2P(1 - P)$ . For longer filters the decisions on  $\vartheta_n$  and  $\vartheta_{n-1}$  are correlated and then  $P_e$  can be less than  $2P$ .

### *MSK Receivers for the Fading Channel*

The average error probability for a fading channel is derived in Ref. 17. Slow fading is assumed and the averaging is performed over one block of length  $N_F$  intervals typically smaller than 10. The instantaneous signal-to-noise ratio in diversity branch  $k$  is assumed to be  $\gamma_k$  with equal average value for all branches. For Rayleigh fading,  $\gamma_k$  has the probability density function  $f(\gamma) = (1/\Gamma)e^{-\gamma/\Gamma}$ , where  $\Gamma$  is the average signal-to-noise ratio.

For maximal ratio combining the error probability of coherent MSK-type detection of partial response continuous phase modulated signals is

$$\begin{aligned} P = & \frac{1}{2m} \sum_{j=1}^m \left\{ 1 - \left( \frac{d_j^2 \Gamma / 2}{1 + d_j^2 \Gamma / 2} \right)^{1/2} \left[ 1 + \frac{1}{1!2} \left( 1 + \frac{d_j^2 \Gamma}{2} \right)^{-1} \right. \right. \\ & \left. \left. + \frac{1 \cdot 3}{2!2^2} \left( 1 + \frac{d_j^2 \Gamma}{2} \right)^{-2} + \dots + \frac{1 \cdot 3 \cdot 5 \cdots (2M-1)}{(M-1)!2^{(M-1)}} \left( 1 + \frac{d_j^2 \Gamma}{2} \right)^{-(M-1)} \right] \right\} \end{aligned} \quad (8.19)$$

where  $d_j^2$ ,  $j = 1, \dots, m$  depend on the modulation scheme and the receiver filter.  $\Gamma$  is the average per branch signal-to-noise ratio and  $M$  is the number of diversity branches. For selection combining, the error probability is given by

$$P = \frac{1}{2m} \sum_{j=1}^m \sum_{k=0}^M \frac{(-1)^k \binom{M}{k}}{(1 + 2k/d_j^2 \Gamma)^{1/2}} \quad (8.20)$$

These expressions are found by averaging (8.18) over the density functions for  $\gamma = E_b/N_0$  with  $M$ -branch diversity, which are for ideal maximal ratio combining

$$f(\gamma) = \frac{1}{\Gamma} \left( \frac{\gamma}{\Gamma} \right)^{M-1} \frac{1}{(M-1)!} e^{-\gamma/\Gamma} \quad (8.21)$$

and ideal selection combining

$$f(\gamma) = \frac{\mathcal{M}}{\Gamma} e^{-\gamma/\Gamma} (1 - e^{-\gamma/\Gamma})^{\mathcal{M}-1} \quad (8.22)$$

Note that  $\mathcal{M}$  here is not the alphabet size ( $M$ ) of the modulation.

### 8.2.2. The Optimum Receiver Filter

In this section we find the optimum receiver filter for the parallel MSK-type receiver. The problem of finding the optimum receiver filter for a linear MSK-type receiver has been addressed in Refs. 19, 21, 14, 15, and 37. Most of the theoretical background is given in these papers. Galko<sup>(21)</sup> gives an algorithm to solve for the optimum filter for high SNR, which typically requires the solution of a quadratic programming problem. We present a simpler alternative algorithm from Refs. 14, 15, and 37. Numerical maximization methods giving the optimum receiver filter for a given SNR both for the Gaussian channel and the Rayleigh fading channel are also presented.

The optimum receiver filter is given in (8.16). From (8.17) it is clear that an increase in the energy of the receiver filter will not change the performance. Thus the coefficients  $a_i$  have been normalized such that  $\sum_{i=1}^{m/2} a_i = 1$  throughout this section.

#### *Low SNRs on the Gaussian Channel*

The average error probability for the additive Gaussian channel is given in (8.18). For very small SNRs, i.e., when  $E_b/N_0 \rightarrow 0$ , the error function  $Q$  is approximated by  $Q(x) \approx 1/2 - x/(2\pi)^{1/2}$ . This means that

$$P = \frac{1}{2} - \left( \frac{E_b}{2\pi N_0} \right)^{1/2} \sum_{j=1}^{m/2} \frac{2}{m} d_j, \quad \frac{E_b}{N_0} \rightarrow 0 \quad (8.23)$$

where the symmetry of the two signal sets have been used. Thus  $P$  is minimized if  $(2/m) \sum_{j=1}^{m/2} d_j$  is maximized.

From (8.16), (8.17), and the Schwartz inequality, we get

$$\frac{2}{m} \sum_{j=1}^{m/2} d_j = \left( \frac{2}{T} \right)^{1/2} \frac{\langle \sum_{j=1}^{m/2} (2/m) s_j^+, \sum_{i=1}^{m/2} a_i s_i^+ \rangle}{|\sum_{i=1}^{m/2} a_i s_i^+|} \leq \left( \frac{2}{T} \right)^{1/2} \left| \sum_{j=1}^{m/2} \frac{2}{m} s_j^+ \right| \quad (8.24)$$

with equality if and only if  $\sum_{j=1}^{m/2} (2/m) s_j^+ = \sum_{i=1}^{m/2} a_i s_i^+$ . By choosing  $a_i = (2/m)$ ,  $i = 1, \dots, m/2$ , the average error probability is minimized. This is the so-called average matched filter (AMF).<sup>(42,37)</sup>

### *Large SNRs on the Gaussian Channel*

In this subsection an algorithm giving the optimum receiver filter for large SNRs, i.e.,  $E_b/N_0 \rightarrow \infty$ , is presented. For large SNRs the error probability is determined by the squared minimum distance  $d_{\min}^2$ , since for large SNRs  $Q(x) \approx e^{-x^2/2}$ . Thus the error probability is minimized if the squared minimum distance  $d_{\min}^2$  is maximized. Galko and Pasupathy<sup>(19)</sup> point out that since we are trying to maximize the minimum of a set of inner products, it follows that an optimum receiver vector  $\mathbf{a}$  is characterized by the properties

$$\begin{aligned} d_j^2 &= d_{\min}^2 && \text{for } j \in J \\ d_j^2 &> d_{\min}^2 && \text{for } j \notin J \end{aligned} \quad (8.25)$$

for some  $d_{\min}^2$  and set of indices  $J \subset \{1, 2, \dots, m/2\}$ , and that no other receiver filter  $\mathbf{a}$  exists which satisfies (8.25) with a greater  $d_{\min}^2$  and any set of indices  $J$ . The signal vectors  $\mathbf{s}_j^+$  with  $j \in J$  are referred to as the *active vectors*, following Refs. 19, 21, 37.

From (8.16) it is known that the receiver filter is a linear combination of all the signals. In Ref. 19 it is shown that, for  $E_b/N_0 \rightarrow \infty$  in fact the receiver filter is a linear combination of the active signals only, the signals corresponding to the active vectors. Thus  $\mathbf{a} = \sum_{j \in J} a_j \mathbf{s}_j^+$ .  $\mathbf{a}$  is unique, but it can be given by several different linear combinations, owing to the linear dependency of the signals in  $S^+$ . In Ref. 19 it is also shown that it is possible to find at least one combination with nonnegative coefficients  $a_i$ ,  $i = 1, \dots, m/2$ , which means that the receiver filter is in the convex canonical hull of the set  $S^+$ .

Our problem is thus to find the active signals and the corresponding coefficients. One difficulty is that the number of signals  $m$  is very large in most of the interesting cases. For a modulation scheme based on 3RC and an observation length of  $N_F = 4$ , the number of signals in  $S^+$  is 32 and  $m$  is 64. However, in some cases not all of these signals have to be considered, owing to the linear dependency of the signals; in the above example only eight signals have to be considered. Only a small part of the candidate signals are symmetric, but since the ensemble of signals in  $S^+$  form a symmetric eye pattern and the signals have equal *a priori* probability, it is clear that the receiver filter impulse response must be symmetric. It can easily be shown that the nonsymmetric signals occur in pairs having a symmetric sum. This means that the coefficients for these two signals must be equal in order to give a symmetric filter. Thus instead of considering all the nonsymmetric signals in  $S^+$  these signals can be combined pairwise and only the average signals of these combinations have to be considered. Furthermore it can be shown that if  $L \leq 3$  only the symmetric signals in  $S^+$  have to be considered because the above linear combinations of the

nonsymmetric signals are linearly dependent on the symmetric signal set.<sup>(14,15)</sup> Unfortunately this is not so when  $L \geq 4$ . However, based on numerical calculations, it has been empirically concluded that the sum of two nonsymmetrical signals are very close to a properly chosen linear combination of symmetric signals.

We now explore a simple procedure for calculating the asymptotically optimum filter. The main idea behind the algorithm is the observation that often only a small number of signals contribute to the filter. The algorithm first checks if one signal is enough to give the optimum filter. Then the algorithm considers all pairs of symmetric signals and if the optimum filter is not found the algorithm considers all 3-tuples of symmetric signals, and so on until the filter is found. It is known from (8.25) that all the active vectors give the minimum distance for the optimum filter. Therefore, for every  $n$ -tuple the coefficients are chosen so that the signals contributing to the filter give the same distance. To find these coefficients,  $n - 1$  linear equations must be solved. (The last coefficient is one minus the other  $n - 1$  coefficients.) Since for a given filter  $|\mathbf{a}|$  is constant independent of  $\mathbf{s}_j^+$ , these equations are

$$\sum_{i \in n\text{-tuple}} a_i s_{ij} = \sum_{i \in n\text{-tuple}} a_i s_{ik}, \quad \text{each } j \in n\text{-tuple}, j \neq k \quad (8.26)$$

where  $s_{ij} = \langle \mathbf{s}_i^+, \mathbf{s}_j^+ \rangle$  is the correlation between signal  $\mathbf{s}_i^+$  and  $\mathbf{s}_j^+$  and  $k$  is one signal in the  $n$ -tuple. It is known that at least one of the combinations giving the optimum filter is a combination having nonnegative coefficient; therefore if at least one  $a_i$  is negative the next  $n$ -tuple is considered, otherwise this  $n$ -tuple is continued. Then the minimum distances for all the symmetric signals are calculated. The  $n$ -tuple giving the largest minimum distance is found and if this distance is given by the signals contributing to the filter we know from (8.25) that the optimum filter is found; otherwise the filter can be improved by letting at least one more signal contribute to the filter. In this way the algorithm proceeds until the optimum filter is found. For  $L \geq 4$ , this filter is optimum only for the symmetric signal set as shown before. Therefore if  $L \geq 4$  the distances for the whole set  $S^+$  are calculated and if the minimum distance for this set is the same as the minimum distance of the symmetric set the filter is optimum also in the set  $S^+$  of signals. Otherwise some nonsymmetric signals must be used to improve the filter, and the algorithm gives a suboptimum filter.

Finally the average error probability is calculated for the optimum filter; all the distances for the signals in  $S^+$  are calculated when  $L \leq 3$ . A block diagram of the algorithm is given in Figure 8.11. All the results presented in the next section were calculated with the above algorithm. For these cases at most four symmetric signals contribute to the filter and so

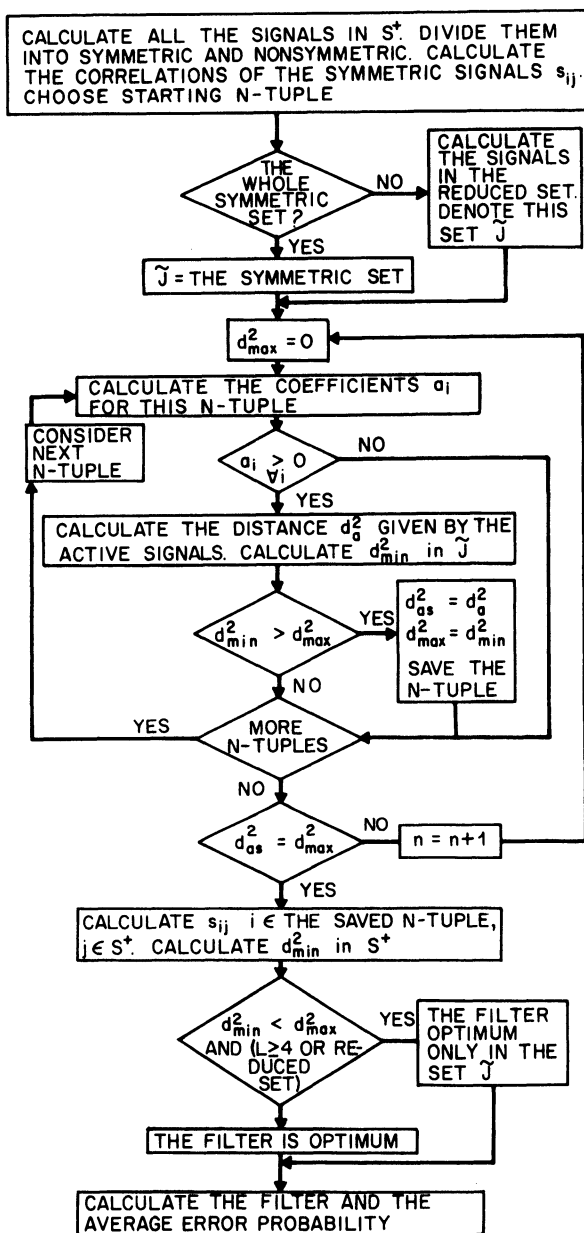


Figure 8.11. Flow chart for the algorithm giving the asymptotic optimum filter on the Gaussian nonfading channel.

the algorithm works very fast. If many signals had contributed to the filter this algorithm would be impractical.

### *Intermediate SNRs on the Gaussian Channel*

For intermediate values of  $E_b/N_0$  no analytic solution to the optimum filter problem has been found. This is a difficult minimization problem, where a sum of  $Q$  functions has to be minimized. The arguments of the  $Q$  function depend on the coefficients  $a_i$ , which have to be chosen to minimize  $P$ . Of course it is possible to find the derivatives of  $P$  on  $a_i$ , and set these equations equal to zero, but this will result in a quite large number of nonlinear equations which cannot be solved analytically. The minimizations can be done numerically with a steepest descent algorithm.<sup>(12,37)</sup> As shown before only the symmetric signals contribute to the filter if  $L$  is less than four and this can again be used to reduce the dimensionality of the minimization; if  $L = 4$ , the filter obtained is optimum in the symmetric set only, but for the cases in Section 8.2.3 this suboptimum filter seems very close to the optimum filter.

### *Optimum Filters for Fading Channels*

Now the optimum filter for the MSK-type receiver on the fading channel will be considered. The average error probability for this channel is given in (8.19) for maximal ratio combining and in (8.20) for selection combining. The error probability without diversity is obtained for  $M = 1$ .

In the low SNR case, i.e.,  $\Gamma \rightarrow 0$ , the average error probability is approximated by

$$P = \frac{1}{2} - K \left( \frac{\Gamma}{2} \right)^{1/2} \sum_{j=1}^{m/2} \frac{1}{m} d_j, \quad \Gamma \rightarrow 0 \quad (8.27)$$

where  $K$  is a constant independent of  $a_i$ ,  $i = 1, \dots, m/2$ . It is seen that minimizing  $P$  is equivalent to maximizing  $\sum_{j=1}^{m/2} d_j$  and for (8.23) it is known that the solution to this is the AMF filter. Therefore the same filter as on the Gaussian channel is optimum at low SNR.

For high SNRs, the asymptotic behavior

$$P = \frac{1}{m\Gamma} \sum_{j=1}^{m/2} \frac{1}{d_j^2}, \quad \Gamma \rightarrow \infty \quad (8.28)$$

can be used. Thus  $\sum_{j=1}^{m/2} 1/d_j^2$  has to be minimized. The derivatives on  $a_i$ ,  $i = 1, \dots, m/2$  of this sum can of course be calculated and set to zero but a nonlinear system of equations will result which appears to be hard to solve. Thus when  $\Gamma$  is not near zero on the Rayleigh fading channel, or for the diversity cases, a numerical approach is called for.

### 8.2.3. Numerical Results

Selected numerical results are now given for the impulse response of the optimum filter, as well as the error probability in detecting the phase node for the different receivers. Different transmitted schemes are compared according to both their detection and spectral efficiencies. The receivers are also compared with the optimum Viterbi receivers.

First we will concentrate on the nonfading Gaussian channel. The schemes are divided into classes according to the main-lobe width of the power spectrum.

#### *3RC-Type Schemes*

These schemes have a power spectral density main-lobe of the same order as 3RC. Figure 8.12 shows the optimum filters with response length  $N_F = 6$  for 3RC. Figure 8.13 shows the corresponding error probabilities, as well as the error probability for the asymptotically high SNR optimum filter of length  $N_F = 9$ . From Figure 8.13 it is seen that the asymptotic optimum filter is close to optimum for intermediate SNR. The minimum distances are given in Table 8.2. The asymptotic loss for  $N_F = 9$  compared to the Viterbi receiver is about 0.16 dB while the loss compared to MSK is 0.70 dB. The loss at  $P_e = 10^{-4}$  compared to MSK is, however, only 0.3 dB for the asymptotic optimum receiver. The number of signals contributing to this filter is 4 out of 64 symmetric signals.

The TFM, SRC, and GMSK pulses are not time limited, and they must be truncated symmetrically to a width  $L_T$  symbol intervals. The frequency pulse is then normalized to have integral 1/2, as usual for CPM pulses. The truncated schemes are denoted  $\text{TFML}_T$ ,  $\text{LSRCL}_T$ , and  $\text{GMSKL}_T$ .

GMSK4 with  $B_b T = 0.25$  and 3SRC6 with  $\beta = 0.8$  have lower side-lobes than 3RC, and a main-lobe of the same order as 3RC. The error probability for these schemes is given in Figure 8.13 as well and the minimum distances are given in Table 8.2. It is known<sup>(37)</sup> that  $\beta = 0.75$  gives the best asymptotic performance for 3SRC6. From Figure 8.13 it is seen that 3SRC6 with  $\beta = 0.75$  performs slightly better than 3RC while GMSK4 with  $B_b T = 0.25$  has a larger error probability than 3RC.

#### *TFM-Type Schemes*

TFM5 and GMSK5 with  $B_b T = 0.20$  both have spectra with about the same main-lobe, while GMSK5 has lower side-lobes. The optimum filters for TFM5 have not been found, but the filters optimum in the symmetric signal set are very close to optimum for the whole set of signals; for  $N_F = 6$ , the minimum distance in the symmetric set, for the filter optimum in this set, is 1.3131, while the minimum distance in the whole set for the same

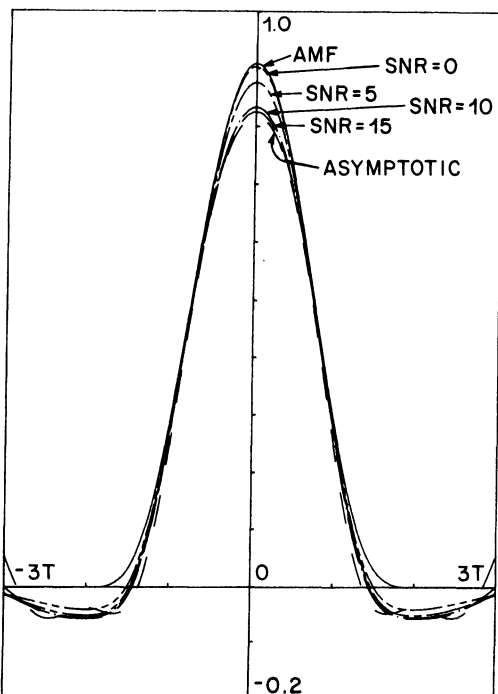


Figure 8.12. The optimum filters for 3RC with  $N_F = 6$ .

filter is 1.3079. The difference is of the same order for  $N_F = 7$  and 8. The optimum filter for GMSK5 with  $B_b T = 0.20$  has, however, been found. The error probability for all these schemes is given in Figure 8.14 when  $N_F = 8$ , and minimum distances are given in Table 8.3. The asymptotic loss for TFM5 compared to the optimum Viterbi receiver is about 0.82 dB, while the asymptotic loss compared to MSK is about 1.82 dB. The loss at  $10^{-4}$  compared to MSK is only 1.1 dB. The loss of GMSK5 compared to the optimum receiver is smaller but the loss compared to MSK is slightly larger than for TFM5. Figure 8.14 gives the error probability for TFM5 with a SPAM filter of length  $N_F = 6$  as comparison. The SPAM filter is based on a PAM approximation of the eye pattern.<sup>(16,27,37,21)</sup>

#### 4RC-Type Schemes

It is known that 4RC and GMSK5 with  $B_b T = 0.18$  have similar spectra, and these schemes will now be considered. Figure 8.15 shows the asymptotic optimum filter for 4RC when  $N_F = 9$ . The error probability for the above schemes is given in Figure 8.16. It is seen that the asymptotic optimum filter for 4RC gives an error probability very close to the filters that are optimum

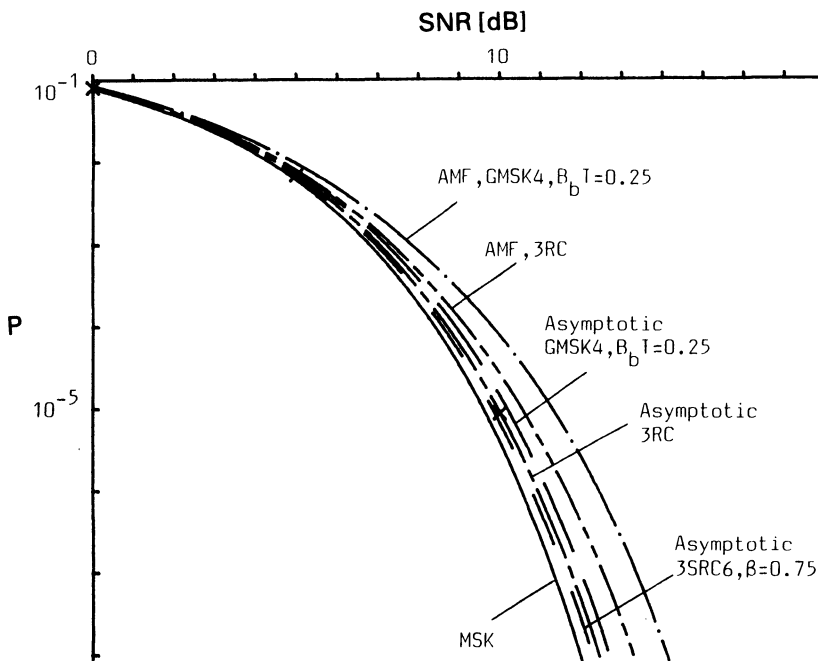


Figure 8.13. The error probability for 3RC with optimum filters of length  $N_F = 6$  ( $\times$ ) together with the error probability for the asymptotic optimum filters for 3RC with  $N_F = 9$ , GMSK4 with  $B_b T = 0.25$  and  $N_F = 9$  and 3SRC6 with  $\beta = 0.75$  and  $N_F = 7$ . As comparison the probability for AMF filters to 3RC and GMSK4 are shown.

at an intermediate value of SNR, and this filter is thus close to optimum for all practical SNR values. The minimum distances are given in Table 8.4. The asymptotic loss compared to a Viterbi receiver is about 0.91 dB for 4RC, while the asymptotic loss compared to MSK is about 2.12 dB; the

**Table 8.2. Minimum Distance for Various Receivers to 3RC-Type Schemes**

Asymptotic optimum									
	$N_F = 2$	$N_F = 3$	$N_F = 4$	$N_F = 5$	$N_F = 6$	$N_F = 7$	$N_F = 8$	$N_F = 9$	Viterbi
3RC	1.4886	1.6328	1.6841	1.6928	1.6967	1.7001	1.7004	1.7005	1.7647
GMSK4 $B_b T = 0.25$	1.3185	1.4811	1.5653	1.5805	1.5854	1.5896	1.5899	1.5899	1.6890
3SRC6 $\beta = 0.75$	1.6757	1.6989	1.7102	1.7119	1.7131	1.7135	—	—	1.8959

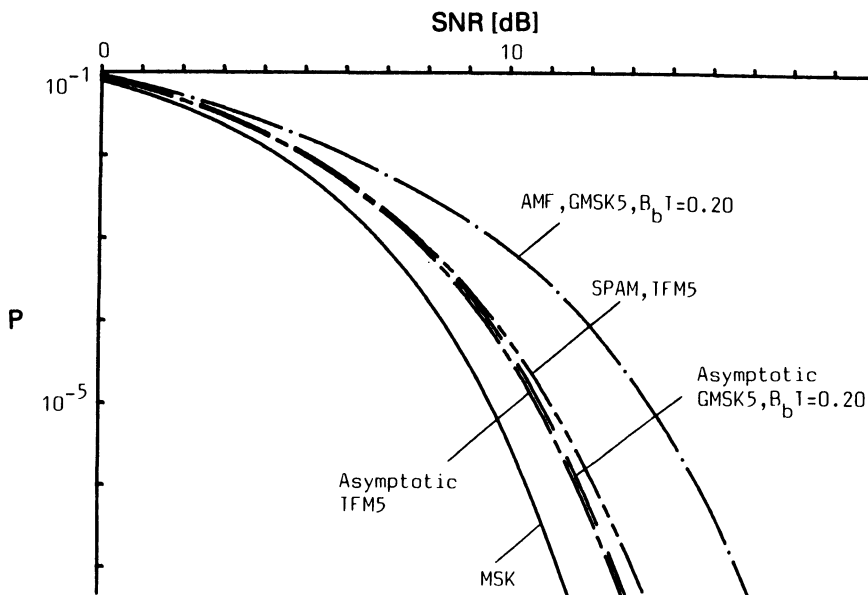


Figure 8.14. The error probability for the asymptotic optimum receivers to TFM5 (this filter is only optimum in the symmetric set) with  $N_F = 8$  and GMSK5 with  $B_b T = 0.20$  and  $N_F = 8$ . As comparison the error probability for TFM5 with a SPAM filter<sup>(3)</sup> with  $N_F = 6$  and for GMSK5 with an AMF filter of length  $N_F = 5$  are shown.

loss at  $10^{-4}$  compared to MSK is about 1.4 dB. The loss for GMSK5 is slightly larger.

### The Fading Channel

Some results are now given for the Rayleigh fading channel. Numerical optimizations have been done for the average SNR equal to 0, 5, 10, and 15 dB. Figure 8.17 gives error probabilities for 3RC both with two branch combiners and without diversity. In all cases a small gain compared to

**Table 8.3. Minimum Distance for Various Receivers to TFM-Type Schemes<sup>a</sup>**

	Asymptotic optimum								Viterbi
	$N_F = 2$	$N_F = 3$	$N_F = 4$	$N_F = 5$	$N_F = 6$	$N_F = 7$	$N_F = 8$		
TFM5	1.0239	1.1564	1.2751	1.3016	1.3079	1.3126	1.3144	1.5865	
GMSK5	0.9335	1.1153	1.2591	1.2905	1.2994	1.3089	1.3113	1.5331	
$B_b T = 0.20$									

<sup>a</sup> The filters for TFM5 are optimum in the symmetric set only.

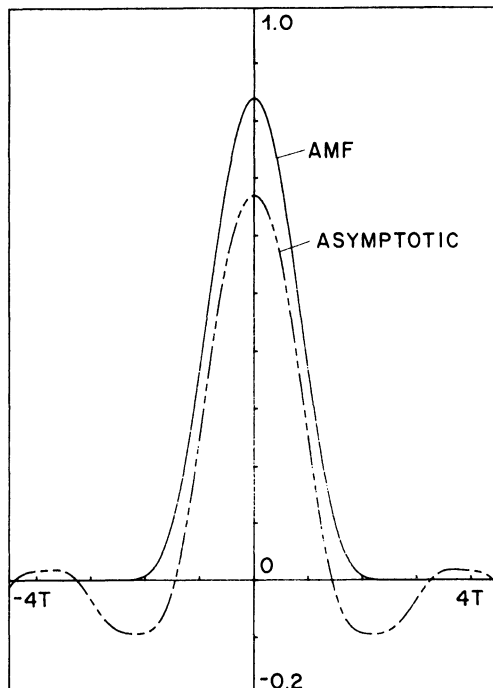


Figure 8.15. The asymptotic optimum filter for 4RC with  $N_F = 9$ .

the AMF receiver is obtained. The performance is close to the MSK performance.

Figure 8.18 shows the filters on a fading channel for 4RC with  $N_F = 5$ . (Since this scheme has  $L = 4$ , these filters are optimum only in the symmetric signal set.) Figure 8.19 shows the corresponding error probabilities. A gain of about 0.5 dB relative to the AMF is obtained at  $10^{-2}$ . The loss at  $10^{-2}$  compared to MSK is of about the same order. Figure 8.19 shows the error probability when the asymptotic optimum filter for the nonfading channel is used on the fading channel. It can be concluded that this filter is very close to the optimum filters, and for practical purposes the nonfading filter can be used at most SNRs on the fading channel. Figure 8.19 also shows the error probabilities for 4RC with two-branch combining. It appears again that in practice the asymptotic optimum filter on the nonfading channel can be used also at lower fading channel SNRs.

#### 8.2.4. Discussion and Comparisons

We have shown that for CPM schemes with  $h = 1/2$  and  $M = 2$ , the loss with an optimum MSK-type receiver compared to the optimum Viterbi

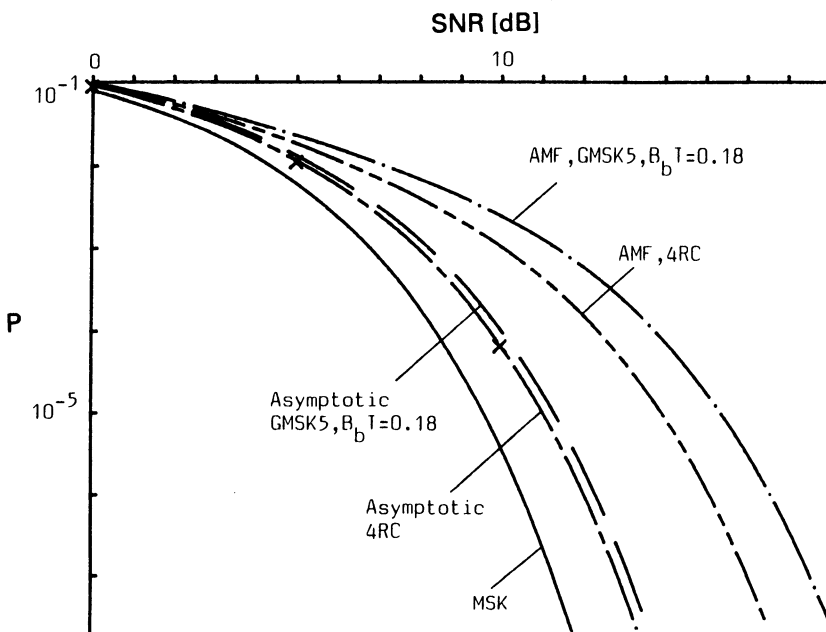


Figure 8.16. The error probability for 4RC with optimum filters of length  $N_F = 7$  ( $\times$ ) (these are optimum only in the symmetric signal set) together with error probability for the asymptotic optimum filters for 4RC with  $N_F = 9$  and GMSK5 with  $B_b T = 0.18$  and  $N_F = 8$ . As comparison the error probabilities for AMF filters to 4RC and GMSK5 with  $B_b T = 0.18$  and  $N_F = 5$  are shown.

receiver is small for schemes based on a frequency pulse with a main-lobe of length less than or equal to about four symbol intervals. Figure 8.20 summarizes the asymptotic behavior of the different receivers for the RC schemes. As comparison the behavior for the AMF receiver is shown. Also shown is the performance for 3SRC6 with  $\beta = 0.75$  and TFM5, both with an optimum Viterbi receiver and with an optimum MSK-type receiver.

The optimum MSK-type receivers have a performance slightly better than the WAMF receiver considered by El-Tanany, Wight, and Hafez.<sup>(25)</sup>

**Table 8.4. The Minimum Distance for Various Receivers to 4RC-Type Schemes**

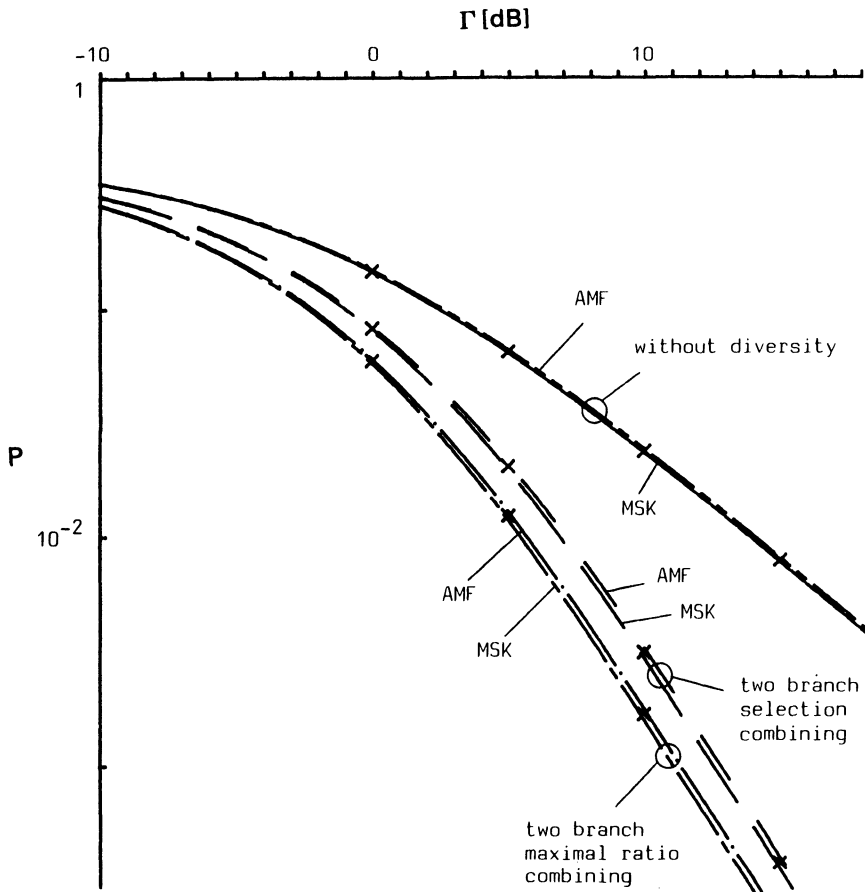


Figure 8.17. The optimum error probability ( $\times$ ) on a Rayleigh fading channel with and without diversity for 3RC. The error probability for an AMF receiver is shown as comparison.

The WAMF filter is based on a minimum squared error approach. The filter consists of a weighted AMF filter, where the trajectories giving the inner boundary of the eye have weight  $1 + \lambda$  and all the others have weight 1. The coefficient  $\lambda$  is then chosen to minimize the error probability. It is surprising that the WAMF receiver performs close to optimum. This receiver has, however, only been applied to TFM5, but for this scheme the loss compared to the optimum filter for most SNRs is only a small fraction of a decibel.

For MSK-type receiver filters generally, as long as the filters do not differ too much from the optimum filter the performance is very close to optimum. For the schemes considered in this section, for example, the

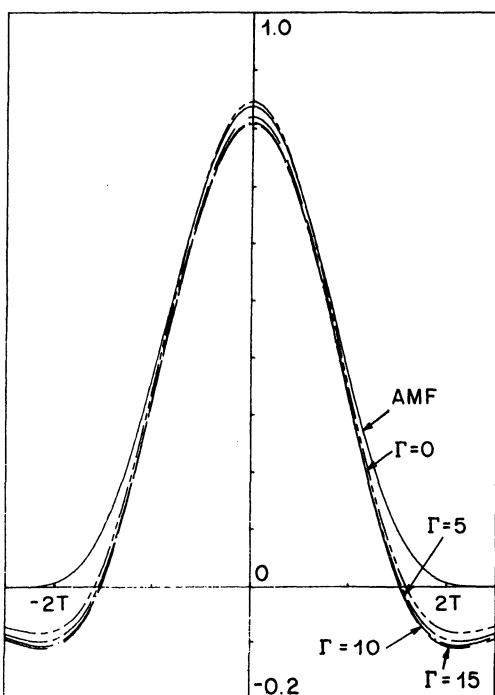


Figure 8.18. The optimum filters in the symmetric signal set, on a Rayleigh fading channel for 4RC with  $N_F = 5$ .

optimum filter for high SNRs on the nonfading channel can be used for both types of channels and all SNRs greater than around 5 dB with a performance close to optimum. In practice the same filter can be used independent of SNR.

Another suboptimum MSK-type receiver for TFM is given in de Jager and Dekker.<sup>(10)</sup> In this paper the TFM eye pattern is approximated with a 4RC PAM eye and the optimum filter for this PAM system is used in the receiver. The results of the approximate analysis in Ref. 10 show that the loss for this receiver at intermediate SNRs is about 1 dB. This type of filter has also been investigated in Refs. 16, 21. We have shown here that the minimum distance is 1.02 and thus that the asymptotic loss is about 2.9 dB. From these papers it is known that these filters give good performance for some schemes. In Ref. 16 truncated filters of this type are considered for smooth partial response schemes and the loss for these filters is quite large for some CPM schemes. From the distance results it is not to be expected that the performance increases significantly with longer filters. A problem is to find a good PAM approximation to these CPM schemes.<sup>(16)</sup> The PAM type of filter seems to be quite good for error probabilities greater than about  $10^{-4}$ .

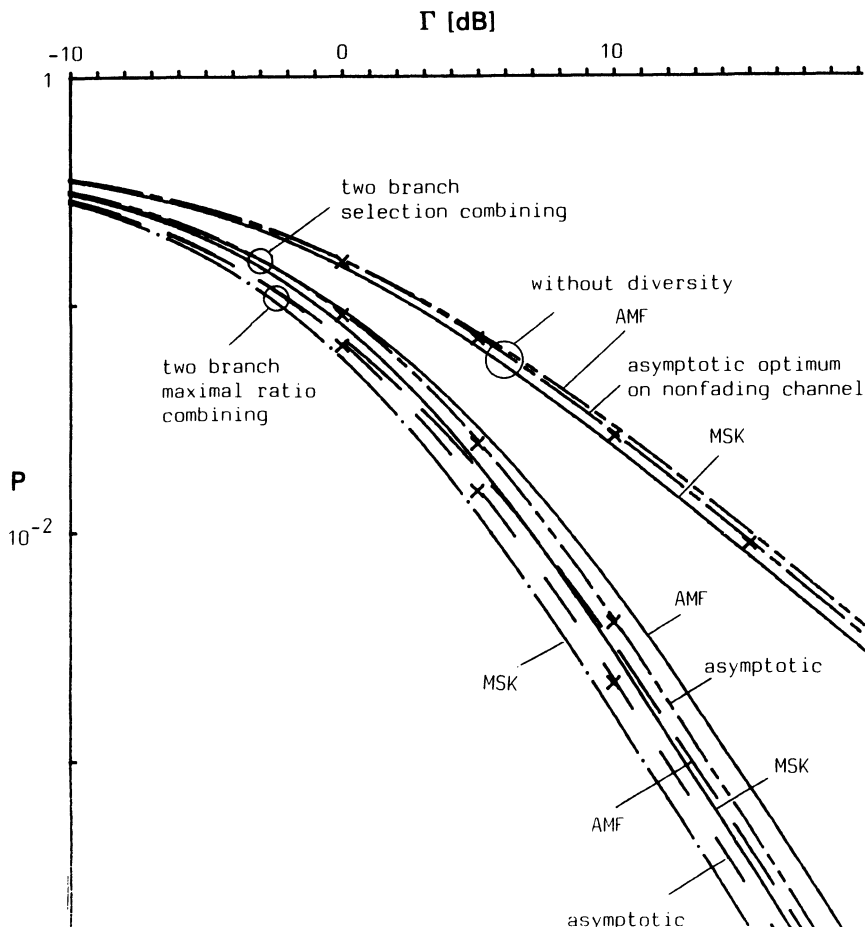


Figure 8.19. The optimum error probability ( $\times$ ) for the receiver optimum in the symmetric signal set on a Rayleigh fading channel with and without diversity for 4RC. The error probability for an AMF receiver is shown as comparison. Also shown is the error probability for the asymptotic optimum receiver on the nonfading channel used on the fading channel.

In Murota and Hirade<sup>(23)</sup> an MSK type receiver for a GMSK scheme is considered. This receiver uses a predetection Gaussian bandpass filter with a normalized 3-dB-down bandwidth of 0.63. It was found by experiment that this bandwidth was close to optimum. From actual tests the loss compared to ideal MSK is found to be around 1.7 dB at  $10^{-3}$  for  $B_b T = 0.25$  and around 3.0 dB for  $B_b T = 0.20$ . The paper also contains some measurements for fast Rayleigh fading.

The MSK-type receiver has also been studied in Galko and Pasupathy.<sup>(19-21)</sup> Another algorithm giving the asymptotic optimum filter is

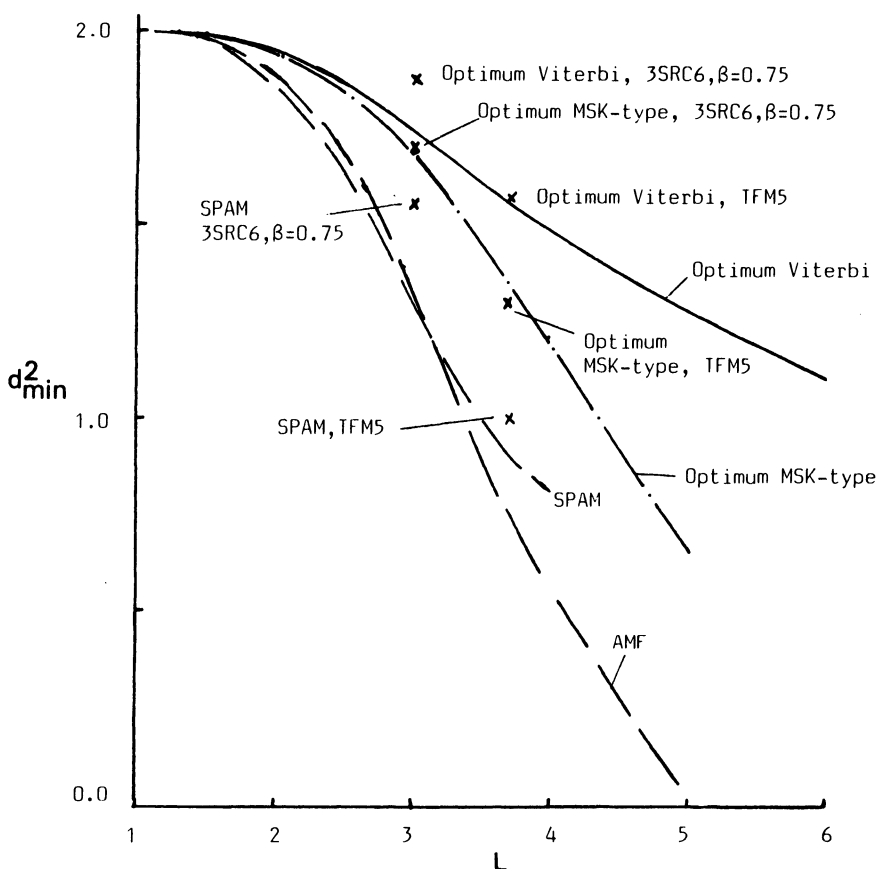


Figure 8.20. Asymptotic performance for various receivers on the nonfading channel to transmitted RC schemes of length  $LT$ . The performance is also shown for 3SRC6, TFM5, and 4SRC8.

given, but it has only been applied to schemes with piecewise constant frequency responses. These schemes are not very attractive in terms of spectral efficiency, if low sidelobes are required.

A modulation scheme called frequency shift offset quadrature modulation (FSOQ) is introduced in Rhodes.<sup>(22)</sup> With our notations this scheme is 2REC (see Table 2.1). This is a modulation scheme of the OQPSK type, but the pulse shape of the two modulation bit streams is varied, depending on the data bits. Since it is an OQPSK type of modulation, an MSK-type receiver can be used. It is claimed that the average bit error probability is minimized by optimizing the filter to obtain the pulse shape of least energy. This idea has also been investigated in Ref. 16. However, in this section we

have shown that this filter is not optimum. For most schemes the filter is optimum for observation length  $N_F = 2$ , but not for a longer observation length.

### 8.3. Serial MSK-Type Receivers

We have shown that the parallel MSK-type receiver works well for schemes based on smooth frequency pulses with a mainlobe width of four symbols or less. One disadvantage with this type of receiver is that decisions must be made alternately in the quadrature arms, which adds hardware complexity in a practical receiver. Recently another receiver of serial type has been investigated,<sup>(28-34,37,44)</sup> which avoids this disadvantage. It is also easier to implement and is less sensitive to phase errors.<sup>(28,29)</sup> The serial receiver has been studied for MSK<sup>(28,34)</sup> and optimum receiver filters have been found; its error performance has been analyzed and results for phase errors have been presented.

In this section the serial receiver will be generalized to include partial response schemes based on smooth frequency pulses. A distance measure giving the asymptotic error probability performance is derived for the serial receiver and an error probability formula is presented. It is shown that the serial and parallel receiver structures have identical performance under the assumption of no phase and timing errors. The error probability for various schemes is calculated, along with the degradation due to phase and timing errors. Comparisons to BPSK and QPSK are given. As in Section 8.2, the modulation index is always 1/2.

#### 8.3.1. The Concept of Serial Detection

The optimum serial receiver for MSK has been derived in Ref. 30. This receiver is shown in Figure 8.21, alongside the parallel receiver of Section 8.2. From Section 2.7, we have that the filter  $a(t)$  in the parallel receiver for MSK is

$$a(t) = \begin{cases} \cos\left(\frac{\pi t}{2T}\right), & |t| \leq T \\ 0 & \text{otherwise} \end{cases} \quad (8.29)$$

We have introduced a phase error  $\Phi$  in the figure, in anticipation of the phase recovery analysis to follow; perfect synchronization corresponds to  $\Phi = 0$ . The serial receiver for MSK uses two filters defined by

$$h_1(t) = \begin{cases} \cos^2(\pi t/2T), & |t| \leq T \\ 0 & \text{otherwise} \end{cases} \quad (8.30a)$$

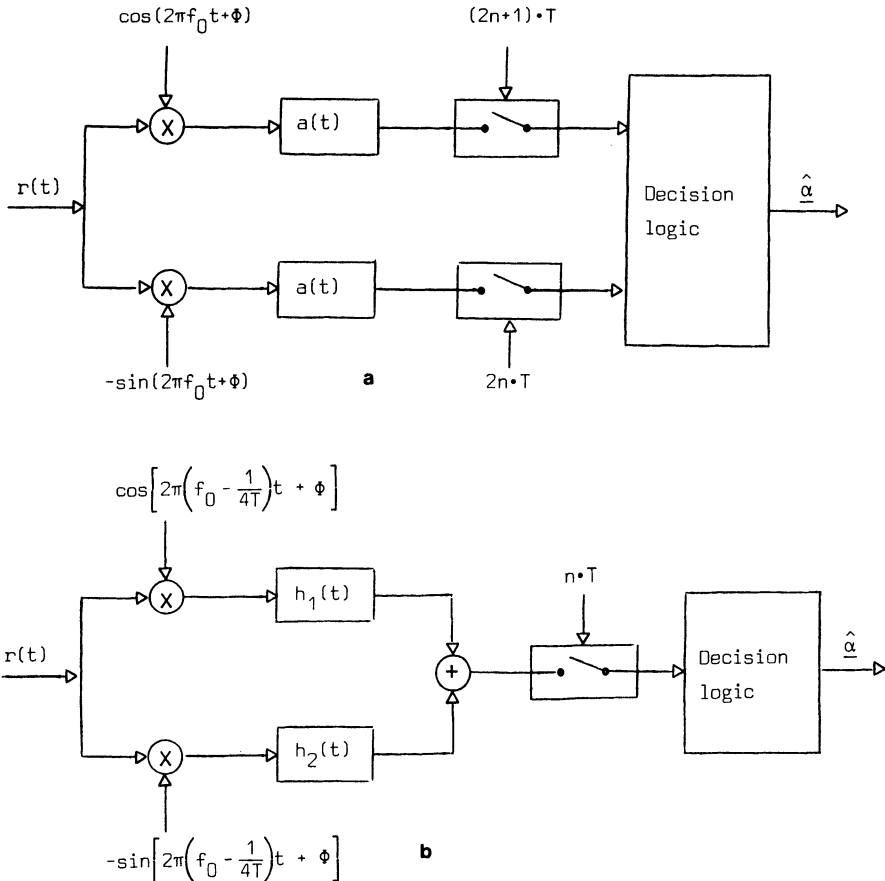


Figure 8.21. (a) Receiver structure for a parallel MSK-type of receiver for CPM. Compare the parallel MSK-type of receiver without phase error  $\Phi$  in Figure 8.9. (b) Receiver structure for a serial MSK type of receiver for CPM. Compare the parallel MSK-type receiver without phase error  $\Phi$  in Figure 8.9.

$$h_2(t) = \begin{cases} -\frac{1}{2} \sin(\pi t/T), & |t| \leq T \\ 0 & \text{otherwise} \end{cases} \quad (8.30b)$$

The difference from the parallel receiver is the demodulation frequency (IF). In the serial receiver the signal is demodulated with the frequency  $f_1 = f_0 - 1/4T$ . This frequency corresponds to the transmitted frequency, for the transmitted data sequence  $\dots, -1, -1, -1, \dots$ , i.e., the all  $-1$  sequence. Thus the signals in the quadrature arms of the serial receiver are  $\cos \phi_1(t, \alpha)$  and  $\sin \phi_1(t, \alpha)$ , where

$$\phi_1(t, \alpha) = \phi(t, \alpha) + \pi t/2T$$

These are equivalent to the unfiltered quadrature signals for a parallel receiver when the transmitted constant amplitude signal has the phase function  $\phi_1(t, \alpha)$ . Note that a transmitted all  $-1$  sequence now corresponds to a zero phase trajectory. These quadrature signals are then filtered and added. The detection eye (after the filters) for MSK is shown in Figure 8.22a. This eye pattern can be compared with the corresponding eye pattern for a parallel MSK receiver given in Figure 8.22b. The advantage of the serial eye is the opened eye at every symbol interval, which means that all the symbols can be detected from this eye. The eye opening is the same as the parallel eye, and therefore the ideal performances for these two receivers are equal.

The filters  $h_1(t)$  and  $h_2(t)$  in equation (8.30) can be easily derived from the MSK filter for the parallel receiver in equation (8.29). The relation is given by

$$\begin{aligned} h_1(t) &= a(t) \cos(\pi t/2T) \\ h_2(t) &= -a(t) \sin(\pi t/2T) \end{aligned} \quad (8.31)$$

where  $a(t)$  is the filter used in the parallel receiver. It is reasonable, therefore, that the serial receiver could also be used for partial response schemes, with the filters chosen according to (8.31) and  $a(t)$  the corresponding filter for the parallel receiver; we will now investigate such "serial MSK-type" receivers. To distinguish the different types, we will use the notation SMSK, where the first  $S$  is for serial, and PMSK, where  $P$  is for parallel.

### 8.3.2. Error Probability Analysis

We will now derive the minimum Euclidean distance and an exact expression of the error probability in estimating the phase node  $\vartheta_n$  for the

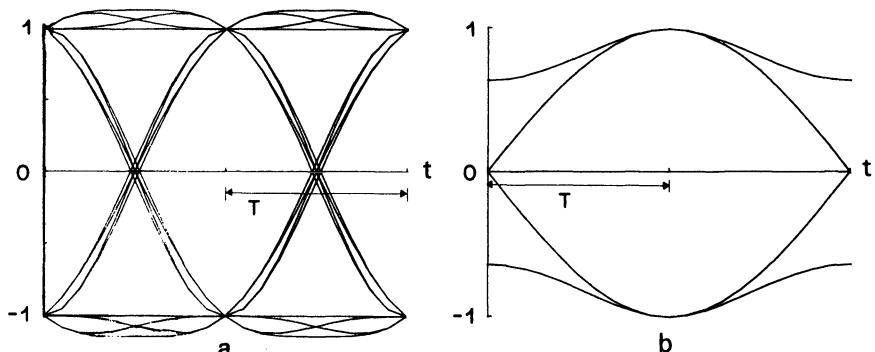


Figure 8.22. (a) Decision eye for a serial MSK receiver for 1REC. (b) Decision eye for a parallel MSK receiver for 1REC.

coherent, serial MSK-type receiver. Note that the phase node  $\vartheta_n$  for the serial receiver is defined in the phase tree traced out by phases  $\phi_1(t, \alpha)$ . Thus  $\vartheta_n$  takes only two values, 0 and  $\pi$ .

We assume zero-mean additive white Gaussian noise and perfect synchronization and timing for the receiver. The receiver observes the signal over  $N_F$  symbol intervals and makes an optimum decision on one symbol. The decision variable  $\lambda$  is a Gaussian random variable, so that its mean and variance determine the error probability.

Assume that the sequence  $\alpha_j$  is transmitted. The mean value of the decision variable is

$$E\{\lambda_j\} = \left(\frac{E_b}{2T}\right)^{1/2} \int_I a(-t) \cos \phi(t, \alpha_j) dt$$

where (8.31) has been used for the filters and  $I$  denotes the observation interval. This is equal to the expected value of the decision variable in the parallel receiver, which means that the eye openings for the two receivers are equal. The variance  $\text{Var}\{\lambda_j\} = E\{(\lambda_j - E\{\lambda_j\})^2\}$  is independent of any particular transmitted sequence, and the usual methods give

$$\text{Var}\{\lambda_j\} = \frac{N_0}{4} \int_I a^2(t) dt$$

This is also the variance for the parallel receiver. Thus the normalized squared distance, defined by

$$d_j^2 = \frac{E\{\lambda_j\}^2}{\text{Var}\{\lambda_j\}} \frac{N_0}{E_b} \quad (8.32)$$

is equal for the two receivers. This is not a Euclidean distance in signal space, but from an error probability point of view it plays the same role. The minimum normalized squared distance is

$$d^2 = \min_j \left\{ \frac{2 \left[ \int_I \cos \phi(t, \alpha_j) a(-t) dt \right]^2}{T \int_I a^2(t) dt} \right\} \quad (8.33)$$

The error probability in estimating the phase node  $\vartheta_n$  is then obtained by averaging over all possible transmitted waveforms to get the same expression as in Section 8.2.1,

$$P = \frac{1}{m} \sum_{j=1}^m Q \left( \left( d_j^2 \frac{E_b}{N_0} \right)^{1/2} \right) \quad (8.18)$$

where  $m$  is the number of different transmitted waveforms. This means that, assuming perfect carrier recovery and timing, the performance of the parallel and serial receiver are identical when the filters are chosen according to (8.31). It is also easily verified that these are the optimum filters for the serial receiver if  $a(t)$  is optimum for the parallel receiver. Using trigonometric formulas on the demodulating frequency in Figure 8.21 and reordering in the terms gives the receiver of Figure 8.23. This is the block diagram of a parallel receiver, whose receive filter is evidently

$$h_1(t) \cos\left(\frac{\pi t}{2T}\right) - h_2(t) \sin\left(\frac{\pi t}{2T}\right) = a(t)$$

This equation is satisfied by the expressions for  $h_1(t)$  and  $h_2(t)$  in (8.31), so that the effects of the parallel and serial filters are the same. It can also be seen that the signal in the other quadrature arm is zero at the sampling instant, just as in the parallel receiver. Thus  $h_1$  and  $h_2$  must be optimal filters for the serial receiver, and the parallel-receiver results of Section 8.2 carry over to the serial case.

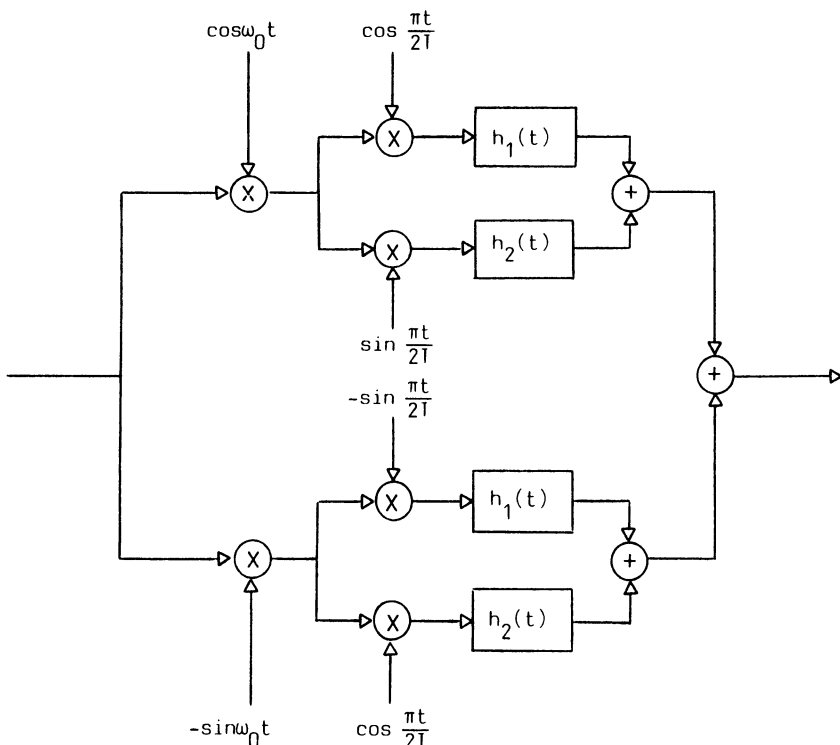


Figure 8.23. Redrawing the serial MSK-type receiver ( $\Phi = 0$ ).

Figure 8.24 shows the error probability with optimum filters for some schemes considered in this section. For the more complex schemes the loss compared to MSK is quite small.

### 8.3.3. Sensitivity to Phase Errors

In this section the performance degradation for a serial receiver due to phase errors will be derived and compared to that of the parallel receiver.

Perfect symbol timing synchronization will be assumed. Several authors have concluded that a serial MSK receiver is less sensitive to phase errors than a parallel receiver (see, e.g., Ref. 29). If a phase error is present, i.e.,  $\Phi \neq 0$  in Figure 8.21, this phase error can be viewed as part of the transmitted phase. In the previous section, however, it is shown that for a specific transmitted phase, the performances for the two receivers are identical, whatever phase is being transmitted, an apparent contradiction to the results

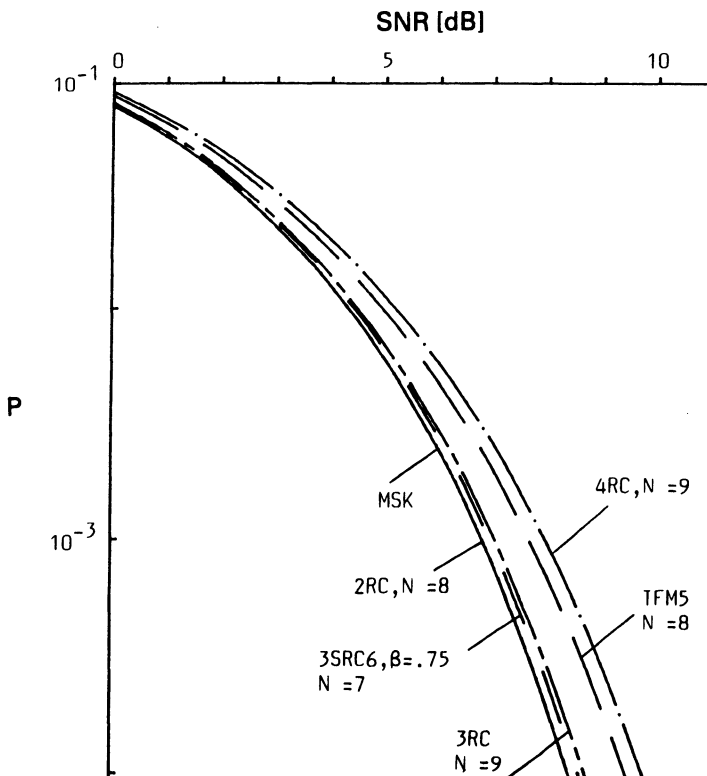


Figure 8.24. The error probability for some CPM schemes. The MSK-type receivers are asymptotically optimum, except for TFM5 where the receiver is asymptotically optimum in the symmetric signal set only.<sup>(15)</sup>  $N = N_F$ .

quoted above. This is not the case. Figure 8.25a shows the detection eye for a serial receiver for MSK when the phase error is  $-10$  deg. The detection eye for the parallel MSK receiver is shown in Figure 8.25b. These figures illustrate that the opening of the eye is equal for a specific phase error for the parallel and serial receiver if the sampling is done strictly according to Figure 8.21. This sampling time is still optimum for the parallel receiver, but it is not for the serial receiver. By changing the sampling time to the time when the eye opening is as large as possible, the performance for the serial receiver is optimized for large SNR, i.e., the minimum distance is optimized.

In general the optimum sampling time will depend on the error probability for which the optimization is desired. By the above choice, however, the error probability will be close to optimum for all signal-to-noise ratios used in practice. Note that with a phase error the eye is symmetrical around an ideal sampling time. The change in sampling time is negative for a negative phase error, the case shown in Figure 8.25, and positive with the same absolute value for a positive phase error.

What is the relationship between the phase error  $\Phi$  and the change of sampling time  $\Delta T_0$  for a serial receiver? From the detection eyes it can be verified that the largest opening in the eye is obtained at the time  $t$  when the trajectories for the transmitted sequences  $\alpha_1 = -1, -1, -1, \dots$  and  $\alpha_2 = 1, 1, 1, \dots$  are equal. Assume the no-error sampling time is  $t = 0$ . Then the trajectory in the eye diagram corresponding to the transmitted sequence  $\alpha_1 = -1, -1, -1, \dots$  is  $y(t, \alpha_1) = T \cos \Phi$ . This is the straight line seen in the eye diagram. In the same way the trajectory corresponding to  $\alpha_2 = 1, 1, 1, \dots$  is  $y(t, \alpha_2) = T \cos(\pi t/T - \Phi)$ .  $\Delta T_0$  is the time when these two trajectories cross each other, when  $\Delta T_0 = 0$  or  $\Delta T_0 = (2\Phi/\pi)T$ . The solution

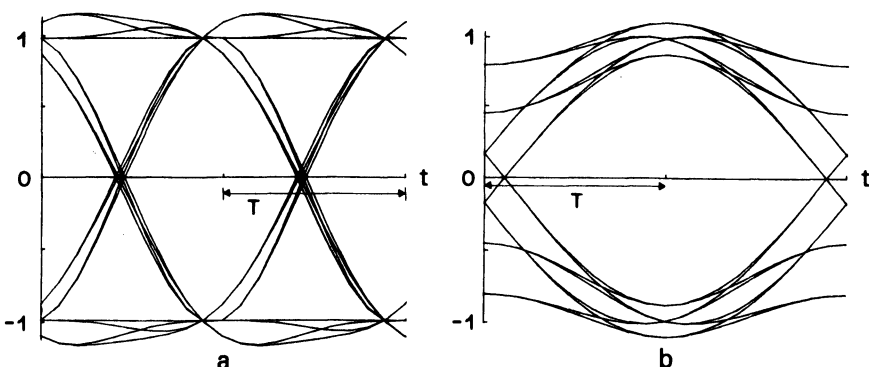


Figure 8.25. (a) Decision eye for a serial MSK receiver for 1REC, when the phase error is  $-10$  deg. (b) Decision eye for a parallel MSK receiver for 1REC, when the phase error is  $-10$  deg.

giving the largest eye opening is the second one,

$$\Delta T_0 = \frac{2\Phi}{\pi} T \quad (8.34)$$

Thus the change in sampling time is directly proportional to the phase error.

We can now ask if this is true for serial-detected partial response schemes. Figure 8.26a shows the serial eye pattern for 3RC with an MSK filter. The serial eye is more complex than the corresponding parallel eye, but it is open every  $T$  seconds. Thus decisions on all the transmitted data symbols can be made from this eye, compared to the parallel receiver where the decisions are made alternately from two different eyes. Figure 8.26b shows the detection eye for 3RC with a SMSK receiver when the phase error is  $-5$  deg and the corresponding detection eye for the PMSK receiver is given in Figure 8.26c. These receivers for 3RC behave just as the receivers for 1REC. To find the optimum sampling time in the serial eye is not easy, and we can only conjecture that the asymptotic optimum is still given by

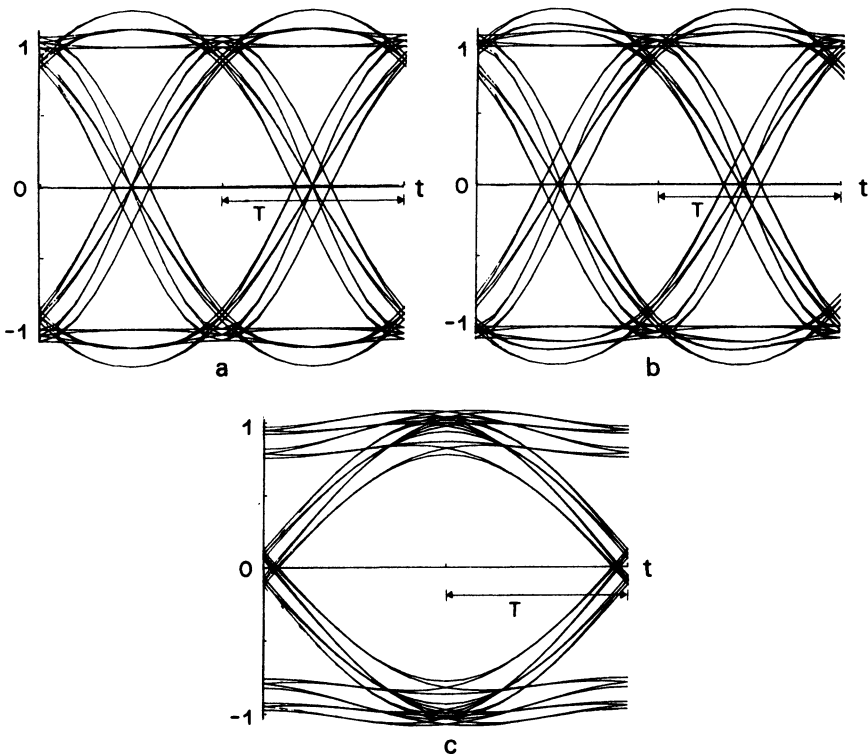


Figure 8.26. (a) Decision eye for a serial MSK receiver for 3RC, no phase error. (b) Decision eye for a serial MSK receiver for 3RC,  $-5$  deg phase error. (c) Decision eye for a parallel MSK receiver for 3RC,  $-5$  deg phase error.

(8.34). In the following this change in sampling time will be used for the serial receivers. This behavior for the serial receiver is observed also for other schemes and receiver filters.<sup>(37)</sup>

Now the performance of the serial receiver can be compared with the performance of the parallel receiver, with the assumption that the optimum sampling time is chosen in both cases. The performance analysis in the previous section must be changed slightly to account for the new sampling time. It is easily verified that the distance is given by

$$d_j^2 = \frac{2}{T} \frac{\left[ \int_I \cos [\phi(t, \alpha_j) - \Phi] a(\Delta T_0 - t) dt \right]^2}{\int_I a^2(t) dt} \quad (8.35)$$

where  $\Delta T_0 = 0$  for the parallel receiver and  $\Delta T_0 = (2\Phi/\pi)T$  for the serial receiver.

Figures 8.27 and 8.28 show error probabilities at several phase errors for transmitted 3RC received in an asymptotically optimum receiver of serial and parallel type, respectively. The observation length is  $N_F = 9$ . For a phase error of 20 deg the degradation at  $P = 10^{-6}$  for the serial receiver is about 0.7 dB, while it is about 4.7 dB for the parallel receiver. More results of this type can be found in Ref. 37. These results show that the parallel receiver is indeed much more sensitive to phase errors than the serial receiver, provided that the optimum sampling time is chosen.

Figure 8.29 summarizes the degradation due to phase errors for various schemes. The degradation in decibels relative to BPSK and QPSK is given versus the phase error  $\Phi$ , for the error probability equal to  $10^{-6}$ . The bit error probability for BPSK, when a phase error is present, is given by

$$P = Q((2E_b/N_0)^{1/2} \cos \Phi) \quad (8.36)$$

while the bit error probability for QPSK is

$$P = \frac{1}{2} \left[ Q \left( \left( \frac{4E_b}{N_0} \right)^{1/2} \cos \left( \frac{\pi}{2} - \Phi \right) \right) + Q \left( \left( \frac{4E_b}{N_0} \right)^{1/2} \sin \left( \frac{\pi}{4} - \Phi \right) \right) \right] \quad (8.37)$$

QPSK is much more sensitive to phase errors than BPSK.

The figure shows various schemes with MSK receivers, both serial and parallel, and the degradation for the asymptotically optimum 3RC receiver with  $N_F = 9$  is also given. The degradations for BPSK and QPSK are given as comparison. It is seen that the serial and parallel receivers with the same type of filter have the same performance when  $\Phi = 0$ . For larger phase errors the serial receiver is superior. There is also another advantage for the serial receiver seen in the figure. For the serial receiver with a specific

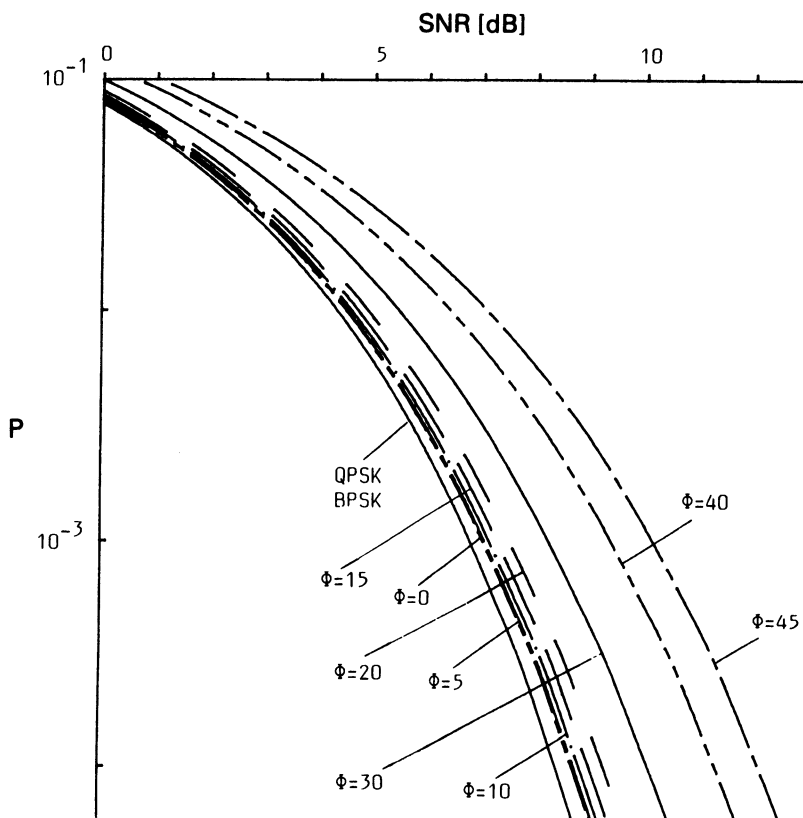


Figure 8.27. The error probability for the asymptotically optimum serial receiver with  $N_F = 9$  for 3RC, for various phase errors  $\Phi$ .

type of filter the relative degradation is nearly independent of the length in symbol intervals of the transmitted pulse, at least for reasonably short pulses. For the parallel receiver, on the other hand, the relative degradation is worse for the longer pulses than for shorter pulses.

For the TFM5 scheme with a serial receiver the degradation pattern is somewhat different. This is due to the frequency pulse shape  $g(t)$ , which is not strictly positive. It has a  $\sin(x)/x$  shape outside the main lobe which is seen in the eye diagram. This scheme is also more sensitive to phase errors than the RC schemes.

The only results for asymptotically optimum MSK-type receivers are for 3RC with  $N_F = 9$ . These results show that the degradation is increasing slightly faster for these filters compared to the MSK filters. The degradation for the serial receiver is still much smaller than the degradation for the parallel receiver. Another type of filter, which is based on a pulse amplitude

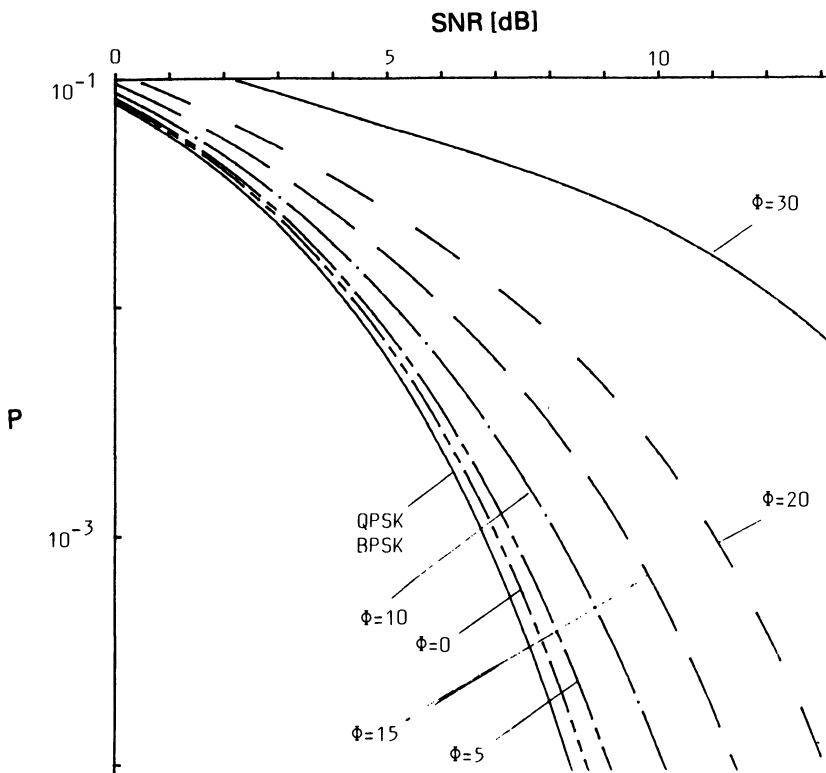


Figure 8.28. The error probability for the asymptotically optimum parallel receiver with  $N_F = 9$  for 3RC, for various phase errors  $\Phi$ .

modulation (PAM) approximation of the decision eye, is investigated in Ref. 37. This filter has a shape which is more like the shape of the optimum filter than the MSK filter. It has been found that this filter is also slightly more sensitive to phase errors for all schemes considered. No results are given for other schemes, but it is expected that the optimum receivers for the other schemes have the same relative degradation.

The degradation for large signal-to-noise ratios has also been investigated.<sup>(37)</sup> It is found that the degradation due to phase errors for a specific receiver depends on the error probability level, and is larger at smaller error probability levels. The serial receiver is much less sensitive to phase errors than the parallel receiver at all error probability levels.

### 8.3.4. Sensitivity to Timing Errors

In this section we will concentrate on the degradation due to timing errors. Assuming, for a moment, that no phase error is present, it is easily

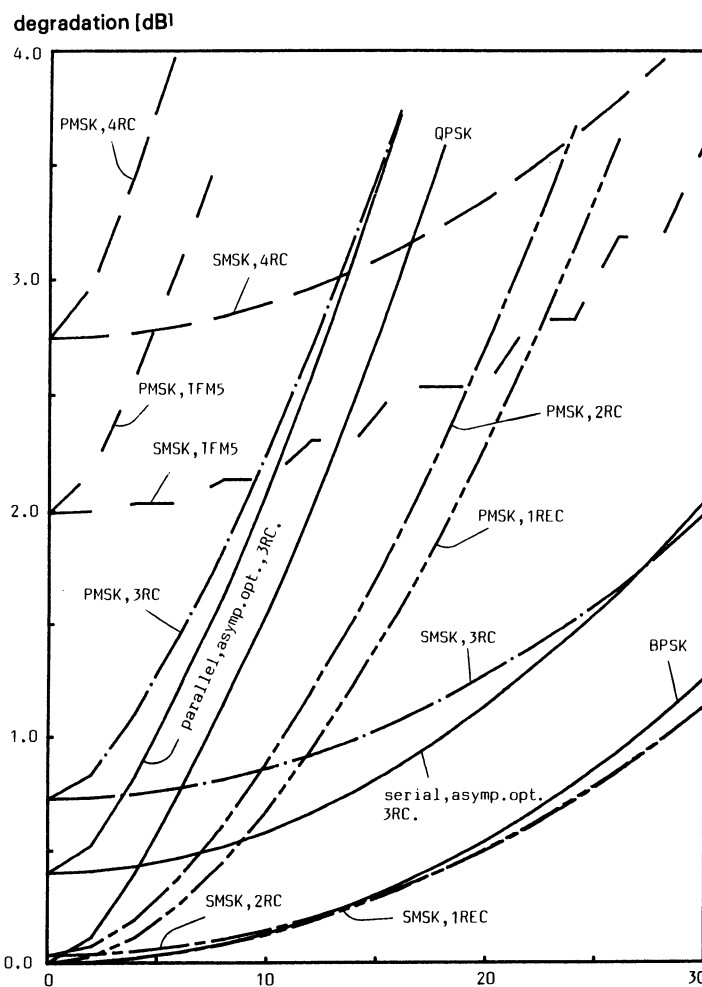


Figure 8.29. Degradation relative to ideal BPSK/QPSK at  $P = 10^{-6}$  versus phase error for various schemes with serial and parallel MSK receivers. The degradation for an asymptotically optimum receiver ( $N_F = 9$ ) for 3RC is also shown.

seen from the eye diagrams in Figures 8.22, 8.25, and 8.26 that the serial receiver is more sensitive to timing errors. For the serial receiver the eye opens every  $T$  seconds and therefore is narrower than the parallel eye, which opens every  $2T$  seconds. The error probability can be calculated also for this case; the distance is given by (8.35) with  $\Delta T_0$  replaced by  $\Delta T + \Delta T_0$  and with  $\Delta T$  equal to the timing error. It is known from Refs. 29, 37 that the serial receiver is more sensitive to timing errors than the parallel receiver.

For comparison the bit error probability for BPSK, with a timing error  $\Delta T$  and a phase error  $\Phi$ , is

$$P = \frac{1}{2} \left[ Q \left( \left( \frac{2E_b}{N_0} \right)^{1/2} \cos \Phi \right) + Q \left( \left( \frac{2E_b}{N_0} \right)^{1/2} \cos \Phi \left( 1 - 2 \left| \frac{\Delta T}{T} \right| \right) \right) \right] \quad (8.38)$$

It can be shown that with  $\Phi = 0$  this result is also valid for QPSK, since the quadrature detection eyes for QPSK are equal to the detection eye for BPSK when  $\Phi = 0$ . Evidently, BPSK is more sensitive to timing errors than to phase errors.

Finally some results for a combined phase error and timing error will be given for certain schemes. Figure 8.30 shows the degradation at  $10^{-6}$  relative to ideal BPSK/QPSK for a phase error of 10 deg, versus a relative timing error  $\Delta T/T$ . Note that the serial eye is not symmetric around the asymptotically optimum sampling time; therefore the degradation results are not symmetric for this receiver. The figure shows the results for MSK receivers for different transmitted schemes. The degradation for an asymptotically optimum MSK-type receiver with  $N_F = 9$  for 3RC is also shown. The degradation for BPSK is given as comparison. It is easily seen that the degradation for the SMSK receiver is much larger than for the PMSK receiver. The relative degradation for the SMSK receiver also gets worse for longer pulses, while it is nearly constant for the PMSK receiver. This is just the opposite of the case for degradation due to phase errors.

From Figure 8.30 it can be concluded that given a phase error  $\Phi$ , the SMSK receiver is superior as long as the timing error is not too large. The region where the serial receiver is superior increases slightly for schemes based on longer pulses. For 1REC the region where the SMSK receiver performs better than the PMSK receiver at  $P = 10^{-6}$  is  $-0.13 \leq \Delta T/T \leq 0.07$ . The same region for 4RC is  $-0.12 \leq \Delta T/T \leq 0.10$ .

The only results given for asymptotically optimum receivers are for 3RC. From Figure 8.30 it appears that the relative degradation due to timing errors for the optimum receiver is slightly larger than that of the SMSK receivers. This is also true for the filters based on PAM-approximations.<sup>(37)</sup> It is believed that the above conclusions for the optimum 3RC receiver also holds for optimum receivers for other schemes.

The asymptotic-SNR degradation has also been calculated.<sup>(37)</sup> It was found that the degradation due to timing errors for a specific receiver is larger at small error probability levels, but still the trends are the same. These results support the conjecture made in Section 8.3.3 about the optimum sampling time for the serial receiver. If the sampling time was not optimum a small timing error would give a better performance there and this is not the case for the schemes considered here.

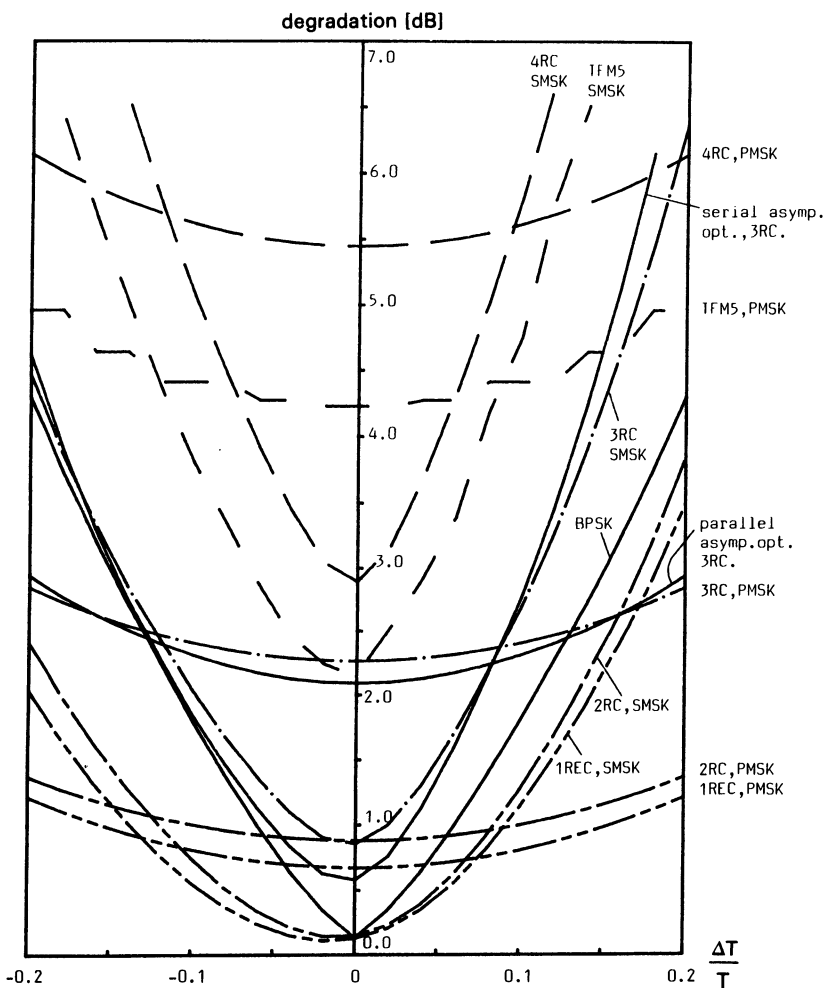


Figure 8.30. Degradation at  $P = 10^{-6}$  relative to ideal BPSK/QPSK, versus a relative timing error, for a phase error of 10 deg, for various schemes with MSK receivers. The degradation for an asymptotically optimum receiver ( $N_F = 9$ ) for 3RC is also shown.

### 8.3.5. Summary

We have shown that the error performance of the serial and parallel receivers is the same under perfect synchronization conditions. An advantage of the serial receiver lies in its implementation. All the decisions on the transmitted symbols can be made from one decision eye. Another advantage is its reduced sensitivity to phase errors. If the exact phase of the transmitted carrier is not recovered in the receiver, the degradation in

performance is larger with the parallel receiver than with the serial. If the bit time synchronization is not correct, however, the relation is the opposite. Assuming it is easier to obtain a good bit time synchronization than a correct carrier phase recovery, we see that the serial receiver has an advantage over the parallel receiver. The parallel-receiver filters obtained here and elsewhere<sup>(16,14)</sup> can be modified and converted according to the results in this section, and used in the serial receiver. In this way it is possible to obtain schemes with combined very good spectral and detection properties.

Previously we have indicated that differential encoding/decoding has to be employed for the parallel receiver to give the estimated data sequence from the phase node sequence. This is also the case for the serial receiver. If a burst mode transmission is used and a unique synchronization word is used in the beginning of the burst, the serial receiver requires no differential encoding/decoding to resolve the data burst, while the parallel receiver still does. This is because  $\alpha_n = -1$  never changes the phase node for the serial receiver while  $\alpha_n = +1$  always changes the phase node, a property which is not true for the parallel receiver.

The serial MSK-type receiver has previously been studied for transmitted MSK.<sup>(6-12)</sup> We have shown that the trends reported for serial MSK are also valid for serial partial response schemes for a variety of different smoothing pulse shapes proposed in the literature.

There is also the issue of serial *generation* of  $h = 1/2$ , binary partial response CPM. This problem is addressed in Section 6.4. One approximate technique is to use BPSK plus a suitable bandpass filter followed by a hard limiter, or a serial MSK unit<sup>(28,34)</sup> (which is a filtered BPSK signal) followed by a linear filter and a hard limiter. For details about similar schemes and comparisons to ideal CPM schemes, see Ref. 36 and Chapter 6.

#### 8.4. Average Matched Filter Receivers

We will now consider the problem of coherent detection of CPM signals with simple receivers of yet another kind. In Chapter 7 we have derived the optimum coherent receiver for CPFSK, assuming an observation interval of  $N$  symbols of the CPFSK waveform which produces an optimum decision of one symbol. This receiver is often too complex. It is possible to find a receiver optimum for low SNR which is simple as it turns out, and is useful at other SNR. This is the average matched filter receiver introduced by Osborne and Luntz.<sup>(42)</sup> This receiver has been further considered for some specific full response signaling schemes in Ref. 43.

We will generalize the idea of an average matched filter receiver. The AMF receiver is introduced for partial response schemes, and some other possibilities for choosing the filter bank are investigated. This generalized

receiver is called the multiple-symbol AMF receiver; it represents a compromise between the optimum and AMF receivers. This simplified receiver is of course suboptimum and the performance is perhaps not acceptable for some schemes. It works well only for schemes based on relatively short frequency pulses. Performance may be improved by increasing the number of receiver filters and matching them better to the transmitted signals.

#### 8.4.1. AMF Receiver Principles and Structure

Suppose that the receiver observes the signal over  $N_F$  intervals and that it seeks to make a decision on the first transmitted signal  $\alpha_0$ . The pure AMF receiver is a bank of  $M$  filters matched to the *average* of all signals having  $\alpha_0 = -(M - 1)$ ,  $\alpha_0 = -(M - 3), \dots, \alpha_0 = (M - 1)$ , respectively. The filter outputs are sampled every symbol interval and the estimate of  $\alpha_0$  taken from the filter giving the highest correlation. This will be a maximum likelihood estimate as the SNR tends to zero. Osborne and Luntz<sup>(42)</sup> introduced the AMF receiver for 1REC pulses; Hirt and Pasupathy<sup>(43)</sup> extended it to other full response schemes.

For partial response schemes this receiver concept has to be modified. In this case the signal depends on the  $L - 1$  prehistory symbols, the  $L - 1$  symbols prior to  $\alpha_0$ .  $L$  is the duration in symbol intervals of the frequency pulse. Thus the average signal is in general nonzero for  $-(L - 1)T \leq t \leq 0$ . There are two possible choices.  $M$  filters can still be used, one for each value of  $\alpha_0$ , with impulse responses equal to the average over all other symbols, including the prehistory symbols. These filters are poorly matched to the signals and it is known that they give a very bad performance. The other possibility is to use one filter set for each prehistory and choose the set according to previous decisions. In this case the impulse response of the filters is the average over all symbols except the prehistory symbols and the decision symbol. This is the receiver we will use.

This receiver can be generalized further to a *multiple-symbol* AMF receiver. Instead of having only  $M$  filters in each set,  $M^{N_A}$  filters can be used, where  $M^{N_A-1}$  of these filters assume the same value of  $\alpha_0$ . The impulse response of each filter is the average of all symbols except  $\alpha_{-(L-1)}, \dots, \alpha_0, \dots, \alpha_{N_A-1}$ . Consider the transmitted sequence  $\alpha_{N_F-1} = \dots, \alpha_{-L}, \alpha_{-(L-1)}, \dots, \alpha_{-1}, \alpha_0, \alpha_1, \dots, \alpha_{N_A-1}, \alpha_{N_A}, \dots, \alpha_{N_F-1}$ . The phase in the interval  $0 \leq t \leq N_F T$  corresponding to this sequence does not depend on the symbols  $\alpha_i$ ,  $i \leq -L$ , except through a constant phase shift

$$\theta = \pi h \sum_{i=-\infty}^{-L} \alpha_i$$

This constant phase shift gives a constant phase rotation of the average signal and thus "rotates" the filter. Now define a prehistory data symbol

vector  $\mathbf{A}_{-1} = \alpha_{-(L-1)}, \dots, \alpha_{-1}$ . The symbols  $\alpha_0, \dots, \alpha_{N_F-1}$  are divided into two vectors  $\mathbf{A}_0 = \alpha_0, \dots, \alpha_{N_A-1}$  and  $\mathbf{A}_1 = \alpha_{N_A}, \dots, \alpha_{N_F-1}$ .  $\alpha_{N_F-1}$  in short notation can be written  $\alpha_{N_F-1} = \alpha_{-L}$ ,  $\mathbf{A}_{-1}$ ,  $\mathbf{A}_0$ ,  $\mathbf{A}_1$ ; when  $N_A = N_F$ , there is no  $\mathbf{A}_1$ . The filter bank consists of a set of filters for every possible prehistory  $\mathbf{A}_{-1}$ , i.e.,  $M^{(L-1)}$  different sets in total. The filters in every set are matched to the average of all transmitted waveforms that have the given prehistory  $\mathbf{A}_{-1}$ , and contain the same symbols  $\mathbf{A}_0$  in the beginning of the observation interval. This means that the  $N_A$  first symbols are fixed when the average is made. In every set of filters, there is one filter corresponding to every possible sequence  $\mathbf{A}_0$ , a total of  $M^{N_A}$  filters per set. Altogether the receiver consists of  $M^{(L-1+N_A)}$  filters. This is a maximum number of filters, since for some schemes and modulation indices, some filters may be identical.

With the new definitions,  $s(t, \alpha_{N_F-1})$  can be written  $s(t, \mathbf{A}_{-1}, \mathbf{A}_0, \mathbf{A}_1, \theta)$ . Thus the average signal, given  $\mathbf{A}_{-1}$  and  $\mathbf{A}_0$ , is

$$\bar{s}(t, \mathbf{A}_{-1}, \mathbf{A}_0, \theta) = \frac{1}{m} \sum_{i=0}^{m-1} s(t, \mathbf{A}_{-1}, \mathbf{A}_0, \mathbf{A}_{1i}, \theta) \quad (8.39)$$

where  $m = M^{(N_F - N_A)}$  is the total of sequences having a given  $\mathbf{A}_{-1}$  and  $\mathbf{A}_0$ .  $\mathbf{A}_{1i}$  is all possible sequences with  $N_F - N_A$   $M$ -ary symbols and index  $i$  is an enumeration of these sequences. The impulse response  $h(t, \mathbf{A}_{-1}, \mathbf{A}_0, \theta)$  of a filter in the bank is

$$h(t, \mathbf{A}_{-1}, \mathbf{A}_0, \theta) = \bar{s}(N_F T - t, \mathbf{A}_{-1}, \mathbf{A}_0, \theta)$$

The receiver chooses one of the sets of filters and computes

$$l_j = \int_0^{N_F T} r(t) \bar{s}(t, \hat{\mathbf{A}}_{-1}, \mathbf{A}_{0j}, \hat{\theta}) dt$$

for all possible sequences  $\mathbf{A}_{0j} = (\alpha_0, \alpha_1, \dots, \alpha_{N_A-1})_j$  in this set and chooses the  $\alpha_0$ , corresponding to the sequence  $\mathbf{A}_{0j}$  giving the largest  $l_j$ , as an estimate of  $\alpha_0$ , the decision symbol. Index  $j$  is an enumeration of the different sequences  $\mathbf{A}_0$ ,  $\hat{\mathbf{A}}_{-1}$  and  $\hat{\theta}$  are estimates of  $\mathbf{A}_{-1}$  and  $\theta$  given by the previous decisions. The receiver model is shown in Figure 8.31.

The constant phase shift  $\theta$  can be handled by multiplications of  $\cos \theta$  and  $\sin \theta$ . This is easily seen by using (8.39) and the definition of the CPM signal:

$$\begin{aligned} \bar{s}(t, \mathbf{A}_{-1}, \mathbf{A}_0, \theta) &= \left( \frac{2E}{T} \right)^{1/2} \{ \cos \omega_0 t [\mathcal{A}(t, \mathbf{A}_{-1}, \mathbf{A}_0) \cos \theta \right. \\ &\quad \left. - \mathcal{B}(t, \mathbf{A}_{-1}, \mathbf{A}_0) \sin \theta] + \sin \omega_0 t [\mathcal{B}(t, \mathbf{A}_{-1}, \mathbf{A}_0) \cos \theta \right. \\ &\quad \left. + \mathcal{A}(t, \mathbf{A}_{-1}, \mathbf{A}_0) \sin \theta] \} \end{aligned} \quad (8.40)$$

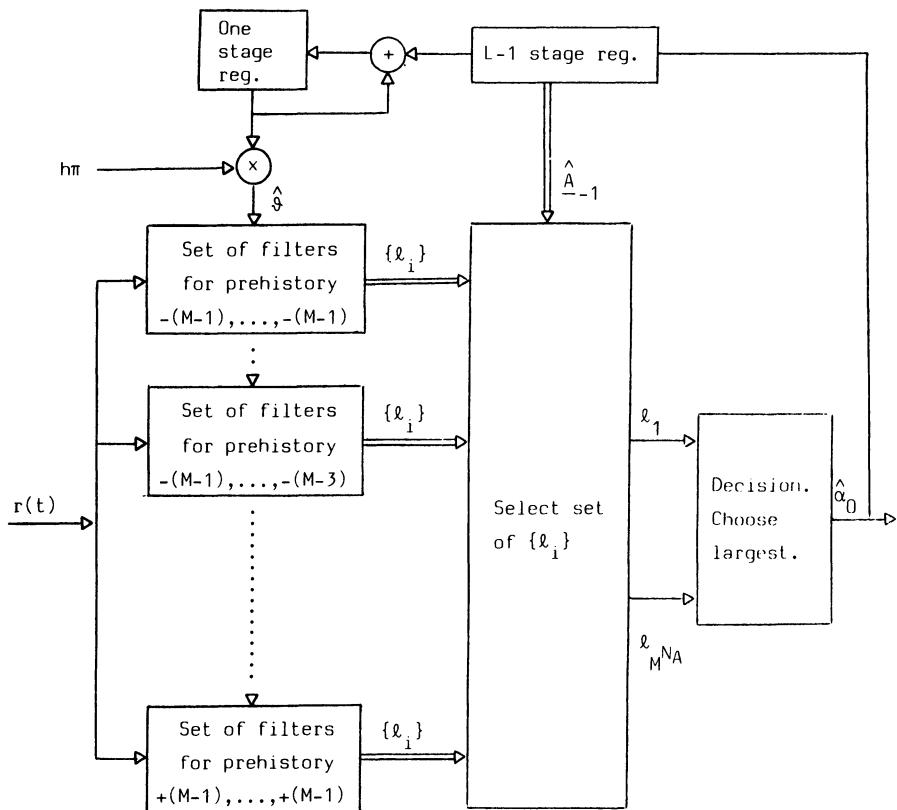


Figure 8.31. Receiver model for an AMF receiver.

where

$$\mathcal{A}(t, \mathbf{A}_{-1}, \mathbf{A}_0) = \frac{1}{m} \sum_{i=0}^{m-1} \cos \phi(t, \mathbf{A}_{-1}, \mathbf{A}_0, \mathbf{A}_{1i})$$

and

$$\mathcal{B}(t, \mathbf{A}_{-1}, \mathbf{A}_0) = \frac{1}{m} \sum_{i=0}^{m-1} \sin \phi(t, \mathbf{A}_{-1}, \mathbf{A}_0, \mathbf{A}_{1i})$$

Thus the filters can be realized in baseband as in Figure 8.32.

#### *Nonuniformly Weighted AMF Filters*

So far only AMF filters where all the signals have equal weight have been considered. In many cases the performance can be improved by using

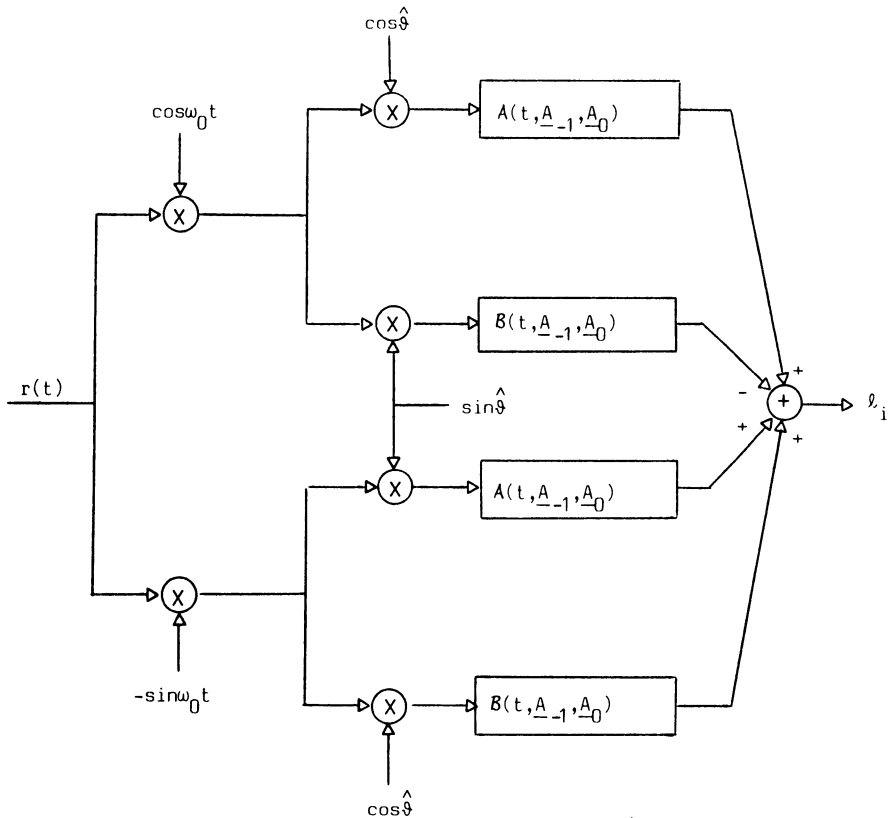


Figure 8.32. Baseband filter for an AMF receiver.

a nonuniformly weighted AMF filter instead. These weights can be optimized to give the best performance at a given error probability. This is a difficult optimization problem. For some schemes weighted AMF filters have been considered<sup>(39)</sup> and they improved performance slightly. These filters were found by trial and error.

#### 8.4.2. Error Performance of AMF Receivers

In this section, the equivalent minimum Euclidean distance and an expression for the symbol error probability of the coherent multiple-symbol AMF receiver are derived. We assume zero-mean additive white Gaussian noise and a receiver that observes the CPM signal over  $N_F$  symbol intervals and makes an optimum decision on one symbol. The updating of prehistory  $\hat{A}_{-1}$  and constant phase  $\hat{\theta}$  will affect the symbol error probability in general but in this section they are assumed to be error free, which means that the

correct filter set is chosen,  $\hat{\theta}$  can be set to zero in the following, without loss of generality. It is easily seen that the decision variable  $l_j$  is a Gaussian random variable; therefore its mean and variance determine the symbol error probability.

Assume the  $M$ -ary sequence  $\alpha_{N_F-1} = \alpha_{-L} A_{-1}, A_0, A_1$  is transmitted. The decision variables  $l'_j$  giving a correct decision are given by

$$l'_j = \int_0^{N_F T} r(t) \bar{s}(t, A_{-1}, A'_0) dt, \quad j = 1, 2, \dots, M^{(N_A-1)}$$

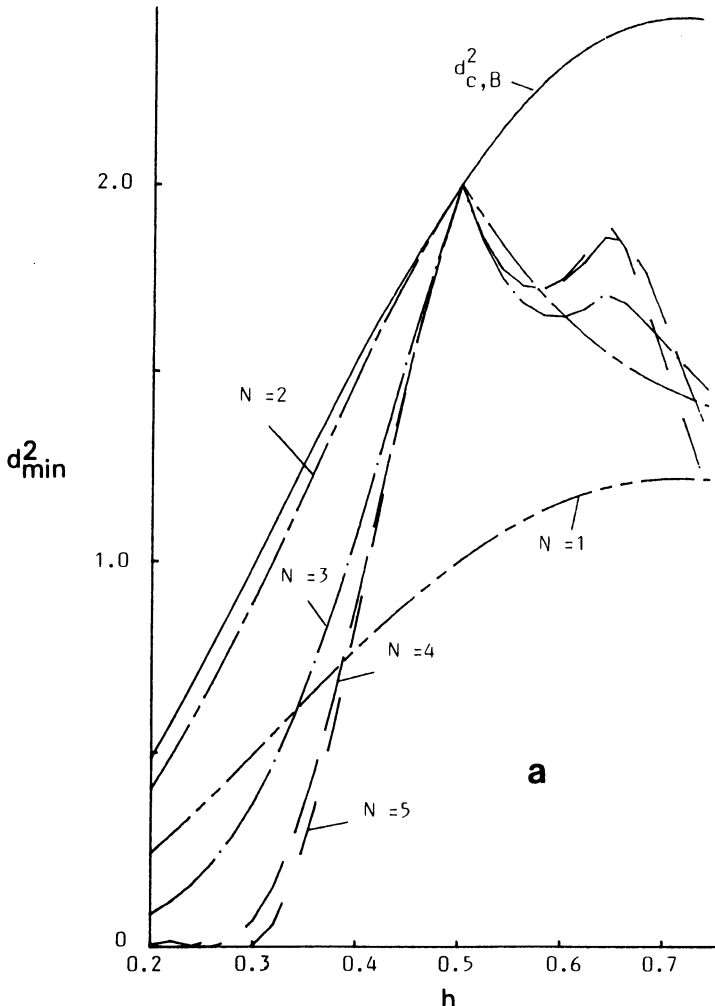


Figure 8.33(a). Minimum Euclidean distance for a binary 1REC AMF receiver with  $N_A = 1$  as a function of  $h$  and  $N_F$ .  $N = N_F$ .

where  $\alpha'_0 = \alpha_0$ . The decision variables  $\tilde{l}_j$  giving a wrong decision are given by

$$\tilde{l}_j = \int_0^{N_F T} r(t) \bar{s}(t, \mathbf{A}_{-1}, \tilde{\mathbf{A}}_0) dt, \quad j = 1, 2, \dots, (M - 1)M^{(N_A - 1)}$$

where  $\tilde{\alpha}_0 \neq \alpha_0$ . The receiver compares  $\max l'_j$  and  $\max \tilde{l}_j$ , and an error is made if  $\max_j \tilde{l}_j$  is greater than  $\max_j l'_j$ . Thus the symbol error probability

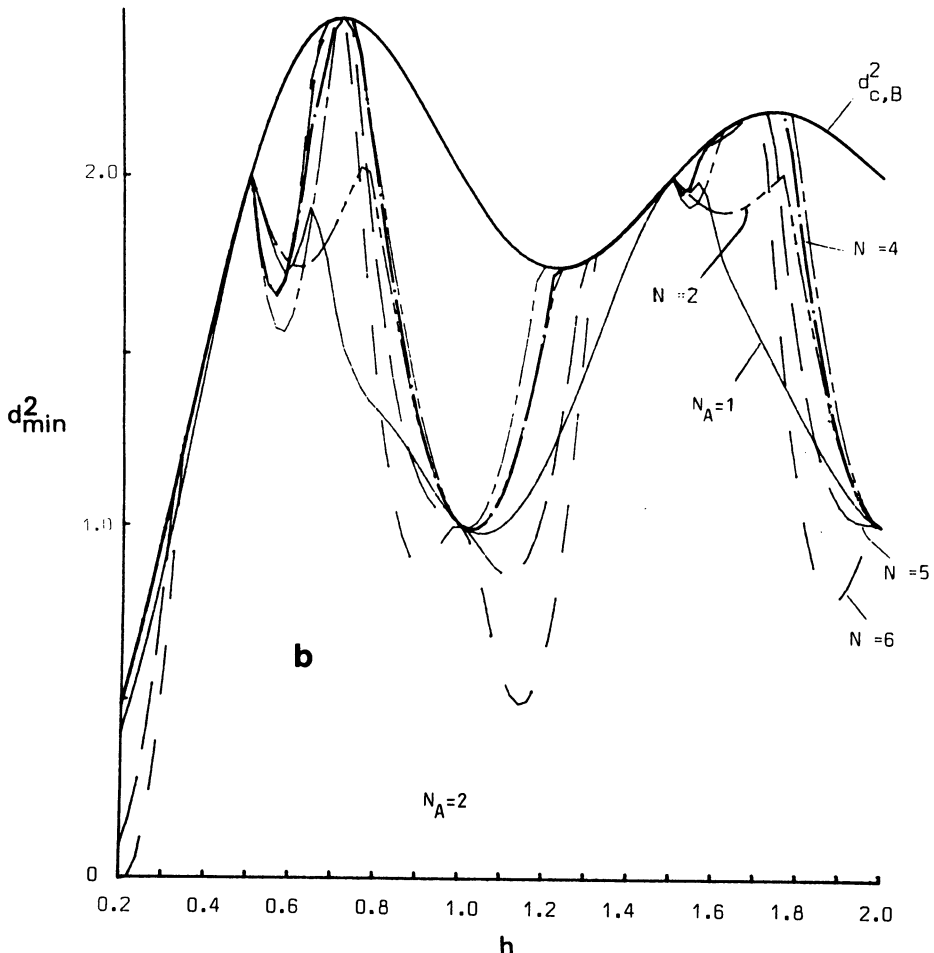


Figure 8.33(b). Minimum Euclidean distance for a binary 1REC AMF receiver with  $N_A = 2$  as a function of  $h$  and  $N_F$ . The upper bound  $d_{c,B}^2$  for the optimum receiver, and maximum on  $d_{\min}^2$  for the AMF receivers with smaller  $N_A$  values are shown as comparison.  $N = N_F$ .

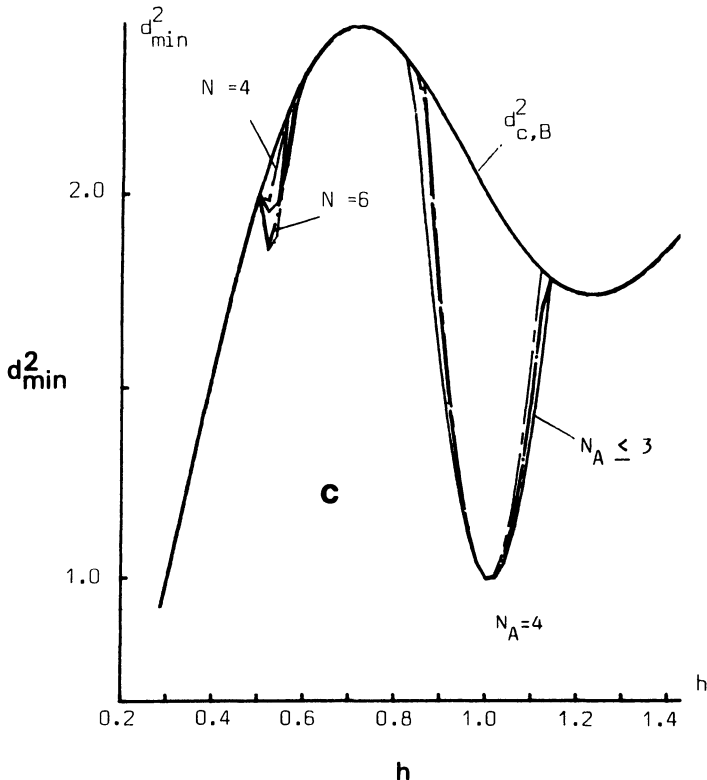


Figure 8.33(c). Minimum Euclidean distance for a binary 1REC AMF receiver with  $N_A = 4$  as a function of  $h$  and  $N_F$ . The upper bound  $d_{c,B}^2$  for the optimum receiver, and maximum on  $d_{\min}^2$  for the AMF receivers with smaller  $N_A$  values are shown as comparison.  $N = N_F$ .

when  $\alpha_{N_F-1}$  is transmitted is given by

$$P[\varepsilon | \alpha_{N_F-1}] = \Pr \{ \max_j l'_j < \max_j \tilde{l}_j \}$$

This symbol error probability is difficult to calculate but can be upper bounded by comparing  $l_1$ , the decision variable from the filter  $h(t, \mathbf{A}_{-1}, \mathbf{A}_0)$ , with  $\max_j \tilde{l}_j$ .  $l_1$  is not greater than  $\max_j l'_j$  because  $l_1$  is equal to  $l'_j$  for one value of  $j$ . Thus

$$P[\varepsilon | \alpha_{N_F-1}] \leq \Pr \{ l_1 < \max_j \tilde{l}_j \} \leq \sum_j \Pr \{ l_1 < \tilde{l}_j \} = \sum_j \Pr \{ l_1 - \tilde{l}_j < 0 \} \quad (8.41)$$

where the union bound technique has been used. Now define  $\lambda_j = l_1 - \tilde{l}_j$ ;

$\lambda_j$  is given by

$$\lambda_j = \int_0^{N_F T} r(t) [\bar{s}(t, \mathbf{A}_{-1}, \mathbf{A}_0) - \bar{s}(t, \mathbf{A}_{-1}, \tilde{\mathbf{A}}_0)] dt$$

The probability that  $\tilde{l}_j$  is greater than  $l_1$ , conditioned on  $\alpha_{N_F-1}$ , is

$$\Pr \{ \tilde{l}_j > l_1 \} = \Pr \{ \lambda_j < 0 \} = Q \left( \left( \frac{\bar{\lambda}_j^2}{\sigma^2} \right)^{1/2} \right)$$

where  $\sigma^2$  is the variance of the gaussian variate  $\lambda_j$ . The mean of  $\lambda_j$ , conditioned on  $\alpha_{N_F-1}$ , is  $\bar{\lambda}_j = \mathbb{E}\{\lambda_j | \alpha_{N_F-1}\}$ , and  $\sigma^2$  is independent of any

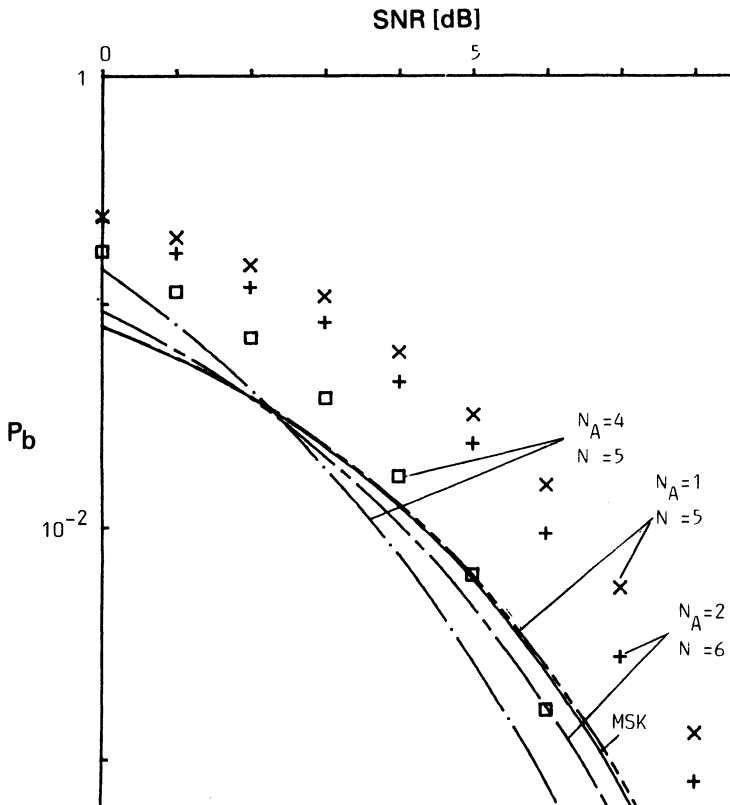


Figure 8.34. Simulated and calculated error probabilities for 1REC with  $h = 0.6$ . The receivers are given above. The calculated results for  $N_A \geq 2$  are upper bounds.  $N = N_F$ .

particular transmitted  $\alpha_{N_F-1}$ .  $\sigma^2$  can be written in the form

$$d_j^2 = \frac{\bar{\lambda}_j^2 N_0}{\sigma^2 E_b}$$

if we define  $d_j^2$  to be

$$d_j^2 = \frac{2}{T} (\log_2 M)$$

$$\frac{\left\{ \int_0^{N_F T} [[\mathcal{A}(t, \mathbf{A}_{-1}, \mathbf{A}_0) - \mathcal{A}(t, \mathbf{A}_{-1}, \tilde{\mathbf{A}}_0)] \cos \phi(t, \mathbf{A}_{-1}, \mathbf{A}_0, \mathbf{A}_1) + [\mathcal{B}(t, \mathbf{A}_{-1}, \mathbf{A}_0) - \mathcal{B}(t, \mathbf{A}_{-1}, \tilde{\mathbf{A}}_0)] \sin \phi(t, \mathbf{A}_{-1}, \mathbf{A}_0, \mathbf{A}_1)] dt \right\}^2}{\int_0^{N_F T} \{[\mathcal{A}(t, \mathbf{A}_{-1}, \mathbf{A}_0) - \mathcal{A}(t, \mathbf{A}_{-1}, \tilde{\mathbf{A}}_0)]^2 + [\mathcal{B}(t, \mathbf{A}_{-1}, \mathbf{A}_0) - \mathcal{B}(t, \mathbf{A}_{-1}, \tilde{\mathbf{A}}_0)]^2\} dt} \quad (8.42)$$

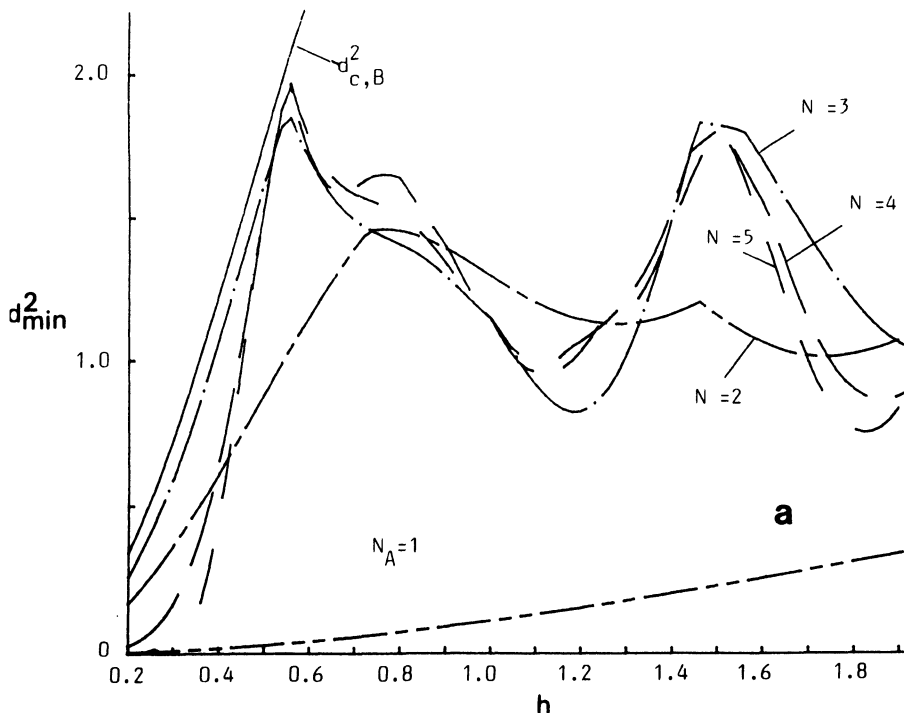


Figure 8.35(a). Minimum Euclidean distance for a binary 3RC AMF receiver with  $N_A = 1$  as a function of  $h$  and  $N_F$ .  $N = N_F$ .

As was the case in Section 8.3, this  $d$  is not a distance in signal space, but it acts like one in the symbol error probability expression at high SNR. We will call  $d$  a normalized Euclidean distance.

As usual, the least of the  $d_j$  dominates the error calculation at high SNR, so we will define the normalized minimum distance

$$d_{\min}^2 = \min_{\substack{\mathbf{A}_{-1}, \mathbf{A}_0, \mathbf{A}_1, \tilde{\mathbf{A}}_0 \\ \alpha_0 \neq \tilde{\alpha}_0}} (d_j^2) \quad (8.43)$$

Unfortunately, a careful study shows that (8.43) in fact gives a lower bound on the minimum distance. In many cases, however, especially when the filters are short,  $\max_j l'_j$  is given by  $l_1$  for large signal-to-noise ratios, i.e.,  $E\{l_1\} = \max_j E\{l'_j\}$ , and thus the minimum distance is exact. There is only

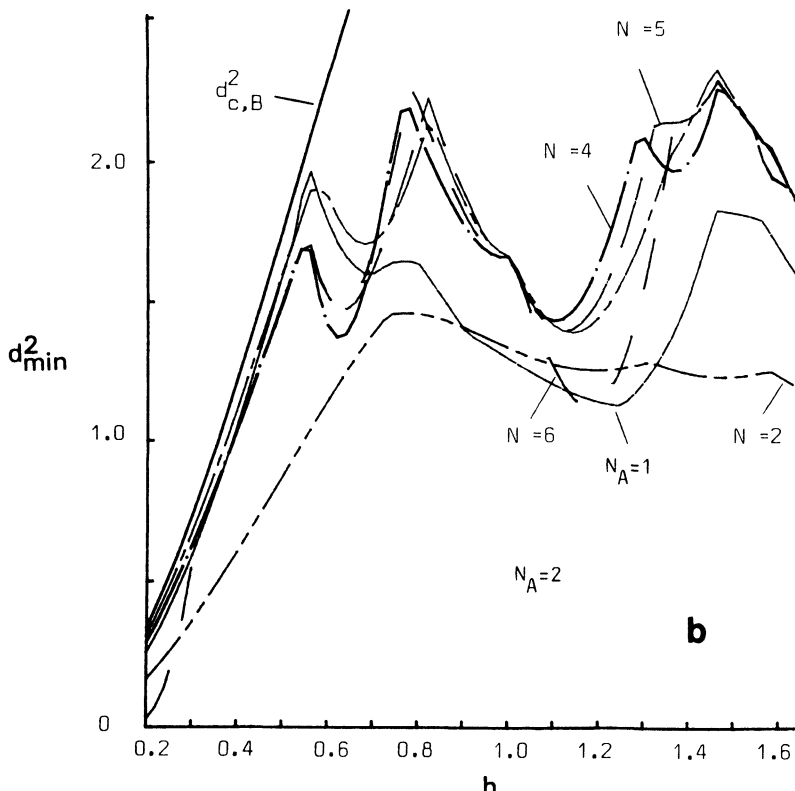


Figure 8.35(b). Minimum Euclidean distance for a binary 3RC AMF receiver with  $N_A = 2$  as a function of  $h$  and  $N_F$ . The upper bound for the optimum receiver and maximum on  $d_{\min}^2$  for the AMF receiver with  $N_A = 1$  are shown as comparison.  $N = N_F$ .

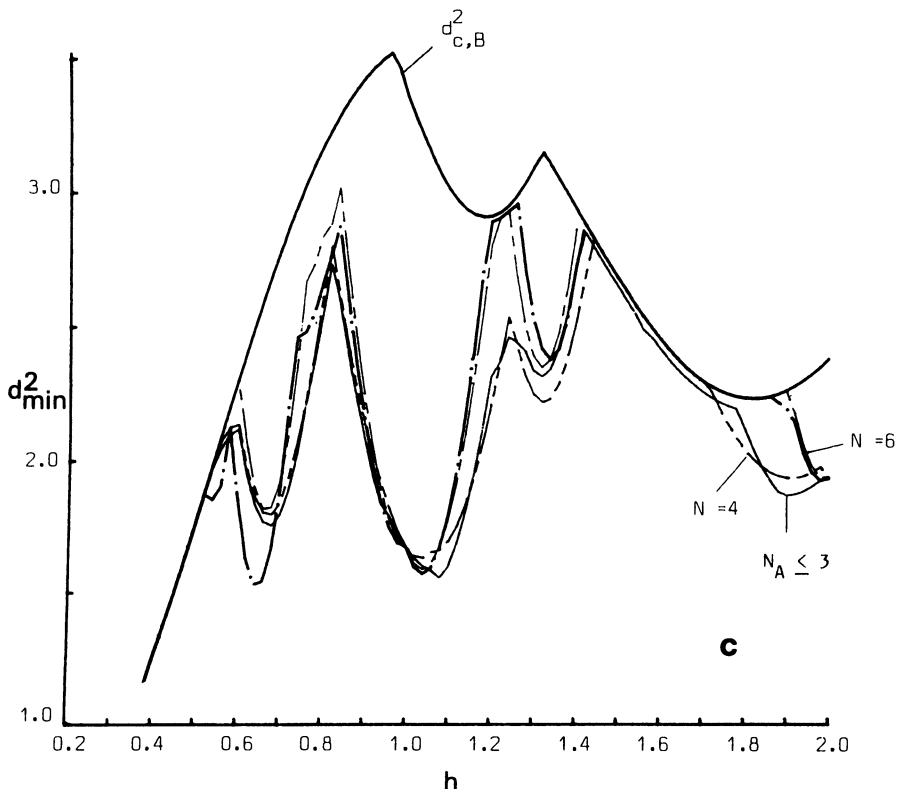


Figure 8.35(c). Minimum Euclidean distance for a binary 3RC AMF receiver with  $N_A = 4$  as a function of  $h$  and  $N_F$ . The upper bound for the optimum receiver and maximum on  $d_{\min}^2$  for the AMF receivers with  $N_A \leq 3$  are shown as comparison.  $N = N_F$ .

one variable giving a correct decision when  $N_A = 1$  and thus the distance is exact in these cases.

Thus it is seen that a distance has to be calculated for every possible transmitted sequence and prehistory. For one specific transmitted sequence the pairwise distance has to be calculated between the correct decision variable and all the variables giving an incorrect decision, given that the correct set of filters have been selected. Fortunately some distances are equal and therefore not all of them have to be calculated, as shown in the next section.

The symbol error probability for a specific transmitted sequence is upper bounded by (8.41). The symbol error probability is then obtained as a function of  $E_b/N_0$  by averaging over all possible transmitted waveforms,

to get

$$P_e = \frac{1}{m_1} \sum_{\alpha_{N_F-1}} P\{\epsilon | \alpha_{N_F-1}\} \leq \frac{1}{m_1} \sum_{\alpha_{N_F-1}} \sum_j Q\left(\left(d_j^2 \frac{E_b}{N_0}\right)^{1/2}\right) \quad (8.44)$$

where the total number of  $\alpha_{N_F-1}$  is  $m_1 = M^{(N_F+L-1)}$ .  $d_j^2$  ranges over all distances corresponding to an erroneous decision, when  $\alpha_{N_F-1}$  has been transmitted. For a binary AMF receiver with  $N_A = 1$  there is only one decision variable corresponding to every  $\alpha_{N_F-1}$  giving a wrong decision, and thus the expression for  $P_e$  holds with equality in this case.<sup>(37)</sup>

#### 8.4.3. Properties of the Distance and the Uniformly Weighted AMF

In this section some properties of the Euclidean distance are derived. It was mentioned in Section 8.4.2 that quite a large number of distances in principle have to be calculated, to get the minimum distance  $d_{\min}^2$ . Fortunately, some symmetries exist so that not all have to be calculated.

The Euclidean distance for the multiple-symbol AMF receiver is independent of the prehistory  $A_{-1}$ , and this means that only one set of filters has to be considered when  $d_{\min}^2$  and the upper bound on the error-probability are calculated. To show this, we assume a sequence  $\alpha_{N_F-1} = A_{-1}, A_0, A_1$  is transmitted and calculate the distance  $d_j^2$  between the output of the filter  $h(t, A_{-1}, A_0)$  giving the correct decision and the filter  $h(t, A_{-1}, \tilde{A}_0)$  giving a wrong decision, i.e.,  $A_0$  and  $\tilde{A}_0$  are chosen so that  $\alpha_0 \neq \tilde{\alpha}_0$  ( $\theta$  is assumed to be zero just as in Section 8.4.2). The phase function can be divided into two terms

$$\phi(t, \alpha_{N_F-1}) = 2\pi h \sum_{i=-\infty}^{-1} \alpha_i q(t - iT) + 2\pi h \sum_{i=0}^{N_F-1} \alpha_i q(t - iT)$$

where all information about the prehistory is contained in the first term. By using this in (8.42) it is easily verified that the distance is independent of the first term and thus of  $A_{-1}$ .

The distance also has a sign symmetry, so that the transmitted sequence  $\alpha$  gives the same set of distances as the sequence  $-\alpha$ . From (8.42) it is seen that changing  $A_0$  for  $-A_0$  and  $A_1$  for  $-A_1$  give the same expressions if  $\tilde{A}_0$  is changed to  $-\tilde{A}_0$ . Since  $\alpha_0 \neq \tilde{\alpha}_0$ , also  $-\alpha_0 \neq -\tilde{\alpha}_0$ ; thus half of the distances required are given. With these symmetries we have reduced the number of calculations by a factor  $2M^{(L-1)}$ , if  $L$  is the duration in symbol intervals of the frequency response.

The AMF filters are time limited if  $h = \frac{1}{2}(2n - 1)$ , where  $n$  is an integer. To show this, the fact that  $q(t) \equiv 0$ ,  $t \leq 0$  and  $q(t) = \frac{1}{2}$ ,  $t \geq LT$  will be used.

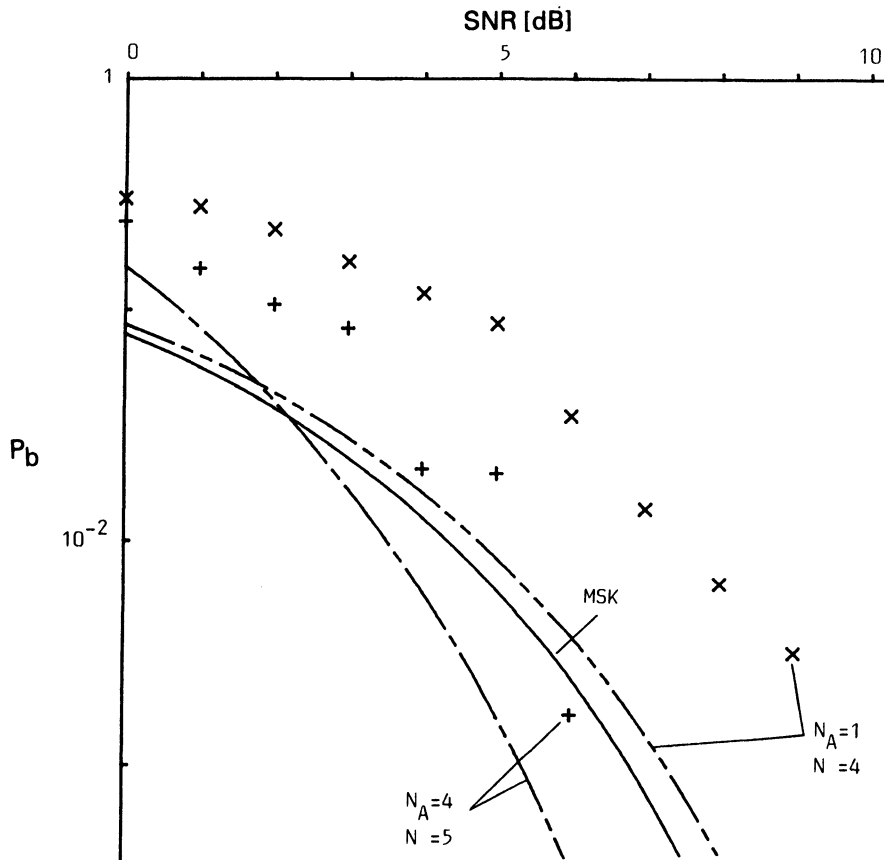


Figure 8.36. Simulated and calculated error probabilities for 3RC with  $h = 0.8$ . The receivers are given above. The calculated result for  $N_A = 4$  is an upper bound.  $N = N_F$ .

From the previous sections it is known that if  $\mathcal{A}(t, \mathbf{A}_{-1}, \mathbf{A}_0)$  and  $\mathcal{B}(t, \mathbf{A}_{-1}, \mathbf{A}_0)$  are time limited, then  $\bar{s}(t, \mathbf{A}_{-1}, \mathbf{A}_0)$  is time limited.  $\mathcal{A}(t, \mathbf{A}_{-1}, \mathbf{A}_0)$  and  $\mathcal{B}(t, \mathbf{A}_{-1}, \mathbf{A}_0)$  are given in (8.40); from Chapter 3 it is seen that the transmitted phase can be written ( $\theta = 0$ )

$$\phi(t, \alpha_{N_F-1}) = 2\pi h \left[ \sum_{i=-\infty}^{N_A-1} \alpha_i q(t - iT) + \sum_{i=N_A}^{N_F-1} \alpha_i q(t - iT) \right]$$

Thus

$$\mathcal{A}(t, \mathbf{A}_{-1}, \mathbf{A}_0)$$

$$= \cos \left[ 2\pi h \sum_{i=-\infty}^{N_A-1} \alpha_i q(t - iT) \right] \frac{1}{m} \sum_{k=0}^{m-1} \cos \left[ 2\pi h \sum_{i=N_A}^{N_F-1} \alpha_{i,k} q(t - iT) \right]$$

$$- \sin \left[ 2\pi h \sum_{i=-\infty}^{N_A-1} \alpha_i q(t - iT) \right] \frac{1}{m} \sum_{k=0}^{m-1} \sin \left[ 2\pi h \sum_{i=N_A}^{N_F-1} \alpha_{i,k} q(t - iT) \right]$$

where  $m = M^{(N_F - N_A)}$ . The second term is zero for  $t \geq N_A T$  because to every sequence  $(\alpha_{N_A}, \alpha_{N_A+1}, \dots, \alpha_{N_F-1})$  giving a phase  $\phi_1(t)$ , there is always a sequence  $(-\alpha_{N_A}, -\alpha_{N_A+1}, \dots, -\alpha_{N_F-1})$  giving the phase  $-\phi_1(t)$ . Since  $\sin \phi(t) + \sin [-\phi_1(t)] = 0$  the sum in the second term is zero. The first term is zero if  $h = \frac{1}{2}(2n - 1)$ ,  $n$  an integer, and  $t \geq (L + N_A)T$ , because to every sequence  $(\alpha_{N_A}, \alpha_{N_A+1}, \dots, \alpha_{N_F-1})$  giving a phase  $\phi_1(t)$ , there is always

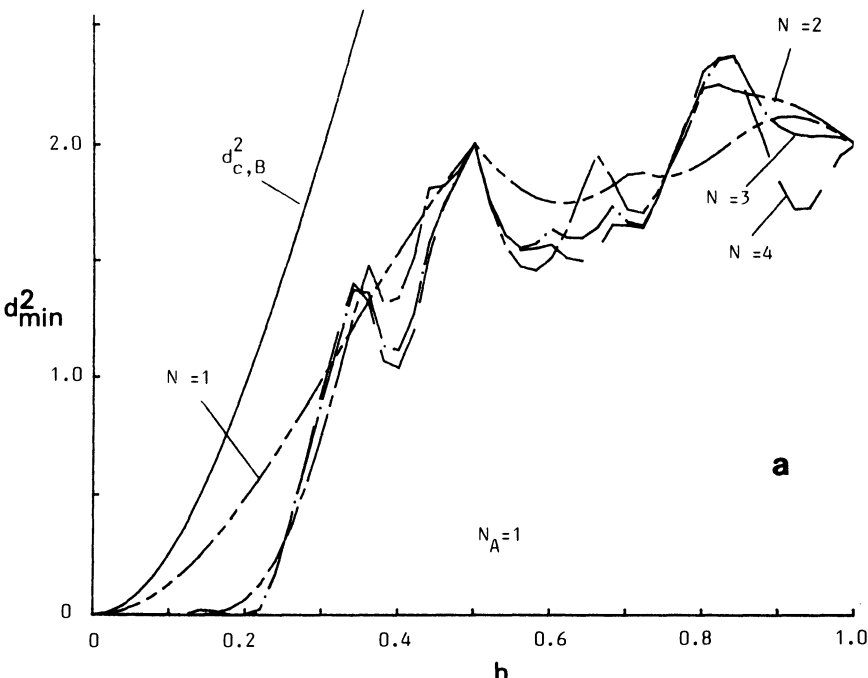


Figure 8.37(a). Minimum Euclidean distance for a quaternary 1REC AMF receiver with  $N_A = 1$  as a function of  $h$  and  $N_F$ .  $N = N_F$ .

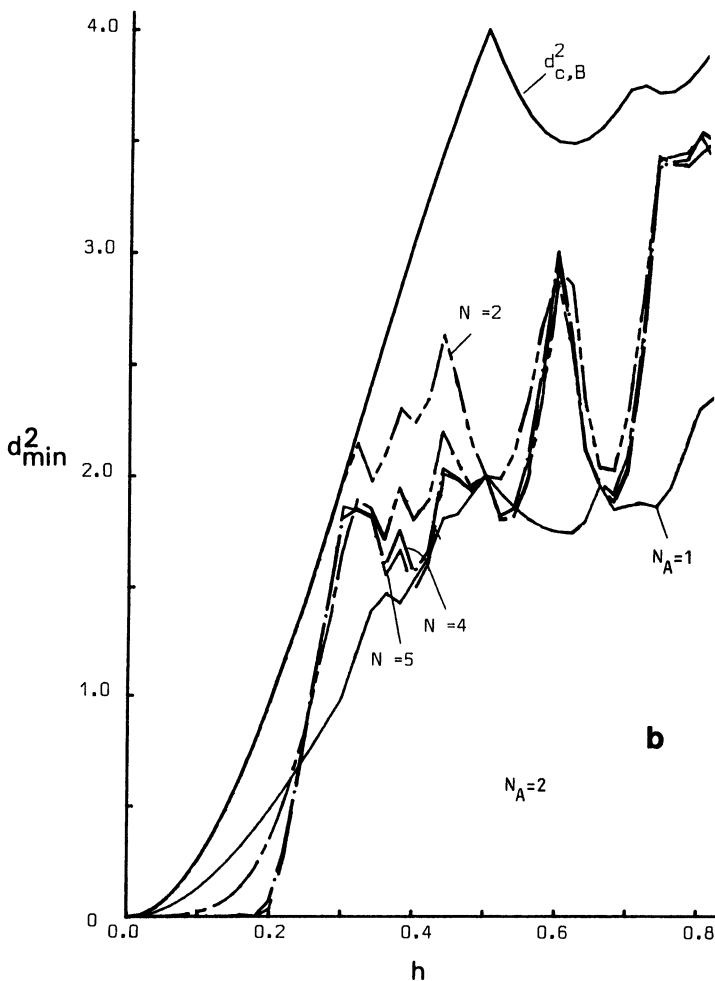


Figure 8.37(b). Minimum Euclidean distance for a quaternary 1REC AMF receiver with  $N_A = 2$  as a function of  $h$  and  $N_F$ . The upper bound for the optimum receiver and maximum on  $d_{\min}^2$  for the AMF receiver with  $N_A = 1$  are shown as comparison.  $N = N_F$ .

a sequence  $(\alpha_{N_A}, -\alpha_{N_A+1}, \dots, -\alpha_{N_F-1})$  giving a phase  $\phi_2(t)$ ; then  $\phi_1(t)$  and  $\phi_2(t)$  are symmetric around  $(\pi/2)(2n-1)$ , for  $t \geq (L + N_A)T$ , and  $\cos \phi_1(t) + \cos \phi_2(t) = 0$ ,  $t \geq (L + N_A)T$ . The proof for  $\mathcal{B}(t, \mathbf{A}_{-1}, \mathbf{A}_0)$  is analogous. This means that even weighted AMF filters have a maximum length of  $L + N_A$  symbol intervals when  $h = \frac{1}{2}(2n-1)$ , and in particular when  $h = \frac{1}{2}$ . This is not true for weighted AMF filters in general. For further details, see Refs. 37, 38, 40.

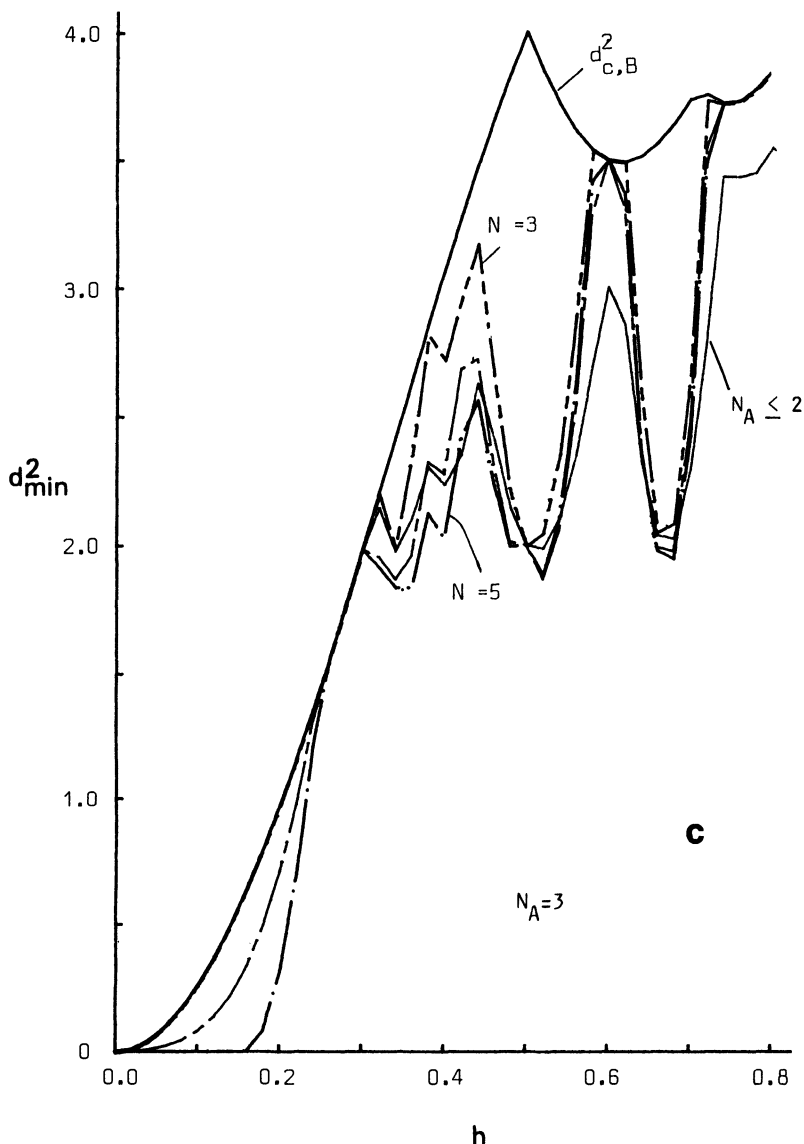


Figure 8.37(c). Minimum Euclidean distance for a quaternary 1REC AMF receiver with  $N_A = 3$  as a function of  $h$  and  $N_F$ . The upper bound for the optimum receiver and maximum on  $d_{\min}^2$  for the AMF receivers with  $N_A \leq 2$  are shown as comparison.  $N = N_F$ .

#### 8.4.4. Numerical Results

We will present Euclidean distances for binary, quaternary, and octal schemes. All distances are normalized by the energy per bit  $E_b$ . The results are given in plots of  $d_{\min}^2$  versus modulation index  $h$ . The upper bound on the Euclidean distance for the optimum receiver (see Chapter 3) is shown in some plots for comparison. The maximum on  $d_{\min}^2$  for AMF receivers with smaller  $N_A$  values and given observation lengths is also shown for comparison.

For some selected modulation indices the error probability is given. These error probabilities are exact for binary schemes with  $N_A = 1$ ; otherwise they are upper bounds. Simulated error probabilities are also shown. The updating in the simulated receiver is very simple:  $A_{-1}$  is estimated from the previous  $L - 1$  decisions and  $\theta$  is estimated from all the other previous

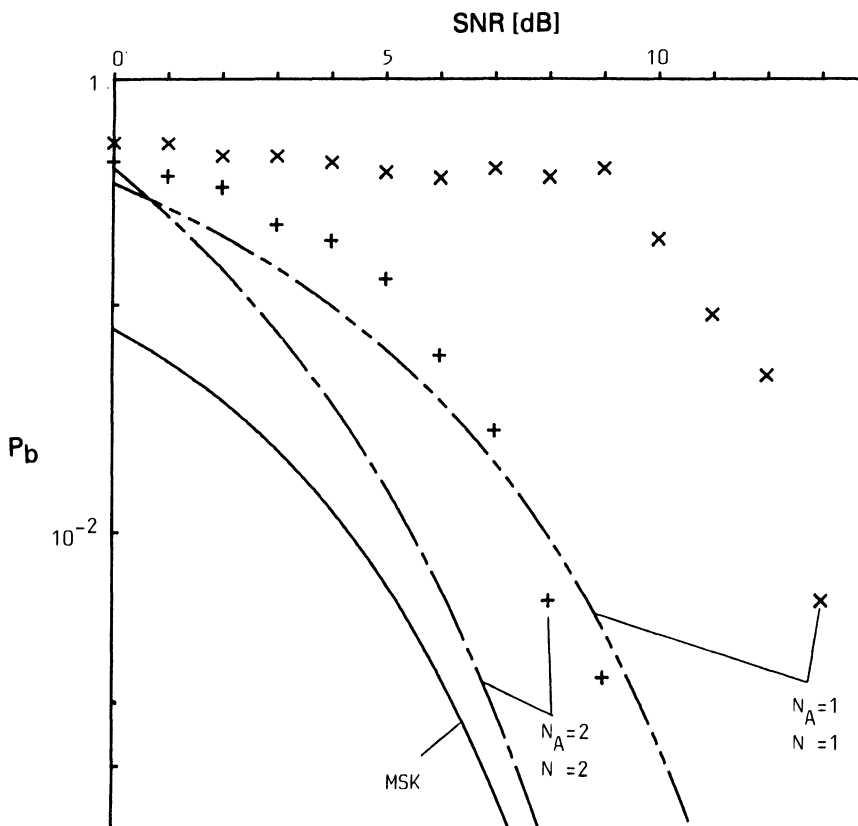


Figure 8.38. Simulated error probability and calculated upper bound for quaternary 1REC with  $h = 0.3$ . The receivers are given above.  $N = N_F$ .

decisions. This is the only method considered, although others might improve the performance.

The normalized squared Euclidean distance for AMF receivers for binary 1REC is shown in Figure 8.33, for various  $N_A$  and  $N_F$  values. The upper bound for the optimum receiver, and maximum on  $d_{\min}^2$  for AMF receivers with smaller  $N_A$ , are shown as comparison. The distance for the AMF receiver with  $N_A = 1$  does not reach the upper bound for the optimum receiver except for  $h = 1/2$ . The AMF receiver with  $N_A = 2$  has a distance that reaches the upper bound in several regions of  $h$ . Note that the distance for an AMF receiver with  $N_A = N_F$  is equal to the distance for the optimum receiver with observation length  $N_F = N$ . When  $N_A = 2$  the performance is bad in some regions, and this performance can be improved by choosing  $N_A = 4$ . A peculiarity of Figure 8.33 is that distance does not always grow with observation length.

Figure 8.34 shows error probabilities and simulations for the receivers when  $h = 0.6$ . The simulated results differ from the calculated ones owing to the updating of phase and prehistory. From simulations it has been noted that the loss compared to the bounds is larger for  $h = 0.6$  than for many other  $h$  values.

Figure 8.35 depicts the situation for 3RC, a scheme with a longer, smoother pulse.  $N_A = 3$  is needed to reach the upper bound of the optimum

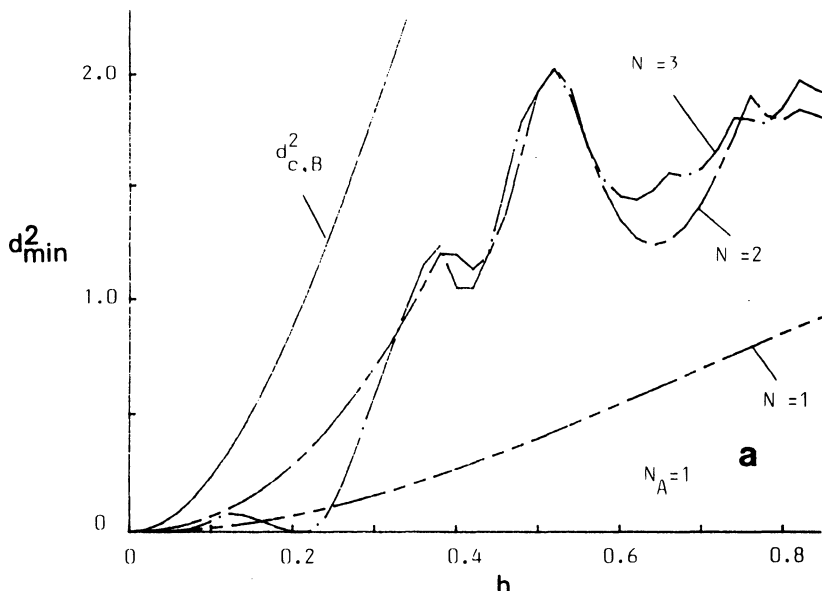


Figure 8.39(a). Minimum Euclidean distance for a quaternary 2RC AMF receiver with  $N_A = 1$  as a function of  $h$  and  $N_F$ .  $N = N_F$ .

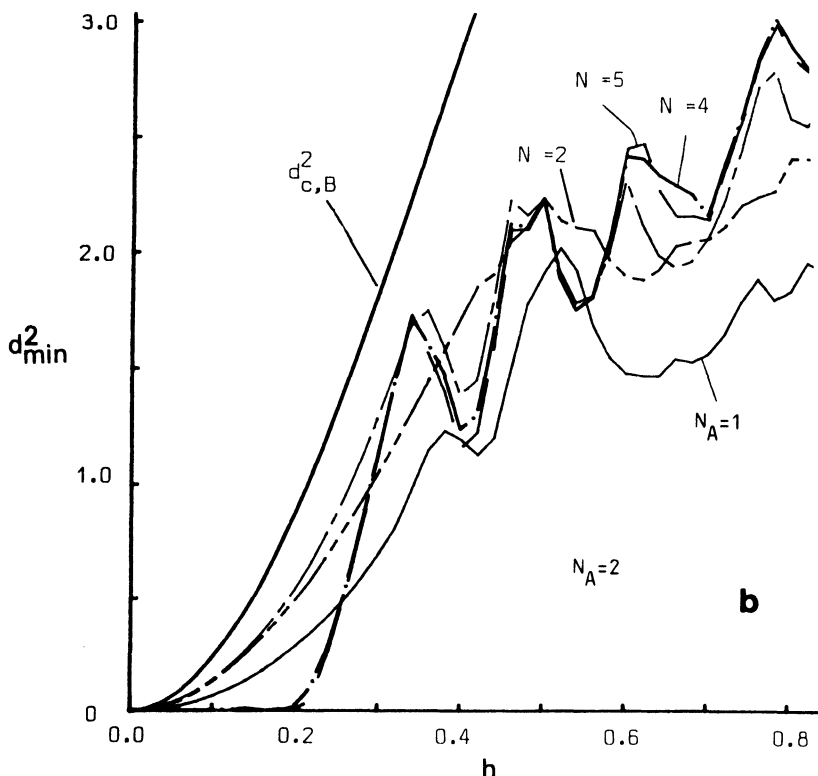


Figure 8.39(b). Minimum Euclidean distance for a quaternary 2RC AMF receiver with  $N_A = 2$  as a function of  $h$  and  $N_F$ . The upper bound for the optimum receiver and maximum on  $d_{\min}^2$  for the AMF receiver with  $N_A = 1$  are shown for comparison.  $N = N_F$ .

receiver. This figure shows the distance for AMF receivers with  $N_A = 1, 2$ , and 4. For modulation indices larger than 0.5,  $N_A = 3$  is needed to give a good distance, and in some regions an even larger  $N_A$  is needed. Figure 8.36 shows calculated and simulated error probabilities for  $h = 0.8$ . It has been reported from simulations for other  $h$  values that the simulated error probabilities sometimes are very large because of updating. If the receiver makes an error, the wrong filters are used for the next decision and this causes the receiver to lose track for a long period. Apparently the updating algorithm of phase and prehistory used in this simulation sometimes does not work well for schemes based on longer pulses.

Figure 8.37 shows the distance for AMF receivers for quaternary 1REC.  $N_A = 2$  is needed to reach the upper bound and for most regions of  $h$ ,  $N_F = N_A$  gives the best performance. Figure 8.38 shows calculated and simulated error probabilities for  $h = 0.3$ . The loss due to the updating of phase is quite large, around 2 dB for  $N_A = 2$ . Figure 8.39 gives the same

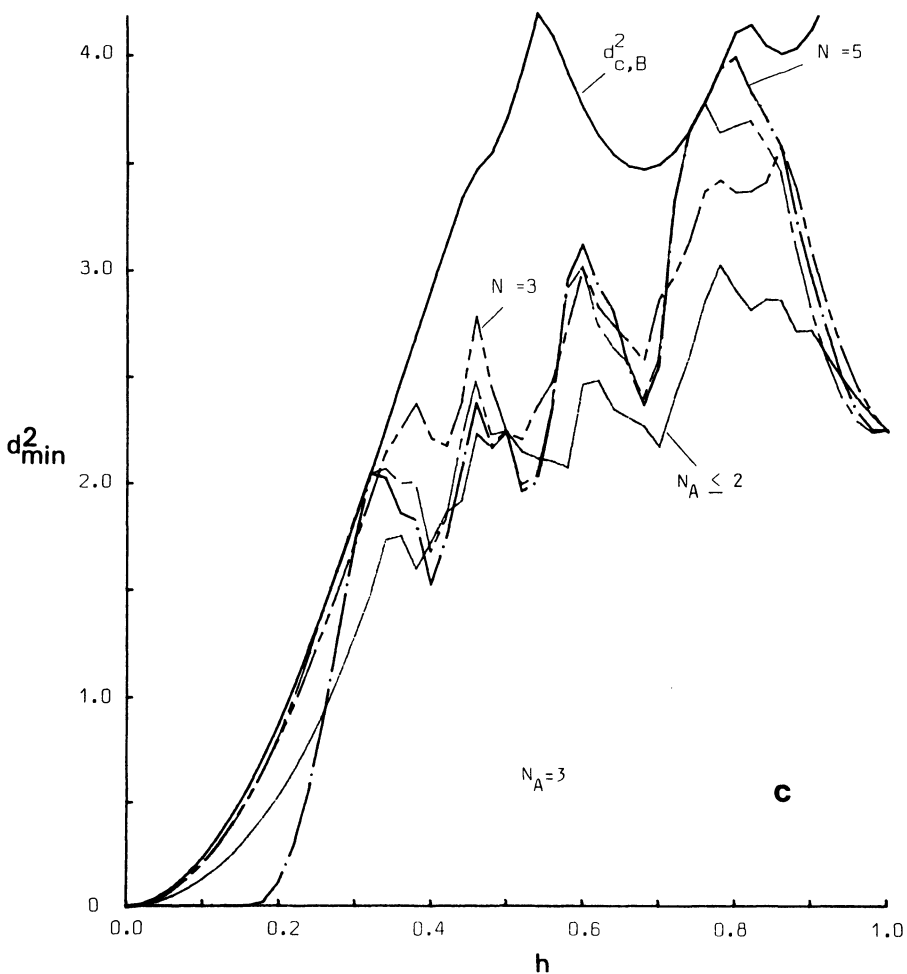


Figure 8.39(c). Minimum Euclidean distance for a quaternary 2RC AMF receiver with  $N_A = 3$  as a function of  $h$  and  $N_F$ . The upper bound for the optimum receiver and maximum on  $d_{\min}^2$  for the AMF receiver with  $N_A \leq 2$  are shown for comparison.

results for quaternary 2RC. For low  $h$  values  $N_F = N_A + 1$  gives the best performance while the  $N_F$  value giving best performance varies for larger  $h$  values.  $N_A$  equal to 3 is needed to reach the bound. Figure 8.40 shows error probabilities for  $h = 0.3$ ; the data are not as reliable as before.

#### 8.4.5. Summary

The degradation in minimum Euclidean distance for some suboptimum multiple symbol AMF receivers compared to the optimum Viterbi receiver

are shown in Figure 8.41, for the binary  $h = 0.5$  case. The minimum Euclidean distance is given for the RC family as a function of the frequency pulse duration  $L$ . The minimum Euclidean distance for the weighted AMF receivers with  $N_A = 1$ , considered in Ref. 39, are also shown, and comparisons are made with the simpler MSK-type receivers (offset quadrature receivers) of Sections 8.2 and 8.3. For high SNRs the different AMF receivers perform mainly in between the optimum Viterbi receiver and the offset quadrature receiver. It appears that the AMF receiver should not be used for  $h = 0.5$  schemes. In this case the MSK-type receiver is very simple and has a performance which is better than an AMF receiver with  $N_A = 1$ . It is also clear that the minimum Euclidean distance is increased by matching filters to sequences of symbols in the AMF receiver. This of course increases the number of filters, but some of these filters may be equal.

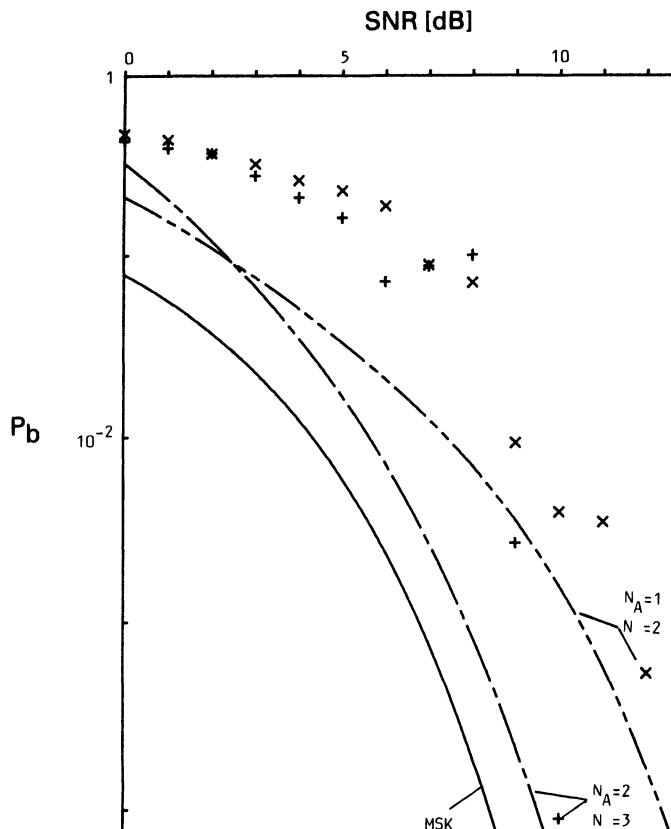


Figure 8.40. Simulated error probability and calculated upper bound for quaternary 2RC with  $h = 0.3$ . The receivers are given above.  $N = N_F$ .

The AMF receiver concept with decision feedback updating of the prehistory and phase based on previous decisions gives good asymptotic-SNR performance for short pulses and for schemes with low  $h$  values. Filter impulse response length is an important parameter when the distance is to be optimized. The distance decreases with the filter length for some modulation indices. For the more complex schemes the AMF receiver has a tendency to lose track, which causes an unacceptable performance. For the quaternary schemes the performance is acceptable only for the 1REC schemes.

The complexity of some AMF receivers is of the same order as the complexity of the reduced-complexity Viterbi receiver of Section 8.1. Of course this comparison depends on the modulation index; if  $h$  is chosen such that the number of phase states in the Viterbi receiver is large, the complexity of this receiver is artificially large. It is difficult to compare

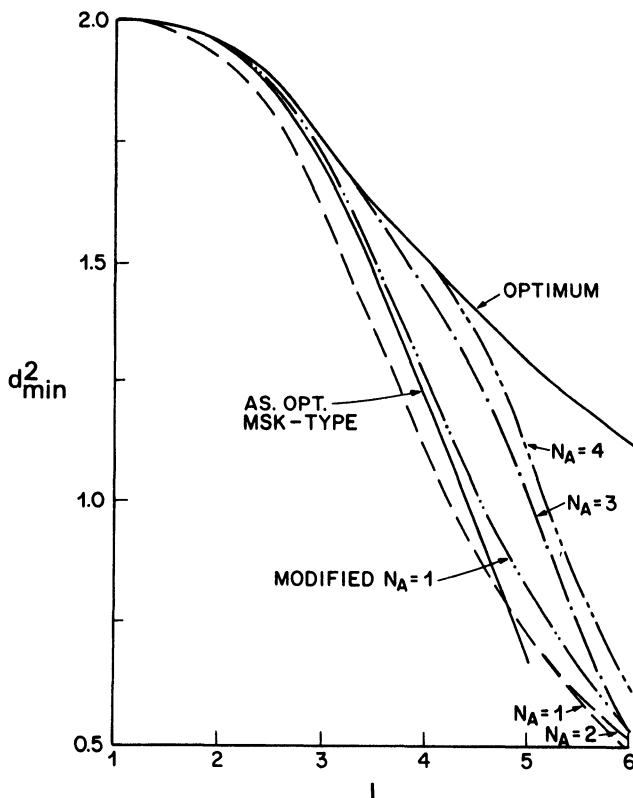


Figure 8.41. Minimum Euclidean distance versus the frequency pulse duration  $L$ , for the binary RC family, with AMF receivers with  $N_A$  fixed symbols. The minimum distance for the optimal receiver and the offset quadrature type of receivers considered in Refs. 9-11 are also shown as comparison. The modulation index is  $h = 1/2$ .

complexity accurately, because it depends on the implementation of the receivers. The AMF receiver clearly has less processing. The metric calculations and comparisons in the Viterbi receiver are time consuming, while the filtering in the AMF receiver can be done parallel and much faster, even if the number of filter is large. Surface acoustic wave implementations can make particular use of these features.<sup>(45,46,47)</sup>

The complexity of the AMF receiver might be reduced using the same idea as for the reduced-complexity Viterbi receiver: An AMF receiver for a less complex scheme is used for the more complex schemes. This idea has not been examined for AMF receivers but the relative degradation should be about the same as for the reduced-complexity Viterbi receivers.<sup>(8)</sup> The idea of reducing the complexity also reduces the problem of updating prehistory, since this works better for short pulses.

Simulations indicate that the simple phase and prehistory updating considered here does not work well if  $L$  greater than 2. One idea to improve the updating could be to use a Viterbi detector for updating the phase.

## 8.5. Limited Trellis Search Receivers

In Section 8.1 we explored how to simplify a receiver by reducing the complexity of the receive state trellis. This was called a reduced-complexity Viterbi detector; the receiver executed a complete Viterbi algorithm search of a reduced state trellis. Another approach is to retain the full state trellis, but scrutinize only certain parts of it, ignoring the rest. We will call this kind of receiver a *limited search* receiver.

The Viterbi algorithm scrutinizes every node in a state trellis. This means that a matched filter (or correlator) operation must be performed for each signal possibility in the  $n$ th interval, and the results of these correlations must be compared among themselves to find the maximum likelihood trellis path into each state at time  $n + 1$ . A limited search receiver performs only a small subset of these matched filterings and comparisons, choosing which ones to perform by some kind of search regime. A number of such regimes have been proposed and we have discussed these in a survey paper.<sup>(52)</sup> Perhaps the best known is the Fano algorithm of sequential decoding. A limited search develops only a few state paths in the trellis and may not execute a maximum likelihood search for the transmitted state path; however, it can be hoped that the path the search finds is virtually optimal.

In Simmons and Wittke<sup>(13)</sup> a limited search is used to decode certain CPFSK schemes. It is claimed that a receiver that pursues only two state trellis paths has the same high-SNR error performance for some (low) modulation indices as the much more complex Viterbi receiver. Note that

a two-path search is only one path more than a single-interval detector, which develops one path. Results that are similarly striking have been reported informally to the authors for more complex CPM schemes. At this writing we can only predict that limited searches will be a fruitful approach for simplifying receivers. It appears that these receivers hold far more promise than their performance with, for instance, convolutional codes, would indicate.

## References

1. A. Svensson and C-E. Sundberg, "Optimized Reduced-Complexity Viterbi Detectors for CPM," GLOBECOM'83, San Diego, California, November 1983, Conference Record, pp. 22.1.1-22.1.8.
2. A. Svensson, C-E. Sundberg, and T. Aulin, "A Class of Reduced Complexity Viterbi Detectors for Partial Response Continuous Phase Modulation," *IEEE Transactions on Communications* COM-32(10), 1079-1087 (1984).
3. A. Svensson, C-E. Sundberg, and T. Aulin, "A Distance Measure for Simplified Receivers," *Electronics Letters* 19(23), 953-954 (1983).
4. T. Aulin, C-E. Sundberg, and A. Svensson, "Viterbi Detectors with Reduced Complexity for Partial Response Continuous Phase Modulation," National Telecommunications Conference, NTC'81, New Orleans, 1981, Conference Record, pp. A7.6.1-A7.6.7.
5. T. Aulin and C-E. Sundberg, "Continuous Phase Modulation—Part I: Full Response Signaling," *IEEE Transactions on Communications* COM-29(3), 196-209 (1981).
6. T. Aulin, N. Rydbeck, and C-E. Sundberg, "Continuous Phase Modulation—Part II: Partial Response Signaling," *IEEE Transactions on Communications* COM-29(3), 210-225 (1981).
7. T. Aulin, "Three Papers on Continuous Phase Modulation (CPM)," Dr. Techn. Thesis, University of Lund, November 1979.
8. T. Aulin, N. Rydbeck, and C-E. Sundberg, "Transmitter and Receiver Structures for M-ary Partial Response FM," 1980 International Zürich Seminar on Digital Communications, Conference Record, pp. A.2.1-A.2.6.
9. N. Rydbeck and C-E. Sundberg, "Recent Results on Spectrally Efficient Constant Envelope Digital Modulation Methods," International Conference on Communications, Boston 1979, ICC'79, Conference Record, pp. 42.1.1-42.1.6.
10. F. de Jager and C. B. Dekker, "Tamed Frequency Modulation, A Novel Method to Achieve Spectrum Economy in Digital Transmission," *IEEE Transactions on Communications* COM-26, 534-542 (1978).
11. T. Aulin and C-E. Sundberg, "An Easy Way to Calculate Power Spectrum for Digital FM," *IEE Proceedings, Pt F: Communications, Radar and Signal Processing* 130(6), 519-526 (1983).
12. R. Fletcher and M. J. D. Powell, "A Rapidly Convergent Descent Method for Minimization," *Computer Journal* 6(2), 163-168 (1963).
13. S. J. Simmons and P. H. Wittke, "Low Complexity Decoders for Constant Envelope Digital Modulations," Global Telecommunications Conference, Miami, Florida, November 1982, Conference Record, pp. E7.7.1-E7.7.5.
14. A. Svensson and C-E. Sundberg, "Optimum MSK-Type Receivers for Partial Response CPM on Fading Channels," ICC'84, Amsterdam, The Netherlands, May 1984, Conference Record, pp. 933-936.

15. A. Svensson and C.-E. Sundberg, "Optimum MSK-Type Receivers for CPM on Gaussian and Rayleigh Fading Channels," *IEE Proceedings, Pt F* 131(5), 480-490 (1984).
16. T. Aulin, C-E. Sundberg, and A. Svensson, "MSK-Type Receivers for Partial Response Continuous Phase Modulation," International Conference on Communications, ICC'82, Philadelphia, June 1982, Conference Record, pp. 6F.3.1—6F.3.6.
17. C-E. Sundberg, "Error Probability of Partial Response Continuous Phase Modulation with Coherent MSK-Type Receiver, Diversity and Slow Rayleigh Fading in Gaussian Noise," *The Bell System Technical Journal* 61(8), 1933-1963 (1982).
18. A. Svensson and C-E. Sundberg, "Serial Detection of Partial Response Continuous Phase Modulation," Global Telecommunication Conference, GLOBECOM'83, San Diego, 1983, Conference Record, pp. 44.1.1-44.1.8.
19. P. Galko and S. Pasupathy, "Optimal Linear Receiver Filters for Binary Digital Signals," International Conference on Communications, ICC'82, Philadelphia, June 1982, Conference Record, pp. 1H.6.1-1H.6.5.
20. P. Galko and S. Pasupathy, "Linear Receivers for Generalized MSK," International Conference on Communications, ICC'82, Philadelphia, June 1982, Conference Record, pp. 6F.5.1-6F.5.6.
21. P. Galko, "Generalized MSK," Ph.D. thesis, University of Toronto, Toronto, Canada, August 1982.
22. S. A. Rhodes, "FSQO, A New Modulation Technique that Yields a Constant Envelope," National Telecommunication Conference, NTC'80, Houston, 1980, Conference Record, pp. 51.1.1-51.1.7.
23. K. Murota and K. Hirade, "GMSK Modulation for Digital Mobile Radio Telephony," *IEEE Transactions on Communications* COM-29(7), 1044-1050 (1981).
24. R. de Buda, "Coherent Demodulation of Frequency Shift Keying with Low Deviation Ratio," *IEEE Transactions on Communications* COM-20(3), 429-435 (1972).
25. M. S. El-Tanany, J. S. Wight, and H. M. Hafez, "On Optimization of a Quadrature Coherent Detector for Partial Response Continuous Phase Modulation with Modulation Index 1/2," Global Telecommunication Conference, GLOBECOM'82, Miami, 1982, Conference Record, pp. D7.2.1-D7.2.7.
26. A. Svensson and C-E. Sundberg, "Serial MSK-Type Detection of Partial Response Continuous Phase Modulation," *IEEE Transactions on Communications*, COM-33(1), 44-52 (1985).
27. R. W. Lucky, J. Salz, and E. J. Weldon Jr., *Principles of Data Communication*, McGraw-Hill, New York (1968).
28. F. Amoroso and J. A. Kivett, "Simplified MSK Signaling Technique," *IEEE Transactions on Communications* COM-25(4), 433-441 (1977).
29. J. M. Liebetreu and C. R. Ryan, "Performance Simulation of Receiver Filters for Serial Detection of MSK Signals," Allerton Conference Proc., October 1980, pp. 351-358.
30. R. E. Ziemer, C. R. Ryan, and J. H. Stilwell, "Conversion and Matched Filter Approximations for serial Minimum-Shift Keyed Modulation," *IEEE Transactions on Communications* COM-30(3), 495-509 (1982).
31. C. R. Ryan, A. R. Hambley, and D. E. Vogt, "760 Mbit/s Serial MSK Microwave Modem," *IEEE Transactions on Communications* COM-28(5), 771-777 (1980).
32. R. E. Ziemer and C. R. Ryan, "Near Optimum Delay-Line Detection Filters for Serial Detection of MSK Signals," International Conference on Communications, ICC'81, Denver, June 1981, Conference Record, pp. 56.2.1-56.2.5.
33. C. R. Ryan, "Advances in Serial MSK Modems," National Telecommunication Conference, NTC'81, New Orleans, December 1981, Conference Record, pp. G3.6.1-G3.6.5.
34. F. Amoroso, "Experimental Results on Constant Envelope Signaling with Reduced Spectral Sidelobes," International Conference on Communications, ICC'81, Denver, June 1981, Conference Record, pp. 47.1.1-47.1.5.

35. J. M. Wozencraft and I. M. Jacobs, *Principles of Communication Engineering*, Wiley, New York (1965).
36. T. Aulin and C-E. Sundberg, "Optimum and Sub-Optimum Detectors for Band and Amplitude Limited Continuous Phase Modulation," International Conference on Communications, ICC'83, Boston, 1983, Conference Record, pp. A6.1.1-A6.1.6.
37. A. Svensson, "Receivers for CPM," Techn. Dr. Thesis, University of Lund, Lund, May 1984.
38. A. Svensson and C-E. Sundberg, "Performance of AMF Receivers for CPM," GLOBECOM'84, Atlanta, Georgia, to be presented.
39. T. Aulin, C-E. Sundberg, and A. Svensson, "Modified Average Matched Filter Receivers for Partial Response CPM," Technical Report TR-151, June 1981, Telecommunication Theory, University of Lund. Presented at the International Symposium on Information Theory, Les Arcs, France, June 20-25, 1982. Book of Abstracts, p. 169.
40. A. Svensson and C-E. Sundberg, "Performance of Generalized AMF Receivers for Continuous Phase Modulation," *IEE Proceedings, Part F*, 132(7), 541-547 (1985).
41. A. Svensson and C-E. Sundberg, "Simulations of Coherent Average Matched Filter Receivers for Partial Response CPM," University of Lund, Telecommunication Theory, Technical Report TR-178, September 1983.
42. W. P. Osborne and M. B. Luntz, "Coherent and Noncoherent Detection of CPFSK," *IEEE Transaction on Communications* COM-22, 1023-1034 (1974).
43. W. Hirt and S. Pasupathy, "Suboptimal Reception of Binary Continuous Phase Shift Keying Signals," September 1980, *IEE Proceedings, Part F* 128(3), 125-134 (1981).
44. C-E. Sundberg and A. Svensson, "Parallel and Serial MSK-type Detection of Partial Response Continuous Phase Modulation," The 1983 Mediterranean Electrotechnical Conference, MELECON'83, Athens, Greece, Conference Record, p. B8.01.
45. S. Nanayakkara and J. B. Anderson, "High Speed Receiver Designs Based on Surface Acoustic Wave Devices," The Sixth International Conference on Digital Satellite Communications, Phoenix, Arizona, September 1983, Conference Proceedings, pp. VI-16-VI-22.
46. J. B. Anderson and S. Nanayakkara, "Surface Acoustic Wave Devices and the Design of Optimal High Speed Receivers," 1983 International Tirrenia Workshop on Digital Communications, Tirrenia (Pisa) 30th August-2 September 1983, Proceedings, pp. D3.1-D3.9.
47. T. Aulin, B. Persson, N. Rydbeck, and C-E. Sundberg, "Spectrally-Efficient Constant-Amplitude Digital Modulation Schemes for Communication Satellite Applications," May 1982, Study Report. European Space Agency—ESTEC, Contract 4765/81/NL/MD, Vol. I and Vol. II, in part published in Conference Proceedings, The Sixth International Conference on Digital Satellite Communications, Phoenix, Arizona, September 1983.
48. D. Muilwijk and J. H. Schadé, "Correlative Phase Modulation for Fixed Satellite Services," January 1983, Study Report, ESTEC 4485/80/NL/MS, Philips Telecommunicatie Industrie B.V., Hilversum, The Netherlands.
49. D. Muilwijk and J. H. Schadé, "Correlative Phase Modulation for Fixed Satellite Services," Supplementary Report, August 1983, ESTEC 44/80/NL/MS(SC), Philips' Telecommunicatie Industrie B.V., Hilversum, The Netherlands.
50. S. Nanayakkara, J. B. Anderson, T. Aulin, and C-E. Sundberg, "Phase Coded Sinusoidal Signal Transmitter/Receiver Structure Including Saw Device-Based Structure," Vols. I and II, Final Report, Intelsat Contract No. INTEL-216, December 1982.
51. D. Muilwijk, "Correlative Phase Shift Keying—A Class of Constant Envelope Modulation Techniques," *IEEE Transactions on Communications* COM-29(3), 226-236 (1981).
52. J. B. Anderson and S. Mohan, "Sequential Coding Algorithms: A Survey and Cost Analysis," *IEEE Transactions on Communications* COM-32, 169-176 (1984).

# Synchronization

For coherent detection, reference signals comprising the carrier with correct frequency and phase and also the data symbol transition instants must be available. This is referred to as synchronization. To avoid wasting power, these signals should not be transmitted separately, but should instead be regenerated at the detector in an optimum manner. Actually, both the transmitted data sequence and the reference signals should be estimated jointly according to some suitable optimization criterion, e.g., the maximum likelihood (ML) principle. We shall outline such an approach.

The joint optimization approach leads to complex mathematical problems to solve, and in those simple cases where they can be solved, complex synchronizer structures are obtained. This motivates another approach where the structure of the synchronizer is specified *a priori*. This structure is chosen to be fairly simple; the choice is motivated by engineering arguments. We will also pursue this approach.

It is also possible to MAP (maximum *a posteriori*) estimate phase and data symbol transition instants jointly and then detect the data using these estimates. Yet further possibilities are outlined in Section 9.3.

The emphasis of this chapter is on synchronization for a CPM scheme of reasonable complexity. Phase acquisition for BPSK and QPSK is relatively easily done by squaring and quadrupling circuits, or by Costas loops. These include or are in conjunction with a phase-lock loop, a structure that is a considerable study in itself. We must defer to introductory texts like Ref. 4, 19, or 20 for a discussion of these topics.

## 9.1. Synchronization with a Specified Structure

One way of obtaining the reference signals is to try to regenerate them at the detector by removal of the modulation, fully or partly. A simple way

to do this is to use a nonlinearity. This regeneration will yield imperfect reference signals if the modulation cannot be fully removed, and the result is a degraded detection performance. This section is an introductory study of these problems. We will concentrate at first on single index CPM, and then, in Section 9.1.5, on multi- $h$  formats.

Within the large class of CPM schemes, mainly one specific case has been studied with regard to synchronization, MSK, or FFSK. A synchronizer for this modulation scheme has been proposed by de Buda.<sup>(1)</sup> This synchronizer has been analyzed by Matyas<sup>(5)</sup> and also others.<sup>(6)</sup> The detector for MSK is simple, and therefore also simple to analyze. A similar approach to synchronization is taken in Ref. 7 for unbalanced QPSK and in Ref. 8 for offset QPSK. Unfortunately, the analysis problem for a general CPM system is far more complicated, as will soon be evident. This is because the detector in general is nonlinear.

The synchronizer for MSK (FFSK) was generalized by Lee<sup>(2)</sup> to include  $M$ -ary data and any rational modulation index. The frequency pulse was still 1REC, however. This synchronizer has now been further developed<sup>(11)</sup> to be useful for any scheme within the CPM family. A schematic of the synchronizer appears in Figure 9.1. It can by no means be called optimum, but it is simple and, as will be seen below, yields in many cases reference signals of good quality. A detailed description of this synchronizer follows.

### 9.1.1. Spectral Considerations

The modulation index for the CPM signal is assumed to be rational

$$h = k_1/k_2, \quad k_1/k_2 = 1, 2, \dots \quad (9.1)$$

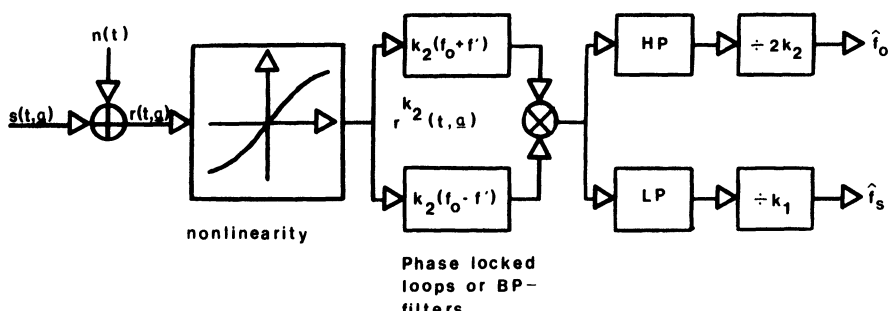


Figure 9.1. A synchronizer circuit for a CPM system with carrier frequency  $f_0$  and modulation index  $h = k_1/k_2$ . The frequency  $f'$  is a multiple of  $1/2T$ , where  $T$  is the symbol rate.

and the available CPM signal  $s(t, \alpha)$  is also corrupted with AWGN,  $n(t)$ . From Figure 9.1, the first step in the synchronization signal regeneration is to form the signal

$$[r(t, \alpha)]^{k_2} = [s(t, \alpha) + n(t)]^{k_2} \quad (9.2)$$

and the signal component of (9.2) around the frequency  $k_2 f_0$  is<sup>(11)</sup>

$$\frac{[2E/T]k_2/2}{2^{k_2-1}} \cos [2\pi k_2 f_0 t + k_2 \phi(t, \alpha)] \quad (9.3)$$

This is recognized as a CPM signal with carrier frequency  $k_2 f_0$  and phase

$$k_2 \phi(t, \alpha) = k_2 2\pi \frac{k_1}{k_2} \sum_i \alpha_i q(t - iT) \quad (9.4)$$

and since the factors  $k_2$  cancel, the result is a CPM signal with modulation index  $k_1$ , which is an integer. From Chapter 4 it is known that CPM signals with noninteger valued modulation index have power spectra absolutely free from discrete components (for equally probable data symbols). For integer valued modulation indices, however, discrete spectral components occur. It is shown in Section 4.2 how to calculate the continuous and discontinuous part of the power spectrum; it is also demonstrated how to calculate the (baseband) autocorrelation functions  $R_{\text{con}}(\tau)$  and  $R_{\text{dis}}(\tau)$  yielding the two different components of the power spectrum [see equation (4.22)].

It is clear from (4.26) that the discrete frequency components occur at odd or even multiples of the quantity  $1/2T$ , relative to the "carrier" frequency. This depends on whether  $h$  is odd or even, respectively, and is illustrated in Figure 9.2. When  $h$  is an odd integer the autocorrelation

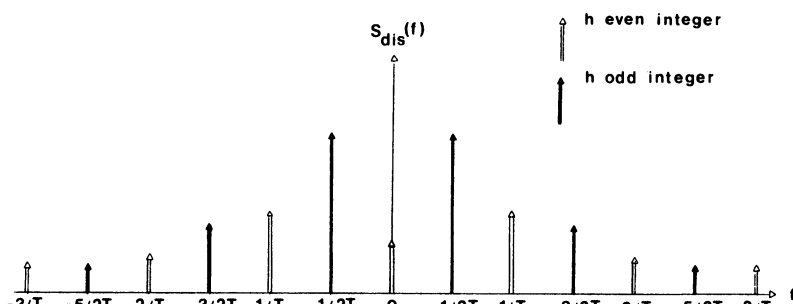


Figure 9.2. Possible locations of discrete frequency components on the baseband frequency axis when  $h$  is an integer. There are in general infinitely many components.

function  $R_{\text{dis}}(\tau)$  is periodic with period  $2T$ , but it is also odd symmetric over a suitable  $2T$  interval. This has an influence on the Fourier coefficient in the Fourier series expansion of  $R_{\text{dis}}(\tau)$ ; every other of them are in this case equal to zero. From Section 4.2 we also know that  $R_{\text{con}}(\tau) = 0$  when  $|\tau| \geq LT$  and thus the continuous part of the spectrum can be found numerically by the Fourier transform relationship

$$S_{\text{con}}(f) = 2 \int_0^{LT} R_{\text{con}}(\tau) \cos 2\pi f\tau d\tau \quad (9.5)$$

The total power in the signal is  $R(0) = 1$ , i.e., the power is normalized to unity as in Chapter 4. This unit total power is divided into two parts  $R_{\text{con}}(0)$  and  $R_{\text{dis}}(0)$ . Thus the total power in the discrete components can be found by calculating either  $R_{\text{con}}(0)$  or  $R_{\text{dis}}(0)$ . Actually,  $R_{\text{dis}}(0) = |R(LT)|$  since  $R_{\text{con}}(LT) = 0$ .

As an example, Figure 9.3 shows the autocorrelation function  $R(\tau)$  for the scheme 3RC,  $M = 2$  when  $h = 2$ , (solid line). In this case  $R(\tau)$  is periodic when  $|\tau| \geq 3T$  and equals  $R_{\text{dis}}(\tau)$  over this interval. By picking one full period of  $R_{\text{dis}}(\tau)$  and then subtracting it from  $R(\tau)$  over the interval  $0 \leq \tau \leq 3T$  with the proper time alignment, the autocorrelation function  $R_{\text{con}}(\tau)$  is obtained. This one is shown dash-dotted in Figure 9.3; it is actually shown over the interval  $0 \leq \tau \leq 3T$ , after which  $R_{\text{con}}(\tau) = 0$ .

By looking at  $R(\tau)$  and  $R_{\text{con}}(\tau)$  at  $\tau = 0$  in Figure 9.3, it can be seen how the total power in the signal is divided between the continuous and discrete parts. A discrete component occurs at the frequency  $f = 0$  since  $R_{\text{dis}}(\tau)$  contains a constant component.  $R_{\text{dis}}(\tau)$  looks very sinusoidal with period  $T$ , and it is likely that most of the power  $R_{\text{dis}}(0)$  [or  $R(3T)$ ] is contained in the two discrete spectral components at  $fT = \pm 1$ . Of course

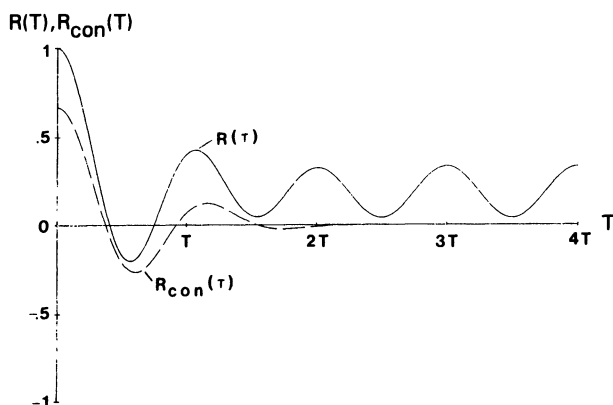


Figure 9.3. The autocorrelation functions  $R(\tau)$  for the scheme 3RC when  $M = 2$  and  $h = 2$ .  $R_{\text{dis}}(\tau) = R(\tau)$  when  $\tau \geq 3T$  for a length three pulse.

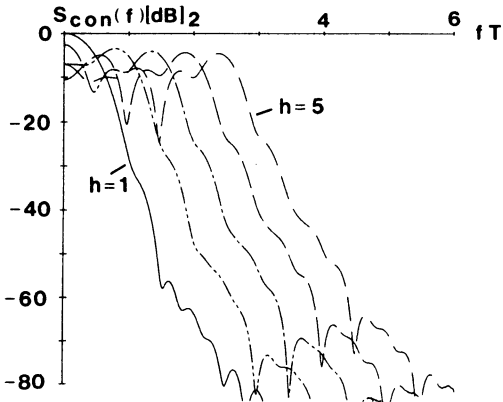


Figure 9.4. Power spectra  $S_{\text{con}}(f)$  in decibels vs.  $fT$  for the schemes 3RC,  $M = 2$ , when  $h = 1, 2, 3, 4, 5$ . The frequency  $f$  is normalized to the symbol rate  $1/T$ .

the magnitudes of the discrete spectral components can be calculated accurately by computing the Fourier coefficients.

In Figure 9.4 the power spectra  $S_{\text{con}}(f)$  are shown for the schemes 3RC,  $M = 2$  when  $h = 1, 2, 3, 4$ , and 5. Equation (9.5) was numerically evaluated. The frequency  $f$  is normalized by the symbol rate  $1/T$  instead of the bit rate, since in synchronization we are interested in the symbol timing. When  $h$  increases from 1 to 5, the width of the main lobe of  $S_{\text{con}}(f)$  is widened by an approximately equal amount for every unit step in  $h$ . The global maximum of  $S_{\text{con}}(f)$  is located around  $fT = h/2$ , and this location in frequency is in most cases also where the strongest discrete component occurs.

As another example, we take the scheme 2RC with  $M = 4$ . Figure 9.5 shows the autocorrelation functions  $R(\tau)$  and  $R_{\text{con}}(\tau)$  over the interval  $0 \leq \tau \leq 3T$ . In this case  $R(\tau)$  equals  $R_{\text{dis}}(\tau)$  over the interval  $2T \leq \tau \leq 3T$ .

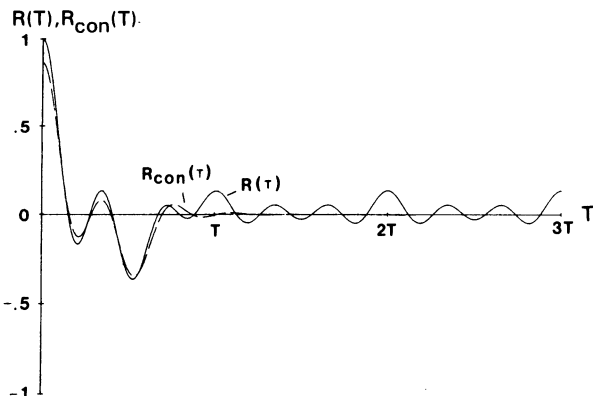


Figure 9.5.  $R(\tau)$  and  $R_{\text{con}}(\tau)$  for the scheme 2RC when  $M = 4$  and  $h = 2$ . In this case  $R_{\text{con}}(\tau) = 0$  when  $\tau \geq 2T$ .

Note the even symmetry about  $\tau = 5T/2$ .  $R_{\text{dis}}(\tau)$  does not have a shape which is very sinusoidal, because there is more than one discrete spectral component which is of comparable size. Here the components with periods  $T$  and  $3T$  are the strongest. Compared to the scheme of Figure 9.3, the total power  $R(2T)$  in the discrete components is now smaller.

Figure 9.6 shows  $S_{\text{con}}(f)$  in decibels for the schemes 2RC,  $M = 4$  having  $h = 1, 2, 3, 4$ , and 5. The main lobe of  $S_{\text{con}}(f)$  again increases by approximately the same amount when  $h$  is increased in steps of 1. It is also seen that the dominant maxima in the spectra now occur around the frequencies  $h/2T$  and  $3h/2T$ , although the spectra are rather flat in the interval  $0 \leq f \leq 3h/2T$ .

For a fixed integer valued modulation index and number of levels  $M$ , the magnitudes of the discrete frequency components are affected by the shape and the duration of the frequency pulse  $g(t)$ . It is possible to design the pulse  $g(t)$  so that straight lines occur in the phase tree. This means that there are data sequences  $\alpha$  such that a discrete frequency is transmitted, and this frequency can be related to the carrier frequency, the symbol rate, or both. It seems realistic that such straight lines should yield strong discrete components at the respective frequencies. This will be studied by means of a numerical example below.

It can be shown that sufficient conditions for a pulse  $g(t)$  to produce a linearly increasing (or decreasing) phase for constant data of suitable duration is that

$$g(t) = g_R(t) * g_0(t) \quad (9.6)$$

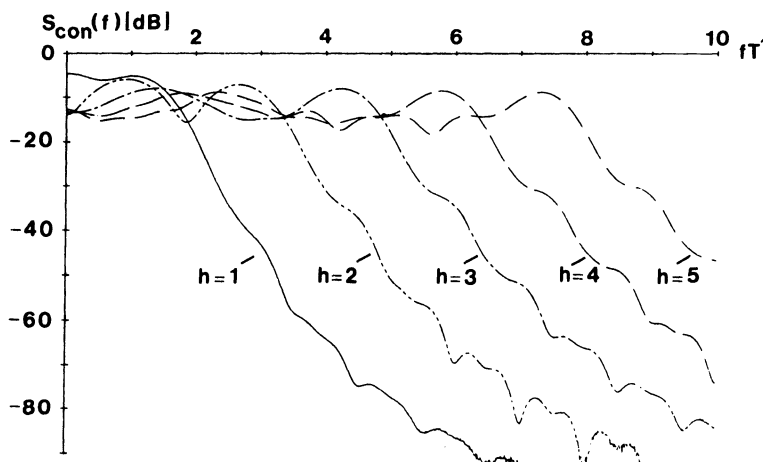


Figure 9.6. Power spectra  $S_{\text{con}}(f)$  for the schemes 2RC,  $M = 4$ , when  $h = 1, 2, 3, 4, 5$ .

where  $g_R(t)$  is the 1REC pulse and  $g_0(t)$  can have any shape. A necessary and sufficient condition for this kind of straight phase trajectory in the phase tree is that

$$G\left(i \frac{1}{T}\right) = 0, \quad i = \pm 1, \pm 2, \dots \quad (9.7)$$

where  $G(\cdot)$  is the Fourier transform of  $g(t)$ .

A sufficient condition for horizontal straight lines to occur in the phase tree for alternating data ( $\dots, +1, -1, +1, -1, \dots$  in the binary case) is that

$$g(t) = \frac{1}{2}[\delta(t) + \delta(t - T)] * g_0(t) \quad (9.8)$$

where  $g_0(t)$  is an arbitrary frequency pulse. A necessary and sufficient condition for this case is that

$$G\left(i \frac{1}{2T}\right) = 0, \quad i = \pm 1, \pm 3, \pm 5, \dots \quad (9.9)$$

### 9.1.2. The Synchronizer Structure

Now that the nonlinear element in Figure 9.1 produces a signal having discrete frequency components, it is possible to understand the operation of the synchronizer circuit. The two phase locked loops (or bandpass filters) are centered at a symmetric pair of the discrete components. These frequencies are  $k_2(f_0 \pm f')$ , say. The output signals are then multiplied, yielding a discrete component at the sum of the two frequencies,  $2k_2f_0$ , and another one at the difference of the two frequencies,  $2k_2f'$ . Since in most cases the strongest component occurs at  $f' = h/2T = k_1/2k_2T$ , the latter of the two sinusoids has the frequency  $k_1/T$ . Next the signal is high-pass filtered with cutoff  $2k_2f_0$  and frequency divided by  $2k_2$ , and also low-pass filtered with cutoff  $k_1/T$  and frequency divided by  $k_1$ . The result is two sinusoids with frequencies  $f_0$  and  $1/T$ ; these are the carrier and symbol rate.

The estimated carrier component has a phase ambiguity of  $2k_2$  because of the frequency divider. Since the modulation index is rational and there are  $p$  phase states in the signal, it is obvious that the phase of the carrier only has to be known modulo  $2\pi/p$  when using a Viterbi detector. This is because in a CPM scheme a phase shift of magnitude  $2\pi/p$  merely renames the phase states, the trellis itself remaining the same. This greatly reduces the carrier phase ambiguity and in most cases eliminates it completely. With the symbol rate, there is a  $k_1$ -fold ambiguity which has to be resolved in some way.

Of great importance to the performance of the synchronizer in Figure 9.1 is the bandwidth of the phase locked loops or bandpass filters following the nonlinearity. With narrow bandwidths, long synchronization times can be expected. On the other hand, the reference signals, when established, can be expected to be very free from channel noise and noise created by remaining modulation. Special problems are presented by cheap, mobile receivers, which often suffer from drift at UHF and microwave frequencies. A wide loop bandwidth greatly aids these receivers in acquiring and keeping phase lock, but the wide bandwidth also admits data noise into the synchronizer.

For TDMA applications, it is known from Gardner,<sup>(17,18)</sup> that the synchronizer must contain two very narrow bandpass filters instead of phase locked loops. This is because the phase locked loops have a tendency to hang up, giving synchronization times that are occasionally very long. Bandpass filters, being linear elements, have no such drawbacks. The acquisition times that may be expected from bandpass filter synchronizers with "zero state start" are carefully investigated in Refs. 17 and 18. These results are directly applicable to the CPM synchronizer described here, if the correct bandwidths are used.

### 9.1.3. Discrete Component CNRs

Because of the foregoing problems we will assume that bandpass filters are used after the nonlinearity. These filters are assumed to be ideal brick-wall filters with total bandwidth  $WT$ , whose purpose is tracking of the discrete frequency component. We can define a carrier to noise ratio (CNR) at the outputs of these bandpass filters as

$$\text{CNR} \triangleq 10 \log_{10} \frac{b_k}{\int_{-W/2}^{W/2} S_{\text{con}}(f_k + f) d(fT)} \quad (9.10)$$

where  $f_k$  is the location of the discrete frequency component and  $b_k$  is the corresponding magnitude. The CNR is given in decibels. The influence of the channel noise has been neglected in (9.10). The reason for this is that the bandwidth  $WT$  will turn out to be much narrower than the bandwidths of the filters used for the detection, so that, as far as the synchronization is concerned, the remaining modulation in the signal is the dominant source of noise.

Figure 9.7 gives an example of a CNR calculation. The scheme is  $M = 2$ , 3RC with  $h = 2$ , just as in Figures 9.3 and 9.4. The CNR defined in (9.10) is shown as a function of the bandwidth  $WT$  by the solid curves;  $WT$  runs from 1/500 to 2 and the discrete components at  $fT = 0$  and  $fT = \pm 1$  have been considered.

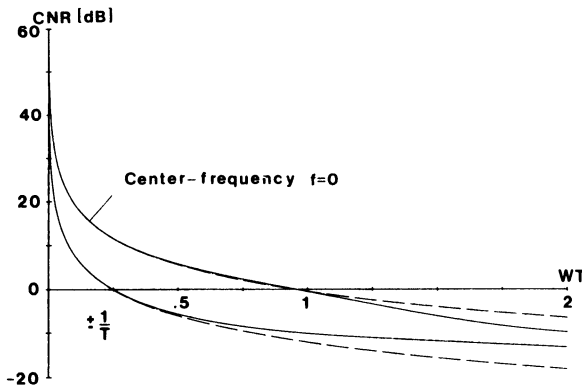


Figure 9.7. CNR in decibels vs. WT for the scheme 3RC,  $M = 2$ , when  $h = 2$ .  $W$  runs from  $1/500$  to  $2$ . The dashed lines indicate that approximation (9.11) was used.

The dash-dotted curves in Figure 9.7 are approximations of the CNR curves according to

$$\begin{aligned} \text{CNR} &\approx 10 \log_{10} \frac{b_k}{WS_{\text{con}}(f_k)} \\ &= 10 \log_{10} b_k - 10 \log_{10} S_{\text{con}}(f_k) - 10 \log_{10} W \end{aligned} \quad (9.11)$$

This approximation is based on the observation that the spectra  $S_{\text{con}}(f)$  are very smooth and therefore can be approximated by a constant value over the filter bandwidth. This constant is taken as the magnitude of  $S_{\text{con}}(f)$  at the discrete frequency considered.

The approximation (9.11) is very accurate for CNRs of practical interest (10-15 dB). Thus only the magnitude of the discrete frequency component  $b_k$  and the value of the continuous part of the power spectrum at that frequency need to be known to be able to calculate the CNR. Both of these quantities can easily be obtained from  $R(\tau)$  in Figure 9.3. A good way of examining the synchronization properties of a CPM scheme is to produce tables of  $b_k$  and  $S_{\text{con}}(f_k)$ . The necessary bandwidth  $WT$  for achieving a specific CNR is then easily obtained from (9.11).

Of course the approximation (9.11) does not exist if  $S_{\text{con}}(f_k) = 0$ . This occurs only rarely. Only two cases have been found,  $g(t) = 1\text{RC}$ ,  $M = 2$  when  $h = 2$  or 4. The CNR is very large in these cases.

CNR curves for the scheme previously considered in Figures 9.5 and 9.6, 2RC with  $M = 4$  and  $h = 2$ , are shown in Figure 9.8. Here the discrete frequency components at  $fT = 0, \pm 2/T, \pm 4/T$ , and  $\pm 6/T$  have been used for calculation of the CNR by means of (9.11). More than one synchronizer of the kind shown in Figure 9.1 can be used for different pairs of discrete frequency components. The outputs from these subsynchronizers can then

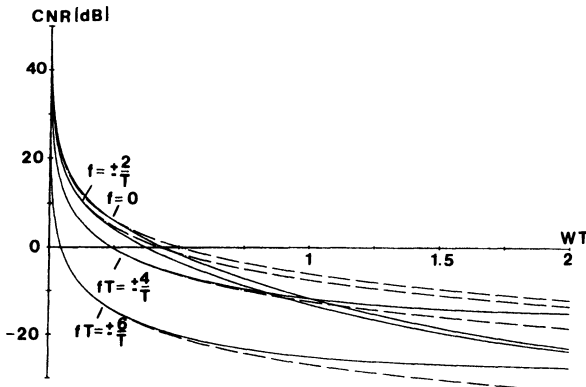


Figure 9.8. CNR for the scheme 2RC,  $M = 4$  when  $h = 2$ . The dashed lines indicate (9.11) was used. Four frequencies  $f$  are considered.

be used to improve the CNR, and also to resolve any ambiguities in the phase of the carrier and the data symbol transition instant.

It has been found that the magnitudes of the discrete frequency components roughly track the continuous part of the spectrum,  $S_{\text{con}}(f)$ . The strongest frequency component is in most cases located at the frequency  $fT = \pm h/2$  in the binary case, and at  $fT = \pm h/2, \pm 3h/2$  in the quaternary case ( $M = 4$ ). The total power of the discrete frequency components,  $R_{\text{dis}}(0)$ , in general decreases with the pulse length  $L$ , when  $h$ ,  $M$ , and the shape of  $g(t)$  are fixed, and it decreases with the integer valued  $h$  for fixed  $g(t)$ ,  $L$ , and  $M$ .  $R_{\text{dis}}(0)$  is in general also a decreasing function of  $M$ , when everything else is fixed. There are exceptions to all of these observations, however.<sup>(11)</sup>

It is of interest to compare the CNR for systems based on the frequency pulses RC and HCS (half cycle sinusoid), both of duration  $L$  symbol intervals. This is because the RC scheme generates straight lines with slope  $\pm h/2T$  in the phase tree when  $L \geq 2$ , while HCS schemes do not in general. When  $L = 4$ , there is also a straight horizontal line in 4RC (see Figure 3.13). By calculating the approximation (9.11) to the CNR for schemes of type LRC and LHCS, we obtain the CNRs  $\text{CNRLRC}(W)$  and  $\text{CNRLHCS}(W)$ .

By forming the difference a comparison can be made. This quantity

$$\Delta\text{CNR} = \text{CNRLRC}(W) - \text{CNRLHCS}(W) \quad (9.12)$$

is independent of the bandwidth  $W$ , when  $W$  takes the same value for the LRC and the LHCS system. In Table 9.1 the result of such a comparison is shown for the discrete frequency components at  $fT = \pm h/2$  when  $M = 2$ .

Approximately 2 dB in CNR is gained by using RC pulses instead of HCS pulses. 3HCS does have lines in the phase tree, and this is also reflected in Table 9.1 where the gain in CNR drops for  $L = 3$ .

**Table 9.1. The Quantity  $\Delta CNR$  Comparing the CNRs for the Binary Schemes LRC and LHCS at  $f \cdot T = h/2$**

	$h = 1$	$h = 2$	$h = 3$	$h = 4$	$h = 5$
$L = 2$	1.80	2.15	2.50	2.59	2.69
$L = 3$	2.72	2.12	1.77	1.72	1.82
$L = 4$	2.91	2.63	2.43	2.14	1.94
$L = 5$	3.21	2.81	2.66	2.61	2.47

#### 9.1.4. Error Performance

So far only the spectral performance of the synchronizer in Figure 9.1 has been considered. It is of interest also to study the detection efficiency for a CPM scheme utilizing such a synchronizer. This is a formidable theoretical problem, for which no solution is presently available. A simpler problem is to calculate the detection efficiency for a given phase error  $\Delta\phi$  between transmitter and receiver. Assuming a Gaussian channel with AWGN and one-sided power spectral density  $N_0$ , the symbol error probability for large SNR is

$$P_e \sim Q\left(\left(d_{\min}^2 \frac{E_b}{N_0}\right)^{1/2}\right) \quad (9.13)$$

according to Chapter 3.

The transmitter now operates with the phase tree  $\phi(t, \alpha)$  and the receiver with the mismatched phase tree  $\phi(t, \tilde{\alpha}) + \Delta\phi$ .

The results of Section 3.5.1 concerning the Euclidean distance measure for mismatched signal sets are directly applicable. The normalized squared Euclidean distance is now

$$d^2 = \frac{d_A^4}{d_R^2} \quad (9.14)$$

where

$$\begin{aligned} d_A^2 &= \log_2 M \frac{1}{T} \int_0^{NT} \{ \cos \Delta\phi - \cos [\phi(t, \gamma) - \Delta\phi] \} dt \\ d_R^2 &= \log_2 M \frac{1}{T} \int_0^{NT} [1 - \cos \phi(t, \gamma)] dt \end{aligned} \quad (9.15)$$

and  $\gamma = \alpha - \tilde{\alpha}$  is the difference between the transmitted and detected data sequences.  $N$  is the duration of the observation interval and  $d_{\min}^2$  in (9.13) is obtained from (9.14) by minimization over the difference sequence  $\gamma$ .

For an optimum detector the distance measure is insensitive to the sign of the sequence  $\gamma$  but this is not true for the phase offset suboptimum detector. If  $\gamma$  yields  $d_{\min}^2$  for the suboptimum detector, the difference sequence  $-\gamma$  does not. Since the difference sequence  $\gamma$  puts restrictions upon the transmitted sequence  $\alpha$ , the relative occurrence of the error event with which  $d_{\min}^2$  is associated is more rare for the suboptimum detector. The performance degradation indicated by the reduction of  $d_{\min}^2$  has to be used with extreme care. Very, very large SNR must be considered. For a realistic SNR,  $d_{\min}^2$  is a pessimistic performance indicator. This will be apparent below.

To illustrate the calculation of  $d_{\min}^2$  by (9.14) and (9.15), the binary scheme 2RC has been selected. The phase errors are  $\Delta\phi = \varepsilon 2\pi$ , where  $\varepsilon = 0, 0.01, 0.02, 0.03, 0.04$ , and  $0.05$ . Figure 9.9 shows the upper bounds  $d_B^2$  for each case; the upper bounds have been constructed using the difference sequences  $\gamma$  yielding the first two mergers, just as in Section 3.2.2, as well as also the corresponding sequence  $-\gamma$ . It is seen that even small phase errors give large reductions in  $d_B^2$ . In Figure 9.10, actual  $d_{\min}^2$  curves are shown for the same scheme now with  $\varepsilon = 0.02$ . The upper bound  $d_B^2$  is also shown (dash-dotted).  $N = 1, 2, \dots, 8$  observed bit intervals are used in the calculation of  $d_{\min}^2$ .

We could attempt to improve the error estimate provided by  $d_{\min}^2$  by upper and lower bounding the symbol error probability, as in Section 3.4.2. A major problem is that the Euclidean distance measure (9.14) is not additive from symbol interval to symbol interval as it is for optimum detectors. In

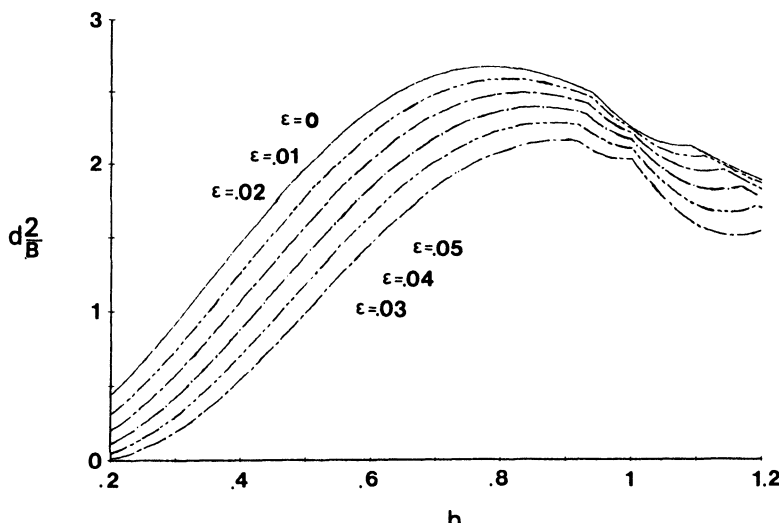


Figure 9.9. Upper bounds  $d_B^2$  on  $d_{\min}^2$  for the binary scheme 2RC. The receiver has a phase error of  $\Delta\phi = 2\pi\varepsilon$  radians relative to the transmitter.

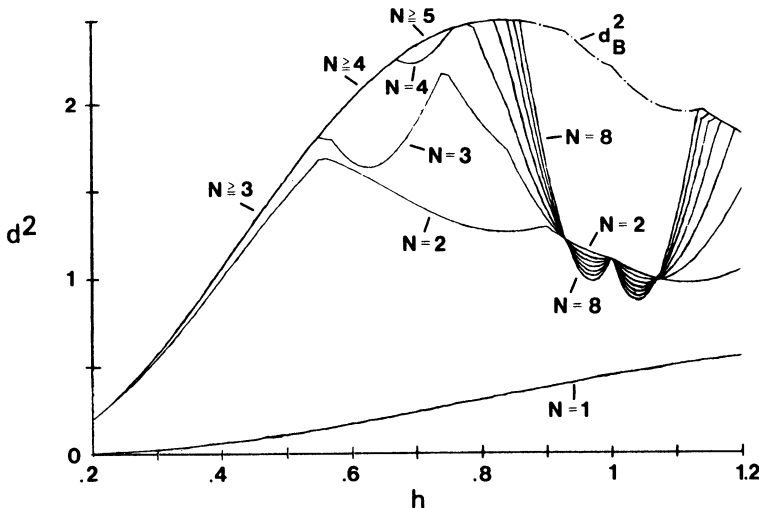


Figure 9.10. Minimum squared Euclidean distance vs. modulation index  $h$ . The scheme is binary 2RC and the phase error is  $\Delta\phi = 2\pi\epsilon$  with  $\epsilon = 0.02$ ;  $N$  is the receiver observation interval in bits and the upper bound  $d_B^2$  is shown dashed.

consequence, the numerical method of calculating transfer function bounds in Section 3.4.2 does not work, and a closed form expression of the transfer function  $T(L, I, D)$  must be found analytically. This is in general very complicated. Only simple schemes can be considered and we therefore turn to MSK.

Figure 9.11 shows the upper and lower bounds on the MSK, bit error probability when  $\epsilon = 0$  and 0.04. The upper and lower bounds are very close and thus one can say that Figure 9.11 shows the true bit error probability. Figure 9.12 shows the loss in decibels in terms of  $E_b/N_0$  as a function of the error rate for different phase errors. It is seen that all the curves are monotonically increasing and that the loss for realistic error rates ( $10^{-4}$ - $10^{-5}$ ) is smaller than when the error probability approaches zero. The latter is what is obtained from a calculation using  $d_{\min}^2$  only. The losses at large  $E_b/N_0$  for MSK are 0.37, 0.79, 1.26, 1.77, and 2.34 dB when  $\epsilon = 0.01$ , 0.02, 0.03, 0.04, and 0.05, respectively. The conclusion from Figure 9.12 is that  $d_{\min}^2$  is a very pessimistic performance measure for realistic error rates, when the effect of a synchronizer is considered.

### Combined Performance Evaluation

Up to this point two different aspects of the synchronization have been considered, the spectral issues and the error performance at a given phase error. To have a complete analysis of the performance degradation these

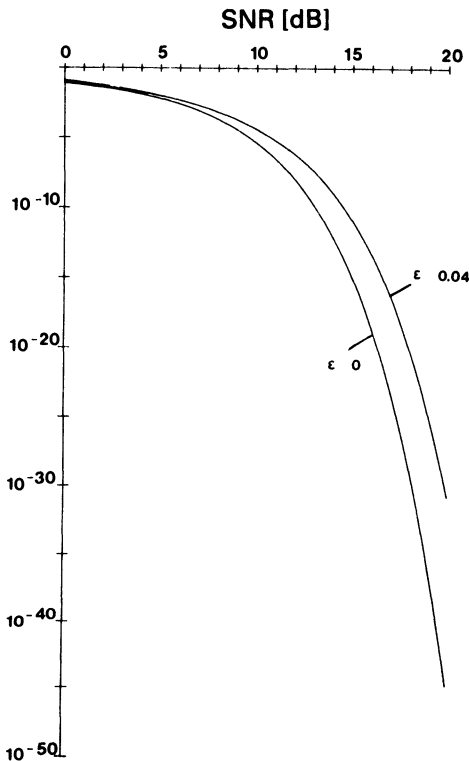


Figure 9.11. Upper and lower bounds on the error event probability for MSK when  $\epsilon = 0$  and 0.04. In a plot of this scale, upper and lower bounds are not distinguishable. The phase error is  $\Delta\phi = 2\pi\epsilon$ .

two must be put together. This could be done by calculation of the steady state probability density function  $p_{\Delta\phi}(\cdot)$  of the phase error associated with the synchronizer<sup>(3)</sup>; then we could calculate

$$P(\epsilon) = \int_{-\pi}^{\pi} P(\epsilon | \Delta\phi) p_{\Delta\phi}(\Delta\phi) d(\Delta\phi) \quad (9.16)$$

where  $P(\epsilon | \Delta\phi)$  is the symbol error probability for a given phase error  $\Delta\phi$ . Unfortunately there is no simple expression for  $P(\epsilon | \Delta\phi)$  in general and we cannot even calculate it numerically for realistic values of  $E_b/N_0$ . Matyas<sup>(5)</sup> has considered the problem of calculating  $P(\epsilon | \Delta\phi)$  for MSK detected by the simple linear offset quadrature detector. He also finds numerically the average error rate  $P(\epsilon)$  via (9.16) when the phase error has a Tikhonov distribution.<sup>(3)</sup> He finds MSK to be less sensitive than QPSK and OQPSK but more sensitive than BPSK.

From the MSK bit error probability results of Refs. 5 and 6 it appears that the slowly varying CNR of the phase reference simply adds to the incoming channel noise. In the following this will be assumed to be the case also for CPM systems. Our assumption is supported by the fact that,

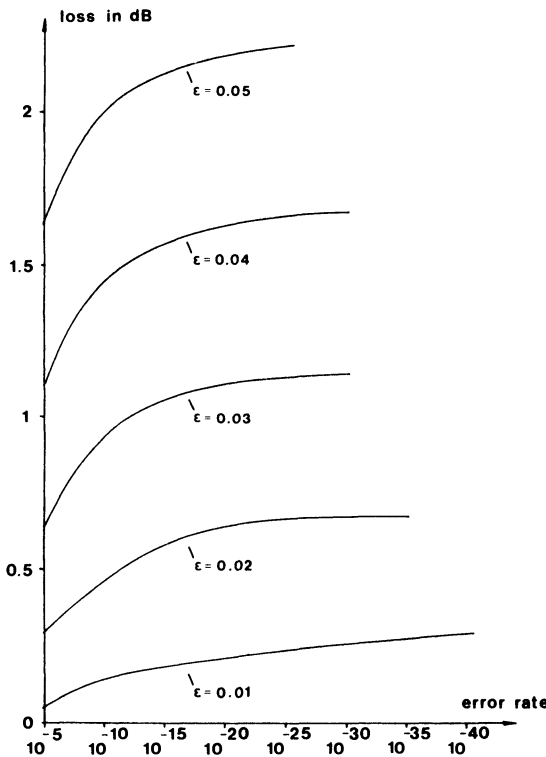


Figure 9.12. Loss in  $E_b/N_0$  in terms of decibels for MSK at different error rates and phase errors  $2\pi\epsilon$ .

although the worst case error event indicated a higher loss, the sequences that determine the worst path are increasingly less probable for more complex schemes.

The bandwidths of the synchronizer filters are determined both by the CNR of the discrete components compared to the white additive channel noise. Thus the reference signal to channel noise ratio  $\text{SNR}_R$  can be calculated from the SNR of the CPM signal and the synchronizer bandwidth  $B$  by means of

$$\text{SNR}_R = \frac{\text{SNR} \cdot b_k}{BT} \quad (9.17)$$

where  $b_k$  is the power level of the  $k$ th discrete component relative to the signal power level. Normally the minimum SNR needed for acceptable detection is somewhere around 10 dB. If we assume that the reference noise produced by both channel and data noise is not allowed to influence the

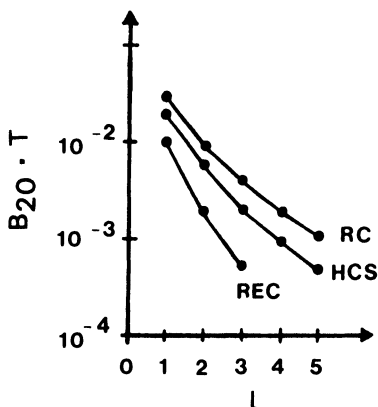


Figure 9.13. Synchronizer bandwidth for 20-dB CNR for binary ( $M = 2$ ) RC, HCS, and REC schemes with  $h = 1/n$ ; all synchronizers raise to the power  $n$ .

performance of the CPM system by more than say 1 dB, the channel and data noise must be at least  $-20$  dB below the discrete signal power. With the  $\text{SNR}_R$  equation we then need a synchronizer bandwidth of

$$B_{20} T = 0.1 b_k \quad (9.18)$$

for achieving less than 0.5 dB loss of signal power from the additive channel noise.

From CNR plots like, e.g., Figures 9.7 and 9.8, the synchronizer bandwidth  $B_{20}$  giving 20 dB signal to data noise in the reference signal can be calculated for different modulation schemes. Figures 9.13–9.15 show the bandwidth when only data noise is considered and the input SNR is high. The modulation index is  $h = 1/n$  and the input signal is raised to the power  $n$  in the synchronizer. The synchronizer thus gets a signal with  $h = 1$  and is tuned to the two frequencies  $n f_c \pm 1/2T$  with filters whose bandwidths are  $B_{20}$ . Figure 9.13 shows the bandwidth  $B_{20} \cdot T$  versus the pulse length  $L$  for binary RC-, HCS- and REC-schemes. The bandwidth is wider for the

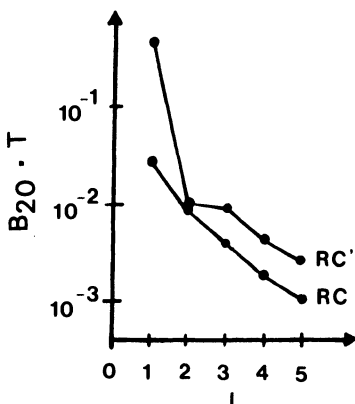


Figure 9.14. As in Figure 9.13, but RC schemes only; RC denotes raising to the minimum power  $n$ , while RC' denotes raising to the optimum power.

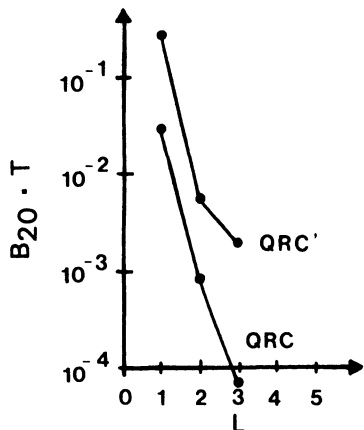


Figure 9.15. Synchronizer bandwidth for 20-dB CNR for quaternary ( $M = 4$ ) RC schemes with  $h = 1/n$ ; QRC denotes raising to the minimum power  $n$ , while QRC' denotes raising to the optimum power.

RC-schemes compared to the two other schemes. This is in agreement with the previous pulse shaping considerations. Note that the bandwidth must be smaller for long  $g(t)$ -pulses (large  $L$ ). This is because the data sequences, giving discrete tones, are longer and thus less probable.

Figure 9.14 shows the 20-dB bandwidth versus  $L$  for RC schemes. The curve denoted RC is the same as in the previous figure. The curve denoted RC' does not use the first frequency pair as does the other; instead it uses the best frequency pair or the component of  $f = 0$  directly if this has the highest power. For 1RC the best synchronizer uses the carrier, obtained by raising to the power  $2n$  in the synchronizer; for 2RC we may use this same carrier, or alternatively a frequency pair located  $\pm\frac{3}{2}(1/T)$  from the carrier and a synchronizer raising to the power  $n$ . None of these are very much better than the original frequency pair, located  $\pm 1/2T$  from the carrier. For 3RC and 4RC we use the same carrier as for the 1RC case. For 5RC the best frequency pair emerges with a synchronizer that raises to the power  $3n$ . The frequency pair is located  $\pm 1/2T$  from the carrier just as for the curve noted RC.

Figure 9.15 shows two curves for quaternary ( $M = 4$ ) raised cosine systems (QRC). The curve denoted QRC uses a synchronizer raising to the power  $n$  and the first frequency pair ( $\pm 1/2T$  from the carrier) just as in the previous figure. The curve QRC' selects the optimum frequency pair or the carrier if this is optimum. 1QRC and 2QRC use the carrier emerging from a synchronizer that raises to the power  $2n$ . 3QRC also uses the power  $2n$ . The optimum frequency pair is now located  $\pm 1/T$  from the carrier. It is important to note that no bit clock information is obtained if the synchronizer produces the carrier directly; in these cases a normal baseband bit synchronizer circuit must be used.

Figures 9.16–9.18 show the synchronizer bandwidths for achieving 20 dB  $\text{SNR}_R$  for the same schemes. Bandwidths are now calculated by (9.18).

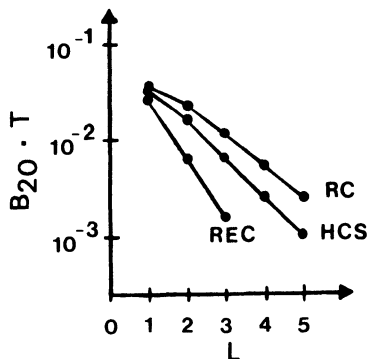


Figure 9.16. Synchronizer bandwidths for 20-dB SNR<sub>R</sub> for binary RC, HCS, and REC schemes with  $h = 1/n$ ; all synchronizers raise to power  $n$ .

These three figures show the identical cases as the three previous figures. Now the curves marked RC' or QRC' are almost always lower than the curves without the prime mark. This indicates that the first frequency pair located  $\pm 1/2T$  from the carrier is almost always the preferred frequency pair for synchronizers.

In Figures 9.19 and 9.20 we have combined the bandwidth requirements for data noise and channel noise into one plot. Most often, the data noise case is the dominating case; that is, the data noise is higher since it determines the synchronizer filter bandwidth calculation. We can compare these results to the case of pure QPSK. The spectrum after raising the QPSK signal to the power 4 consists only of a discrete carrier frequency, which contains the whole power ( $b_0 = 1$ ), and no continuous spectrum. Therefore there is no data noise. A Nyquist QPSK produces more power for synchronization than do complicated CPM schemes.

### 9.1.5. Multi- $h$ Full Response Synchronization

For multi- $h$  signals the synchronizer must not only produce the correctly phased carrier and the data symbol transition instants, but must also give

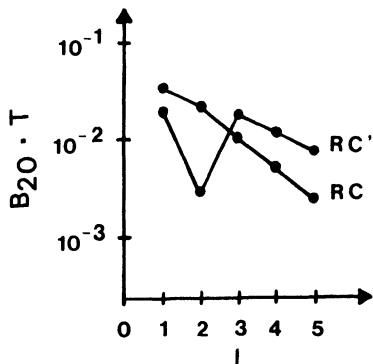


Figure 9.17. As in Figure 9.16, but RC only; RC denotes raising to minimum power  $n$ , while RC' denotes raising to power giving maximum CNR.

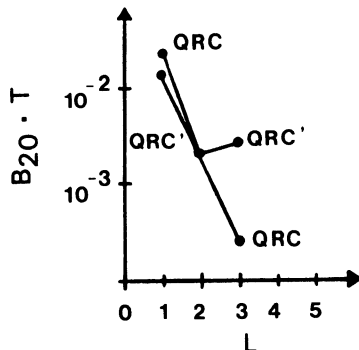


Figure 9.18. As in Figure 9.17, but quaternary.

the timing of the modulation indices. This is called superbaud timing<sup>(14)</sup> and it is clear that the superbaud timing and symbol timing are harmonically related by the number of modulation indexes,  $H$ . These problems are considered by Mazor and Taylor in Ref. 14, but the main concern of the work reported there is the generation of the carrier with correct phase. An analysis was also provided and this will now be briefly summarized. Only the binary case ( $M = 2$ ) with frequency response 1REC was considered in Ref. 14.

A block diagram of the multi- $h$  detector together with a carrier recovery loop appears in Figure 9.21. This loop illustrates a type called a *decision-directed* loop, since it uses previously detected data symbols. The front part of the detector [inner product calculator and phase rotation network (PRN)] is identical to the bank of matched filters and “alternative processor” in Figure 7.7. The branch metrics to be used by the Viterbi detector are produced there.

In the carrier reconstruction loop, an estimate  $\hat{\Delta}\phi_j$  of the phase error  $\Delta\phi_j$  and a tentative decision  $\hat{a}_j$  are extracted from the Viterbi algorithm detector at the end of each signaling interval  $jT \leq t \leq (j+1)T$ , and these are used to cancel the modulation in the selected pair of matched filter

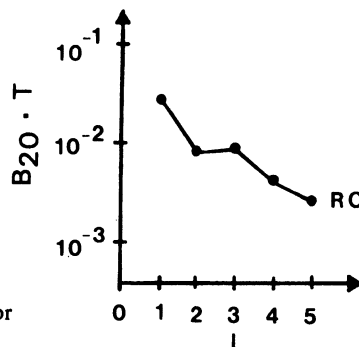


Figure 9.19. Maximum synchronizer bandwidth for less than 1 dB loss; binary RC.

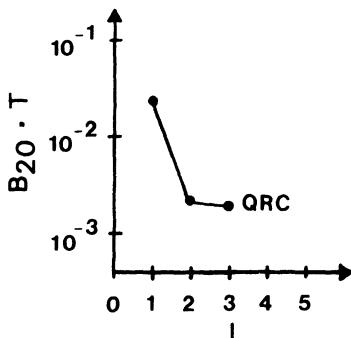


Figure 9.20. As in Figure 9.19, but quaternary RC.

(inner product calculator) outputs and to develop the carrier phase error signal  $\epsilon_j$ . The outputs of the matched filters are functions of the phase error  $\Delta\phi_j$ . The error signal  $\epsilon_j$  is fed through a loop filter  $F(p)$  and is used to correct the phase of a local reference oscillator.

The authors of Ref. 14 have analyzed this synchronization procedure and found the steady-state probability density function of the carrier phase error, modulo  $2\pi/p$ , where  $p$  is the total number of phase states. The result is

$$p_{\Delta\phi}(\Delta\phi) = C e^{SNR_L(\cos \Delta\phi - 1)}, \quad |\Delta\phi| \leq \pi/p \quad (9.19)$$

where  $C$  is a constant such that  $p_{\Delta\phi}(\cdot)$  integrates to unity. The loop SNR

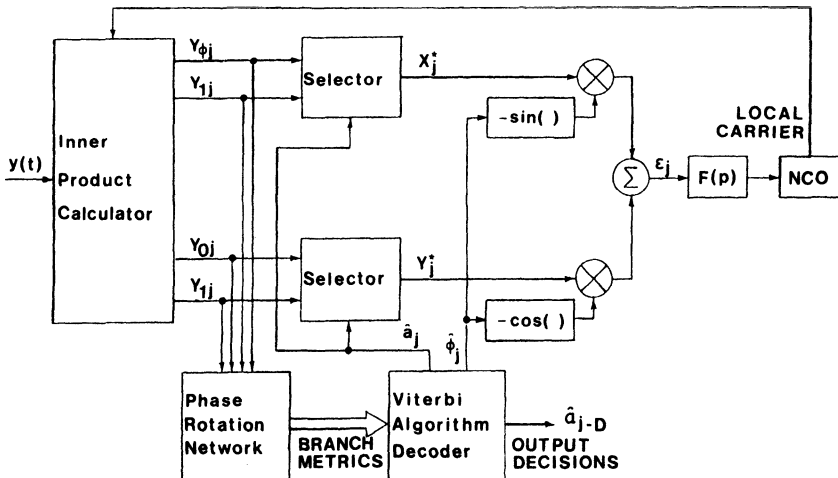


Figure 9.21. A multi- $h$  Viterbi receiver that uses a decision-directed carrier recovery loop; the Viterbi algorithm is used in the phase error computation. From B. A. Mazur and D. P. Taylor,<sup>(14)</sup> © IEEE 1981.

is given by

$$\text{SNR}_L = \frac{4E}{K_0 N_0} = \frac{P}{B_L N_0} \quad (9.20)$$

where  $P = E/T$  is the signal power and  $B_L = K_0/4T$  is the loop noise bandwidth.<sup>(3)</sup>

In Ref. 14 results of simulations are also presented. It was assumed that the symbol and superbaud timing are perfect. The structure in Figure

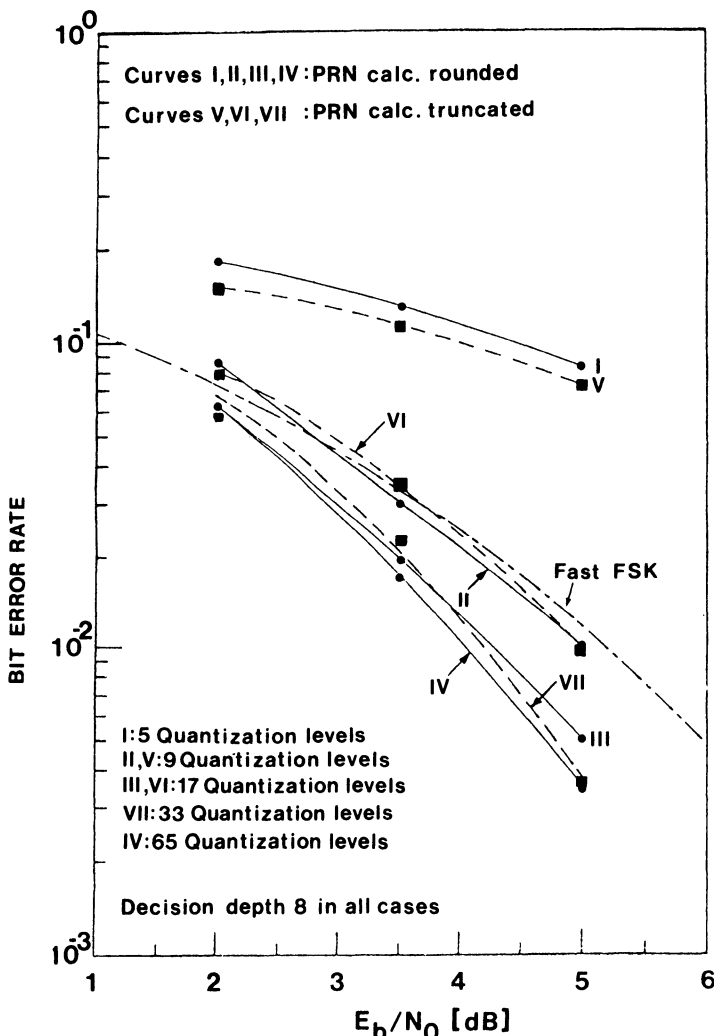


Figure 9.22. The error performance of the (3/8, 4/8) multi- $h$  system; the effect is shown of quantizing the outputs of the inner product calculator in Figure 9.21. The path memory length is 8 and Fast FSK denotes MSK. From B. A. Mazur and D. P. Taylor,<sup>(14)</sup> © IEEE 1981.

9.21 was implemented in software. The outputs from the inner product calculation were quantized to  $Q$  levels, and the channel was AWGN.

The error performance as obtained from simulations for the multi- $h$  scheme {3/8, 4/8} appears in Figure 9.22. In each case a large number of independent trials have been done.  $Q$  is the number of quantization levels, and it is seen that  $Q = 33$  seems to be quite adequate. There are also two kinds of curves in Figure 9.22. These represent the case where the PRN calculations are either rounded or truncated, in both cases to integer form. It is seen that rounding gives a better performance, especially for small  $Q$  values. As a reference, Figure 9.22 also shows the ideal performance for MSK. From the results in Chapter 3, an asymptotic gain of 1.45 dB should be attainable for the multi- $h$  scheme relative to MSK. The results in Figure 9.22 show that this is almost the case.

Because a finite number of quantization levels is used, the phase detector has a characteristic where a saturation phenomenon can be traced. This saturation effect was not taken into account in the previous analytical results. It was found in Ref. 14 that this effect caused only a minor performance degradation.

One way of investigating the saturation effect is by means of the steady state probability density function for the phase error. In Figure 9.23, a

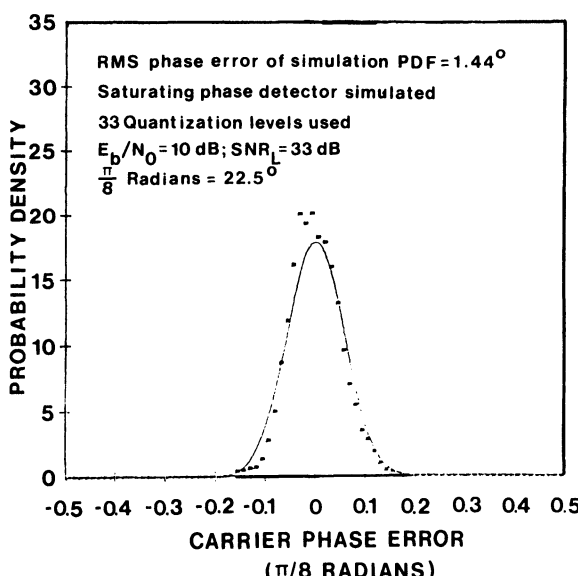


Figure 9.23. Measured phase error density function at steady state and a loop SNR of 33 dB; (3/8, 4/8) multi- $h$  system with receiver in Figure 9.21. From B. A. Mazur and D. P. Taylor,<sup>(14)</sup> © IEEE 1981.

simulation derived density function is compared with the theoretical expression given in (9.19).

## 9.2. ML Estimation of Data, Phase, and Timing

In Ascheid, Chen, and Meyr<sup>(12,13)</sup> the problem of jointly estimating the carrier phase, symbol timing, and data symbol sequence by using the ML (maximum likelihood) principle is considered, with emphasis on CPM-like schemes. In this case the structure of the synchronizer is not specified but is instead achieved as a result of the maximization of a likelihood function. The realization of this joint optimal receiver in digital hardware is stressed in Refs. 12, 13.

Denoting the received signal (AWGN channel) by  $r(t)$ , the phase error by  $\Delta\phi$ , and the timing error by  $\Delta T$ , the log-likelihood function

$$\Lambda(\Delta\phi, \Delta T, \alpha_N) = \int_0^{NT} r(t)s(t, \Delta\phi, \Delta T, \alpha_N) dt \quad (9.21)$$

is derived.<sup>(12)</sup> The joint ML estimate of  $\Delta\phi$ ,  $\Delta T$ , and  $\alpha_N$  is now obtained by simultaneously maximizing (9.21) with respect to its arguments. Two of these are continuous and the sequence  $\alpha_N$  is discrete. The maximization can be done by applying the Viterbi algorithm for all values of  $\Delta T$  and  $\Delta\phi$ . Of course there are infinitely many such values. Thus it is suggested in Ref. 12 that the possible outcome of  $\Delta\phi$  and  $\Delta T$  be quantized to  $N_{\Delta\phi}$  and  $N_{\Delta T}$  equally spaced values. The maximization of (9.21) can now be performed in a digital processor for all the  $N_{\Delta\phi}N_{\Delta T}$  possible outcomes of  $\Delta\phi$  and  $\Delta T$  while the maximizing parameters  $\widehat{\Delta\phi}$ ,  $\widehat{\Delta T}$  and  $\alpha_N$  are searched for. A sampled and stored version of the received signal is assumed to be available.

The procedure outlined above is complex, and can in practice only be used for low data rates. When using the Viterbi algorithm for detection of the transmitted data sequence, it is assumed that  $\Delta\phi$  and  $\Delta T$  are known. This is not the case now, but a realistic assumption is that  $\Delta T$  and  $\Delta\phi$  are slowly varying relative to the symbol rate  $1/T$ , so that  $\Delta T$  and  $\Delta\phi$  are almost constant over several symbol intervals. In this case the maximization in (9.21) can be divided into two separate maximization procedures, and still be a joint maximization.

Instead of using the unknown symbol sequence  $\alpha_N$  in (9.21), the symbol sequence  $\tilde{\alpha}_N$  obtained from the Viterbi detector is used. Having done this, the synchronization parameters  $\Delta\phi$  and  $\Delta T$  are obtained by maximization of

$$\Lambda_s(\Delta\phi, \Delta T) = \Lambda(\Delta\phi, \Delta T, \alpha_N = \tilde{\alpha}_N) \quad (9.22)$$

This is now a decision directed synchronization, previously considered in Section 9.1.2. With the estimates  $\Delta\phi$ ,  $\Delta T$  the Viterbi detector now operates with the metric

$$\Lambda_v(\alpha_N) = \Lambda(\Delta\phi = \widehat{\Delta\phi}, \Delta T = \widehat{\Delta T}, \alpha_N) \quad (9.23)$$

to estimate the data symbol sequence  $\alpha_N$ . The procedure is illustrated in Ref. 12 for MSK. In that case we have

$$s(t, \alpha_n) = (2P)^{1/2} \cos \left[ \omega_0 t + \Delta\phi + \alpha_n \frac{\pi}{2T} (t - nT - \Delta T) + \theta_n \right], \quad (9.24)$$

$nT + \Delta T < t < (n+1)T + \Delta T$

where  $\alpha_n$  is the data symbol and  $\theta_n$  is the phase state present in the  $n$ th bit interval. Approximating the integral in (9.21) by a sum gives

$$\begin{aligned} \Lambda(\Delta\phi, \Delta T, \theta_n, \alpha_n) &= \sum_{m=0}^{S-1} r(t_{nm} + \Delta T) \\ &\times \cos \left( \omega_0 t_{nm} + \Delta\phi + \alpha_n \frac{\pi}{2T} m \frac{T}{S} + \theta_n \right) \end{aligned} \quad (9.25)$$

where  $t_{nm} = nT + mT/S$  and  $S$  is the number of samples in each bit interval. Using trigonometric identities, (9.25) can be written

$$\begin{aligned} \Lambda(\Delta\phi, \Delta T, \alpha_n, \theta_n) &= \cos \Delta\phi K_c(\Delta T, \alpha_n, \theta_n) \\ &- \sin \Delta\phi K_s(\Delta T, \alpha_n, \theta_n) \end{aligned} \quad (9.26)$$

where

$$\begin{aligned} K_c(\Delta T, \alpha_n, \theta_n) &= \sum_{m=0}^{S-1} \left[ r_I(t_{nm} + \Delta T) \cos \left( \alpha_n \frac{\pi}{2T} m \frac{T}{S} + \theta_n \right) \right. \\ &\quad \left. - r_Q(t_{nm} + \Delta T) \sin \left( \alpha_n \frac{\pi}{2T} m \frac{T}{S} + \theta_n \right) \right] \\ K_s(\Delta T, \alpha_n, \theta_n) &= \sum_{m=0}^{S-1} \left[ r_I(t_{nm} + \Delta T) \sin \left( \alpha_n \frac{\pi}{2T} m \frac{T}{S} + \theta_n \right) \right. \\ &\quad \left. + r_Q(t_{nm} + \Delta T) \cos \left( \alpha_n \frac{\pi}{2T} m \frac{T}{S} + \theta_n \right) \right] \end{aligned} \quad (9.27)$$

and  $r_I(t) = r(t) \cos \omega_0 t$ ,  $r_Q(t) = r(t) \sin \omega_0 t$  are the quadrature components.

The log-likelihood function (9.26) will now be maximized with respect to  $\Delta T$  and  $\Delta\phi$ . Quantization of these parameters leads to the processor structure in Ref. 12, shown in Figure 9.24.

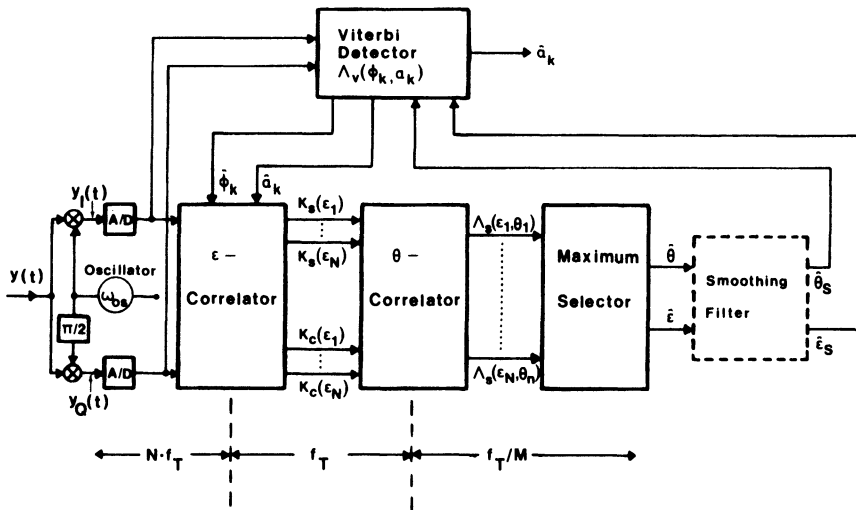


Figure 9.24. Block diagram of a digital open-loop synchronizer for CPM. From G. Ascheid, Y. Chen, and H. Meyr,<sup>(12)</sup> © NTZ Archiv, 1982.

The received signal  $r(t)$  is mixed with an oscillator having the frequency  $\omega_0$  approximately, to give  $r_1(t)$  and  $r_Q(t)$ . These quadrature components are then sampled  $S$  times each bit interval. Then the Viterbi detector uses the metric  $\Lambda_v(\alpha_n, \theta_n)$  to detect the data symbol sequence. In parallel with this, the quantities  $K_c(\Delta T, \tilde{\alpha}_n, \tilde{\theta}_n)$  and  $K_s(\Delta T, \tilde{\alpha}_n, \tilde{\theta}_n)$  are calculated for the  $N_{\Delta T}$  possible outcomes of  $\Delta T$ . In the  $\Delta\phi$ -correlator that follows, the  $N_{\Delta T}N_{\Delta\phi}$  quantities  $\Lambda_s(\Delta T_i, \Delta\phi_j)$  are then calculated. The largest of these is found and the corresponding values of  $\Delta T$ ,  $\Delta\phi$  are taken as the estimates.

The structure in Figure 9.24 is referred to in Ref. 12 as an open loop estimator. By forming partial derivatives of (9.26) with respect to  $\Delta\phi$  and  $\Delta T$ , a closed loop structure can be obtained. These derivatives are now interpreted as error signals, controlling the phase and the timing; when (9.26) is maximized, they are zero and synchronization is obtained.

### 9.3. Other Approaches

Other approaches than those presented above are possible for the construction of synchronizers for CPM. Booth<sup>(10)</sup> has applied the MAP (maximum *a posteriori*) technique for a joint estimation of carrier phase and data symbol timing for MSK. The technique has previously been applied to modulation formats such as BPSK and QPSK to show the reasonableness of certain loops such as the Costas loop.<sup>(19)</sup> The closed-loop synchronizer

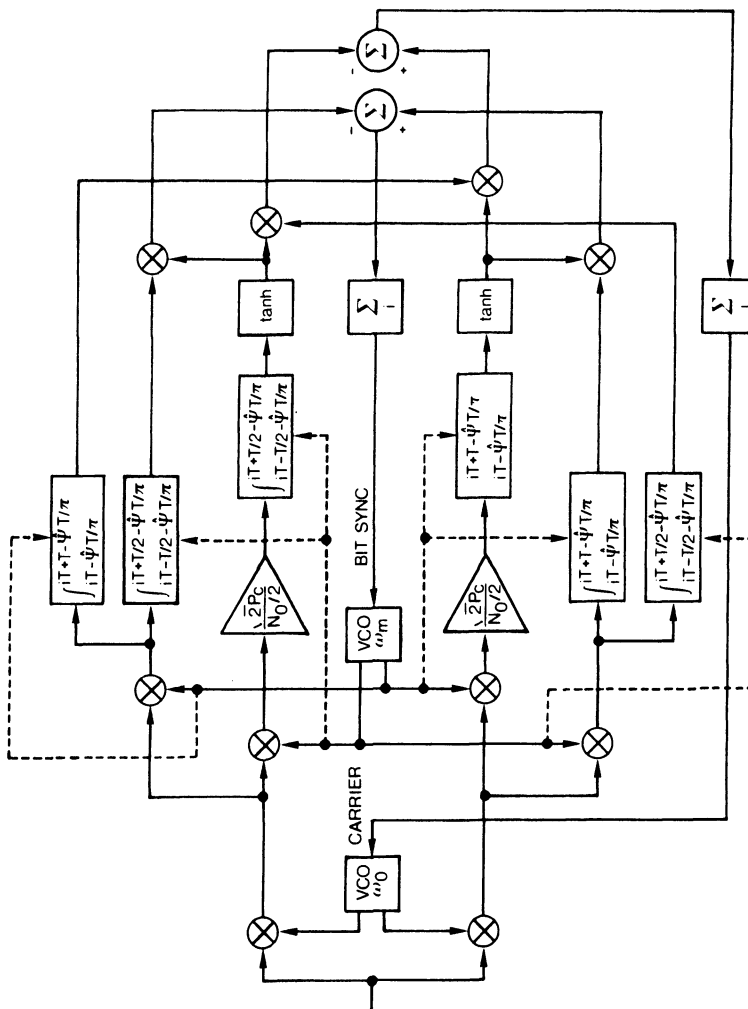


Figure 9.25. Block diagram of an MAP closed-loop synchronizer that estimates both phase and symbol timing. From R. W. D. Booth,<sup>(10)</sup> © IEEE 1980.

for MSK derived in Ref. 10 is shown in Figure 9.25; the estimation of carrier phase and data symbol timing occurs jointly here.

The synchronizer in Figure 9.25 is fairly complex. This is normally the case when the synchronizer is derived from an ML or MAP criterion. Simpler structures appear in Ref. 9.

Another interesting approach to carrier phase estimation for a general CPM scheme has been used by Wilson and Hsu<sup>(16)</sup> and Omura and Jackson<sup>(15)</sup> independently. The principle is to quantize the interval  $(0, 2\pi)$  into  $R$  equally spaced regions and then denote the carrier phase error by which of the  $R$  intervals it falls into. The carrier phase error is time varying, but if it varies slowly enough, the phase error may be viewed as constant over each symbol interval.

Additionally, we can assume that the phase error is first-order Markov, so that

$$p(\Delta\phi_0, \Delta\phi_1, \dots, \Delta\phi_N) = \frac{1}{R} \prod_{k=1}^N p(\Delta\phi_k | \Delta\phi_{k-1}) \quad (9.28)$$

if  $\Delta\phi_0$  is assumed to be uniformly distributed. The index denotes symbol interval number. Since the phase error is slowly varying, it can be assumed that the allowed transitions are to the same phase error or to one of the two neighboring intervals. These transitions are assigned probabilities. By taking the middle in each phase error interval as a representative of the phase error, a trellis description of the phase error is now obtained.

Since for rational modulation indices the phase of the CPM signal has a trellis description, it follows that the information carrying phase plus the phase error also has one. By making  $R$  equal to a small multiple of the number of phase states  $p$ , the number of states of the resulting trellis is  $RM^{(L-1)}$  instead of  $pM^{(L-1)}$  for the CPM signal alone. If the data and carrier phase error are independent, the MAP criterion becomes

$$\max_{\alpha, \Delta\Phi} p(r(t) | \alpha, \Delta\Phi) P(\Delta\Phi) \quad (9.29)$$

Here  $\Delta\Phi = (\dots, \Delta\phi_0, \Delta\phi_1, \Delta\phi_2, \dots)$  is the sequence of quantized carrier phase errors. In AWGN, the joint MAP sequence estimator will compute

$$\sum_{k=1}^N \left[ \frac{2}{N_0} \int_{(k-1)T}^{kT} r(t)s(t, \alpha, \Delta\Phi) dt + \ln p(\Delta\phi_k | \Delta\phi_{k-1}) \right] \quad (9.30)$$

and maximize over the sequences  $\alpha$  and  $\Delta\Phi$ . Since (9.30) lends itself to recursive computation, a Viterbi algorithm operating on the appropriate state trellis can determine the joint MAP sequence estimate.

In both Refs. 15 and 16 it is found by simulation that this detector has a performance close to the optimum coherent one if  $\Delta\phi$  is not too rapidly varying and  $R/p$  is 2-4. Rapid variation of the phase reference is fatal: If  $\Delta\phi$  varies with the same rate as the modulation itself, one cannot tell what is modulation and what is carrier phase error.

Several different approaches to the problem of establishing synchronization for a general CPM scheme have been presented in this chapter. To each of these synchronizers corresponds a detection performance and an overall complexity of the detector. The time for acquisition of synchronization is also of importance.

It is clear that in most cases it is extremely difficult to calculate the detection performance and acquisition time statistics. These are still open problems which deserve attention. There are undoubtedly new synchronizers, not yet discovered, which will prove attractive.

## References

1. R. de Buda, "Coherent Demodulation of Frequency Shift Keying with Low Deviation Ratio," *IEEE Transactions on Communications* COM-20(6), 429-435 (1972).
2. W. U. Lee, "Carrier Synchronization of CPFSK Signals," NTC '77, Conference Record, pp. 30.2.1-30.2.4.
3. A. J. Viterbi, *Principles of Coherent Communication*, McGraw-Hill, New York (1966).
4. W. C. Lindsey and M. K. Simon, *Telecommunication Systems Engineering*, Prentice-Hall, Englewood Cliffs, New Jersey (1973).
5. R. Matyas, "Effect of Noisy Phase References on Coherent Detection of FFSK Signals," *IEEE Transactions on Communications* COM-26(6), 807-815 (1978).
6. J. R. Cruz and R. S. Simpson, "Minimum-Shift-Keying Signal Detection with Noisy Reference Signals," *IEEE Transactions on Communications* COM-26(6), 896-902 (1978).
7. H. C. Osborne, "Effect of Noisy Phase Reference on Coherent Detection of Unbalanced QPSK Signals," NTC '78, Conference Record, pp. 2.2.1-2.2.6.
8. S. A. Rhodes, "Effect of Noisy Phase Reference on Coherent Detection of Offset-QPSK Signals," *IEEE Transactions on Communications* COM-22(8), 1046-1055 (1974).
9. R. W. D. Booth, "Carrier Phase and Bit Sync Regeneration for the Coherent Demodulation of MSK," NTC '78, Conference Record, pp. 6.1.1-6.1.5.
10. R. W. D. Booth, "An Illustration of the MAP Estimation for Deriving Closed-Loop Phase Tracking Topologies: The MSK Signal Structure," *IEEE Transactions on Communications* COM-28(8), 1137-1142 (1980).
11. T. Aulin and C-E. Sundberg, "Synchronization Properties of Continuous Phase Modulation," Global Telecommunications Conference, GLOBECOM '82, Miami, Florida, USA, November 29-December 2, 1982, Conference Record, pp. D7.1.1-D7.1.7.
12. G. Ascheid, Y. Chen, and H. Meyr, "Synchronisation, Demodulation und Dekodierung bei bandbreiteneffizienter Übertragung," *NTZ Archiv* 4(12) 355-363 (1982).
13. G. Ascheid and H. Meyr, "Synchronisation bei Bandbreiten-Effizienter Modulation," NTG-Fachtagung, Conference Record, March 23-25, 1983, Garmisch-Partenkirchen, BRD, pp. 107-114.
14. B. A. Mazur and D. P. Taylor, "Demodulation and Carrier Synchronization of Multi- $h$  Phase Codes," *IEEE Transactions on Communications* COM-29(3), 259-266 (1981).

15. J. K. Omura and D. Jackson, "Cutoff Rates for Channels Using Bandwidth Efficient Modulations," National Telecommunications Conference, NTC '80, Houston, Texas, November 30-December 4, 1980, Conference Record, pp. 26.1.1-26.1.5.
16. S. G. Wilson and C.-D. Hsu, "Joint MAP Data/Phase Estimation for Trellis Phase Codes," International Conference on Communications, ICC '80, Seattle, Washington, USA, June 8-12, 1980, Conference Record, pp. 26.1.1-26.1.5.
17. F. M. Gardner, "Carrier and Clock Synchronization for TDMA Digital Communications," ESA TM 169, December 1976.
18. F. M. Gardner, "Clock and Carrier Synchronization, Prefilter and Antihang-up Investigations," ESA CR-984, November 1977.
19. W. C. Lindsey, *Synchronization Systems*, Prentice-Hall, Englewood Cliffs, New Jersey (1972).
20. R. E. Ziemer and W. H. Tranter, *Principles of Communications*, Houghton-Mifflin, Boston (1976).

---

# Partially Coherent Receivers

As was made clear in the previous chapter on synchronization, an ideal coherent detector with no carrier phase error does not exist in practice. The best we can hope for is a phase error that constantly fluctuates around the mean value zero. In this chapter we will give a statistical description of the steady state phase error and study both optimum and suboptimum detection at high SNR. A parameter called the minimum equivalent Euclidean distance is derived and used. First, however, we will precisely define the notion of partially coherent detection.

## 10.1. Notions of Phase Coherence

Throughout this chapter it is assumed that the carrier frequency  $\omega_0$  is exactly known to the receiver. We define  $\phi_0$  and  $\hat{\phi}_0$  as the carrier phase at the transmitter and receiver, respectively, and the carrier phase error  $\Delta\phi_0$  as  $\phi_0 - \hat{\phi}_0$ . If  $\Delta\phi_0$  is not known at all to the receiver  $\Delta\phi_0$  is generally taken to be a random variable with the uniform probability density function (PDF)

$$p_{\Delta\phi_0}(\Delta\phi_0) = \begin{cases} 1/2\pi, & |\Delta\phi_0| \leq \pi \\ 0, & |\Delta\phi_0| > \pi \end{cases} \quad (10.1)$$

The reception is referred to now as *noncoherent*.

The receiver may extract information about the statistical nature of  $\Delta\phi_0$  by means of a carrier tracking device like a phase-lock loop. Once this device has acquired phase lock, the phase reference that it provides is different from the true phase by a slowly varying error  $\Delta\phi_0$ . Now we will assume that  $\Delta\phi_0$  locally has the density function

$$p_{\Delta\phi_0}(\Delta\phi_0) = \begin{cases} \frac{e^{a \cos \Delta\phi_0}}{2\pi I_0(a)}, & |\Delta\phi_0| \leq \pi \\ 0, & |\Delta\phi_0| > \pi \end{cases} \quad (10.2)$$

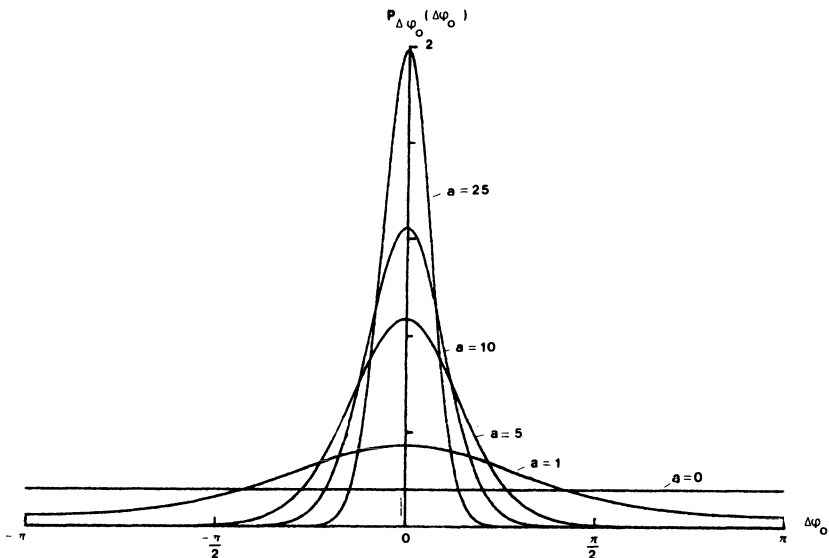


Figure 10.1. The PDF for the estimated phase error, equation (10.2), when  $a = 0, 1, 5, 10$ , and  $25$ .

the Tikhonov distribution,<sup>(1,3)</sup> instead of (10.1).  $I_0(\cdot)$  is the modified Bessel function of zero order and first kind. The parameter  $a$  generates a whole class of models for the steady state carrier phase error, and is often referred to as the loop-SNR of the synchronizer.<sup>(1,6)</sup>

Several PDFs given by (10.2) are shown in Figure 10.1 for different values of  $a$ ; the PDF is always symmetric with respect to  $\Delta\phi_0 = 0$  and the PDF narrows as  $a$  increases. For the case when  $a = 0$ , (10.2) and (10.1) are the same. In the limiting case

$$\lim_{a \rightarrow \infty} p_{\Delta\phi_0}(\Delta\phi_0) = \delta(\Delta\phi_0) \quad (10.3)$$

which means that  $\Delta\phi_0 = 0$  with probability 1 and the detection is coherent. For all other finite and nonzero values of  $a$  we say that the detection is *partially coherent*.

## 10.2. Partially Coherent Detection; Equivalent Distance

In this section the notation of Chapter 3, with slight modification, will be used. Our first goal is to derive the MLSE detector. The received signal is

$$r(t, \alpha, \phi_0) = s(t, \alpha, \phi_0) + n(t) \quad (10.4)$$

where

$$s(t, \alpha, \hat{\phi}_0) = \left( \frac{2E}{T} \right)^{1/2} \cos [\omega_0 t + \phi(t, \alpha) + \hat{\phi}_0] \quad (10.5)$$

and  $n(t)$  is AWGN with zero mean and one-sided power spectral density  $N_0$ .

The detector is allowed to observe several symbol intervals of the received signal in order to ML-estimate one of the transmitted data symbols, say  $\alpha_0$ . This observation interval is  $[-N_1 T, N_2 T]$ , which includes the interval  $[0, T]$  corresponding to  $\alpha_0$ . In the coherent case treated in Chapter 3 the observation interval was  $[0, NT]$ ; later it will be shown that in this case there is no need to observe the received signal prior to  $t = 0$ .

The detector has knowledge of the mean value of  $\phi_0$ , which it uses to force the equality  $E\{\hat{\phi}_0\} = \phi_0$  and it also knows the loop SNR  $a$ . It forms the likelihood function<sup>(3)</sup>

$$\Lambda[r(t)] = \int_{-\pi}^{\pi} p_{\Delta\phi_0}(\Delta\phi_0) \times \exp \left[ (2/N_0) \int_{-N_1 T}^{N_2 T} r(t, \alpha, \phi_0) s(t, \tilde{\alpha}, \hat{\phi}_0) dt \right] d\Delta\phi_0 \quad (10.6)$$

for all possible received sequences  $\tilde{\alpha}_{-N_1}, \tilde{\alpha}_{-N_1+1}, \dots, \tilde{\alpha}_0, \tilde{\alpha}_1, \dots, \tilde{\alpha}_{N_2}$ , in order to find the maximizing one. The value of  $\tilde{\alpha}_0$  in this sequence is taken as an estimate of the transmitted data symbol  $\alpha_0$ . Some analysis shows that the integrand in the exponential is only a function of  $\Delta\phi_0 = \phi_0 - \hat{\phi}_0$ ,<sup>(6)</sup> assuming that  $\omega_0 T \gg 1$ .

Equation (10.6) can be integrated analytically.<sup>(1,7)</sup> A monotone transformation of the result is

$$\Lambda'[r(t)] = \left[ c(\alpha, \tilde{\alpha}) + (T/E)^{1/2} n_c(\tilde{\alpha}) + \frac{1}{2} \frac{a}{E/N_0} \right] + [s(\alpha, \tilde{\alpha}) + (T/E)^{1/2} n_s(\tilde{\alpha})]^2 \quad (10.7)$$

This expression will be used for analysis of the detector (10.6). Here

$$\begin{aligned} c(\alpha, \tilde{\alpha}) &= \frac{1}{T} \int_{-N_1 T}^{N_2 T} \cos [\phi(t, \alpha) - \phi(t, \tilde{\alpha})] dt \\ s(\alpha, \tilde{\alpha}) &= \frac{1}{T} \int_{-N_1 T}^{N_2 T} \sin [\phi(t, \alpha) - \phi(t, \tilde{\alpha})] dt \end{aligned} \quad (10.8)$$

and

$$\begin{aligned} n_c(\tilde{\alpha}) &= \frac{1}{T} \int_{-N_1 T}^{N_2 T} n_c(t) \cos \phi(t, \tilde{\alpha}) \\ &\quad + \frac{1}{T} \int_{-N_1 T}^{N_2 T} n_s(t) \sin \phi(t, \tilde{\alpha}) dt \\ n_s(\tilde{\alpha}) &= \frac{1}{T} \int_{-N_1 T}^{N_2 T} n_c(t) \sin \phi(t, \tilde{\alpha}) dt \\ &\quad - \frac{1}{T} \int_{-N_1 T}^{N_2 T} n_s(t) \cos \phi(t, \tilde{\alpha}) dt \end{aligned} \quad (10.9)$$

are Gaussian random variables with zero mean. The white Gaussian processes are defined through the usual formula

$$n(t) = \sqrt{2} n_c(t) \cos \omega_0 t - \sqrt{2} n_s(t) \sin \omega_0 t \quad (10.10)$$

Another philosophy for building a detector might be to use

$$\begin{aligned} c_{\Delta\phi_0}(\alpha, \tilde{\alpha}) &= (1/T) \int_{-N_1 T}^{N_2 T} \cos [\phi(t, \alpha) - \phi(t, \tilde{\alpha}) + \Delta\phi_0] dt \\ s_{\Delta\phi_0}(\alpha, \tilde{\alpha}) &= (1/T) \int_{-N_1 T}^{N_2 T} \sin [\phi(t, \alpha) - \phi(t, \tilde{\alpha}) + \Delta\phi_0] dt \end{aligned} \quad (10.11)$$

instead of (10.8) in (10.7). This new measure must then be averaged with respect to the PDF (10.2) in order to implement a detector, since  $\Delta\phi_0$  is not known.

### 10.2.1. Derivation of $d_e^2$

To stress the fact that (10.7) is a function of the  $M$ -ary data sequences  $\alpha$  and  $\tilde{\alpha}$  the notation

$$R(\alpha, \tilde{\alpha}) = \Lambda'[r(t)] \quad (10.12)$$

will be more appropriate. In the receiver (10.6), an error occurs if the sequence  $\tilde{\alpha}$  which maximizes  $R(\alpha, \tilde{\alpha})$  satisfies  $\tilde{\alpha}_0 \neq \alpha_0$ . There are in general several sequences  $\tilde{\alpha}$  giving an erroneous estimate of  $\alpha_0$ , and there are also several sequences  $\tilde{\alpha}$  giving correct estimates of  $\alpha_0$ . For large SNR, only the sequence  $\tilde{\alpha}$ , among those with  $\tilde{\alpha}_0 \neq \alpha_0$ , which gives a value  $R(\alpha, \tilde{\alpha})$  closest to the value corresponding to the correct sequence,  $R(\alpha, \alpha)$ , significantly contributes to the probability of error. For large SNR, we thus have

$$P_e = P\{R(\alpha, \alpha) < R(\alpha, \tilde{\alpha})\} \quad (10.13)$$

where the two sequences  $\alpha$  and  $\tilde{\alpha}$  satisfy  $\alpha \neq \tilde{\alpha}_0$  and are chosen to minimize  $R(\alpha, \alpha) - R(\alpha, \tilde{\alpha})$  in the noiseless case.

Now, both  $R(\alpha, \alpha)$  and  $R(\alpha, \tilde{\alpha})$  are Rician random variables,<sup>(3)</sup> and in (10.13) we have the problem of calculating the probability of one Rician variable exceeding another. This problem is solved in Ref. 5. Express  $R(\alpha, \tilde{\alpha})$  and  $R(\alpha, \alpha)$  as the squared magnitude of the two complex random variables

$$\begin{aligned} Z_1 &= c(\alpha, \tilde{\alpha}) + \left(\frac{T}{E}\right)^{1/2} n_c(\tilde{\alpha}) + \frac{1}{2} \frac{a}{E/N_0} + j \left[ s(\alpha, \tilde{\alpha}) + \left(\frac{T}{E}\right)^{1/2} n_s(\tilde{\alpha}) \right] \\ Z_2 &= c(\alpha, \alpha) + \left(\frac{T}{E}\right)^{1/2} n_c(\alpha) + \frac{1}{2} \frac{a}{E/N_0} + j \left[ s(\alpha, \alpha) + \left(\frac{T}{E}\right)^{1/2} n_s(\alpha) \right] \end{aligned} \quad (10.14)$$

respectively. We have

$$P_e = P(|Z_2|^2 < |Z_1|^2) = P(|Z_2| < |Z_1|) \quad (10.15)$$

This probability is given<sup>(5)</sup> by

$$P_e = \frac{1}{2} [1 - Q_M(\sqrt{B}, \sqrt{A}) + Q_M(\sqrt{A}, \sqrt{B})] \quad (10.16)$$

where  $Q_M(\cdot, \cdot)$  is Marcum's  $Q$  function

$$Q_M(x, y) = \int_y^{\infty} u e^{-(u^2+x^2)/2} I_0(xu) du \quad (10.17)$$

and where the parameters  $A$  and  $B$  are given<sup>(2)</sup> by

$$\begin{cases} A \\ B \end{cases} = \frac{1}{2\sigma^2} \left[ \frac{|M_1|^2 + |M_2|^2 - 2 \operatorname{Re} \{M_1^* M_2\}}{1 - |\rho|^2} \pm \frac{|M_2|^2 - |M_1|^2}{(1 - |\rho|^2)^{1/2}} \right] \quad (10.18)$$

Here the minus of the  $\pm$  sign gives  $A$  and the plus gives  $B$ . The parameters above are defined by

$$M_i = E\{Z_i\}$$

$$\sigma^2 = \operatorname{Var} \{Z_i\} = E\{(Z_i - M_i)^*(Z_i - M_i)\}, \quad i = 1, 2 \quad (10.19)$$

$$\rho = \frac{1}{\sigma^2} E\{(Z_2 - M_2)^*(Z_1 - M_1)\}$$

where the expectation is with respect to the channel noise. Expressions for  $A$  and  $B$  can be found in Ref. 7, but a more compact description will follow below.

An approximation to the Marcum  $Q$  function is<sup>(5)</sup>

$$\frac{1}{2}[1 - Q_M(\sqrt{B}, \sqrt{A}) + Q_M(\sqrt{A}, \sqrt{B})] \approx Q(\sqrt{B} - \sqrt{A}) \quad (10.20)$$

where  $Q(\cdot)$  is the usual error function associated with the Gaussian distribution defined in (2.13). This approximation is good if  $B \gg 1$ ,  $A \gg 1$ , and  $\sqrt{B} \gg \sqrt{B} - \sqrt{A} > 0$ . Since  $E/N_0$  is assumed to be large these inequalities are satisfied, and it follows that  $P_e$  has the asymptotic form

$$P_e \sim Q\left(\left(d^2 \frac{E_b}{N_0}\right)^{1/2}\right) \quad (10.21)$$

at large  $E_b/N_0$ . The constant  $d^2$  is an equivalent normalized squared Euclidean distance, defined as [compare (10.20) and (10.21)]

$$d_e^2 = (\sqrt{B} - \sqrt{A})^2 / (E_b/N_0) \quad (10.22)$$

From the expressions for  $A$  and  $B$  in Ref. 6 we have

$$d_e^2 = \log_2 M \cdot \frac{\eta_N^2}{\xi_N + (\xi_N^2 - \xi_D \eta_N^2)^{1/2}} \quad (10.23)$$

where

$$\begin{aligned} \xi_N &= (N_1 + N_2 + \beta)[(N_1 + N_2)^2 - \Delta^2(\alpha, \tilde{\alpha})] + (\beta^2/2)[N_1 + N_2 - c(\alpha, \alpha)] \\ \xi_D &= (N_1 + N_2)^2 - \Delta^2(\alpha, \tilde{\alpha}) \\ \eta_N &= (N_1 + N_2)^2 - \Delta^2(\alpha, \tilde{\alpha}) + \beta[N_1 + N_2 - c(\alpha, \tilde{\alpha})] \end{aligned} \quad (10.24)$$

and the quantities  $\Delta^2(\alpha, \tilde{\alpha})$  and  $\beta$  are defined as

$$\begin{aligned} \Delta^2(\alpha, \tilde{\alpha}) &= c^2(\alpha, \tilde{\alpha}) + s^2(\alpha, \tilde{\alpha}) \\ \beta &= a/(E/N_0) \end{aligned} \quad (10.25)$$

Note that  $\beta$  is the Tikhonov parameter, normalized by  $E/N_0$ .

Observe that  $d_e^2$  is only a function of  $\gamma = \alpha - \tilde{\alpha}$  since  $c(\alpha, \tilde{\alpha})$  and  $s(\alpha, \tilde{\alpha})$  are so. More important, however, is that  $d_e^2$  plays the same role as the squared Euclidean distance  $d^2$  for coherent detection. Thus for large SNR, the error probability is given by

$$P_e \sim Q\left(\left(d_{e,\min}^2 \frac{E_n}{N_0}\right)^{1/2}\right) \quad (10.26)$$

where the minimization of  $d_e^2$  is over the difference sequences  $\gamma$  with  $\gamma_0 \neq 0$ . It is easily checked that  $d_e^2 = 0$  when  $\gamma = 0$ .

In the limiting cases for coherent and noncoherent detection,  $d_e^2$  becomes

$$\begin{aligned} \lim_{a \rightarrow \infty} d_e^2 &= [N_1 + N_2 - c(\alpha, \tilde{\alpha})] \log_2 M \\ \lim_{a \rightarrow 0} d_e^2 &= [N_1 + N_2 - \Delta(\alpha, \tilde{\alpha})] \log_2 M \end{aligned} \quad (10.27)$$

and thus  $\lim d_e^2$  coincides with  $d^2$  used for coherent detection. An interesting property of  $d_e^2$  in the noncoherent case is that  $d_e^2 = 0$  for two parallel but offset phase trajectories,  $\phi(t, \tilde{\alpha}) = \phi(t, \alpha) + \Delta\phi$ . Thus parallel phase trajectories are indistinguishable from each other in this case, and need to be different in shape somewhere in the interval  $[-N_1 T, N_2 T]$  to give  $d_e^2 > 0$ .

Another interesting property with noncoherent detection is the case when (10.11) is used in (10.7). By performing the calculation of (10.7) with  $a = 0$ , it is found that (10.7) is independent of  $\Delta\phi_0$ . Thus the two detection philosophies given in (10.6) [either use (10.6) or use (10.7) with (10.11) instead of  $c(\alpha, \tilde{\alpha}), s(\alpha, \tilde{\alpha})$ ], coincide in this case. It can also be shown that  $d_e^2$  is independent of  $\Delta\phi_0$  if (10.11) is used instead of (10.8) in the expression for  $d_e^2$ , in the noncoherent case. Thus the two detection strategies coincide when  $a = 0$ .

### 10.2.2. Some Properties of $d_e^2$

Phase trees are useful also for the understanding of the behavior of  $d_e^2$  for partially coherent detection. Figure 10.2 shows the familiar example binary 1REC with  $H = 1$ . (In what follows  $H$  is always 1.) Here the solid tree is used by the transmitter ( $\phi_0 = 0$  without loss of generality) and the dotted one by the detector. The phase offset between the two trees is  $\Delta\phi_0$  and the ML detector performs (10.6) by averaging over the offsets  $\Delta\phi_0$ . This means that the dotted tree in Figure 10.2 must be generated for all values of  $\Delta\phi_0$  in the interval  $|\Delta\phi_0| \leq \pi$ . In practice this can be done by a proper quantization of  $\Delta\phi_0$ .

The expression for  $d_e^2$  is independent of  $\Delta\phi_0$  since the parameter has been integrated out by averaging. In effect, only the solid tree has to be considered, and actually only the phase difference tree (see Chapter 3) has to be traced in the calculation of  $d_e^2$ . The components of the difference

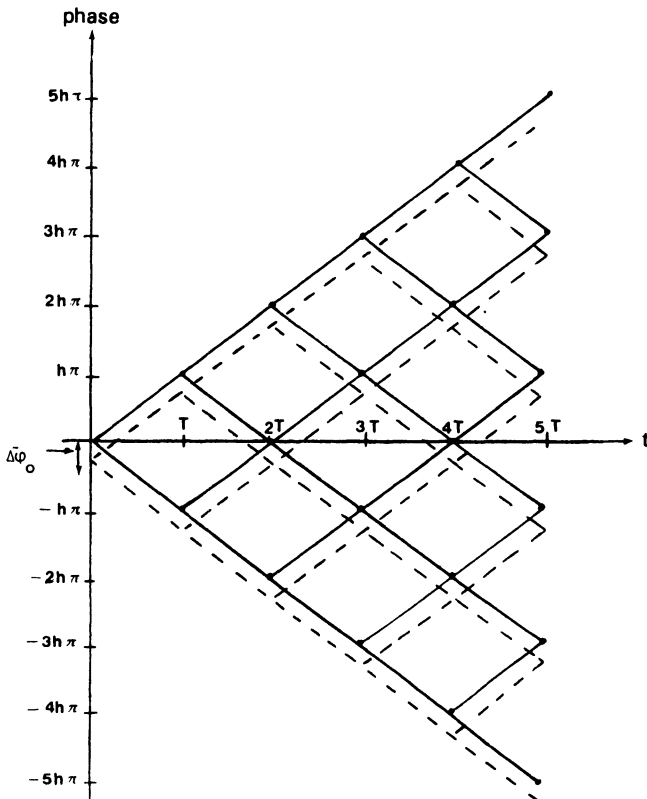


Figure 10.2. Transmitter phase tree (solid) and detector phase tree (dotted) for the binary 1REC scheme. The error of the carrier phase is  $\Delta\phi_0$ .

sequence  $\gamma$  are

$$\begin{aligned}\gamma_i &= 0, \quad i < -N_1, \quad i \geq N_2 \\ \gamma_i &= 2, 4, \dots, 2(M-1), \quad i = 0 \\ \gamma_i &= 0, \pm 2, \pm 4, \dots, \pm 2(M-1), \quad i = -N_1, -N_1 + 1, \dots, \\ &\quad -1, 1, 2, \dots, N_2 - 1\end{aligned}\tag{10.28}$$

when the observation interval for detection of  $\alpha_0$  is  $[-N_1 T, N_2 T]$ .

It is possible to construct an upper bound  $d_{e,B}^2$  on  $d_{e,\min}^2$  for all values of  $N_2$  including infinity. The principle is to use infinitely long  $\gamma$  sequences associated with mergers, just like in Section 3.2. Assuming for instance a binary scheme, the first merger occurs at  $t = (L+1)T$  for  $\gamma_0 = 2$ ,  $\gamma_1 = -2$  and all other components equal to zero. Assuming also that  $N_2 \geq (L+1)$

we have

$$\begin{aligned} c(\alpha, \tilde{\alpha}) &= N_1 + \frac{1}{T} \int_0^{(L+1)T} \cos \phi(t, \gamma) dt + N_2 - L - 1 \\ s(\alpha, \tilde{\alpha}) &= \frac{1}{T} \int_0^{(L+1)T} \sin \phi(t, \gamma) dt \end{aligned} \quad (10.29)$$

and an upper bound on  $d_{e,\min}^2$  is obtained by using  $c(\alpha, \tilde{\alpha})$  and  $s(\alpha, \tilde{\alpha})$  in (10.23) and letting  $N_2 \rightarrow \infty$ . For a 1REC frequency pulse and  $M$ -ary data it turns out that

$$d_{e,\min}^2 \leq \min_{k=1,2,\dots,M-1} 2 \left( 1 - \frac{\sin 2\pi hk}{2\pi hk} \right) \log_2 M \quad (10.30)$$

which is exactly the upper bound on  $d_{\min}^2$  for coherent detection, previously derived in Section 3.2.1. This is natural, since a partially coherent detector cannot perform better than a coherent one. It can also be shown that for  $N_2 \geq L + 1$  and finite, the same merger sequences yield exactly the same upper bound, as  $N_2 \rightarrow \infty$ . Actually the expression for  $d_e^2$  is the same for all combinations of  $N_1$  and  $N_2$  provided that  $N_2 \geq L + 1$  and  $N_1 + N_2$  is fixed.

By choosing all  $\gamma_i = 0$  except  $\gamma_0$ , the effect of first-order weak modulation indices can be studied. In this case

$$\begin{aligned} c(\alpha, \tilde{\alpha}) &= N_1 + \frac{1}{T} \int_0^{LT} \cos \phi(t, \gamma) dt + (N_2 - L) \cos(h\pi\gamma_0) \\ s(\alpha, \tilde{\alpha}) &= \frac{1}{T} \int_0^{LT} \sin \phi(t, \gamma) dt + (N_2 - L) \sin(h\pi\gamma_0) \end{aligned} \quad (10.31)$$

Again choosing the 1REC pulse as an example and letting  $N_2 \rightarrow \infty$ , we have

$$d_{e,\min}^2 \leq \min_{k=1,\dots,M-1} \frac{\left[ 1 - \frac{\sin 2\pi hk}{2\pi hk} + (N_1 + \beta/2)(1 - \cos 2\pi hk) \right]^2}{1 - \frac{\sin 2\pi hk}{2\pi hk} + N_1(1 - \cos 2\pi hk)} \log_2 M \quad (10.32)$$

For weak modulation indices  $h_w$  the upper bound equals  $\log_2 M$ , independently of both  $N_1$  and  $\beta$ . By taking the minimum of the two upper bounds (10.30) and (10.32), a better bound is obtained.

It can be noted that

$$\lim_{\beta \rightarrow \infty} d_{e,B}^2 = \lim_{N_1 \rightarrow \infty} d_{e,B}^2 = \begin{cases} d_{c,B}^2, & h \neq h_w \\ \log_2 M, & h = h_w \end{cases} \quad (10.33)$$

where  $d_{c,B}^2$  is the coherent upper bound from Section 3.2.1. This is the same bound as with coherent detection but now more refined.

At the weak modulation indices  $h_w$  the upper bound for coherent detection,  $d_{c,B}^2$ , has been forced down to its lowest possible value. When both  $N_1$  and  $\beta$  are zero,  $d_{e,B}^2$  equals  $d_{c,B}^2/2$ . Thus, with noncoherent detection of the first data symbol in the observed interval, the performance cannot be better than a 3-dB loss in  $E_b/N_0$  compared to coherent detection. This is true even if  $N_2$  is infinite; the performance of even this noncoherent detector is the same as the coherent one with an observation of just one symbol (see Section 3.3.1.). These general results not only apply to the  $M$ -ary 1REC scheme, but also to all full response schemes having a symmetric frequency pulse  $g(t)$ .

We now plot  $d_{e,B}^2$  for the 1REC (or CPFSK) scheme with  $M = 2$ . In Figure 10.3 the case  $\beta = 0$  with  $N_1 = 0, 1, 2, 3$  and 10 bit intervals is given. The valleys in  $d_{e,B}^2$  around  $h = h_w$  are the result of using the component (10.32) in the construction of the upper bound; they narrow as  $N_1$  grows. When  $N_1 \rightarrow \infty$ ,  $d_{e,B}^2$  tends to  $d_{c,B}^2$  as (10.33) tells, provided  $h \neq h_w$ . The same phenomenon occurs also for  $M = 4, 8$  etc., but the density of weak modulation indices is higher and larger  $N_1$  are required to force  $d_{e,B}^2$  up to the value of  $d_{c,B}^2$ .

Figure 10.4 shows the case of  $N_1 = 0$  and degrees of coherence  $\beta = 0, 0.2, 0.4, 1$ , and 4; the scheme is still binary 1REC. This means that detection takes place on the first bit in the observed interval. For low values of  $\beta$  the bound component (10.32) completely determines the upper bound. As  $\beta$  grows, (10.32) affects  $d_{e,B}^2$ , but only around  $h = h_w$ ; we have  $d_{e,B}^2 = d_{c,B}^2$  for larger regions of  $h$ .

For the binary 1REC scheme considered it is possible to conclude that when either  $N_1$  or  $\beta$  or both are not too small, the upper bound  $d_{e,B}^2$  on

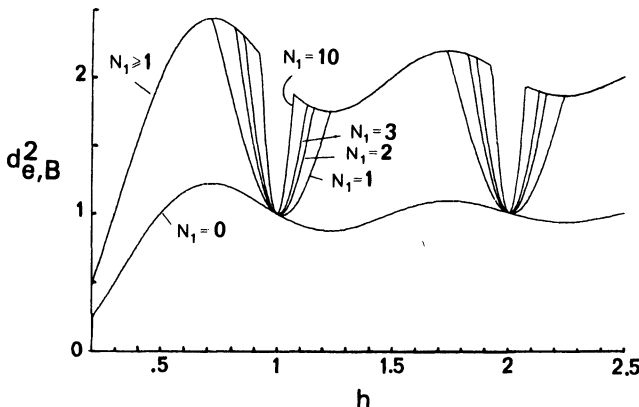


Figure 10.3. Upper bounds on the minimum normalized squared equivalent distance for the binary 1REC noncoherent scheme when  $N_1 = 0, 1, 2, 3$  and 10 symbol intervals;  $N_2 = \infty$ .

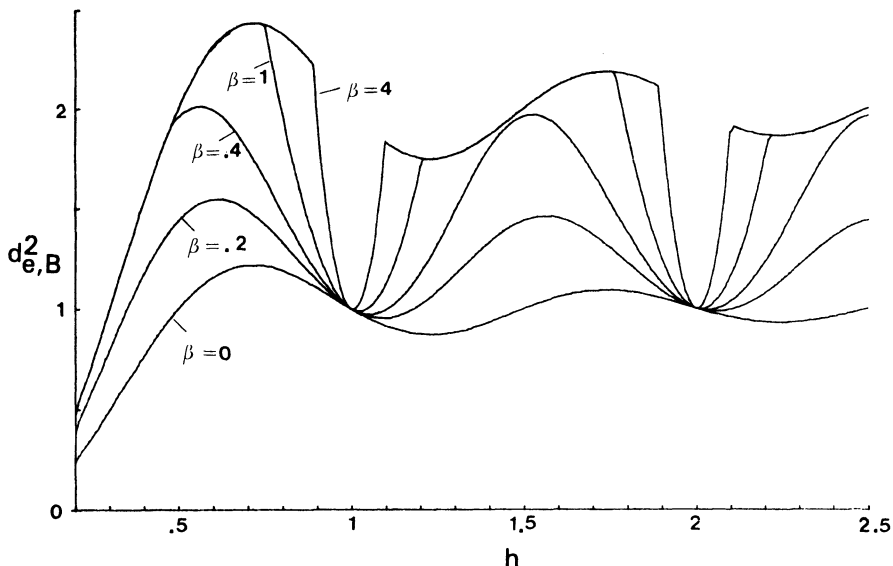


Figure 10.4. Upper bounds on the minimum normalized squared equivalent distance for the binary 1REC scheme with detection in the first symbol interval;  $\beta = 0, 0.2, 0.4, 1$ , and  $4$ .

$d_{e,\min}^2$  coincides with the coherent upper bound  $d_{c,B}^2$  considered in Chapter 3. Although only the 1REC frequency pulse has been depicted here, the conclusion is true also for other pulse shapes, for partial response schemes, and for all  $M$ . The bounding technique for partial response schemes is analogous to the one presented here; later mergers than the first are used in that case, as in Section 3.2.2. Some partial response bounds appear in the next section, which gives numerical results for  $d_{e,\min}^2$  for partial response schemes.

### 10.3. Minimum Equivalent Distance Results

To illustrate the behavior of  $d_{e,\min}^2$  for various schemes and also its relation to  $d_{e,B}^2$  numerical results in the form of plots will be given. In each plot  $g(t)$ ,  $M$ ,  $N_1$ , and  $\beta$  are fixed and  $d_{e,\min}^2$  curves as functions of  $h$  for various  $N_2$  are shown. The upper bound on  $d_{e,\min}^2$ ,  $d_{e,B}^2$  is also given as a function of  $h$  and in some cases also the coherent bound  $d_{c,B}^2$  appears.

#### Full Response Schemes

As a first example we choose binary 1REC with  $\beta = 0$  and  $N_1 = 0$ . Thus we have noncoherent detection of the first bit in the observation

interval. This observation interval coincides with that of a coherent detector having  $N = N_1$ , which is optimum for a coherent detector since we do not gain anything there by making observations prior to  $t = 0$ . Figure 10.5 shows  $d_{e,\min}^2$  when  $N_2 = 1, 2, 3$ , and 4. The upper bound on the minimum normalized squared Euclidean distance for coherent detection is shown dashed. For the difference sequence ( $\gamma_0 = 2$ ;  $\gamma_i = 0$ ,  $i \neq 0$ ) we have

$$\begin{aligned} c(\alpha, \tilde{\alpha}) &= \frac{\sin 2\pi h}{2\pi h} + (N_2 - 1) \cos 2\pi h \\ s(\alpha, \tilde{\alpha}) &= \frac{1 - \cos 2\pi h}{2\pi h} + (N_2 - 1) \sin 2\pi h \end{aligned} \quad (10.34)$$

This  $\gamma$  sequence was found to give the minimum  $d_e^2$  except when  $N_2 = 2$  and  $h \leq 0.65$ . With  $\beta = 0$  (10.23) for this difference sequence gives

$$d_{e,\min}^2 = N_2 - \left[ \left( \frac{\sinh \pi}{h\pi} \right)^2 + (N_2 - 1)^2 + 2(N_2 - 1) \frac{\sin 2\pi h}{2\pi h} \right]^{1/2} \quad (10.35)$$

which is a mathematical description of the  $d_{e,\min}^2$  curves in Figure 10.5 with

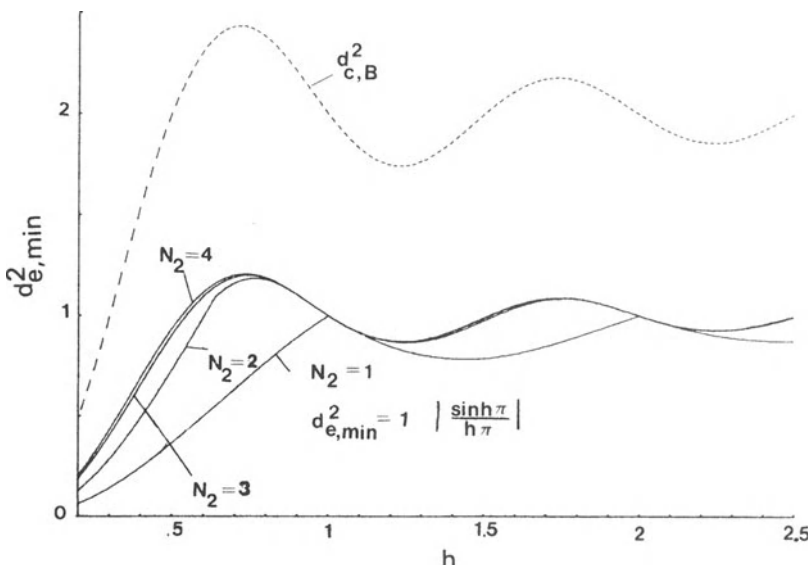


Figure 10.5. Minimum equivalent Euclidean distance  $d_{e,\min}^2$  for the binary 1REC scheme. Noncoherent ( $\beta = 0$ ) detection on the first bit ( $N_1 = 0$ ). The upper bound for coherent detection is shown dashed. In this case  $d_{e,\min}^2$  can never exceed  $d_{c,B}^2/2$ .

the exception noted. When  $N_2 = 1$ , (10.35) becomes

$$d_{e,\min}^2 = 1 - \left| \frac{\sinh \pi}{h\pi} \right|^2, \quad N_2 = 1 \quad (10.36)$$

By letting  $N_2 \rightarrow \infty$  in (10.35), we get

$$\lim_{N_2 \rightarrow \infty} d_{e,\min}^2 = 1 - \frac{\sin 2\pi h}{2\pi h} \quad (10.37)$$

which is exactly half of  $d_{c,B}^2$ , a loss of 3 dB in terms of  $E_b/N_0$  compared to the coherent case. For  $h = h_w = 1, 2, \dots$ , however, the performance of the noncoherent detector is the same as for the coherent when both have a one-symbol observation interval (see Section 3.3.1). Most of the early FSK systems in fact suggested an integer  $h$  and a 1-bit observation interval. The binary 1REC scheme with  $h = 1$  is often referred to as Sunde's FSK.

In Figure 10.6  $N_1$  has been increased from 0 to 1. The scheme is still binary 1REC with noncoherent detection; the upper bound  $d_{e,\min}^2$  is shown dashed. In the region  $0.5 \leq h \leq 0.8$  there is a saturation effect in that  $d_{e,\min}^2$

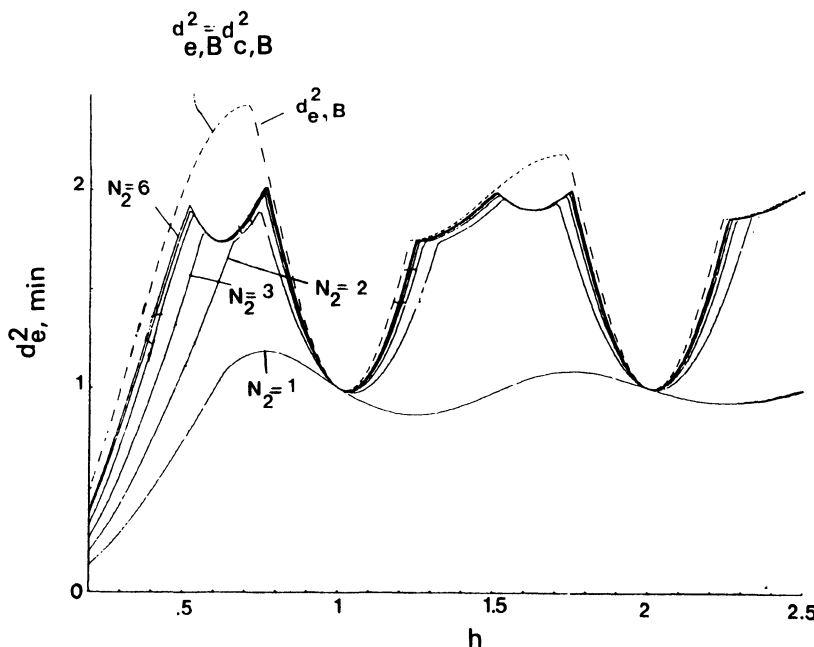


Figure 10.6. Minimum equivalent Euclidean distance for the binary 1REC scheme. Noncoherent detection ( $\beta = 0$ ) at the second bit ( $N_1 = 1$ ). Note that  $d_{e,B}^2$  can be made smaller in the region  $0.5 < h < 0.8$ .

does not seem to grow up to  $d_{e,B}^2$  when  $N_2$  is increased. It is possible to further tighten  $d_{e,B}^2$  in this region by taking  $\gamma_{-1} = \gamma_0 = 2$  and all other  $\gamma_i = 0$ . When this upper bound component is incorporated it is found that  $d_{e,\min}^2$  for  $N_2 \geq 3$  is very close to the new upper bound. Unlike Figure 10.5 it is now possible to make  $d_{e,\min}^2$  larger than  $d_{c,B}^2/2$ , and when  $h \leq 0.5$   $d_{e,\min}^2$  is actually close to  $d_{c,B}^2$ . Here  $d_{e,B}^2$  equals  $d_{c,B}^2$  and  $d_{e,\min}^2$  will grow up to  $d_{e,B}^2$  when  $N_2 \rightarrow \infty$  (since  $d_{e,B}^2$  was constructed in this way).

By increasing  $N_1$  further to  $N_1 = 2$  in Figure 10.7, the distance is improved in the region  $0.5 \leq h \leq 0.8$ . The upper bound is shown dashed in Figure 10.7; for  $d_{e,B}^2$  see Figure 10.3. It is now possible to make  $d_{e,\min}^2$  close to  $d_{e,B}^2$  in the region  $h \approx 0.715$ , where  $d_{c,B}^2$  takes its maximum value 2.43. With  $N_2$  equal about 3 or 4 we thus have a noncoherent scheme which outperforms MSK, BPSK, or QPSK.

We will now concentrate on the partially coherent case. For easy comparison with the previous cases the scheme is still binary 1REC. Figure 10.8 shows the case where  $\beta = 0.2$  and  $N_1 = 0$ ,  $N_2 = 1, 2, 3$ , and 4. The upper bound  $d_{c,B}^2$  is shown dashed and  $d_{e,B}^2$  is shown in Figure 10.4; now  $d_{e,B}^2$  is always smaller than  $d_{c,B}^2$ . Compared to Figure 10.5 (where  $\beta = 0$ ) the performance has been improved, however. By increasing  $\beta$  further it is possible to make  $d_{e,B}^2 = d_{c,B}^2$  over most regions of  $h$ , with  $N_1 = 0$ . It has also been found that  $d_{e,\min}^2$  can be made almost equal to  $d_{e,B}^2$  even with

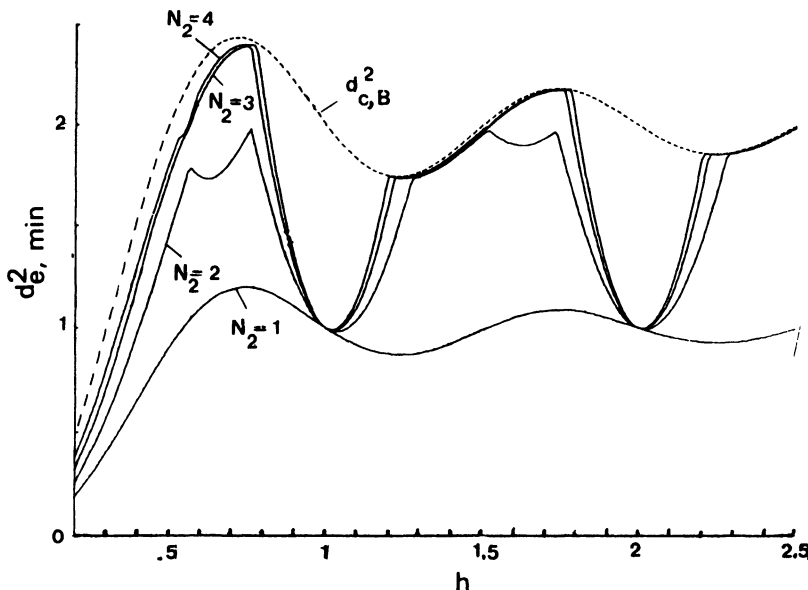


Figure 10.7. Minimum equivalent Euclidean distance for binary 1REC; noncoherent detection ( $\beta = 0$ ) at the third bit ( $N_1 = 2$ ). The upper bound for coherent detection  $d_{c,B}^2$  is shown dashed.

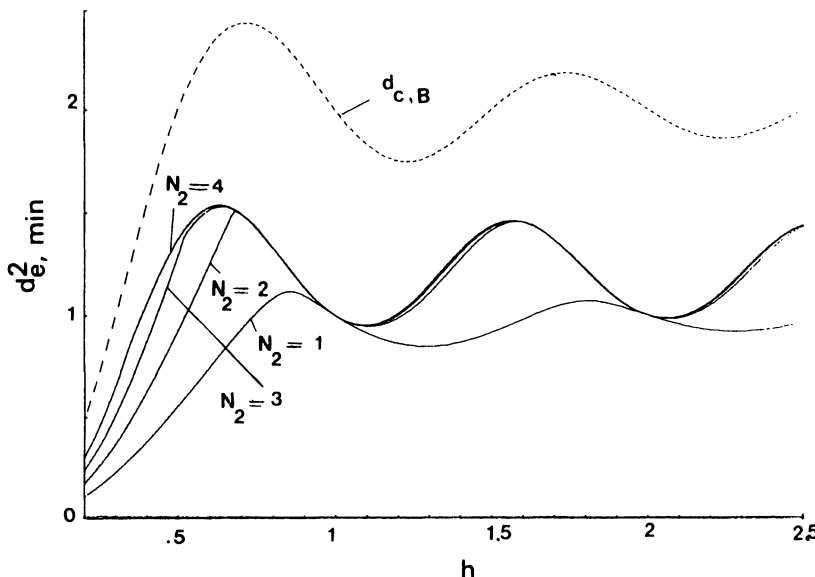


Figure 10.8. Minimum equivalent Euclidean distance versus modulation index  $h$  for the binary 1REC scheme with linear phase trajectories. Partially coherent detection ( $\beta = 0.2$ ) at the first bit ( $N_1 = 0$ ).  $d_{e,\min}^2$  will never come close to  $d_{c,B}^2$ . Compare Figure 10.4 where  $N_2 = \infty$ .

fairly small values of  $N_2$ , and by allowing  $N_1$  larger than zero, the distances are improved even more. An increase in  $\beta$  can be traded for a decrease in  $N_1$ , or vice versa, for the same distance. For further examples see Ref. 6 or 7. The general trend outlined here has been found also for binary schemes with other full response frequency pulses, including for example the plateau [or " $(\alpha, \beta)$ "] function in Chapter 3.

Now we turn to the performance of multilevel systems, choosing for attention the quaternary 1REC scheme. In Figure 10.9 the case  $\beta = 0$ ,  $N_1 = 0$  is considered, and the behavior of  $d_{e,\min}^2$  is evidently similar to the corresponding binary case in Figure 10.5. Both  $d_{c,B}^2$  and  $d_{e,B}^2$  are shown in Figure 10.9 and we have  $d_{e,B}^2 = d_{c,B}^2/2$  just as for  $M = 2$ .  $d_{e,B}^2$  is seen to be a tight bound.

Next  $N_1$  is increased to 1 and the effect on  $d_{e,\min}^2$  is shown in Figure 10.10. Just as for  $M = 2$  it is now possible to have  $d_{e,\min}^2$  larger than  $d_{c,B}^2/2$ . Figure 10.10 shows both upper bounds  $d_{c,B}^2$  and  $d_{e,B}^2$ ; it is possible to tighten  $d_{e,B}^2$  by incorporating a bound from the  $\gamma$  sequence ( $\gamma_{-1} = \gamma_0 = 2, 4, \text{ or } 6$ ;  $\gamma_i = 0$ , otherwise). For small  $h$  values,  $d_{e,B}^2$  equals  $d_{c,B}^2$  and  $d_{e,\min}^2$  can be made arbitrarily close to  $d_{e,B}^2$  by increasing  $N_2$ .

The trend with  $N_1$  and  $\beta$  discovered for binary schemes has been found to apply also to multilevel full response schemes. Larger values of  $N_1$  and/or

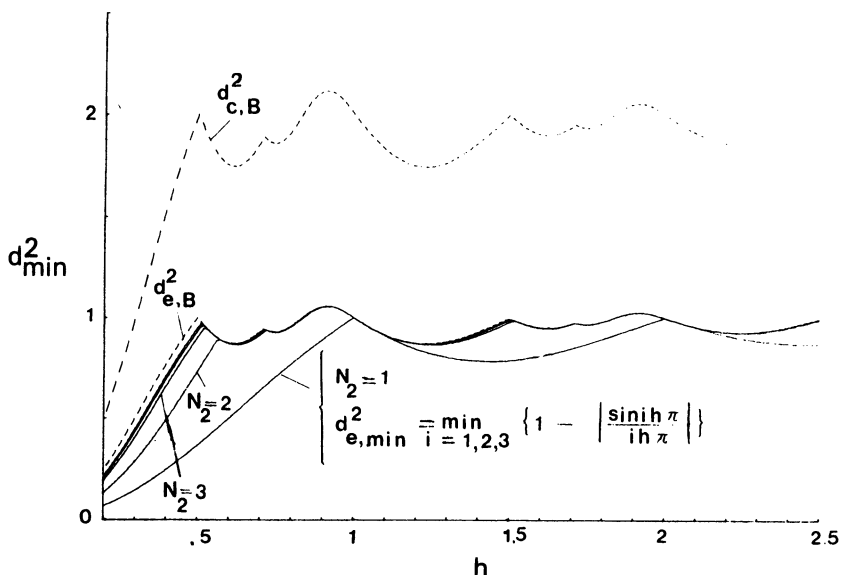


Figure 10.9. Minimum normalized squared equivalent distance for the quaternary 1REC system with noncoherent detection ( $\beta = 0$ ); detection of the first symbol ( $N_1 = 0$ ) and  $N_2 = 1, 2, 3, 4$ , and 5. The upper bounds are shown dashed.

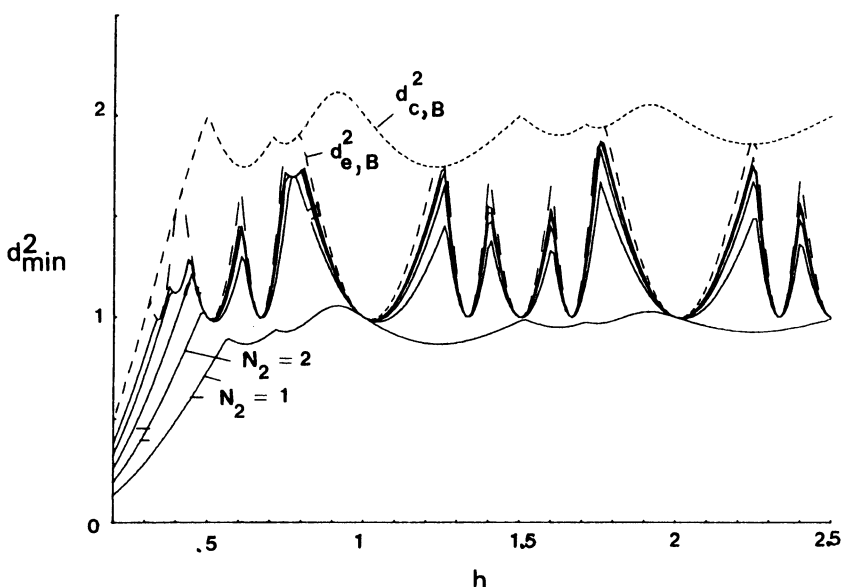


Figure 10.10. Minimum equivalent distance for the quaternary 1REC system with noncoherent detection ( $\beta = 0$ ); detection of the second symbol ( $N_1 = 1$ ) and  $N_2 = 1, 2, 3, 4$ , and 5. The upper bounds are shown dashed.

$\beta$  are needed for the multilevel schemes, however, to force  $d_{e,B}^2 = d_{c,B}^2$ , and larger values of  $N_2$  are needed to make  $d_{e,\min}^2$  close to  $d_{e,B}^2$ .

### Partial Response Schemes

To exemplify the behavior of  $d_{e,\min}^2$  for a partial response scheme the frequency pulse 3RC is chosen with a binary alphabet. Figure 10.11 shows  $d_{e,\min}^2$  when  $N_1 = 0$ ,  $\beta = 0$ , and  $N_2 = 1, 2, \dots, 10$  together with the bounds

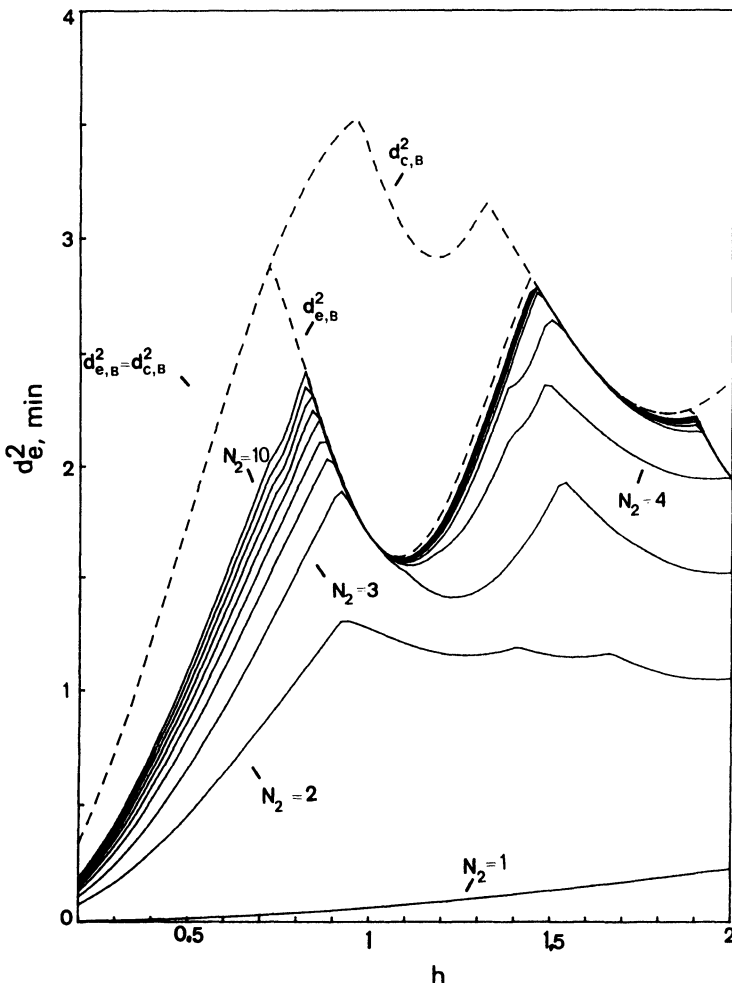


Figure 10.11. The minimum equivalent distance  $d_{e,\min}^2$  for binary 3RC with  $N_1 = 0$  and  $\beta = 0$  when  $N_2 = 1, 2, \dots, 10$ . The upper bounds  $d_{c,B}^2$  and  $d_{e,B}^2$  are also shown.

$d_{e,B}^2$ . In the full response cases considered before we had  $d_{e,B}^2 = d_{c,B}^2/2$ . As is seen in Figure 10.11 this does not apply to the binary 3RC scheme. There are regions of  $h$  for which we have  $d_{e,B}^2 = d_{c,B}^2$ , and it is possible to make  $d_{e,\min}^2$  arbitrarily close to  $d_{e,B}^2$  by making  $N_2$  large. This behavior is quite different from the full response case and it shows that *this* partial response scheme behaves in a better way.

Figure 10.12 shows the same scheme with  $N_1 = 5$ ,  $\beta = 0$  and Figure 10.13 with  $N_1 = 0$ ,  $\beta = 0.4$ . In both cases  $N_2 = 1, 2, \dots, 10$  and the usual

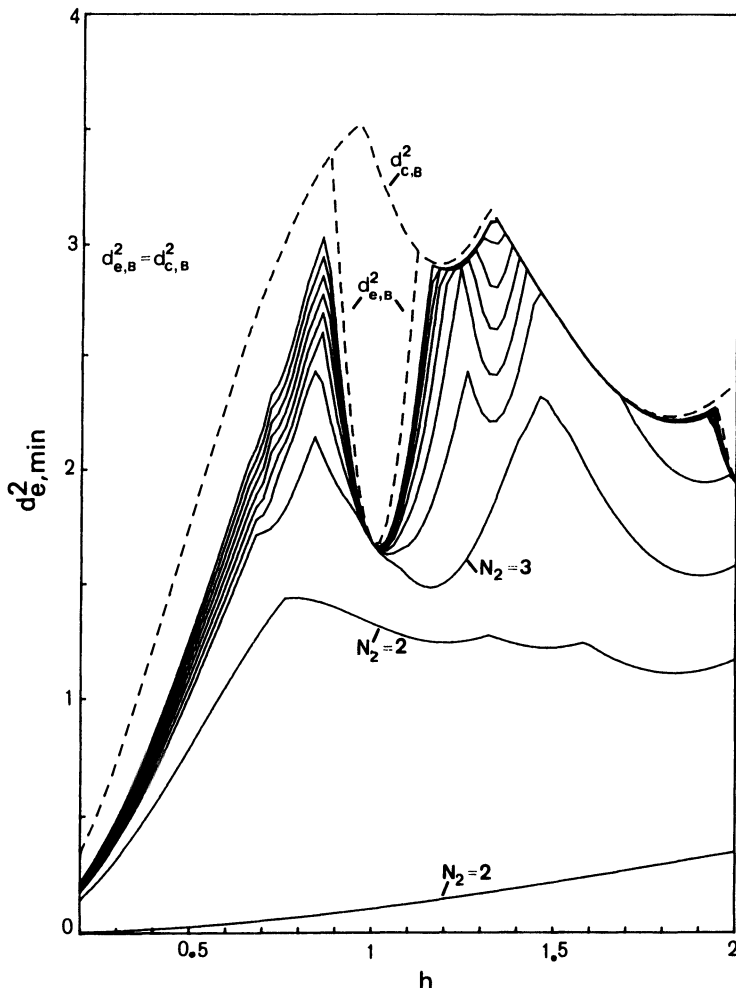


Figure 10.12. The minimum equivalent distance  $d_{e,\min}^2$  for noncoherent detection of binary 3RC when  $N_1 = 5$  and  $N_2 = 1, 2, \dots, 10$ . The upper bounds  $d_{c,B}^2$  and  $d_{e,B}^2$  are also shown.

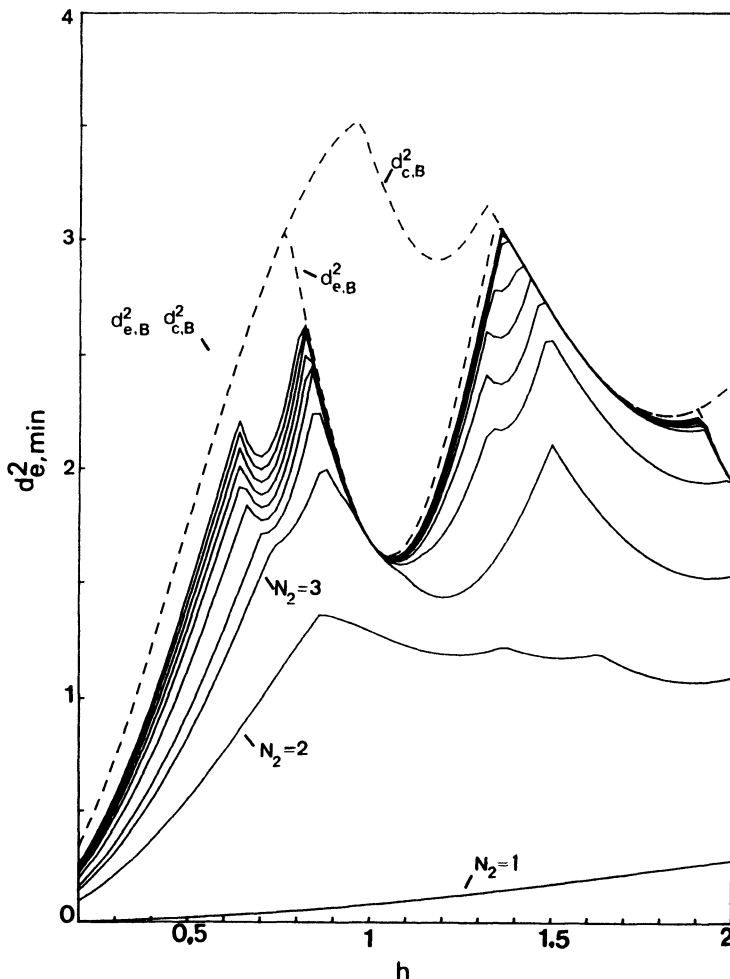


Figure 10.13.  $d_{e,\min}^2$  for partially coherent detection ( $\beta = 0.4$ ) of binary 3RC when  $N_1 = 0$  and  $N_2 = 1, 2, \dots, 10$ .  $d_{c,B}^2$  and  $d_{e,B}^2$  are also shown.

bounds appear. It can be seen that either increasing  $N_1$  or  $\beta$  improves the distances.

Finally a quaternary partial response scheme is considered, with frequency pulse 2RC. Figure 10.14 shows the case of noncoherent ( $\beta = 0$ ) detection of the first symbol ( $N_1 = 0$ ). For  $h \geq 0.3$ ,  $d_{e,B}^2$  always falls below  $d_{c,B}^2$  but they are equal otherwise. If  $N_2$  is about 7 or larger,  $d_{e,\min}^2$  is close to  $d_{e,B}^2$  except at low modulation indices.

In Figures 10.15 and 10.16 the same quaternary scheme is considered for  $N_1 = 5$ ,  $\beta = 0$  (a larger  $N_1$ ) and  $N_1 = 0$ ,  $\beta = 1$  (a larger coherence).

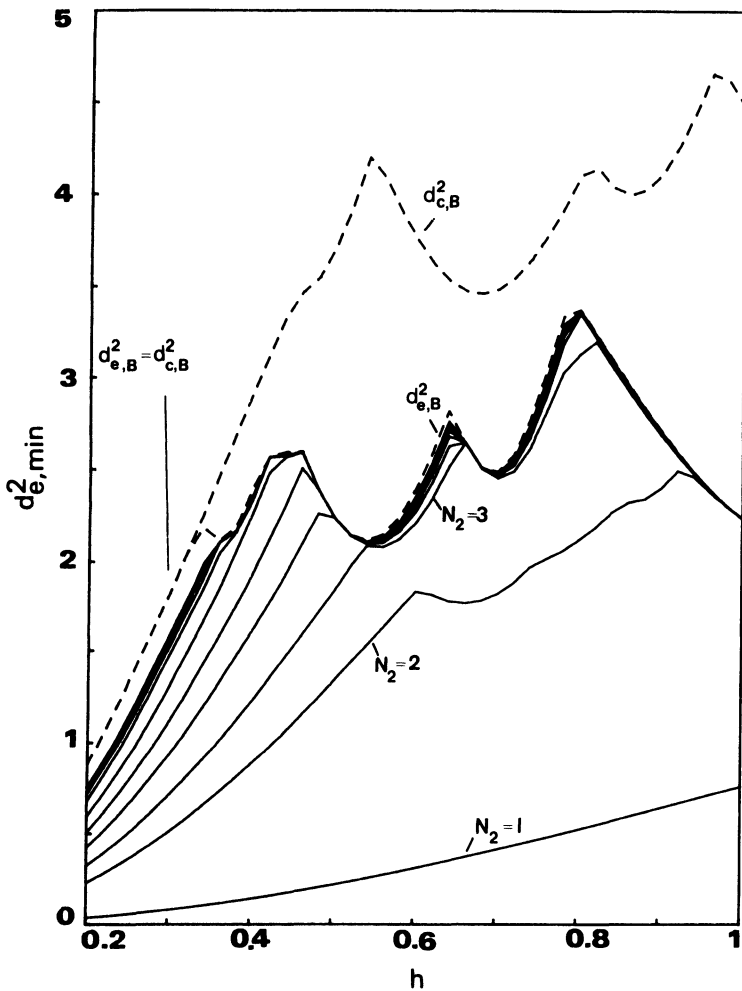


Figure 10.14.  $d_{e,\min}^2$ ,  $d_{c,B}^2$  and  $d_{e,B}^2$  for quaternary 2RC with  $\beta = 0$ ,  $N_1 = 0$ , and  $N_2 = 1, 2, \dots, 10$ .

$N_2$  runs from 1 to 10. In both cases the performance is improved relative to  $N_1 = 0$ ,  $\beta = 0$ ; a smaller  $N_2$  is required and new distance peaks appear for  $h \geq 0.35$ .

#### 10.4. Discussion

From the numerical results in the previous section it is possible to conclude that noncoherent digital phase modulated systems can have an

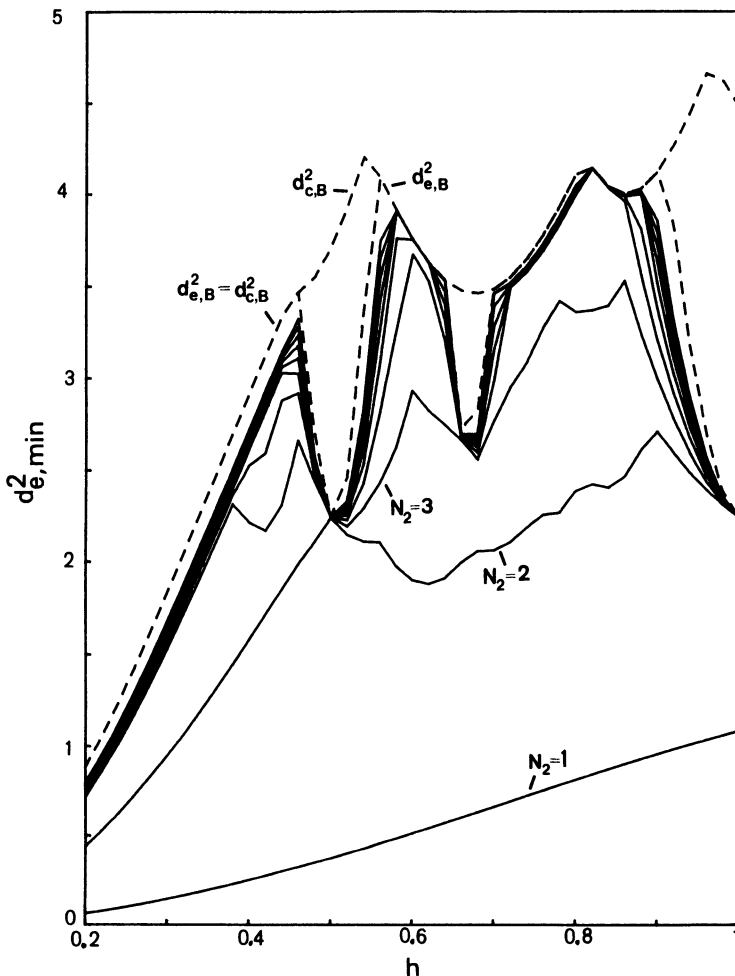


Figure 10.15.  $d_{e,\min}^2$ ,  $d_{c,B}^2$  and  $d_{e,B}^2$  for quaternary 2RC with  $\beta = 0$ ,  $N_1 = 5$ , and  $N_2 = 1, 2, \dots, 10$ .

asymptotic detection performance in terms of  $E_b/N_0$  which is the same as a coherent detector would have. It is important that the observation interval  $[-N_1 T, N_2 T]$  extends to both sides of the data symbol and that  $N_1$  is not too small. Systems were found saving several decibels in  $E_b/N_0$  relative to coherent detection of MSK, BPSK, or QPSK.

An interesting question is how to choose  $N_1$  in a given situation to maximize  $d_{e,\min}^2$  when  $N_1 + N_2$  is large and constant. In Osborne and Luntz<sup>(2)</sup> it is found that for noncoherent detection of binary 1REC, it is optimum to detect the data symbol in the middle of the observation interval when

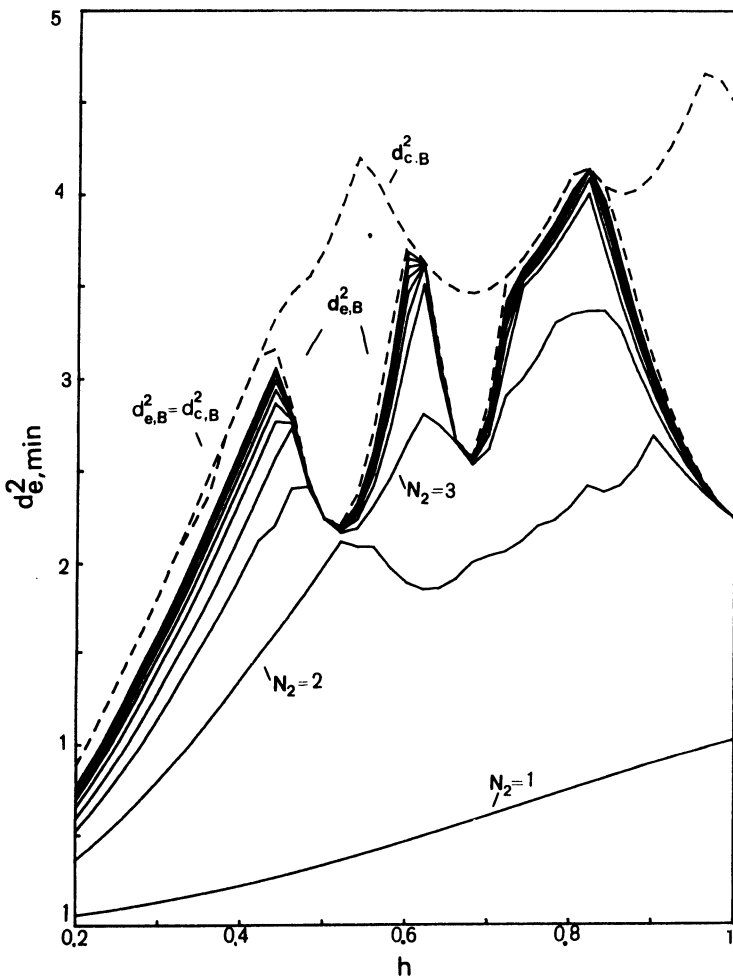


Figure 10.16.  $d_{e,\min}^2$ ,  $d_{c,B}^2$  and  $d_{e,B}^2$  for quaternary 2RC with  $\beta = 1$ ,  $N_1 = 0$ , and  $N_i = 1, 2, \dots, 10$ .

$N_1 + N_2$  is odd. This was found through bounds on the error probability. The general problem is easily solved by displaying  $d_{e,\min}^2$  in the format of Figure 10.17 and 10.18. The scheme here is binary 1REC with  $N_1 + N_2 = 15$  and  $N_1$  runs from 0 to 14; both partially and noncoherent detectors are considered. When  $N_1 + N_2$  is as large as 15 two cases can be distinguished: Figure 10.18 shows the behavior close to a weak modulation index and Figure 10.17 shows the behavior for the other  $h$  values. In Figure 10.17, where  $h = 0.715$ , it is clear that if  $\beta = 0$  and  $h$  is not close to  $h_w$  it does not matter where in the observation interval we choose to detect the data

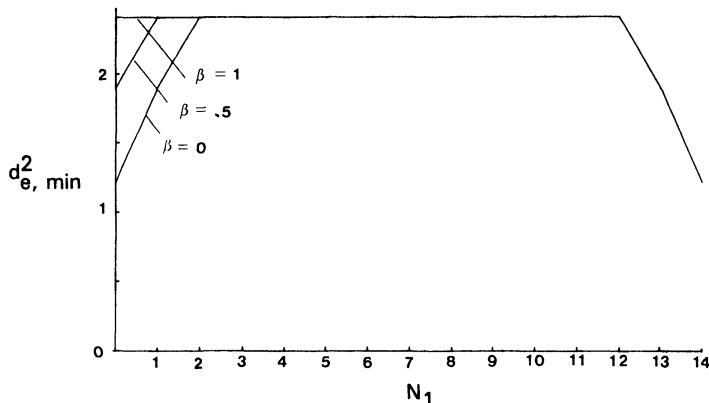


Figure 10.17. Minimum Euclidean distance for the binary 1REC system. The number of observed bit intervals is fixed,  $N_1 + N_2 = 15$ , and  $N_1$  varies from 0 to 14; the cases  $\beta = 0, 0.5$ , and 1 are shown. The modulation index is  $h = 0.715$ .

symbol, as long as  $N_1 \neq 0, 1, 13$  or 14. (This corresponds to detection of either the first, second, or last two bits in the observation interval.) When  $h$  is close to a weak index we see from Figure 10.18 that it is indeed optimum to detect the data symbol in the middle of the interval that is observed. From both Figure 10.17 and 10.18 it is seen that when  $\beta$  is increased, the best place to detect the data symbol moves over toward the beginning of the observation interval.

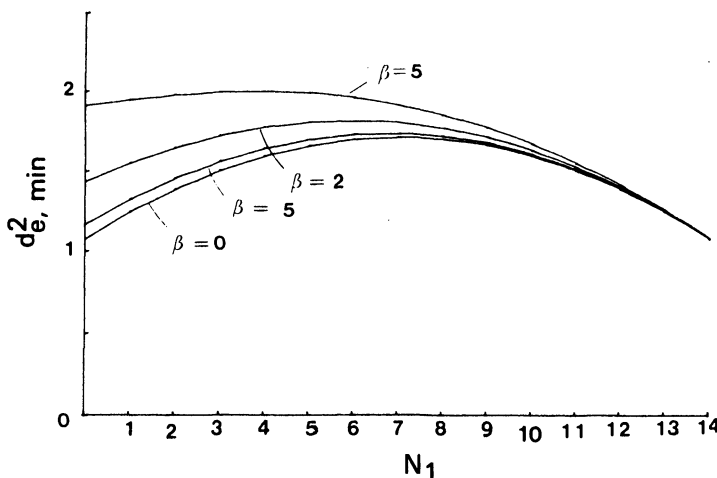


Figure 10.18. Minimum equivalent Euclidean distance for the binary 1REC system. The number of observed bit intervals is fixed  $N_1 + N_2 = 15$ , and  $N_1$  varies from 0 to 14; the cases  $\beta = 0, 0.5, 2, 5$  are shown. The modulation index is  $h = 0.9$ .

The implementation of the general partially coherent detector is rather complex since the operations in (10.6) must be performed. An exception is the noncoherent case. Here the decision variable can be found by insertion of (10.11) into (10.7), yielding

$$R(\alpha, \tilde{\alpha}) = \left[ c_{\Delta\phi_0}(\alpha, \tilde{\alpha}) + \left( \frac{T}{E} \right)^{1/2} n_c(\tilde{\alpha}) \right]^2 + \left[ s_{\Delta\phi_0}(\alpha, \tilde{\alpha}) + \left( \frac{T}{E} \right)^{1/2} n_s(\tilde{\alpha}) \right]^2 \quad (10.38)$$

which can be shown to be independent of  $\Delta\phi_0$  from a statistical point of view. This means that (10.38) indicates a simple implementation, since from (10.11)

$$\begin{aligned} c_{\Delta\phi_0}(\alpha, \tilde{\alpha}) &= \frac{1}{T} \int_{-N_1 T}^{N_2 T} \cos [\phi(t, \tilde{\alpha}) + \hat{\phi}_0] \cos [\phi(t, \alpha) + \phi_0] dt \\ &\quad + \frac{1}{T} \int_{-N_1 T}^{N_2 T} \sin [\phi(t, \tilde{\alpha}) + \hat{\phi}_0] \sin [\phi(t, \alpha) + \phi_0] dt \\ s_{\Delta\phi_0}(\alpha, \tilde{\alpha}) &= \frac{1}{T} \int_{-N_1 T}^{N_2 T} \sin [\phi(t, \tilde{\alpha}) + \hat{\phi}_0] \cos [\phi(t, \alpha) + \phi_0] dt \\ &\quad - \frac{1}{T} \int_{-N_1 T}^{N_2 T} \cos [\phi(t, \tilde{\alpha}) + \hat{\phi}_0] \sin [\phi(t, \alpha) + \phi_0] dt \end{aligned} \quad (10.39)$$

$c_{\Delta\phi_0}(\alpha, \tilde{\alpha})$  and  $s_{\Delta\phi_0}(\alpha, \tilde{\alpha})$  can be obtained by filtering the recovered quadrature components  $\cos [\phi(t, \alpha) + \phi_0]$  and  $\sin [\phi(t, \alpha) + \phi_0]$  with filters matched to  $\cos [\phi(t, \tilde{\alpha}) + \hat{\phi}_0]$  and  $\sin [\phi(t, \tilde{\alpha}) + \hat{\phi}_0]$ . The Viterbi algorithm can be employed as a detector in the noncoherent case, when  $h$  is rational, but this is now a *suboptimum* detection strategy. The quantities  $c_{\Delta\phi_0}(\alpha, \tilde{\alpha})$  and  $s_{\Delta\phi_0}(\alpha, \tilde{\alpha})$  can be calculated recursively from symbol interval to symbol interval. From these the decision variable  $R(\alpha, \tilde{\alpha})$  in (10.38) is formed. What makes the Viterbi algorithm suboptimum is the following. For each state in the trellis we choose as the survivor the sequence  $\tilde{\alpha}$  that maximizes  $R(\alpha, \tilde{\alpha})$ . Denoting two different  $\tilde{\alpha}$ -sequences leading to the same state by  $\tilde{\alpha}_1$  and  $\tilde{\alpha}_2$  we might have, say,  $R(\alpha, \tilde{\alpha}_1) > R(\alpha, \tilde{\alpha}_2)$  with the sequence  $\tilde{\alpha}_1$  the survivor. Assuming that we have reached symbol interval  $nT \leq t \leq (n+1)T$  we denote the decision variables by  $R_n(\alpha, \tilde{\alpha}_1)$  and  $R_n(\alpha, \tilde{\alpha}_2)$ . At the interval  $(n+1)T \leq t \leq (n+2)T$ , we form  $R_{n+1}(\alpha, \tilde{\alpha}_3)$  and  $R_{n+1}(\alpha, \tilde{\alpha}_4)$  by calculating the increments  $\Delta c_{\Delta\phi_0}$  and  $\Delta s_{\Delta\phi_0}$ , adding these to  $(c_{\Delta\phi_0}(\alpha, \tilde{\alpha}_1), s_{\Delta\phi_0}(\alpha, \tilde{\alpha}_1))$  and  $(c_{\Delta\phi_0}(\alpha, \tilde{\alpha}_2), s_{\Delta\phi_0}(\alpha, \tilde{\alpha}_2))$ , and then calculating  $R_{n+1}(\alpha, \tilde{\alpha}_3)$  and  $R_{n+1}(\alpha, \tilde{\alpha}_4)$ . Here  $\tilde{\alpha}_3$  is the sequence  $\tilde{\alpha}_1$  followed by a specific data

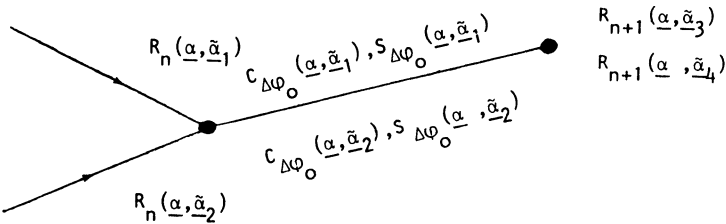


Figure 10.19. A transition and metrics in a trellis diagram. The sequence  $\tilde{\alpha}_3$  is  $\tilde{\alpha}_1$  followed by a specific data symbol and  $\tilde{\alpha}_4$  is  $\tilde{\alpha}_2$  followed by the same data symbol.

symbol and  $\tilde{\alpha}_4$  is the sequence  $\tilde{\alpha}_2$  followed by the same data symbol. Figure 10.19 shows the relevant part of the trellis. If we now assume that  $R_{n+1}(\underline{\alpha}, \tilde{\alpha}_3) > R_{n+1}(\underline{\alpha}, \tilde{\alpha}_4)$  it does not necessarily follow that  $R_n(\underline{\alpha}, \tilde{\alpha}_1) > R_n(\underline{\alpha}, \tilde{\alpha}_2)$ ; thus the sequence  $\tilde{\alpha}$  maximizing  $R(\underline{\alpha}, \tilde{\alpha})$  cannot be calculated recursively.

Although the Viterbi algorithm cannot be used for optimal maximization of  $R(\underline{\alpha}, \tilde{\alpha})$ , we have tested its performance by simulation. We could not find any significant degradation from the performance that can be expected from the  $d_{e,\min}^2$  calculations.

## References

1. A. J. Viterbi, "Optimum Detection and Signal Selection for Partially Coherent Binary Communication," *IEEE Transactions on Information Theory* IT-11(2), 239-246 (1965).
2. W. P. Osborne and M. B. Luntz, "Coherent and Non-Coherent Detection of CPFSK," *IEEE Transactions on Communications*, COM-22(8), 1023-1036 (1974).
3. H. L. van Trees, *Detection, Estimation and Modulation Theory*, Part I, Wiley, New York (1968).
4. T. Aulin and C.-E. Sundberg, "On Partially Coherent Detection of Digital Continuous Phase Modulated Signals," International Conference on Communications, ICC '80, Seattle, Washington, June 8-12, 1980, Conference Record, pp. 26.2.1-26.2.6.
5. M. Schwartz, W. R. Bennett, and S. Stein, *Communication Systems and Techniques*, McGraw-Hill, New York (1965).
6. T. Aulin and C.-E. Sundberg, "Differential Detection of Partial Response Continuous Phase Modulated Signals," International Conference on Communications, ICC '81, Denver, Colorado, June 14-18, 1981, Conference Record, pp. 56.1.1-56.1.6.
7. T. Aulin and C.-E. Sundberg, "Partially Coherent Detection of Digital Full Response Continuous Phase Modulated Signals," *IEEE Transactions on Communications*, COM-30(5), 1096-1117 (1982).
8. A. Svensson, C.-E. Sundberg, and T. Aulin, "Partial Response Continuous Phase Modulation with Partially Coherent Detection," International Conference on Communications, ICC '83, Boston, Massachusetts, June 19-22, 1983, Conference Record, pp. A6.5.1-A6.5.9.

# Phase Modulation and Convolutional Codes

In previous chapters we have seen that the memory in the continuous phase of the CPM signal can be utilized to improve the minimum Euclidean distance; so also can the memory introduced by the controlled intersymbol interference in partial response CPM. Even more memory can be built into the signals by means of multi- $h$  coding (see Chapter 3) or convolutional codes. In this chapter we will present some recent results on combinations of many-level PSK and CPM with convolutional codes. Section 11.2 covers binary and quaternary CPFSK with rate 1/2 convolutional codes, and presents combinations with the best free Euclidean distance. Section 11.3 covers eight-level CPM with rate 2/3 codes, 16-level CPM with rate 3/4 codes, etc. Finally Section 11.4 presents some simulations of eight- and 16-level CPFSK with rate 2/3 and rate 3/4 codes. Viterbi detection is used throughout.

## 11.1. PSK Set Partition Codes

Conventional coding with BPSK and QPSK modulation is discussed in standard textbooks, e.g., Refs. 5–7. Optimizing the Euclidean distance is in this case equivalent to optimizing the Hamming distance of the error correcting code. This is not the case with 8PSK or 16PSK modulation. Ungerboeck<sup>(8)</sup> devised the so-called *set partition* codes for use with many-level PSK modulators. The idea behind these codes is to start with a large constellation of signal space points in the  $I/Q$  plane, and then restrict the signaling to a pattern of subsets of this. The choice of this subset is driven by the data symbols, and until now the mechanism to do so has always been a convolutional encoder circuit. The PSK may be either pure or Nyquist PSK.

To illustrate the technique, we first give some examples of 8PSK constellations combined with rate 2/3 convolutional codes. Figure 11.1 shows the 4PSK (QPSK) and 8PSK signal constellations. The 8PSK constellation is normalized with the rate 2/3 code rate to facilitate comparisons in normalized distance at equal  $E_b/N_0$  between uncoded QPSK and rate 2/3 coded 8PSK. Note that the asymptotic difference in  $E_b/N_0$  between uncoded 8PSK and uncoded 4PSK at high SNRs is

$$10 \log_{10} \left( \frac{3d_0^2}{2d_4^2} \right) = 10 \log_{10} \left[ \frac{3}{4} (2 - \sqrt{2}) \right] = -3.57 \text{ dB} \quad (11.1)$$

a loss of 3.57 dB. For the uncoded case a Gray code representation of the eight different phase values should be used, as in Figure 11.1.b. For the coded case, both the Gray code and the natural binary code mapping rule have been proposed; see Refs. 28 and 8. Other points are discussed in Refs. 15 and 24–30.

Figures 11.2–11.4 show three examples of coded 8PSK where the decoder has 4, 8, and 16 states, respectively. The natural binary mapper in Figure 11.1 is used. In the scheme of Figure 11.2, the most significant bit of the natural binary mapper word is left uncoded. Thus the free squared Euclidean distance can be no larger than the distance between two antipodal phase values in the signal constellation, i.e., 4. The minimum distance path in the trellis is also shown in Figure 11.2. Larger gains are obtained with the codes shown in Figures 11.3 and 11.4, where the most significant bit of the natural binary mapper is also coded. This is necessary to achieve larger

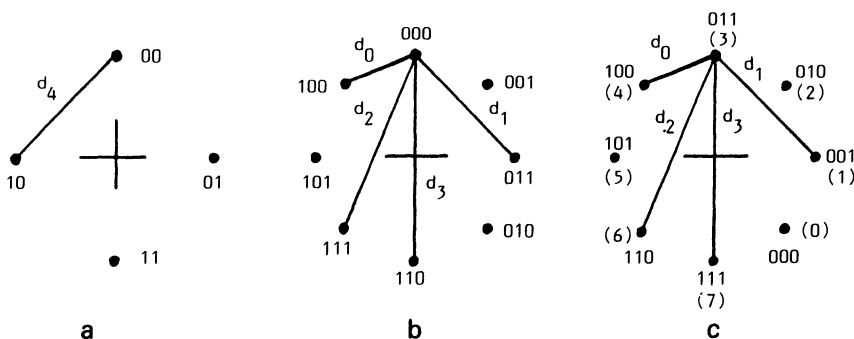


Figure 11.1. Signal constellations and distances for uncoded 4PSK (QPSK) and coded 8PSK with rate 2/3 coding. All distances are normalized with respect to  $2E_b$  as before. Two different mapping rules (binary representations of the signal points) are shown for 8PSK, viz., Gray mapping and Natural binary mapping. (a) 4PSK = QPSK.  $d_4^2 = 2$ . (b) 8PSK. Gray mapping.  $d_0^2 = 2 - \sqrt{2}$ ,  $d_1^2 = 2$ ,  $d_2^2 = 2 + \sqrt{2}$ ,  $d_3^2 = 4$ . (c) 8PSK. Natural binary mapping. The octal number corresponding to each phase is also shown.

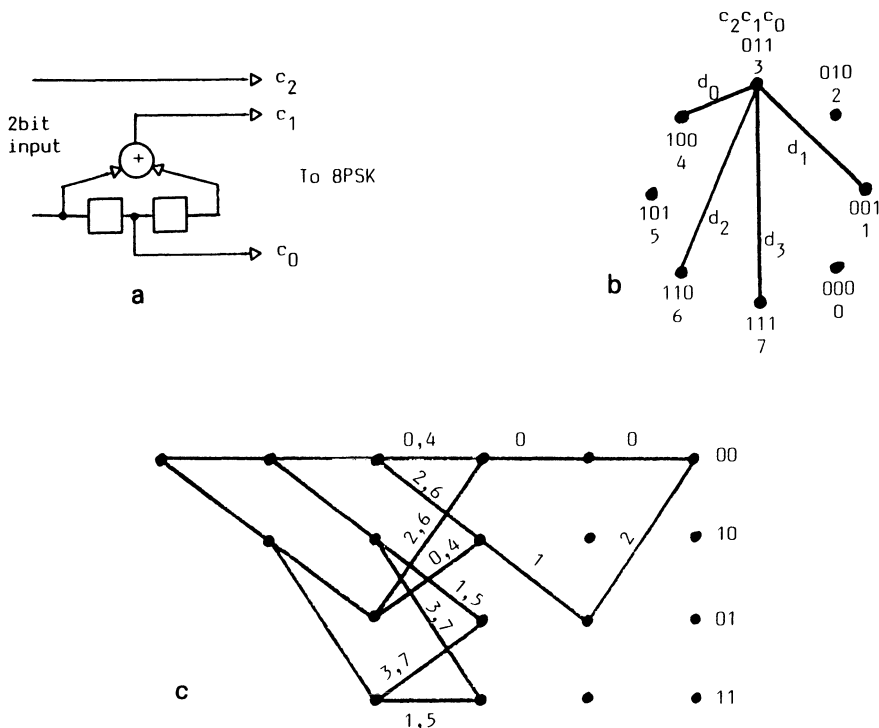


Figure 11.2. Example of a rate 2/3 code with 8PSK, four states. Note that the most significant bit  $c_2$  of the natural binary word is left uncoded in this example. Therefore each transition in the trellis can correspond to two different output values (phase values) at the 8PSK modem. It can be shown that  $d_f^2 = d_s^2 = 4.000$ , i.e., 3.0 dB gain over 4PSK. (a) Encoder; (b) 8PSK and mapper; (c) partial trellis.

coding gains than 3 dB with the concept of 8PSK and rate 2/3 coding in Figure 11.2. For details of codes with high-SNR gains approaching 6 dB, see the tables in Refs. 8, 28, 7.

Wilson, Schottler, and Sleeper<sup>(23)</sup> list the results of a search for 16PSK codes with rate 3/4 coding. Set partition codes have also found application to high rate (4–6 bits/interval) QAM-style signalling in telephone-line modems,<sup>(36)</sup> where gains of 3–6 dB have been observed. Here the QAM constellation has 32–128 points and the subset mechanism is in the manner of Figure 11.2. The number of data bits appearing per interval,  $b$ , is divided into groups of  $b_1$  and  $b_2$ . The group of  $b_2$  bits drives the choice of a sequence of subsets, in which each subset contains  $2^{b_1}$  QAM points; the selection of one of these points carries the remaining  $b_1$  bits.

These QAM codes of course incorporate amplitude modulation, so we will not pursue them further. The set partition idea has not explicitly been

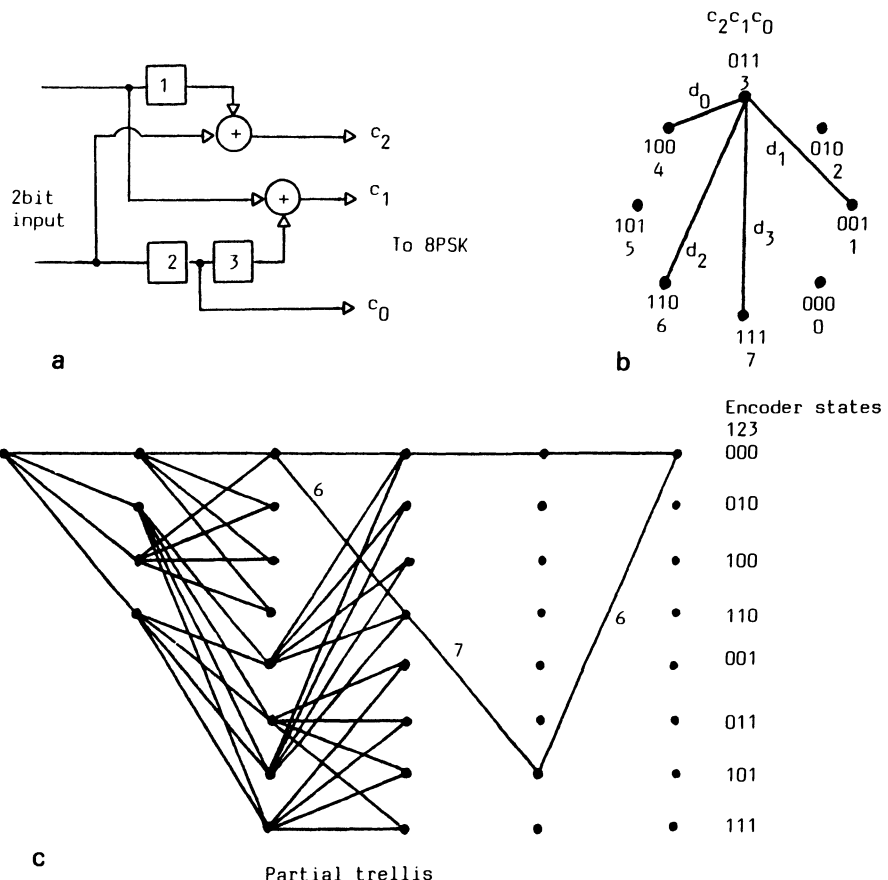


Figure 11.3. Example of a rate 2/3 code with eight states. Natural binary mapper. It can be shown that  $d_f^2 = 2d_1^2 + d_0^2 = 4.584$ , i.e., 3.6 dB gain over 4PSK. (a) Encoder; (b) 8PSK and mapper; (c) partial trellis.

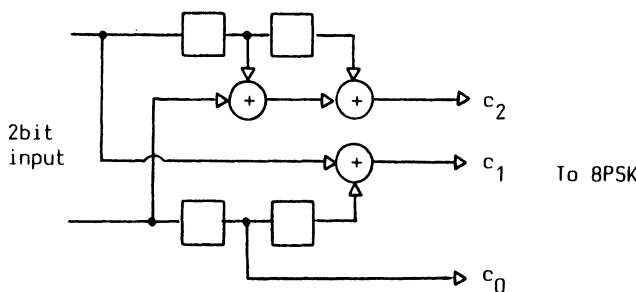


Figure 11.4. Example of a rate 2/3 code with 16 states. Natural binary mapper. It can be shown that for this code,  $d_f^2 = 2d_0^2 + 2d_1^2 = 5.171$ . This corresponds to a gain of 4.1 dB over 4PSK.

applied to continuous phase schemes; we will now turn to coded CPM schemes.

## 11.2. Coded Binary and Quaternary CPFSK

Now we list good schemes that combine convolution codes and  $M$ -ary continuous phase FSK. Memory is introduced in the signal both by means of the convolutional code and by means of the continuous phase FSK modulator. A Viterbi detector is used that takes into account both types of memory. The advantage of CPFSK is its constant envelope and low spectral tails; by introducing convolutional coding, the error probability is improved. We will assume that the detector is coherent, that the rate of the convolutional encoder equals 1/2, and that the CPFSK has 2 or 4 levels. More general cases appear in Section 11.3. The convolutional code implies a bandwidth expansion by 2, compared to the uncoded CPFSK, which strongly affects the energy-bandwidth trade-off of the combined scheme.

By optimal combination is meant that combination of rate 1/2 convolutional encoder and  $M$  level mapping rule which, for a given code memory  $\nu$  and a given modulation index  $h$ , gives the largest minimum Euclidean distance when combined with the CPFSK modulator. It is assumed that the observation interval over which the minimum distance is calculated is large enough so that the maximum obtainable minimum distance is reached. Minimum distance growth with the observation interval length will also be studied.

### 11.2.1. System Description

Let  $\mathbf{u}$  be a sequence of independent binary (0, 1) data symbols. This sequence is encoded by a conventional convolutional encoder (rate  $k/n$ ) whose output is a sequence of coded binary (0, 1) symbols  $\mathbf{v}$ ; see Figure 11.5. It is convenient to use the following notation  $\mathbf{u} = (\dots, u_{-2}, u_{-1}, u_0, u_1, u_2, \dots) = (\dots, \mathbf{u}^{-2}, \mathbf{u}^{-1}, \mathbf{u}^0, \mathbf{u}^1, \mathbf{u}^2, \dots)$  where  $u_m \in \{0, 1\}$ ,  $\mathbf{u}' = (u'_1, u'_2, \dots, u'_k)$  and  $u'_m = u_{l_k-1+m}$ . Similarly  $\mathbf{v} = (\dots, v_{-2}, v_{-1}, v_0, v_1, v_2, \dots) = (\dots, \mathbf{v}^{-2}, \mathbf{v}^{-1}, \mathbf{v}^0, \mathbf{v}^1, \mathbf{v}^2, \dots)$  where  $v_m \in \{0, 1\}$ ,  $\mathbf{v}' = (v'_1, v'_2, \dots, v'_n)$  and  $v'_m = v_{l_n-1+m}$ . Thus  $\mathbf{u}$  and  $\mathbf{v}$  consist of subsequences  $\mathbf{u}'$  and  $\mathbf{v}'$  of length  $k$  and  $n$ , respectively. The encoding operation performed

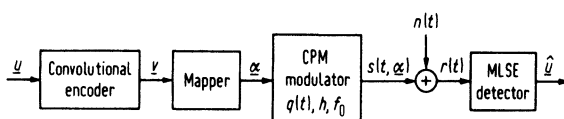


Figure 11.5. The modulation scheme, channel, and receiver.

by the convolutional encoder can now be written as

$$v_m^l = \sum_{j=1}^k \sum_{i=0}^{\mu} q_{m,j}(i) u_j^{l-i}, \quad l = \dots, -2, -1, 0, 1, 2, \dots, \\ m = 1, 2, \dots, n \quad (11.2)$$

$g_{m,j}(i) \in \{0, 1\}$  and represents the connection between  $u_j^{l-i}$  and  $v_m^l$ ; the summations are modulo 2 and  $k\mu$  is the maximum possible number of delay elements in the encoder. This encoder produces blocks of coded symbols,  $\mathbf{v}^l$ , of length  $n$  each time blocks of data symbols,  $\mathbf{u}^l$ , of length  $k$  enter the encoder. The rate,  $R_c$ , of the convolutional encoder is therefore  $R_c = k/n$  data symbols/coded symbol. The number of delay elements in the encoder is  $\nu$  and the state of the encoder,  $\mathbf{x}$ , has  $\nu$  binary components. Another useful way to describe a convolutional encoder is by means of the “code-generating polynomials”  $G_{ij}(D)$ .<sup>(6,16)</sup> Using for the moment the notation of Massey and Sain,<sup>(16)</sup> the  $D$ -transform of the  $k$  input sequences and  $n$  output sequences is  $I_1(D), \dots, I_k(D)$  and  $T_1(D), \dots, T_n(D)$ . The input-output relationship of the convolutional encoder can then be written as  $T(D) = \bar{G}(D)I(D)$ , where  $\bar{G}(D)$  is the  $n \times k$  matrix whose  $ij$ th entry is  $G_{ij}(D)$ , and where  $T(D)$  and  $I(D)$  are vectors whose components are  $T_j(D)$  and  $I_j(D)$ .

The coded sequence  $\mathbf{v}$  is the input to a mapper which associates levels in an  $M$ -ary alphabet with blocks of coded symbols. The output from the mapper is a sequence  $\alpha = (\dots, \alpha_{-2}, \alpha_{-1}, \alpha_0, \alpha_1, \alpha_2, \dots)$  of channel symbols according to the mapping rule. It is assumed that  $M$  is a power of 2 and  $\alpha_l \in \{\pm 1, \pm 3, \dots, \pm(M-1)\}$ . The mapper has rate  $R_m = \log_2(M)$  code symbols/channel symbol and the overall rate,  $R$ , is  $R = R_c R_m$  data symbols/channel symbol. The natural  $M$ -level mapping rule is defined by

$$\alpha_l = \sum_{i=0}^{s-1} v_{ls+i} \cdot 2^{(2-i)} - M + 1, \quad l = 0, \pm 1, \pm 2, \dots \quad (11.3)$$

with  $s = R_m$ . The symbols  $v_{ls}$  and  $v_{(l+1)s-1}$  are referred to as the most significant bit (MSB) and the least significant bit (LSB). When  $M$  equals 2 or 4 the corresponding natural mapping rule will be referred to as B1 or Q1, respectively. Table 11.1 gives the mappers for quaternary schemes considered in Section 11.2. The final stage of the transmitter is the CPFSK modulator of Chapter 3 or 6.

With the notations introduced above the transmitted energy per information bit,  $E_b$ , and the information bit symbol time,  $T_b$ , can be written as  $E_b = E/R$  and  $T_b = T/R$ . The signal available for observation is  $r(t) = s(t, \alpha) + n(t)$  where  $n(t)$  is a Gaussian random process having zero mean and one-sided power spectral density  $N_0$ . A coherent detector which minimizes the probability of erroneous decisions must observe the received signal

Table 11.1. Four-Level Mapping Rules

Input coded symbol to the mapper		Output channel symbol												
1st (MSB)	2nd (LSB)	Q1	Q11	Q12	Q13	Q14	Q15	Q2	Q21	Q22	Q23	Q24	Q25	
0	0	-3	-3	-3	-3	-3	-3	-1	-1	-1	-1	-1	-1	
0	1	-1	-1	1	1	3	3	-3	-3	1	1	3	3	
1	0	1	3	3	-1	-1	1	1	3	3	-3	-3	1	
1	1	3	1	-1	3	1	-1	3	1	-3	3	1	-3	

$r(t)$  over the entire time axis and choose the infinitely long sequence  $\hat{u}$  which minimizes the error probability. As discussed in Chapter 7, this is referred to as maximum likelihood sequence estimation (MLSE).

### 11.2.2. Error Probability and Minimum Euclidean Distance

As was done in Chapter 2, we can overbound  $P(\varepsilon)$  by the union bound<sup>(17)</sup>

$$P(\varepsilon) = \frac{1}{S} \sum_{i=0}^{S-1} P(\varepsilon | s_i) \leq \frac{1}{S} \sum_{i=0}^{S-1} \sum_{j=0, j \neq i}^{S-1} Q\left(\left(d_{ij}^2 \frac{E_b}{N_0}\right)^{1/2}\right) \quad (11.4)$$

where  $S$  is the total number of signal alternatives  $s_0, s_1, \dots, s_{S-1}$ .  $d_{ij}^2$  is the squared Euclidean distance (ED) in signal space between  $s_i$  and  $s_j$ , normalized by  $2E_b$ . When  $E_b/N_0$  is large the union bound becomes increasingly tight and

$$P(\varepsilon) \sim Q\left(\left(d_{\min}^2 \frac{E_b}{N_0}\right)^{1/2}\right) \quad (11.5)$$

In our present coding context,  $d_{\min}^2$  will be referred to as the normalized squared free Euclidean distance (NSFED)

$$d_{\min}^2 = \min_{\mathbf{u}_\alpha, \mathbf{u}_\beta} \frac{1}{2E_b} \int_0^\infty [s(t, \alpha) - s(t, \beta)]^2 dt \quad (\text{NSFED}) \quad (11.6)$$

where  $\alpha$  and  $\beta$  are the output sequences from the mapper when the input data sequences to the convolutional encoder are  $\mathbf{u}_\alpha = (\dots, 0, 0, 0, \mathbf{u}_\alpha^{-\mu}, \mathbf{u}_\alpha^{-\mu+1}, \dots, \mathbf{u}_\alpha^{-1}, \mathbf{u}_\alpha^0, \mathbf{u}_\alpha^1, \mathbf{u}_\alpha^2, \dots)$  and  $\mathbf{u}_\beta = (\dots, 0, 0, 0, \mathbf{u}_\beta^{-\mu}, \mathbf{u}_\beta^{-\mu+1}, \dots, \mathbf{u}_\beta^{-1}, \mathbf{u}_\beta^0, \mathbf{u}_\beta^1, \mathbf{u}_\beta^2, \dots)$ , respectively. The minimization in (11.6) is carried out for all possible  $\mathbf{u}_\alpha^0 \neq \mathbf{u}_\beta^0$ .

We seek modulation schemes which have large  $d_{\min}^2$ . For comparison,  $d_{\min}^2 = 2$  for uncoded minimum shift keying (MSK), uncoded binary phase shift keying (BPSK), or uncoded quaternary phase shift keying (QPSK). A more general parameter of interest is the minimum normalized squared Euclidean distance (MNSED)  $d_{\min,N}^2$  defined by

$$d_{\min,N}^2 = \min_{\mathbf{u}_\alpha, \mathbf{u}_\beta} \frac{1}{2E_b} \int_0^{NT} [s(t, \alpha) - s(t, \beta)]^2 dt \quad (\text{MNSED}) \quad (11.7)$$

with  $\mathbf{u}_\alpha$  and  $\mathbf{u}_\beta$  the same as in (11.6).  $d_{\min,N}^2$  is the minimum distance between signals defined up to time  $NT$ . It is a nondecreasing function of  $N$  with maximum value equal to  $d_{\min}^2$ . It is interesting to know for which value of  $N$  the free Euclidean distance is reached, i.e., the smallest  $N$  for which  $d_{\min}^2 = d_{\min,N}^2$  because the path memory of the MLSE detector at large  $E_b/N_0$  is closely related to this.<sup>(12,18,32)</sup> It is also of interest to know how fast  $d_{\min,N}^2$  grows with  $N$ .

An example of a coded modulation scheme of the present type is given in Figure 11.6. The rate 1/2 code is defined by means of an octal representation of the upper and lower connection polynomials. This notation will be used throughout this chapter. The code in Figure 11.6 is denoted (13, 4), where 13 and 4 are octal representations of the two polynomials. We are looking for those combinations of a noncatastrophic rate 1/2 convolutional encoder  $[\bar{G}(D)]$  and mapping rule such that, for fixed  $v$  and  $h$ ,  $d_{\min}^2$  is maximized. Formally, this can be written as

$$\max_{\substack{\text{mapping} \\ \text{rule}}} \max_{\{\bar{G}(D)\}} d_{\min}^2 \quad (11.8)$$

### 11.2.3. Minimum Euclidean Distance: Properties and Calculation

It is always possible to find two data symbol sequences  $\mathbf{u}_\alpha$  and  $\mathbf{u}_\beta$  in (11.6) such that  $s(t, \alpha) = s(t, \beta)$  for  $t \geq N_m T$ , where  $N_m$  is some positive

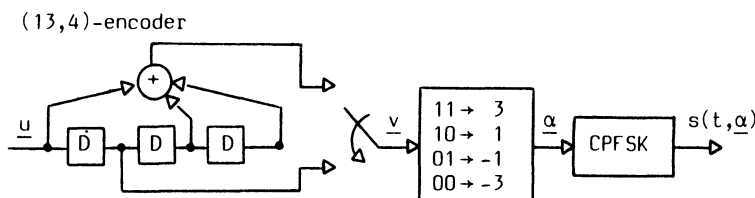


Figure 11.6. An example of a modulation scheme considered in this chapter. (13, 4) are the octal representation of the upper and lower polynomial, respectively. The mapping rule used in this example is mapping rule Q1; see Table 11.1.

integer; this must yield an upper bound,  $d_B^2(h)$ , on  $d_{\min}^2(h)$ . This bound is the normalized squared ED in signal space between  $s(t, \alpha)$  and  $s(t, \beta)$ ,

$$d_B^2(h) = \frac{1}{2E_b} \int_0^{N_m T} [s(t, \alpha) - s(t, \beta)]^2 dt \quad (11.9)$$

Clearly,  $d_{\min, N}^2(h) \leq d_{\min}^2(h) \leq d_B^2(h)$  and the bound is tight [ $d_{\min}^2(h) = d_B^2(h)$ ] for properly chosen sequences  $\mathbf{u}_\alpha$  and  $\mathbf{u}_\beta$ . The situation described above is an example of a phase and state merger. The conditions for a phase and state merger can be formulated as

$$\sum_{i=0}^{N_m-1} \gamma_i = \frac{2l}{h} \quad \text{for some } l, l = 0, \pm 1, \pm 2, \dots$$

$$\gamma_j = 0, \quad j \geq N_m - L + 1 \quad (11.10)$$

where  $\gamma_i = \alpha_i - \beta_i$  is the  $i$ th element in the difference sequence  $\gamma = \alpha - \beta = (\dots, \gamma_{-2}, \gamma_{-1}, \gamma_0, \gamma_1, \gamma_2, \dots)$  and  $\gamma_i \in \{0, \pm 2, \pm 4, \dots, \pm 2(M-1)\}$ . If  $l=0$  in (11.10) a phase and state merger has occurred independent of  $h$  while if  $l \neq 0$  a phase and state merger has occurred only for specific  $h$  values according to (11.10). This is important because in the former case an upper bound can be calculated for all  $h$ , while in the latter case an upper bound can only be calculated for those specific  $h$  values given by (11.10). Such specific  $h$  values are referred to as weak modulation indices.

Figure 11.7 shows examples of phase and state mergers for two specific coded binary CPFSK schemes. Calculations show that the phase and state merger given in Figure 11.7a is a minimum ED merger when the modulation index is small. It is also found that the phase and state merger (all  $h$ ) given in Figure 11.7b is a minimum ED merger for almost all modulation indices in the interval  $0 \leq h \leq 0.5$ ; furthermore, for this  $h$  interval, there does not exist any shorter minimum ED merger than those two given in Figure 11.7. Note that the phase and state merger (all  $h$ ) in Figure 11.7b has length  $14T$ , but there are only  $10T$  intervals giving any distance contribution. Assuming  $f_0 \gg 1/T$ , the expression (11.7) for  $d_{\min, N}^2(h)$  can be reduced to

$$d_{\min, N}^2(h) = \min_{\mathbf{u}_\alpha, \mathbf{u}_\beta} R \left( N - \sum_{m=0}^{N-1} C_m \right) \quad (11.11)$$

with

$$C_m = \int_0^1 \cos \left[ \pi h \xi_m + 2\pi h \sum_{i=0}^{L-1} \gamma_{m-i} q((x-i)T) \right] dx$$

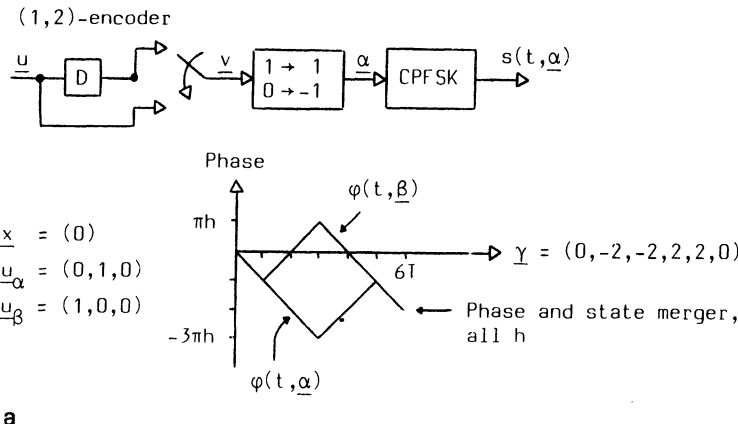


Figure 11.7a. Examples of phase and state mergers for binary CPFSK with the (1, 2)-encoder.

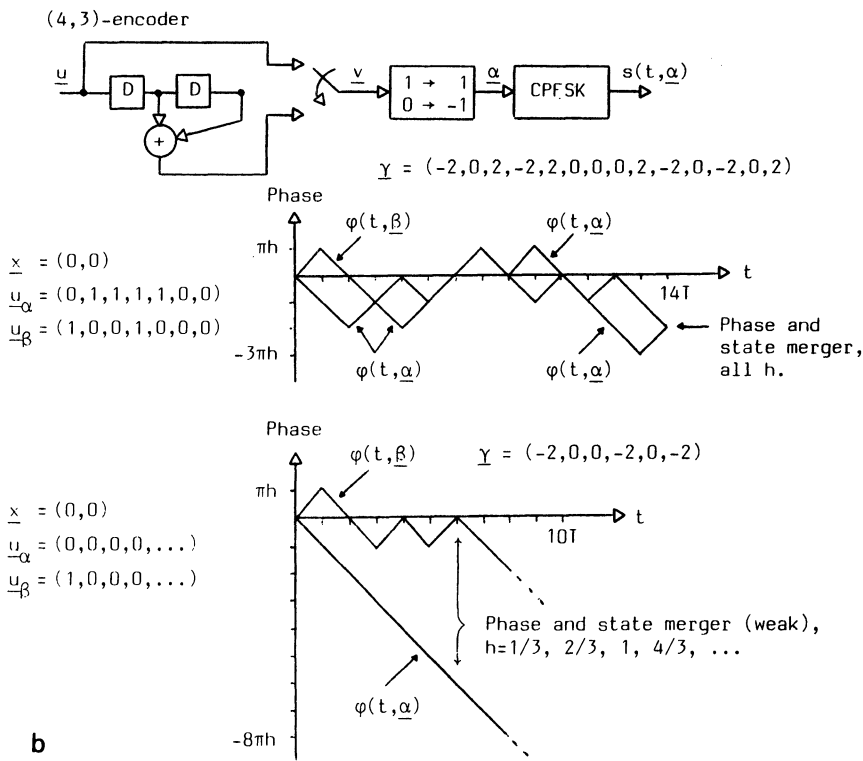


Figure 11.7b. Examples of phase and state mergers for binary CPFSK with the (4, 3)-encoder.

where

$$\xi_m = \sum_{i=-\infty}^{m-L} \gamma_i$$

Since  $\gamma_i = 0$  for all  $i \leq -1$ ,  $\xi_m = 0$  for all  $m \leq L-1$ . When  $g(t)$  is LREC [ $g(t) = 1/2LT$ ,  $0 \leq t \leq LT$ ], further simplification is possible since  $C_m$  is

$$C_m = \begin{cases} \frac{\sin(y_m + z_m) - \sin(y_m)}{z_m}, & z_m \neq 0 \\ \cos(y_m), & z_m = 0 \end{cases} \quad (11.12)$$

with

$$z_m = \frac{\pi h}{L} \sum_{i=0}^{L-1} \gamma_{m-i}$$

and

$$y_m = \pi h \left( \xi_m + \frac{1}{L} \sum_{i=0}^{L-1} i \gamma_{m-i} \right)$$

The algorithm used for the calculation of  $d_{\min, N}^2(h)$  is a natural extension of the algorithm described in Appendix A. The modulation scheme in Figure 11.5 is called *catastrophic* if there exist two data symbol sequences  $\mathbf{u}_\alpha$  and  $\mathbf{u}_\beta$  with infinite Hamming distance such that the corresponding ED in signal space between  $s(t, \alpha)$  and  $s(t, \beta)$  is finite. This type of scheme must of course be avoided. It is quite easy to show that if the convolutional encoder is noncatastrophic,<sup>(16,5-6)</sup> then the modulation scheme is also non-catastrophic for all rational  $h$  values.<sup>(19-20)</sup>

#### 11.2.4. Symmetries for the Combination of Convolutional Encoder and Mapping Rule

In this section we shall take a closer look at the combination of convolutional encoder and mapping rule. The reason for this is that in the search for the best combinations [largest  $d_{\min}^2(h)$ ] we would like to minimize the number of combinations to be investigated. It is assumed that  $R_c = 1/n$ , ( $k = 1$ ). Let us first state four conditions for the convolutional encoder  $\tilde{G}(D)$ . It is also assumed that (1) The convolutional encoder is noncatastrophic; (2)  $g_{j,1}(0) = 1$  for some  $j$ ,  $1 \leq j \leq n$ ; (3)  $g_{j,1}(\nu) = 1$  for some  $j$ ,  $1 \leq j \leq n$ ; and (4)  $g_{j,1}(i) = 1$  for some  $i$ ,  $0 \leq i \leq \nu$ , and all  $j$ ,  $1 \leq j \leq n$ . The total

number of different mapping rules is  $M!$ . From (11.11), however, it is seen that  $d_{\min, N}^2(h)$  would be the same if  $\gamma$  was replaced with  $-\gamma$ . Consequently only  $M!/2$  mapping rules need to be investigated. Also, time reversal of phase and state mergers does not change  $d_{\min}^2$ .

### *Rate 1/n Convolutional Encoder and Binary Mapping Rule*

First we reduce the number of rate  $1/n$  convolutional encoders in the search when  $M = 2$ . In this binary case there is only one mapping rule of interest, namely, mapping rule B1. Consider now two convolutional encoders  $\bar{G}(D)$  and  $\bar{G}'(D)$ , where

$$g'_{j,1}(i) = g_{(n+1-j),1}(\nu - i), \quad 1 \leq j \leq n, \quad 0 \leq i \leq \nu \quad (11.13)$$

$\bar{G}(D)$  and  $\bar{G}'(D)$ , together with mapping rule B1 will have the same  $d_{\min}^2(h)$  but not the same  $d_{\min, N}^2(h)$ . This is now shown.

Let  $\mathbf{u}$  and  $\mathbf{u}'$ , defined as  $\mathbf{u} = (\dots, 0, 0, u_0, u_1, \dots, u_m, 0, 0, \dots)$  and  $\mathbf{u}' = (\dots, 0, 0, u'_0, u'_1, \dots, u'_m, 0, 0, \dots)$ , be the input data symbol sequences to the convolutional encoders  $\bar{G}(D)$  and  $\bar{G}'(D)$ , respectively, and let the corresponding output sequences be  $t_j$  and  $t'_j$ ,  $j = 1, 2, \dots, n$ . If  $g'_{j,1}(i) = g_{(n+1-j),1}(\nu - i)$ ,  $i \leq j \leq n$ ,  $0 \leq i \leq \nu$ , and  $u'_i = u_{m-i}$  then the  $i$ th element in  $t'_j$  is  $t'_{j,i} = t_{(n+1-j),(m+\nu-i)}$ . Consequently, after the binary mapping rule, the channel symbol sequence  $\alpha'$  is only a time reversed delayed variant of  $\alpha$ . Those pairs of data symbol sequences,  $\mathbf{u}_\alpha$  and  $\mathbf{u}_\beta$ , which give  $d_{\min}^2(h)$  can always be written as  $\mathbf{u}$  and  $\mathbf{u}'$ . Suppose now that the convolutional encoder  $\bar{G}(D)$  is used and  $\mathbf{u}_\alpha$  and  $\mathbf{u}_\beta$  causes a state and phase merger. Then, as was shown above, it is always possible to create a new convolutional encoder  $\bar{G}'(D)$ , according to (11.13), which together with the two input data symbol sequences  $\mathbf{u}'_\alpha (u'_{\alpha,i} = u_{\alpha,(m-i)})$  and  $\mathbf{u}'_\beta (u'_{\beta,i} = u_{\beta,(m-i)})$  produces a state and phase merger which is just a time reversed delayed variant of the phase and state merger created by  $\mathbf{u}_\alpha$ ,  $\mathbf{u}_\beta$  and  $\bar{G}(D)$ . Since these two state and phase mergers have the same ED it is clear that  $\bar{G}(D)$  and  $\bar{G}'(D)$  are equivalent from the  $d_{\min}^2(h)$  point of view. However,  $\bar{G}(D)$  and  $\bar{G}'(D)$  have different  $d_{\min, N}^2(h)$ ; see Refs. 1 and 38 for details.

### *Rate 1/n Convolutional Encoder and $2^n$ -Level Mapping Rule*

Consider two convolutional encoders  $\bar{G}(D)$  and  $\bar{G}'(D)$ , where

$$g'_{j,1}(i) = g_{j,1}(\nu - i), \quad 1 \leq j \leq n, \quad 0 \leq i \leq \nu$$

$\bar{G}(D)$  and  $\bar{G}'(D)$ , together with a  $2^n$  level mapping rule, will have the same  $d_{\min}^2(h)$  but not the same  $d_{\min, N}^2(h)$ . The arguments and notations used in

the proof above will be repeated. Let  $\mathbf{u}$  and  $\mathbf{u}'$  be the input data symbol sequences to the convolutional encoders  $\bar{G}(D)$  and  $\bar{G}'(D)$ , respectively, and let the corresponding output sequences be  $\mathbf{t}_j = \mathbf{t}'_j$ ,  $j = 1, 2, \dots, n$ . If  $g'_{j,1}(i) = g_{j,1}(\nu - i)$ ,  $1 \leq j \leq n$ ,  $0 \leq i \leq \nu$  and  $u'_i = u_{m-i}$  then the  $i$ th element in  $\mathbf{t}'_j$  is  $t'_{j,i} = t_{j,(m+\nu-i)}$ . Consequently, after any  $2^n$  level mapping rule, the channel symbol sequence  $\alpha'$  is only a time reversed delayed variant of  $\alpha$ . Using the same argument as in the earlier proof, it is clear that  $\bar{G}(D)$  and  $\bar{G}'(D)$  are equivalent from the  $d_{\min}^2(h)$  point of view, but do not have the same  $d_{\min,N}^2(h)$ ; see details in Refs. 1, 38, 19, 20.

### *Rate 1/2 Convolutional Encoder and Four-Level Mapping Rule*

We now look at the specific case when a rate 1/2 convolutional encoder is combined with a four-level mapping rule. Consider the mapping rules Q1 and Q2 (defined in Table 11.1). Any combination of a rate 1/2 convolutional encoder and a four-level mapping rule can be transformed to another combination of a rate 1/2 encoder and a four-level rule, where the rule is either Q1 or Q2. Furthermore, the transformed combination will be identical to the original combination. Consequently, only mapping rules Q1 and Q2 are needed in the search. Another useful property is that the combinations  $\{\bar{G}(D), Q2\}$  and  $\{\bar{G}(D), Q11\}$  (Q11 defined in Table 11.1) are equivalent from the  $d_{\min,N}^2(h)$  point of view if  $\bar{G}(D)$  has an odd number of connections in its lower polynomial. This fact reduces the number of convolutional encoders needed in the search when Q2 is used, since the combination  $\{\bar{G}(D), Q11\}$  can be transformed to an identical combination using mapping rule Q1.

The proof of these two properties will now be given. Take an arbitrary convolutional encoder, say the (13, 4)-encoder, and an arbitrary mapping rule, say Q11. Consider in Table 11.1 how the mapping rules Q11–Q15 and Q21–Q25 are created from each other by changing two levels in the previous mapping rule. Note that the two corresponding pairs of input coded symbols always have a “1” in the same position. Now it is clear that by successively adding the lower (upper) polynomial to the upper (lower) polynomial of the convolutional encoder the following combinations are identical:  $\{(13, 4), Q11\} \Leftrightarrow \{(17, 4), Q12\} \Leftrightarrow \{(17, 13), Q13\} \Leftrightarrow \{(4, 13), Q14\} \Leftrightarrow \{(4, 17), Q15\} \Leftrightarrow \{(13, 17), Q1\}$ . If the original mapping rule belongs to Q21–Q25, it is clear that the procedure above can be used to transform the original combination to an identical combination using mapping rule Q2. This shows the first property. To show the second property it is enough to note that if the combination  $\{\bar{G}(D), Q2\}$  is used, and the number of connections in the lower polynomial is odd, then this combination, with input sequence  $\mathbf{u}$ , is identical to the combination  $\{\bar{G}(D), Q11\}$  fed with the input sequence  $\mathbf{u} \oplus \mathbf{1}$ , where  $\mathbf{1}$  is the all-one sequence. Therefore, the combinations

$\{\bar{G}(D), Q2\}$  and  $\{\bar{G}(D), Q11\}$  must yield the same  $d_{\min,N}^2(h)$  when the number of connections in the lower polynomial is odd. Further details of these proofs appear in Ref. 19.

### 11.2.5. Numerical Results

Numerical results are presented now for a rate 1/2 convolutional encoder and two- or four-level CPFSK modulation. Every combination of  $\nu$  and  $h$  requires a search, and each search produces the optimum  $d_{\min}^2(h)$  together with those combinations of a convolutional encoder and a mapping rule which maximizes  $d_{\min}^2(h)$ . These combinations will be referred to as optimal combinations. The results in Refs. 1, 2, 19, 20 are presented in the figures below and in the tables in Appendix D.

#### *Rate 1/2 Convolution Encoder and Binary CPFSK*

In this case the search is only over the noncatastrophic convolutional encoders since there is only one mapping rule of interest, namely, rule B1. The symmetry properties in Section 11.2.4 were used to reduce the search. The modulation indices  $h = 0.05, 0.10, \dots, 0.95$  and  $h = 1$  are employed and  $1 \leq \nu \leq 4$ . The optimum  $d_{\min}^2(h)$  for different  $\nu$  and  $h$  are given in Tables D.1 and D.2, together with the corresponding optimal convolutional encoders. The second argument within the brackets in Tables D.1 and D.2 is the least even  $N$  for which  $d_{\min,N}^2(h) = d_{\min}^2(h)$ . Note that the free Hamming distance for the convolutional code equals  $2d_{\min}^2(1)$ ; this is so because for  $h = 1$  there is no memory introduced by the CPFSK modulator, and phase merger takes place after each channel symbol interval. Consequently, when  $h = 1$  the optimal convolutional encoders from the  $d_{\min}^2(1)$  point of view are identical with the optimal convolutional encoders from the free Hamming distance point of view.

When  $\nu = 1$  the optimum  $d_{\min}^2(h)$  is significantly increased compared to the uncoded binary case. As an example, when  $h = 1/2$  the optimum  $d_{\min}^2(1/2) = 4$  (compare with uncoded MSK which yields  $d_{\min}^2 = 2$ ), and this is reached for the (2, 3)-encoder or (3, 1)-encoder. Furthermore, for modulation indices in the interval  $0 \leq h \leq 0.30$  the (1, 2)-encoder is optimal and for modulation indices around (but not equal to)  $h = 1/2$  the (2, 1)-encoder is optimal. Figure 11.8 shows  $d_{\min,40}^2(h)$  for all six noncatastrophic  $\nu = 1$  convolutional encoders. This figure can be used to find the optimal  $\nu = 1$  encoder for a specific modulation index.

When  $\nu = 2$  the optimum  $d_{\min}^2(h)$  is significantly increased compared to the  $\nu = 1$  case, except for very small modulation indices where a decrease in the optimum  $d_{\min}^2(h)$  actually occurs. When  $h = 1/2$ , the optimum  $d_{\min}^2(1/2)$  is increased from 4 to 6 and this reached when the (4, 3)-encoder is used. The (4, 3)-encoder is in fact optimal for modulation indices in the

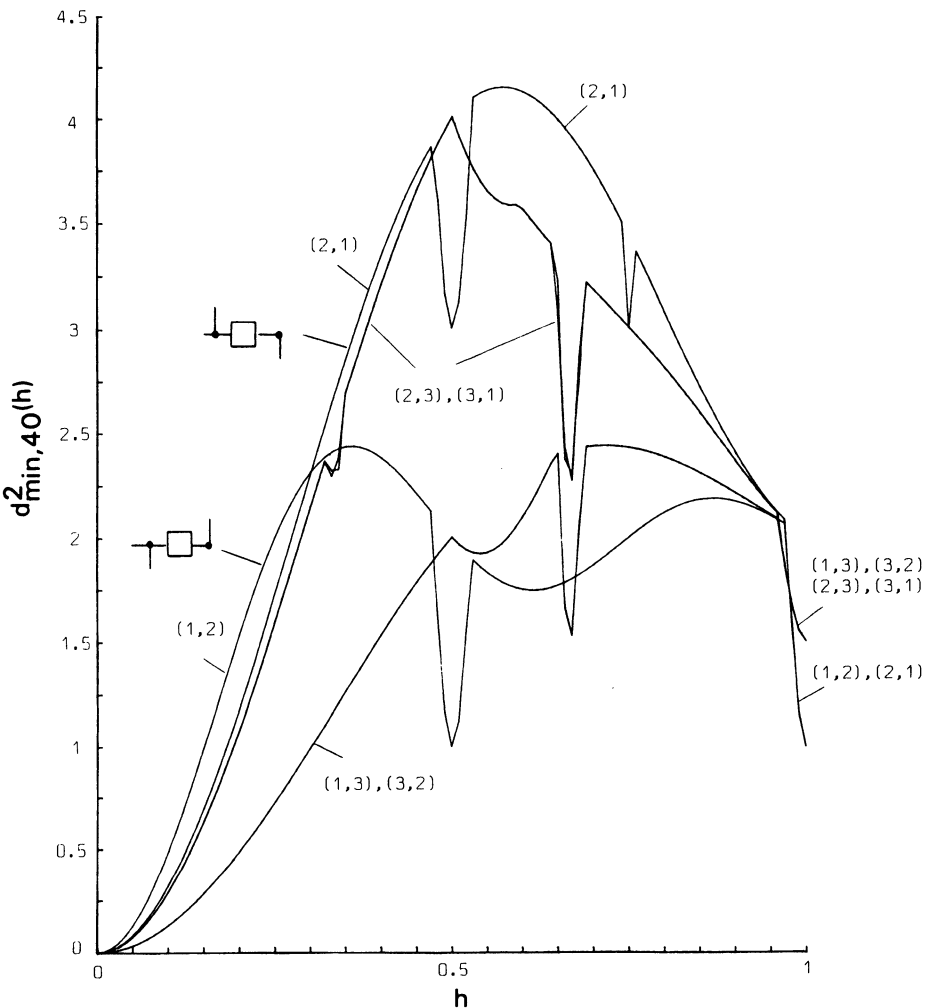


Figure 11.8.  $d_{\min,40}^2(h)$  as a function of  $h$  for all noncatastrophic  $\nu = 1$  rate  $1/2$  convolutional encoders. Binary CPFSK modulation is used.

interval  $0 \leq h \leq 0.75$ . Figure 11.9 shows  $d_{\min,N}^2(h)$  as a function of  $h$  with  $N$  as a parameter for the  $(4, 3)$ -encoder. It is seen that for modulation indices around  $1/3$ ,  $2/3$ , and  $1$ , the growth with  $N$  is very slow. This is typical behavior around  $h$  values for which a phase and state merger has occurred modulo  $2\pi$ . Figure 11.10 shows  $d_{\min,N}^2(h)$  as a function of  $h$  with  $N$  as a parameter for the  $(7, 5)$ -encoder. This encoder is optimal from the free Hamming distance point of view, but it is clear that in general it is

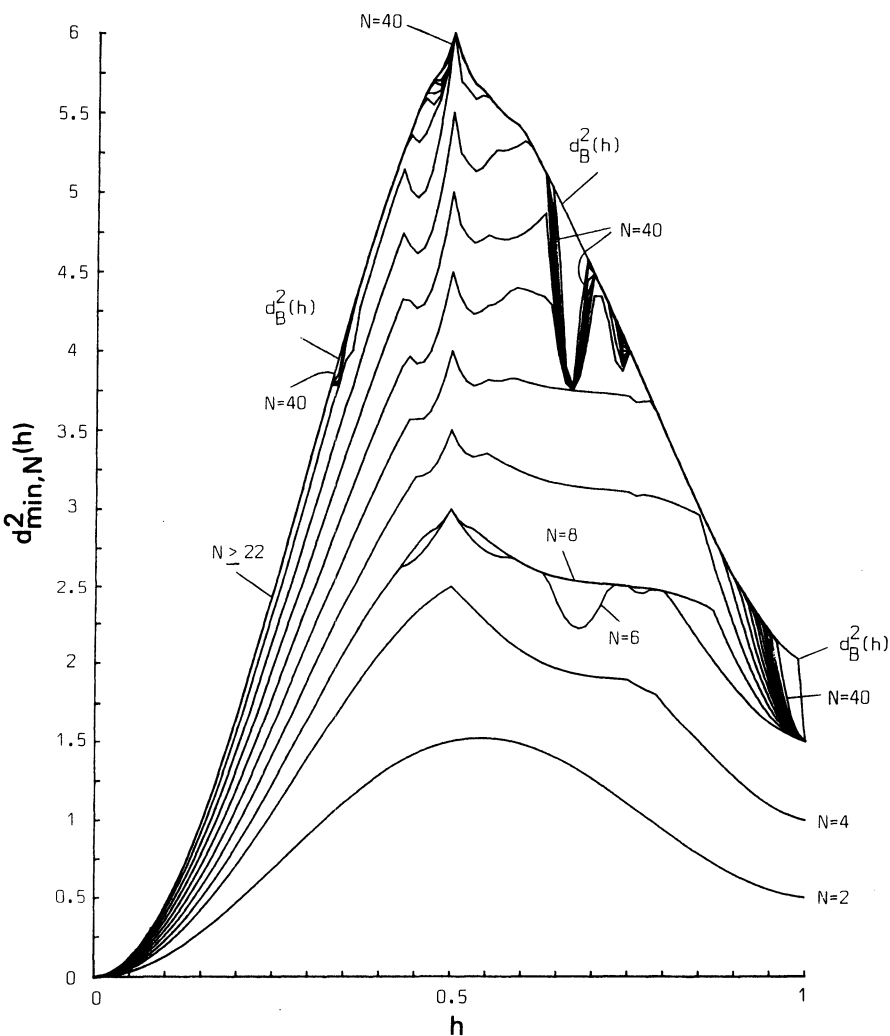


Figure 11.9.  $d^2_{\min,N}(h)$  as a function of  $h$  with  $N$  as a parameter when the rate 1/2 (4, 3)-convolutional encoder with binary CPFSK modulation is used.

suboptimal from the  $d^2_{\min}(h)$  point of view. Figure 11.11 shows  $d^2_{\min,40}(h)$  for all 24  $\nu = 2$  noncatastrophic convolutional encoders and the optimality of the (4, 3)-encoder in the interval  $0 \leq h \leq 0.75$  is clearly demonstrated.

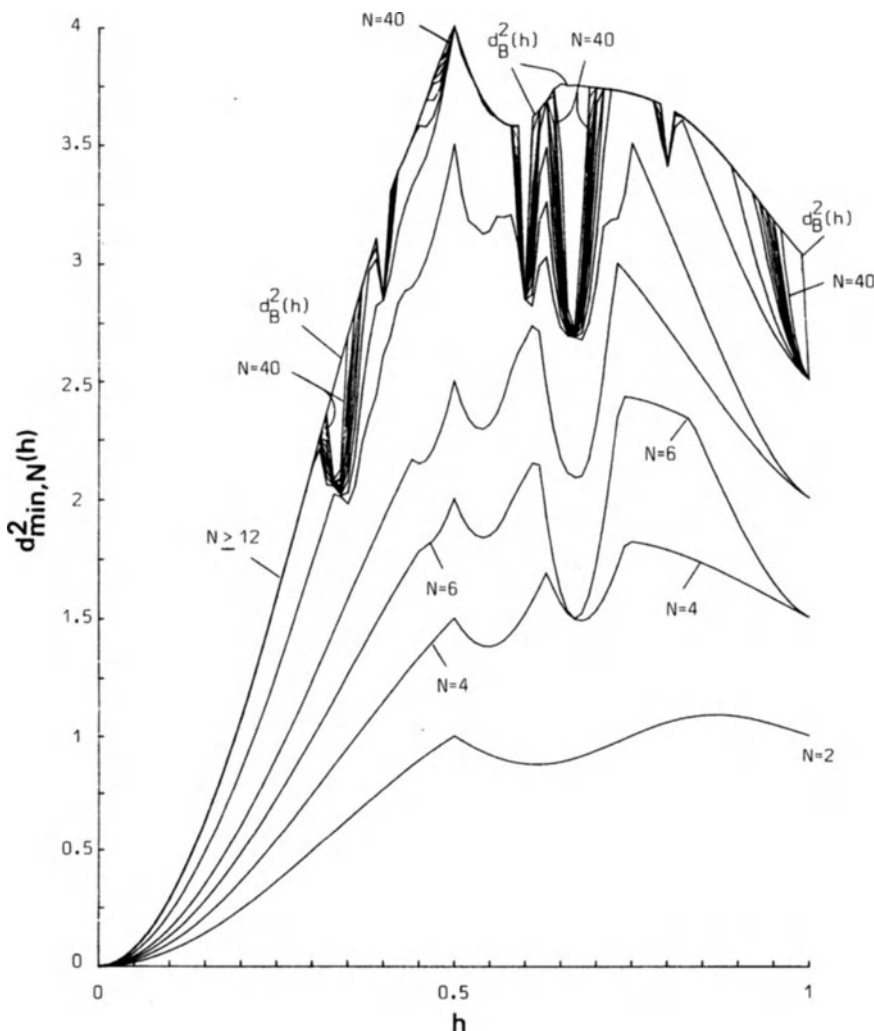


Figure 11.10.  $d_{\min, N}^2(h)$  as a function of  $h$  with  $N$  as a parameter when the rate 1/2 (7, 5)-convolutional encoder with binary CPFSK modulation is used.

When  $\nu = 3$  there is no significant increase in the optimum  $d_{\min}^2(h)$  compared to the  $\nu = 2$  case when  $0 \leq h \leq 1/2$ . However, for  $1/2 < h \leq 1$  the increase is significant. As an example, when  $h = 1/2$  the optimum  $d_{\min}^2(1/2) = 6$ , which is the same as in the  $\nu = 2$  case. The (12, 7)-encoder

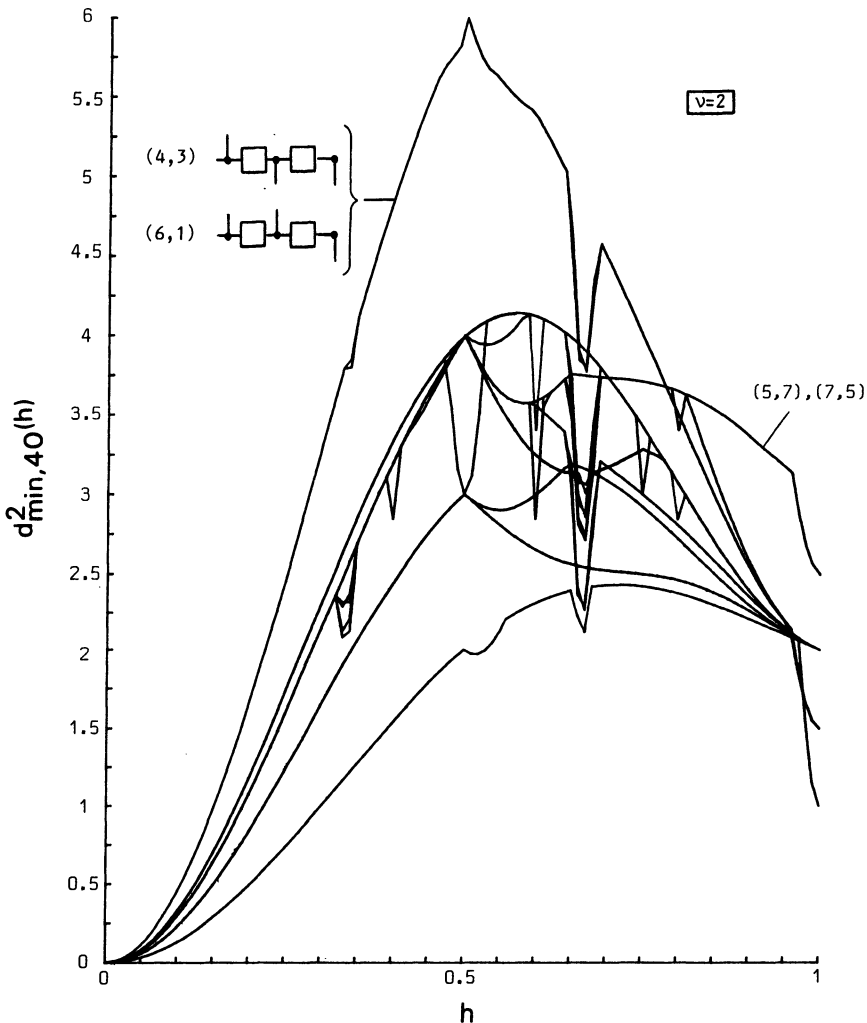


Figure 11.11.  $d_{\min,40}^2(h)$  as a function of  $h$  for all noncatastrophic  $v = 2$  rate 1/2 convolutional encoders. Binary CPFSK modulation is used.

and the  $(10, 3)$ -encoder are optimal encoders when  $0 \leq h \leq 0.50$  and  $0.5 \leq h \leq 0.70$ , respectively. For very small modulation indices the optimal  $v = 1$  encoder is better than both the optimal  $v = 2$  and  $v = 3$  encoders. (This can be understood by studying the two mergers (all  $h$ ) in Figure 11.7.) When  $v = 4$  the optimum  $d_{\min}^2(h)$  is significantly increased compared to schemes with smaller  $v$  values. For example, when  $h = 1/2$ , the optimum

$d_{\min}^2(1/2) = 8$ . The (31, 17) encoder and the (32, 17) encoder are both optimal when  $0 < h < 0.30$  and when  $h = 1/2$ .

### Rate 1/2 Convolutional Encoder and Four-Level CPFSK

In this case the search is over all noncatastrophic convolutional encoders and all four-level mapping rules. The modulation indices  $h = 0.05, 0.10, \dots, 0.55$  and  $h = 0.60$  are considered and  $1 \leq \nu \leq 4$ . The optimum  $d_{\min}^2(h)$  for different  $\nu$  and  $h$  are given in Tables D.3–D.5 in Appendix D together with the corresponding optimal combinations of encoder and mapping rule, and the minimum  $N$  for which  $d_{\min,N}^2(h) = d_{\min}^2(h)$ .

When  $\nu = 1$  the optimum  $d_{\min}^2(h)$  is significantly increased compared to the uncoded four-level case when  $0 \leq h \leq 0.35$ . Furthermore, when  $h = 1/2$  the optimum  $d_{\min}^2(1/2) = 3$  (the corresponding uncoded value is 2), and this is reached when the  $\{(1, 2), Q1\}$ ,  $\{(3, 1), Q1\}$ , or  $\{(1, 3), Q2\}$  combinations are used. However, there also exist modulation indices for which coding decreases the optimum  $d_{\min}^2(h)$  compared to the uncoded case. Note that when  $0 \leq h \leq 0.45$  no combination using mapping rule Q2 is optimal and when  $h = 0.55$  and  $h = 0.60$  no combination using mapping rule Q1 is optimal.

When  $\nu = 2$  the optimum  $d_{\min}^2(h)$  is significantly increased over the  $\nu = 1$  case. When  $h = 1/2$ , the optimum  $d_{\min}^2(1/2)$  is increased from 3 to 5 and this can be reached with the  $\{(1, 7), Q1\}$  combination or with the  $\{(1, 6), Q2\}$  combination. The combinations  $\{(7, 2), Q1\}$  and  $\{(7, 5), Q2\}$  are optimal when  $0 \leq h \leq 0.30$ . Note that whenever a combination  $\{\bar{G}(D), Q11\}$  is optimal the combination  $\{\bar{G}(D), Q2\}$  is also optimal even when the number of connections in the lower polynomial is even. Calculations indicate that these two combinations are almost (but not exactly) identical from the  $d_{\min,N}^2(h)$  point of view.<sup>(19)</sup> Figure 11.12 shows  $d_{\min,N}^2(h)$  as a function of  $h$  with  $N$  as a parameter for the  $\{(7, 2), Q1\}$  combination. To compare the uncoded four-level CPFSK scheme with the coded  $\nu = 2$  schemes Figure 11.13 is included. This figure shows the right upper bounds on  $d_{\min}^2(h)$  for some optimal  $\nu = 2$  combinations. A significant increase in  $d_{\min}^2(h)$  can be achieved with coding for almost all modulation indices in the interval  $0 < h \leq 1$ . On the other hand, the corresponding  $N$  values are significantly larger.

When  $\nu = 3$  the optimum  $d_{\min}^2(h)$  again increases compared to the  $\nu = 2$  case. As an example, when  $h = 1/2$  the optimum  $d_{\min}^2(h)$  is increased from 5 to 6 and this can be reached with the  $\{(1, 15), Q1\}$  combination or the  $\{(1, 14), Q2\}$  combination. When  $0 \leq h \leq 0.25$  the combinations  $\{(13, 4), Q1\}$  and  $\{(13, 17), Q2\}$  are optimal, and the  $\{(3, 10), Q1\}$  combina-

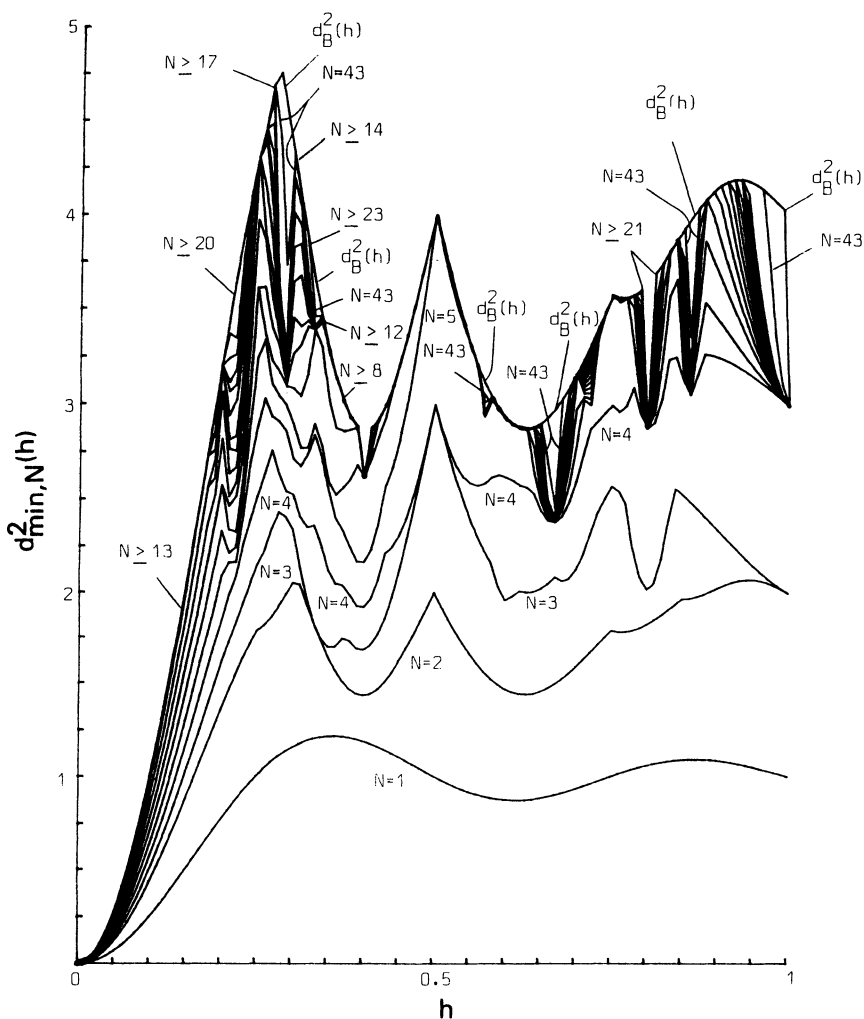


Figure 11.12.  $d_{\min, N}^2(h)$  as a function of  $h$  with  $N$  as a parameter when the rate 1/2 (7, 2)-convolutional encoder with four-level CPFSK modulation is used (mapping rule Q1).

tion is optimal in  $0.30 \leq h \leq 0.40$ . Just as in the  $\nu = 2$  case, whenever a combination  $\{\bar{G}(D), Q11\}$  is optimal, the combination  $\{\bar{G}(D), Q2\}$  is also optimal, even when the number of connections in the lower polynomial is even.

For  $\nu = 4$  a complete search has only been done for  $h = 1/4$ . The optimum  $d_{\min}^2(1/4) = 6.151$  and the corresponding optimal combinations

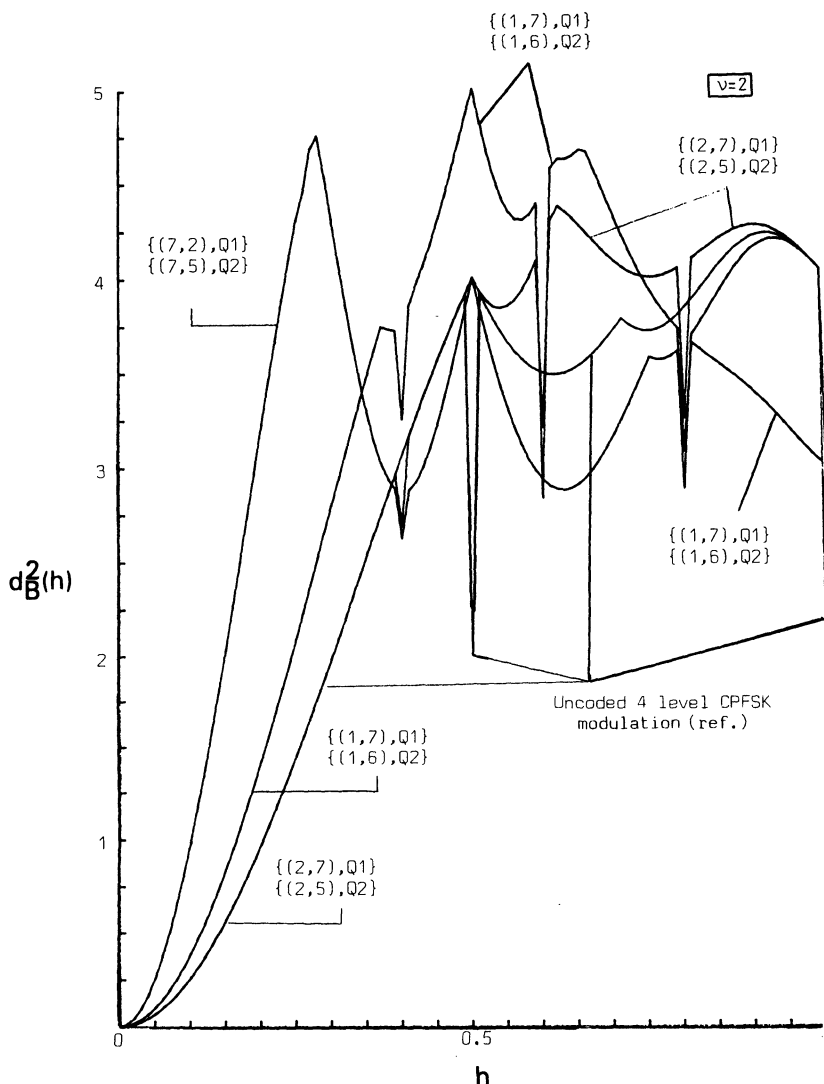


Figure 11.13. Upper bounds on  $d_B^2(h)$  for some combinations of a rate 1/2 convolutional encoder and a four-level mapping rule. CPFSK modulation is used. These upper bounds are tight for all modulation indices of practical interest.

are  $\{(23, 10), Q1\}$  and  $\{(23, 33), Q2\}$ . For other modulation indices, combinations have been found which significantly increase  $d_{\min}^2(h)$  compared to the  $\nu = 3$  case. As an example, when  $h = 1/2$  the  $\{(4, 23), Q1\}$  combination achieves  $d_{\min}^2(1/2) = 7$ .<sup>(19,20)</sup>

### Summary of Distance Results

Figure 11.14 summarizes the rate 1/2 encoders that are optimal with two- and four-level CPFSK when the modulation index is small. Figures

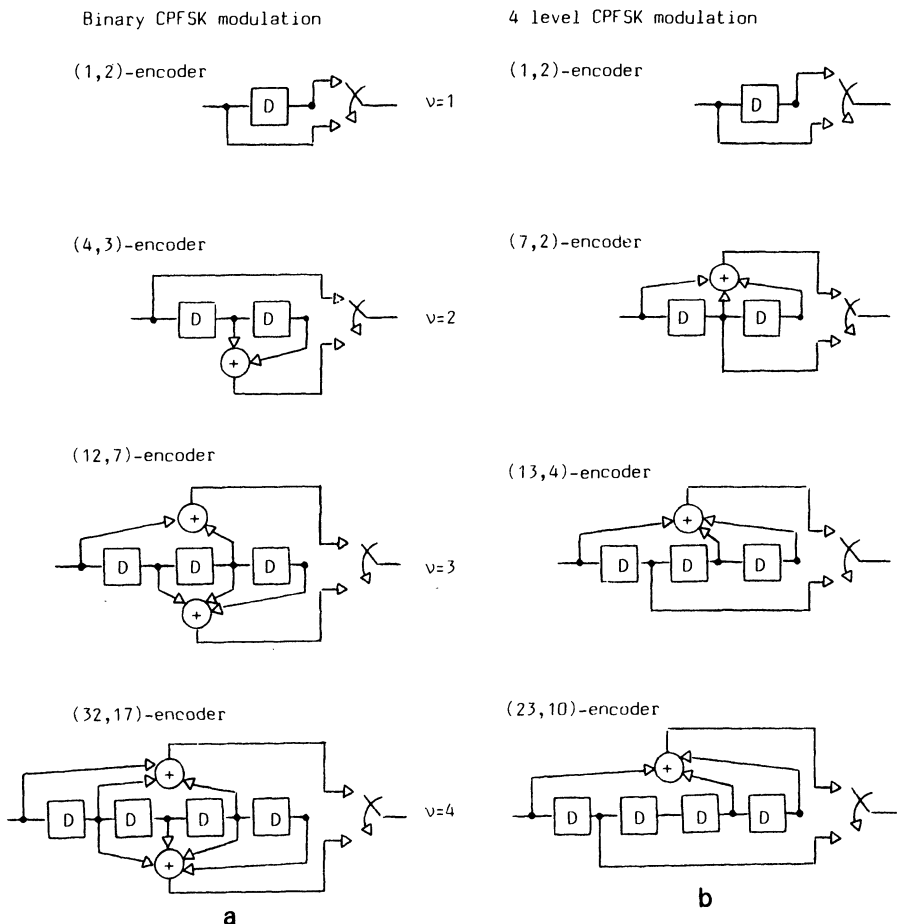


Figure 11.14.(a) Examples of optimal rate 1/2 convolutional encoders when the modulation index  $h$  is small. Binary CPFSK modulation. (b) Examples of optimal rate 1/2 convolutional encoders when the modulation index is small. Four-level CPFSK modulation with mapping rule Q1.

11.15 and 11.16 summarize the behavior of  $d_{\min}^2(h)$  vs.  $h$  that we have found for the best codes. Uncoded CPFSK appears for reference, and it is clear that coding leads to large gains. One penalty for this is a much longer requirement for the path memory, which is closely related to  $N$ ; another penalty is bandwidth expansion.

Just as the error probability for the combined schemes is dominated by the term  $Q((d_{\min}^2 E_b / N_0)^{1/2})$ , the probability for a rate 1/2 code combined with BPSK or QPSK is  $Q((d_f E_b / N_0)^{1/2})$ , where  $d_f$  is the free Hamming distance. From the coding literature we can construct Table 11.2, which compares the  $d_{\min}^2$  and  $d_f$  from these two approaches. The table shows that the coded CPFSK approach is as good as or even a little better than the coded QPSK method, and it can achieve better spectral tails for a fixed signal envelope than can QPSK. The most important fact is not depicted

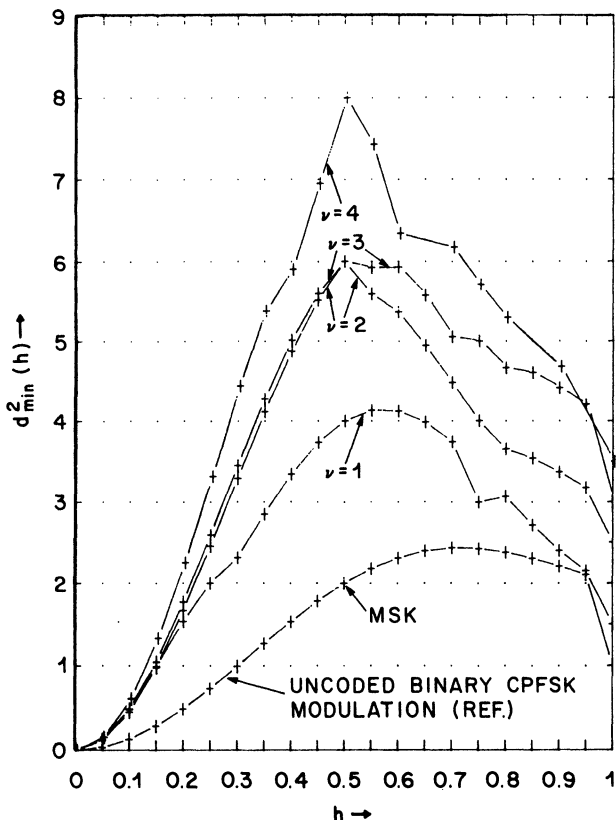


Figure 11.15. Rate 1/2 convolutional encoder and binary CPFSK modulation. The optimum  $d_{\min}^2(h)$  for different  $v$  and  $h$ . See also Tables D.1-D.2. Note that the connection lines do not contain any numerical results.

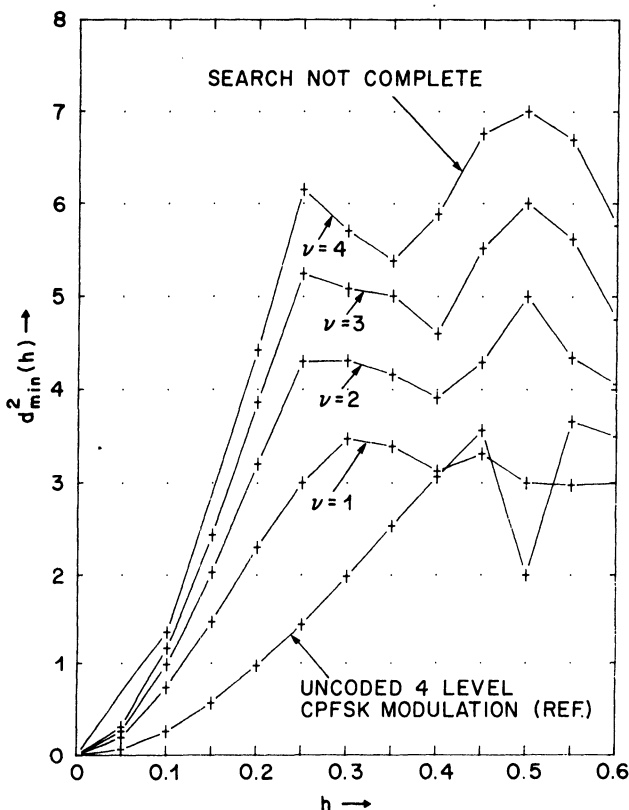


Figure 11.16. Rate 1/2 convolutional encoder and four-level CPFSK modulation. The optimum  $d_{\min}^2(h)$  for different  $v$  and  $h$ . See also Tables D.3-D.5. Note that the connection lines do not contain any numerical results.

**Table 11.2. Comparison between the Optimal Rate 1/2 Convolutional Codes for  $d_{\min}^2(1/2)$  and  $d_f$**

$v$	$d_f$ best code	$d_{\min}^2(1/2)$ : Optimal combination	
		$M = 2$	$M = 4$
1	3	4	3
2	5	6	5
3	6	6	6
4	7	8	7 <sup>a</sup>

<sup>a</sup> Search not complete.

in the table: That the optimal encoders for QPSK and CPFSK are quite different.

### 11.2.6. Energy–Bandwidth Tradeoff

The considerable distance gains of coded CPFSK are bought with an increase in bandwidth over uncoded CPFSK. Denote by  $2BT_b$  the double-sideband positive-frequency bandwidth of uncoded CPFSK, just as was done in Chapter 5. With the introduction of coding, this increases to approximately  $2B_cT_b = 2BT_b/R_c$ .

Figure 11.17 gives a detailed picture of the bandwidth of the CPFSK family of modulations without coding. 99% and 99.9% out of band powers

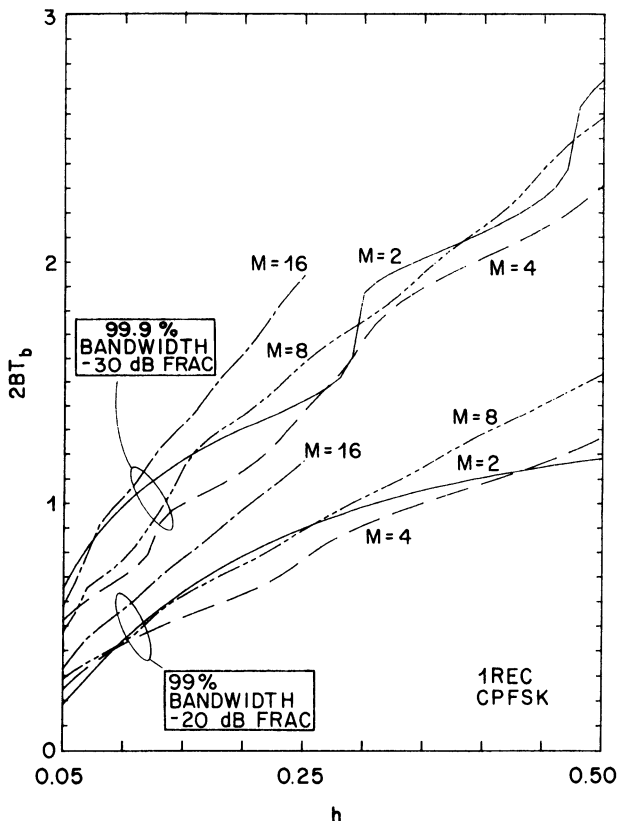


Figure 11.17. The normalized bandwidth  $2BT_b$  as a function of the modulation index  $h$  when  $M$  level CPFSK modulation is used,  $M = 2, 4, 5$ , and  $16$ . The levels in the fractional out of band power function used in the definitions of bandwidth are  $-20$  dB (99% power within the band) and  $-30$  dB (99.9%).

(defined in Section 5.1) are shown, calculated by the method of Chapter 4. By comparison, Figure 11.18 gives an energy-bandwidth plot for coded CPFSK in the style of Section 5.1;  $d_{\min}^2$  relative to MSK is plotted against the 99% power bandwidth  $2B_c T_b$ . (No separate measurement of the coded spectra was performed.) It is clear that the energy-bandwidth performance of coded CPFSK becomes rapidly better as the convolutional constraint length increases, and that much better schemes than MSK exist. However, a comparison with the energy-bandwidth trajectory of two- and four-level uncoded CPFSK, also plotted in the figure, shows that coding with these short constraint lengths does not really lead to an overall improvement throughout the plane. In the coded two-level schemes particularly, the factor-of-2 bandwidth expansion is quite damaging. But the coding is effective at achieving large distances with simple hardware, and we shall see in the next section that a higher encoder rate and more FSK levels will improve performance.

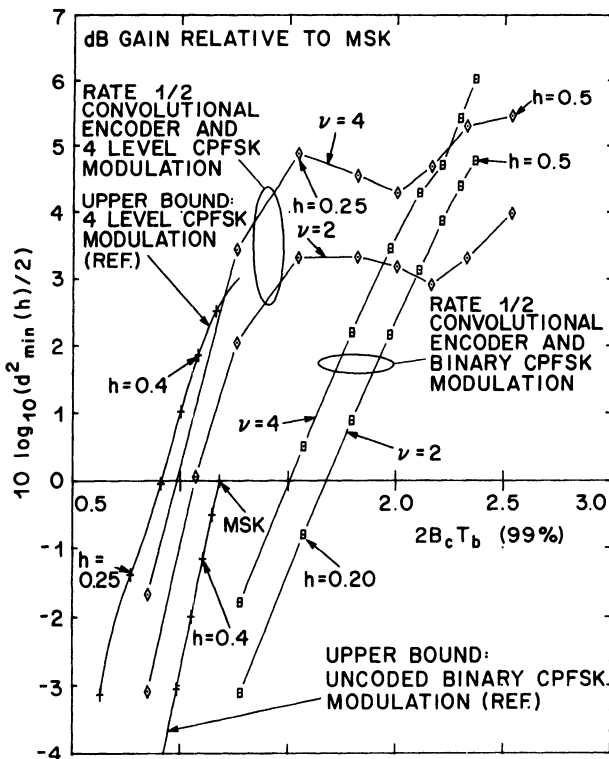


Figure 11.18. Power-bandwidth trade-off for some of the coded CPFSK schemes considered in Section 11.2. Note that the connection lines do not contain any numerical results.

### 11.3. Coded Multilevel CPM

In this section we will increase the encoder rate and the alphabet size of the FSK in an attempt to find coded schemes with a more attractive energy-bandwidth performance. Following Refs. 3 and 4, we will typically deal with eight- and higher level CPFSK. The encoder rate with eight-level schemes will be  $2/3$ , that is, two information bits per eight-level FSK symbol. We will also give a method generalizing the eight-level results to 16-level CPM with rate  $3/4$  codes and 32-level CPM with rate  $4/5$  codes. All of these schemes combine energy and bandwidth efficiency with constant envelope. Significant improvements are obtained over the CPM and multi- $h$  schemes of Chapter 3. The price for this is increased complexity in the FSK and the complexity in the encoder.

We will also propose a way to extend the CPFSK method to smoothed partial response CPM. The principal idea is to use the optimal encoders for CPFSK in a CPM scheme with weak partial response.

Lists of good encoder/modulator combinations appear in Appendix D.

#### 11.3.1. System Description

The general system description in Section 11.2.1 and Figure 11.5 still holds, but in this section we study a restricted class of high rate convolutional encoders. These have  $k = n - 1$ ,  $n = 3, 4, 5, 6$ . Furthermore, the first  $(n - 2)$  data symbols in each block are not coded at all.

$$v_m^l = u_m^l, \quad m = 1, 2, \dots, n - 2, \quad \text{all } l \quad (11.14)$$

The only coding used is a conventional (in general nonsystematic) rate  $1/2$  convolutional encoder which encodes the data symbol sequence  $\dots, u_k^{-1}, u_k^0, u_k^1, \dots$  to produce the two coded symbol sequences  $\dots, v_{n-1}^{-1}, v_{n-1}^0, v_{n-1}^1, \dots$  and  $\dots, v_n^{-1}, v_n^0, v_n^1, \dots$ . Formally this can be written as

$$v_m^l = \sum_{i=0}^{\nu} g_{m,k}(i) u_k^{l-i}, \quad l = \dots, -1, 0, 1, \dots, \quad m = n - 1, n \quad (11.15)$$

where  $g_{m,k}(i) \in \{0, 1\}$  and represents the connection between  $u_k^{l-i}$  and  $v_m^l$ . The summation is modulo 2 and  $\nu$  is the number of delay elements in the encoder. The state  $x$  of the encoder has  $\nu$  binary components and there are  $2^\nu$  states. Since the encoder described above has  $(n - 1)$  inputs and  $n$  outputs, the rate  $R_c$  of the encoder is  $(n - 1)/n$  data symbols/coded symbol.

As before, the coded sequence  $v$  is the input to a mapper which associates levels in an  $M$ -ary alphabet with blocks of coded symbols. The output from the mapper is a sequence  $\alpha$  of channel symbols  $\alpha_l \in \{\pm 1, \pm 3, \dots, \pm(M - 1)\}$  all  $l$ , where  $M$  is a power of 2. The mapper has rate  $R_m = \log_2(M)$  coded symbols/channel symbol, which is fixed at  $n$ . The overall rate  $R$  is therefore  $R = R_c R_m = (n - 1)$  binary data symbols/channel symbol. The (natural)  $M$  level mapping rule used is defined by

$$\alpha_l = \sum_{i=0}^{n-1} v_{ln+i} \cdot 2^{(n-i)} - M + 1, \quad l = 0, \pm 1, \pm 2, \dots \quad (11.16)$$

The symbols  $v_{ln}$  and  $v_{(l+1)n-1}$  are referred to as the most significant bit (MSB) and the least significant bit (LSB), respectively. The channel encoding in this section can be viewed as a conventional rate 1/2 convolutional encoder of the least significant symbol in the mapping rule. For further details, see Refs. 3–7.

In this section it is assumed that the frequency pulse of the CPM modulator is given by

$$g(t) = \begin{cases} [1 - \cos(\pi t/\varepsilon T)]/4T, & 0 < t < \varepsilon T \\ 1/2T, & \varepsilon T \leq t \leq T \\ [1 + \cos(\pi(t-T)/\varepsilon T)]/4T, & T < t < (1 + \varepsilon)T \\ 0, & \text{otherwise} \end{cases} \quad (11.17)$$

with  $0 \leq \varepsilon \leq 1$ . When  $\varepsilon = 0$  and  $\varepsilon = 1$  we have the CPFSK scheme and the 2RC scheme, respectively. Thus (11.17) defines a class of frequency pulses in between CPFSK and 2RC, and a certain degree of smoothness and partial response can be controlled by the parameter  $\varepsilon$ .

For CPFSK modulation ( $\varepsilon = 0$ ) we will search for the optimal rate 1/2 noncatastrophic convolutional encoders such that, for given  $v$  and  $h$ ,  $d_{\min}^2$  is maximized. Formally this can be written as (11.8). Some of the optimal encoders are then used together with a frequency pulse with a small  $\varepsilon$ ,  $\varepsilon > 0$ . The idea is to create a modulation scheme which has roughly the same  $d_{\min}^2$  as the corresponding coded CPFSK scheme but with considerably smaller side lobes in the spectrum because of the smoothing and partial response.

### 11.3.2. Bounds on the Free Euclidean Distance

As an example of the upper bound defined in Section 11.2 consider the modulation scheme in Figure 11.19. This scheme consists of the rate

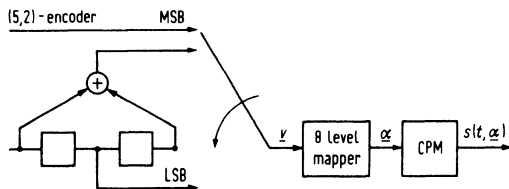


Figure 11.19. The rate 2/3 (5, 2)-encoder combined with eight-level CPM modulation.

2/3 (5, 2)-encoder combined with eight-level CPFSK modulation. Now assume that the start state of the encoder is  $x = (0, 0)$ . If the two sequences  $u_\alpha = (01, 10, 00, 01)$  and  $u_\beta = (10, 01, 10, 01)$  are fed into the encoder the corresponding phase functions are  $\phi(t, \alpha)$  and  $\phi(t, \beta)$ . These phase functions are linearly increasing or linearly decreasing depending on the corresponding channel symbols; see the example in Figure 11.20. It is easy to see that the two data symbol sequences  $u_\alpha$  and  $u_\beta$  given above generate a phase and state merger after four channel symbol intervals. Thus an upper bound on  $d_{\min}^2(h)$  for the specific coded CPFSK scheme given in Figure 11.19 can be calculated from (11.9), to get the upper bound

$$d_{\min}^2(h) \leq 2 \left( 4 - \frac{2}{3} \frac{\sin(2\pi h)}{2\pi h} - \frac{10}{3} \frac{\sin(4\pi h)}{4\pi h} \right) \quad (11.18)$$

Let us now employ a frequency pulse  $g(t)$  with the parameter  $\epsilon \neq 0$ . Using the sequences  $u_\alpha$  and  $u_\beta$  we again generate phase and state mergers

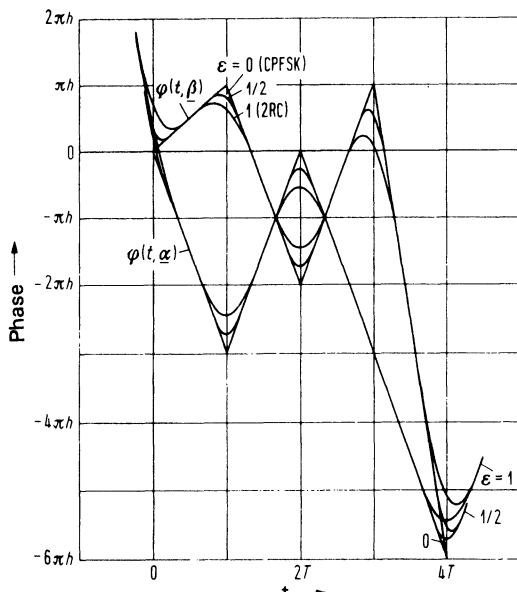


Figure 11.20. Examples of phase and state mergers for the modulation scheme in Figure 11.19. The underlying channel symbol sequences are  $\alpha = (-3, 3, -3, -3)$  and  $\beta = (1, -3, 3, -7)$ .

for these cases. We add a common channel symbol at the end of the two channel symbol sequences  $\alpha$  and  $\beta$  generated by  $u_\alpha$  and  $u_\beta$ , and because of the partial response we must also specify a common start-symbol. Figure 11.20 shows the corresponding phase functions  $\phi(t, \alpha)$  and  $\phi(t, \beta)$  when  $\epsilon = 1/2$  and  $\epsilon = 1$ ; the start symbol is  $-7$  and the added channel symbol is  $3$ . Note that the phase functions are shown with different delays for different values of the parameter  $\epsilon$ . This makes Figure 11.20 easier to read. It is seen that a phase and state merger occurs after five channel symbol intervals, and an upper bound on  $d_{\min}^2(h)$  for the specific coded CPM scheme ( $0 < \epsilon \leq 1$ ) given in Figure 11.19 can be calculated from this merger. By increasing the parameter  $\epsilon$  the phase function  $\phi(t, \alpha)$  becomes more smooth, and it is this smoothing that reduces the sidelobes in the spectrum.

In Chapter 3 it was shown that the Euclidean distance between any two transmitted signals  $s(t, \alpha)$  and  $s(t, \beta)$  is a function only of the difference sequence  $\gamma$ . By making the  $k$ th encoder input  $0$  (i.e., the second in Figure 11.19), it is possible to generate phase and state mergers corresponding to the difference sequences  $\gamma = (\dots, 0, 8l, -8l, 0, \dots)$ ,  $l = 1, 2, \dots, 2^{n-2} - 1$ . These phase and state mergers are independent of the actual rate  $1/2$  convolutional encoder used, and thus encoder-independent upper bounds on  $d_{\min}^2$  can be calculated from them. Taking the minimum of these ( $2^{n-2} - 1$ )

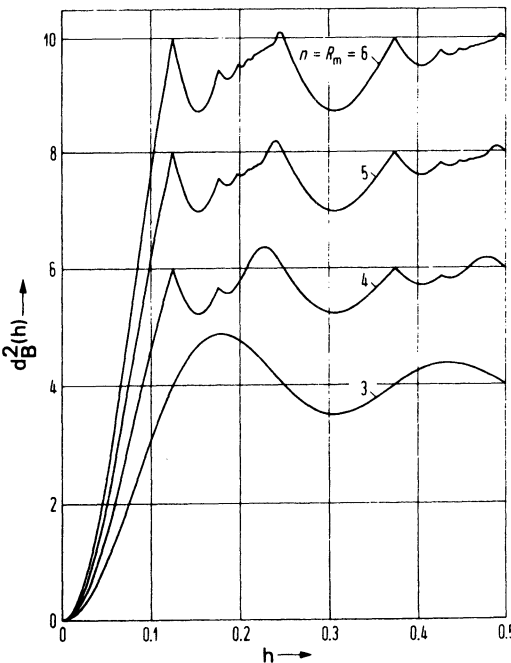


Figure 11.21. Encoder-independent upper bounds on  $d_{\min}^2(h)$ , equation (11.19). Coded eight-level to 64-level CPFSK modulation is assumed.

upper bounds and assuming CPFSK modulation yields the encoder-independent upper bound (see Refs. 3, 4)

$$d_{\min}^2(h) \leq 2(n-1) \min_{1 \leq l \leq A} \left( 1 - \frac{\sin(l8\pi h)}{l8\pi h} \right) \quad (11.19)$$

where  $A = 2^{n-2} - 1$ . Figure 11.21 shows this upper bound with  $n$  as a parameter. Two questions arise: Are the upper bounds tight, and if they are tight, which rate  $(n-1)/n$  convolutional encoders together with  $2^n$ -level CPFSK modulation reach this bound? In particular we are interested in encoders with small  $\nu$  values. As we increase  $n$  the number of encoder-independent weak modulation indices is also increased, owing to the distance properties of the encoded  $2^{n-2}$  level CPFSK scheme; see Refs. 3 and 4 for details.

### 11.3.3. Code Search and Tables of Good Codes

For the case of rate 2/3 convolutional encoders with eight-level CPFSK modulation, the encoder consists of an uncoded MSB and a rate 1/2 code on the remaining bit, as in Figure 11.19. The optimum [largest  $d_{\min}^2(h)$ ] rate 1/2 convolutional encoders for this case have been found when  $1 \leq \nu \leq 4$ .<sup>(3,4,21)</sup> Some of these rate 1/2 encoders can then be used in rate 3/4 and rate 4/5 convolutional encoders combined with 16-level and 32-level CPFSK modulation. The specific modulation indices studied were  $h = 2/22$ ,

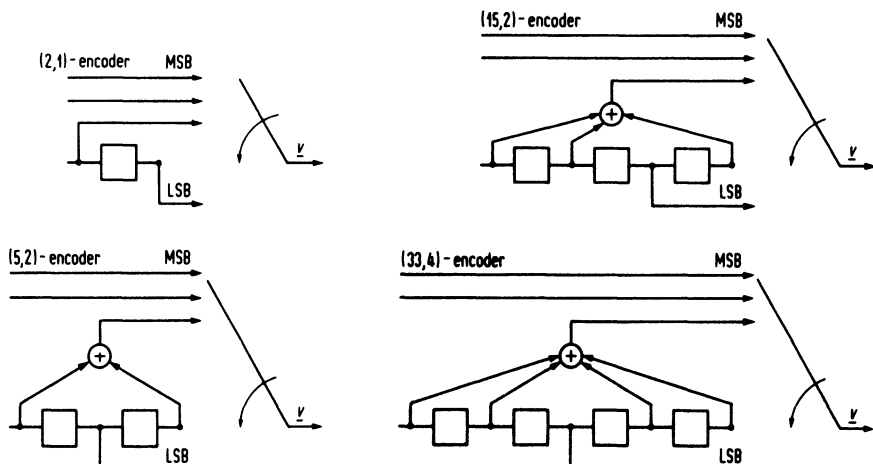


Figure 11.22. Examples of good rate 3/4 convolutional encoders when combined with 16-level CPFSK modulation (assuming small modulation indices).

$2/21, \dots, 2/9, 2/8$ . The numerical results are presented in Appendix D in Tables D.6–D.13.

### Rate 2/3 Convolutional Encoders and Eight-Level CPFSK

The optimal rate 1/2 convolutional encoders with  $\nu = 1, 2, 3$ , and 4 are listed in Appendix D, Tables D.6–D.9, together with their distances. At  $\nu = 1$  and  $h = 1/10$ , for example, the best code has square distance 0.983 and there are four encoders with this distance. At  $\nu = 2$ , the distances achieved are significantly larger than at constraint 1; at  $h = 2/9$ , eight encoders all achieve square distance 4.46, which is also the upper bound value at this  $h$ . At  $\nu = 3$ , distances are again somewhat larger. At constraint 4, heavy calculation is required and complete searches have been performed only for a few  $h$ ; at other indices distances have been calculated for the (33, 4) encoder only. Distance again increases and the upper bound is not reached at a number of modulation indices.

### Rate 3/4 and Rate 4/5 Convolutional Encoders

For rate 3/4 and rate 4/5 convolutional encoders combined with 16- and 32-level CPFSK modulation no complete search for the optimal rate

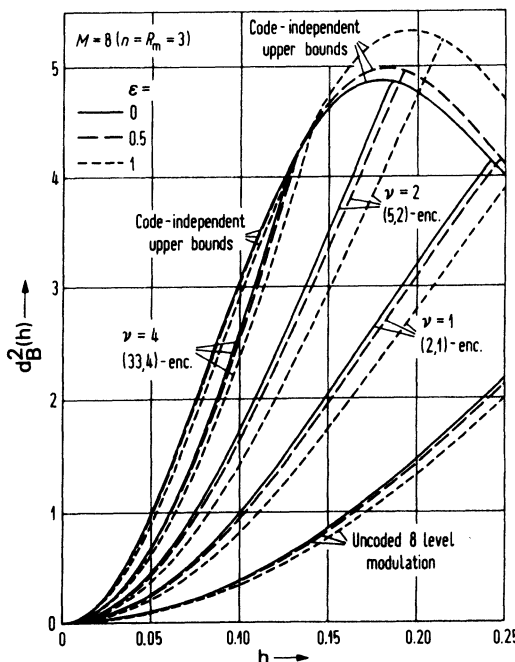


Figure 11.23. Upper bounds on  $d_{\min}^2(h)$  when a rate 2/3 convolutional encoder and eight-level CPM are used. The frequency pulse  $g(t)$  follows equation (11.17).

1/2 encoders has been performed. Instead, the (2, 1), (5, 2), (15, 2), and (33, 4) encoders found for the rate 2/3 case have been explored. The calculated  $d_{\min}^2(h)$  values are given in Tables D.10-D.13. There is quite a significant increase in the  $d_{\min}^2(h)$  values when  $\nu$  is increased. For small modulation indices ( $h \leq 2/17$ ) the upper bound is not reached at  $\nu \leq 4$ .

### *Summary of Numerical Results*

Very good schemes of combined rate  $(n - 1)/n$  convolutional encoders and  $2^n$  level CPFSK modulation,  $n = 3, 4, 5$ , have been found when the modulation index is in the interval  $0 \leq h \leq 1/4$ . Examples of good rate 1/2 encoders are the (2, 1)-encoder, the (5, 2)-encoder, the (15, 2)-encoder, and the (33, 4)-encoder. These are shown in Figure 11.22 assuming  $n = 4$ . When using these four rate 1/2 encoders, the shortest minimum distance mergers at small  $h$  are  $\gamma = (-4, 6, -2)$ ,  $\gamma = (-4, 6, -6, 4)$ ,  $\gamma = (-4, 8, -6, 6, -4)$ , and  $\gamma = (-4, 4, 2, 0, -2, -4, 4)$ , respectively. If we use these  $\gamma$  sequences to construct upper bounds on  $d_{\min}^2(h)$  we obtain (CPFSK modulation)

$$d_{\min}^2(h) \leq (n - 1) \left( 3 - \frac{4}{3} \frac{\sin(2\pi h)}{2\pi h} - \frac{5}{3} \frac{\sin(4\pi h)}{4\pi h} \right), \quad (2, 1)\text{-encoder}$$

$$d_{\min}^2(h) \leq (n - 1) \left( 4 - \frac{2}{3} \frac{\sin(2\pi h)}{2\pi h} - \frac{10}{3} \frac{\sin(4\pi h)}{4\pi h} \right), \quad (5, 2)\text{-encoder}$$

$$d_{\min}^2(h) \leq (n - 1) \left( 5 - \frac{2}{3} \frac{\sin(2\pi h)}{2\pi h} - \frac{13}{3} \frac{\sin(\pi h)}{4\pi h} \right), \quad (15, 2)\text{-encoder}$$

$$d_{\min}^2(h) \leq (n - 1) \left( 7 - 2 \frac{\sin(2\pi h)}{2\pi h} - 4 \frac{\sin(4\pi h)}{4\pi h} - \cos(2\pi h) \right), \quad (33, 4)\text{-encoder}$$

Some of the encoder-dependent upper bounds on  $d_{\min}^2(h)$  are shown in Figures 11.23 ( $n = 3$ ) and 11.24 ( $n = 4$ ). Also shown are the corresponding encoder-independent upper bound (11.19) and uncoded upper bound. Since many of the upper bounds in Figures 11.23 and 11.24 are tight in the CPFSK case, these figures actually show  $d_{\min}^2(h)$  for some specific coded CPFSK schemes.

For the same four encoders, we can replace the CPFSK frequency pulse with a smoother one from (11.17) and look at the effect of the smoothness parameter  $\epsilon$  on the upper bounds. As shown in Figures 11.23–11.24 the bounds do not change much if  $0 \leq \epsilon \leq 1/2$ . We can expect that  $d_{\min}$  for small  $\epsilon$  will be similar to the CPFSK case. More details appear in Refs. 3 and 21.

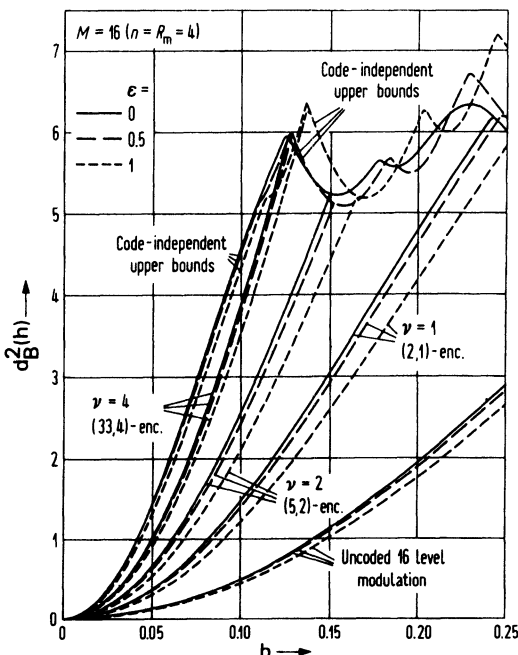


Figure 11.24. Upper bounds on  $d_{\min}^2(h)$  when a rate 3/4 convolutional encoder and 16-level CPM are used. The frequency pulse  $g(t)$  follows equation (11.17).

### 11.3.4. Energy and Bandwidth Efficiency of Coded CPM

The true power spectral density for coded CPM schemes is not known. Instead we use estimates defined by

$$\hat{G}_c(\beta) = R_c G(R_c \beta), \quad \beta = fT_b$$

where  $G(\beta)$  is the normalized power spectral density of Chapter 4 for the corresponding uncoded  $2^n$  level CPM schemes. Figure 11.25 shows examples of estimated power spectral densities when a rate 2/3 convolutional encoder and eight-level CPM is used. The modulation index in this figure is  $h = 0.091 (\approx 1/11)$ , and a reduction of the sidelobes with increasing  $\epsilon$  is clearly demonstrated. Figure 11.26 shows estimated power spectral densities for two useful coded CPFSK schemes, with the power spectra for conventional uncoded MSK also given as a reference. The rate 2/3 (33, 4)-encoder combined with eight-level CPFSK and  $h = 1/11$  yields a spectrum which is much better than the MSK spectrum, even though the coded scheme has  $d_{\min}^2 = 2.1615$ , which is slightly larger than  $d_{\min}^2$  for MSK. Thus this coded CPFSK scheme saves bandwidth compared to MSK without loss of energy efficiency. The rate 3/4 (33, 4)-encoder combined with 16-level CPFSK and

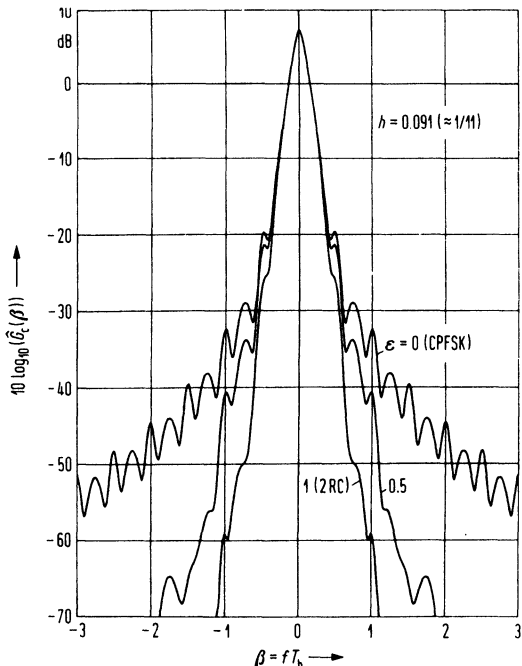


Figure 11.25. Examples of estimated power spectra when a rate 2/3 convolutional encoder and eight-level CPM is used.

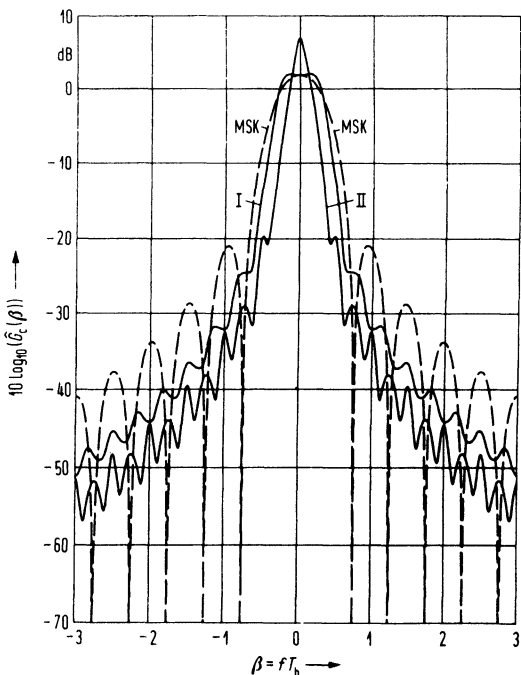


Figure 11.26. Estimated power spectra for some interesting coded CPFSK schemes.

$h = 2/15$  also yields a better spectrum than MSK, but has  $d_{\min}^2 = 5.64$ ! This coded CPFSK schemes saves both power and bandwidth relative MSK. Still more spectrally efficient schemes can easily be obtained by using a small  $\epsilon > 0$  instead of CPFSK.

Figure 11.27 plots bandwidth vs.  $h$  using the 99% power in band definition of bandwidth as in Section 5.1. This is estimated by the relation  $2\hat{B}_c T_b = 2BT_b/R_c$ , in which  $BT_b$  is the single-sideband rf normalized bandwidth of the uncoded CPM scheme. Some uncoded schemes are shown for reference. Also compare Figure 11.17.

Figure 11.28–11.30 show power-bandwidth tradeoffs for some of the schemes considered in Section 11.3. On the vertical axis is the gain in  $d_{\min}^2$  compared to MSK and on the horizontal axis is the estimated normalized double sideband 99% bandwidth. (The connection lines between schemes with different  $h$  in these figures do not contain any numerical results.) Figure 11.28 depicts the rate 2/3 encoders given in Tables D.5–D.9 combined with eight-level CPFSK modulation. Specific schemes are shown as rectangles; note that coded systems with the same  $h$  value have the same estimated bandwidth for all  $n$  values. The coded schemes become more power efficient with increasing  $n$ , until the encoder-independent upper bound is reached. Figure 11.29 considers schemes consisting of the rate 3/4 encoders given in Tables D.10 and D.11 combined with 16-level CPFSK

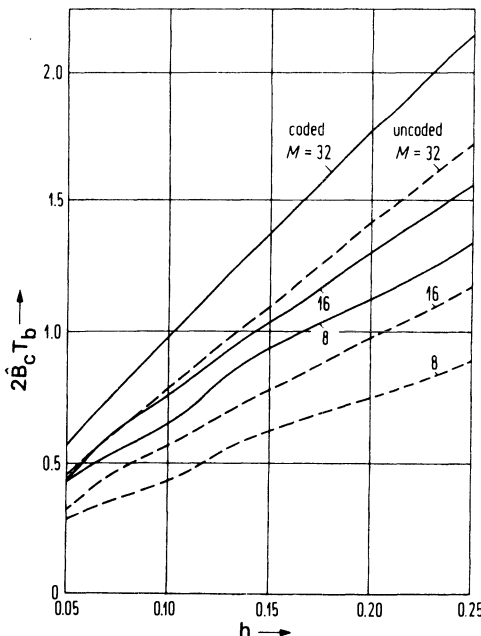


Figure 11.27. The estimated normalized double-sided bandwidth as a function of the modulation index  $h$  when a rate  $(n - 1)/n$  convolutional encoder and  $2^n$  level CPFSK modulation are used,  $n = 3, 4$ , and 5.

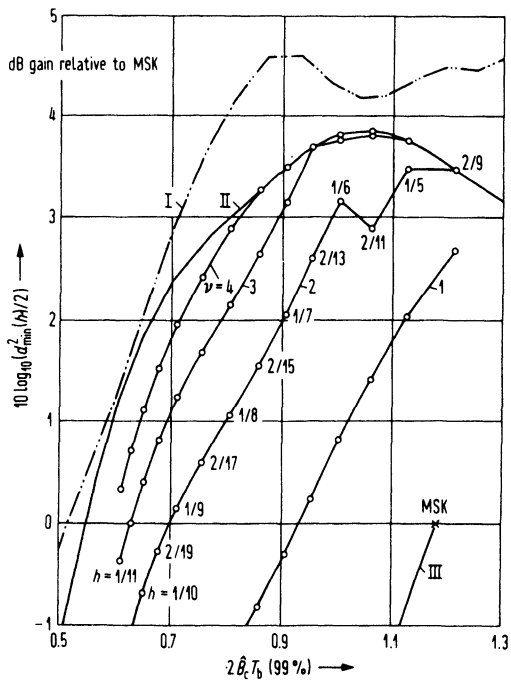
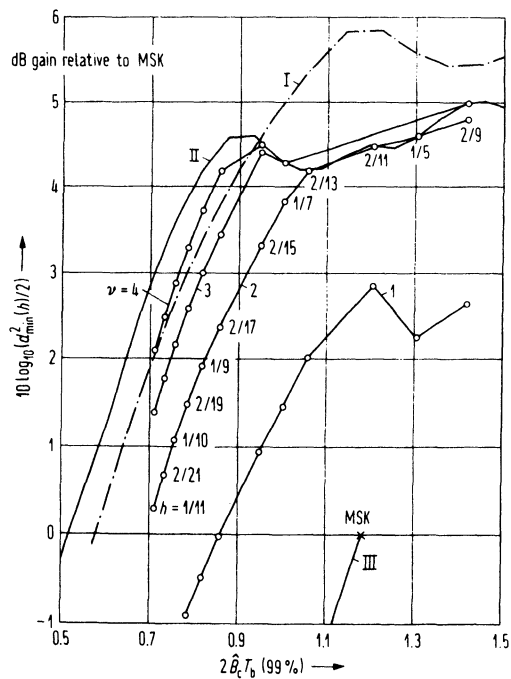


Figure 11.28. Power-bandwidth trade-off for some of the coded eight-level CPFSK schemes considered in this chapter.  $\nu = 1, 2, 3$ , and 4. The 99% power in band definition of bandwidth is used. I is the upper bound for coded 16-level CPFSK schemes, II is the upper bound for coded 8-level CPFSK, and III is binary CPFSK.



**Figure 11.29.** Power-bandwidth trade-off for some of the coded 16-level CPFSK schemes considered in this chapter.  $\nu = 1, 2, 3$ , and  $4$ . The 99% power in band definition of bandwidth is used. I is the upper bound for the coded 32-level CPFSK, II is the upper bound for coded 16-level CPFSK, and III is binary CPFSK.

modulation. These schemes also become more power efficient with increasing  $\nu$ , until the encoder-independent upper bound is reached.

Figure 11.30 considers the best schemes found in Refs. 3 and 4. It is quite obvious from this figure that schemes have been found that are much better than the MSK scheme both in terms of asymptotic error performance and of bandwidth. An example of such a scheme is the rate 3/4 (33, 4)-encoder combined with 16-level CPFSK modulation and  $h = 2/17$ . This scheme has an asymptotic gain of  $\approx 4.2$  dB and the bandwidth is only  $\approx 74\%$  of the MSK bandwidth. Other schemes appear that have the same asymptotic error performance as MSK but with roughly only half the MSK bandwidth; alternately, schemes with the same spectral efficiency as MSK but with an asymptotic performance gain of 5–6 dB have been found. Figure 11.30 shows some of the best available multi- $h$  CPFSK schemes (denoted A–D) for comparison.<sup>(10)</sup> These are clearly outperformed by the coded CPFSK schemes considered here.

### 11.3.5. Conclusions

Good coded CPFSK schemes have been found by utilizing a high rate convolutional code, and a modulation scheme with a large number of levels and a low modulation index. Relative to MSK, these schemes can either

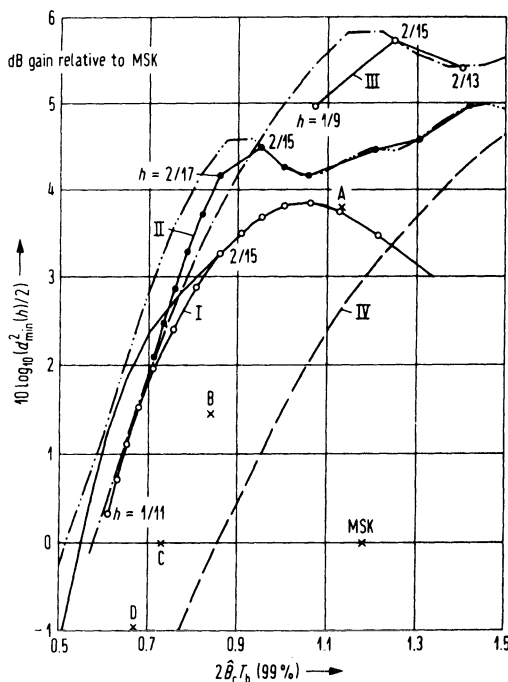


Figure 11.30. Power-bandwidth trade-off for the best schemes found in this chapter. As reference points some four-level multi- $h$  schemes have been given (A, B, C, and D).<sup>(10,4)</sup> The 99% power in band definition of bandwidth is used. I is coded 8-level CPFSK, II is coded 16-level CPFSK, III is coded 32-level CPFSK, and IV is uncoded 8-level CPFSK.

reduce bandwidth by a factor of 2 or reduce power by 5 dB. By varying the system parameters, notably the modulation index, schemes can be obtained with different combinations of bandwidth and power savings.

Code-independent upper bounds on minimum distance are useful because once they are achieved for a certain code constraint length, no increase in this length will give better performance. Upper bounds were often reached in this section. This means that for even better performance, new encoder structures and mapper must be explored. The results for coded CPM schemes in this section have been given in terms of the minimum

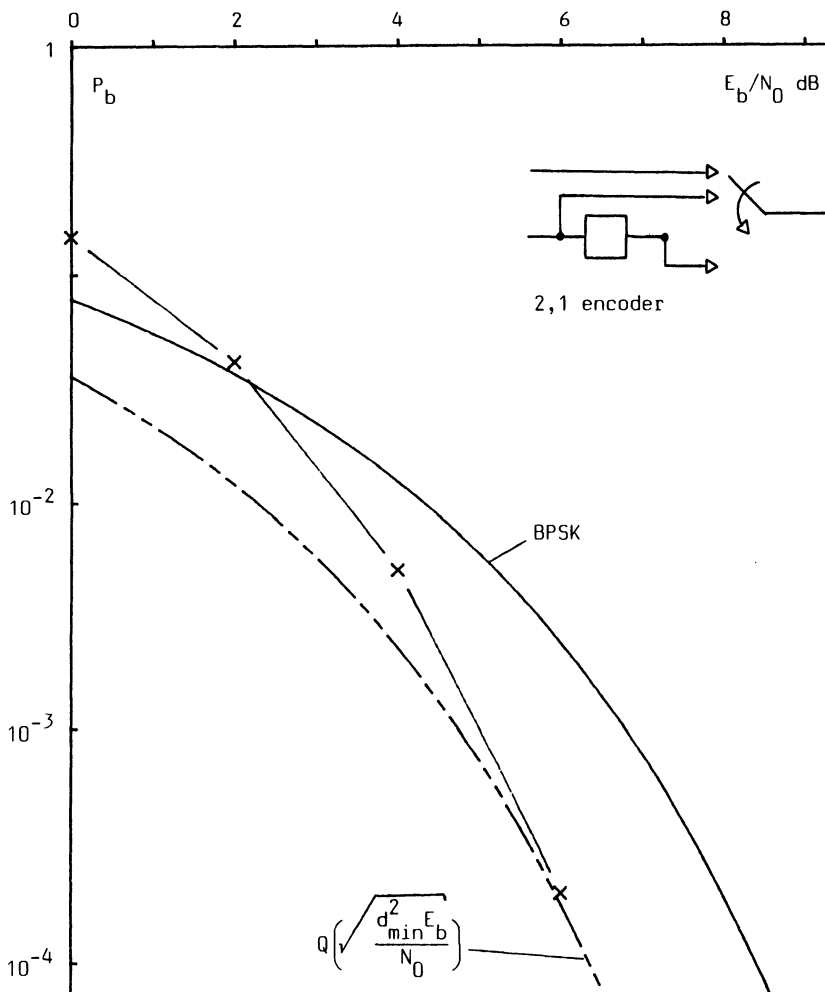


Figure 11.31. Simulated bit error probability for a rate 2/3 encoder with memory  $\nu = 1$  and polynomials (2, 1), combined with an eight-level CPFSK scheme with  $h = 1/5$ .

Euclidean distance. Recently, tight upper bounds on the bit error probability have been developed. For details, see Refs. 37 and 38.

We have discussed only one type of smooth partial response modulation in combination with coding. It had significantly lower side lobes than did the CPFSK schemes, but the spectral main lobe was not much changed. The best encoders for CPFSK were simply carried over to these smoother

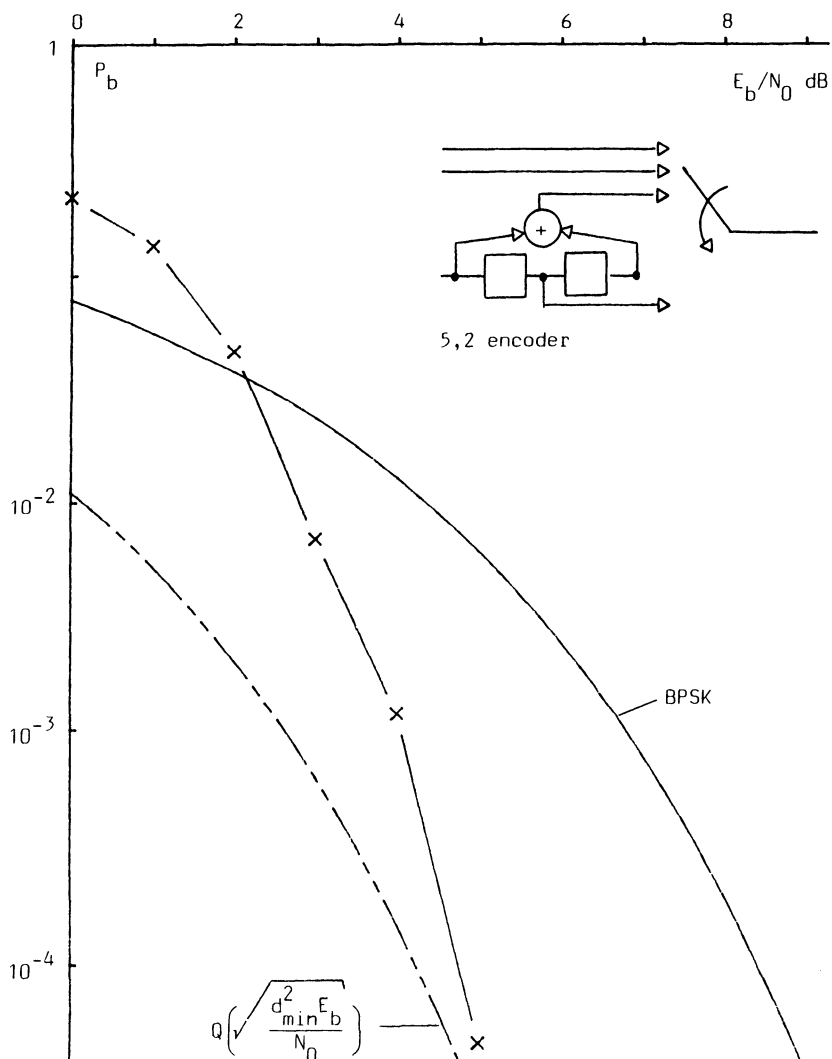


Figure 11.32. Simulated bit error probability for a rate 3/4 encoder with  $v = 2$  and polynomials (5, 2), combined with a 16-level CPFSK scheme with  $h = 2/13$ .

modulations. Except for scattered work,<sup>(24,25)</sup> little is known about how to combine partial response and coding.

Achieving the good signal properties of coded CPM requires a more complex receiver, and one that employs sequence detection. It is shown in Ref. 4 that the MLSE receiver has

$$S = p \cdot 2^{\nu+(L-1)k}$$

states in its Viterbi processor, if the modulation index is  $h = 2i/p$  ( $i$  and  $p$

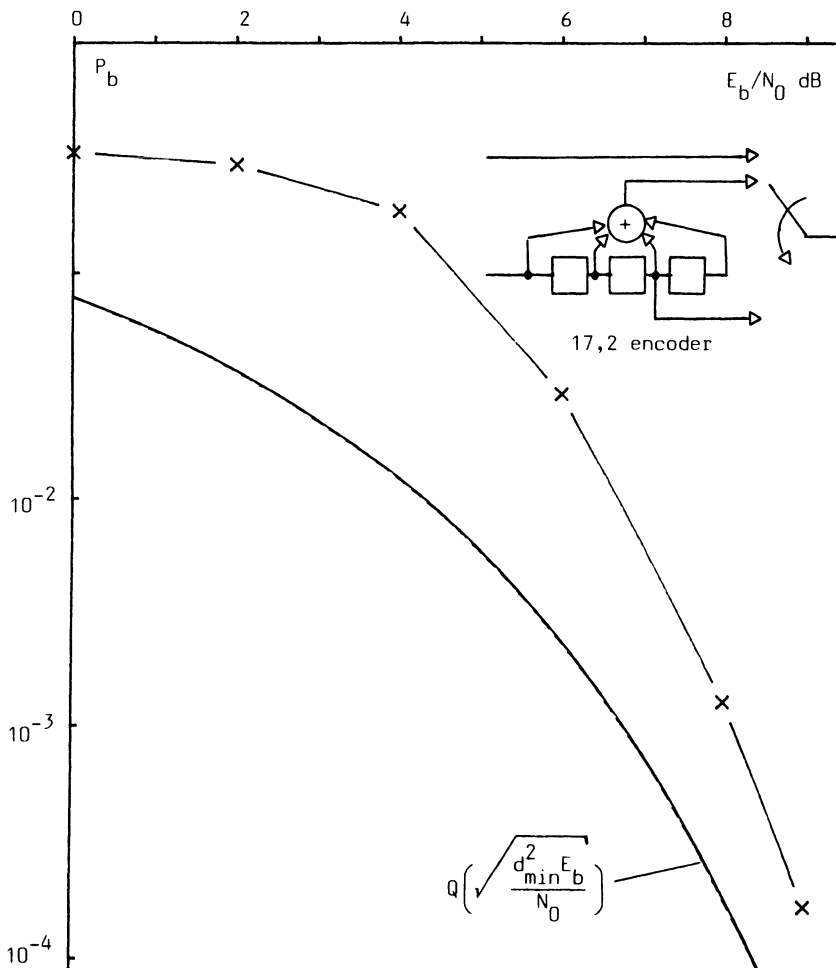


Figure 11.33. Simulated bit error probability for a rate 2/3 encoder with  $\nu = 3$  and polynomials (17, 2), combined with an eight-level CPFSK scheme with  $h = 2/21$ .

are integers without common divisor).  $\nu$ ,  $L$ , and  $k$  have an exponential effect on  $S$ ; the small  $h$ , which we would like to have, leads to a growth proportional to  $1/h$ . Some of the complexity-reducing approaches of Chapter 7 and 8 or of Ref. 33 can be applied to the coded case.

#### 11.4. Simulations of Coded CPFSK Schemes

The technique described in Chapter 7 and Appendix C has been applied to coded CPFSK, with results that we will review in this section. Tables 11.3 and 11.4 parameters for the simulated schemes and their energy-bandwidth tradeoffs appear in Figure 11.30.

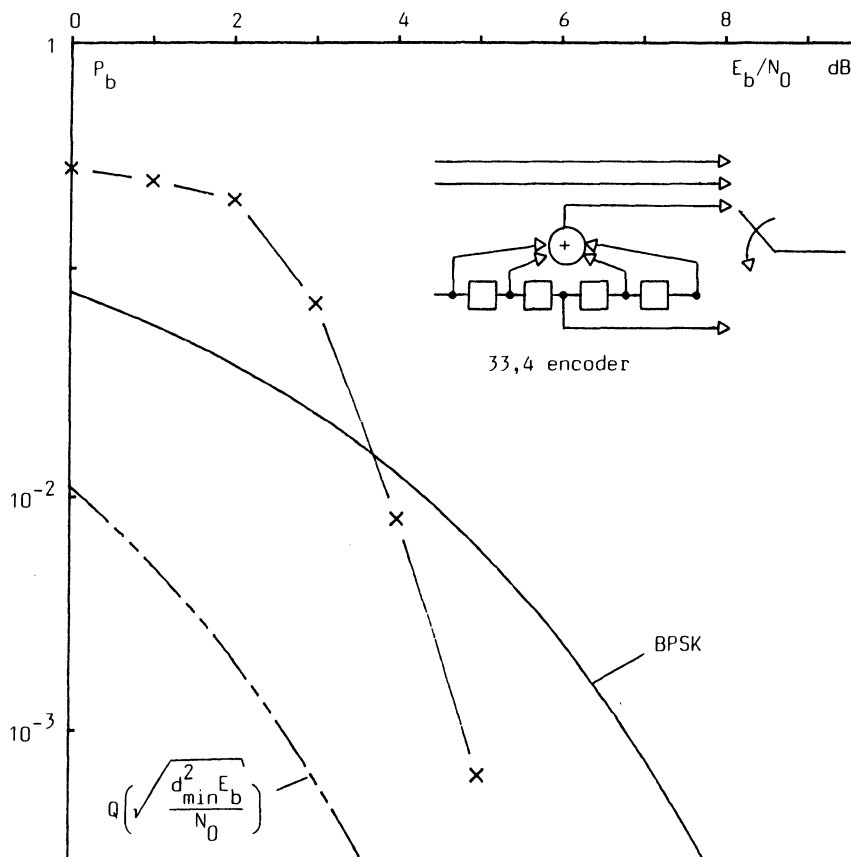


Figure 11.34. Simulated bit error probability for a rate 3/4 encoder with  $\nu = 4$  and polynomials (33, 4), combined with a 16-level CPFSK scheme with  $h = 2/17$ .

**Table 11.3. Details of Some Selected Coded and Uncoded CPFSK Schemes.  
 $2B_c T_b$  Is the 99% Bandwidth**

Scheme	$M$	$h$	$\nu$	Code	$d_{\min}^2$	$N$	$2B_c T_b$ 99%	$S$
H	8	1/5	1	2, 1	3.20	4	1.13	20
K	16	2/13	2	5, 2	5.23	19	1.06	52
L	8	2/21	3	17, 2	2.00	18	0.63	168
F	16	2/17	4	33, 4	5.23	28	0.86	272
E	8	1/10	4	33, 4	2.59	28	0.65	320
G	32	2/15	4	33, 4	7.51	29	1.25	240
Q	8	1/4	—	—	2.18	2	0.89	8
P	8	5/11	—	—	5.41	5	1.41	22

The path memory (see Section 7.3) for the Viterbi detector is 50 intervals. The simulation method of Section 7.4.1 is used with  $\xi = 20$  samples per interval. As the reference, the symbol error probability of BPSK,  $Q((2E_b/N_0)^{1/2})$ , is always given. Simulation results and bounds for CPFSK were presented in Section 7.4.2; for coded schemes the multiplicative factor in front of the  $Q$ -function in Section 7.4.2 is not known, and it has been set to 1.

Figure 11.31 shows the bit error probability for a rate 2/3 encoder with memory length  $\nu = 1$ . The polynomials are (2, 1) and the mapper is a natural binary mapper. The modulation index for the eight-level CPFSK scheme is  $h = 1/5$ . The squared free distance for this scheme is 3.20 and the number of states is 20. The number of bit errors simulated is 1000 except for 6 dB where it is 209 bit errors.

A rate 3/4 encoder with  $\nu = 2$  and the polynomials given by (5, 2) is considered in Figure 11.32. A natural binary mapper is used and  $h$  is 2/13 for the 16-level CPFSK scheme. The squared free distance is 5.23 and the number of states is 52. 1000 bit errors are simulated for 0 and 1 dB, 500 for 2 dB, 100 for 3 and 4 dB, and 11 for 5 dB.

**Table 11.4. Parameters of  $M = 4$  Level 2 –  $h$  Multi- $h$  Schemes  
from Ref. 10.  $2BT_b$  Is the 99% Bandwidth**

Scheme	$h_1$	$h_2$	$d_{\min}^2$	$N$	$2BT_b$ 99%	$S$
A	0.40	0.46	4.80	30	1.13	100
B	0.25	0.29	2.80	30	0.84	200
C	0.25	0.23	2.00	30	0.73	200
D	4/16	3/16	1.60	$\leq 30$	0.67	32

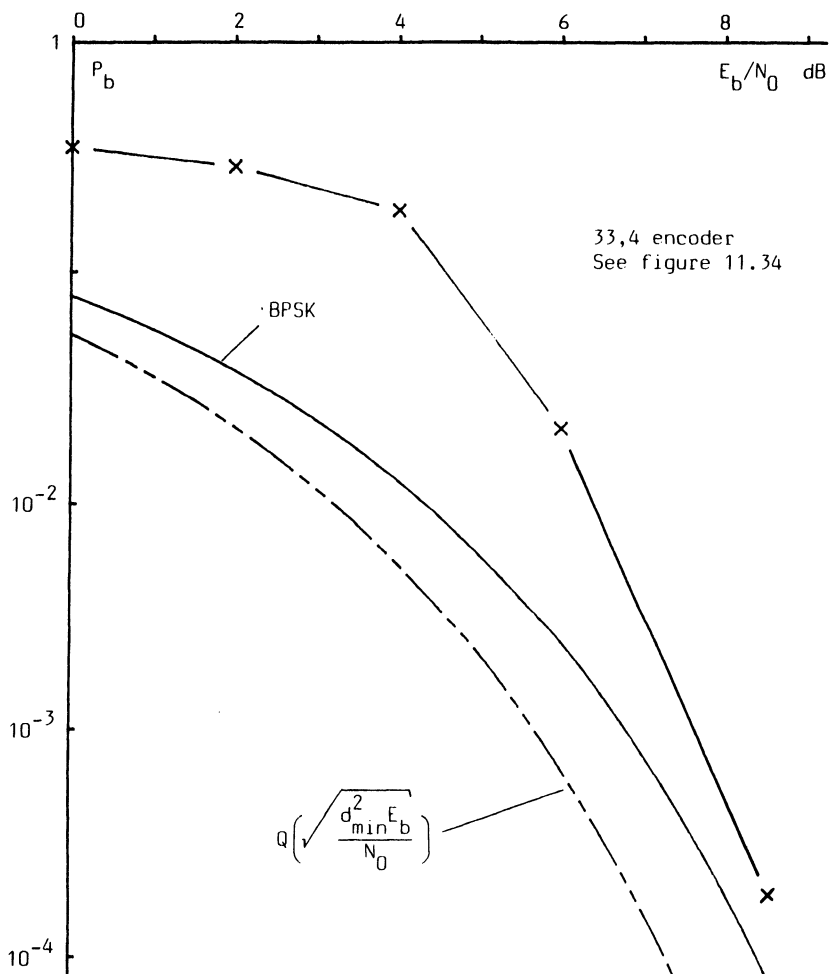


Figure 11.35. Simulated bit error probability for a rate 2/3 encoder with  $\nu = 4$  and polynomials (33, 4), combined with an eight-level CPFSK scheme with  $h = 1/10$ .

An eight-level CPFSK scheme with  $h = 2/21$  and a rate 2/3 encoder with  $\nu = 3$  and polynomials given by (17, 2) is considered in Figure 11.33. A natural binary mapper is used. The squared free distance is 2.00 and the number of states is 168. 1000 bit errors are simulated for 0 to 6 dB, 135 for 8 dB, and 30 for 9 dB.

Figure 11.34 shows the bit error probability for rate 3/4 encoder with  $\nu = 4$  and polynomials given by (33, 4). The mapper is a natural binary and the modulation index in the 16-level CPFSK scheme is 2/17. This scheme has squared free distance equal to 5.23 and 272 states. 190 bit errors are

simulated for the 5-dB point. Finally, Figure 11.35 shows the results for a rate 2/3 code and with  $\nu = 4$  and polynomials given by (33, 4). A natural binary mapper is used and  $h = 1/10$  for eight-level CPFSK. The squared free distance is 2.59 and the number of states is 320. 2000 bit errors are used for 0 and 2 dB, 1000 bit errors for 4 and 6 dB, and 55 for 8.5 dB.

## References

1. G. Lindell, C-E. Sundberg, and T. Aulin, "Minimum Euclidean Distance for Combinations of Short Rate 1/2 Convolution Codes and CPFSK Modulation," *IEEE Transactions on Information Theory*, IT-30(3), 509-519 (1984).
2. T. Aulin, G. Lindell, and C-E. Sundberg, "Minimum Euclidean Distance for Short Convolution Codes and Continuous Phase Modulation," GLOBECOM '82, Conference Record, pp. E.7.2.2-E.7.2.5.
3. G. Lindell and C-E. Sundberg, "Multilevel Continuous Phase Modulation with High Rate Convolutional Codes," GLOBECOM '83, San Diego, November 1983, Conference Record, pp. 30.2.1-30.2.6.
4. G. Lindell, C-E. Sundberg, and A. Svensson, "Error Probability of Multilevel CPM with High Rate Convolutional Codes," International Zürich Seminar on Digital Communications, March 1984, Conference Record, pp. 93-100.
5. G. C. Clark Jr. and J. B. Cain, *Error Correction Coding for Digital Communications*, Plenum Press, New York (1981).
6. A. J. Viterbi and J. K. Omura, *Principles of Digital Communications and Coding*, McGraw-Hill, New York (1979).
7. R. Blahut, *Error Control Coding*, Addison-Wesley, Reading, Massachusetts (1983).
8. G. Ungerboeck, "Channel Coding with Multilevel/Phase Signals," *IEEE Transactions on Information Theory* IT-28(1), 55-67 (1982).
9. J. B. Anderson and C. P. Taylor, "A Bandwidth-Efficient Class of Signal Space Codes," *IEEE Transactions on Information Theory* IT-24(6), 703-712 (1978).
10. T. Aulin and C-E. Sundberg, "On the Minimum Euclidean Distance for a Class of Signal Space Codes," *IEEE Transactions on Information Theory* IT-28(1), 43-55 (1982).
11. T. Aulin and C-E. Sundberg, "Minimum Euclidean Distance and Power Spectrum for a Class of Smoothed Phase Modulation Codes with Constant Envelope," *IEEE Transactions on Communications* COM-30(7), 1721-1729 (1982).
12. T. Aulin and C-E. Sundberg, "Continuous Phase Modulation—Part I: Full Response Signaling," *IEEE Transactions on Communications* COM-29(3), 196-209 (1981).
13. T. Aulin, N. Rydbeck, and C-E. Sundberg, "Continuous Phase Modulation—Part II: Partial Response Signaling," *IEEE Transactions on Communications* COM-29(3), 210-225 (1981).
14. J. B. Anderson, C-E. Sundberg, T. Aulin, and N. Rydbeck, "Power-Bandwidth Performance of Smoothed Phase Modulation Codes," *IEEE Transaction on Communications* COM-29(3), 187-195 (1981).
15. S. W. Pizzi, "Modulation and Convolutional Coding for Power and Bandwidth Efficiency," thesis, May 1982, Dept. Elec. Eng., University of Virginia.
16. J. L. Massey and M. K. Sain, "Inverses of Linear Sequential Circuits," *IEEE Transactions on Computers* C-17, 330-337 (1968).
17. J. M. Wozencraft and I. M. Jacobs, *Principles of Communication Engineering*, Wiley, New York (1965).

18. T. Aulin, "Symbol Error Probability Bounds for Coherently Viterbi Detected Continuous Phase Modulated Signals," *IEEE Transactions on Communications* COM-29(11), 1707-1715 (1981).
19. T. Aulin, G. Lindell, and C-E. Sundberg, "Minimum Euclidean Distance for the Best Combination of Short Rate 1/2 Convolutional Codes and Binary CPFSK Modulation," Technical Report TR-160, Telecommunication Theory, University of Lund, November 1981.
20. G. Lindell, C-E. Sundberg, and T. Aulin, "Minimum Euclidean Distance for the Best Combination of Short Rate 1/2 Convolutional Codes and Quaternary CPFSK Modulation," Technical Report TR-170, Telecommunication Theory, University of Lund, August 1982.
21. G. Lindell and C-E. Sundberg, "High Rate Convolutional Codes and Multilevel Continuous Phase Modulation," Technical Report TR-180, Telecommunication Theory, University of Lund, November 1983.
22. G. Lindell and C-E. Sundberg, "Power and Bandwidth Efficient Coded Modulation Schemes with Constant Amplitude," *Achiv Elektronik und Übertragungstechnik*, Band 39, Heft 1, 45-56 (1985).
23. S. G. Wilson, P. J. Schottler, and H. A. Sleeper, "Rate 3/4 16-PSK Phase Codes," IEEE International Conference on Communications, ICC '82, Philadelphia, June 1982, Conference Record, pp. 6F.1.1-6F.1.5.
24. S. G. Wilson *et al.*, "Convolutional Coding Combined with Continuous Phase Modulation," University of Virginia, Charlottesville, Report NAG-3-141, November 1982.
25. M. G. Mulligan and S. G. Wilson, "An Improved Algorithm for Evaluating Trellis Phase Codes," University of Virginia, Charlottesville, Report No. UVA/528200/EE82/104, September 1982.
26. S. A. Rhodes and S. H. Lebowitz, "Performance of Coded OPSK for TDMA Satellite Communications," Fifth International Conference on Digital Satellite Communications, Genoa, March 1981, Proceedings, pp. 79-87.
27. S. H. Lebowitz and S. A. Rhodes, "Performance of Coded 8PSK Signaling for Satellite Communications," International Conference on Communications ICC '81, Denver, June 1981, Conference Record, pp. 47.4.1-47.4.8.
28. S. A. Rhodes, R. J. Fang, and P. Y. Chang, "Coded Octal Phase Shift Keying in TDMA Satellite Communications," *COMSAT Technical Review* 13(2), 221-258 (1983).
29. J. Hui, "Joint Coding and Modulation Designs for Bandlimited Satellite Channels," Master's thesis, MIT Dept. of Electrical Engineering and Computer Science, MIT, Cambridge, Massachusetts, June 1981.
30. J. Hui and R. J. F. Fang, "Convolutional Code and Signal Waveform Design for Bandlimited Satellite Channels," International Conference on Communications ICC '81, Denver, June 1981, Conference Record, pp. 47.5.1-47.5.10.
31. T. Aulin and C-E. Sundberg, "An Easy Way to Calculate Power Spectrum for Digital FM," *IEE Proceedings, Part F* 130(6), 519-525 (1983).
32. T. Aulin, N. Rydbeck, and C-E. Sundberg, "Transmitter and Receiver Structures of  $M$ -ary Partial Response FM," 1980 International Zürich Seminar on Digital Communications, Zürich, March 1980, Conference Proceedings, pp. A2.1-A2.6.
33. A. Svensson and C-E. Sundberg, "Optimized Reduced-Complexity Viterbi Detectors for CPM," GLOBECOM '83, San Diego, November 1983, Conference Record, pp. 22.1.1-22.1.8.
34. G. Lindell, C-E. Sundberg, and A. Svensson, "Error Probability of Coded CPM with Viterbi Detection—Bounds and Simulations," Technical Report, Telecommunication Theory, University of Lund, 1984.

35. W. C. Lindsey and M. K. Simon, *Telecommunication Systems Engineering*, Prentice Hall, Englewood Cliffs, New Jersey (1973).
36. G. D. Forney, Jr., R. G. Gallager, G. R. Lang, and S. U. Qureshi, "Efficient Modulation for Band-limited Channels" *IEEE Journal on Selected Areas in Communications*, SAC-2(5), 632-647 (1984).
37. G. Lindell, C-E. Sundberg, and A. Svensson, "Bit Error Probability of Coded CPM—Bounds and Simulations," *GLOBECOM '85*, New Orleans, Louisiana, December 1985, Conference Record, pp. 21.3.1-21.3.7.
38. G. Lindell, "On Coded Continuous Phase Modulation," Dr. Techn. Thesis, University of Lund, Lund, Sweden, May 1985.

---

## Appendix A

# Minimum Distance Calculation Algorithms

In a Euclidean vector space it is possible for us to calculate distances (here squared and normalized) between signal elements in the space, without knowing anything about the geometry or the dimensionality of the space that we are exploring. This is obvious from Chapter 4 of Ref. 1. This we will use.

In dealing with tree or trellis codes/modulation structures we are interested in finding the two elements in the vector space (signal space) that are closest together. These two are most easily mixed up by an observer.

There is a difference between tree and trellis codes in that the latter has a finite number of possible transmitted waveforms. This is not the case for a tree code.

Two algorithms for calculation of minimum distances are presented. The first one operates in a tree code and uses a pruning rule to keep the computational effort low. A nonordered list is used.

The other algorithm operates with super- or pair-states, the one in the pair belonging to the transmitter, the other to the receiver. The pruning rules of the first algorithm can be applied also in this case, to cut down the amount of calculation. The number of pair-states should be kept low. Instead of the term pair-states, superstates can be used.<sup>(2)</sup>

The general problem of exponential growth in the amount of calculation of minimum distances for optimum detectors is avoided here. Approximate linearity is achieved by both algorithms.

These algorithms are here given for the application to digital phase modulation. Their usefulness is for general tree or trellis codes, however.

### A.1. Limited Sequential Tree Search

From Chapter 3, the normalized squared Euclidean distance measure is (assuming  $H = 1$ )

$$d^2(\gamma_{N-1}, h) = N - \frac{1}{T} \int_0^{NT} \cos \phi(t, \gamma_{N-1}) dt \quad (\text{A.1})$$

where  $N$  is the number of observed symbol intervals,  $T$  the symbol duration, and  $h$  the modulation index. Furthermore,

$$\phi(t, \gamma_{N-1}) = 2\pi h \sum_{i=0}^{N-1} \alpha_i q(t - iT), \quad 0 \leq t \leq NT \quad (\text{A.2})$$

where  $q(\cdot)$  is the phase response. The problem is to find

$$d_{\min, N}^2(h) = \min_{\substack{\gamma_{N-1} \\ \gamma_0 \neq 0}} \{d^2(\gamma_{N-1}, h)\} \quad (\text{A.3})$$

where  $\gamma_i = 0, \pm 2, \pm 4, \dots, \pm 2(M-1)$ . A brute force method for finding  $d_{\min, N}^2(h)$  for a given  $N$  and  $h$  is to compute  $d^2(\gamma_{N-1}, h)$  for all possible sequences  $\gamma_{N-1}$  and take the minimum of all the achieved quantities. The number of required computations grows exponentially with  $N$  since the number of distinct  $\gamma_{N-1}$ 's is  $(M-1)(2M-1)^{N-1}$ . Even for  $M = 2$  it is unrealistic to proceed in this way when  $N$  is larger than, say, 8.

A fast algorithm to solve this problem is now described. It is sequential (or iterative) in  $N$ . This property is obtained by noting that Euclidean distances are additive in  $N$ , i.e.,

$$d^2(\gamma_N, h) = d^2(\gamma_{N-1}, h) + 1 - \frac{1}{T} \int_{NT}^{(N+1)T} \cos \phi(t, \gamma_N) dt \quad (\text{A.4})$$

where (A.1) was used. We also use the basic properties of the minimum Euclidean distance, namely, that it is upper bounded and also a nondecreasing function of  $N$  for fixed  $h$ .

A flowchart for the algorithm is shown in Figure A.1. It is assumed that  $d_{\min, N}^2(h)$  is to be calculated when the modulation index is  $h = h_{\min}, h_{\min} + \Delta h, \dots, h_{\max} - \Delta h, h_{\max}$  and for  $N = 1, 2, \dots, N_{\max}$  observed symbol intervals.

The first step is to calculate the upper bound  $d_B^2(h)$  for the relevant  $h$  values, according to the method presented in Section 3.2. Then all the Euclidean distances for  $N = 1$  observed symbol interval are computed. The difference sequence is  $\gamma_0 = 2, 4, \dots, 2(M-1)$ . If any of these distances are larger than the upper bound for that  $h$  value, the entire subtree having the corresponding  $\gamma_0$  value will never be used again. This can be done since the Euclidean distance is a nondecreasing function of  $N$  for fixed  $h$ . The minimum of these Euclidean distances gives  $d_{\min, 1}^2(h)$ .

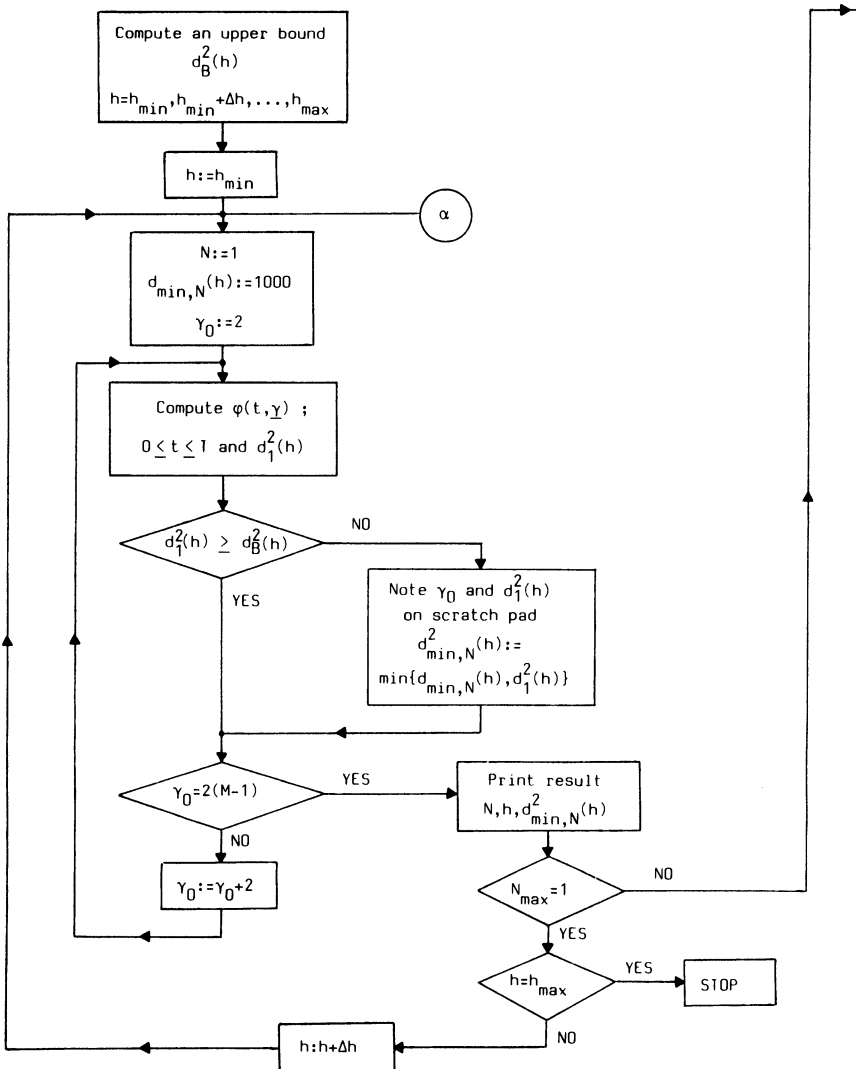


Figure A.1. Flowchart for the limited sequential tree search algorithm for computation of minimum distances  $d_{\min,N}^2(h)$ ,  $N = 1, 2, \dots, N_{\max}$ ,  $h_{\min} \leq h \leq h_{\max}$ .

When  $d_{\min,2}^2(h)$  is to be computed, only those  $\gamma_0$  values whose corresponding distances for  $N = 1$  did not exceed the upper bound are used. The second component is chosen as  $\gamma_1 = -2(M - 1), -2(M - 2), \dots, 2(M - 1)$  and the Euclidean distance is calculated by the use of (A.4). Again only those sequences whose corresponding Euclidean distances are not above the upper bound will be stored as possible difference sequences.

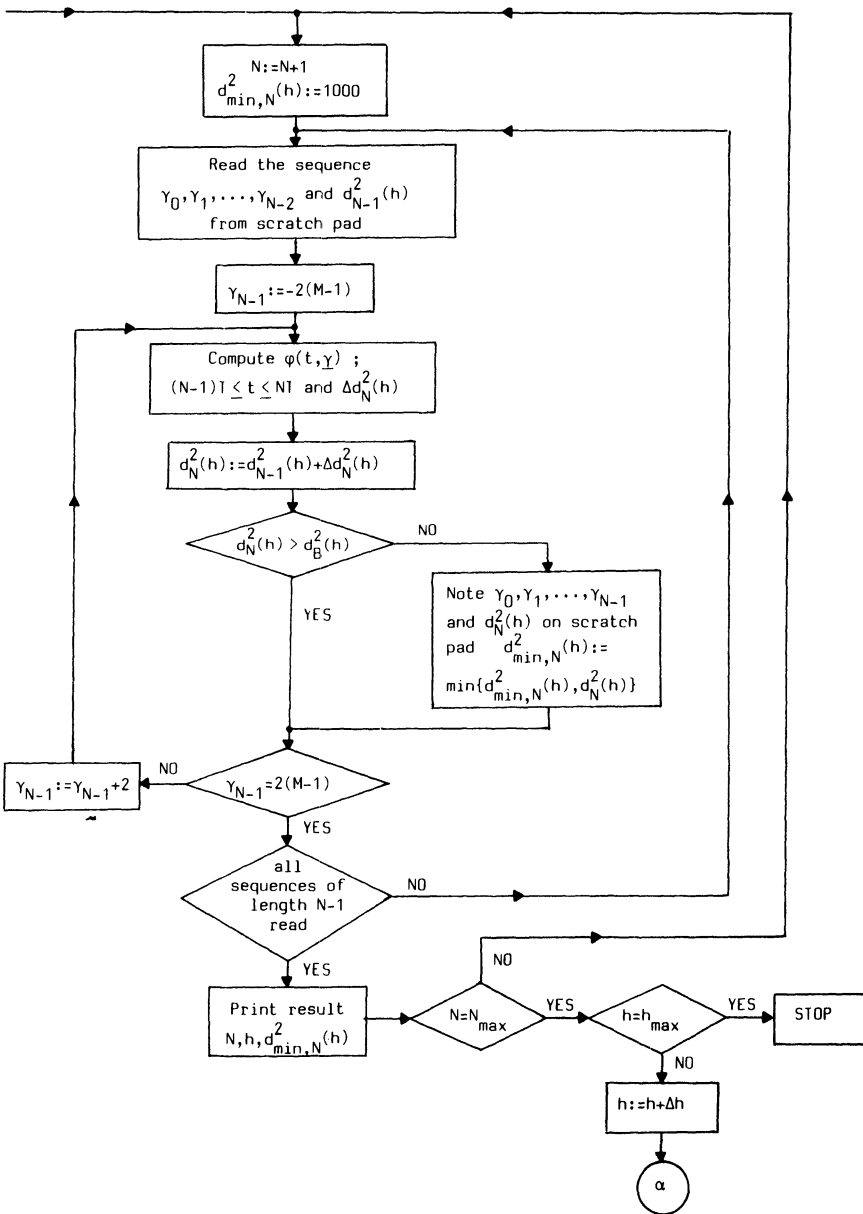


Figure A.1 (cont.)

for  $N = 3$ . The algorithm continues like this up to the maximum  $N$  value,  $N_{\max}$ .

In this way subtrees are deleted all the time since only possible extensions of the sequences are made. It is clear that the upper bound does not need to be tight for the algorithm to work. If the upper bound is too large, however, the number of possible sequences will grow. The algorithm will be as fast as possible if the lowest possible upper bound is used. It has been found empirically that this algorithm increases only linearly in computational complexity with  $N$ , not exponentially as with the brute force method. A flowchart for the algorithm is shown in Figure A.1.

One possible way to speed up the calculations and to reduce the amount of storage is obtained by noting that (A.2) can be written

$$\phi(t, \gamma_N) = 2\pi h \sum_{i=\max(0, N-L+1)}^N \gamma_i q(t - iT) + 2\pi h q(LT) \sum_{i=0}^{N-L} \gamma_i \quad (\text{A.5})$$

where the latter term is a constant phase shift over each symbol interval. Instead of storing the whole sequence  $\gamma_0, \gamma_1, \dots, \gamma_N$ , only the sequence in the first sum and  $\sum_{i=0}^{N-L} \gamma_i$  need be stored. The effect of this is noticeable when  $N > L$ . Another way to reduce memory requirements is to store nothing at all when  $N = N_{\max}$ .

The algorithm described above first appeared in Ref. 3.

## A.2. The Viterbi Algorithm in a Superstate Trellis

When using the tree search algorithm in the previous section for, e.g., multi- $h$  schemes ( $H > 1$ ) or convolutionally encoded schemes like those in Chapter 11, it is important that all starting conditions are used when the algorithm is initialized. This means that the algorithm must be run  $H$  times for a multi- $h$  scheme and  $S$  times for a convolutionally encoded  $H = 1$  scheme ( $S$  is the number of states for the convolutional encoder). The minimum of the results from all these runs is the desired result.

A way out of this problem is to consider only rational  $h$  values where the transmitted signal has a trellis structure. This holds for both examples given above. Denoting the state of the transmitter at symbol interval  $n$  by  $\sigma_{i,n}$ ,  $i = 1, 2, \dots, S$  and the state of the detector at the same symbol interval by  $\sigma_{j,n}$ ,  $j = 1, 2, \dots, S$ , it is seen that all error events are described by the sequence of superstates  $(\sigma_{i,n}, \sigma_{j,n})$ . The error event of course starts in any of the  $S$  error-free superstates  $(\sigma_{i,0}, \sigma_{i,0})$  and also ends in some of these, not necessarily the same. Since both  $\sigma_{i,n}$  and  $\sigma_{j,n}$  have finite state, discrete time Markov structures, the same property applies to the superstates  $(\sigma_{i,n}, \sigma_{j,n})$ . It is possible to use a supertrellis to describe this process. Figure A.2 illustrates this. This trellis has  $S^2$  states and out of these  $S$  are error-free.

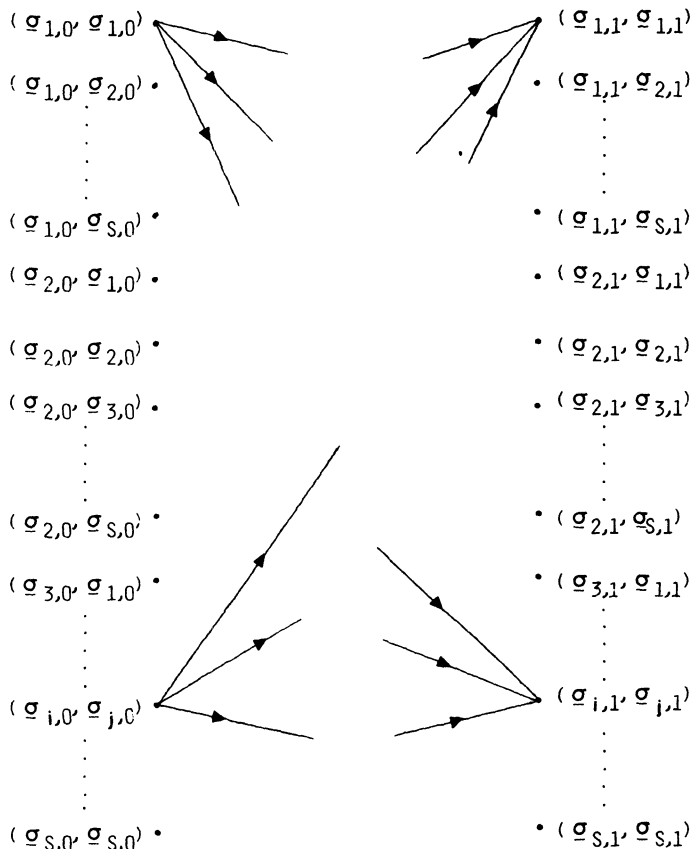


Figure A.2. A supertrellis for the superstates  $(\sigma_{i,n}, \sigma_{j,n})$ ;  $i, j = 1, 2, \dots, S$ . This trellis has  $S^2$  states.

Each transition in this supertrellis is defined by the modulation/coding scheme. With each transition is associated a normalized squared Euclidean distance increment. For sequences of transitions we simply add these increments [see equation (A.4)] to have the normalized Euclidean distance associated with this sequence. Transitions from an error-free state to the same error-free state have increment 0.

We now use the Viterbi algorithm to find the shortest route ( $d_{\min,n}^2$ ,  $n = 1, 2, \dots$ ) through this supertrellis. By the principle of optimality the Viterbi algorithm does this by finding the superpath leading into each superstate having the shortest route, in each iteration.

The first iteration is different from the others and we also have to initialize the algorithm properly. The latter is done by assigning a cumulative distance equal to zero for the error-free states and very large ( $\sim 1000$ ) for

the error-states. In the first iteration, transitions from the error-free states to the error-free states are not allowed. This corresponds to the initial split in the supertrellis. In all subsequent iterations, all possible transitions are allowed.

In each iteration we form the smallest distance associated with each superstate and by taking the minimum of these we find  $d_{\min,n}^2$ ,  $n = 1, 2, \dots$ . As a stopping rule, we use that the minimum cumulative distance is associated with an error-free superstate for the first time. This means that the error event has terminated and all the subsequent distance increments are zero.

It is possible to use an upper bound on  $d_{\min}^2$  also in this case to speed the calculation. If the cumulative distance is larger than this upper bound, we do not allow any superpaths leading out from that superstate in the next iteration. We have killed that state.

The advantage with this algorithm is that all possible starts of the error event are handled in one pass. Another advantage is that the amount of calculation in each iteration is exactly the same and can be estimated beforehand. It has also been noticed that considering all possible starts of error events in a single pass is faster than starting with a new single superstate and making multiple runs.

The disadvantage with the superstate Viterbi algorithm for finding  $d_{\min}^2$  is that the number of states in the underlying modulation/coding scheme must be kept relatively small.

This method for finding the minimum distance first appeared in the literature in Ref. 4, where it was referred to as double dynamic programming. A roughly similar approach was apparently used by G. Ungerboeck in 1976.

## References

1. J. M. Wozencraft and I. M. Jacobs, *Principles of Communication Engineering*, Wiley, New York (1965).
2. J. K. Omura, "Performance Bounds for Viterbi Algorithms," International Conference on Communications, ICC'81, Conference Record, pp. 2.2.1-2.2.5, June 14-18, 1981, Denver, Colorado.
3. T. Aulin, "CPM—A Power and Bandwidth Efficient Digital Constant Envelope Modulation Scheme," Telecommunication Theory Department, Univ. of Lund, Sweden, Doctoral thesis, November 1979.
4. J. B. Anderson and D. P. Taylor, "A Bandwidth Efficient Class of Signal Space Codes," *IEEE Transactions on Information Theory* IT-24, 703-712 (1978).

---

## Appendix B

# Specification of the Markov Distance Chain and Calculation of $R_0$

In Chapter 5 the exponential bound parameter  $R_0$  was given for random codes whose code words are CPM modulator outputs driven by random sequences. This appendix performs two technical details in the derivation of  $R_0$ , the specification of a Markov chain for the distance between a pair of code words, and the calculation of the  $P_{2,e}$ , the probability of decoding one word in the randomly chosen pair when the other was sent.

### B.1. A Markov Distance Chain

In order to have a finite-state chain for the distance between two code words, we must restrict the modulation index  $h$  to be  $\mu/\eta$ , where  $\mu$  and  $\eta$  are both integers. To see this, we can consider (5.13), which gives the phase vs. time for a CPM signal in terms of the randomly chosen symbols  $\alpha_i$ ; we can rewrite this in terms of the difference sequence  $\gamma_i = \alpha_i(1) - \alpha_i(2)$  to get an expression for the phase difference between the two code words:

$$\Delta\phi(t, \alpha) = 2\pi h \sum_{i=n-L+1}^n \gamma_i q(t - iT) + \Delta\theta_n, \quad nT < t < (n+1)T \quad (\text{B.1})$$

$$\Delta\theta_n = \left[ \pi h \sum_{i=n-L}^n \gamma_i \right] \bmod 2\pi$$

In thinking about this phase difference, it is useful to imagine the phase-time cylinder introduced in Chapter 2 with time extending down the cylinder and phase around it. The restriction on  $h$  can be expressed by spacing  $\eta$  underlying phase levels around the cylinder, one each  $2\pi/\eta$ . A code word

is a sequence of smoothed transitions from level to level with each symbol  $\alpha_i$  causing a smoothed, eventual jump to a new level. Compared to the old level, the new level differs by  $\pm \pi\mu/\eta, \pm 3\pi\mu/\eta, \dots, \pm(M-1)\pi\mu/\eta$ , assuming  $M$  is even. The choice of these jumps is random.

Figure B.1 depicts a pair of smoothed phase trajectories and their underlying phase levels. As given in equation (B.1), the difference between the trajectories is determined by a set of  $L$  differences  $\gamma_i$  and the offset  $\Delta\theta_0$ . The difference between the underlying levels is set by the present difference and the sum of all the previous ones, modulo  $2\pi$ . To avoid confusion, we will call this a *separation*, or an underlying separation, rather than a difference.

Unfortunately, these underlying separations are not quite enough to define a state. The phase between a pair of paths is ambiguous in the sense that it could be increasing toward the new underlying separation or it could be decreasing. In the example of Figure B.1, the separation has been  $\pi$  for a long time, changing via a decrease in phase to  $\pi/2$  in the  $n$ th interval. In interval  $n+1$  there is a renewed widening to an underlying separation of  $\pi$  again, followed by another widening to  $5\pi/2$ . The last separation is  $\pi/2$ , modulo  $2\pi$ , a smaller separation than  $\pi$ ; but unlike the case in interval  $n$ , the phase separation has increased instead of decreased to  $\pi/2$ . If the underlying separation increases during an interval, we will say that the path pair *diverges* during that interval and otherwise that it *converges* (see Figure

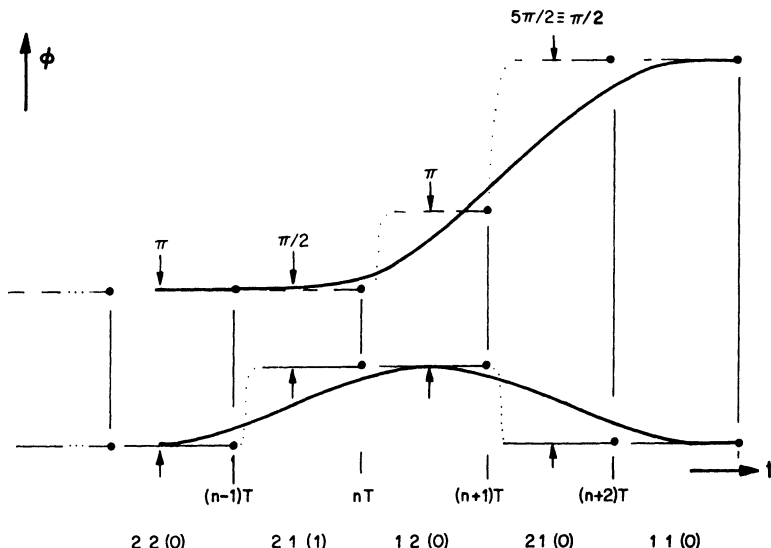


Figure B.1. A pair of second-order ( $L = 2$ ) smoothed phase paths, showing the underlying phase separations. Second-order state notation appears at bottom.

5.8). Over a span of intervals relevant to a distance calculation, one path must consistently be called the “first” and the other the “second,” and  $\Delta\phi(t)$  must be taken to mean first minus second.

We can now define the states of a Markov chain for the distance growth between the path pair. The transition from time  $n - 1$  to  $n$  generates the  $n$ th distance increment. Out of the  $L + 1$  separations, counting  $\Delta\theta_n$  as the first, that affect an order- $L$  smoothed phase, we associate the first  $L$  with the state at time  $n - 1$  and the last  $L$  with the state at  $n$ . We will let an integer  $i$  denote an underlying phase separation of  $2\pi i/\eta$ . For second-order smoothing, the definition is as follows:

Let the chain be in state  $[j, k, (c)]$  at time  $n - 1$  if the underlying phase separation is  $j2\pi/\eta$  in interval  $n - 2$  and  $k2\pi/\eta$  in interval  $n - 1$ ; if  $c = 1$ , the pair is converging, and if  $c = 0$ , the pair is diverging.

For the third-order case:

Let the chain be in state  $[i, j, (b), k, (c)]$  at time  $n - 1$  if  $j, k$ , and  $c$  are as defined before and the level difference is  $i2\pi/\eta$  in interval  $n - 3$ ;  $b$  is the convergence in interval  $n - 2$ .

Transition probabilities are for the most part zero in these chains. Only transitions of the type  $[j, k, (c)] \rightarrow [k, l, (e)]$  or  $[i, j, (b), k, (c)] \rightarrow [j, k, (c), l, (e)]$  are allowed since otherwise the underlying separations and convergences will not match from state to state. By assuming equiprobable choices for the outcome of the choice of  $\alpha_n$  in each path, we can calculate the nonzero transition probabilities. There will be  $M^2$  configurations of the separations in the next interval, each with probability  $1/M^2$ . Starting from an initial underlying separation of  $j2\pi/\eta$  and transiting to one of size  $k2\pi/\eta$ , there are  $M - k + j$  cases when  $k > j$  and  $M - \eta - k + j$  when  $k < j$  for which the convergence variable is 0 (divergence); similarly, there are  $M - \eta + k - j$  cases when  $k > j$  and  $M + k - j$  when  $k < j$  when the variable is 1 (convergence). For  $j = k$ , there are always  $M$  cases. If any of these expressions are negative or zero, there are no cases of that type. Dividing the number of cases by  $M^2$  gives the transition probability to a state with a terminating  $j, k$ , and convergence; the remaining state variables have no effect.

For first-order (full response) modulations, a simpler state description exists that does not need the concept of convergence.

## B.2. Calculation of $R_0$

From the state variables, one can reconstruct the true difference sequence  $\gamma_i$  and the offset  $\Delta\theta_n$ . Substituting these into (B.1) leads to the actual phase difference  $\Delta\phi(t)$  in the  $n$ th interval. Care must be taken with

the convergence variable. For instance, in Figure B.1 with  $h = 1/4$ , the separations expressed as integers are  $\dots, 2, 2, 1, 2, 1, 1, 1, \dots$ ; but the proper difference sequence for (B.1) is  $2 \cdot (\dots, 0, 0, -1, 0, 3, 3, 3, \dots)$  with a constant offset of  $\pi$ .

Solution for  $R_0$  is made possible by the theorem that follows, which expresses  $R_0$  in terms of the largest eigenvalue of a certain matrix. We first make a list of all the states, ignoring the convergence variable, and assign to them a serial order. We then let  $p_{uv}$  be the probability of a transition from state  $u$  to state  $v$  among states in the newly ordered list, and let  $d_{uv}$  be the increment of distance accrued as a product of this transition. An element in the matrix  $\Lambda$  is defined by

$$\Lambda_{uv} = p_{uv} \mathcal{E}[e^{\lambda d_{uv}^2}], \quad \lambda = -E/4N_0 \quad (\text{B.2})$$

where the expectation is over the distance distribution given  $u$  and  $v$ . The increment may take on several values depending on the phase convergence, which we ignore in the renumbering of the states. As usual,  $E$  is the interval energy.

*Theorem.* For some constant  $A$ ,

$$p_{2,e} \leq A \exp_2(N \log_2 \rho_{\max}) \quad (\text{B.3})$$

for all  $N$ , where  $N$  is the phase code word length and  $\rho_{\max}$  is the largest eigenvalue of the matrix  $\Lambda$ . As a consequence of Section 5.4,  $R_0 = -\log_2 \rho_{\max}$ .

*Proof.* Consider a pair of paths of length  $N$  intervals, square-distant from each other a total  $y$ . Clearly,  $\mathcal{E}[Y]$  must grow linearly but at a rate as yet unknown. For any  $\lambda$ ,  $y$  has the Chernoff bound,

$$\Pr\{Y \leq m - z\} \leq \mathcal{E}[e^{\lambda Y}] e^{-\lambda(m-z)}, \quad m = \mathcal{E}[Y]$$

The best bound occurs for  $\lambda_0$ , the solution of

$$\frac{\mathcal{E}[Y e^{\lambda_0 Y}]}{\mathcal{E}[e^{\lambda_0 Y}]} = (m - z) \quad (\text{B.4})$$

$\lambda_0$  is a continuous function of  $z$ .

Making use of (5.14) and the optimal bound  $\lambda_0(z)$  at each  $z$ , one gets

$$\begin{aligned} p_{2,e} &= \mathcal{E}[Q((YE/2N_0)^{1/2})] \leq \mathcal{E}[e^{-YE/4N_0}] \\ &\leq \int_0^\infty \Pr\{Y \leq y\} e^{-yE/4N_0} dy \\ &\leq \int_{-\infty}^{\mu} \mathcal{E}[e^{\lambda_0 Y}] e^{-\lambda_0(m-z)} e^{-(m-z)E/4N_0} dz \end{aligned}$$

It is straightforward to show that the log of this expression tends in ratio as  $N \rightarrow \infty$  to the maximum of the log of the integrand,

$$\ln \mathcal{E}[e^{\lambda_0 Y}] - \lambda_0(m-z) - (m-z)E/4N_0$$

which occurs at  $z$  the solution of

$$0 = \frac{\mathcal{E}[Ye^{\lambda_0 Y}]}{\mathcal{E}[e^{\lambda_0 Y}]} \frac{d\lambda_0}{dz} - (m-z) \frac{d\lambda_0}{dz} + \lambda_0 + E/4N_0$$

The first two terms cancel by (B.4) so that evidently the maximizing  $z$  is the one for which  $\lambda_0 = -E/4N_0$ . Thus,

$$\ln p_{2,e} \leq \ln \mathcal{E}[e^{-YE/4N_0}]$$

as  $N \rightarrow \infty$  where  $\leq$  means “tends to or is less than in ratio.”

### B.3. Evaluation of $\mathcal{E}[e^{-YE/4N_0}]$

For a one-step transition from state  $v$  to  $w$ ,

$$\mathcal{E}[e^{\lambda d_{vw}^2} | v] = \sum_w \Lambda_{vw}$$

For a two-step transition  $u$  to  $v$  to  $w$ ,

$$\begin{aligned} \mathcal{E}[e^{\lambda d^2(u \rightarrow v \rightarrow w)} | u] &= \sum_v \mathcal{E}[e^{\lambda d_{uv}^2} e^{\lambda d_{vw}^2} | u, v] p_{uv} \\ &= \sum_v \mathcal{E}[e^{\lambda d_{uv}^2} | u, v] \mathcal{E}[e^{\lambda d_{vw}^2} | u, v] p_{uv} \\ &= \sum_v \Lambda_{uv} \mathcal{E}[e^{\lambda d_{vw}^2} | v] \end{aligned}$$

where in the first line we have used the additivity of  $d^2$ , in the second the fact that the increments are independent under the conditioning, and in the third the definition of  $\Lambda_{uv}$ .

By the one-step result, the last line is

$$= \sum_v \Lambda_{uv} \sum_w \Lambda_{vw} = \sum_w \Lambda_{uw}^{(2)}$$

where  $\Lambda^{(2)}$  denotes the second power of  $\Lambda$ .

By induction one gets for an  $N$  step transition that (letting  $y$  equal the total square distance)

$$\mathbb{E}[e^{\lambda y} | \text{start in state } u] = \sum_w \Lambda_{uw}^{(N)}$$

If  $\{b_u\}$  is some starting distribution, then

$$\mathbb{E}[e^{\lambda y}] = \sum_u b_u \sum_w \Lambda_{uw}^{(N)}$$

which is just a weighted sum of the elements of  $\Lambda^{(N)}$ .

By a basic theorem of algebra, such a sum grows asymptotically as  $\rho_{\max}^N$ , where  $\rho_{\max}$  is the largest eigenvalue of  $\Lambda$ , so long as  $b$  is not perpendicular to this value's eigenvector. (The proof follows by examining the Jordan canonical form of  $\Lambda$ .) From this follows the theorem.

---

# Appendix C

## Simulation Techniques

This appendix serves two purposes. First we develop a statistical view of demodulator error events which provides the means to interpret simulation results. Then we present the “signal space method” of simulation, an alternative to the method of Section 7.4.1. We illustrate both the method and the analysis by multi- $h$  code simulations, taken from Ref. 1.

### C.1. Statistical Analysis of Error Events

As was developed in Chapter 2, the probability of decoding a “neighbor” signal  $s_2$ , given that  $s_1$  was transmitted, is  $Q(d(E_b/N_0)^{1/2})$ , assuming white Gaussian noise of power  $N_0/2$ . Here  $d$  is the normalized Euclidean distance between the two signals. As the energy grows, the worst case combination of  $s_1$  and  $s_2$  comes to dominate the total probability of incorrectly decoding the transmitted signal;  $d_{\min}$  denotes the distance between these two signals.

An *error event* occurs when the decoder releases a trellis path section not on the transmitted path. The event begins when the decoded path splits from the transmitted path and ends when it merges again with it. This is illustrated in Figure C.1. Once a path has split, it generates various descendants, and the first of these that can merge does so  $H + 1$  intervals after the split point; thereafter, one descendant merges each level ad infinitum in a binary scheme, or three descendants in a quaternary scheme. Typically, the paths in the transmitted/neighbor pair that give rise to  $d_{\min}$  lie separate just for  $H + 1$  intervals, but sometimes this worse-case pair is a longer error event. When  $E_b$  is small, an error event is often not the one connected with  $d_{\min}$ , because many events have similar probability. In any case, error events always cause an initial decoded data bit error in a CPM scheme. The

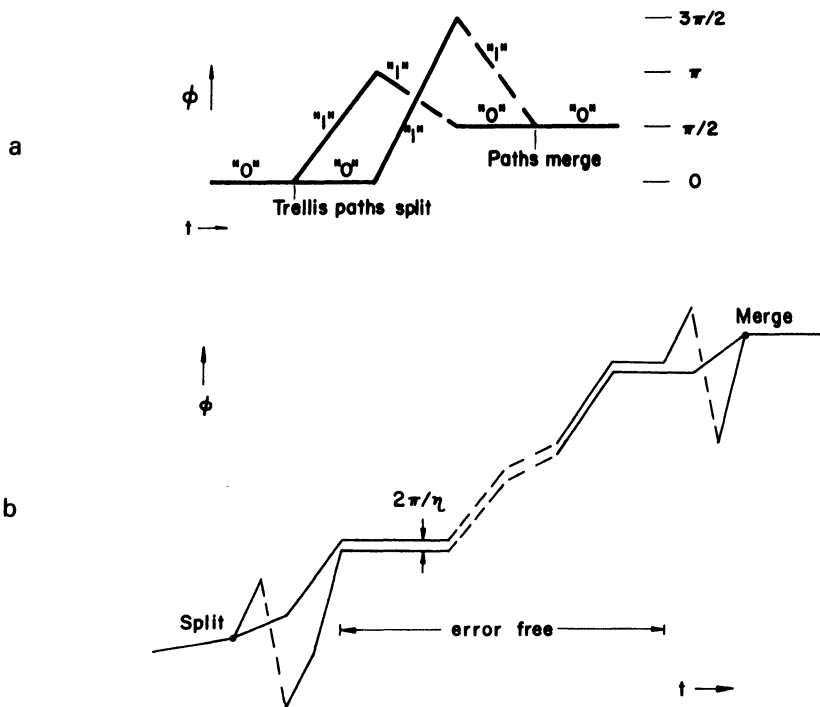


Figure C.1. Transmitted and neighbor paths in multi- $h$  codes; a "long" error event (above) and a "short" event in the two- $h$  code ( $h_1 = 2/4$ ,  $h_2 = 3/4$ ). From Ref. (1).

remaining data bits are sometimes mostly correct. Even so, for an accurate statistical analysis it is essential to keep track of the progress of events, not of individual bit errors.

As was developed in Chapters 3 and 7, decoders retain paths for the path memory length  $N_T$ . If after  $N_T$  intervals the decoder is still considering trellis paths that descend from more than one branch out of some node, then a forced decision must be made among branches out of that node. In order for  $d_{\min}$  to dominate the high- $E_b/N_0$  error probability,  $N_T$  must be at least the size of  $N_B$ , where here we are interpreting  $N_B$  as the first depth in a signal trellis at which no unmerged neighbor lies closer than  $d_{\min}$  to the transmitted path, for any transmitted path. Multi- $h$  codes and convolutional code/CPFSK combinations often have  $N_B$  much longer than the length of their shortest merged error event. A short memory  $N_T$  is often useful, but then the high- $E_b$  error probability is determined by the worst case unmerged path distance at depth  $N_T$ , if this distance is smaller than  $d_{\min}$ .

Decoder error events can be put into two categories, long and short events. The short events have length close to the length of the  $d_{\min}$ -causing

error event(s), and they account for almost all events at high  $E_b/N_0$ . The long events occur when the decoder is "lost," typically because of an incorrect forced decision or low  $E_b/N_0$ . These two event types are pictured in Figure C.1; the long event there is a type that occurs in multi- $h$  codes, in which two phase trellis paths sometimes run very close to each other for many intervals.

In order to make a statistical analysis of error events, we hypothesize that the events strike at random whenever they are free to strike, that is, whenever an event is not already in progress. Under this hypothesis, the waiting time  $A$  between the end of one event and the beginning of the next is geometrically distributed and successive waiting times are independent; for such events,  $\Pr\{A > k\} = (1 - \rho)^k$ , where  $\rho$  is the probability that an event begins at some interval and  $k$  is an integer number of intervals. This is the "backward" cumulative distribution function, or BCDF, of  $A$ . It decays exponentially to zero with  $k$ , and we can test our hypothesis by plotting the log BCDF for experimentally measured waiting times.

Figure C.2 is such a plot for the binary multi- $h$  code ( $h_1 = 4/6$ ,  $h_2 = 3/6$ ). Information on this and other codes used in the sequel appear in Table C.1. The path memory is 3, significantly less than  $N_B$ , which is 6, so that many long events occur; the plot is based on a run of 10,000 encoded data bits. The log BCDF here is very close to linear, even when  $E_b/N_0 = 2$  dB, which leads to a decoder bit error rate of 0.12! The slope of the log BCDF is an estimate of  $\rho$ , the probability that an event occurs. This

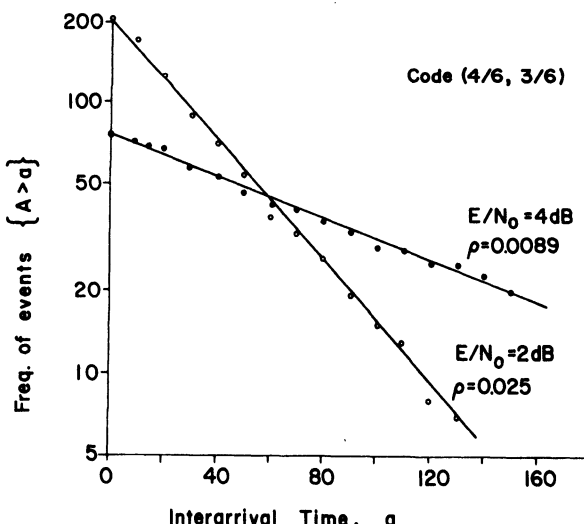


Figure C.2. Log-scale backward CDF for event interarrival times; path memory  $N_T = 3$ . Data from 10 000 decoded data bits.  $E$  denotes energy/data bit. From Ref. (1).

**Table C.1. Important Characteristics of Multi- $h$  Codes Used in Appendix C<sup>a</sup>**

Code ( $h_k$ )	$H + 1$	$N_B$	Minimum distance at $H + 1$ (dB)	$d_{\min}$ (dB)
3/4, 2/4	3	4	—	+1.44
4/6, 3/6	3	6	—	2.37
6/8, 5/8, 4/8	4	10	+0.79	2.78
10/13, 9/13, 8/13	4	20	1.30	3.19
12/16, 10/16, 11/16, 8/16	5	38	0.97	3.66

<sup>a</sup> Distances are shown in decibels relative to the square distance of QPSK, which is 2. These codes are the best for a given  $\eta$ .

can be compared to the observed event frequency, the number of events divided by the number of event-free symbol intervals, in order to obtain another confirmation of our hypothesis.

Plots like Figure C.2 have proven to be the rule, both with CPM schemes and convolutional decoding.<sup>(1,2)</sup> The linearity of the log BCDF and the agreement of its slope with the event frequency are very strong tendencies, and we may conclude that in any practical sense error events are indeed random. Note that this is not true for individual bit errors, which occur in groups dictated by the events. Additional statistical tests of independence, including the serial correlation test and the “poker” test, are described in Cox and Lewis.<sup>(3)</sup> These require more experimental data, but applications to convolutional decoding<sup>(2)</sup> have again verified the random-event hypothesis.

Figure C.3 illustrates the effect of increasing path memory length in the decoder; three multi- $h$  codes are depicted, whose characteristics are given in Table C.1. It can be seen that the bit error rate improves as  $N_T$  grows, until  $N_T$  is approximately equal to  $N_B$ . Thereafter the error rate does not improve, reflecting the fact that among all merged and unmerged neighbors of the transmitted path, the  $d_{\min}$ -causing one is the closest. Alternatively, one can plot the error rate against  $E_b/N_0$ , for a fixed path memory length. Then the error rate will fall off asymptotically as  $Q(d(E_b/N_0)^{1/2})$ , where  $d$  is the distance to the closest neighbor of length  $N_T$ , whether merged or unmerged. In general,  $d$  depends on which path is transmitted, and in the case of multi- $h$  codes, which index is operating in the first interval.

Whether or not an error event occurs at all depends primarily on  $d$ , but the overall bit error rate depends as well on the length of the events. At shorter path memories, long events take over and the average length grows considerably; this effect is strongly influenced by the properties of

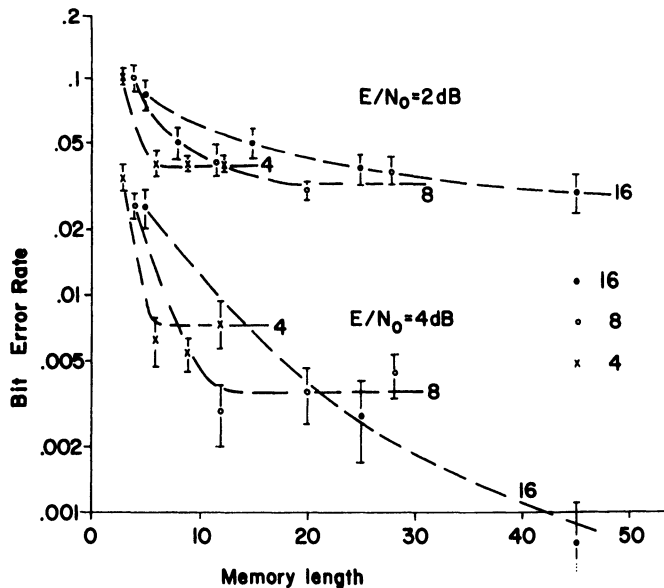


Figure C.3. Overall bit error rate versus decoder path memory for the codes in Table C.1 with  $\eta = 4, 8$ , and  $16$  codes; one-sigma confidence intervals are shown.  $E$  denotes energy/bit. From Ref. (1).

unmerged neighbors. In all cases, the average event length acts as a constant multiplying the probability  $Q(\cdot)$ , to create the total bit error probability.

#### *Confidence Intervals*

From the empirical independence of error events, we can derive confidence estimates on the experimental data. Once an error event terminates, each symbol interval can be viewed as a new Bernoulli trial with success probability  $1 - \rho$ . Presented with  $K$  such intervals, we expect to see  $\rho K$  error events with a variance of  $\rho(1 - \rho)K$ . If we make the additional assumption that the distribution of the number of events is approximately normal, the quantity  $\pm[\rho(1 - \rho)K]^{1/2}$  represents the one-sigma statistical confidence interval of the data, a range inside which the true mean lies with probability 0.68.

When the basic event probability  $\rho$  is small, the one-sigma interval is close to  $\pm(\rho K)^{1/2}$ . As a fraction of the sample mean, this is  $\pm 1(\rho K)^{1/2}$ , a quantity we estimate by replacing  $\rho K$  with the observed number of events. Thus the fractional confidence interval is inversely proportional to the square root of the number of events. An accurate simulation depends not on the number of bit errors observed, but on the number of events.

One-sigma confidence intervals are given in Figure C.3. In a plot like this of  $\log P_e$  the same fractional interval appears as a constant interval everywhere in the plot.

## C.2. The Signal Space Method of Simulation

To simulate the effect of an AWGN channel on a decoder, we perform a Gram-Schmidt orthogonalization on the phase signals to produce a basis for the vector space of transmitted signals. The encoder chooses from the signals expressed over this basis, the channel adds Gaussian noise of power  $N_0/2$  to each component, and the decoder finds the signal closest to this received vector in Euclidean distance.

In our multi- $h$  code example, four signal space dimensions are required during each interval, two to represent carrier frequency  $\omega_c$  (data 0), and two for carrier frequency  $\omega_c + 2\pi h_k/T$  (data 1). These pairs can express all phase shifts of the two frequencies. For the first basis pair, we simply choose the pair of signals

$$\Phi_1(t) = (2/T)^{1/2} \cos \omega_c t, \quad \Phi_2(t) = (2/T)^{1/2} \sin \omega_c t \quad (\text{C.1})$$

Without loss of generality, we can assume  $t \in [0, T]$ . These signals are of unit energy, and as  $\omega_c \rightarrow \infty$ ,  $(\Phi_1, \Phi_2) \rightarrow 0$ . [Here  $(u, v) = \int_0^T u(t)v(t) dt$ .] For the second pair, we begin with the pair

$$s_3(t) = (2/T)^{1/2} \cos (\omega_c + 2\pi h_k/T)t \quad (\text{C.2})$$

$$s_4(t) = (2/T)^{1/2} \sin (\omega_c + 2\pi h_k/T)t \quad (\text{C.3})$$

These are mutually orthogonal in the sense that  $(s_3, s_4) \rightarrow 0$  as  $\omega_c \rightarrow \infty$ , but not orthogonal to  $\Phi_1$  and  $\Phi_2$ . From the Gram-Schmidt procedure come  $\theta_3$  and  $\theta_4$  which are orthogonal,

$$\begin{aligned} \theta_3(t) &= (2/T)^{1/2} \cos (\omega_c + 2\pi h_k/T)t - b_{31}\Phi_1 - b_{32}\Phi_2 \\ b_{31} &= (s_3, \Phi_1), \quad b_{32} = (s_3, \Phi_2) \end{aligned} \quad (\text{C.4})$$

$$\begin{aligned} \theta_4(t) &= (2/T)^{1/2} \sin (\omega_c + 2\pi h_k/T)t - b_{41}\Phi_1 - b_{42}\Phi_2 - b_{43}\Phi_3 \\ b_{41} &= (s_4, \Phi_1), \quad b_{42} = (s_4, \Phi_2), \quad b_{43} = (s_4, \theta_3) \end{aligned} \quad (\text{C.5})$$

After considerable algebra, it develops that

$$\begin{aligned} b_{31} &= S_0, \quad b_{41} = -C_0, \quad b_{43} = 0 \\ b_{32} &= C_0, \quad b_{42} = S_0 \end{aligned} \quad (\text{C.6})$$

plus terms of order  $1/\omega_c$ , where

$$S_0 = \sin(2\pi h_k)/2\pi h_k, \quad C_0 = [\cos(2\pi h_k) - 1]/2\pi h_k$$

The functions  $\theta_3$  and  $\theta_4$  are still not normal; to normalize them we must divide by  $(1 - S_0^2 - C_0^2)^{1/2}$ , to obtain  $\Phi_3$  and  $\Phi_4$ .

In terms of these four basis vectors, the transmitter outputs beginning at zero phase are as follows:

*Data 0:*

$$(2E/T)^{1/2} \cos \omega_c t = \sqrt{E}(1, 0, 0, 0) \quad (C.7)$$

$$(2E/T)^{1/2} \sin \omega_c t = \sqrt{E}(0, 1, 0, 0)$$

*Data 1:*

$$(2E/T)^{1/2} \cos(\omega_c + 2\pi h_k/T)t = \sqrt{E}(S_0, C_0, (1 - S_0^2 - C_0^2)^{1/2}, 0) \quad (C.8)$$

$$(2E/T)^{1/2} \sin(\omega_c + 2\pi h_k/T)t = \sqrt{E}(-C_0, S_0, 0, (1 - S_0^2 - C_0^2)^{1/2})$$

while the outputs phase shifted by  $2\pi j/\eta$  radians are, for data 0,

$$\sqrt{E}[\cos(2\pi j/\eta)(1, 0, 0, 0) - \sin(2\pi j/\eta)(0, 1, 0, 0)] \quad (C.9)$$

and similarly for data 1. Table C.2 gives as an example all  $H\eta$  vectors for the (4/6, 3/6) code. The parameter  $\eta$  is the denominator of the  $h$  values; see Chapters 3 and 5.

**Table C.2. All Transmitted Signal Space Vectors for the (3/6, 4/6) Multi- $h$  Code<sup>a</sup>**

Initial phase	Phase slope	Signal space vector components			
		1	2	3	4
0	0	1	0	0	0
1	0	0.5	-0.8660	0	0
2	0	-0.5	-0.8660	0	0
3	0	-1	0	0	0
4	0	-0.5	0.8660	0	0
5	0	0.5	0.8660	0	0
0	4/6	-0.2067	-0.3581	0.9105	0
1	4/6	-0.4135	0	0.4553	-0.7885
2	4/6	-0.2067	0.3581	-0.4553	-0.7885
3	4/6	0.2067	0.3581	-0.9105	0
4	4/6	0.4135	0	-0.4553	0.7885
5	4/6	0.2067	-0.3581	0.4553	0.7885
0	3/6	0	-0.6366	0.7712	0
1	3/6	-0.5513	-0.3183	0.3856	-0.6679
2	3/6	-0.5513	0.3183	-0.3856	-0.6679
3	3/6	0	0.6366	-0.7712	0
4	3/6	0.5513	0.3183	-0.3856	0.6679
5	3/6	0.5513	-0.3183	0.3856	0.6679

<sup>a</sup> The initial phase is in multiples of  $2\pi/6$ .

## References

1. J. B. Anderson, "Simulated Error Performance of Multi- $h$  Phase Codes," *IEEE Transactions on Information Theory* IT-27, 357–362 (1981).
2. K. Srivatsa and J. B. Anderson, "Independence of Error Event Waiting Times in Convolutional Decoders," 18th Allerton Conf. on Commun., Control and Computing, Proc., October 1980, pp. 68–77.
3. D. R. Cox and P. R. Lewis, *The Statistical Analysis of Series of Events*, Methuen, London (1966).

---

## Appendix D

### Tables of Optimum Codes

In Chapter 11 we have given results for combined convolutional codes and CPFSK modulation. In this appendix tables of the best codes found are given. The notations used are explained in Chapter 11. For further code tables, see the reference list in Chapter 11.

#### D.1. Optimal Codes for Binary and Quaternary CPFSK

The results for the optimal codes for binary and quaternary CPFSK are shown in Tables D.1–D.5. The  $N$  value given in these tables is the value of  $N$  for which  $d_{\min}(h) = d_{\min,N}(h)$ . It should be observed that Tables D.1–D.5 are written in a “minimal” way. If, for example, all optimal combinations, using mapping rules Q1 or Q2, are wanted when  $\nu = 1$  and  $h = 0.15$ , Table D.3 and the results in Section 11.2.4 must be used. Doing this, it is seen that the combinations  $\{(1, 2), \text{Q1}, 4\}$  and  $\{(2, 1), \text{Q1}, ?\}$  are the only optimal combinations. Note that no calculations have been performed for the latter combination (see Section 11.2.4). Doing the same example when  $\nu = 2$  and  $h = 0.35$  yields the optimal combinations  $\{(3, 4), \text{Q1}, 40\}$ ,  $\{(3, 7), \text{Q2}, 40\}$ ,  $\{(6, 1), \text{Q1}, ?\}$ , and  $\{(6, 7), \text{Q2}, ?\}$ . Note that the combinations  $\{(3, 7), \text{Q2}, 40\}$  and  $\{(6, 7), \text{Q2}, ?\}$  are found by using the properties discussed in Section 11.2.4.

**Table D.1. The Optimal Rate 1/2 Convolutional Encoders and the Corresponding Optimum  $d_{\min}^2(h)$  for Different  $\nu$  and  $h$**

Coded binary CPFSK modulation				
$h$	$\nu = 1$		$\nu = 2$	
	Encoder, $N$	$d_{\min}^2(h)$	Encoder, $N$	$d_{\min}^2(h)$
0.05	{(1, 2), 6}	0.1290	{(4, 3), 22}	0.1144
0.10	{(1, 2), 6}	0.4863	{(4, 3), 22}	0.4490
0.15	{(1, 2), 6}	0.9909	{(4, 3), 22}	0.9786
0.20	{(1, 2), 6}	1.532	{(4, 3), 22}	1.664
0.25	{(1, 2), 6}	2.000	{(4, 3), 22}	2.454
0.30	{(1, 2), 8}	2.312	{(4, 3), 22}	3.291
0.35	{(2, 1), 8}	2.852	{(4, 3), 26}	4.116
0.40	{(2, 1), 10}	3.341	{(4, 3), 22}	4.874
0.45	{(2, 1), 12}	3.732	{(4, 3), 24}	5.514
0.50	{(2, 3), 12}	4.000	{(4, 3), 20}	6.000
0.55	{(2, 1), 18}	4.130	{(4, 3), 20}	5.592
0.60	{(2, 1), 10}	4.121	{(4, 3), 20}	5.366
0.65	{(2, 1), 10}	3.984	{(4, 3), 54}	4.943
0.70	{(2, 1), 10}	3.741	{(4, 3), 16}	4.484
0.75	{(2, 1), 8}	3.000	{(4, 3), 14}	4.000
0.75	{(2, 3), 8}	3.000		
0.80	{(2, 1), 8}	3.069	{(4, 5), 14}	3.652
0.85	{(2, 1), 8}	2.715	{(5, 7), 14}	3.536
0.90	{(2, 1), 8}	2.399	{(5, 7), 16}	3.368
0.95	{(2, 1), 16}	2.152	{(5, 7), 30}	3.175
1.00	{(2, 3), 4}	1.500	{(5, 7), 12}	2.500
1.00	{(1, 3), 6}	1.500		

**Table D.2. The Optimal Rate 1/2 Convolutional Encoders and the Corresponding Optimum  $d_{\min}^2(h)$  for Different  $\nu$  and  $h$**

Coded binary CPFSK modulation					
$h$	$\nu = 3$		$\nu = 4$		$d_{\min}^2(h)$
	Encoder, $N$	$d_{\min}^2(h)$	Encoder, $N$	$d_{\min}^2(h)$	
0.05	{(2, 11), 26}, {(12, 7), 32}	0.1225	{(31, 17), 34}, {(32, 17), 36}	0.1553	
0.10	{(2, 11), 26}, {(12, 7), 32}	0.4800	{(31, 17), 34}, {(32, 17), 36}	0.6090	
0.15	{(2, 11), 26}, {(12, 7), 32}	1.043	{(31, 17), 34}, {(32, 17), 36}	1.326	
0.20	{(2, 11), 26}, {(12, 7), 32}	1.766	{(31, 17), 34}, {(32, 17), 36}	2.252	
0.25	{(2, 11), 26}, {(12, 7), 32}	2.590	{(31, 17), 34}, {(32, 17), 36}	3.317	
0.30	{(2, 11), 26}, {(12, 7), 32}	3.450	{(31, 17), 34}, {(32, 17), 36}	4.441	
0.35	{(2, 11), 28}, {(12, 7), 32}	4.278	{(22, 13), 54}, {(34, 17), 78}	5.380	
0.40	{(12, 7), 30}	5.012	{(22, 13), 32}	5.905	
0.45	{(12, 7), 30}	5.599	{(30, 13), 36}	6.950	
0.50	{(1, 14), 22}, {(1, 17), 22}	6.000	{(22, 13), 32}, {(22, 15), 34}	8.000	
0.50	{(2, 11), 22}, {(2, 17), 22}	6.000	{(22, 31), 32}, {(30, 13), 34}	8.000	
0.50	{(3, 15), 20}, {(4, 17), 22}	6.000	{(31, 17), 30}, {(32, 17), 34}	8.000	
0.50	{(6, 13), 24}, {(10, 3), 22}	6.000	{(34, 17), 32}	8.000	
0.50	{(10, 5), 22}, {(12, 7), 26}	6.000			
0.50	{(12, 15), 26}, {(14, 7), 20}	6.000			
0.50	{(14, 13), 24}	6.000			
0.55	{(10, 3), 24}	5.923	{(32, 17), 32}	7.422	
0.60	{(10, 3), 24}	5.930	{(22, 15), 28}	6.344	
0.65	{(10, 3), 22}	5.572	—	—	
0.70	{(10, 3), 20}	5.051	{(24, 7), 26}	6.174	
0.75	{(14, 7), 20}	5.000	{(24, 7), 24}, {(31, 17), 22}	5.712	
0.75			{(20, 35), 24}, {(32, 17), 24}	5.712	
0.75			{(24, 37), 28}, {(30, 13), 26}	5.712	
0.75			{(34, 27), 26}	5.712	
0.80	{(13, 15), 18}	4.663	{(22, 31), 24}	5.295	
0.85	{(13, 15), 20}	4.606	—	—	
0.90	{(13, 15), 22}	4.416	{(23, 35), 26}	4.679	
0.95	{(13, 15), 30}	4.207	—	—	
1.00	{(7, 13), 20}, {(7, 15), 22}	3.000	—	—	
1.00	{(13, 7), 20}, {(13, 15), 20}	3.000			
1.00	{(13, 17), 16}, {(15, 7), 22}	3.000			
1.00	{(15, 13), 20}, {(15, 17), 18}	3.000			

**Table D.3. The Optimal Combinations of a Rate 1/2 Convolutional Encoder and a Four-Level Mapping Rule (Quaternary CPFSK), and the Corresponding Optimum  $d_{\min}^2(h)$  for  $\nu = 1$  and 2**

Coded four-level CPFSK modulation				
$\nu = 1$		$\nu = 2$		
$h$	Encoder, mapping rule, $N$	$d_{\min}^2(h)$	Encoder, mapping rule, $N$	$d_{\min}^2(h)$
0.05	$\{(1, 2), Q1, 4\}$	0.1935	$\{(7, 2), Q1, 13\}, \{(7, 5), Q2, 13\}$	0.2587
0.10	$\{(1, 2), Q1, 4\}$	0.7295	$\{(7, 2), Q1, 13\}, \{(7, 5), Q2, 13\}$	0.9826
0.15	$\{(1, 2), Q1, 4\}$	1.486	$\{(7, 2), Q1, 13\}, \{(7, 5), Q2, 13\}$	2.029
0.20	$\{(1, 2), Q1, 5\}$	2.298	$\{(7, 2), Q1, 12\}, \{(7, 5), Q2, 12\}$	3.202
0.25	$\{(1, 2), Q1, 6\}$	3.000	$\{(7, 2), Q1, 10\}, \{(7, 5), Q2, 10\}$	4.302
0.30	$\{(1, 2), Q1, 11\}$	3.468	$\{(7, 2), Q1, 14\}, \{(7, 5), Q2, 14\}$	4.312
0.35	$\{(1, 2), Q1, 36\}$	3.389	$\{(3, 4), Q1, 40\}$	4.164
0.40	$\{(1, 2), Q1, 5\}$	3.126	$\{(1, 4), Q1, 6\}, \{(1, 5), Q2, 7\}$	3.911
0.45	$\{(1, 2), Q1, 7\}$	3.312	$\{(1, 7), Q1, 8\}, \{(1, 6), Q2, 8\}$	4.296
0.50	$\{(1, 2), Q1, 3\}$	3.000	$\{(1, 7), Q1, 8\}, \{(1, 6), Q2, 7\}$	5.000
0.50	$\{(3, 1), Q1, 3\}$	3.000	$\{(3, 7), Q1, 7\}$	5.000
0.50	$\{(1, 3), Q2, 3\}$	3.000		
0.55	$\{(1, 3), Q2, 4\}$	2.977	$\{(1, 7), Q1, 7\}, \{(1, 6), Q2, 7\}$	4.346
0.55			$\{(3, 7), Q1, 7\}$	4.346
0.60	$\{(1, 3), Q2, 4\}$	2.998	$\{(1, 4), Q1, 6\}, \{(1, 6), Q2, 6\}$	4.060

**Table D.4. The Optimal Combinations of a Rate 1/2 Convolutional Encoder and a Four-Level Mapping Rule (Quaternary CPFSK), and the Corresponding Optimum  $d_{\min}^2(h)$  for  $\nu = 3$**

Coded four-level CPFSK modulation		
$h$	$\nu = 3$ ; Encoder, mapping rule, $N$	$d_{\min}^2(h)$
0.05	$\{(13, 2), Q1, 20\}, \{(13, 11), Q2, 20\}, \{(13, 4), Q1, 26\}, \{(13, 17), Q2, 26\}$	0.3075
0.10	$\{(13, 2), Q1, 20\}, \{(13, 11), Q2, 20\}, \{(13, 4), Q1, 26\}, \{(13, 17), Q2, 26\}$	1.171
0.15	$\{(13, 2), Q1, 20\}, \{(13, 11), Q2, 20\}, \{(13, 4), Q1, 23\}, \{(13, 17), Q2, 23\}$	2.430
0.20	$\{(13, 4), Q1, 23\}, \{(13, 17), Q2, 23\}$	3.863
0.25	$\{(13, 4), Q1, 22\}, \{(13, 17), Q2, 22\}$	5.241
0.30	$\{(3, 10), Q1, 20\}$	5.080
0.35	$\{(3, 10), Q1, 26\}$	5.006
0.40	$\{(3, 10), Q1, 13\}$	4.602
0.45	$\{(1, 15), Q1, 12\}, \{(1, 14), Q2, 12\}$	5.514
0.50	$\{(1, 15), Q1, 9\}, \{(1, 14), Q2, 9\}, \{(2, 15), Q1, 10\}, \{(2, 17), Q2, 10\}$	6.000
0.50	$\{(3, 13), Q1, 9\}, \{(3, 15), Q1, 9\}, \{(3, 16), Q1, 8\}, \{(7, 13), Q1, 9\}$	6.000
0.50	$\{(7, 14), Q2, 9\}, \{(13, 7), Q1, 9\}, \{(13, 14), Q2, 9\}, \{(17, 13), Q1, 9\}$	6.000
0.55	$\{(1, 15), Q1, 11\}, \{(1, 14), Q2, 11\}, \{(2, 15), Q1, 10\}, \{(2, 17), Q2, 10\}$	5.611
0.55	$\{(3, 13), Q1, 11\}$	5.611
0.60	$\{(3, 10), Q1, 9\}$	4.751

**Table D.5. The Optimal Combinations of a Rate 1/2 Convolutional Encoder and a Four-Level Mapping Rule (Quaternary CPFSK), and the Corresponding Optimum  $d_{\min}^2(h)$  for  $\nu = 4$**

Coded four-level CPFSK modulation, $\nu = 4$		
$h$	Encoder, mapping, $N$	$d_{\min}^2(h)$
0.10 <sup>a</sup>	{(23, 10), Q1, 27}	1.362
0.20 <sup>a</sup>	{(23, 10), Q1, 24}	4.427
0.25	{(23, 10), Q1, 24}	6.151
0.25	{(23, 33), Q2, 24}	6.151
0.30 <sup>a</sup>	{(7, 20), Q1, 19}	5.702
0.35 <sup>b</sup>	{(4, 23), Q1, 30}	5.380
0.40 <sup>a</sup>	{(4, 23), Q1, 15}	5.881
0.45 <sup>a</sup>	{(4, 23), Q1, 14}	6.760
0.50 <sup>b</sup>	{(4, 23), Q1, 13}	7.000
0.55 <sup>b</sup>	{(4, 23), Q1, 13}	6.696
0.60 <sup>a</sup>	{(4, 23), Q1, 11}	5.761

<sup>a</sup> Search not complete, only all combinations  $\{\bar{G}(D), Q1\}$  have been searched.

<sup>b</sup> Search not complete.

## D.2. Optimal Codes for 8-, 16-, and 32-Level CPFSK

Tables D.6–D.13 give results for the best found codes for 8-, 16-, and 32-level CPFSK. The mapper is the natural binary mapper and the code is a rate 1/2 code applied to the two least significant natural binary bits. The modulation indices considered range from  $h = 2/22, 2/21, \dots$  to  $2/9, 2/8$ . The tables D.6–D.13 give the information {rate 1/2 encoder,  $N, N_m$ }, where  $N$  is the smallest value of  $N$  for which  $d_{\min, N}^2 = d_{\min}^2$  and  $N_m T$  is the length of the shortest phase and state merger giving a tight upper bound on  $d_{\min}^2$ . The  $d_{\min}^2(h)$  values given in these tables are underlined if the encoder-independent upper bound on  $d_{\min}^2(h)$  is reached. Note that if the upper bound is reached it is not possible to increase  $d_{\min}^2(h)$  regardless of how many delay elements we use in the rate 1/2 encoder. For further details see Section 11.3.

**Table D.6. The Optimal  $d_{\min}^2(h)$  and Corresponding Optimal Encoders When a Rate 2/3 Convolutional Encoder and Eight-Level CPFSK Modulation Are Used;  $\nu = 1$**

Rate 2/3 convolutional encoder and eight-level CPFSK modulation		
$h$	$d_{\min}^2(h)$	Optimal $\nu = 1$ rate 1/2 convolutional encoder, $N, N_m$
1/11(0.0909)	0.8218	{(1, 2), 8, 3}, {(2, 1), 3, 3}, {(3, 1), 3, 3}, {(3, 2), 8, 3}
2/21(0.0952)	0.8970	{(1, 2), 8, 3}, {(2, 1), 3, 3}, {(3, 1), 3, 3}, {(3, 2), 8, 3}
1/10(0.1000)	0.9826	{(1, 2), 8, 3}, {(2, 1), 3, 3}, {(3, 1), 3, 3}, {(3, 2), 8, 3}
2/19(0.1053)	1.0807	{(1, 2), 8, 3}, {(2, 1), 3, 3}, {(3, 1), 3, 3}, {(3, 2), 8, 3}
1/9(0.1111)	1.1937	{(1, 2), 8, 3}, {(2, 1), 3, 3}, {(3, 1), 3, 3}, {(3, 2), 8, 3}
2/17(0.1176)	1.3246	{(1, 2), 8, 3}, {(2, 1), 3, 3}, {(3, 1), 3, 3}, {(3, 2), 8, 3}
1/8(0.1250)	1.4771	{(1, 2), 8, 3}, {(2, 1), 8, 3}, {(3, 1), 3, 3}, {(3, 2), 8, 3}
2/15(0.1333)	1.6560	{(1, 2), 8, 3}, {(2, 1), 3, 3}, {(3, 1), 3, 3}, {(3, 2), 8, 3}
1/7(0.1429)	1.8670	{(1, 2), 8, 3}, {(2, 1), 3, 3}, {(3, 1), 3, 3}, {(3, 2), 8, 3}
2/13(0.1538)	2.1175	{(1, 2), 8, 3}, {(2, 1), 3, 3}, {(3, 1), 3, 3}, {(3, 2), 8, 3}
1/6(0.1667)	2.4164	{(1, 2), 7, 3}, {(2, 1), 3, 3}, {(3, 1), 3, 3}, {(3, 2), 7, 3}
2/11(0.1818)	2.7741	{(1, 2), 7, 3}, {(2, 1), 10, 3}, {(3, 1), 10, 3}, {(3, 2), 7, 3}
1/5(0.2000)	3.2022	{(1, 2), 7, 3}, {(2, 1), 4, 3}
2/9(0.2222)	3.7109	{(1, 2), 13, 3}, {(2, 1), 5, 3}, {(3, 1), 5, 3}, {(3, 2), 13, 3}
1/4(0.2500)	<u>2.0000</u>	{(1, 2), 3, 1}, {(2, 1), 1, 1}, {(3, 1), 1, 1}, {(3, 2), 3, 1}

**Table D.7. The Optimal  $d_{\min}^2(h)$  and Corresponding Optimal Encoders When a Rate 2/3 Convolutional Encoder and Eight-Level CPFSK Modulation Are Used;  $\nu = 2$**

Rate 2/3 convolutional encoder and eight-level CPFSK modulation		
$h$	$d_{\min}^2(h)$	Optimal $\nu = 2$ rate 1/2 convolutional encoder, $N, N_m$
1/11	1.4297	{(5, 2), 12, 4}, {(7, 2), 12, 4}
2/21	1.5595	{(5, 2), 12, 4}, {(7, 2), 12, 4}
1/10	1.7072	{(5, 2), 12, 4}, {(7, 2), 12, 4}
2/19	1.8761	{(5, 2), 12, 4}, {(7, 2), 12, 4}
1/9	2.0703	{(5, 2), 12, 4}, {(7, 2), 12, 4}
2/17	2.2947	{(5, 2), 12, 4}, {(7, 2), 12, 4}
1/8	2.5554	{(5, 2), 12, 4}, {(7, 2), 12, 4}
2/15	2.8602	{(5, 2), 12, 4}, {(7, 2), 12, 4}
1/7	3.2181	{(5, 2), 12, 4}, {(7, 2), 12, 4}
2/13	3.6406	{(5, 2), 21, 4}, {(7, 2), 21, 4}
1/6	4.1407	{(5, 2), 11, 4}, {(7, 2), 11, 4}
2/11	3.8994	{(3, 4), 20, 5}, {(6, 1), 19, 5}, {(7, 1), 19, 5}, {(7, 4), 17, 5}
1/5	4.4636	{(5, 2), 10, 3}, {(7, 2), 10, 3}
2/9	<u>4.4604</u>	{(1, 4), 18, 2}, {(3, 4), 18, 2}, {(4, 1), 9, 2}, {(5, 2), 9, 2} {(6, 1), 12, 2}, {(7, 1), 12, 2}, {(7, 2), 9, 2}, {(7, 4), 18, 2}

**Table D.8. The Optimal  $d_{\min}^2(h)$  and Corresponding Optimal Encoders When a Rate 2/3 Convolutional Encoder and Eight-Level CPFSK Modulation Are Used;  $\nu = 3$**

Rate 2/3 convolutional encoder and eight-level CPFSK modulation		
$h$	$d_{\min}^2(h)$	Optimal $\nu = 3$ rate 1/2 convolutional encoder, $N, N_m$
1/11	1.8372	$\{(13, 4), 23, 5\}, \{(15, 2), 18, 5\}, \{(17, 2), 18, 5\}, \{(17, 4), 23, 5\}$
2/21	2.0039	$\{(13, 4), 23, 5\}, \{(15, 2), 18, 5\}, \{(17, 2), 18, 5\}, \{(17, 4), 23, 5\}$
1/10	2.1935	$\{(13, 4), 23, 5\}, \{(15, 2), 18, 5\}, \{(17, 2), 18, 5\}, \{(17, 4), 23, 5\}$
2/19	2.4104	$\{(13, 4), 23, 5\}, \{(15, 2), 18, 5\}, \{(17, 2), 18, 5\}, \{(17, 4), 23, 5\}$
1/9	2.6596	$\{(13, 4), 23, 5\}, \{(15, 2), 18, 5\}, \{(17, 2), 18, 5\}, \{(17, 4), 23, 5\}$
2/17	2.9476	$\{(13, 4), 23, 5\}, \{(15, 2), 18, 5\}, \{(17, 2), 18, 5\}, \{(17, 4), 23, 5\}$
1/8	3.2822	$\{(13, 4), 23, 5\}, \{(15, 2), 18, 5\}, \{(17, 2), 18, 5\}, \{(17, 4), 23, 5\}$
2/15	3.6730	$\{(13, 4), 22, 5\}, \{(15, 2), 18, 5\}, \{(17, 2), 18, 5\}, \{(17, 4), 22, 5\}$
1/7	4.1320	$\{(13, 4), 22, 5\}, \{(15, 2), 16, 5\}, \{(17, 2), 16, 5\}, \{(17, 4), 22, 5\}$
2/13	4.6733	$\{(13, 4), 34, 5\}, \{(15, 2), 32, 5\}, \{(17, 2), 32, 5\}, \{(17, 4), 34, 5\}$
1/6	4.7624	$\{(11, 2), 14, 5\}, \{(11, 4), 15, 5\}, \{(13, 2), 14, 5\}, \{(15, 4), 15, 5\}$
2/11	4.8170	$\{(3, 10), 26, 5\}, \{(14, 1), 25, 5\}$
1/5	<u>4.7568</u>	$\{(11, 2), 11, 2\}, \{(11, 4), 13, 2\}, \{(13, 2), 11, 2\}, \{(13, 4), 13, 2\}$ $\{(15, 2), 14, 2\}, \{(15, 4), 13, 2\}, \{(17, 2), 14, 2\}, \{(17, 4), 13, 2\}$

**Table D.9. The Optimal  $d_{\min}^2(h)$  and Corresponding Optimal Encoders When a Rate 2/3 Convolutional Encoder and Eight-Level CPFSK Modulation Are Used;  $\nu = 4$**

Rate 2/3 convolutional encoder and eight-level CPFSK modulation		
$h$	$d_{\min}^2(h)$	Optimal $\nu = 4$ rate 1/2 convolutional encoder, $N, N_m$
1/11	2.1615	$\{(33, 4), 28, 7\}, \{(37, 4), 28, 7\}$
2/21 <sup>a</sup>	2.3596	$\{(33, 4), 28, 7\}$
1/10 <sup>a</sup>	2.5854	$\{(33, 4), 28, 7\}$
2/19 <sup>a</sup>	2.8442	$\{(33, 4), 28, 7\}$
1/9 <sup>a</sup>	3.1425	$\{(33, 4), 28, 7\}$
2/17 <sup>a</sup>	3.4882	$\{(33, 4), 28, 7\}$
1/8 <sup>a</sup>	3.8916	$\{(33, 4), 28, 7\}$
2/15 <sup>a</sup>	4.2482	$\{(33, 4), 26, 2\}$
1/7 <sup>a</sup>	4.4834	$\{(33, 4), 23, 2\}$
2/13 <sup>a</sup>	4.6860	$\{(33, 4), 32, 2\}$
1/6	<u>4.8270</u>	$\{(21, 4), 17, 2\}, \{(21, 16), 19, 2\}, \{(23, 4), 18, 2\}, \{(23, 10), 16, 2\}$ $\{(23, 12), 16, 2\}, \{(23, 16), 17, 2\}, \{(25, 2), 17, 2\}, \{(25, 4), 17, 2\}$ $\{(25, 10), 15, 2\}, \{(27, 2), 17, 2\}, \{(27, 4), 18, 2\}, \{(27, 16), 17, 2\}$ $\{(31, 2), 18, 2\}, \{(31, 4), 18, 2\}, \{(31, 12), 16, 2\}, \{(31, 16), 17, 2\}$ $\{(33, 2), 18, 2\}, \{(33, 10), 16, 2\}, \{(35, 4), 18, 2\}, \{(35, 10), 15, 2\}$ $\{(35, 16), 17, 2\}, \{(37, 16), 19, 2\}$
2/11	<u>4.8664</u>	$\{(7, 20), 27, 2\}, \{(13, 20), 29, 2\}, \{(17, 34), 29, 2\}, \{(23, 4), 26, 2\}$ $\{(23, 34), 27, 2\}, \{(27, 4), 26, 2\}, \{(27, 20), 29, 2\}, \{(31, 4), 28, 2\}$ $\{(31, 7), 26, 2\}, \{(32, 1), 18, 2\}, \{(33, 1), 18, 2\}, \{(33, 20), 27, 2\}$ $\{(34, 1), 18, 2\}, \{(35, 1), 18, 2\}, \{(35, 4), 28, 2\}, \{(36, 7), 26, 2\}$

<sup>a</sup> Best found results, no complete search.

**Table D.10. The Best Found  $d_{\min}^2(h)$  and Corresponding Encoders When a Rate 3/4 Convolutional Encoder and 16-Level CPFSK Modulation Are Used;  
 $\nu = 1$  and  $\nu = 2$**

Rate 3/4 convolutional encoder and 16-level CPFSK modulation				
$h$	$\nu = 1$		$\nu = 2$	
	$d_{\min}^2(h)$	Encoder, $N, N_m$	$d_{\min}^2(h)$	Encoder, $N, N_m$
1/11	1.2327	{(2, 1), 3, 3}	2.1445	{(5, 2), 12, 4}
2/21	1.3455	{(2, 1), 3, 3}	2.3392	{(5, 2), 12, 4}
1/10	1.4739	{(2, 1), 3, 3}	2.5608	{(5, 2), 12, 4}
2/19	1.6210	{(2, 1), 3, 3}	2.8141	{(5, 2), 12, 4}
1/9	1.7905	{(2, 1), 3, 3}	3.1054	{(5, 2), 12, 4}
2/17	1.9868	{(2, 1), 3, 3}	3.4420	{(5, 2), 12, 4}
1/8	2.2156	{(2, 1), 3, 3}	<u>3.0000</u>	{(5, 2), 8, 1}
2/15	2.4839	{(2, 1), 3, 3}	4.2903	{(5, 2), 12, 4}
1/7	2.8005	{(2, 1), 3, 3}	4.8272	{(5, 2), 12, 4}
2/13	3.1763	{(2, 1), 3, 3}	<u>5.2298</u>	{(5, 2), 19, 2}
1/6	<u>3.0000</u>	{(2, 1), 2, 1}	—	—
2/11	3.8501	{(2, 1), 8, 2}	<u>5.6019</u>	{(5, 2), 19, 2}
1/5	3.3511	{(2, 1), 2, 2}	<u>5.7661</u>	{(5, 2), 8, 2}
2/9	3.6725	{(2, 1), 5, 2}	6.0405	{(5, 2), 15, 3}
1/4	<u>3.0000</u>	{(2, 1), 1, 1}	—	—

**Table D.11. The Best Found  $d_{\min}^2(h)$  and Corresponding Encoders When a Rate 3/4 Convolutional Encoder and 16-Level CPFSK Modulation Are Used;  
 $\nu = 3$  and  $\nu = 4$**

Rate 3/4 convolutional encoder and 16-level CPFSK modulation				
$h$	$\nu = 3$		$\nu = 4$	
	$d_{\min}^2(h)$	Encoder, $N, N_m$	$d_{\min}^2(h)$	Encoder, $N, N_m$
1/11	2.7558	{(15, 2), 18, 5}	3.2422	{(33, 4), 28, 7}
2/21	3.0058	{(15, 2), 18, 5}	3.5394	{(33, 4), 28, 7}
1/10	3.2903	{(15, 2), 18, 5}	3.8781	{(33, 4), 28, 7}
2/19	3.6156	{(15, 2), 18, 5}	4.2663	{(33, 4), 28, 7}
1/9	3.9894	{(15, 2), 18, 5}	4.7137	{(33, 4), 28, 7}
2/17	4.4214	{(15, 2), 18, 5}	5.2324	{(33, 4), 28, 7}
2/15	5.5096	{(15, 2), 19, 5}	<u>5.6359</u>	{(33, 4), 21, 2}
1/7	<u>5.3467</u>	{(15, 2), 15, 2}	—	—
2/9	<u>6.3101</u>	{(15, 2), 14, 2}	—	—

**Table D.12. The Best Found  $d_{\min}^2(h)$  and Corresponding Encoders When a Rate 4/5 Convolutional Encoder and 32-Level CPFSK Modulation Are Used;  
 $\nu = 1$  and  $\nu = 2$**

Rate 4/5 convolutional encoder and 32-level CPFSK modulation				
$h$	$d_{\min}^2(h)$	$\nu = 1$		$\nu = 2$
		Encoder, $N, N_m$	$d_{\min}^2(h)$	Encoder, $N, N_m$
1/11	1.6437	{(2, 1), 3, 3}	2.8593	{(5, 2), 12, 4}
2/21	1.7939	{(2, 1), 3, 3}	3.1189	{(5, 2), 12, 4}
1/10	1.9652	{(2, 1), 3, 3}	3.4143	{(5, 2), 12, 4}
2/19	2.1614	{(2, 1), 3, 3}	3.7522	{(5, 2), 12, 4}
1/9	2.3874	{(2, 1), 3, 3}	4.1405	{(5, 2), 12, 4}
2/17	2.6491	{(2, 1), 3, 3}	4.5893	{(5, 2), 12, 4}
1/8	2.9542	{(2, 1), 3, 3}	4.0000	{(5, 2), 8, 1}
2/15	3.3119	{(2, 1), 3, 3}	5.7203	{(5, 2), 16, 4}
1/7	3.7340	{(2, 1), 3, 3}	4.0000	{(5, 2), 5, 1}
2/13	4.2350	{(2, 1), 3, 3}	6.9730	{(5, 2), 19, 2}
1/6	4.0000	{(2, 1), 2, 1}	—	—
2/11	5.1335	{(2, 1), 8, 2}	.4692	{(5, 2), 19, 2}
1/5	4.0000	{(2, 1), 2, 1}	—	—
2/9	4.8966	{(2, 1), 5, 2}	7.7933	{(5, 2), 14, 2}
1/4	4.0000	{(2, 1), 1, 1}	—	—

**Table D.13. The Best Found  $d_{\min}^2(h)$  and Corresponding Encoders When a Rate 4/5 Convolutional Encoder and 32-Level CPFSK Modulation Are Used;  
 $\nu = 3$  and  $\nu = 4$**

Rate 4/5 convolutional encoder and 32-level CPFSK modulation				
$h$	$d_{\min}^2(h)$	$\nu = 3$		$\nu = 4$
		Encoder, $N, N_m$	$d_{\min}^2(h)$	Encoder, $N, N_m$
1/11	3.6744	{(15, 2), 18, 5}	4.3230	{(33, 4), 28, 7}
2/21	4.0077	{(15, 2), 18, 5}	—	—
1/10	4.0000	{(15, 2), 15, 1}	—	—
2/19	4.8208	{(15, 2), 18, 5}	—	—
1/9	5.3192	{(15, 2), 18, 5}	6.2850	{(33, 4), 28, 7}
2/17	5.8952	{(15, 2), 21, 5}	—	—
2/15	7.3119	{(15, 2), 27, 5}	7.5145	{(33, 4), 29, 2}

# Index

- Acquisition time: *see* Synchronization  
 $(\alpha, \beta)$  phase pulses, 69–71
- Alphabet size  
cutoff rate, effect on, 203, 206–208  
definition, 25  
discrete components, relation to, 366  
energy-bandwidth plot, effect on, 182–186, 206–207  
Shannon theory, 187  
strength of  $M=4$ , 183–186; weakness of  $M=2$ , 182–186
- Average-matched filter (AMF)  
in AMF receiver, 330–333  
nonuniformly weighted, 332–333, 344  
in parallel MSK receiver, 300, 304–313
- AMF receiver  
complexity, 351–352  
distance in, 334–352  
error probability, 333–341  
multiple symbol approach, 330, 348–349  
nonuniform weighted, 332–333  
simulations, 342, 346, 350  
structure, 330–333  
symbol updating, 347–348
- Amoroso, F., with Kivett, J. A., 232
- Amplitude limitation  
CPM, effect of, 136–144  
definition, 33  
distance, effect on, 136–144  
distance formula, 33  
spectra  
calculation methods for, 178  
effect on, 173–178  
transmitter based on, 227
- Anderson, J. B., 12, 59
- Anderson, R. R., with Salz, J., 148
- Ascheid, G., with Chen, Y. and Meyr, H., 379
- Augmented state vector, 129–131
- Aulin, T., 12, 56, 59
- Autocorrelation function, of modulated signals  
at baseband, 150  
discrete and continuous parts  
definition, 153–154  
RC examples, 360–361  
in synchronization, 359–362  
filtering, effect on, 174–176  
geometric decay of, 152–153  
hardlimiting effect on, 174–176  
real and imaginary parts, 151  
in spectra calculation, 147–154
- Autocorrelation method: *see* Spectra (calculation methods)
- Average-matched filter: *see* AMF
- Backwards state transition, 259
- Baker's property, 168–171
- Bandwidth; *see also* Energy-bandwidth plots  
capacity, relation to, 195  
compaction, 7, 11  
consumption, 8, 181  
dimensionality, relation to, 192–195  
power out of band (POB), 99%, 99.9%, 182–186, 205–208; for CPFSK/convolutional code combs., 437–438, 448–450  
in synchronizers, 372–376
- Baseband components, or signals; *see also* Eye diagram or Envelope diagram  
in AMF receiver, 333  
definition, 31–35  
distance (*formula*) from, 33

- Baseband components, or signals (*cont.*)**
- eye diagram, relation to, 36–38
  - filter effects, 128–131
  - after filtering (*formula*), 33–34
  - after hardlimiting (*formula*), 33
  - in MSK, 50–51
  - in Nyquist QPSK, 43–44
  - transmitter, based on, 212–215, 228–230
  - in Viterbi receiver, 250–251
- Basis functions**
- in coding theorems, 193
  - definition, 16–18
  - in Nyquist PSK, 42, 46–47
- Bayes rule, 16**
- Bessel function, 244, 387–388**
- Binary coding: *see* Error correcting codes**
- Blahut, R. E., 10**
- Booth, R. W. D., 381–382**
- Bounds; *see also* Error probability bounds or Distance (bounds to)**
- cutoff rate, as bound, 200–201
  - E(R) function bound, 190, 200–201
  - Marcum Q function bound, 391
  - minimum distance calculation, use of
    - bounds in, 462–465
  - phase error, sensitivity of distance bound to, 368–369
- Q function bounds, 21–22**
- BPSK**
- channel model, 189
  - cutoff rate, 203
  - definition, 48
  - differential BPSK, 48–49
  - distance, 28–29
  - error probability, 28–29; under phase and timing error, 327–328
  - Nyquist BPSK, 42–48
  - receiver, ML, 34–35
  - spectra, 38–41
  - synchronizers, 357–358, 370
- Burst mode, parallel and serial MSK, 329**
- Butterworth filter: *see* Filtering**
- Capacity**
- antipodal modulation channel, 191
  - AWGN, 192, 194–195, 209
  - bandwidth, as function of, 195, 209
  - BSC, 190
  - per dimension, 194–195
  - IDMC, 190–191
  - of phase modulation channel, 199
  - power, as function of, 195
  - quantization, effect on, 191
- Catastrophic modulation index, 91–92**
- Channels; *see also* Capacity or Cutoff rate**
- analog vs. digital, 4
  - antipodal modulation, 189–191
  - AWGN, 16–17, 189, 193, 197
  - BSC, 188, 191
  - coaxial cable, 6
  - fading, 196, 299–300, 308–313
  - IDMC, 188, 190–191, 200–201
  - input distribution of, 190
  - ISI, 196
  - microwave, 3–4
- Chebychev filter: *see* Filtering**
- Chernoff bound, 472–474**
- Clark, G. C., with Cain, J. B., 10**
- Coding theorem**
- for AWGN channel, 194–195
  - converses, 190
  - for IDMC, 190
- Coherent receiver; *see also* Simulations, Receiver**
- for CPFSK, optimal, 238–242
  - definition, 57
  - Viterbi, for CPM, 246–255
- Compatibility, 2, 4**
- Completeness, of basis, 17**
- Complexity**
- of AMF receiver, 351–352
  - of minimum distance calculation, 465–467
  - of reduced complexity Viterbi receivers, 294–295
- Confidence intervals, 479–480**
- Convergence, in phase difference states, 470–472**
- Convolutional codes**
- catastrophic, 423
  - CPFSK, combined with, 417–457
    - energy-bandwidth plots, 437–438, 446–450
    - minimum distance, rate  $\frac{1}{2}$  codes, 427–437, 483–487
    - minimum distance, rate  $\frac{2}{3}$  and above, 440–454, 487–493
    - multi-h modulation, comparison to, 450
  - definition, 417–418, 439–440
  - in set partition codes, 414–417
  - simulation of, with CPFSK, 451–457
    - with smooth phases pulses, 444–446
    - symmetries, from mapping rules, 423–426
    - tables of good codes, 434, 483–492
- CORPSK, 53, 295**
- Correlative PSK: *see* CORPSK**
- Correlation receiver, 20, 249**

- Correlative state vector, 112, 115, 246–247  
Costello, D. J., with Lin, S., 10  
Cox, D. R., with Lewis, P. R., 478  
CPFSK: *see* 1REC  
CPM, definition of, 56  
Cubic smoothing, 204  
Cutoff rate, 199–209, 469–474  
    alphabet size, effect of, 203, 206–208  
    for BSC, hard and soft decision, 207–208;  
        sequential decoding, 201  
    capacity, relation to, 200–201  
    difference chain, calculation from, 201–202,  
        469–474  
    E(R), relation to, 200–201  
    input distribution, dependence on, 201  
    modulation index, effect of, 202, 206–207  
    numerical results, 202–205  
    smoothing, effect of, 203–204  
Cyclostationarity, 150  
Cylinder, phase, 24, 247, 255–256, 469
- DeBuda, R., 24, 59, 358; with Kassem, W.,  
    195
- Decoding: *see also* Receiver; Viterbi algorithm  
    of codes, 7, 10  
    in Shannon theory, 187  
    soft decision, 10
- DeJager, F., with Dekker, C. B., 211, 214,  
    312
- Detection theory, 9
- Difference chain: *see* States (Markov)
- Difference sequence  
    difference tree, 72  
    distance, related to, 59–61  
    minimum distance, calculation from, 90  
    in mismatched receivers, 285–286  
    in multi-h modulation, 80–84, 88  
    weak indices, relation to, 91
- Difference states  
    in error bound calculation, 114–115  
    under filtering, 130  
    split averaged difference state, 114–120
- Differential encoding, parallel MSK receivers,  
    297–299; Serial MSK receivers, 329
- Differential PSK, 48–49, 272–275
- Differential receiver  
    for differential PSK, 48–49, 272–275  
    error probability of, 267–269  
    for partial response CPM, 263–269  
    phase eye diagrams, 266
- Dimensionality, 192–195, 197
- Direct approach: *see* Spectra, calculation  
    methods
- Discrete (spectral) components; *see also*  
    Spectra  
    alphabet size, relation to, 366  
    CNR of, 364–374  
    definition, 154–155  
    for HCS, 366–367  
    modulation index, relation to, 366  
    pulse length, relation to, 366  
    for RC, 361–362, 366–367  
    in synchronizers, 359–366
- Discriminator receiver  
    clicks in, 269–270  
    error probability, 269–271  
    sequence detection in, 275–276  
    simulations (1REC and 1RC), 271–275
- Distance  
    algorithms to find, 461–467  
    in AMF receiver, 334–352  
    amplitude limitation, effect of, 136–142  
    from baseband components, 32  
    bounds to ( $d_B$ )  
        full response CPM, 61–71  
        multi-h CPM, 80–89  
        partial response CPM, 65–80  
        tightness, 94–96  
    definition, for CPM, 26–27, 32, 59, 182,  
        199–202  
    from difference sequence, 59  
    energy consumption, as measure of, 182  
    equivalent distance ( $d_e$ ), 392–408  
    error probability, relation to, 368–369  
    frequency pulse, relation to, 64–71  
    justification of use, 55–56  
    Markov nature, 201–202  
    minimum distance; *see also under* modula-  
        tion name  
    CPFSK/convolutional code combs., 419–  
        457, 483–492  
    definition, 27–28  
    multi-h, full response, 105–109; partial  
        response, 106–110  
    1REC, 3REC, 92–98  
    2RC, 3RC, 98–104  
    with mismatched signals, 123, 127–136  
    normalization of, 27  
    with Nyquist pulses, 43–44  
    in parallel MSK receiver, 298–304  
    receiver distance ( $d_R$ ), 124–125, 283–284  
    in reduced complexity receiver, 282–295  
    in serial MSK receiver, 318  
    in synchronization, 367–369  
    2-signal distance, 199  
    in unmerged path pairs, 476–479

- Distance bound: *see* Distance
- Doelz, M. L., with Heald, E. T., 24
- Double dynamic programming minimum distance algorithm, 465–467
- Dupontel, D., 49
- Dynamic programming, 11, 465–467
- E(R) function, 190, 200–201
- Eigenvalue method, capacity and cutoff rate, 199, 202, 471–474
- Encoder, Shannon, 187
- Energy; *see also* energy-bandwidth plots  
 bit energy ( $E_b$ ), 27  
 consumption, 182  
 cutoff rate, relation to, 202–208  
 per dimension, 194–195  
 interval energy (E), 27
- Energy-bandwidth plots  
 for CPFSK/convolutional code combs., 437–438, 446–450  
 via cutoff rates, 205–208  
 via distance, 182–186  
 trade-off examples, 205–207
- Entropy, 187
- Envelope  
 definition, 32  
 of Nyquist signals, 42, 47  
 variations, with filtering, 8, 40
- Envelope diagram, 133–139; of Filtered MSK, 264; of Filtered 3RC, 139, 265
- Equalization, 8, 11, 12
- Equivalent distance ( $d_e$ )  
 bound to, 394–397  
 definition, 392–393  
 minimum equivalent distance, 397–408
- Error correcting codes  
 combined with modulator  
 CPFSK, 417–457; error bound, 419–420;  
 compared to coded QPSK, 435–437;  
 simulations, 451–457  
 CPM, 209  
 PSK, 413–417  
 with smooth pulses, 444–446
- history, 10–11
- ISI related to, 36
- in systems and channels, 3, 6–7
- tables of good codes, 434, 483–492
- Error events  
 in convolutional codes, 478  
 in CPM, 475–478  
 definition, 114, 475  
 geometrical distribution, 477–479  
 high *vs.* low SNR, 476–477
- Error event (*cont.*)  
 length, 478–479  
 long and short, 476  
 statistical analysis, 475–480  
 in trellis (Viterbi) decoding, 259–260
- Error exponent: *see* E(R) function; Cutoff rate
- Error probability; *see also* Error probability bounds; Simulations  
 in AMF receiver, 333–341  
 in differential PSK, 272–275  
 in differential receivers, 267–269, 271–272  
 in discriminator receiver, 269–276  
 first symbol, 30–31  
 in MSK, 29–31  
 multi-symbol, 21–22  
 non-Gaussian, 22  
 Nyquist pulse, 43–44, 46–47  
 in parallel MSK receivers, 298, 300, 307–314  
 phase signals, general, 22–25  
 PSK, 23  
 in reduced complexity Viterbi receiver, 282–284  
 in serial MSK receiver, 317–328  
 with synchronizers, 367–371  
 2-signal, 20–21
- Error probability bounds; *see also* Distance  
 for AMF receiver, 336–341  
 for CPFSK/convolutional code combs., 419–420, 442–443  
 for differential receiver, 268–269  
 for maximum likelihood receiver (CPM), 240–242  
 from minimum distance, 27–28  
 in reduced complexity Viterbi receiver, 284  
 transfer function bounds, 114–123  
 finite path memory, 119–121  
 4RC, 120–121; 1REC, 117–119  
 multi-h, 121–122
- Viterbi receiver simulations, relation to, 260–262
- Estimation, of channel parameters, 9
- Euclidean distance: *see* Distance
- Excess bandwidth factor: *see* Nyquist pulses
- Exponential bound parameter: *see* Cutoff rate
- Eye diagram  
 definition, 36–38  
 in differential receiver, 266  
 in parallel MSK (3RC), 297  
 in serial MSK (1REC, 3RC), 317, 321–322
- Fano algorithm, 10, 352
- FFSK: *see* MSK

- Fidelity of reproduction, 3  
Filtering; *see also* Nyquist pulses; Matched filter  
average-matched filters, 330–333  
baseband conversion (*formulas*), 33–34  
BPSK, effect on, 38–41  
Butterworth, 38–40  
channel, 7, 8, 126–142, 173–178  
Chebychev, 38–40  
envelope, variations with, 40, 133, 139  
lattice filters, 9  
mismatched distance, due to filters, 123–125  
on MSK, 38–41  
optimum and suboptimum receiver, for filtered channel, 126–139  
for parallel MSK, 298–312  
pulse length, relation to, 133–136  
on QPSK, 38–41  
RC and REC responses, filters with, 126–142  
for serial MSK, 315–317, 319–320  
in synchronizers: *see* Synchronization transmitters, realized from filters, 227–231  
First mergers, 73–75, 81, 89, 286–287  
SRC, 75–76 (distance bound), 171 (spectrum)  
FM, 5, 6  
Forney, G. D., 11  
4RC  
parallel MSK receiver, 306–313  
phase tree (bin.), 77  
quantization of, 220–222  
reduced complexity approximation, 291–293  
spectrum (bin.), 157–159, 171–172  
transfer function bound, 120–121  
weakness of, 78  
4S, 107–108  
Fractional out of band power: *see* Power out of band  
Frequency pulse  $g(t)$ ; *see also* Phase pulse  
definition of, 25–26, 56–57  
in reduced complexity receiver, 280–282, 287–292  
straight line phase, condition for, 362–363  
synchronizer bandwidth, relation to, 372–376  
FSK, 23–25, 50–53; *see also* IREC  
FSQ modulation, 314–315  
Full response modulation  
definition, 59  
distance bound, 60–71  
minimum distance, 91–96  
multi-h, minimum distance, 105–106  
Galko, P., 298–300; with Pasupathy, S., 301, 313; Galko's algorithm, 300  
Gallager, R. J., 10, 190, 193, 199, 201  
Gardner, F. M., 364  
Garrison spectral calculation, 148  
Geometrical distribution, error events, 477–479  
Gilbert-Elliott model, 196  
GMSK  
definition, 50–53  
parallel MSK receiver, 305–314  
reduced complexity receiver, 295  
Gram-Schmidt orthogonalization, 17, 480–481  
Gray code, 260–261 (oct. CPFSK), 414 (set partition codes)  
Greenstein, L., 148  
Group delay, 127  
  
Half-cycle sinusoidal modulation: *see* HCS  
Hard limiting: *see* Amplitude limitation  
Hardware, advances and costs, 1, 2, 4, 8; *see also* Surface acoustic wave devices  
HCS  
definition, 64–65  
discrete spectral lines, 366–367  
distance bound, 65–66, 70  
synchronizer bandwidth, 372–374  
Helstrom, C. W., 15  
Hirt, W., with Pasupathy, S., 330  
  
Independence, tests for, 477–478  
In phase component: *see* Baseband components, or signals  
Information content, 187  
Integrate and dump, 34–35, 269; *see also* Receiver  
Interarrival times, error events, 477–479  
Interference  
adjacent channel, 5  
co-channel, 5  
intersymbol ISI (ISI), 11–12, 36–38, 41, 196  
Markov ISI model, 196  
ISI: *see* Interference  
  
Karhunen-Loeve expansion, 17, 22  
Kotelnikov, V. A., 9  
Krauss, H. L., with Bostian, C. W., and Raab, F. H., 32  
  
Landau, H. J., with Pollak, H. O., 193  
Lee, W. U., 358  
Lender, A., 12

- Likelihoods: *see* Metrics, or Maximum likelihood
- Limited search receiver, 352–353
- Limited sequential search algorithm, for minimum distance (Aulin), 462–465
- Lin, S., 10
- Lindell, G., 417–454
- Linear receiver, 34–38, 46–47, 298; *see also* Receiver
- Lucky, R. W., 9
- Mapping rule
- in CPFSK/convolutional code combs., 418–419, 423–426, 440, 455–457
  - natural mapping, 414
  - in oct. CPFSK, 260–261
  - in set partition codes, 414
- Marcum Q function, 391–392
- Markov chain; *see also* States, Markov
- for distance, 199, 201–202, 469–472
  - for superstates, 465
- Massey, J. L., 201; with Sain, M. K., 418
- Matched filter
- average-matched filter, 330–333
  - matched filter receiver, 20, 193
  - for Nyquist pulses, 42–47
  - for QPSK, BPSK, 34–35
  - in Viterbi receiver (CPM), 249–251
- Matyas, R., 358, 370
- Maximal ratio combining, 299, 311
- Maximum likelihood
- detection, 15–16, 192–193
  - in partially coherent receiver, 388–390
  - sequence estimation (MLSE), 58, 248–249, 252, 275–276, 388–389
  - synchronizers, 379–381
- Mazor, B. A., with Taylor, D. P., 375–378
- Mean modulation index, 85–88
- Merges (tree or trellis)
- in CPFSK/convolutional code combs., 421, 440–442, 445
  - distance bound, effect on, 62–73, 92
  - under filtering, 130–131
  - first merger, 73–75, 81, 89; second & later, 73–75, 84, 89
  - inevitable, 61
  - minimum distance, effect on, 92–95
  - mismatched receiver, applied to, 286–287
  - in multi-h codes, 79–81, 88–89
  - in 3REC, 97–98
- Metrics, in Viterbi algorithm (CPM), 249–252, 255
- Minimum distance: *see* Distance; *see under modulation name*
- Minimum-shift keying: *see* MSK
- Mismatched receiver distance ( $d_R$ )
- definition, 124–125; in reduced complexity receiver, 283–284
  - merges in, 286–287
  - minimum receiver distance, 289–292
  - in synchronizers, 367
- Miyakawa, H., with Harashima, H., and Tanaka, Y., 12, 59
- MLSE: *see* Maximum likelihood
- Mobile radio, digital, 3, 6, 218; *see also* Channels
- Modulation index,  $h$
- in CPFSK/convolutional code combs., 421, 427–457, 483–492
  - cutoff rate, relation to, 202, 206–207
  - definition, 23–26, 56–57
  - discrete spectral components, relation to, 361–362, 366
  - energy-bandwidth plot, relation to, 182–185, 205–206
  - mean index, 85–88
  - minimum distance, relation to
    - with amplitude limitation, 136–142
    - with filtering, 123–136
    - multi-h, 105–110
    - single h, 92–104
  - in partially and noncoherent receiver, 396–408
- Modulation (data) noise, 364, 371–372, 374
- MSK; *see also* 1REC
- CPFSK/convolutional code combs., compared with, 446–450
  - cutoff rate, 202–204, 206
  - definition, 49–53
  - distance derivation, 30–31
  - energy-bandwidth view, 183–185, 446–450
  - error probability, 29–31, 35
  - invention of, 24
  - parallel MSK, 231–233 (transmitter), 295–315 (receiver)
  - as QPSK, shaped, 49–51, 67
  - serial MSK, 231–234 (transmitter), 315–329 (receiver)
  - spectrum, 38–41, 156–158, 167
  - synchronizers, 358, 369–371, 380–383
- MSK-type receiver: *see* Parallel MSK receiver; Serial MSK receiver
- Multi-h modulation
- alphabet size, effect of, 86–88

- Multi-h modulation (*cont.*)**
- basis, signal space, 480–481
  - CPFSK/convolutional code combs., comparison to, 450
  - definition, 26, 52, 79–89
  - distance bounds
    - full response, 80–88
    - partial response, 87–89
    - 2 indices, 80–83; above 2, 83–88
  - error events, 475–479; geometric distribution, 477–479
  - invention, 12
  - merges in, 79–81, 84
  - minimum distance, 105–106 (full response), 106–110 (partial response)
  - number of h's, effect of, 86–88
  - phase trees, 81, 89
  - simulations, 475–481
  - synchronizers, 374–379
- Multiple-symbol AMF receiver:** *see* AMF receiver
- Murota, K., with Hirade, K., 313
- N<sub>B</sub>, 94**
- Noncoherent receiver**
- coherent receiver, comparison to, 406–409
  - for CPFSK, optimal, 242–246
  - definition, 387
  - differential receiver (CPM), 263–269
  - discriminator receiver (CPM), 269–276
  - implementation, 410–411
  - minimum distance for IREC, 397–402
- Nonlinearity, rf amplifiers, 11, 209**
- Nyquist pulses**
- criterion for pulses, 41
  - definition, 41–42
  - dimensionality, 192, 194
  - excess bandwidth, 46–47
  - filters for, 47
  - QPSK, BPSK, 42
  - raised cosine, 45–47
  - sinc( ), 41–44
  - transmitter/receiver for, 43
- Nyquist sampling theorem, 45**
- Observation interval**
- in AMF receivers, 334–49
  - with amplitude limiting, 136–142
  - in CPFSK/convolutional code combs., 427–429, 431–432, 455–456, 483–492
  - definition, 30–31, 94
  - distance bound tightness, 94–96
- Observation interval (*cont.*)**
- with filtering, 131–138
  - for multi-h modulation, 105–110
  - in non- and partially coherent receivers, 389, 396–409
  - in REC modulations, 92–98; in RC, 98–104
  - in reduced complexity receivers, 289–292
- Offset QPSK:** *see* OQPSK
- Omura, J., with Jackson, D., 383; with Viterbi, A. J., 11, 24, 116, 190–191, 201
- IRC**
- autocorrelation, 155–158
  - distance bound, 65, 75–76 (bin.); 66, 77–78 (quat.); 66, 77–80 (oct.)
  - filtering effects, 131–136
  - spectra, 171–172
- IREC**
- AMF receiver distance, 334–337, 344–347
  - channel model, 198–199
  - coherence of receiver, effect, 406–409
  - convolutional codes, combined with, 417–457
  - cutoff rate, 201–208
  - distance bound, 65–66; multi-h, 81–87
  - energy-bandwidth plot, 182–183, 437–438, 446–450
  - equivalent distance d<sub>e</sub>, 393–397
  - minimum distance
    - multi-h, 105–109
    - in partially coherent receiver, 398–403
    - single h, 92–93 (bin.), 92–94 (quat.), 93–95 (oct.)
  - observation interval, 92–95, 105–109, 398–403
  - phase trees, 60–61
  - QPSK, coded, comparison to, 435–437
  - simulations, 260–261, 271–273, 451–457
  - spectra, 167; asymptotic, 168; with filtering or limiting, 176–177
  - transfer function bound, 117–119
- OQPSK, 49, 67, 358, 370; *see also* QPSK**
- Orthonormality, 16–17; of sinc, Nyquist functions, 42, 46–47**
- Osborne, W. P., with Luntz, M. B., 25, 58, 329–330, 407
- Osborne and Luntz receiver, 237–241, 245, 252
- Pair states:** *see* Superstates
- Papoulis, A., 15
- Parallel MSK receiver**
- distance in, 298–299

- Parallel MSK receiver (*cont.*)  
     error probability results, 307–314; under  
         phase and timing error, 320–328  
     fading channels, 299–300, 304, 308–314  
     filters, in arms, 298–312  
     FSQ receiver, 314–315  
     optimal receiver, 298  
     with predetection filter, 313  
     serial MSK receiver, comparison to, 323–  
         328  
     structure, 296–298  
     WAMF receiver, 310–311
- Partial response modulation  
     bound calculation, 71–79  
     channel model, 189, 196–199  
     definition, 59  
     history, 12  
     minimum distance calculation, 96–104 (single h), 106–110 (multi-h)
- Partially coherent receiver  
     coherence degree,  $\beta$ , 392  
     coherent receiver, comparison to, 406–409  
     definition, 387–388  
     equivalent distance, 391–409  
     ML receiver derivation, 388–390  
     minimum distance, 397–403 (full response),  
         403–408 (partial response)  
     observation interval, 389, 406–409  
     weak indices, 395–396
- Pasupathy, S., 50–51; with Galko, P., 301;  
     with Hirt, W., 330
- Path memory; *see also* Observation interval  
     in CPFSK/convolutional code combs., 435,  
         455–456  
     definition, 116  
     with filtering, 131  
     infinite lengths, 116  
      $N_B$ , relation to, 253, 476  
     short length, effect of, 119–122  
     in Viterbi receiver, 253, 259–262
- Pelchat, M. G., with Davis, R. C., and Luntz,  
     M. B., 25, 58
- Phase ambiguity, 363
- Phase cylinder, 24, 61, 247, 255–256, 469
- Phase errors, synchronization  
     distribution of, 387–388  
     in eye diagram, 37  
     Markov model, 383
- QPSK error probability, with phase error,  
     323, 326
- in serial and parallel MSK, 320–328
- Phase-lock loop  
     bandwidth of, 364  
     loop filter, in synchronizers, 376–377  
     in synchronization, 358  
     transfer function, 225  
     transmitter based on, 224–227
- Phase node sequence, 297–299, 317–318
- Phase pulse; *see also* Frequency pulse  
     definition, 25–26, 56–57  
     discrete spectral components, relation to,  
         366  
     filter losses, effect on, 133–136  
     optimized, for distance, 68–71  
     synchronizer bandwidth, relation to, 372–  
         376  
     truncation of, 100–101  
     weak, 64, 97–98
- Phase state  
     augmented, 129  
     definition, 112, 246–247  
     difference state, 115  
     superstate, 465–467
- Phase tree  
     for amplitude limiting, 141–142  
     on cylinder, 24, 61, 247, 255–256, 469  
     definition, 23–24, 60–61  
     difference tree, 72  
     filtered, 263–264  
     for 4RC, 77  
     incorrect subtree, 30  
     merges, 61  
     MSK, filtered, 263  
     multi-h, 79–81, 89  
     for 1REC, 60  
     for OQPSK, 49  
     partial response, 71  
     in partially coherent receiver, 393–394  
     in reduced complexity receiver, 281, 291  
     for 3RC, 100, 264  
     for 3REC, 71  
     for 2RC, 79  
     trellises, 24
- Phase trellis: *see* Phase tree
- Pierobon, G. L., with Pupolin, S. G., and  
     Tronca, G. P., 163
- Plateau function, 69–70
- Polar representation, differential receivers,  
     263–265
- Pollak, H. O., with Slepian, D. and Landau,  
     H. J., 193
- Power consumption, 8

- Power out of band (POB), 160–161, 166  
Power spectral density: *see* Spectra, or under modulation name  
Prehistory, data, 71–72, 287, 292, 330–331, 340–341, 352  
Proakis, J. G., 9  
PSK; *see also* BPSK or QPSK  
    definition, BPSK & QPSK, 23, 48–49  
    differential reception, 48, 272–275  
    generalized PSK, 68–71  
    history, 9–10  
    spectra, M-ary, 167; asymptotic, 168  
Pulse amplitude modulation (PAM), 42  
Pulse shaping: *see also* Nyquist pulses, Phase pulse, Frequency pulse  
    CPM/convolutional code combs., 444–446  
    cutoff rate, effect on, 203–204  
    energy-bandwidth plot, effect on, 182–186  
    history, 10–12  
    Nyquist, 35, 41–47  
    truncation, 53
- Q function, 21–22
- QPSK  
    channel model, 189  
    coded QPSK, 208  
    cutoff rate, 203, 208  
    definition, 48  
    distance of, 28–29  
    error probability, 28; with phase and timing errors, 327–328  
    Nyquist QPSK, 42–48  
    OQPSK, 49, 67, 358, 370  
    receiver, ML, 34–35  
    spectra, 38–41, 167; asymptotic, 168  
    synchronizers, 357–358, 370
- Quadratic smoothing, 89, 203–204; *see also* 2S
- Quadrature components: *see* Baseband components
- Quadrature modulation, 48–50
- Quantization  
    capacity, effect on, 191  
    in ROM transmitter, 217–233  
    in synchronizer (multi-h), 377–378  
    of Viterbi metrics, 225
- Raised cosine modulation: *see* RC, general or under 1RC, 2RC, etc.
- Random codes: *see* Shannon codes
- Rate; *see also* Cutoff rate  
    of a code, 182  
    of data, 182  
    per dimension, 194
- Rayleigh fading, 299
- RC, general; *see also* under 1RC, 2RC, etc.  
    AMF receiver distance, 350–351  
    amplitude limiting effects, 136–142  
    definition, 50–52  
    discrete lines, spectral, compared to HCS, 366–367  
    distance bounds, 75–76  
    filters, effect on distance, 131–139  
    minimum distance, 98–104  
    REC, approximation by, 280–281; by other pulses, 287–292  
    spectra, 1RC–5RC, 171  
    synchronizer, bandwidth, 372–376
- REC, general; *see also* under 1REC, 2REC, etc.  
    definition, 50–52  
    RC, REC used to approximate, 280–281  
    synchronizer bandwidth, 372–374
- Receiver; *see also* under type of receiver; *see* Simulations  
    AMF receiver, 329–352  
    amplitude limiting, effects of, 136–142  
    baseband circuits for, 31, 34–35  
    correlation receiver, 20, 249  
    for CPFSK, 238–242  
    differential receiver (CPM), 263–269  
    discriminator receiver, 269–276  
    filtering, effects of, 36–41, 126–136  
    integrate and dump, 34–35, 38–40  
    limited trellis search receiver, 352–353  
    linear receiver, 35–38, 43  
    matched filter receiver, 20, 42–43, 46–47, 58, 193  
    maximum likelihood (ML) receiver, 15–16, 19, 42–43, 46–47, 58, 113–114, 239–246; *see also* Viterbi receiver  
    noncoherent receiver, CPFSK, 242–246  
    optimal receiver, 8, 15–16, 40–41  
    parallel MSK type receiver, 295–315  
    for QPSK/BPSK, 34–35  
    reduced complexity Viterbi receiver, 279–295  
    serial MSK type receiver, 315–329  
    signal space receiver, 20, 480–481  
    Viterbi receiver, CPM, 246–255  
    WAMF receiver, 310–311

- Receiver distance: *see* Mismatched receiver distance
- RECtangular (REC) modulation: *see* REC, general or under IREC, 2REC, etc.
- Reduced complexity Viterbi receiver
- complexity reduction, 294–295
  - concept, 279–281
  - distance in, 282–289
  - optimal mismatched receiver, 287–292
  - simulations, 292–294
  - spectral sidelobes, reduction of, 295
  - symbol timing, 285
- Rhodes, S. A., 314
- Rice function, 267–268
- Rician distribution, 244, 391
- ROM: *see* Transmitters
- Ryan, C. R., with Hambley, A. R. and Vogt, D. E., 232
- Rydbeck, N., 12
- S modulations: *see under* 2S, 3S, or 4S
- Salz, J., with Anderson, R. R., 148; with Lucky, R. W. and Weldon, E. J., 9
- Schonhoff, T. A., 25, 238
- Security, data, 3, 6
- Sequence estimation, 7, 9–12, 58, 248–249, 252, 275–276, 388–389; *see also* Equalization or Viterbi algorithm
- Serial MSK receiver, 315–329
- filters, 315–317, 319–320
  - parallel MSK receiver, comparison to, 323–328
  - phase errors in, 320–328
  - structure, 315–317
  - timing errors in, 325–328
- Services, new digital, 2
- Set partition codes, 12, 413–417
- Shannon, C. L., 63, 188, 193
- Shannon codes, 181, 188
- vs. modulations, 197–198
  - as phase codes, 197–199
- Shannon theory, 186–209
- Signal interval, 22–23
- Signal space; *see also* States
- derivation of, 16–20, 189
  - non-gaussian, 22
  - in reduced complexity receiver, 283
  - simulation in, 480–481
  - volume of, 195
- Signal space simulation, 480–481
- Simmons, S. J., with Wittke, P. H., 352
- Simon, M. K., with Wang, C. C., 267
- Simulations; *see also under* modulation name
- AMF receiver, 342, 346, 350
  - of CPFSK/convolutional code combs., 451–457
  - by correlated noise method, 258
  - of differential PSK receiver, 272–275
  - by discrete-time approximation, 257–259
  - of discriminator receiver, 271–275
  - of reduced complexity Viterbi receiver, 292–294
  - by signal space method, 259, 480–481
  - of synchronizers (multi-h), 377–378
  - of Viterbi receiver (CPM), 257–262
- Sinc(t), 192–194
- 6RC (bin.)
- distance bound, 75–76
  - minimum distance, 99–102
  - observation interval, 99–102
  - spectra, 159–162
- 6SRC (spectra), 159–163, 166
- Slepian, D., 193
- Smoothing: *see* Phase pulse, Nyquist pulse
- SPAM filter, 306
- Spectra; *see also under* modulation name; *see also* Bandwidth
- accuracy, 159, 168–171, 173
  - alphabet size, effect of, 172
  - amplitude limitation, effect of, 173–178
  - asymptotic, 168–173
  - calculation methods
    - autocorrelation method, 148–150
    - direct method, 148, 170
    - Garrison's method, 148
    - Markov chain methods, 148–149, 162–163
    - new method, 149–154, 163–166
    - orthogonal pulses, 44–45
    - for time limited phase pulse, 148  - closed forms, 166–167
  - of CPFSK/convolutional code combs., 446–447
  - data distribution effect, 155–165; correlated data, 162–163
  - discrete components, 154–155
  - filters, effect of, 39, 173–178
  - lobes, main & side, 38, 186; side lobe reduction, 295
  - modulation index, effect of, 161, 166, 172, 361–362
  - for MSK, 38–41, 156–158, 167, 173
  - multi-h spectra, 161–162
  - of Nyquist pulses, 43–47, 167

- Spectra (*cont.*)  
phase pulse length, effect of, 171–172  
PSK, M-ary, 167; QPSK/BPSK, 38–41  
power out of band, 160–161  
RC family, 157–160, 162, 164, 171–173, 178  
REC family, 167, 176–177  
SRC family, 159–161, 163, 165–166  
TFM, 157–159
- Spectral raised cosine modulation: *see* SRC
- Split averaged difference state: *see* Difference state
- SRC, general; *see also* 6SRC  
autocorrelation, 155  
definition, 50–52  
parallel MSK receiver, 305–314  
RC, similarity to, 78–79, 101–102  
reduced complexity receiver, 295
- States, Markov  
cardinality, 197  
convergence variable, 470–472  
correlative state vector, 197, 469–470  
decomposable states, 197, 199  
difference chain, 199, 201–202, 469–472  
transition probabilities, 196, 473–474
- States; *see also* States, Markov  
backward state transitions, 259  
in coherent receiver, 238–240  
in CPFSK/convolutional code combs., 421, 441–442, 453–454  
definition, modulator states, 111–114  
even and odd, 114  
under filtering, 128–131  
in noncoherent receiver, 242–244  
superstates (pair states), 465–467  
for 3RC (bin.), 100, 113  
in transmitters, 213–216  
trellis, 112, 129  
in Viterbi receiver, 246–248, 259
- State trellis  
definition, 112  
error events, in, 259–260  
under filtering, 129  
superstate trellis, 465–466
- State vector: *see* States, Markov or States
- Sundberg, C.-E., 12, 56, 59
- Sunde's FSK, 399
- Superbaud timing, 374–375
- Superstates (pair states), 465–467
- Surface acoustic wave (SAW) devices, 227, 233, 352
- Svensson, A., 279–352
- Switching, 3
- Synchronization  
acquisition time, 364  
bandpass filters for, 364–365, 371–372  
bandwidth, synchronizer, 372–376  
bit synchronization, 371  
CNR, of spectral lines, 364–374  
decision directed, 375–376  
MAP, 381–383  
maximum likelihood, 379–381  
nonlinearity, based on, 358–374  
for TDMA, 364
- Tamed FM: *see* TFM
- Taylor, D. P., 12, 59; with Mazor, B. A., 375–378
- TFM  
definition, 50–52  
discriminator reception of, 276  
generalized TFM, 276  
minimum distance, 102  
observation interval, 102  
parallel MSK reception of, 296, 305–314  
reduced complexity receiver for, 295  
spectra, 157  
transmitter, 214  
truncation, of pulse, 101–102
- 3RC  
AMF reception, 338–340  
approximation, by 2REC, 281  
autocorrelation, 360  
cutoff rate, 204–205, 207–208  
discriminator simulations, 272–275  
distance bounds, 75–77 (bin.), 77–78 (quat.), 77–80 (oct.)  
eye pattern, parallel MSK receiver, 297  
filter effects on, 131–139, 178  
minimum distance & observation interval  
with filtering, 131–139  
multi-h, 108–110  
single h, 99–102 (bin.), 102–103 (quat.), 104 (oct.)  
parallel MSK reception, 297, 305–310  
partially coherent reception, 403–405  
phase tree and cylinder, 100, 239, 247, 253, 255  
reduced complexity reception, 289–291  
serial MSK reception, 322–328  
spectra, 160, 164 (quat.), 171 (bin.), 178, 361  
states, 100; trellis, 247–248, 254–256  
synchronization, 360–374

- 3RC (*cont.*)  
     transfer function bound, 120–122  
     Viterbi receiver simulations, 260–262
- 3REC  
     difference tree, 72  
     distance bound, 75  
     minimum distance and observation interval  
         (bin.), 96–98  
     phase tree, 71
- 3S, 107–108
- 3SRC, 101–102, 160, 165
- Tikhonov distribution, 370, 388
- Timing errors, 327–328 (PSK), 45 (Nyquist pulses)
- Tjhung, T. T., with Wittke, P. H., 271
- Transfer function bound: *see* Error probability bounds
- Transition probabilities: *see* States, Markov
- Transmitters  
     BPF/hardlimiter implementation, 227–231  
     direct forms, 31, 43, 211  
     high speed, 220–226, 233  
     Nyquist, 43  
     parallel MSK, 231–233; *vs.* serial, 231–233  
     PLL implementations, 224–227  
     ROM implementations, 212–224  
     serial MSK type, 231–234
- Trellis: *see* State trellis; Phase tree
- 2-4PSK, 49
- 2RC  
     AMF reception, 347–351  
     autocorrelation, 361  
     differential reception, 266  
     distance bounds, 75–77 (bin.), 77–78  
         (quat.), 77–80 (oct.)  
     energy-bandwidth plot, 184–186  
     filter, effects on, 131–137, 139–142  
     minimum distance and observation interval  
         with filtering, 131–137  
         multi-h, 107–110  
         single h, 98–99, 103–104  
     partially coherent reception, 405–408  
     phase tree, 79  
     quantization effects, transmitter, 217–223  
     reduced complexity approximation, 291–294  
     spectra, 171, 362  
     synchronization, 361–374  
     synthesis, by BPF and limiting, 230–231
- 2REC  
     channel model, 198  
     cutoff rate, 204–205, 207–208
- 2S  
     definition, 89  
     multi-h, 89, 107–108  
     2-signal error probability, 21, 199
- Underlying phases, 469–472
- Ungerboeck, G., 11, 22, 413, 467
- Van Trees, H. L., 9, 17, 22
- Viterbi, A. J., 10, 11; with Omura, J., 11, 64, 116, 190–191, 201
- Viterbi algorithm; *see also* Maximum likelihood  
     for CPFSK/convolutional code combs., 417, 453–454  
     for CPM, coherent, 246–255  
     in discriminator receiver, 275  
     history, 11  
     limited trellis search receiver, 352–353  
     in minimum distance calculation, 465–467  
     modulation states, related to, 112–114  
     in noncoherent receiver, 410–411  
     path memory, 113, 116, 119–121; truncation of, 252–255  
     in reduced complexity Viterbi receiver, 279–295  
     simulation of (CPM), 255–262  
     in synchronizers, 375–383
- VLSI, 212, 222–224
- Wald, A., 10
- WAMF receiver, 310–311
- Weak index  
     catastrophic, 91–92  
     in CPFSK/convolutional code combs., 421  
     definition, 70, 90–92  
     distance bound, relation to, 94–96  
     in multi-h modulation, 85, 106  
     in partially coherent reception, 395–397  
     in REC modulations, 92–98
- Weak modulation, of order L, 75, 77, 91, 100
- Weak phase pulses: *see* Phase pulse
- Wide sense stationarity, 147
- Wilson, S. G., with Hsu, C.-D., 383; with Schottler, P. J., and Sleeper, H. A., 415
- Wittke, P. H., with Tjhung, T. T., 271; with Simmons, S. J., 352
- Wozencraft, J. M., 9; with Jacobs, I. M., 9, 17, 22, 63, 183, 193, 195, 201
- Ziemer, R. E., with Tranter, W. H., 15